Partially-drained loading of shallow foundations on sand

by

Jan Krishna Mangal

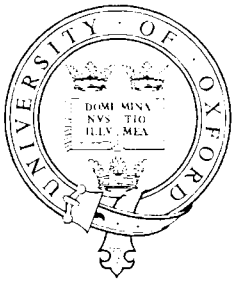

A thesis submitted for the degree of

Doctor of Philosophy

at the University of Oxford

Brasenose College, Hilary Term 1999

Abstract

Partially-drained loading of shallow foundations on sand

A thesis submitted for the degree of Doctor of Philosophy

Jan Krishna Mangal

Brasenose College, Oxford

Hilary Term 1999

Wave loading on offshore structures founded on sand can result in partially-drained response of the foundation soil. The characteristics of the rate of loading, the permeability of the soil, and the size of the foundation affect the degree of partial drainage. Partial drainage refers to situations where pore pressures develop in the soil, and the response of the soil is neither fully drained nor undrained. This thesis is concerned with the effects of loading rate, and consequent drainage, on the behaviour of a flat circular footing that is founded on the surface of a saturated sand base. The results of physical tests performed in the laboratory on a model-size footing are reported. The footing was founded on oil-saturated fine sand and was subjected to combined loading. The effect of the vertical, horizontal, and rotational displacement rate are reported. The response of the footing is analysed in the context of existing drained foundation models that are based on work hardening plasticity theory. The rate dependency of the vertical load:deformation behaviour and the combined load yield surfaces is described.

Acknowledgements

I am indebted to my supervisor, Prof. Guy Houlsby, for his encouragement, invaluable guidance, and above all, for his enduring patience. He also wrote the computer program used to control the experiments.

Mr. Bob Earl constructed most of the apparatus and made many suggestions on the design. The loading rig was developed by Dr. Chris Martin as part of a previous research programme.

Contents

1 Introduction

1.1 Offshore foundations

The development of offshore foundations has been mainly driven by the needs of the petroleum industry. Reservoirs of oil and gas are located in geological structures offshore as well as onshore. Oil has been extracted from offshore locations for about half a century. But the world's two main offshore production areas, in the Gulf of Mexico and in the North Sea, have only been substantially developed over the last thirty years. The development of some offshore fields has posed huge engineering problems because of the water depth and the sometimes severe loading conditions (mainly wave loading).

The offshore extraction process has required the construction of large structures (platforms) that are fixed to the seabed. There are different types of platforms but these can be grouped into three general categories. Steel jacket structures are usually supported by steel piles that are driven deep into the seabed. Concrete gravity base structures are founded on the surface of the seabed. Tension leg platforms are used in very deep water and the tethers are fixed to piled foundations in most cases. Large offshore platforms are only cost effective when the reservoirs are large and when they are expected to be in production for decades.

Many large fields have recently reached (or will soon reach) the end of their production lives. This has led the petroleum industry to develop marginal (smaller) oil and gas reservoirs. The development of marginal fields has required novel engineering solutions. Smaller platforms have been used, and in some cases even totally sub-surface production systems have been used. Piled or large gravity base foundations are usually not cost effective solutions for small platforms. Small shallow foundations, such as suction caisson foundations, have been shown to be viable alternatives. Small shallow foundation systems can also be used for other purposes such as supporting wind turbines.

1.1.1 Suction caissons and partially-drained behaviour

Some aspects of the behaviour of a small shallow foundation on a clay seabed can be

predicted using established design procedures. This is because the response of such a foundation/soil system under severe wave loading is mainly undrained. The behaviour of a small shallow foundation on a sand seabed is neither fully drained or undrained, but is partially-drained. The partially-drained behaviour of sand is not well understood, and consequently, design procedures have not been established.

The foundations of offshore structures are subject to vertical, horizontal, and moment loads. Foundations also have to withstand tensile loads (negative vertical loads) in some cases. To withstand tensile loads, small shallow foundations have to be designed to induce negative pore fluid pressures on their bases. The factors affecting the development of pore pressures in the foundation soil (or the partially-drained behaviour) are the loading rate, the permeability of the soil, and the drainage length. The loading rate is dependent on the wave period, and the permeability is dependent on the size of the sand particles. These two factors cannot be altered but the drainage length of the foundation can be set to ensure that the required degree of partial-drainage is attained.

The drainage length of a shallow foundation can be increased by incorporating skirts around the periphery. Skirts not only increase the drainage length, they also increase the vertical, horizontal, and moment capacity of the foundation as well. Circular foundations with skirts are generally referred to as suction caisson foundations (or skirt-plate or bucket foundations). This type of foundation has been only recently used to support steel jacket platforms on sand. That is, in the Europipe and Sleipner West fields in the North Sea (Aas & Andersen, 1992; Bye *et al.*, 1995; Erbrich, 1996). The recent use of suction caisson foundations required extensive offshore and laboratory modelling because of the lack of knowledge of partially-drained behaviour. The understanding of partially-drained behaviour is poor because soil mechanics research has focused on the two extremes of soil behaviour (drained and undrained behaviour) about which simplifying assumptions can be made.

1.1.2 Modelling of foundation behaviour

In the offshore industry, bearing capacity methods are commonly used to calculate the ultimate drained and undrained capacity of foundations under vertical, inclined, and eccentric

loads (Brinch Hansen, 1970 and Vesic, 1975). Recent research has successfully interpreted the drained and undrained behaviour of shallow foundations in terms of plasticity theory (Tan, 1990; Nova & Montrasio, 1991; Martin, 1994; Gottardi *et al.*, 1997). Foundation models based on plasticity theory are simple and powerful methods for analysing the behaviour of shallow foundations. These models can incorporate vertical as well as horizontal and moment loads, and also link loads and displacements.

1.1.3 Current knowledge of the behaviour of shallow footings

The behaviour of circular footings subject to vertical loads and under the limiting conditions of drained and undrained loading will be outlined. The discussions below serve as an introduction to the current knowledge associated with some aspects of the problem addressed by this thesis.

Mechanisms of failure

Experimental evidence in the literature indicates that mechanisms can be categorised as general shear, local shear, or punching shear. These mechanisms differ in the extent of the failure surface or slip lines. General shear refers to mechanisms with extensive slip lines, where the failure surface extends all the way to the surface of the foundation material. Punching shear is the opposite extreme, where slip lines are only evident beneath the footing. Local shear refers to mechanisms where the development of the failure surface is between that of general shear and punching shear.

The failure mechanisms that are expected with various combinations of material characteristics and loading conditions are listed in Table 1.1 (note that geometrical effects are not mentioned in Table 1.1; these will be discussed below). There is substantial evidence which indicates that under drained loading conditions, a general shear mechanism is probable in materials of low compressibility (dense sand and over-consolidated clay). While a punching shear mechanism is probable in materials of high compressibility (loose sand and normally-consolidated clay). This evidence is summarised by Vesic (1975). These characteristics can be explained by the volumetric strains associated with drained shearing. Dilation results in volumetric expansion and general movement in a material of low compressibility. Conversely, contraction results in volumetric compression and local movement in a material of high compressibility.

Under undrained loading conditions, a general shear mechanism is probable in a material of high compressibility. Vesic (1975) indicates that there is substantial evidence for this with regard to normally-consolidated clay. The failure mechanism of a footing on loose sand under undrained conditions should be similar considering the constant volume condition and that a relatively low undrained shear strength is characteristic of loose sand.

In the case of undrained loading of footings on materials of low compressibility, the tests of Vesic *et al.* (1965) on dense sand indicate that punching shear is probable. Vesic (1975) indicated that this was the case with over-consolidated clay as well. The undrained loading of a shallow footing on a dilatant material can result in very high effective stresses due to negative pore pressures; where the undrained strength might be dependent on the cavitation pressure of the pore fluid.

The size of a footing also affects the failure mechanism. It is well documented that the average shear strength along a slip line decreases with footing size (Vesic, 1975). This manifests itself as an increase in the relative compressibility of the foundation material with increasing footing size. Thus for a particular soil, a small footing might develop a general shear mechanism while a large footing might develop a punching shear mechanism.

Response on elastic soil

It is sometimes acceptable to assume that the foundation soil can be modelled as a linear elastic material. In such cases, standard elastic solutions can be used to estimate the response of footings. Some of these solutions are outlined in Poulos and Davis (1974) for example.

The elastic parameters which are usually used in these solutions are the Young's modulus E' and the Poisson's ratio ν'. Under axi-symmetric conditions with the radial stress held constant, the Young's modulus is deduced from the ratio of the increments of effective axial stress and elastic axial strain. Under similar conditions, the Poisson's ratio is deduced from the ratio of the increments of elastic radial strain and elastic axial strain.

The drained and undrained cases are modelled using appropriate values for Young's modulus and Poisson's ratio. Under drained loading conditions, the values of E' and ν' which are representative of the effective stress state are applicable. Under undrained loading conditions,

values of E_u and $\nu_u = 0.5$ which are representative of undrained or constant volume loading are applicable. The constant volume condition implies that the Poisson's ratio is 0.5 since the undrained bulk modulus is infinite.

The relationships between the parameters of an isotropic elastic material imply that the undrained and drained values of Young's modulus are not independent (most notably, the relationship between the drained and undrained values of shear modulus). Hence the undrained value of Young's modulus can be deduced from the drained parameters as follows,

$$E_u = \frac{3E'}{2(1+\nu')} \qquad [1.1]$$

Since the settlement of a surface footing on an elastic base is a function of Young's modulus and Poisson's ratio (and of the applied load and footing geometry), the ratio between the undrained and drained values of settlement can be expressed as,

$$\frac{w_u}{w_d} = \frac{1}{2(1-\nu')} \qquad [1.2]$$

Taking a typical value of $\nu' = 0.2$ implies that $w_u = 0.625 w_d$. The difference between the drained and undrained settlement is equal to the settlement which occurs during consolidation. Note that this is for a footing on an infinite base. Solutions do exist, however, for footings on finite bases. For the extreme case of one-dimensional loading, the undrained settlement is zero.

Load:displacement response

The load:displacement response of a footing under conditions of drained and undrained loading are discussed below. The response of a footing on an elastic soil and on an inelastic soil will be addressed separately.

It was mentioned previously that the ratio between the undrained and drained settelment of a footing on an infinite elastic base could be deduced using the value of the drained Poisson's ratio. For a given load increment, the ratio between the undrained and drained load:displacement response could be deduced from the ratio of w_u / w_d. Using the example given previously, where $\nu' = 0.2$ and $w_u = 0.625 w_d$, the undrained stiffness of the footing would be 1.6 times higher than the drained stiffness. Thus the stiffness of a footing under undrained loading conditions should be

higher than under drained loading conditions.

Soils are highly non-linear and inelastic. In most practical situations, the elastic solutions cannot be used to predict the load:displacement response of footings. Some insight into the effect that loading conditions have on the load:displacement response of footings on inelastic soil can be gained, however, by considering the relationship between soil stiffness and effective stress. If one assumes that the load:displacement response (or footing stiffness) is proportional to some value of soil stiffness (be it the shear modulus or bulk modulus; shear and volumetric effects being coupled because the soil is inelastic), then the response of a footing will be dependent on the effective stress. In soils that are prone to dilate, undrained loading might result in higher effective stresses and stiffer response than for drained loading. Conversely, undrained loading might result in lower effective stresses and less stiff response than drained loading in soils which are prone to contract.

Pore pressures under conditions of undrained loading

The pore pressure distribution on the base of a footing under conditions of undrained loading is discussed below. The distribution on a footing on an elastic soil and on an inelastic soil will be addressed separately.

On an elastic soil, where shear and volumetric effects are not coupled, undrained conditions imply that any change in total stress results in an equivalent change in pore pressure. The change in the total stress distribution, which can be deduced using the standard solutions of elasticity outlined in Poulos and Davis (1974), is equal to the change in the pore pressure distribution. Thus a saddle shaped total stress and pore pressure distribution, where the total stress and pore pressure is highest around the perimeter of the footing, is expected for a rigid footing.

Undrained loading of a rigid footing on an inelastic soil should result in a saddle shaped total stress distribution similar to that for an elastic soil. The pore pressure distribution is unlikely to be similar to the total stress distribution, however, because of the coupling between shear and volumetric effects.

Bearing capacity and the effect of embedment

Simple bearing capacity equations for drained and undrained loading and the effects of footing embedment will be introduced.

The bearing capacity of a shallow foundation under conditions of drained loading is given by,

$$q_f = \tfrac{1}{2}\gamma' B N_\gamma + \gamma' D N_q \qquad [1.3]$$

where N_γ is the bearing capacity factor for soil self-weight, N_q is the bearing capacity factor for surcharge, γ' is the effective unit weight of the soil, B is the foundation width, and D is the depth of embedment. These two bearing capacity factors are dependent on the friction angle of the soil and increase with the value of the friction angle. It is apparent from Equation 1.3 that for a constant value of friction angle and effective unit weight, the bearing capacity is proportional to the depth of embedment. If Equation 1.3 were used to estimate load:displacement response by calculating the bearing capacity at different depths, for a range of friction angle values, then a series of linear load:displacement curves would be produced. Each of these curves would start from the q_f axis at a value dependent on the friction angle and equal to the term in Equation 1.3 which is representative of the soil self-weight. The gradients of the load:displacement curves would increase with the value of the friction angle. A limiting load:displacement curve equivalent to penetration of a foundation in a material of zero frictional resistance (water for example) could also be postulated.

The bearing capacity under conditions of undrained loading is given by,

$$q_f = s_u N_c + \gamma D \qquad [1.4]$$

where N_c is the bearing capacity factor for cohesion, s_u is the undrained strength of the soil, and γ is the total unit weight of the soil. The bearing capacity factor N_c depends on the shape and depth of the foundation, and increases with embedment to a constant value at a D/B ratio of about four. Equation 1.4 predicts a non-linear load:displacement response at values of embedment of relevance to a shallow foundation. If the undrained strength were zero and the unit weight were constant, Equation 1.4 would predict a linear load:displacement curve.

1.1.4 The need for more research

The traditional bearing capacity methods and the more recent plasticity foundation models can only be used to analyse the drained and undrained behaviour of shallow foundations. The use of small shallow foundations to support offshore structures on sand requires an understanding of

the partially-drained behaviour. Although the partially-drained behaviour of suction caissons has been investigated, previous studies have mainly focused on the design for specific prototypes and were not generic studies of the partially-drained foundation problem. The partially-drained behaviour of a simple flat foundation should also be investigated before that of the more complex geometry of a suction caisson.

1.2 Aims of present work

This investigation was intended to provide a database of experimental evidence of partially-drained foundation behaviour. The vertical, horizontal, and moment partially-drained response of a model footing under 1-g conditions was to be explored. Partially-drained behaviour was to be investigated by varying the displacement rates of the footing.

More specifically, the aim of this project was the investigation of the effects of partial drainage on the monotonic load:deformation behaviour of a flat circular footing. The following aspects of behaviour were to be investigated:

— Virgin-penetration behaviour. The effect of the vertical penetration rate on the virgin-penetration behaviour was to be explored.

— Consolidation behaviour. A simple partially-drained consolidation model was to be developed and compared to the results of vertical loading partially-drained tests.

— Combined load behaviour. The effect of the horizontal and rotational displacement rates on the combined load yield surfaces was to be studied.

Because of the novelty of this research, it was difficult to postulate what the outcome would be. It was expected, however, that the partially-drained behaviour would be rate dependent.

1.3 Outline of thesis

In **Chapter 2**, information of relevance to this investigation is reviewed. Literature on the drained and partially-drained response of footings is presented. At the end of Chapter 2, the scaling of model footing tests is discussed and scaling relationships are presented. **Chapter 3** describes the apparatus used in the footing tests, as well as that used in the miniature cone penetrometer tests and the sample preparation process. In **Chapter 4**, the properties of the sand and of the oil-

saturated sand samples are discussed. The results of element tests, and of the miniature cone penetrometer results, are analysed. **Chapter 5** outlines the test programme and describes the procedures involved in some typical tests. **Chapter 6** analyses the vertical load results and **Chapter 7** the combined load results. **Chapter 8** summarises the findings of this investigation. Suggestions for further research are also made.

2 Literature Survey

2.1 Introduction

The aspects of footing behaviour that are of relevance to the investigation of partially-drained behaviour are reviewed. The drained elastic and plastic behaviour of footings are discussed. Theoretical elastic solutions are compared with unload-reload data in the literature. The traditional bearing capacity methods and the more recent combined load solutions based on plasticity theory are outlined. Evidence of partially-drained behaviour and the factors affecting this type of behaviour are investigated. Theoretical and empirical data on the pore pressure and effective stress distributions on footings is outlined. Solutions for the consolidation behaviour of footings are detailed. The issues associated with the scaling of model behaviour are also addressed.

2.2 Elastic behaviour

The working loads that shallow offshore foundations are subjected to are usually lower than the loads required to induce significant plastic deformation. The working loads are generally below the combined load bearing capacity and therefore within the combined load failure surface. Loads resulting in plastic deformation are usually only encountered during installation of the structure and during periods of severe environmental loading. The load:deformation response is governed by essentially elastic soil behaviour for loads within the combined load failure surface.

2.2.1 Available elastic solutions

Estimates of deformation can be made for unload-reload behaviour assuming the soil to be an isotropic homogeneous elastic material. Short-term static loading results in this form of deformation. It is more or less the instantaneous response of the foundation to loading and primarily results from shear straining of the soil. The elastic solutions of Poulos and Davis (1974) for a rigid flat circular footing provide a useful means for estimating deformation and have been adopted by the American Petroleum Institute in their offshore platform design guidelines (API, 1993). These solutions are as follows,

$$V = \left[\frac{4GR}{1-\nu}\right] w \; ; \qquad H = \left[\frac{32\,GR(1-\nu)}{7-8\nu}\right] u \; ; \qquad M = \left[\frac{8\,GR^3}{3(1-\nu)}\right] \theta \qquad [2.1; 2.2; 2.3]$$

where the loads and displacements are defined in Figure 2.1, and G and ν are the elastic shear modulus and Poisson's ratio. Gazetas *et al.* (1985) proposed an empirically derived equation for the vertical stiffness that is almost identical to Equation 2.1. An empirically derived equation for the horizontal stiffness was also proposed by Gazetas *et al.* (1987), which predicts stiffness values that are not less than 95% of those that are predicted by Equation 2.2 (for a Poisson's ratio of 0.2). Equations 2.1 and 2.3 are applicable to smooth footings and Equation 2.2 is applicable to rough footings. Spence (1968) derived the following solution for the case of a rough footing subjected to vertical loading,

$$V = \left[\frac{4GR\ln(3-4\nu)}{1-2\nu}\right] w \qquad [2.4]$$

Bell (1991) used the finite element method to investigate the effect of the depth of footing penetration and the variation of Poisson's ratio on the elastic stiffness of circular footings. He found that the vertical, horizontal, and rotational stiffness increased with the depth of penetration. Bell also detected coupling between the horizontal and rotational displacements of rough footings. In general, a horizontal load does not only displace the footing horizontally, but also results in rotation. Similarly, a pure moment load results in some horizontal displacement. The degree of coupling was found to increase with footing penetration, to be higher for lower Poisson's ratios, and to be dependent on the position of the load reference point. Bell expressed this mathematically as,

$$\begin{Bmatrix} V \\ H \\ M/R \end{Bmatrix} = GR \begin{bmatrix} K_1 & 0 & 0 \\ 0 & K_2 & K_3 \\ 0 & K_4 & K_5 \end{bmatrix} \begin{Bmatrix} w \\ u \\ R\theta \end{Bmatrix} \qquad [2.5]$$

Ngo-Tran (1996) investigated the effect of the cone angle of conical footings, footing penetration, and Poissons ratio using the finite element method. He derived values for the factors in Equation 2.5 and a selection of these are shown in Table 2.1. Shallow foundations on dense sand generally satisfy the surface condition. Thus the effect of footing penetration can be ignored.

2.2.2 Elastic parameters

There is great uncertainty in the choice of appropriate elastic shear moduli for soils, especially for sands. Soils are not isotropic or elastic materials as assumed in the derivation of Equations 2.1-2.3. Soils exhibit non-linear and stress path dependent behaviour. The elastic moduli of soils are also dependent on the density, the state of effective mean stress, and the magnitude of shear strain. Wroth and Houlsby (1985) found that the elastic shear modulus was generally proportional to the square root of the effective mean stress. Atkinson (1992) noted that the elastic shear modulus reduced with increasing shear strain. Hicher (1996) found that the unload-reload behaviour of granular materials ceased to be linear and reversible at strain amplitudes of 0.001% to 0.01%. The effect of the soil density on the elastic shear modulus is less dramatic. The findings of Iwasaki *et al.* (1978) and Lo Presti (1987) indicate that the elastic shear modulus of a dense soil is approximately twice that of a loose soil. An appropriate elastic shear modulus is best estimated by carrying out "laboratory tests in which the field state and stress path (including cyclic loading) is reproduced as closely as possible", as stated by Poulos (1988).

Barltrop and Adams (1991) suggested relationships for deriving the elastic shear moduli for very small strains. These values of the elastic shear moduli are compared with values derived from other relationships in the literature in Figure 2.2. This comparison is based on a stress level and strain magnitude that is representative of the model foundation problem, where R = 0.075 m and V = 1000 N. The moduli shown in Figure 2.2 are representative of axial strain magnitudes of 0.025% and 0.05%, where the representative strain of a footing is assumed to be equal to $w/2R$. The predicted small-strain elastic shear moduli range from 10 MPa to 20 MPa.

The influence of the effective mean stress on the elastic shear moduli measured in the model footing tests of Gottardi and Houlsby (1995), and calculated from the relationship suggested by Iwasaki *et al.* (1978), are compared in Figure 2.3. Although the moduli from the footing tests are greater than the values calculated using the relationship of Iwasaki *et al.*, they can still be modelled using a power relationship.

Elastic theory can be used to predict that $H/u = 0.86V/w$ and $M/(R^2\theta) = 0.71V/w$. These relationships are derived from Equation 2.5 and the values in Table 2.1 for $\nu = 0.2$ and $w/R = 0$.

The horizontal and rotational stiffness values from the model footing tests of Gottardi and Houlsby (1995) were approximately one fifth of the vertical stiffness values, and therefore less than implied from the theory. The vertical stiffness was about 17 kN/mm, and the horizontal and the moment stiffness were both about 3 kN/mm.

2.3 Bearing capacity of shallow foundations

Bearing capacity analyses can be used to determine a suitable foundation size for a specified load and soil type. Load:deformation behaviour cannot be estimated using bearing capacity theory but the calculated failure load can be used in the development of a load:deformation model. The bearing capacity of shallow foundations on sand subjected to vertical and combined loads will be discussed.

2.3.1 Central vertical loading

There are only a few specific bearing capacity problems for which analytical solutions have been derived. Prandtl (1921) solved the problem of a strip footing on a weightless, perfectly plastic material. The axisymmetric case was solved by Shield (1955) for a Tresca material and by Cox *et al.* (1961) for a weightless Mohr-Coulomb material. Cox (1962) extended the solution of Cox *et al.* (1961) to include Mohr-Coulomb material with self-weight, but results were not generated for a wide range of friction angle (ϕ) values.

Terzaghi (1943) used the results of Prandtl to develop the well known semi-empirical bearing capacity formula for shallow strip footings. He suggested that the effects of self-weight, cohesion, and surcharge could be separated and superimposed. Bearing capacity factors N_c, N_γ, and N_q, which were dependent on the effective friction angle and the undrained strength, were used to represent the effects of cohesion, self-weight, and surcharge respectively. Shape factors were introduced so circular and square footings could be analysed using the plane-strain bearing capacity formula. Terzaghi's formula is still widely used although various workers have suggested different bearing capacity factors (Meyerhof, 1963; Brinch Hansen, 1970).

Terzaghi's formulation was extended by Brinch Hansen (1970) and Vesic (1975) to account for load inclination, vertical load eccentricity, footing shape, depth of embedment, and the

inclination of the base. Most workers have adopted the empirically derived shape factors of de Beer (1970). The bearing capacity formula and the factors suggested by some researchers are given in Appendix A. Vesic also includes a reduction factor to account for soil compressibility. Vesic's formula is recommended by the API (1993) guidelines for estimating the foundation capacity of offshore structures.

Recent research by the Cambridge Soil Mechanics Group (Lau, 1988; Shi, 1988; Tan, 1990) has extended the Cox solution for axisymmetric footings on Mohr-Coulomb material with weight by calculating bearing capacity factors for a range of friction angles. Bolton and Lau (1993) summarise this work and compare their analytical results with empirical results.

Values of N_γ derived from the bearing capacity formula and values suggested by Bolton and Lau (1993) are compared with some experimental results in Figure 2.4. The experimental results taken from the literature are of tests using rough circular footings. The factors derived from the Brinch Hansen (1970) formula are compared in Figure 2.4[a] and the rough axisymmetric factors proposed by Bolton and Lau (1993) are compared in Figure 2.4[b]. The factors derived from the theoretical methods are approximately double most of the experimental factors. The experimental factors of Montrasio and Nova (1997) and of Byrne and Houlsby (1999), however, are larger than the theoretical predictions. One would expect all of the theoretical predictions to be conservative, as is generally accepted. But in this comparison it is obvious that the experimental failure loads are generally less than the theoretical values. The various methods employed in the derivation of the friction angles are listed in Figure 2.4. The difference between the results of Montrasio and Nova (1997), of Byrne and Houlsby (1999), and of the other investigators cannot be explained by the effect of footing size on the bearing capacity factor. It should be noted that the friction angles for most of the tests are limited by the restriction on the dilatancy index implied in Bolton's (1986) method. If this restriction were ignored, the friction angles of Byrne's tests would be about two degrees greater than shown in Figure 2.4—or almost equal to the relevant theoretical values.

A number of assumptions are made in the solution of the bearing capacity problem. The foundation material is assumed to be rigid perfectly plastic. Only very dense sand develops the *general shear* mechanism (shown Figure 2.5) that is expected of a rigid perfectly plastic material.

Full mobilisation of the shear strength in the plastic zone is assumed. Sand is not a homogeneous material. The friction angle is dependent on the density and the stress level (de Beer, 1965a; Bolton, 1986; Hettler & Gudehus, 1988; Simonini, 1993).

The bearing capacity formulae are very sensitive to variations in the friction angle. This problem is exacerbated as there are a number of factors that contribute to the uncertainty in the friction angle. There is also confusion on whether to use plane strain or triaxial friction angles. Meyerhof (1963) recommended plane strain angles for strip footings and triaxial angles for circular footings. Brinch Hansen (1970), however, suggested that the plane strain angle be used as the theoretical bearing capacity factors were developed for the plane strain case. The plane-strain angle is approximately 10% larger than the triaxial angle. Ingra and Baecher (1983) and Basma (1994) performed statistical analyses to investigate the effect of uncertainty in the friction angle on the bearing capacity. The variation in the bearing capacity coefficient N_γ was found to be as much as 100% for a standard deviation of 2° in the friction angle.

The scale effects of foundation size are not taken into account in the general bearing capacity formulae. de Beer (1965b) investigated the scale effect, and Vesic (1975) found that an increase in the foundation size caused an increase in the relative compressibility of soils and a substantial decrease in N_γ. These effects are greatest for small surface footings (B < 100 mm) and care is needed when extrapolating the results from small model tests to large footings. The scaling of the foundation problem is discussed in Section 2.8.

Some workers have investigated the problem of smooth footings but the smooth case is usually only applicable to model tests, where machined footings are used. At the prototype level, footings can generally be classed as rough or semi-rough. Experiments have also shown that foundation roughness sometimes has practically no effect on bearing capacity (Vesic, 1975). The effect, however, does increase with increasing cone angle for conical footings (Tan, 1990).

Meyerhof (1961) found the bearing capacity of shallow cones to be very similar to that of flat footings. Investigations by Tan (1990) led to similar conclusions but differences were detected for the case of sharp cones on dense sand. Noble Denton and Associates (1987) suggested methods for analysing cones in the joint industry report based on work performed by the Cambridge Soil

Mechanics Group.

The finite element method has been used to predict bearing capacity loads, and in some cases the results have been in agreement with traditional bearing capacity predictions (Griffiths, 1982; Simonini, 1993).

2.3.2 Combined loading: Introduction

The horizontal and moment components of load in the offshore environment are substantially greater than the components on onshore structures. Offshore combined loads are caused by environmental forces, such as current, wave, and wind forces, acting on the platform structure. Footings have to withstand simultaneous vertical, horizontal, and moment loads.

The bearing capacity formulae of Meyerhof (1963), Brinch Hansen (1970), and Vesic (1975) can be used to calculate the degrading effect of horizontal and moment load on the vertical capacity. And thereby derive failure surfaces for the load combinations. Meyerhof (1953) suggested that the load in situations involving V, H, and M could be modelled as an equivalent inclined and eccentric point load acting on an effective foundation area. The inclined load tests conducted by Meyerhof were on strip footings. He suggested that the results could be applied to circular footings using a shape factor. Most researchers have retained the concept of an equivalent inclined and eccentric point load. Brinch Hansen (1970) and Vesic (1975), however, suggested the modified effective foundation area shown in Figure 2.6 to account for load eccentricity. The bearing capacity formulae and the factors of Meyerhof, Brinch Hansen, and Vesic are summarised in Appendix A. The API (1993) recommendations on the calculation of the effective dimensions are also included in Appendix A.

Roscoe and Schofield (1956) may have been the first researchers to use plasticity theory to analyse foundations subjected to combined loading. Butterfield and Ticof (1979) and Butterfield (1981) used a similar approach to develop interaction diagrams for describing the combined load problem of footings on granular materials and of foundations of offshore gravity platforms. A number of researchers have recently developed footing models based on plasticity theory, and calibrated with experimental data. Tan (1990) developed a model based on the results of centrifuge tests of circular footings embedded in loose sand. Nova and Montrasio (1991) analysed the results

of 1-g tests of strip footings on the surface of loose sand. A plasticity approach was outlined by Gottardi *et al.* (1997) for circular footings on dense sand. And Martin (1994) developed a plasticity model for circular footings embedded in clay.

2.3.3 Combined loading: *V*:*H* failure surfaces

Combinations of vertical and horizontal load can be modelled as a single load, with an inclination angle α to the vertical, acting at the centre of the footing as shown in Figure 2.6. Meyerhof (1953) noted that the bearing capacity reduced to zero and that sliding failure occurred when the inclination angle approached the soil-footing friction angle. The inclination factors in the bearing capacity formulae were derived from a combination of experimental evidence and theoretical analyses of the strip footing problem.

The following relationship, which describes a *V*:*H* failure surface for a circular footing on sand, can be deduced from Meyerhof's formulae (listed in Table A.1),

$$\frac{V}{V_m} = \left[1 - \frac{\tan^{-1}(H/V)}{\phi}\right]^2 \qquad [2.6]$$

where V is the vertical load, V_m is the bearing capacity under a central load, H is the horizontal load, and ϕ is the friction angle of the sand. Corresponding relationships can be derived from Brinch Hansen's bearing capacity formula,

$$\frac{V}{V_m} = \frac{1}{3}\left[5 - 2\left(1 - 0.7\frac{H}{V}\right)^5\right]\left(1 - 0.7\frac{H}{V}\right)^5 \qquad [2.7]$$

and from Vesic's formula,

$$\frac{V}{V_m} = \left[1 - \frac{H}{V}\right]^{5.2} \qquad [2.8]$$

The normalised failure surfaces obtained using Equations 2.6-2.8 are compared in Figure 2.7. The Brinch Hansen method predicts a larger normalised capacity against bearing failure than the other two methods. The Meyerhof formula predicts a lower capacity than the methods of Brinch Hansen and Vesic.

Andersen (1972) reviewed experimental data and performed simple stability analyses before

concluding that the inclination factor was not a function of the friction angle. Ingra and Baecher (1983) suggested relationships for the inclination factor based on statistical analysis of available data. They noted that the inclination factor was dependent on the footing shape and was less for strip footings than for square footings. The failure surfaces derived above must be applied with caution, as the bearing capacity formulae were not developed with combined loading in mind.

There is a great deal of experimental evidence (Georgiadis & Butterfield, 1988; Ricceri & Simonini, 1989; Nova & Montrasio, 1991; Gottardi & Butterfield, 1993) from plane-strain load controlled tests on sand that supports the approximately parabolic form of the *V*:*H* failure surface predicted by Equations 2.6-2.8 . Butterfield and Gottardi (1994) found that a simple parabola,

$$\frac{h}{h_0} = 4v(1-v) \qquad [2.9]$$

where $h = H/V_m$, $v = V/V_m$ and $h_0 = 0.13$ fit the experimental data from three different series of plane-strain tests of rough footings on dense sand. The peak horizontal load occurred at $V/V_m = 0.5$. Butterfield (1981) noted that the peak normalised horizontal load h_0 of a smooth footing on dense sand was dependent on the embedment, and increased to 0.15 at $w/R = 1$. Equation 2.9 can also be used to fit parabolas in V_0-normalised space, where h and v are defined as H/V_0 and V/V_0 respectively.

Tan (1990) investigated the *V*:*H* failure surface of flat circular and conical footings using a geotechnical centrifuge apparatus. Tan's tests were performed on medium dense and loose sand at w/R ratios of 0.2 to 1.8. The V_m parameter is not applicable to situations where a general shear failure mechanism does not occur, such as situations involving loose sand and to post bearing capacity behaviour. Thus Tan normalised his results by the maximum vertical load previously experienced by the footing. This parameter will be referred to as V_{ol} in this thesis. Tan found that a *V*:*H* failure surface, for a particular ratio of w/R, could be traced in one test by subjecting a footing to a horizontal displacement whilst maintaining a constant vertical displacement. Tan termed this type of displacement controlled test a *sideswipe*. The typical path of a sideswipe test and of a constant-*V* test in *w*:*V*:*H* space are shown in Figure 2.8[a]. The details of the vertical load:deformation behaviour is also illustrated in Figure 2.8[b]. Plastic vertical displacement occurs

even in a constant vertical displacement sideswipe as shown in Figure 2.8[b]. Tan used the predictions from an elastic-plastic model to illustrate how the plastic vertical displacement during a sideswipe, and consequent expansion of the failure surface, was negligible when the ratio of elastic to plastic stiffness was high.

Tan (1990) found that the peak of the *V*:*H* failure surface occurred at a normalised vertical load of approximately 0.4. The peak normalised horizontal load was found to be a function of embedment; h_o was equal to 0.15 for surface footings and to 0.24 for footings at an embedment of w/R = 1. Tan's peak normalised horizontal load for an embedded footing was higher than that recorded by Butterfiled (1981). It should be noted that Tan (1990) did not measure the moment load on his footings. Thus his *V*:*H* surfaces surfaces may in fact be *V*:*H*:*M* surfaces.

Martin (1994) performed a comprehensive series of displacement controlled tests in which the combined load failure surface of a spudcan footing on clay was defined. His sideswipe tests indicated that h_o was equal to 0.127 at a V/V_{oi} value of 0.464. As with Tan (1990), Martin used V_{oi} values to normalise his results since his sideswipe tests were performed on a soft material. Martin used the following modified parabola to fit his data,

$$\frac{h}{h_o} = \left[\frac{(\beta_1+\beta_2)^{\beta_1+\beta_2}}{(\beta_1)^{\beta_1}(\beta_2)^{\beta_2}}\right](v)^{\beta_1}(1-v)^{\beta_2} \qquad [2.10]$$

where β_1 = 0.764 and β_2 = 0.882. β_1 and β_2 are constants to adjust the curvature of the failure surface at low and high vertical load. Martin (1994) utilised the Cam-clay soil model to suggest that the expansion of a failure surface during a sideswipe test on normally consolidated clay was negligible when the ratio of elastic to plastic stiffness was about 50.

Gottardi and Houlsby (1995) investigated the pre-V_m combined load behaviour of a rough circular footing on the surface of dense sand. Their tests were also reported in Cassidy (1996) and Gottardi *et al.* (1997). The results of the sideswipe tests are shown normalised by V_o in Figure 2.9[a]. Equation 2.9 with h_o = 0.12 is also shown. The experimental values of V_o were not equal to the V_{oi} values because of the increase in the vertical penetration that occurred during the tests. This was caused by the flexibility of the experimental rig. The symbol V_{oi} is used to denote the maximum vertical load that the footing was previously subjected to and V_o is used to denote the

extrapolated virgin-penetration load that is representative of the current state. These terms are illustrated in Figure 2.8[b]. Plastic straining during a sideswipe test results in expansion or contraction of the surface, depending on the slope of the virgin penetration curve. The sideswipe tests do not track along a single surface but traverse adjacent surfaces as illustrated in Figure 2.8[a], and described in Gottardi *et al.* (1997). The constant vertical penetration sideswipe ($\delta w = 0$) is labelled "E" and the penetrating sideswipe ($\delta w > 0$) is labelled "D".

Two sideswipe tests on overconsolidated ("OC") samples, which were unloaded from V_{oi} before commencing the sideswipes, and a constant-V test are also shown in Figure 2.9[a]. Constant-V tests are not usually plotted using V_o values, but are usually plotted using the constant V_{oi} value. Plotting against V_o produces a path similar to a sideswipe as the test tracks up and across adjacent surfaces in w:V:H space. This is illustrated by the path labelled "B" in Figure 2.8. The peak of the constant-V path in Figure 2.9[a] represents a point on the V_m:H failure surface. This point is represented by the intersection of path "B" and "C" in Figure 2.8[a].

The peak normalised horizontal load in Figure 2.9[a] seems to be dependent on the value of V_{oi}. The peak value is larger for smaller values of V_{oi}. The observed relation between h_o and V_{oi}/V_m is illustrated in Figure 2.10. The results of sideswipe tests conducted by Byrne and Houlsby (1999) on Baskarp Cyclone sand with a relative density of 95% are also included in Figure 2.10. The following equation is a fit to the data in Figure 2.10,

$$h_o = -0.045 \ln\left(\frac{V_{oi}}{V_m}\right) + 0.11 \qquad [2.11]$$

Normalisation by V_{oi} may not be applicable to sideswipe tests initiated at vertical loads less than V_m. The data of Gottardi and Houlsby (1995) is shown normalised by V_m in Figure 2.9[b]. The V_m values used in the normalisation were estimated from vertical bearing capacity tests on similar samples. One would expect all the load paths from tests initiated at vertical loads less than V_m to be inside the V_m failure surface. This is the case as all the load paths converge on the parabola described by Equation 2.9 with h_o = 0.12. Even the tests from low V/V_m values and the overconsolidated tests converge. The shape of the sideswipe surfaces in Figure 2.9[b] is dependent on the ratio of V_{oi}/V_m at which the sideswipes were initiated. Cassidy (1996) used the failure

surface defined by Equation 2.10 with $h_0 = 0.116$, $\beta_1 = 0.9$ and $\beta_2 = 0.99$ to fit the data of Gottardi and Houlsby (1995).

The variation in size may have been due to changes in the mechanism occurring beneath the footing. The development of slip lines under a general failure mechanism beneath a vertically loaded footing should be proportional to the value of V_{oi}/V_m. Thus a sideswipe from a high V_{oi}/V_m value will result in a different failure mechanism than a sideswipe from a low V_{oi}/V_m value. After bearing capacity failure and full slip line development, the mechanism should remain relatively unchanged and V_{oi} should work as a normalising parameter.

Sideswipe tests were initially employed by Tan (1990) and Martin (1994) to define the post-bearing failure surface of footings on soft work-hardening materials. Their results are of particular relevance to the design of jackup structures that undergo significant vertical penetration. Knowledge of the failure surface allows the factor of safety to be set by pre-loading the foundation. The design of foundations on stiff materials, in which a general shear mechanism is probable, cannot employ significant pre-loading because of the risk of work-softening at the vertical failure load. These foundations are usually designed without pre-loading, and it is usually assumed that the behaviour within the V_m failure surface is mainly elastic. The pre-V_m sideswipe tests of Gottardi and Houlsby (1995) indicate that significant yielding occurs within the V_m failure surface. The term *yield surface* is used in this thesis to describe the path of sideswipe tests performed within the V_m *failure surface*. The yield surfaces tracked by sideswipe tests can be used to differentiate between areas of predominantly elastic and plastic behaviour. They can also be used to gauge the effect of pre-loading within the failure surface.

Nova and Montrasio (1991), Montrasio and Nova (1997), and Tan (1990) found that sand density did not affect the shape of the failure surface. Tan also made a similar conclusion about the effects of footing roughness but Nova and Montrasio (1997) noted that the normalised horizontal capacity of smooth footings was 73% that of rough footings. Nova and Montrasio also investigated the effects of footing shape and embedment. They concluded that the shape of the V:H failure surface was not affected by the shape of the footing but increased in size with embedment.

2.3.4 Combined loading: *V*:*M* failure surfaces

The bearing capacity of footings subjected to vertical and moment loads has traditionally been calculated using the statically equivalent eccentric load and effective area concept that is shown in Figure 2.6. The calculation of effective area, length, and breadth is outlined in Appendix A. The following *V*:*M* interaction equation can be derived using the aforementioned procedure in combination with Meyerhof's (1963) method,

$$\frac{V}{V_m} = \frac{A'B'}{AB}\left[\frac{1+0.1\tan^2(45+\phi/2)(B'/L')}{1+0.1\tan^2(45+\phi/2)}\right] \qquad [2.12]$$

where the prime indicates an effective dimension. Moment load is incorporated into Equation 2.12 via the effective dimensions that are functions of the load eccentricity. A similar equation can be deduced using the methods of Brinch Hansen (1970) and Vesic (1975),

$$\frac{V}{V_m} = \frac{A'B'}{3AB}\left(5-2\frac{B'}{L'}\right) \qquad [2.13]$$

Normalised failure surfaces obtained using Equations 2.12-2.13 are compared in Figure 2.11. The curves are all approximately parabolic and thus similar to the *V*:*H* failure surfaces shown Figure 2.7. The most notable difference being the lower magnitude of the peak normalised moment load as compared to that in *V*:*H* space. The Brinch Hansen and Vesic method predict a larger normalised capacity against bearing failure than that predicted by the Meyerhof method. At low vertical load, the normalised failure surfaces converge. Ingra and Baecher (1983) suggest a relationship for an eccentricity factor based on statistical analysis of available data. Their method predicts a peak normalised moment load of 0.084 at V/V_m = 0.446. This is greater than that predicted by the methods shown in Figure 2.11. It is widely accepted that the equivalent area method is conservative.

Most of the researchers mentioned in the previous review of *V*:*H* surfaces also addressed the *V*:*M* problem. The main difference between *V*:*M* and *V*:*H* surfaces being the smaller size of the *V*:*M* surfaces, when normalised by V_m and using the *M*/2*R* convention. Equation 2.9 can be altered to represent the *V*:*M* surface,

$$\frac{m}{m_o} = 4v(1-v) \qquad [2.14]$$

where $m = M/2RV_m$ and m_o is the peak normalised moment load. Butterfield and Ticof (1979) found that a peak normalised moment load of 0.1, occurring at $V/V_m = 0.5$, was representative of model footing tests on sand. Recent research conducted by Butterfield and Gottardi (1994) and Montrasio and Nova (1997) on strip footings suggests a lower peak value of 0.0875. Montrasio and Nova also found that the size of the normalised failure surface increased with footing embedment and suggested that $m_o = 0.125$ at $w/R = 1$. Sand density and footing roughness were found not to affect the *V*:*M* failure surface.

The *V*:*M* sideswipe tests of Gottardi and Houlsby (1995) are shown normalised by V_o in Figure 2.12[a]. Equation 2.14 with $m_o = 0.09$ is also shown in Figure 2.12[a]. The changes in the vertical displacement that occurred during the sideswipe tests are accounted for in the values of V_o. A sideswipe test on an overconsolidated sample and a constant-*V* probe are also shown in Figure 2.12[a]. The peak normalised moment load in Figure 2.12[a] seems to be dependent on the value of V_{oi}. This is consistent with *V*:*H* behaviour. The following expression is used to fit the m_o:V_{oi}/V_m data shown in Figure 2.10,

$$m_o = -0.039 \ln\left(\frac{V_{oi}}{V_m}\right) + 0.07 \qquad [2.15]$$

The moment sideswipe results of Byrne and Houlsby (1999) are included in the derivation of Equation 2.15.

The data of Gottardi and Houlsby (1995) is normalised by V_m in Figure 2.12[b]. All the load paths from tests initiated at vertical loads less than V_m are inside the parabola described by Equation 2.14 with $m_o = 0.09$. Cassidy (1996) used the failure surface defined by Equation 2.10 (with h and h_o replaced by m and m_o respectively) with $m_o = 0.086$, $\beta_1 = 0.9$ and $\beta_2 = 0.99$ to fit the data of Gottardi and Houlsby.

2.3.5 Combined loading: *V*:*H*:*M* failure surfaces

The *V*:*H*:*M* problem can be modelled using the traditional bearing capacity methods and an equivalent inclined load centred on a reduced footing area as shown in Figure 2.6 and described in

Appendix A. Meyerhof 's (1963) method may be used to derive the following *V*:*H*:*M* failure surface,

$$\frac{V}{V_m} = \frac{A'B'}{AB}\left[\frac{1+0.1\tan^2(45+\phi/2)(B'/L')}{1+0.1\tan^2(45+\phi/2)}\right]\left[1-\frac{1}{\phi}\tan^{-1}\left(\frac{H}{V}\right)\right]^2 \qquad [2.16]$$

Similarly, the theory of Brinch Hansen (1970) gives,

$$\frac{V}{V_m} = \frac{A'B'}{3AB}\left[5-2\left(1-0.7\frac{H}{V}\right)^5\frac{B'}{L'}\right]\left(1-0.7\frac{H}{V}\right)^5 \qquad [2.17]$$

and the theory of Vesic (1975) gives,

$$\frac{V}{V_m} = \frac{A'B'}{3AB}\left(5-2\frac{B'}{L'}\right)\left(1-\frac{H}{V}\right)^{m+1} \qquad [2.18]$$

where m is defined in Table A.1. It should be noted that Equations 2.16-2.18 are only valid in the 1st and 3rd quadrants of *H*:*M* space. The *H*:*M* surfaces in the 1st quandrant are shown in Figure 2.13. The degrading effect that a horizontal load has on the moment capacity at V/V_m = 0.5, and vice versa, is evident.

Butterfield and Ticof (1979) used the results of numerous combined load tests of strip footings on sand to derive parabolic shaped *V*:*H* and *V*:*M* surfaces. They also postulated a cigar shaped *V*:*H*:*M* surface as shown in Figure 2.14. The cigar shaped *V*:*H*:*M* failure surface has been verified in (+*H*):(+*M*) space by Georgiadis and Butterfield (1988) and Nova and Montrasio (1991) for strip footings on sand, and by Dean *et al.* (1992a) for conical footings on sand. Butterfield and Gottardi (1994) and Gottardi *et. al* (1997) have since verified the applicability of a cigar shaped failure surface to both positive and negative combinations of horizontal and moment load, for strip and circular footings respectively. Both of these investigations indicated an elliptical *H*:*M* surface rotated by about 14°. Gottardi *et al.* used the following expression to fit their *V*:*H*:*M* data,

$$\left(\frac{h}{h_o}\right)^2 + \left(\frac{m}{m_o}\right)^2 - 2a\frac{hm}{h_o m_o} - \left[4v(1-v)\right]^2 = 0 \qquad [2.19]$$

where a defines the rotation of the failure surface in *H*:*M* space. The latter two surfaces mentioned above are compared in Figure 2.15. Butterfield and Gottardi assumed that anti-clockwise moments were positive and Gottardi *et al.* assumed the opposite. The effect of the sign convention on the

rotation of the *H*:*M* ellipse is illustrated in Figure 2.16. The surface of Butterfield and Gottardi shown in Figure 2.15 is plotted assuming clockwise moment positive. These failure surfaces are very similar considering that one represents a strip footing and the other a circular footing. The rotation of the ellipse in *H*:*M* space is dependent on the sign convention used to describe the combined loads and also on the location of the point to which these loads are referenced. The above is also true for displacements, and the effect of the load/displacement reference point is illustrated in Figure 2.17. At some reference point R, the ellipse is symmetrical. At points above R the ellipse is rotated anti-clockwise, and at points below R the rotation is clockwise. Butterfield *et al.* (1996) discussed the different standardised sign conventions for footings subjected to combined loads.

2.4 Modelling of foundation behaviour

2.4.1 Introduction

The load:deformation behaviour and stability of an offshore structure is dependent on the interaction between the structure and the soil on which it is founded. Understanding the foundation:soil interaction problem and developing a means (or a model) for predicting load:deformation response is essential. A complete foundation:soil interaction model should incorporate all aspects of a foundation's behaviour. This is not usually possible because of the complexity of the loads and resulting foundation response. The important aspects of foundation behaviour and some foundation models in the literature will be discussed.

Soils do not behave in a purely elastic or plastic way, or in a linear way. For a foundation:soil interaction model (as for a soil model of triaxial tests) to be accurate, it would have to capture non-linear elastic, plastic work-hardening, and plastic work-softening load:deformation response. The boundary conditions of soil beneath a foundation and in a triaxial test are broadly similar. The elements of a soil model derived from triaxial tests should also be applicable to foundation behaviour. The basic elements of foundation behaviour which have to be modelled are described in the framework of an elastic-plastic soil model (Wood, 1990) as follows:

— Vertical load:deformation response links the absolute magnitude of vertical plastic

deformation to the changing size of the failure surface. A *hardening rule* can be used to model this link.

— There is a boundary in *V*:*H*:*M* load space within which behaviour can be described as elastic or non-linear elastic. A description of this *failure surface* is required.

— The vertical, horizontal, and rotational unload and reload foundation response within the failure surface can usually be modelled assuming *elastic behaviour*.

— The relative magnitudes of the various components of plastic deformation (δw, δu, and $\delta\theta$) can be describe by a *plastic potential*. The absolute magnitudes can be deduced from the plastic vertical displacement δw; this value is given by the hardening rule.

The elastic behaviour of foundations and the shape of failure surfaces were discussed in Sections 2.2 and 2.3.

2.4.2 Vertical and combined loading

The vertical load:deformation behaviour of footings on sand is non-linear even at small displacements. Butterfield (1981) suggested that a modified exponential relationship deduced from plate bearing tests be used to model this behaviour. The three variables in his relationship were the initial slope of the load:deformation curve k, the bearing capacity load V_m, and the slope of the curve after bearing capacity failure. Butterfield did not differentiate between plastic and elastic displacement, as the influence of elastic displacement was negligible. Butterfield adopted the technique commonly used in plasticity theory of plotting loads and their associated displacement vectors on the same diagram, so as to model the displacements associated with combined loading. It is likely that Roscoe and Schofield (1956) were the first to use this procedure to analyse the foundation problem. The results of strip footing tests on dense sand (reported by Butterfield, 1981) showed that displacement vectors along a radial load path in *V*:*H* space were generally parallel and that the magnitude of the vectors increased as the load path approached the parabolic failure surface. An elliptic, and hence non-associated, plastic potential was found to fit the displacements associated with radial load increments close to the failure surface. The displacement vectors were also found to be approximately the same irrespective of the load path taken to reach the failure

surface. Butterfield made an analogy to the plastic potentials used in plasticity theory.

Tan (1990) used the bearing capacity theory of Terzaghi to predict vertical load:deformation and develop a hardening rule for circular footing tests on loose sand. He assumed that the depth of overburden was equivalent to the penetration of the footing. This was coupled with the elastic solutions of Poulos and Davis (1974). Tan's model predicts that the footing does not penetrate the soil before reaching the bearing capacity load V_m. He was only trying to model post-V_m work-hardening behaviour of footings on loose sand and his approach worked well. A non-associated flow rule was required to model vertical and horizontal displacement. He derived a plastic potential, based on the Cam-clay constitutive soil model, that predictes a change from work-softening to work-hardening behaviour at $V/V_o = 0.135$ as shown in Figure 2.18[a]. The point of transition was called a *parallel point*. His experiments indicated that there was indeed a load state at which horizontal displacement could take place with no change in vertical displacement or vertical and horizontal load. Plastic displacement on the left side of the parallel point resulted in heave whilst on the right side settlement resulted. The term critical state is used to refer to such states in this thesis. Tan (1990) combined a failure surface, plastic potential, theoretical definitions of elastic behaviour, and a hardening rule to produce a work-hardening plasticity model. His model gave good retrospective predictions of both load and displacement controlled tests.

Nova and Montrasio (1991) used a similar hardening rule to that suggested by Butterfield (1981) in their rigid plastic work-hardening model for strip footings on loose sand. Only three tests were required to calibrate the model: one under central vertical loading, one with $M = 0$ and one with $H = 0$. Experimental results, such as an increase in vertical displacement with decreasing vertical load, indicated that a non-associated flow rule was required. Also, it was noted that an associated flow rule would over predict the foundation heave linked to sliding at low V/V_m. Nova and Montrasio adjusted their failure surface to create a non-associated plastic potential by incorporating constants to alter the horizontal and moment load. The failure surface and plastic potential incorporated a history parameter that was not only a function of vertical displacement but of horizontal and rotational displacement as well. This indicates that a hardening rule may be a function of the three components of displacement and not just of vertical displacement. The model

accurately predicted combined load tests that included load reversals.

More recently, Nova and Montrasio (1997) investigated the effects of foundation shape on the behaviour of rectangular footings on dense sand and noted that the hardening rule was more representative of square footing behaviour. This was for a constant value of the non-dimensional ratio $V_m/2Rk$. It was suggested that $V_m/2Rk$ was a function of sand density only. Normalised experimental load:deformation curves were also found to be very similar.

Martin (1994) developed an incremental work-hardening plasticity model from the results of spudcan footing tests on clay. Theoretical stiffness factors were used to define elastic behaviour. A theoretical vertical load:deformation relationship was derived using the Method of Characteristics to solve the bearing capacity problem. An elliptical paraboloid shape was used to represent the failure surface. Martin noted that an associated flow rule would over predict vertical footing displacements occurring during failure in the *V*:*H* and *V*:*M* planes. He used a non-associated flow rule in which only the vertical plastic displacement was adjusted so as to be different than that predicted by normality. His experimental evidence supported the applicability of associated flow in the *H*:*M* plane.

Gottardi and Butterfield (1995) noted that the displacement increments of a strip footing on sand in the *H*:*M* plane were non-associated. Their *w*:*u* and *w*:θ displacement increments were also non-associated but differ in form from Tan's non-associated flow rule. For example, the displacement increments from a constant-*V* test remained parallel although the relative position along the failure surfaces changed. On the other hand, the displacement increments from a radial load path test did not remain parallel although the relative position along the failure surfaces did not change. The difference in behaviour mentioned above may be due to the fact that Tan's tests were post-V_m and the tests of Gottardi and Butterfield were pre-V_m.

Cassidy (1996) and Gottardi *et al.* (1997) used the following empirical expression relating vertical load to the plastic component of displacement to fit data from circular footing tests on dense sand,

$$V_o = \frac{k_p w_p}{1 + \left(\frac{k_p w_{pm}}{V_m} - 2 \right) \left(\frac{w_p}{w_{pm}} \right) + \left(\frac{w_p}{w_{pm}} \right)^2} \qquad [2.20]$$

where k_p is the initial plastic stiffness and w_{pm} is the plastic displacement at the bearing capacity load V_m. The total displacement w is equal to the sum of the plastic and elastic components of displacement (w_p and w_e respectively). Equation 2.20 incorporates one more parameter, w_{pm}, than the modified exponential relationship of Butterfield (1981). This makes it more representative of footing response because it can be used to model work-softening behaviour that is common beyond V_m.

Some of the experimental data shown in Figure 2.19[a] suggests that the vertical bearing capacity V_m is inversely proportional to w_{pm}. Also, the k_p:V_m data shown in Figure 2.19[b] supports the evidence of Montrasio and Nova (1997) that V_m is proportional to k_p. The linear relationship between the normalised initial penetration stiffness and the relative density that was suggested by Montrasio and Nova is shown in Figure 2.20. Although the data of de Beer (1970) supports the evidence of Montrasio and Nova, the other data were inconclusive because of the small ranges of the relative density values. The considerable variation between the different tests shown in Figure 2.20 does not seem to be dependent on the footing size.

Cassidy (1996) developed an incremental work-hardening plasticity model similar to Martin's (1994) model. Equation 2.20 was used as the hardening rule and a more sophisticated form of Equation 2.19 was used to represent the failure surface. The normalised *V*:*H* failure surface and plastic potentials are shown in Figure 2.18[b]. A transition from work-softening to work-hardening behaviour occurs at V/V_m = 0.265. Cassidy used this model to perform retrospective predictions of the footing tests conducted by Gottardi and Houlsby (1995) on dense sand.

The *V*:*H* experimental evidence of Gottardi and Houlsby does not support the existence of a critical state point at V/V_m = 0.265. If a *V*:*H* critical state point did exist, then its value would be less than V/V_m = 0.05. This is indicated by the failure surfaces shown in Figure 2.9[b] and by the u:H/V_m response of the sideswipe tests shown in Figure 2.21[a]. The horizontal load in the

sideswipe with V_{oi} = 1800 N is still reducing linearly at the end of the test. The load:deformation paths of the other sideswipes shown in Figure 2.21[a] are of a similar shape to that of the test with V_{oi} = 1800 N and probably would have reduced in a similar fashion as well.

On the other hand, the *V*:*M* sideswipe tests shown in Figure 2.12[b] converge at $V/V_m \cong 0.25$. This convergence was is evident in load:deformation space as shown in Figure 2.21[b]. The moment load of the sideswipe tests tend to a $M/2RV_m$ value of 0.06 at large rotational displacements. These results suggest that there is a critical state point in *V*:*M* space.

Intuitively, one would not expect a critical state point in *V*:*H* space, since there can be no horizontal resistance when sliding from zero vertical load at a constant vertical displacement. In *V*:*M* space, however, rotation from zero vertical load at a constant vertical displacement would result in moment resistance. The above findings indicate that different plastic potentials may be required for *V*:*H* and *V*:*M* behaviour.

2.5 Partially-drained behaviour

2.5.1 Introduction

The loads that an offshore foundation are subjected to can be categorised as static, transient, or cyclic. The terms static and transient refer to situations where the load changes by a single increment. A static load is applied in an instant and a transient load is applied over a finite time. During the application of a static load one assumes that the change in effective stress is equal to the change in total stress (drained condition) or is equal to the difference between the total stress and the pore pressure (undrained condition). The load is said to be transient (partially-drained condition) if the effective stress changes during the period that the load is applied as illustrated in Figure 2.22. Cyclic loading is similar to transient loading but there is a continuous change of load by alternating positive and negative increments. Foundation response is different for each type of load and becomes increasingly complex as the load type changes from static, to transient, through to cyclic.

The sand beneath a shallow foundation of an offshore platform is likely to behave in a partially-drained manner mainly because of the extreme wave loading experienced during storm

conditions. Wave loading, which typically has cyclic periods in the range of 10-20 seconds, results in simultaneous cyclic vertical, horizontal, and moment foundation loads. The extent to which the foundation soil behaves in a partially-drained manner is dependent on the size of the foundation, the loading rate, and the drainage and deformation characteristics of the soil. Under partially-drained conditions, the effective stresses of the foundation soil may decrease or increase.

The partially-drained behaviour of submerged shallow foundations has been investigated by a number of researchers. Vesic *et al.* (1965) investigated the effect of loading rate on the drained and partially-drained bearing capacity of model sized footings on dense sand. Research into the transient loading of foundations has been mainly focused on the behaviour of suction caissons. In sand, suction caissons rely on the partially-drained capacity to generate uplift resistance. Goodman *et al.* (1961) investigated the feasibility of vacuum anchorage in a range of soils. Wang *et al.* (1977) studied the effect of an applied suction on the breakout capacity of caissons and Byrne and Finn (1978) investigated the effect of pullout rate on suction caissons in clay. In terms of the more conventional types of offshore foundations, McNeilan (1985) noted partially-drained effects during the installation of spudcans in silt, and Finnie (1993) investigated the effect of loading rate on the behaviour of spudcans on carbonate sands. Dean (1991) suggested approximate methods for estimating the pore pressures on spudcans. Recently, there has been considerable interest in the use of suction caissons for fixed offshore platforms founded on dense sand (Aas & Andersen, 1992; Bye *et al.*, 1995; Erbrich, 1996).

2.5.2 Evidence of partially-drained behaviour with sand

Vesic *et al.* (1965) performed dynamic loading tests on submerged sand and an apparent cohesion was noticed for rapid loading. The fastest displacement rates shown in Figure 2.23[a] result in bearing capacities twice that recorded at the drained displacement rate. The API (1993) guidelines state that an undrained bearing capacity analysis is required in cases where the rate of loading is such that no drainage occurs. And in such cases, the friction angle should be assumed to be zero and an appropriate undrained strength parameter be used. Janbu (1985) notes that undrained tests on sand indicate an apparent cohesion a and a frictional resistance. Janbu recommends using undrained a-ϕ soil data to calculate effective stress bearing capacities using

limit equilibrium analyses. A dilatancy parameter derived from triaxial tests was also used to account for the effects of shear deformation on the excess pore pressures along the failure surface.

The potential for the dilatancy of sand to affect the excess pore pressures will not be fully realised where loading rates are such that the conditions are not undrained. Drainage will result in bulk deformation, and dilatancy will have a reduced effect on the excess pore pressures. The results of partially-drained element tests on sand could not be found in the literature. Intuitively, one would expect the partially-drained bearing capacity to be bounded by the drained and undrained bearing capacity. And for it to be inversely proportional to the degree of drainage (proportional to the rate of loading). This proportionality is evident in Figure 2.23[a]. The undrained bearing capacity can be less than the drained capacity in collapsible soils, such as in loose and medium dense sand. The effect of density on the partially-drained bearing capacity is illustrated in Figure 2.23[a]. A test in which the relative density is nine percentage points less than the average, has a bearing capacity a factor of about 2.5 less than the tests on the denser sand.

Kolk and Campbell (1997) discussed the findings of Finnie (1993) relating to the partially-drained bearing capacity of spudcan foundations on carbonate sands and silts. Finnie defined the displacement rate in terms of a non-dimensional relative penetration velocity,

$$v_n = \frac{v\ D}{c_v} \qquad [2.21]$$

where v was the spudcan penetration velocity, D the diameter, and c_v the coefficient of consolidation. The bearing stress under undrained conditions, which was normalised with respect to the initial vertical effective stress at unit depth, was about half that under drained conditions. The response was found to be fully drained when $v_n < 0.01$ and fully undrained when $v_n > 10$.

The partially-drained model footing tests of Vesic *et al.* (1965) shown in Figure 2.23[b] illustrate the effect of the penetration rate on the ultimate settlement. As the degree of drainage reduces, the load:deformation behaviour becomes more ductile and the ultimate settlement dramatically increases. The maximum settlement was taken to be representative of the ultimate settlement in the fast partially-drained tests as the peak value was not reached. The initial slope of the load:deformation curves of the fastest partially-drained tests was also slightly less than the

slope of the drained tests.

The pull-out capacity (tension capacity) of suction caissons is dependent on the rate of displacement. The effect of the pull-out rate on the stress:strain behaviour of laboratory and offshore tests of suction caissons is shown in Figure 2.24. The values on the vertical scales are not shown for reasons of confidentiality. The pull-out velocity and total stress are shown in non-dimensional form. Only the Oxford and NGI tests are at equivalent stress and time scales. From Figure 2.24[a] it is evident that there was a general trend of increasing total stress with increasing velocity. The values from each test were measured at a constant value of strain. The dotted line is drawn between the Sleipner T and B tests because these were performed at different sites with slightly different drainage characteristics. Actual stress:strain curves from some of the Oxford and NTH/SINTEF tests are shown in Figure 2.24[b] and [c] respectively. The Oxford and NTH/SINTEFF tests were not at equivalent scales; the size of the NTH/SINTEFF caisson was a factor of about 1.5 greater than the effective size of the Oxford caisson. This difference in size may have explained the larger stiffness and load response observed in the Oxford tests. But the general trend of increasing stiffness with velocity was clearly evident in both sets of tests. Note that the fastest of the Oxford tests shown in Figure 2.24[b] might have resulted in cavitation of the pore fluid, as the pore pressure at the base of the footing was very low.

2.5.3 Factors affecting effective stress

Terzaghi's (1943) Principle of Effective Stress states that the effective stress is related to total stress as follows,

$$\sigma' = \sigma - u \qquad [2.22]$$

where σ' is the effective stress, σ is the total stress, and u is the pore fluid pressure. The application of this principle to the loading of a foundation is illustrated in Figure 2.22. The loading of sand results in particle rearrangement and a change in the volume of inter-particle voids. The change in volume may induce excess pore fluid pressures if the rate of volume change is greater than the rate of fluid flow between the voids. The induced excess pore pressures cause changes in effective stress and result in partially-drained behaviour.

The characteristics of the volume change arising from a load increment are dependent on the relationship between the shear and volumetric behaviour of the sand. It is dependent on the *dilatancy* when sand tries to increase in volume during shearing, and on the *contractancy* when sand tries to reduce in volume during shearing. Sand will tend to dilate, thereby inducing negative excess pore pressures under rapid shearing, when the ratio of shear stress to normal stress is high. And sand will tend to contact, thereby inducing positive excess pore pressures under rapid shearing, when the ratio is low. The density of the sand also affects this tendency. Dense sand is likely to dilate and loose sand is likely to contract when sheared. The rate of pore fluid flow is controlled by the permeability of the sand, by the size of the foundation, and by the rate of loading. The lower the permeability, the longer the drainage length, and the faster the loading rate, the lower is the rate of pore fluid flow. And, therefore, the greater is the tendency for excess pore pressures to develop.

Yamamuro and Lade (1998) noted that silty sands could exhibit *reverse* dilatant behaviour. Their specimens of silty sand became more dilatant with increasing confining stress under undrained conditions.

In dense sands, the coupling of dilatancy with a low rate of pore fluid flow can induce enormous effective stresses. The effective stress has an upper bound that is dependent on the cavitation pressure of the pore fluid, which in turn is dependent on the ambient water pressure at foundation level. Cavitation of the pore fluid in triaxial tests was investigated by McManus and Davis (1996), and Os and Van Leussen (1987) detailed the effects of cavitation on the response of a submerged plough.

2.5.4 Calculation of effective stress

As outlined previously, the effective stress state of a soil is dependent on the interaction between the soil skeleton and the pore fluid. The fundamental principles of mechanics, which are the conditions of equilibrium and compatibility, can be applied to analyse this situation. Equilibrium ensures that the forces (and stresses) acting on a body do not result in accelerations, and compatibility ensures that the displacements (and strains) in a body do not result in discontinuities. The relationship between stress and strain is governed by the characteristics of the

material. The governing equations (in two dimensions) for equilibrium, compatibility and material behaviour for a saturated soil mass are outlined below.

Equilibrium

Consider a body in which the stress components vary with x and z, and on which there is a body force acting in the z direction. Equilibrium is satisfied if,

$$\frac{\partial \sigma'_x}{\partial x} + \frac{\partial \tau_{zx}}{\partial z} - i_x \gamma_w = 0 \qquad [2.23a]$$

$$\frac{\partial \sigma'_z}{\partial z} + \frac{\partial \tau_{xz}}{\partial x} - \gamma' - i_z \gamma_w = 0 \qquad [2.23b]$$

where τ is shear stress and i is hydraulic gradient. Note that $i_x = -(\partial h/\partial x)$ where h is total head which is assumed increasing in directions x and z (x direction positive rightwards and z direction positive downwards).

Compatibility

If the components of displacement in the x and z directions are denoted by u and w respectively, then the normal strains are given by,

$$\varepsilon_x = -\frac{\partial u}{\partial x} \qquad \varepsilon_z = -\frac{\partial w}{\partial z}$$

and the shear strains by,

$$\gamma_{zx} = -\frac{\partial u}{\partial z} + \frac{\partial w}{\partial x}$$

The above strains must be compatible with each other if the body is to remain continuous. This leads to the following relationship,

$$\frac{\partial^2 \varepsilon_x}{\partial z^2} + \frac{\partial^2 \varepsilon_z}{\partial x^2} - \frac{\partial^2 \gamma_{xz}}{\partial x \partial z} = 0 \qquad [2.24]$$

Compatibility also requires continuity of fluid flow through the body. The following relationship applies for a body in which there is a net outflow of an incompressible fluid having velocities v_x and v_z,

$$\left(\frac{\partial v_x}{\partial x} + \frac{\partial v_z}{\partial z} \right) dx\, dy\, dz = -\frac{dV}{dt} \qquad [2.25]$$

where dV/dt is the change in volume per unit time.

Material characteristics

A constitutive relation for the soil skeleton is required. This can be defined incrementally in terms of effective stress as follows,

$$d\sigma' = f(d\varepsilon) \qquad [2.26]$$

A relationship for fluid flow is also required. The following relationships for an isotropic soil mass are applicable if Darcy's law is assumed to be valid.

$$v_x = k\, i_x = -k\frac{\partial h}{\partial x} \qquad v_z = k\, i_z = -k\frac{\partial h}{\partial z} \qquad [2.27a; 2.27b]$$

where k is permeability and $h = z + u/\gamma_w$, with u representing the pore pressure in this case.

The equation for continuity of fluid flow can now be written as,

$$\frac{k}{\gamma_w}\left(\frac{\partial^2 u}{\partial x^2} + \frac{\partial^2 u}{\partial z^2}\right) = \frac{1}{1+e}\frac{\partial e}{\partial t} \qquad [2.28]$$

Equation 2.28 links the pore pressure to the volumetric changes (or strain). But the pore pressure is also linked to the strain by Equation 2.26. This closed loop (strain→pore pressure→effective stress→strain) or coupled problem has only been solved for a few limited cases. Biot (1941) solved the equations for a saturated linear-elastic porous solid. Many practitioners have used numerical techniques to model this type of behaviour (Small *et al.*, 1976; Hicks & Smith, 1988). But numerical solutions require external inputs and for the loop to be broken.

2.6 Stress distribution on footings

The pore pressure distribution on the base of a footing was required for the calculation of the pore pressure load U, which was used to derive the effective load V'. Terzaghi's theory of effective stress states that the effective load is equal to the total load minus the pore pressure load. To derive U, the function describing the pore pressure distribution has to be integrated over the area of the footing. The shape of the pore pressure distribution on a footing is dependent on the rate of loading and the drainage characteristics of the soil.

Under undrained conditions, the displacements and stresses in a consolidating material are

the same as those in an elastic material with $\nu = 0.5$ (Davis & Poulos, 1963; Chiarella & Booker, 1975). At $t \cong 0$, the pore pressure distribution beneath a rigid circular footing on an isotropic elastic semi-infinite mass would be equal to the contact stress distribution defined by Bossinesq (1885), and later described by Poulos and Davis (1974). The undrained pore pressure distribution is shown in Figure 2.25[a] and the elastic contact stress distribution is defined as follows,

$$q = \frac{V}{2\pi R\left(R^2 - r^2\right)^{1/2}} \qquad [2.29]$$

where V is the applied load, R is the radius, and r is the distance from the centre. Distributions calculated using the above equation should also be valid for footings on a finite layer when the thickness of the layer is greater than twice the radius of the footing (when $h/R \geq 2$).

Contact stress distributions similar to the Bossinesq solution have been measured on footings founded on clay. Faber (1933) measured a Bossinesq shaped contact stress distribution on a rigid circular footing that was resting on stiff London clay. Conclusive experimental data on the undrained and the partially-drained pore pressure distribution beneath footings on sand could not be found in the literature, but one would expect the undrained distribution to be similar to that described by Equation 2.29.

The shape as well as the magnitude of the pore pressure distribution beneath a consolidating footing is a function time. The distribution gradually changes from the initial undrained shape to a uniform distribution, and finally to a parabolic distribution as drainage progresses. Yue *et al.* (1994) found that the pore pressure distribution was approximately parabolic in shape after a non-dimensional time factor T_v value of about 0.1. They conducted numerical analyses of a poro-elastic semi-infinte mass subjected to a uniform stress. The parabolic distribution is shown in Figure 2.25[b].

In the model tests of this programme, where the pore pressure was only measured at the centre of the footing, the following expression was used to estimate the pore pressure load,

$$U = C_p \pi R^2 u_c \qquad [2.30]$$

where u_c is the pore pressure measured at the centre of the footing and C_p is a parameter that described the pore pressure distribution. C_p is defined as a function of time, and is equal to two for

an undrained distribution and to 0.5 for a parabolic shaped pore pressure distribution. The following relationship between C_p and the non-dimensional time factor T_v is proposed,

$$\begin{aligned} C_p &= 2 && T_v \cong 0 \\ C_p &= 1.51e^{-50T_v} + 0.49 && 0 < T_v < 0.1 \\ C_p &= 0.5 && T_v \geq 0.1 \end{aligned} \qquad [2.31]$$

The constants in Equation 2.31 for $0 < T_v < 0.1$ were chosen assuming that the exponential decay shown in Figure 2.26 was valid between $C_p = 2$ and $C_p = 0.5$. Equations 2.30 and 2.31 indicate that the rate of decay of U is greater than that of u_c. Therefore a more realistic assessment of the effective load V' could be made by assuming that the pore pressure distribution on a consolidating footing is a function of time. Assuming a uniform distribution of pore pressure for all stages of the consolidation process, as is commonly done, underestimates the rate of increase of the effective load.

In the discussions above, it was assumed that a load increment was applied in zero time. Fully undrained loading of sand is only likely in situations involving large footings and very rapid rates of loading. If the load increment is partially-drained, the initial C_p value would be less than two. An elastic base was also assumed, but penetration of a footing on sand may result in local volumetric expansion as well as contraction. Davis and Poulos (1972) found that non-elastic effects on the rate of consolidation were negligible for practical engineering purposes. Thus it was assumed that similar effects on the pore pressure distribution would be negligible.

In terms of drained behaviour, there exists a wealth of information on the problem of a footing interacting with a sand base. Selvadurai (1979) and Kerr (1989) reported the findings of numerous investigations that indicated a tendency for a Bossinesq shaped distribution beneath footings where there had been little plastic deformation and stress re-distribution. They also stated that as the sand beneath the edge of a footing deformed, the contact stress distribution tended to be parabolic in shape. Therefore the contact stress distribution beneath a footing that is undergoing plastic penetration should be similar to that described by the following equation,

$$q = \frac{2V}{\pi R^2}\left[1 - \left(\frac{r}{R}\right)^2\right] \qquad [2.32]$$

A similar parameter to C_p, which was introduced to describe the shape of the pore pressure distribution on a footing, could be used to describe the total stress distribution on the footing. And hence account for the degree of elasticity. This parameter was labelled C_q and defined as follows,

$$q = \frac{V}{C_q \pi R^2} \qquad [2.33]$$

where q is the total stress at the centre of the footing, V is the applied load, and R is the radius of the footing. One would expect C_q to take similar values as C_p for similarly shaped stress distributions. Therefore $C_q = 2$ for an elastic stress distribution (shown in Figure 2.25[a]) and $C_q = 0.5$ for a plastic stress distribution (shown in Figure 2.25[b]). For an elastic material, C_q would be constant throughout the consolidation process but C_p would decrease with dissipation of the pore pressure.

2.7 Consolidation behaviour

2.7.1 Introduction

The one-dimensional consolidation equation is defined as,

$$c_v \frac{\partial^2 u}{\partial z^2} = \frac{\partial u}{\partial t} \qquad [2.34]$$

and can be derived by combining the appropriate forms of the continuity and stress:strain equation (see Equations 2.26 and 2.28 in Section 2.5.4). Terzaghi (1943) developed his well known theory for one-dimensional consolidation by solving Equation 2.34 and expressing the solution in terms of the variation of excess pore pressure with depth and time. The one-dimensional coefficient of consolidation c_v in Equation 2.34 is expressed as follows,

$$c_v = \frac{k}{\gamma_w m_v} = \frac{2kG}{\gamma_w} \frac{(1-\nu)}{(1-2\nu)} \qquad [2.35]$$

where k is the permeability and m_v, the coefficient of compressibility, is equal to the inverse of the constrained modulus M'. Equation 2.34 is a form of diffusion equation that is applicable to many physical problems, and has been solved for a variety of initial and boundary conditions. Solutions, be they Taylor's (1948) analytical solution or the method of parabolic isochrones, are usually expressed in non-dimensional terms. In non-dimensional terms Equation 2.34 becomes (Scott,

1980),

$$\frac{\partial^2 U_v}{\partial Z^2} = \frac{\partial U_v}{\partial T_v} \qquad [2.36]$$

where U_v is equal $(u_i - u)/(u_i - u_f)$ and is called the degree of consolidation (or degree of pore pressure dissipation; subscripts i and f refer to the initial and final states). The non-dimensional depth Z is equal to the vertical dimension divided by the length of the maximum drainage path (z/d), and the time factor T_v is defined as,

$$T_v = \frac{c_v t}{d^2} \qquad [2.37]$$

In practical problems it is the average degree of consolidation $\overline{U}_p$ over the depth of the layer that is of interest and the consolidation process is usually expressed in terms of $\overline{U}_p$ and T_v. The degree of consolidation settlement U_v is also equal to $\overline{U}_p$ in the one-dimensional case. This is because the total stress, as well as the variation between the volume and the effective stress, is assumed constant.

Terzaghi's (1943) theory of one-dimensional consolidation is applicable to oedometer tests and to foundation problems where the depth of the layer is small compared with the width of the foundation. For circular footings on deep layers, where the thickness of the layer is greater than the radius of the footing, three-dimensional effects result in a considerable increase in the rate of consolidation as pore pressures can dissipate horizontally as well as vertically.

Davis and Poulos (1972) discussed the rate of settlement under three-dimensional conditions. They mentioned that theoretical solutions of the Biot (1941) equations for the three-dimensional problem have been only formulated for a few foundation scenarios. Such as for uniformly loaded footings on semi-infinite and finite masses with relatively simple boundary conditions. Nevertheless, Davis and Poulos suggest that solutions for more complex foundation scenarios obtained from simple diffusion theory should be sufficiently accurate for practical use.

2.7.2 Three-dimensional consolidation settlements

The settlement of a footing on a saturated porous elastic medium results from distortion of

the medium as a consequence of shear stresses imposed by the applied load, and from volume changes due to the dissipation of excess pore pressures (consolidation). The settlement of a footing on a consolidating soil is usually calculated assuming that the soil behaves as an elastic medium. The total or drained settlement w_d is given by,

$$w_d = w_u + w_c \qquad [2.38]$$

where w_u is the immediate or undrained settlement and w_c is the final consolidation settlement. The undrained as well as the drained settlement of a rigid circular footing on a finite layer can be calculated using the following equation suggested by Poulos and Davis (1974),

$$w = \frac{V}{2\pi G R(1+\nu)} I_\rho \qquad [2.39]$$

where I_ρ is an influence factor that is dependent on the Poisson's ratio and the ratio h/R. For $h/R \cong 3$, the ratio relevant to this enquiry, the influence factor is approximately equal to 1.16 for drained loading ($\nu = 0.2$) and equal to 0.80 for undrained loading ($\nu = 0.5$). These values indicate that the undrained settlement is less than the drained settlement by a factor of about 0.55 (note that $G' = G_u$ for an elastic material in which shear and volumetric effects are not coupled). The final consolidation settlement is taken as the difference between the drained and the undrained settlements. The settlement during the consolidation process at any time t after the application of the load increment is given by,

$$w_t = w_u + U_s w_c \qquad [2.40]$$

where U_s is the degree of consolidation settlement for the appropriate geometrical conditions.

In the one-dimensional or oedometer case there is no undrained settlement and the influence factor I_ρ is approximately equal to 1.25 for $\nu = 0$ and $h/R \cong 3$. Davis and Poulos (1968) stated that a Poisson's ratio of zero should be used to derive the influence factor but that $\nu = \nu'$ should be used in the following one-dimensional settlement equation,

$$w_{oedo} = \frac{V}{\pi M' R} I_\rho \qquad [2.41]$$

where M' is the constrained modulus which is given by,

$$M' = \frac{2(1-\nu)G}{1-2\nu} \qquad [2.42]$$

Equation 2.41 can be rewritten as,

$$w_{oedo} = \frac{V}{2\pi G R}\frac{(1-2\nu)}{(1-\nu)} I_p \qquad [2.43]$$

Comparing the total settlements under three and one-dimensional conditions (Equations 2.39 and 2.43) indicates that they are approximately equal for ν = 0.2 and $h/R \cong 3$. But using the one-dimensional theory to predict the settlement in three-dimensional situations underestimates the total settlement when the Poisson's ratio is greater than 0.25 (Davis and Poulos, 1968).

The methods outlined in the preceding paragraphs for the calculation of footing settlements where based on the assumption that the foundation soil could be modelled as ideal elastic medium. The stiffness of soil is dependent on the effective stress level. Thus stiffness parameters should be experimental values measured at an appropriate stress level.

2.7.3 Three-dimensional rate of consolidation settlement

The degree of consolidation settlement is usually expressed as a function of the time factor T_v that is dependent on the coefficient of consolidation. The definition of the coefficient of consolidation is dependent on the geometry of the problem, and appropriate coefficients should be used in the solutions of the one-dimensional and three-dimensional consolidation equations. The one-dimensional coefficient of consolidation was outlined in Equation 2.35 and the three-dimensional form is given by,

$$c_3 = \frac{2}{3}\frac{k\,G}{\gamma_w}\frac{(1+\nu)}{(1-2\nu)} \qquad [2.44]$$

Comparing the coefficients for a Poisson's ratio of 0.2 indicates that $c_3 = ½\, c_1$ (note that $c_1 = c_v$). Davis and Poulos (1972) stated that the theoretical one-dimensional and three-dimensional $T_v : \overline{U}_p$ curves would be the same if the appropriate coefficients of consolidation were used (for example when comparing an oedmeter and a triaxial test).

In the three-dimensional problem solved using simple diffusion theory, the degree of settlement is not equal to the average degree of pore pressure dissipation ($U_v \neq \overline{U}_p$). Davis and

Poulos (1972) suggested that $U_v \cong \overline{U}_p$ if the time scale is appropriately adjusted by defining T_v in terms of c_1 for both the one and three dimensional cases. The $T_v : \overline{U}_p$ curves obtained by Davis and Poulos using simple diffusion theory are shown in Figure 2.27. Also shown is an estimate of the curve for $h/R \cong 3$. Although the curves in Figure 2.27 were calculated assuming a Poisson's ratio of 0.5 and a flexible footing, Davis and Poulos stated that their solutions are applicable for all values of ν' and could be applied to rigid footings with reasonable accuracy.

2.8 Scaling

The scaling of the foundation problem will be reviewed although the scaling relationships were not applied to the results of this investigation. The scaling relationships are outlined so as to guide readers who may wish to scale the results according to their own specifications.

2.8.1 Introduction

Scaling is an import element in the design of foundations because of the lack of rigorous theoretical design techniques and the high cost of prototype tests (full-scale tests). Designs rely heavily on observed behaviour, and even the established theories, such as bearing capacity theory, require reference to physical tests. Model (physical) tests are usually used to derive design parameters that have to be scaled to the prototype situation. The scaling of model tests conducted at 1-g is not straightforward, as the behaviour of soil is dependent on the effective stress level. One must consider the effective stress level at homologous points in the soil of the model and prototype. The effective stress level in the model can be increased to the prototype value by conducting the model test in a centrifuge or by imposing a downward gradient on the pore fluid. These methods are more costly and time consuming than tests conducted at 1-g. The cost benefit of using the results of 1-g tests for foundation design has led researchers to propose various ways of overcoming the problems of scaling 1-g model tests. An outline of the scaling of 1-g model tests will be given. The details of scaling the stress:strain response, the elastic stiffness, and the drainage characteristics of sand will also be discussed in the following sections.

2.8.2 Model footings on sand

A satisfactory design will need to predict the stress:strain behaviour of the sand beneath a prototype foundation before the load:deformation response of the foundation can be deduced. The rate of change of stress and strain may also need to be incorporated into the design when dealing with saturated sand. The results from a model test will only be useful if the relation between stress and strain is similar in the prototype and the model. Rate effects must also be similar where these affect the stress:strain response. Dimensional analysis is used to define the set of similarity requirements that have to be satisfied (Isaacson and Isaacson, 1975; Douglas *et al.*, 1985). The similarity can involve length, mass and time or any combination of these. Complete similarity is achieved when all dimensionless groups attain the same values in the model and the prototype. This is usually not feasible, and any departure from complete similarity has to be justified.

An example of the problems encountered when scaling 1-g tests is highlighted by the effect of footing size on the dimensionless bearing capacity factor for self-weight N_γ. It is well known that N_γ decreases with increasing footing size for footings on dense sand. de Beer (1965b) suggested that the progression of a rupture surface beneath a footing might be dependent on footing size. He also suggested that the pressure dependency of the shear strength parameters of sand might be the cause of the size effect. The dependency of the mobilised friction angle on the stress level along a rupture surface beneath a footing was confirmed by Yamaguchi *et al.* (1977). Hettler and Gudehus (1988) also found that the size effect could be explained by the pressure dependence of the shear strength parameters of sand. Thus for a model to be representative, the effective stress state has to be increased to the prototype value by testing in a centrifuge or by imposing a downward hydraulic gradient. Alternatively, the stress:strain response of a 1-g test could be made similar to that of the prototype by reducing the density of the sand in the model. The latter technique is possible because the stress:strain response of sand is a function of void ratio, as well as of confining stress.

Hettler and Gudehus (1988) have shown that departure from similarity with regard to the scaling of the size of sand particles is unimportant. A ratio of footing diameter to sand particle diameter above a threshold value of about 50 has little influence on the bearing capacity. In the

scaling of model tests the effects of chamber size have to be assessed. In centrifuge tests, Ovesen (1979) found that a chamber diameter to footing diameter ratio of five was too small. Lau (1988) found that a chamber diameter to footing diameter ratio of 8.5, and also a height of sand layer to footing radius ratio of 3.5, resulted in no significant chamber size effects. A comprehensive literature review of the scaling of models tests is given in Corté (1989).

2.8.3 Scaling of stress:strain behaviour

The scaling of footing load:deformation behaviour is best illustrated by considering the stress:strain behaviour of an element of soil beneath a footing. This could, for instance, be at a depth equivalent to the radius of the footing. The comparison of the load:deformation behaviour of a footing and the stress:strain response of soil in an element test was utilised by Altaee and Fellenius (1994). The initial vertical stress before application of the foundation load can be used to represent the reference stress state. If the effective mean stress p' is assumed to be representative of the initial vertical stress beneath the footing and the void ratio is used to represent density, then the scaling of a soil element may be illustrated using the concepts of critical state soil mechanics and the state parameter (Roscoe & Poorooshasb, 1963; Been & Jeffries, 1985). The stress:strain behaviour of three model reference soil states, representing three different methods of scaling, will be compared to a prototype reference soil state. The reference soil states, which are shown in Figure 2.28, are characterised by the void ratio and the effective mean stress.

The equivalent void ratio model represents a conventional 1-g model test and the equivalent state parameter model utilises the evidence that the stress:strain behaviour of a soil is similar if the state parameter is the same. Altaee and Fellenius (1994) used the results from drained triaxial tests to illustrate the importance of the state parameter. The results of their tests, which correspond to states M1, M2 and P in Figure 2.28, are shown in Figure 2.29. The similarity between M1 and P is evident in the plots of normalised shear stress and volumetric strain against axial strain, as is the difference between M2 and P. The stress:strain response of the equivalent void ratio model does not scale because of the increased dilation effect. The drained critical state stress of this model will, however, scale by $1/n$. The stress:strain response of the centrifuge model will be the same as that of the prototype. A model state similar to the prototype state is attained in the centrifuge

model by increasing the body acceleration by the geometric scale factor n.

If triaxial stress:strain behaviour is representative of the soil beneath a footing, then the scaling factors listed in Table 2.2 can be deduced. Most of the scaling factors of a downward hydraulic gradient model will be similar to those of the centrifuge model, assuming that the prototype stress state can be attained with a downward hydraulic gradient. The acceleration will, however, be the same in the downward hydraulic gradient model and the prototype.

The scale factors for force from Table 2.2 can be used to scale vertical and horizontal drained capacity. The drained moment capacity of the equivalent state parameter model will scale by $1/n^3$ because of the additional length variable in the definition of a moment. The drained moment capacity of the equivalent void ratio model will scale by a factor of the order of $1/n^4$.

The undrained strength scale factor of the equivalent state parameter model will be the same as the drained factor. The undrained strength scale factor of the equivalent void ratio model will depend on the definition of failure, but it would be between about $1/n$ and 1. If both the model and prototype are sheared to cavitation, then the undrained scale factor would be influenced by the difference in the ambient pore pressure at foundation level between the model and prototype. The scaling of partially-drained strength is even more complex. One would need to know the drained and undrained strengths of the model and prototype, and the degree of drainage in the model and prototype would also have to similar.

In terms of model tests conducted at 1-g, it would seem that the equivalent state parameter model is the most appropriate scaling technique. This is because it correctly models dilatancy. Poorooshasb (1995) drew similar conclusions in his analysis of the problem of scaling in 1-g tests. He used an elasto-plastic constitutive soil model in conjunction with the equilibrium equation to prove that similarity, under quasi static loading conditions, could be achieved with the equivalent state parameter model. This was only if the viscosity of the pore fluid was also appropriately scaled. Under dynamic loading conditions, however, he found that similarity could only be achieved if the soil skeleton was assumed to be poro-elastic.

2.8.4 Scaling of elastic stiffness

The elastic stiffness of sand is highly dependent on the magnitude of strain. A ten-fold

variation in stiffness occurs in the 10^{-4}% to 1% strain range. This review of stiffness will be limited to small strain "linear" elastic behaviour and the initial stress state. The API (1993) recommendations on elastic foundation stiffness (see Equations 2.1-2.3) give the following relationships:

vertical stiffness $\propto GR$

horizontal stiffness $\propto GR$

rotational stiffness $\propto GR^3$

The shear modulus is known to be approximately proportional to the square root of effective mean stress. The radius will scale by the geometric scaling factor $1/n$. The scale factor for p' will depend on the scaling of initial effective stresses, which is $1/n$ for both the equivalent state parameter and void ratio models. This results in a factor of $1/n^{1.5}$ for vertical and horizontal stiffness. The factor for moment stiffness is $1/n^{3.5}$.

2.8.5 Scaling of drainage

Soil behaviour that is not fully drained or undrained will be affected by the drainage characteristics of the sand. Drainage can be scaled using the dimensionless time factor,

$$T = \frac{c_v t}{H^2} \qquad [2.45]$$

where c_v is the coefficient of consolidation, t is time, and H is the drainage length. The radius of a footing can be used as a representative drainage length. The coefficient of consolidation can be expressed by,

$$c_v = \frac{k M'}{\gamma_w} \qquad [2.46]$$

where k is the permeability and M' is a representative constrained modulus (one-dimensional compression modulus). The work of Poorooshasb (1995) indicated that stress:strain similarity under quasi static loading conditions is achieved if the viscosity of the pore fluid in the model is increased by the geometric scale factor n. This would result in a scale factor of $1/n$ for permeability. If the constrained modulus represents plastic stress:strain behaviour, an appropriate scale factor for this variable would be $1/n$. Thus the coefficient of consolidation would scale by

$1/n^2$ and time would scale by a factor of one for the same dimensionless time factor in Equation 2.45. If on the other hand the process is principally elastic, the modulus would scale by $1/n^{1/2}$ and the time would scale by $1/n^{1/2}$.

3 Apparatus

3.1 Introduction

The diameter of the model footing was 150 mm. The behaviour of the footing was investigated using a displacement controlled rig. The rig and all of the data logging processes were controlled from a PC. The miniature cone penetrometer tests were also performed using the same rig and data logging equipment. The sample preparation procedures were novel and required special equipment.

3.2 Model footing tests: Rig

3.2.1 Design of the rig

The test rig was designed by Martin (1994) for model spudcan footing tests on clay. The control of the rig was fully automated and allowed independent control over vertical (w), horizontal (u), and rotational (θ) displacements in a single plane. Displacement control facilitates exploration of the complete V:H:M failure surface using sideswipe tests, which involve either horizontal or moment displacement at a constant vertical displacement. Simultaneous measurement of the resulting load components (V, H and M) was achieved using a Cambridge type load cell.

Independent control over the three components of displacement was accomplished by using separate bearing arrangements, and by superposition of the different motion systems. This is illustrated in Figure 3.1. Linear slides guide the vertical and horizontal systems, and a rotary slide guides the rotational system. The vertical plate displaces along the vertical slide that is attached to the back plate. The back plate is fixed to the specimen container. The horizontal plate displaces along the horizontal slide that is attached to the vertical plate. The bearings guiding the rotational slide are attached to the horizontal plate. The shaft supporting the model footing was attached directly to the rotary slide. Each plate, and the rotary slide, were driven by a motors that were fixed to the plate immediately behind. LVDTs positioned between the adjacent systems measured displacements.

The displacement and load design specifications adopted by Martin were calculated for a 100 mm diameter footing. The choice of this diameter was influenced by the use of 450 mm diameter specimen containers. The vertical, horizontal, and rotational displacement ranges adopted were 300 mm, 50 mm, and 30 ° respectively. The corresponding maximum displacement rates were 1 mm/s, 0.25 mm/s, and 0.25 deg/s respectively. The displacement rates were chosen to achieve an undrained footing response with kaolin clay specimens. Martin used Brinch Hansen's (1970) bearing capacity method to estimate the required load capacity of the footing, and hence of the rig. The rig and the load cell were designed for working loads of V = 1000 N, H = 300 N, and M = 12.5 Nm. A safety factor of 1.5 was used in the design of the load cell.

The rig, as designed by Martin for tests on clay, was not wholly suited for footing tests on dense sand specimens. For a similar sized footing, a dense sand specimen results in stiffer behaviour and larger capacities. The investigation of partially-drained behaviour also required an apparatus that could produce a large range of displacement rates. Slow displacement rates are required for drained loading and fast displacement rates for undrained loading. The rig was adapted to cope with the increased stiffness and displacement rates required for partially-drained footing tests on dense sand. This entailed replacement of some structural elements, a faster and more powerful vertical motion system, an altogether different and more sensitive displacement measuring system, and a new load cell of increased capacity.

The load capacity of the rig was dictated by the capacity of the vertical and horizontal motion systems and by components in the rotational motion system. The motion systems imposed limits of 970 N on the vertical load and 350 N on the horizontal load, for non-lubricated slides. The limits could be increased by a factor of four with lubrication of the slides. The author used an alternative and less effective method of lubrication than that recommended by the manufacturers. Load limits a factor of about two greater than the values for dry slides mentioned above were deemed to be acceptable. A moment capacity of 200 Nm was dictated by the strength of the plastic rack in the rack and pinion system used to rotate the rotary slide.

The vertical load capacity of the rig restricts the maximum footing size that can be used if one is interested in investigating bearing capacity failure. The investigation of partially-drained

behaviour, however, was of overriding importance. Partially-drained considerations dictated a minimum footing size, in addition to rates of displacement and the permeability of the sand specimen. The degree of drainage under partially-drained conditions is dependent on the drainage length, the rate of loading, and the drainage properties of the sand base. To achieve undrained conditions (or a low degree of drainage) at a specific loading rate and permeability, the drainage length has to be sufficiently long. Hence the specification of a minimum footing size.

Rapid loading trials with footings of various sizes on an oil-saturated sand specimen indicated that a 100 mm diameter footing was too small. It was not possible to develop undrained footing response with a 100 mm diameter footing. The degree of drainage was estimated from a pore pressure measurement at the centre of the footing. With a 150 mm footing, the increase in pore pressure was similar to the increase in total stress under rapid loading. A footing diameter of 150 mm was chosen. The estimated bearing capacity load of a 150 mm footing on dense sand was approximately 6000 N. This was three times higher than the capacity of the rig. The footing diameter was ultimately restricted by the 450 mm diameter specimen container and the influence of possible chamber size effects. Minimum and maximum vertical displacement rates of 0.001 mm/s and 5 mm/s (for drained and undrained response respectively) were deemed necessary for the choice of footing size and sand permeability. The permeability of the sand was reduced by using a silicone oil pore fluid with a higher viscosity than that of water.

Martin's (1994) displacement measurements were affected by the flexibility of the rig since his measurements were not recorded at the footing, but between the relevant sliding plates. By measuring the stiffness of the rig under various load combinations, he was able to account for this effect. The relevant flexibility coefficients were as follows,

$$w = -2.75\times10^{-4}\ V \qquad \text{under vertical load only} \qquad [3.1a]$$

$$u = -2.25\times10^{-3}\ H \qquad \text{under horizontal load only} \qquad [3.1b]$$

$$\theta = -4.63\times10^{-3}\ M \qquad \text{under moment load only} \qquad [3.1c]$$

where the units were mm, degrees, N and Nm. The author developed a displacement measurement system that was attached directly to the footing. This removed the influence of the rig flexibility on

the displacement measurements. It was still deemed necessary to increase the rig stiffness because sideswipe tests ideally require a constant vertical displacement. A flexible rig extends on the relaxation of load that is encountered during such a test. It was not possible to reduce the vertical flexibility of the rig without having to perform major alterations. This flexibility was generated in the numerous bearings and sliding parts, and could not be altered by simply replacing the structural elements. The horizontal and rotational flexibility were reduced by approximately 8% by replacing the shaft, onto which the footing was attached, by a stiffer element. A larger shaft was also needed to fit the new load cell. The new shaft and associated connections are shown in Figure 3.2. A removable U-shaped element was machined to fit the base of the shaft and to connect to the top of the load cell. The shaft was positioned so that the centre of the base of the footing was at the centre of rotation of the rotary slide. It was possible to maintain a constant vertical displacement during the slowest sideswipe tests by using a load feedback mechanism. This facility was not adopted because the feedback mechanism would not work in the fast tests.

The vertical stiffness of the rig between the vertical stepper motor and the footing, shown in Figure 3.3, was calculated by comparing the displacement at the stepper motor and at the footing. Note that this stiffness was different from that specified by Martin (1994) as he measured the stiffness between the vertical plate and the footing. There was considerable flexibility in the vertical lead screw and associated bearings situated between the vertical stepper motor and the vertical plate (see Figure 3.3). The slack in the vertical displacement system was also measured. This occurred in the lead screw system. The load increments and displacements are shown in Figure 3.4[a]. The average value of the rig stiffness was 1944 N/mm. The stiffness measurements that were affected by slack are not included in the estimation of the rig stiffness. The slack was approximately 0.2 mm and from Figure 3.4[b] it is clear that the slack occurred at a vertical load of about 450 N.

The range of vertical displacement rates required for partially-drained footing response could not be achieved with the existing vertical motor. In addition, a single motor could not cover the full velocity range of 0.001 mm/s to 5 mm/s. Two different motors were used in tests requiring both drained and undrained response. The vertical drive system was adapted so that the motor

could be changed during a test with minimum disturbance to the footing. The position of the vertical motor was raised above the confined space within the rig so as to accommodate a new larger motor required for undrained loading. An extended couple was introduced between the motor and the lead-screw that drove the vertical plate. This arrangement is shown in Figure 3.3.

3.2.2 Displacement control system

Three stepper motors and an intelligent stepper motor controller were used to control the displacement of the vertical and horizontal plates, and of the rotary slide, and hence the displacement of the footing. The intelligent stepper motor controller received position, velocity and acceleration commands from a PC via an RS232 interface. The vertical and horizontal plates were connected to the appropriate stepper motors by a lead screw and nut arrangement whilst a rack and pinion arrangement was used to drive the rotary slide. The general layout of the stepper motors and drive systems is shown in Figure 3.3.

The stepper motors were supplied by McLennan Servo Supplies Ltd and were all of type 23HS-108, which produce 400 steps of 0.9 ° per revolution. These motors operate best at 400-1000 r.p.m., which result in linear and rotational displacement rates higher than the footing displacement rates required by Martin (1994). Martin incorporated gearboxes to reduce the r.p.m. from all three stepper motors. Gearbox reduction ratios of 50:1, 250:1 and 500:1 were used on the vertical, horizontal and rotational stepper motors. These gearbox reduction ratios, combined with the reductions due to the lead screw/nut and rack/pinion systems, produce the conversion factors in Table 3.1. These relate motor steps and footing displacements. It was mentioned in the previous section that a larger vertical stepper motor was needed to generate the fast displacement rates required for undrained footing response. A 34HS-209 stepper motor (without a gearbox) was used and the conversion factor relating motor steps to footing displacement for this motor is also listed in Table 3.1.

An important characteristic of stepper motors are their working ranges in terms of speed and acceleration. The limits of the working ranges of the three small stepper motors, under minimal footing load, are shown in Figure 3.5. These working ranges reduce with increased footing load. The range of velocities used in this test programme is listed in Table 3.1. Although an undrained

displacement rate of 5 mm/s could be attained using the smaller vertical motor with a lower gearbox reduction ratio, the larger and more powerful motor was required to cope with the anticipated torque. It was also possible to develop faster displacement rates than 5 mm/s with the larger motor, but this would have required a faster data logger to achieve an acceptable data logging resolution.

The SM9343 triple-axis intelligent stepper motor controller was supplied by McLennan Servo Supplies Ltd and included three PM301 stepper motor controllers and three PM164C translators. Each axis corresponds to a motor. Axis one was the rotational motor, axis two was the horizontal motor, and axis three was the vertical motor. The power supply module was replaced by a more powerful 50 V d.c. module to cope with the increased torque required for this test programme. External current switches for each axis were also placed on the intelligent stepper motor controller to accommodate changing of the vertical motor. The three PM301 controllers were daisy chained on the single RS232 serial interface to the host PC. Simple ASCII commands, specifying motor position, velocity, and acceleration were used in the two-way communication between the PM301 controllers and the host PC. These commands could also be stored in the on-board RAM of the controllers and executed as a sequence of moves. Separate PM301 controllers for each motor allowed independent control of the three different displacement components. The PM301 controllers supplied the required direction signal and step pulses to the TM164C translators. The translators converted these into drive currents to drive the stepper motors.

The ASCII commands for the PM301 stepper motor controllers were generated using a QuickBASIC program on an IBM compatible 286 PC. A typical Move Relative (MR) velocity path and the associated PM301 commands are shown in Figure 3.6. The MR command rotates the stepper motor by a fixed number of steps. This move starts at a programmed Base Speed (SB) and ramps up linearly at a rate defined by the Set Acceleration (SA) command, until the desired Slew Speed (SV) is reached. The motor will continue at this SV speed until it decelerates at the SA rate back down to the SB speed. The Creep Steps (CR) command defines the number of final steps at the SB rate. The PM301 controller calculates when to decelerate the motor so as to achieve the programmed steps, and hence footing displacement. Another commonly used feature was the

Constant Velocity (CV) command, which was used to rotate the stepper motors at a specified SV speed for an unspecified number of steps. Many more stepper motor commands were available in addition to those mentioned above. It was possible to simulate sinusoidal cyclic displacements and to have load control via a feedback routine in the QuickBASIC control program. Use of the feedback routine was restricted by the speed of the host PC. Limit switches were attached to the rig to stop the stepper motors from displacing the moving parts of the rig beyond their limits.

3.2.3 Model footing and connection plate

The factors affecting the decision to use a 150 mm diameter footing were discussed in Section 3.2.1. The first factor was the need for a sufficiently large footing to ensure undrained response. The vertical displacement rate of the rig and the permeability of the sand specimen had already been altered as much as possible to reduce drainage rates. The second and conflicting factor was the need for a sufficiently small footing, imposed by the relative size of the specimen container and the desire for the bearing capacity load of the footing to be within the load limits of the test rig. The shape of the footing was circular because most shallow offshore foundations are circular in plan. A circular flat footing shape, as opposed to one with skirts around the periphery, was chosen because it was felt that the partially-drained behaviour of the simplest geometry had to be investigated before that of a more complicated sort.

A 150 mm diameter footing was chosen based on the results of a series of rapid loading preliminary tests. Different size footings and pore pressure measurement arrangements were investigated. The pore pressure was measured at the centre of the footing. This was achieved by attaching the transducer to the centre of the footing or by measuring the pressure at the centre via a tube to an externally located transducer. The nine preliminary tests were conducted on the oil-saturated sand used in the main series of tests. Different combinations of loading apparati, footing sizes, transducer locations, and effective stress arrangements were tested. The preliminary tests and their results are summarised in Table 3.2 and the apparatus is shown in Figure 3.7.

Tests TP01, TP02 and TP03 comprised a 100 mm diameter footing with an external transducer. This arrangement is shown in Figure 3.7[a]. The footing in these tests was loaded using the rig described in the preceding sections. The larger stepper motor was not installed when the

preliminary tests were performed, thus the maximum vertical displacement rate of the rig was about 1 mm/s. The measured pore pressure response was low in the above mentioned tests, even when the length of tubing to the transducer was reduced and the effective stress of the sand was increased by downward hydraulic gradient. The ratio of the increments of pore pressure load to vertical load averaged only 5% and the footing response could not be classified as undrained. This ratio, and hence the magnitude of the pore pressure, was used to indicate how undrained the tests were. The pore pressure load was calculated assuming a uniform pore pressure distribution on the footing.

A faster method of load application was needed to investigate the effect of loading rate, as opposed to footing size, on the pore pressure response. A hanger and weights system was devised that resulted in displacement rates varying between 5 mm/s and 10 mm/s. The results of test TP04, using the hanger and weights arrangement, again resulted in a low pore pressure response ratio. The effect of directly attaching the pore pressure transducer to the centre of the footing was apparent in tests TP06 and TP07 (see Table 3.2). The pore pressure in test TP05 was anomalous. A direct connection reduces the effects of the capillary action in the tubing. A pore pressure response ratio of about 25% was attained with the 100 mm diameter footing, when loaded with the hanger and weights loading system.

A pore pressure response ratio of 64% was attained in tests TP08 and TP09 by increasing the footing diameter to 150 mm. The apparatus of these tests is shown in Figure 3.7[b]. The displacement rate in these two tests averaged about 8 mm/s. This combination of footing size and displacement rate probably resulted in an undrained response. Therefore a footing diameter of 150 mm was chosen for the main series of tests.

The design of the 150 mm diameter footing used in the main series of tests incorporated a wall around the periphery. This was to prevent inundation of the instrumentation in and above the footing. A connecting plate, termed the base plate, was needed between the footing and the load cell. The base plate acted as a spacer for the pore pressure transducer, which was screwed into the centre of the footing, and also facilitated removal of the footing without disconnection of the load cell. Toyoura sand with a mean grain size of 0.16 mm was glued to the base of the footing to create

a rough footing. The footing displacement measuring devise was attached to the wall of the footing. A fine stainless steel woven wire-cloth (supplied by Potter & Soar, nominal aperture = 0.05 mm) was attached at the base of the footing at the pore pressure transducer port. It was felt that a less permeable VYON F filter (supplied by Porvair plc, thickness = 0.75 mm, average pore size = 0.09 mm) or stone filter might have reduced the transducer response. The footing and base plate are shown in Figure 3.8.

3.3 Model footing tests: Instrumentation

The instrumentation consisted of ten transducers, a Mowlem Microsystems "Autonomous Data-acquisition Unit" (ADU) supplied by Measurements Group UK, and an additional "RDP Dataspan 2000" signal-conditioning unit supplied by RDP Electronics. The ten transducers required 12 channels and consisted of six LVDT transducers for measuring displacement, three pore pressure transducers (PPT), and a load cell with three channels. The ADU was connected to the host PC via a RS232 interface.

3.3.1 Data-acquisition and signal-conditioning

The ADU was used to log 12 channels and to provide excitation for six channels. The six LVDTs required a.c. excitation, which was provided using the RDP Dataspan unit. The ADU incorporated a MM720 analogue to digital 12 bit converter (which had an accuracy of 1 in 4096 bits), MM724 and MM740 analogue input boards, a MM718 memory module, and a MM712 microprocessor module with an RS232 interface. The analogue input boards accepted a full scale input range of ±10 mV to ±10 V, and the MM724 module was also capable of supplying an excitation of up to ±10 V. The six load cell and PPT channels were connected to the MM724 module and the six LVDT channels were connected to the MM740 module. The MM720 A/D converter module had gain settings, with a maximum gain of 1024. The MM718 module had an onboard storage capacity of 256 kBytes. The ADU was commanded and interrogated using simple ASCII commands sent from the host PC to the MM712 module.

Two forms of data logging were utilised, fast logging (up to 100 scans per second) of relatively short tests by the MM718 module and slow logging by the host PC (up to 1 scan per

second). Each test, which could be up to 12 hours long, included a series of sub-tests in which fast logging was used. Data from the sub-tests was transferred (and cleared) from the ADU to the host PC immediately after each sub-test. Each test produced an average of 2 MBytes of data.

3.3.2 Load cell

The load cell was designed to measure vertical, horizontal, and moment loads acting on the footing and was similar to the contact stress transducers developed at Cambridge University. Bransby (1973) described the development and design of these transducers. The cell consists of two blocks attached by an arrangement of thin strain-gauged webs as shown in Figure 3.9. The lower block, or active face, is connected to the surface on which loads are measured. The upper block is attached to the loading apparatus. In this study, the active face of the load cell was connected to the base plate and the upper block was connected to the shaft. This is illustrated in Figure 3.2 and Figure 3.8.

Two pairs of vertical webs at each end of the cell (labelled LCV1 and LCV2 in Figure 3.9) measure the vertical and moment load. The moment load is deduced from the difference between the forces in the two pairs of vertical webs. Four horizontal webs (labelled LCH in Figure 3.9) measure the horizontal load. Two horizontal webs were located on each side of cell close to the active face. A compressive vertical load results in compressive strains in both of the vertical web arrangements (LCV1 and LCV2), whilst a pure moment results in compressive strains in one of the vertical web arrangements and tensile strains in the other. A horizontal load results in strains in the horizontal webs. There is some degree of cross coupling depending on the position of the Load Reference Point (LRP).

Three full Wheatstone bridge strain-gauged circuits measure strain in the webs. All of the webs were strain-gauged on both sides, with each circuit comprising eight gauges. There were four "dummy" gauges in each of the vertical circuits that were attached to the solid part of the cell. The three load cell channels were connected to the MM724 module on the ADU that supplied an excitation of 10 V d.c.. The signal from each vertical channel had a load sensitivity of approximately 0.01 mV/N for the specified excitation (with respect to the vertical load acting on each web arrangement, and not the total vertical load). The sensitivity of the horizontal web

arrangement was approximately 0.036 mV/N. A gain of 256 was used in both of the vertical channels, which meant a voltage input range of ±20 mV. In the horizontal channel, a gain of 128 and a voltage input range of ±40 mV was used.

The cell was machined from a single block of dural (E = 70000 MPa and 0.1% proof stress = 220 MPa). The webs were sized to achieve 1000 με under the web design loads. A vertical web design load of 450 N was chosen to give a vertical footing design load of 1800 N. This vertical web design load results in the following relationship between allowable moment footing load and vertical footing load,

$$M = 46.08 - 0.0256\,V \qquad [3.2]$$

where the units are Nm and N. A permanent strain of 0.1% would be expected at a vertical web load a factor of 3 greater than the web design load. The factor of safety calculated using Rankine's theory (Stephens, 1970) was 2.7 assuming a fixed web. The failure load derived from Rankine's theory is a function of the direct compression and Euler failure loads, and is valid for struts of intermediate length. A horizontal web design load of 125 N was chosen to give a horizontal footing design load of 500 N. The factors of safety of the horizontal webs were the same as for the vertical webs. Cambridge In-situ Ltd supplied the strain-gauged and wired load cell.

The load cell was calibrated by applying a load (V, H or M) at the load reference point whist keeping the other two loads constant. The calibration apparatus is shown in Figure 3.10. The load cell was calibrated with the active face directed upwards. A calibration block was connected to the active face of the cell and the loads were applied to this block. Moment load was applied by varying the eccentricity of a constant vertical load on a hanger. Horizontal load was applied by a wire positioned at a height above the active face of the load cell equivalent to the LRP. The distance from the active face to the LRP was 33 mm and represented the thickness of the base plate plus the footing (shown in Figure 3.8). Grooves were made in the calibration block along its axis for positioning the hanger to simulate moment loading. Negative and positive calibrations under horizontal and moment loads were performed separately. The negative and positive calibration gradients were averaged together but these were almost identical. Calibration of the cell with each load resulted in three coefficients, one for each set of webs, relating load and bits. This was

because vertical load also generated strain in the horizontal webs and vice versa. There was some cross coupling.

The gradients of the calibration curves, which relate the output from the load cell to the applied loads, form the entries in the matrix below,

$$\begin{Bmatrix} LC_{v1}\,(\text{bits}) \\ LC_{v2}\,(\text{bits}) \\ LC_{h}\,(\text{bits}) \end{Bmatrix} = \begin{bmatrix} 5.952\times10^{-1} & 8.329\times10^{-1} & -23.188 \\ 5.854\times10^{-1} & -8.127\times10^{-1} & 22.920 \\ -2.760\times10^{-3} & 1.866 & -4.283\times10^{-1} \end{bmatrix} \begin{Bmatrix} V\,(\text{N}) \\ H\,(\text{N}) \\ M\,(\text{Nm}) \end{Bmatrix} \qquad [3.3]$$

where LC_{v1}, LC_{v2} and LC_{h} are the outputs from the three load cell channels and V, H, and M are the applied loads. To derive loads from the outputs of the load cell (in bits), the above matrix is inverted. Inversion results in the following matrix,

$$\begin{Bmatrix} V\,(\text{N}) \\ H\,(\text{N}) \\ M\,(\text{Nm}) \end{Bmatrix} = \begin{bmatrix} 8.422\times10^{-1} & 8.519\times10^{-1} & 4.890\times10^{-3} \\ -3.720\times10^{-3} & 6.332\times10^{-3} & 5.404\times10^{-1} \\ -2.164\times10^{-2} & 2.210\times10^{-2} & 1.929\times10^{-2} \end{bmatrix} \begin{Bmatrix} LC_{v1} \\ LC_{v2} \\ LC_{h} \end{Bmatrix} \qquad [3.4]$$

The accuracy of the load cell calibration matrix was checked by applying various known combinations of the three load components, and comparing these with the values output by the load cell. The results of these checks are listed in Table 3.3 and indicate that the measured loads were accurate to ±5 N, ±3 N and ±0.3 Nm for V, H and M respectively. The standard error in the calibration coefficients of the vertical webs during vertical loading, and of the horizontal webs during horizontal loading, was not more than 0.12%.

Measurements of the three load components were affected by what seemed to be random noise, with ranges of ±4 N, ±3 N and ±0.2 Nm for V, H and M respectively. The load cell readings were monitored after each test to check to see if they returned to their initial values. Any differences were generally less than the accuracy ranges quoted in the preceding paragraph. The load cell was calibrated twice before being used in this project.

3.3.3 Displacement measurement

There were two forms of displacement measurement: coarse measurements by three long LVDTs positioned to measure the relative movement between the three adjacent moving elements of the rig; and fine measurements by an arrangement of three short LVDTs connected to the

footing and referenced to the specimen container. All of the LVDTs were provided with an excitation of 5 V r.m.s. at 5 kHz from the RDP Dataspan 2000 unit. The a.c. output signal from these transducers was transformed to a d.c. signal by the RDP Dataspan 2000 unit before being transferred to the MM740 module on the ADU.

The long vertical LVDT (DLV) was fixed to the back plate and its armature was attached to the vertical plate. The long horizontal LVDT (DLH) was fixed to the vertical plate and its armature was placed against the horizontal plate. The long rotational LVDT (DLM) was pinned at one end to a beam attached to the horizontal plate and at the other end it was pinned onto the shaft connecting the footing to the rig. Linear displacement measured by this LVDT was transformed to rotational displacement using a trigonometric calculation. The specifications of the long LVDTs are listed in Table 3.4 and their positions on the rig are shown in Figure 3.11[a]. The long vertical LVDT was calibrated using a ruler and the other two long ones were calibrated using a micrometer. The random noise levels were ±0.10 mm, ±0.05 mm and ±0.01 ° for vertical, horizontal and rotational displacements respectively. There was no detectable drift in the readings from DLV and DLM but the channel on the RDP Dataspan 2000 unit onto which DLH was connected was subject to drift. This resulted in a typical variation of 0.1 mm in the reading from DLH over the period of a test.

Additional fine displacement measurements of the footing were required for the following reasons:

— Lack of sensitivity in the existing coarse LVDT measurements. The stiffness of dense sand meant that the displacements that were required to produce the necessary variations in load were of the order of a few millimetres to fractions of a millimetre.

— There was considerable flexibility in the rig between the LRP and the points at which the coarse displacement measurements were recorded. The difference between the vertical displacement of the LRP and of the vertical plate was of the order of 0.5 mm under large loads.

Preliminary tests on dense sand indicated that vertical penetrations were unlikely to exceed 10 mm at the maximum load (under a pure vertical displacement path). The fine displacement

measurement system consisted of three short LVDTs (±5 mm range) which were pinned to a beam connected to the footing and pinned to a L-shaped frame. The frame was fixed to the specimen container. The fine displacement measurement system is shown in Figure 3.11[b]. The specifications of the small LVDTs are listed in Table 3.4. The three linear displacement measurements from the two vertically aligned small LVDTs (DSV1 and DSV2) and the approximately horizontally aligned one (DSH) were transformed using a trigonometric calculation to give the vertical (w), horizontal (u) and rotational displacement (θ) of the LRP. The procedure for calculating the displacements from the small LVDTs is outlined in Appendix B.

The non-linearity of these transducers was rated at 0.1%, which translates to 0.01 mm, and the random noise levels were ±0.0075 mm, ±0.0100 mm and ±0.0050 ° for w, u and θ respectively. The three short LVDTs were calibrated using a micrometer. The displacements measured by the LVDT frame were compared with the displacements expected for specified revolutions of the stepper motors, and with dial gauge measurements of the footing displacements. The small LVDT system was accurate and the absolute errors in the measurements of w, u, and θ were similar to the noise levels.

3.3.4 Pore pressure measurement

In addition to the pore pressure transducer in the footing (pp_1), two transducers were placed in the walls of the specimen container (pp_2 and pp_3). The position and dimensions of pp_1 are shown in Figure 3.8, and those of the other two transducers are shown in Figure 3.12. Transducer pp_1 was screwed directly into the centre of the footing, whilst special adapters for connecting pp_2 and pp_3 to the specimen containers were machined. pp_1 was designed for this project and manufactured by Gaeltec Ltd and the other two transducers were standard PDCR910 units supplied by Druck Ltd.. The specifications of the pore pressure transducers are listed in Table 3.5.

Before installing pp_1 in the centre of the footing, an arrangement whereby the transducer was connected to the port by copper tubing was investigated (see Figure 3.7). This arrangement proved unsatisfactory because of the poor transmission of pressure by the tubing. The VYON filter used in the preliminary tests was also replaced by a more permeable wire-cloth. The response time

of the transducers in the specimen container was not a vital factor and the VYON filter was used in the adapters for pp_2 and pp_3.

The transducers were calibrated using positive and negative air pressure. A DPI600 (Druck Ltd.) calibration unit was used to measure the calibration air pressure. The transducers were all supplied with an excitation of 10 V d.c. by the MM724 module on the ADU. The non-linearity of the transducers was ±0.1% and the random noise level was ±0.05 kPa. The signal of the Gaeltec transducer (pp_1) was subject to spurious jumps in a few of the tests. The spurious output was easily corrected since the magnitude of the jump was large and consistent.

3.4 Model footing tests: Control and monitoring

Tests were controlled and monitored using a QuickBASIC program (filename CONT_1.BAS) on the host IBM compatible 286 PC. Houlsby (1995) wrote the program for a previous project but some alterations were performed to the program for this investigation. RS232 serial links were used to communicate with the data logging unit (ADU) and with the displacement control unit (SM9343). A schematic diagram of this arrangement is shown in Figure 3.13.

The control program performed two main functions: real-time control and data logging of testing; and autonomous testing using parameters stored in previously created input files (filename extension: .INP). The autonomous method of testing was used to perform the sub-tests that required fast logging. The term sub-test is used to refer to special events that were performed in the main-tests. The transducer calibration coefficients, the LVDT frame constants, and the sample details were stored in a definition file (filename extension: .DEF) that was loaded by the control program at the start of each main-test. The program logged raw data from the twelve channels of the ADU into files with extension .OUR and also performed real-time processing of the raw data. The processed data was stored in files with extension .OUT. The rate of logging to .OUR and .OUT files (termed background logging) could be varied but was restricted by the maximum background logging rate of the ADU, which was one scan per second.

The scan rate of the ADU could be increased by operating it in an autonomous testing mode. In this mode, the ADU could be configured to perform tests with a maximum logging rate of 100

scans per second. This mode was used to log the sub-tests that required fast logging rates. The sub-tests were stored onboard the ADU and downloaded to the PC immediately after each sub-test. The raw sub-test data transferred from the ADU was stored in files with extension .RAW. The control program was also used to create processed data files with extension .DAT. In addition to the storage of raw and processed background logging data, the data was displayed on the monitor. The data displayed on the monitor was updated at the background logging rate.

Soft limits for the transducers could be set using the control program. The soft limits on the three components of load were used to control the loading of the footing. Hard limits were also permanently set in the program. These limits were set in bits and responded to the unprocessed data. The hard limits ensured that the transducers were not accidentally pushed over their working ranges by unchecked loading. The control program contained a menu system for setting the parameters required by the numerous control functions. There were functions to control constant velocity moves, fixed displacement moves, combined fixed displacement moves (moves involving all three components of displacement), load holding routines, ADU sub-test configuration, data retrieval from the ADU, reading of .INP files, and the zeroing of the fine displacement measuring system, to name but a few. All the necessary real-time control and data logging adjustments could be performed from the control program on the host PC.

3.5 Miniature cone penetrometer tests

Cone tests were performed with a small penetrometer to gauge the relative density and uniformity of the sand samples. The penetrometer was developed by McBean and West (1987) to test pressurised soil samples in the laboratory. The diameter of the cone was 8 mm (cross sectional area of 50 mm^2) and the cone angle was 60 °. The cone was designed to yield at 2500 N and was strain gauged to produce an output signal of 4.8×10^{-3} mV/N with an excitation of 2.5 V.

The transducer on the cone tip was connected to the ADU. The penetrometer loads encountered in this investigation were generally less than 100 N but a resolution of 1 N was produced by setting the relevant channel on the ADU to its maximum gain. Although the resolution of the A/D conversion was adequate, the noise in the signal from the strain gauged cone

was ±20 N. Thus the signal from the cone tip was not used. The measurement from the load cell on the rig was used to represent the penetrometer load instead. Consequently, the penetrometer load comprised the resistance due to the wall friction as well as the tip resistance

The connection of the penetrometer to the rig is shown in Figure 3.14. The penetrometer was clamped to a bracket that was attached to the base plate below the load cell on the rig. The penetrometer tests were controlled and logged using the same apparatus as for the footing tests.

3.6 Preparation of sand samples

Three sand specimens were prepared. One of the specimens consisted of dry sand and the other two consisted of oil-saturated sand. The two similar oil-saturated specimens were prepared to enable concurrent testing and sample preparation. The oil-saturated sand specimens required a novel preparation procedure. The high cost of the silicone oil, and the imported Baskarp Cyclone sand, necessitated recycling of the specimens. The recycling process had to ensure that all disturbances caused by a footing test could be removed, and that the specimen could be reconstituted to the required uniform density. A fluidisation process involving liquefaction and mechanical agitation of the specimens was adopted. A process that entailed applying alternate components of vibration and downward hydraulic gradient was used to densify the specimens. The dry specimen was only used for a single test and was prepared by vibrating the container and the sand itself.

3.6.1 Sand specimen containers

The specimen containers were produced by Gue (1984) for preparing clay specimens and were also used by Martin (1994) for model footing tests on clay. The dural containers consisted of a flanged cylindrical section and a removable base. All three containers had an internal diameter of 450 mm. The effective internal height of the two containers with oil-saturated specimens was 421 mm and that of the container with the dry specimen was 446 mm. The dimensions of the containers are shown in Figure 3.15[a].

A number of alterations were required for this project. The containers for the oil-saturated specimens were made watertight. The incorporation of o-ring seals satisfied this objective. Two

pore pressure transducer ports were incorporated into the walls of the oil-saturated specimen containers. Filters were attached to the base of the containers. The bases were machined to facilitate drainage, and to attach the associated plumbing. The filtering system consisted of a VYON F filter (supplied by Porvair plc; thickness = 0.75 mm and average pore size = 0.09 mm) placed on top a plastic geo-grid. These were screwed to the base by a circular bracket around the periphery of the container. The strong connection of the filter to the base was needed because of the intense vibrations applied to the containers during the densification process. The top flange of the containers was adapted to take the LVDT frame. The layout of the specimen containers and the associated plumbing, required for the liquefaction and densification processes, are shown in Figure 3.15[b].

3.6.2 Densification of sand samples

The dry sand specimen was poured in two layers, which were both vibrated. For the oil-saturated specimens, the Baskarp Cyclone sand had to be saturated with the viscous silicone oil. This process was complicated because of the low permeability (of the order of 10^{-7} m/s) of the resulting mixture. Some methods for saturating low permeability fluid/soil mixtures were suggested in the literature. Tan (1990) used a process of percolation under vacuum for a mixture with a similar permeability. The whole system was also heated to reduce the viscosity of the pore fluid and took approximately four days to complete. Lau (1988) found that 24 hours of vibration was sufficient to de-air a water/silt mixture and assumed that the specimen was fully saturated when bubbles stopped surfacing.

Pilot saturation tests were performed in a perspex tube to assess the feasibility of saturating Baskarp Cyclone sand with silicone oil. A saturation front was evident but air ingress into the apparatus under high vacuums was a problem. Vacuum was not used in the saturation process of the main specimens because of the risk of air ingress, and because the vacuum pump could not be activated for extended periods. Instead, the oil was percolated up through the sand and the specimen was vibrated until bubbles stopped surfacing.

A densification process employing alternating downward hydraulic gradient and vibration was investigated by the NGI (1993) and deemed to be effective. Homogeneous samples with

relative densities of 80% were obtained. The effectiveness of this method in densifying the soil used in this project was assessed. The result of a pilot densification test performed in a perspex tube is shown in Figure 3.16. The surcharge was induced by applying a negative fluid pressure to the base of the sample. A relative density of 97% was achieved in less than two hours. The densification of the main samples, however, took longer. This method of densification would only be efficient if the initial relative density of the specimen is greater than 0%. Vibration is only effective if soil has strength (effective stress greater than zero). Full sedimentation of the sand particles out of the suspension was deemed a necessary precursor to the application of the downward hydraulic gradient and vibration.

The sedimentation of Baskarp Cyclone sand in oil was investigated. The settlement of the oil/sand interface is shown in Figure 3.17. The maximum void ratio (e = 1.075, R_D = 0%) is attained after about two hours. The velocity of the solidification front is about 7×10^{-6} m/s. It is difficult to estimate what the velocity of the solidification front should have been during sedimentation in the large specimen containers (used for the footing tests). The density of the fluidised sand in the large containers was higher and the distance travelled by the solidification front was greater.

Compaction of sand is known to be dependent on the shear strain. The degree of compaction increases with the number of cycles (to a limiting density) for a particular shear strain amplitude (Youd, 1972). The frequency of the shear strain cycles is thought not to be important. In saturated sand, vibration reduces the effective stresses and does not itself cause the particles of sand to settle. Settlement is dependent on the vertical force on the particles. Seepage forces generated by a downward hydraulic gradient increase the vertical force on the particles and induce settlement. An existing pneumatic powered vibrator was adapted to apply horizontal vibrations to the walls of the specimen containers. This apparatus is shown in Figure 3.15[b]. The amplitude of the vibrations could not be controlled but varying the pneumatic pressure altered the intensity as well as the frequency. The downward hydraulic gradient was induced by applying an air pressure of about 15 kPa to the oil surface above the sand. An asynchronous timing switch and two pneumatic solenoid valves were used to automatically control the air supply that drove the vibration and

downward hydraulic gradient systems. The air supply to the specimen container was regulated and relief valves were installed in the lid to prevent the container being over pressurised. The automated densification system was only employed from test T106 onwards. In the previous oil-saturated tests, switching between the alternate densification components was done manually. The different methods of densification used to prepare the specimens are listed in Table 3.6.

The progress of the densification could only be monitored by removing the lid on the container. Density measurements (and cone penetrometer tests in some instances) were taken to chart the densification process. It was not possible to obtain the same relative density measurements in all of the samples prepared for each test. Approximately three days of sedimentation and five days of densification were required to obtain a relative density of 90%. The uniformity of the samples prepared for each test was investigated by measuring the hydraulic gradient along the vertical axis using the two pore pressure transducers in the wall of the container. A linear hydraulic gradient was taken to indicate that the sample prepared for a test was uniform (assuming that the permeability was dependent on the density). The uniformity was also gauged from the miniature cone penetrometer tests.

The footing response and cone penetrometer results of the initial tests suggested that the density distributions in the oil-saturated samples were not uniform. In an attempt to increase the density in the top layer of the samples, a surcharge was applied to the sand surface during the densification process of samples T107 and T309 (listed in Table 3.6). The surcharge consisted of a heavy dural disc with a filter on the base and around the edge. In test T107, a VYON F filter was attached to the base of the disc and a brush filter was placed around the edge. The filter around the edge of the disc was needed as the sand was in a suspended state and was susceptible to flow. On removal of the surcharge, it was evident that sand adhered to the VYON F filter although the surcharge was removed slowly. This indicated the possibility of uplift forces being applied to the sample, and consequent disturbance. It was deemed necessary to use a more permeable filter. In the densification of the sample for test T309, a fine stainless-steel woven wire cloth was used. This was the same material as used on the pore pressure port in the model footing. This filter proved more beneficial but it was still not possible to raise the surcharge at a sufficiently slow rate, and

also to keep the disc level during the retraction process. Thus the surcharge system was not used in the preparation of the later samples. Use of the surcharge system would have entailed the production of a retraction apparatus, incorporating a rigid frame and a stepper motor drive system for example.

3.6.3 Fluidisation of sand samples

The term fluidisation is used to describe a state in which the effective stress of the sand was reduced to zero after total rearrangement of the sand particles by stirring. The fluidisation process was needed to remove heterogeneities, such as localised soil densification under the footing, caused by previous tests. NGI (1993) concluded that full liquefaction of water-saturated fine-grained sand was possible if the hydraulic gradient was applied with caution. In this project, it was not possible to consistently induce full liquefaction of the samples, and agitation was needed to reduce the samples to a fluidised state. In some of the initial attempts at liquefaction, localised piping occurred. Once piping occurred, it was impossible to achieve full liquefaction. The fact that the samples could not be fully liquefied may have been due to the low permeability. The estimated vertical total stresses and the measured pore pressures (at the pore pressure ports) during one of the liquefaction processes are shown in Figure 3.18. The effective stresses reduced to zero between t = 2.5 hr and t = 3 hr. The data in Figure 3.18 implies that the effective stresses are negative after about t = 3 hr. Since effective stresses cannot be negative, the estimates of total stress in Figure 3.18 are probably not representative. The resistance due to wall friction, acting against the upward movement of the sand specimen, may explain this discrepancy. The coefficient of permeability during the liquefaction process was estimated at 7×10^{-7} m/s (assuming a constant head). This value was similar to the results of the permeability tests ($k = 1.8 \times 10^{-7}$ m/s).

An automatic stirring apparatus was built to agitate the samples as manual agitation proved too demanding. The stirrer is shown in Figure 3.19 and consisted of a rotating paddle that was slowly lowered into the sand. Each rotation of the paddle scraped a thin layer of sand from the sample. This sand remained fluidised by the movement of fins that were placed above the paddle. The whole sample was gradually fluidised as the paddle was lowered to the bottom of the

container. An electric motor with a variable speed control was used to power the paddle. This motor incorporated a trip switch to prevent overloading of the motor and was fixed to an elevated platform that was guided by two vertical bearings. It was necessary to devise a cooling system for the electric motor as it was operating at full capacity for long periods. The paddle was connected to the motor by an extended shaft. The lowering of the platform and the paddle was controlled by a lead screw and stepper motor arrangement. A 23HS-108 stepper motor was connected to the stepper motor control box (SM9343), which in turn was controlled by the host PC. Trip switches were incorporated to ensure that the paddle ceased penetration about 30 mm above the base of the tank to protect the filter. The paddle was lowered at approximately 0.01 mm/s and rotated at about 20 r.p.m.. This resulted in an average time for fluidisation of five hours. The fluidisation apparatus in Figure 3.19 proved highly effective but a more powerful electric motor for turning the paddle would have improved performance. It was necessary to manually agitate the bottom 30 mm of sand but this was only done from test T309 onwards. The samples that were fully fluidised before being densified are indicated in Table 3.6.

4 Sand Samples

4.1 Introduction

The Baskarp Cyclone sand that was used as the foundation soil was supplied by A.B. Baskarpsand of Habo, Sweden. Three different sand specimens were prepared: one dry and two oil-saturated. The two saturated sand specimens were saturated with viscous silicone oil. Only one test was performed on the dry specimen. The two oil-saturated specimens were recycled *in-situ* to facilitate multiple testing. Baskarp Cyclone sand was used previously at Oxford and at the Norwegian Geotechnical Institute (Houlsby, 1995; and NGI, 1994b).

4.2 Index properties

The Baskarp Cyclone sand was a silty fine sand produced using a cyclone separation process. The grains were sub-angular to angular and were 84.3% Quartz (NGI, 1994b). The relationship between the void ratio and the coefficient of angularity, suggested by Holubec and D'Appolonia (1973), indicated that the coefficient of angularity for Baskarp Cyclone sand was probably 1.65.

4.2.1 Particle size characteristics

The particle size of soil is usually characterised by a particle size distribution curve. In situations involving submerged sand, the distribution curve can be used as an indicator of drainage related behaviour such as permeability and consolidation. A particle size analysis was performed on Baskarp Cyclone sand at Oxford University using a "CILAS Granulometer" situated in the Geography Department. The sand was mixed with water using an ultrasonic mixer and a calgon dispersing agent, before being placed in the Granulometer. The particle size distribution curves obtained by the aforementioned procedure and by the NGI (1994b) are shown in Figure 4.1. The median grain size d_{50} from the Granulometer curve was 0.058 mm. The d_{60} and d_{10} sizes were 0.069 mm and 0.018 mm, and the uniformity coefficient (defined as the ratio of d_{60} to d_{10}) was 3.8. The value of the uniformity coefficient was on the border between the well-graded and uniform classifications (Jackson and Dhir, 1988).

4.2.2 Specific gravity of solids

The unit weight of the solid fraction was determined to be 26.40 kN/m^3 by the NGI (1994b). This corresponds to a specific gravity of G_s = 2.69. The author measured the volume of solids required for the calculation of G_s using a simple water displacement method with vibration to remove the air bubbles. G_s was found to be 2.71 but the value determined by the NGI was used in this investigation.

4.2.3 Relative density

It is generally accepted that the relative density is a useful parameter for characterising density, and it is defined as follows,

$$R_D = 100\left(\frac{e_{max} - e}{e_{max} - e_{min}}\right) = 100\frac{\gamma_{max}}{\gamma}\left(\frac{\gamma - \gamma_{min}}{\gamma_{max} - \gamma_{min}}\right) \quad [4.1]$$

where e is the void ratio, and γ represents the dry unit weight. The maximum and minimum dry unit weights were determined by the NGI (1994b) using the following methods. A minimum dry unit weight of γ_{min} = 12.72 kN/m^3 was determined by pouring sand into a mould whilst maintaining a minimal free-fall height for the sand particles. Dry and wet tamping, in combination with vibration, was used to determine a maximum dry density of γ_{max} = 16.85 kN/m^3. These values correspond to e_{max} = 1.07 and e_{min} = 0.57. The author calculated a maximum void ratio of 1.01 using the "tilt" method suggested by Kolbuszewski (1948), and a minimum void ratio of 0.59 using a combination of downward hydraulic gradient and vibration. The NGI values were used in this investigation.

4.3 Drainage properties

The use of viscous pore fluids in model testing was initially driven by the need to scale consolidation behaviour in the centrifuge (Tan, 1990). But it becomes increasingly difficult to saturate, densify, and fluidise fine sand samples as the viscosity of the pore fluid increases. Tan used circulatory systems oil with a kinematic viscosity of 437 mm^2/s as the pore fluid in his fine sand samples. He investigated the cyclic behaviour of spudcan footings in the centrifuge, using the

circulatory systems oil instead of silicone oil because of the reduced cost. Tan utilised the temperature dependency of the circulatory systems oil in his sample preparation procedure. He heated the oil to reduce its viscosity during sample preparation.

Allard *et al.* (1994) used a viscous pore fluid developed at Delft Geotechnics in their centrifuge tests of a model skirted gravity platform. This fluid was stated to have similar physical and chemical properties to that of water, but its actual constituents have not been made public. The constitutive behaviour of sand saturated with the Delft fluid and of sand saturated with water is similar. Use of the fluid resulted in consistent samples and overcame some of the problems of saturating sand samples with a viscous pore fluid. The viscous pore fluid was only percolated into the sample (under an applied hydraulic gradient) after full saturation and densification had been achieved. Laboratory tests indicated linearity between the permeability of water-saturated and Delft fluid-saturated samples. The permeability was found to be inversely proportional to the kinematic viscosity. The Delft fluid can be prepared to a range of viscosity values and a value of 300 mm^2/s was used in the model tests of Allard *et al.*.

Watson and Randolph (1997) found that by using silicone oil as the pore fluid in their tests on a model caisson in the centrifuge, they could induce undrained behaviour. Their tests were conducted on calcareous silt and utilised the findings of Finnie (1993) on the relationship between loading rate and sample permeability.

The main disadvantages with using oils were the high cost (especially of silicone oils) and the difficult sample preparation procedures. Silicone oils do, however, possess many beneficial properties: such as being inert; non-hazardous; and having well defined values of viscosity. A water-soluble pore fluid would overcome the sample preparation problems but such fluids were not readily available. The Delft fluid was not widely available and was classified as a hazardous chemical, for the purposes of handling and disposal. Glycerine could be a water-soluble alternative, but information on the use of this fluid in model testing could not been found.

4.3.1 Pore fluid characteristics

Silicone oil was used as the pore fluid in the two saturated sand samples. The choice of the viscosity of the oil was influenced by the need to achieve a low permeability sand sample, and the

difficulties associated with saturating such samples. The silicone oil was a Dow Corning® 200 Fluid with a kinematic viscosity of 100 mm^2/s. This type of water-clear silicone oil was noted for its thermal and chemical stability, low vapour pressure, low surface tension, shear-breakdown resistance, and essentially non-toxic nature. The 100 mm^2/s oil had a specific gravity of 0.96, and its viscosity reduced slightly with increasing temperature. The viscosity of this oil was approximately 100 times that of water, which has a viscosity of 0.897 mm^2/s at 25° C. The bulk modulus of the silicone oil was approximately 800 MPa at a relevant stress level, as compared with a value of about 2300 MPa for water. Dow Corning could not supply information on the cavitation pressure of the silicone oil but Houlsby (1995) concluded that cavitation was probable at low pressures.

4.3.2 Coefficient of permeability

Three constant head permeability tests were performed on oil-saturated Baskarp Cyclone sand. The permeability apparatus is shown in Figure 4.2. The applied head varied by only 0.15% and the results from the permeability tests are shown in Table 4.1. The tests indicated an average coefficient of permeability of 1.8×10^{-7} m/s. The relative density of the samples was approximately $R_D = 84\%$.

The NGI (1994b) performed permeability tests with water-saturated Baskarp Cyclone sand at relative densities of 63% and 89%. The flow rate in a modified triaxial apparatus was measured during loading and unloading, at consolidation stresses from 20 kPa to 110 kPa. The consolidation stress and the state of stress (virgin loading or unloading) did not affect the permeability. If one assumed a linear R_D:k relationship then the NGI data suggests a permeability of 8.0×10^{-6} m/s for water-saturated Baskarp Cyclone sand at a relative density of 84%.

The permeability of the oil-saturated sand measured by the author was approximately 44 times less than the NGI estimate for water-saturated sand. One would have expected the two values to differ by a factor of approximately 100, as the coefficient of permeability defined by the Kozeny-Carman Equation is inversely proportional to the fluid viscosity (Scott, 1980).

4.3.3 Coefficient of consolidation

The one-dimensional coefficient of consolidation c_v of water-saturated Baskarp Cyclone

sand was derived from element tests conducted by the NGI (1994b). The values of c_v are listed Table 4.2. In the one-dimensional tests, the coefficient of consolidation was calculated using Equation 2.35. In the three-dimensional tests, the coefficient of consolidation was calculated using Equation 2.44 and then converted to the one-dimensional value. The average one-dimensional coefficient of consolidation for loading was 3.6 x 10^{-2} m^2/s and for unloading it was 2.7 x 10^{-1} m^2/s. The coefficient of permeability of water-saturated Baskarp Cyclone sand was a factor of 44 greater than that of oil-saturated sand (Section 4.3.2). One would expect the coefficient of consolidation of the oil and water-saturated sand to differ by a similar factor, assuming that the modulus was constant. Thus for oil-saturated sand the one-dimensional coefficient of consolidation should have been approximately 8 x 10^{-4} m^2/s for loading and 6 x 10^{-3} m^2/s for unloading (for elastic shear moduli of about 10 MPa and 70 MPa respectively).

The coefficient of consolidation is a function of the effective stiffness and the permeability of a soil. For a given relative density the permeability does not change significantly but the change in stiffness can be great. For example, consider the difference between the virgin penetration stiffness and the unloading stiffness. Thus the coefficient of consolidation is sensitive to the effective stress level and the state of stress. Wood (1990) states that the coefficient of consolidation is not a satisfactory parameter for describing the movement of pore fluid in general transient problems and recommends the use of the permeability in conjunction with an effective stress model.

4.4 Stiffness properties

The elastic shear moduli G of Baskarp Cyclone sand were derived from element tests reported in NGI (1994b). Moduli for unloading are compared with predictions from the literature in Figure 4.3. The triaxial and oedometer data shown in Figure 4.3 is also listed in Table 4.2. The moduli derived from the NGI tests were all greater than the comparable small-strain theoretical values. At a relative density of 85%, the experimental values were a factor of approximately two to three greater than the relevant theoretical values. At a maximum effective mean stress of 87 kPa and a strain level of 0.04%, an elastic shear modulus of 90 MPa was estimated from triaxial tests BC10 to BC12. The oedometer tests (BC13 and BC14) indicated an elastic shear modulus of about

35 MPa at a maximum effective mean stress of 30 kPa. The elastic shear moduli of the oedometer tests were calculated from the constrained moduli M, using Equation 2.42 and assuming a Poisson's ratio of 0.2. From the data for the triaxial tests in Table 4.2, it is evident that the elastic shear modulus for unloading was a factor of about seven greater than the modulus for loading.

The Poisson's ratio from tests BC10 to BC12 was checked using the following relationship,

$$\nu = \frac{\sigma_r + \frac{\sigma_a}{2}\left(1 - \frac{\varepsilon_v}{\varepsilon_a}\right)}{\sigma_r\left(2 - \frac{\varepsilon_v}{\varepsilon_a}\right) + \sigma_a} \qquad [4.2]$$

where σ_a and σ_r are the axial and radial effective stresses, and ε_a and ε_v are the axial and volumetric strains. The average value of the Poisson's ratio during loading was found to be less in the denser samples and was approximately equal to 0.25 at a relative density of 90%. The Poisson's ratio from the oedo-triaxial test NTH93-2 was calculated using Equation 2.42 and the measured values of the elastic shear modulus and the constrained modulus. Test NTH93-2 indicated a Poisson's ratio of 0.2 during loading for a relative density of 85%.

4.5 Strength properties

Shear strength parameters were derived from triaxial tests. These parameters are compared with predictions of Bolton's (1986) method, and a low stress adjustment to Bolton's method is proposed.

4.5.1 Shear strength of sand

The results from static triaxial tests conducted by the NGI (1994b) on Baskarp Cyclone sand were used to derive strength parameters. The results from six drained and seven undrained compression tests were analysed. A drained and an undrained test with silicone oil as the pore fluid (the same fluid as used in the footing tests, Section 4.3.1) were included in the analysis. Two of the drained tests and four of the undrained tests were performed on samples that had previously been subjected to undrained cyclic tests. These tests are sometimes referred to as tests on "disturbed samples". The results of the drained and undrained triaxial tests are listed in Table 4.3 and Table 4.4 respectively. The drained and undrained tests are also shown in Figure 4.4 and Figure 4.5 respectively. The results from the tests on the disturbed samples are only included in Figure 4.4[d]

and Figure 4.5[d].

The drained tests indicated a peak friction angle, which reduced with increasing effective mean stress, of 43 ° at an effective mean stress of 100 kPa. The peak friction is shown in Figure 4.6. The relative density of the drained samples was approximately 80%. The peak friction angle from the oil-saturated test was about 2 ° less than that from the comparable water-saturated test (tests BC23 and BC15 respectively). The difference in the dilation angle, which is defined as $\beta = \tan^{-1} d\varepsilon_q/d\varepsilon_p$, between tests BC15 and BC23 is evident in Figure 4.4[f]. This reduction in the peak friction angle is consistent with the findings of Eypton (1982) and Bielby (1989), which were reported in Tan (1990). The peak and critical states were highlighted in all the plots in Figure 4.4. The peak state shown in Figure 4.4[c] consistently occurred at a volumetric strain of about -2%. The stress ratio η shown in Figure 4.4[e] tended to a value of approximately 1.3 at the critical state. The stress ratio is equal to q/p'. The critical state friction angles are also shown in Figure 4.6. A critical state friction angle of 33 ° was representative of an effective mean stress of about 100 kPa if one ignores the high value from test BC16. The presence of silicone oil does not seem to affect the critical state friction angle. One would expect the critical state friction angle to reduce with increasing effective mean stress, especially at low levels of stress (Chu, 1995). It was probable that the critical state had been attained at the end of the drained tests. The dilation angle β shown in Figure 4.4[f] is constant and approximately equal to 90 °. The critical state points shown in Figure 4.4[d] indicate a probable critical state line in $\ln(p'):e$. The parameters of the best-fit line are $\lambda = -0.016$ and $\Gamma = 0.75$. These values are similar to those of the steady state lines of some of the sands referred to by Altaee and Fellenius (1994). It should be noted that the sands referred to consisted of larger grain sizes than Baskarp Cyclone sand, and that the steady state is usually derived from undrained tests and the critical state from drained tests. Been *et al.* (1991) found that these lines were coincident for some sands.

The results from the undrained tests are shown in Figure 4.5. The difference in the shear stress and pore pressure responses between the two undrained water-saturated tests, shown in Figure 4.5[a] and [c], is due to the difference in relative density. In test BC1 the relative density was 50% and in test BC2 it was 80%, as listed in Table 4.4. The dilatancy that is evident in the

drained tests manifests itself as negative pore pressures in the undrained tests. The effect of the silicone oil pore fluid is evident in the undrained tests as it is in the drained tests. The oil-saturated undrained test BC24 exhibits a less intense shear stress and pore pressure response than the comparable water-saturated test BC2. The stress ratio response shown in Figure 4.5[e] of the oil-saturated test is also lower. This reinforces the observation from the drained tests that the silicone oil had a degrading effect on stiffness and strength. It is probable that the undrained tests had not reached a steady state even though the values of the stress ratio at the end of the tests are similar to the critical state values observed in the drained tests. The stress paths (shown in Figure 4.5[b]) are moving up and along the critical state line as the pore pressures (shown in Figure 4.5[c]) are still decreasing at the end of the tests. A probable steady state line is plotted in $\ln(p'):e$ space in Figure 4.5[d]. The parameters of the best-fit line are $\lambda = -0.072$ and $\Gamma = 0.87$. These values are similar to those of the steady state lines of some of the sands referred to by Altaee and Fellenius (1994). They are different, however, from the critical state line deduced from the drained tests.

The critical state line of the drained tests and the steady state line of the undrained tests are compared in Figure 4.7. The two state lines do not seem to be coincident. But if one ignores test BC1, the undrained test with $e \cong 0.82$, it is possible that the two state lines are coincident. A reduction in the slope of the critical state line at $p' \cong 1000$ kPa was observed by Been *et al.* (1991). Therefore it is possible that the critical state line of Baskarp Cyclone sand might have a similar shape.

It was probable that the pore pressures in the undrained tests would have continued to decrease until cavitation of the pore fluid occurred. McManus and Davis (1997) found that dilatant sand samples exhibited signs of pore fluid cavitation when the pore fluid pressure reduced to an absolute value of -100 kPa. On the onset of cavitation, their samples behaved as if undergoing drained shearing. The plot of $\varepsilon_q:u$ in Figure 4.5[c] does not indicate if cavitation is probable in the tests on Baskarp Cyclone sand. An indication of the likelihood of cavitation is gained by normalising the excess pore pressure by the pore pressure increment u_{cav} required for an absolute pressure of -100 kPa. The value of u_{cav} is assumed to be equal to the initial excess pore pressure, plus the backpressure, and plus 100 kPa. The samples should cavitate at a value of $u/u_{cav} = -1$. The

normalised pore pressures are shown in Figure 4.8. From this figure it is evident that the absolute pore pressures in the undrained tests do not reach a value of -100 kPa. Therefore cavitation was not probable. Tests BC3 and BC8, which were performed on disturbed samples, exhibited reduced rates of pore pressure change after shear strains of about 16%. The reduction in the rate of pore pressure change in these tests was probably due to the effects of disturbance, as opposed to those of cavitation.

4.5.2 Drained triaxial peak states and Bolton's method

The triaxial friction angles of Baskarp Cyclone sand are compared with predictions of Bolton's (1986) empirically derived R_D:p':ϕ'_{max} relationship. Bolton defined a relative dilatancy index as

$$I_R = R_D(Q - \ln p') - R \qquad [4.3]$$

where R_D is the relative density and p' is the effective mean stress at failure, measured in kPa. The constants Q and R are fitting parameters. Bolton found that values of Q = 10 and R = 1 fit the observed behaviour well (of element tests on quartz and feldspar sands, with fine to coarse sizes). The relationship between the peak and critical state friction angles, and the relative dilatancy index, was defined as

$$\phi'_{max} - \phi'_{crit} = 3I_R \qquad [4.4]$$

for triaxial strain and for $0 < I_R < 4$. The upper bound to I_R of four, which was equivalent to a lower bound to p' of approximately 150 kPa at R_D = 100%, was necessary because the dilatancy of sand below effective mean stresses of 150 kPa was found to be relatively insensitive to changes in stress. It should be noted, however, that some investigators observed no reduction in sensitivity above I_R values of four. This was the case for Berlin and Mol sand (de Beer, 1965a).

An abrupt cessation of further increases in dilatancy at points defined by I_R = 4 probably does not occur in practice. But this limitation provided a conservative check on an aspect of behaviour that was not well defined, and that was of little relevance to prototype-size geotechnical problems. In model-size footing tests on dense sand, the relative dilatancy index of the foundation sand is commonly greater than the limiting value of four. The "at rest" horizontal effective stresses associated with the miniature cone penetrometer tests performed in this investigation where also so

low as to produce I_R values greater than four. It was therefore necessary to formulate a theoretical framework for predicting the R_D:p':ϕ'_{max} behaviour of Baskarp Cyclone sand at low stress states. This theoretical framework is outlined in Section 4.5.3 below.

A comparison of the experimental and the theoretical dilation angles is shown in Figure 4.9. The experimental angles are derived from the drained triaxial tests on Baskarp Cyclone sand and the theoretical angles are assumed equal to $3I_R$. Two different methods are used to estimate the experimental angles: one method using the peak and critical state friction angles listed in Table 4.3; and the other using the volumetric and major principal strain increments. The relationship between the dilation angle and the strain increments

$$\phi'_{max} - \phi'_{crit} = 10\left(-\frac{d\varepsilon_v}{d\varepsilon_1}\right)_{max} \qquad [4.5]$$

is derived from the following relationship given by Bolton (1986)

$$\left(-\frac{d\varepsilon_v}{d\varepsilon_1}\right)_{max} = 0.3I_R \qquad [4.6]$$

and Equation 4.4. The quantities $d\varepsilon_v$ and $d\varepsilon_1$ represent the volumetric and major principal strain increments respectively. The experimental results shown in Figure 4.9 are lower than the predictions but the difference is not greater than about 2 °. The experimental dilation angles for the water-saturated tests that are calculated by the two different methods are also similar. The experimental results for the oil-saturated test differed considerably. One would expect the dilation angle in the oil-saturated test to be approximately 2 ° less than in the equivalent water-saturated test, as is the case when the dilation angle is calculated from the friction angles.

The peak friction angles from the drained triaxial tests are compared with the predictions of Bolton's (1986) method in Figure 4.10. A critical state friction angle of 31.5 ° is used in Bolton's method although the angle measured in the triaxial tests is about 33 °. This is because the lower angle produced a better fit between the triaxial data and Bolton's prediction. It is also probable that the critical state friction angles used in the derivation of Bolton's method were measured at larger values of effective mean stress than those measured in the triaxial tests on Baskarp Cyclone sand. From Figure 4.10, it is evident that the difference between the experimental and theoretical values of the peak friction angle is not greater than 2 °. They were of a similar accuracy as observed by

Bolton.

4.5.3 Low stress adjustment to Bolton's method

It was necessary to formulate a low stress adjustment to Bolton's (1986) R_D:p':ϕ'_{max} relationship to predict the friction angle of the sand samples from the miniature cone penetrometer tests. The cone penetrometer was penetrated to a maximum depth of about 200 mm. The maximum horizontal effective stress of relevance to the cone penetrometer tests was 3.4 kPa for R_D = 100%. Substituting these values into Equations 4.3 and 4.4 results in a relative dilatancy index of 7.8 and a peak friction angle of 55 °. This value of I_R was greater than the suggested limit of four and the estimated friction angle is unreasonably high. If the limit of I_R = 4 is adhered to, the estimated friction angles of all of the sand samples would be 43.5 ° (as deduced from Figure 4.10). Thus it was necessary to devise a low stress R_D:p':ϕ'_{max} relationship.

The chosen low stress adjustment to Bolton's (1986) method is shown in Figure 4.11. The friction angles from the triaxial tests and an additional friction angle estimated from the bearing capacity tests of Byrne and Houlsby (1999) (Section 2.3.1 and Figure 2.4) are also included in Figure 4.11. The characteristics of the adjustment are influenced by the following factors:

— In Bolton (1987), the peak friction angle was shown to be less sensitive to changes in the effective mean stress when I_R > 4. An abrupt cessation of further increases in ϕ'_{max} at a specified value of I_R, however, seemed unreasonable. A reduction in the slope of the ln(p'):ϕ'_{max} curve at low stresses was probably more realistic and this characteristic was adopted.

— In Bolton (1987), the effect of the relative density on the peak friction angle (at a constant effective mean stress) was found to be generally the same at low and high values of stress.

The two additional parameters that are required to define the adjusted relationship are: the value of I_R at R_D = 100% at which the slope of the ln(p'):ϕ'_{max} curve changed, denoted I_{RC}; and a parameter a that affected the slope of the adjusted section. The slope of the ln(p'):ϕ'_{max} curves in Bolton's method is sensitive to the factor that I_R was multiplied by in Equation 4.4. This factor is labelled m_H and is equal to three in Equation 4.4. The equivalent parameter in the adjusted section is labelled m_L, and a is defined as the ratio of m_L to m_H. The subscripts "L" and "H" are used to differentiate

between the low and high stress sections, or the adjusted and normal sections shown in Figure 4.11. It is necessary to alter the value of the parameter Q in the adjusted section. The parameter Q_L is defined as

$$Q_L = I_{RC}\left(\frac{1}{a} - 1\right) + Q_H \qquad [4.7]$$

where Q_H is equal to ten. The effective mean stress at the point at which the slope changed is defined as

$$p' = \exp\left[\frac{R_D(aQ_L - Q_H) + R(1-a)}{R_D(a-1)}\right] \qquad [4.8]$$

where R is equal to one.

Sufficient data were not available to rigorously substantiate the chosen characteristics of the low stress adjustment. Only three data points from triaxial tests, and a point that was estimated from the 16 bearing capacity tests performed by Byrne and Houlsby (1999), were available. Thus the chosen values of the parameters I_{RC} and a (I_{RC} = 5.0 and a = 0.2) are somewhat arbitrary. The value of I_{RC} is probably representative if one assumes that the estimated values of ϕ'_{max} and p' for the bearing capacity tests are accurate.

4.6 Characterisation of samples

The relative density parameter is commonly used in the characterisation of sand behaviour. In the case of footings on sand, the bearing capacity is usually correlated to the relative density, via the peak friction angle. The elastic shear modulus, and hence the elastic response of footings, is also estimated from the relative density.

In this investigation, the relative density of the sand base was initially estimated from the volume and the mass of the samples (it was a bulk relative density measurement). Three different sand specimens were prepared. One of the specimens consisted of dry sand and the other two consisted of oil-saturated sand. The specimen used in each of the tests was identifiable by the second character in the test names; for example T**1**01, T**2**04 and T**3**09. The properties of the three sand specimens are listed in Table 4.5. The oil-saturated specimens were recycled *in-situ* to create a number of different samples.

The relative density measurements could not be used to characterise the sand samples because the correlation between the R_D measurements and the footing response was not good. The characterisation stiffness K_{ch} (which was the virgin-penetration stiffness of the footing measured between 400 N and 500 N) was found to be representative of the load:deformation behaviour of the footing. This parameter was used to characterise the sand samples and is plotted against the relative density in Figure 4.12. A similar load:deformation response was observed in tests on different samples in which the relative density measurements ranged from 88% to 102% (compare tests 6, 12, 19 and 20 in Figure 4.12). At these high values of R_D one would expect the response of the footing to be very sensitive to changes in the value of R_D. It was probable that the bulk relative density measurements were not representative of the state of the sand in the top layer of the samples. The samples may not have been uniform. Byrne and Houlsby (1999) found that even when there was a high degree of confidence in their relative density measurements, where the standard deviation of 16 samples (with $R_D \cong 97.3\%$) was only 1.7%, the initial stiffness and bearing capacity varied by ±33% and ±22% respectively.

In the sections below, it is attempted to qualify the degree of uniformity of the samples, and to use the cone penetrometer results to characterise the top layer of the samples.

4.6.1 Uniformity of samples and possible errors in R_D

The uniformity of the density distribution in the samples (along the vertical axis) was investigated using the pore pressures measured in the downward hydraulic gradient tests. The effect on the relative density measurements of a very dense layer of sand is checked. This layer was at the bottom of some of the samples and was not fluidised. The possible sand losses through the filter are also assessed.

A downward hydraulic gradient was induced in the samples by applying an air pressure to the oil surface and allowing the oil to drain from the base of the container. The pore pressure was measured at two points along the wall of the container and it was assumed that the base of the sample was at atmospheric pressure. The permeability of the VYON F filter at the base of the samples was calculated from the manufacturer's specifications. It was also deduced from permeability tests. This was to ensure that the head loss through the filter was relatively small. The

permeability of the filter was estimated to be six times greater than that of the sand samples (Mangal, 1994).

The results from the downward hydraulic gradient tests are shown in Figure 4.13. It was known that there was a 30 mm thick layer of sand at the bottom of some of the samples that were not fully fluidised. In the preparation of the samples for tests T102, T103, and T105 to T108, the samples were not fully fluidised (Section 3.6.3 and Table 3.6). The effect of the dense layer is evident in the downward hydraulic gradient tests shown in Figure 4.13, as the pore measurements in samples T309 to T311 are closer to the theoretical predictions. The downward hydraulic gradient tests seem to indicate that the samples for test T309 and later tests were uniform. Although downward hydraulic gradient tests were not performed on the samples for test T112 onwards, it is assumed that the degree of uniformity in these samples was similar to that in samples T309 to T311. This is because the preparation procedures did not differ. Even though it is probable that the degree of uniformity was similar in the samples of tests T309 onwards, there were large variations in the bulk density measurements of samples on which the load:deformation footing behaviour was similar. Compare tests T311 and T114 in Figure 4.12.

The effect of the layer of sand that was not fluidised on the bulk relative density measurements was estimated. If it is assumed that the relative density of the layer was 100%, then the relative density of the remainder of the sample would have been about 3 % less than the bulk relative density measurement. This error cannot account for the large difference in the bulk relative density measurements of samples T105 and T311 for instance, which exhibited similar load:deformation footing behaviour as shown in Figure 4.12.

Traces of sand were evident in the drainage system beneath the sample containers and it was possible that sand might have leaked into the drainage channels in the base of the sample containers. This could not be verified, however, as the containers were not dismantled. If there was leakage, the dry weight of the samples would have been reduced by only 1%, lowering the relative density measurements by about three points. If the filter was damaged, the probability of this damage occurring would have been highest during the latter stages of the test programme. The large difference between the relative density measurements of samples T317 and T319 (the penultimate and last tests performed on specimen three) could not be explained by the possible

effects of leakage. Since only trace quantities of sand were evident in the external drainage system, it was not probable that the internal drainage channels were filled with sand.

The variability in the values of R_D could not be explained by the possible sources mentioned in the preceding paragraphs. It was most probable that the samples were not uniform. The downward hydraulic gradient method was too crude an instrument. More pore pressures transducers, and a well defined relationship between the density and the permeability, would have increased the usefulness of this method.

4.6.2 Cone penetrometer results

The miniature cone penetrometer tests were performed at the centre and at the sides of the samples, and the majority of these were performed after the footing tests were conducted. Since none of the penetrometer tests were before-centre tests (performed at the centre of the samples and before the footing tests), it was necessary to estimate the before-centre cone tip resistance values. The estimated cone tip resistance values are compared with the behaviour of the footing and used to estimate the relative density of the top layer of the samples.

The relative density, the characterisation stiffness, and the cone tip resistance measurements are listed in Table 4.6. The characterisation stiffness K_{ch} is the vertical virgin-penetration stiffness of the footing measured between V = 400 N and V = 500 N. The values of the cone tip resistance q_c are the average of the various penetrometer tests that were performed on each sample (Section 5.7 and Table 5.2).

The tip resistance between 50 mm and 100 mm of penetration is taken to be representative, as it is assumed that the characteristics of this layer of the sample had a significant effect on the response of the footing. The values of q_c estimated from the penetrometer tests performed at the centre of the samples, and before the footing tests, are also taken to be representative of the undisturbed characteristics of the samples (the before-centre penetrometer tests are taken to be representative). The footing tests might have resulted in disturbance of the samples, and the cone tip resistance from tests performed at the sides of the samples was probably influenced by the boundary conditions of the sample containers.

Estimation of the before-centre cone tip resistance

The measured q_c values shown in Figure 4.14[a] from the tests on samples 2 to 12 indicate a possible linear relationship between the results from the tests at the side and at the centre of the samples. The cone tip resistance at the side is approximately 43% greater than the resistance at the centre of the samples. This relationship is used to estimate the before-centre values for samples 12 to 20, as listed in Table 4.6. A similar relationship shown in Figure 4.14[c] can be deduced when all of the after-centre and after-side results are plotted against the characterisation stiffness.

The results in Figure 4.14[c] indicate that the variation between the cone tip resistance and the characterisation stiffness could be approximated by a linear relationship. This is expected as it is assumed that $\ln(q_c)$ is proportional to ϕ when σ'_h is constant (Houlsby and Hitchman, 1988), and that $\ln(K_{ch})$ is roughly proportional to ϕ as well. Note that a linear relationship is assumed between K_{ch} and the bearing capacity, and hence between K_{ch} and N_γ (Figure 6.9). The standard error in q_c, when predicted from K_{ch}, is less than 200 kPa in the three relationships shown in Figure 4.14[c].

Both before and after penetrometer tests were only performed on two samples (samples 12 and 13) and the q_c values from the tests on one of these samples were spurious. The before-side and after-side results from the test on sample 12 are compared in Figure 4.14[b]. Due to the low confidence in the results shown in Figure 4.14[b], the relationship deduced by comparing all of the before-side and after-side results in Figure 4.14[c] is taken to be representative. Ideally, one would prefer to have a relationship based on a direct comparison of before-side and after-side data. The degree of variability in the K_{ch}:q_c relationships are, however, acceptable. The before/after ratio shown in Figure 4.14[c] is used to estimate the before-centre q_c values for samples 2 to 11, as listed in Table 4.6. The before/after ratio indicates that the disturbance caused by the footing tests resulted in a 40% reduction in the cone tip resistance. Note that the penetrometer results from the tests on the dry sample (the tests on sample T204) are also assumed to be affected by the footing test. It is probable, however, that the disturbance was mostly due to partially-drained loading effects as opposed to the effects of drained shearing. The majority of the disturbance probably occurred at the end of the footing tests when the footing was retracted, inducing uplift forces in the samples.

It is possible to compare two different estimates of some of the before-centre cone tip resistance values. That is, values estimated from measured before-side values and from measured after-centre values. This comparison is shown in Figure 4.15 and indicates that the estimates from the before-side values are generally larger than those from the after-centre values. This discrepancy might have been due to localisation of the disturbance effects and/or the effect of disturbance on the centre/side relationship. The estimated before-centre values of q_c are plotted against K_{ch} in Figure 4.16. This comparison indicates that the data could be fit by a linear relationship. The variability in the q_c values, resulting from the variability in centre/side and before/after relationships shown in Figure 4.14[a] and [c], is acceptable.

Relative density of the top layer of the samples

The bulk relative density measurements were not consistent with the response of the footing. The results from the cone penetrometer tests, however, indicate that the relationship between the cone tip resistance and the characterisation stiffness could be approximated by a linear expression.

Using the cone tip resistance values, it is possible to estimate the relative density of the top layer of the samples (R_D at a depth of about 75 mm). Two bulk measurements of R_D that were assumed to be accurate are used in the development of a R_D:q_c relationship. The two R_D:q_c points are derived from the dry sand sample. This sample consisted of two layers with different values of density.

The methodology of Houlsby and Hitchman (1988) is used to derive a relationship between the relative density and cone tip resistance. Houlsby and Hitchman found that the cone tip resistance (from calibration chamber tests of a cone penetrometer in sand) could be expressed as a function of the effective horizontal stress and of a cone tip resistance factor,

$$q_c = N_h \, \sigma'_h \qquad [4.9]$$

The cone tip resistance factor N_h is related to the peak friction angle as follows,

$$\ln N_h = 0.16\left(\phi'_{max} - 9\right) \qquad [4.10]$$

The above expression was found to fit the results from calibration chamber tests performed by different investigators on a variety of sands. It is necessary to alter the constants in Equation 4.10 to fit the results from the cone penetrometer tests of this investigation. This difference is probably due

to the lower stress states encountered in this investigation, and to the smaller diameter of the cone penetrometer that was used. The peak friction angle of the Baskarp Cyclone sand is estimated using the low stress adjustment to Bolton's (1986) method that is postulated in Section 4.5.3.

The results from the cone penetrometer test at the centre of the dry sample (CP04C) are used to derive two points in ϕ'_{max}:ln(N_h) space as shown in Figure 4.17[b]. The q_c values shown in Figure 4.17[a] are equal to the measured after-centre values multiplied by 1.66. The effective horizontal stress is also plotted in Figure 4.17[a], and the boundary between the two layers is shown. The horizontal effective stress of the sand samples is assumed to be equal to the vertical effective stress, as the earth pressure coefficient K_0 is assumed equal to one. The vibration that was applied during the sample preparation procedure should have countered any overconsolidating effects. The average values of ln(N_h) and ϕ'_{max} from two sections of the cone penetrometer profile (from a section in the top layer and from a section in the denser bottom layer) are shown in Figure 4.17[b]. These two values are used to derive the following expression

$$\ln N_h = 0.6\left(\phi'_{max} - 33.8\right) \qquad [4.11]$$

which is taken to be representative of the penetrometer tests on dry as well as oil-saturated sand. The two ϕ'_{max}:ln(N_h) data points from the test on the dry sample and Equation 4.11 are shown in Figure 4.18[a]. The similar expression given in Houlsby and Hitchman (1988) (Equation 4.10) and the results from the penetrometer tests on the oil-saturated samples are also plotted in Figure 4.18[a]. The peak friction angles of the oil-saturated samples are estimated from the bulk relative density measurements, which are deemed to be unrepresentative, hence the scatter. The oil-saturated peak friction angles estimated using the low stress adjustment to Bolton's (1986) method are reduced by 1.5 ° to account for the degrading effect of the silicone oil. The triaxial tests discussed in Section 4.5.1 indicated that the silicone oil resulted in a 2 ° reduction in the peak friction angle. This was based on a comparison of only two triaxial tests, hence a reduction of 1.5 ° was reasonable.

Although there is considerable scatter in the results from the tests on the oil-saturated samples shown in Figure 4.18[a], it is probable that Equation 4.11 represented the relationship between the peak friction angle of the sand and the cone tip resistance (at a depth of about 75 mm).

The bulk relative density measurements are either greater than or equal to the actual values of the relative density at 75 mm, assuming that the density did not decrease with depth. Thus the peak friction angles deduced from the bulk relative density measurements were either greater than or equal to the actual values of the peak friction angle at 75 mm. The data in Figure 4.18[a] satisfies this criterion.

The penetrometer results, at a depth of 75 mm, and the proposed relationships are also plotted in R_D:q_c space in Figure 4.18[b]. The dry and the oil-saturated tests, as well as the results from different depths, could be described by one expression in Φ'_{max}:ln(N_h) space (Equation 4.11). In R_D:q_c space, however, the result of changes in the effective unit weight, of changes in the depth of penetration, and of the degrading effect of the silicone oil, is evident. Hence the different curves for the dry and oil-saturated tests. The proposed relationship between the cone tip resistance and the relative density for the tests on the dry sample is,

$$q_c = 0.174 e^{0.11 R_D} \qquad [4.12]$$

and for the tests on the oil-saturated samples is,

$$q_c = 0.044 e^{0.11 R_D} \qquad [4.13]$$

The above equation is an approximation of the actual relationship, which is derived from Equation 4.11 and Bolton's method. The relative density values estimated from the cone penetrometer tests are listed in Table 4.6.

5 Experimental Procedure

5.1 Introduction

This chapter describes the model footing test programme and the procedures employed. One main-test was performed on each soil sample. The term main-test refers to a group of events on a single sample. A typical main-test included sub-tests such as partially-drained tests, unload-reload tests, and consolidation tests. The miniature cone penetrometer tests are also described.

The partially-drained tests could be vertical load tests (VP), horizontal load tests (HSS), or moment load tests (MSS). The horizontal and moment load tests were sometimes referred to as combined load tests or sideswipe tests. The partially-drained tests were conducted at different displacement rates to investigate the effects of drainage. The vertical partially-drained tests investigated the effects of drainage on the load:deformation response of the footing. The combined load partially-drained tests investigated the effects of drainage on the combined load yield surface. In the final main-test of this investigation, the partially-drained tests were performed with alternating rates of slow and fast displacement. These multi-rate partially-drained tests were labelled VPM, HSSM, and MSSM tests (vertical, horizontal, and moment load respectively).

The unload-reload tests were performed to investigate the drained elastic response of the footing. Vertical unload-reload tests (ULRL), horizontal load-unload-reload cycles (HCYC), and moment load-unload-reload cycles (MCYC) were performed. The consolidation tests (CONSL) were vertical load tests, and were performed to investigate the rate of pore pressure dissipation.

Generally, two vertical load partially-drained tests and one horizontal load or moment load partially-drained test were performed as part of each main-test. Twenty samples were prepared and twenty main-tests were performed. One of the main-tests was performed on a dry sand sample. The rest of the tests were all on oil-saturated samples. The following number of successful sub-tests were performed: 29 VP tests; two VPM tests; eleven HSS tests; two HSSM tests; eleven MSS tests; two MSSM tests; six CONSL tests; five ULRL tests; two HCYC tests; and two MCYC tests. A chronological list of all the tests is given in Table 5.1.

The main-tests are named using four characters. The first character in all the tests is the letter

"T". The second character is a digit identifying the sand specimen. The last two digits are used to identify the number of the main-test. Three different specimens were prepared. The one dry specimen is denoted specimen "2". Only one main-test was performed on this specimen. The two saturated specimens are denoted specimen "1" and specimen "3". The majority of the main-tests were performed on these saturated specimens. Specimens 1 and 3 were reformed between tests to give 13 and 6 samples respectively. The main-test numbers range from 01 to 20. For example, test T204 is the fourth main-test and was performed on specimen 2. The main-test name and the sub-test character (usually a single digit), separated by an underscore character, identify the sub-test events that were performed within the main-tests. The events are numbered in chronological order. For example, the third sub-test in main-test T105 is labelled T105_3.

It was necessary to quit and restart the control program a number of times during some of the main-tests. On restarting the control program, a letter was attached to the end of the main-test label. For example, the background logging data files for test T313 are labelled T313, T313A, T313B, T313C, T313D, and the sub-test data files are labelled T313A_1, T313C_1, T313D_1. The first sub-test was performed during part A of the main test, the second during part C, and the third during part D. The control program of test T313 was restarted four times. All of the main-test and sub-test data files are listed in Table 5.1.

Different types of data logging were performed. Data was logged continuously by the host PC at relatively slow rates and data was logged by the ADU during the fast sub-tests. Data logging directly onto the host PC was termed "background logging". Two different files were created of this data. Files with extension .OUR contained the raw data (in bits) and files with extension .OUT contained the processed data (in engineering units). The data logged by the ADU was transferred to host PC and stored in two types of files. Files with extension .RAW contained the raw data and files with extension .DAT contained the processed data.

5.2 Test initialisation

A number of procedures were followed before commencing a test. Two pore pressure transducers were attached to the tank. A pore pressure transducer was connected to the footing and the footing was then attached to the base plate (connected to rig via the load cell). The footing was

lowered onto the sand and the LVDT frame was attached to the footing. Input files for the sub-tests, and the definition file that was required to control the tests, were also produced before the QuickBASIC control program on the host PC was started.

The pore pressure transducers attached to the tank (pp_2 and pp_3) were de-aired by a pressure of approximately -60 kPa that was applied to a port located on the top of the adapters. The adapters were used to connect these transducers to the wall of specimen containers. The test rig was bolted onto the sample container and the oil level was set at approximately 50 mm above the surface of the sand. A rubber seal was placed on the pore pressure port on the underside of the footing and the port was filled with oil. The pore pressure transducer was then screwed into the footing, ensuring that air was not present in the port. After connecting the footing to the base plate, the footing was lowered into the oil and rotated to remove air from the underside of the footing. The rubber seal was then removed and the footing was lowered to the sand surface whilst the oil level was simultaneously lowered, by siphoning, to approximately 15 mm. The footing was centred and levelled. The footing was lowered at 0.001 mm/s to a vertical contact load of 10 N. This load was then held for about three minutes.

The LVDT frame was attached to the flange of the sample container and the small LVDTs were attached to the footing. The frame was levelled and adjusted to achieve the specified length between the pin joints of each of the small LVDTs. This adjustment set the lengths of the LVDTs to within ±0.01 mm of the desired values. The actual lengths were then entered in the definition file. The small LVDT measurements were referenced to their initialised values, but these in turn could be referenced to the sample container by the long LVDT measurements. The sand and oil levels were also recorded in the definition file.

The input files that were used to control some of the sub-tests were created before test initialisation. These files could be altered after test initialisation by exiting the control program or by using the "DOS Shell" function.

Once the procedures listed above were performed, the control program was started and the main-test was initialised. The three pore pressure transducer channels and the three load cell channels were set at the middle of their ranges on initialisation (the initial output was set to zero bits). At this stage there was almost no load on the footing as the small vertical contact load had

inevitably been reduced due to infinitesimal movements of the footing. Thus subsequent changes in the load recorded by the load cell were actual footing loads. The output from the pore pressure transducers in the tank were processed using the oil level measurement (stored in the definition file) to give the ambient pore pressure as an initialised value. The pore pressure transducer in the footing was initialised whilst it was approximately 10 mm below the oil surface. This position was taken to have an ambient pore pressure of 0 kPa. This discrepancy was insignificant as it was of the same order of magnitude as the noise level. The output from the six LVDT channels were not offset to give an output of zero bits on initialisation. These transducers normally give an output of zero volts at the middle of their stroke, and the actual position of the armature of the small LVDTs in relation to their bodies was required.

5.3 Main-tests

The test procedure from the initialisation to the end of two typical main-tests, excluding the details of the any sub-tests, is described in this section. The main-test data was logged directly onto the host PC at rates of between one scan per second to one scan every 20 seconds. This type of data logging was termed background logging. Since the PC could not log faster than one scan per second, the sub-tests that required faster logging (sometimes up to 100 scans per second) were initially stored on the ADU. The data on the ADU was then downloaded to the host PC once the sub-tests were completed.

The main-tests were generally conducted at the drained displacement rates, which were $\dot{w}$ = 0.001 mm/s, $\dot{u}$ = 0.001 mm/s, and $\dot{\theta}$ = 0.001 deg/s. The main-test data (or background logging data) was not generally utilised as it was the sub-tests that were important. There were exceptions, however, since it was not necessary to store some of the slower sub-tests (for example the unload-reload tests and a few of the very slow combined load partially-drained tests) on the ADU. These sub-tests, which required scan rates of less than one scan per second, were stored directly on the host PC as part of the background logging data. The drained virgin-penetration stiffness was also deduced from the background logging data. Tests T101 and T114 will be described in the following sections to highlight the typical features of the main-tests.

5.3.1 Test T101

The procedure for T101 was similar to T204, T108 and T309. These tests generally contained two events, an unload-reload test from 1000 N and a sideswipe test (combined load partially-drained test, HSS or MSS) from 1500 N. The sideswipe test of T101, however, was commenced from about 1600 N. Test T108 also only contained one event, an unload-reload test. These tests were performed to derive unload-reload data that was not affected by the possible disturbance caused by previous events.

Time history plots of T101 (using the data from the processed background logging file T101.OUT) are shown in Figure 5.1. The unit of time in Figure 5.1 is seconds. The test lasted about eight hours. The plots are grouped in sets of three. The first set ([a], [b] and [c]) is of the three load components. The moment load in [c] is shown as an equivalent force (the M/2R representation is used). The second set of plots on the first page of Figure 5.1 ([d], [e] and [f]) show the three displacements measured by the long LVDTs. The rotation of the footing in [f] is shown as an equivalent linear displacement (the $2R\theta$ representation is used). The first set of plots on the second page of Figure 5.1 ([g], [h] and [i]) show the displacements calculated from the LVDT frame. The final set of plots ([j], [k] and [l]) is of the pore pressure measurements. The pore pressure measured at the centre of the footing is pp_1, and the measurements taken at the wall of the specimen container are pp_2 and pp_3.

The initialisation procedure was slightly different in T101 than that mentioned in Section 5.2. The footing was embedded to 10 N and the LVDT frame was zeroed after the control program was started. Point A in Figure 5.1[d] indicates the vertical displacement (long LVDT) associated with embedding the footing to 10 N and point B in Figure 5.1[g] indicates the zeroing of the LVDT frame. At point C in plots [d] and [g], the VLDN command (VeLocity DowN, penetration at a constant velocity to a set load limit) was used to set the footing load to 1000 N at 0.005 mm/s. This was intended to be drained penetration but point D in plot [j] indicates that pore pressure generation was associated with this displacement rate. At point E in [d] and [g], the penetration rate was reduced to 0.001 mm/s.

Although the footing was only displaced vertically, the moment load on the footing

increased as indicated by point F in plot [c]. Changes in H and M with changing w were detected in most tests and were probably due to a slightly uneven sand surface. In some of the later tests, the build up in H or M (with increasing w) was reduced by rotating or sliding the footing slightly.

The pore pressure measured beneath the footing exhibited a peculiar cyclic response in test T101 only. The five sets of spikes indicated by points G_1 to G_5 in Figure 5.1[j] were not due to the behaviour of the relevant transducer and associated instrumentation. This was verified by checking the response of the load cell and displacements at the footing. The response of these transducers during the combined load horizontal sideswipe test at G_5 all mimicked that of pp_1. Also, the fact that the frequency of the spikes is fairly constant within each group (as indicated by G_1 to G_5 in Figure 5.1[j]), but differ between groups, indicates that they were probably not due to the instrumentation. Slippage in the vertical drive system did occur at the maximum vertical load but slippage was not detected at lower loads. The changing frequencies between the groups of spikes suggest that they were not caused by slippage in the drive system. The rate of rotation of the vertical stepper motor, the only moving component in the rig, during the periods of groups G_1 to G_5 was constant. It was possible that the foundation soil was shearing in a cyclic fashion because of partially-drained effects, but slippage in the drive system cannot be ruled out as a possible cause as well.

The penetration of the footing was stopped at point H in Figure 5.1[a] and [g] as the small LVDTs were approaching their limit. The LVDT frame was reset and zeroed at point I. This point is shown in plots [g], [h], and [i]. Resumption of penetration is identified by point J in plots [a] and [g]. The footing reached 1000 N at point K and was held at this load for about 8 minutes. An unload-reload loop (ULRL sub-test T101_U) was started at point L. The VLUP command was used to unload the footing to 200 N at 0.001 mm/s. The footing was then held at 200 N before the VLDN command was used (at point M in [a]) to reload the footing to 2000 N at 0.001 mm/s. The unload-reload data file (T101_U.DAT) was created from the background-logging data.

It was not possible to achieve a vertical load of 2000 N as the couple between the lead screw and the vertical stepper motor began slipping at 1700 N (indicated by point N in Figure 5.1[a]). The vertical stepper motor was stopped at point O and a horizontal sideswipe test was commenced (HSS sub-test T101_1). This is obvious from plots [b], [e], and [h]. The test was a drained

sideswipe test ($\dot{u}$ = 0.001 mm/s) that was recorded directly onto the host PC as part of the background logging data. A separate file for this test was created from the background logging file (T101.OUT) and was labelled T101_1.DAT. The sideswipe test was stopped at point P and the footing was displaced back to zero horizontal displacement at point Q. The footing was then retracted at point R. The negative pore pressures induced by the retracting footing are indicated by point R in plots [j] to [l].

5.3.2 Test T114

The procedure for T114 was similar to that of the majority of the other tests. Main-test T114 contained three events, two vertical load partially-drained tests from 500 N and 1000 N (VP sub-tests T114B_1 and T114D_1), and a combined load partially-drained test from 1500 N (MSS sub-test T114E_1). Time history plots of test T114 (using data from the processed background-logging files of T114.OUT to T114E.OUT) are shown in Figure 5.2. The layout of the plots is the same as described in the previous section. The details of T114 are listed in Table 5.1.

At point A (shown in Figure 5.2[a], [d], and [g]) the VLDN command was used to set the footing to a load of 500 N at 0.001 mm/s. As in test T101, the moment load on the footing increased with vertical penetration (indicated by point B in plot [c]).

A fault occurred with the control program at point C, approximately 3200 seconds into the test, and the program was restarted as T114A after about three minutes. When the control program stopped, all the stepper motors could be stopped using the limit switches on the test rig or the stepper motor controller could be switched off. The ADU was not reinitialised on restarting. This ensured that the previous transducer settings were maintained. After restarting, the drained loading of the footing to 500 N was resumed at point D in plot [a]. The footing reached 500 N at point E and stopped automatically as an upper soft limit of 500 N was set on the vertical load. Two types of limits were set in the control program to monitor the transducer measurements (see Section 3.4). A load of 500 N was then held for a couple of minutes at point F before the small vertical stepper motor was changed to the large one. The large stepper motor was used for the very fast vertical moves ($\dot{w}$ = 5 mm/s).

The large vertical stepper motor was used in the two vertical load partially-drained tests (VP)

of T114 as a penetration rate of w= 5 mm/s was required. The stepper motor controller was switched off whilst the small motor was replaced by the large motor. During this time (indicated by point G in [a]) the control program was still running and background logging was maintained. Before communication with the stepper motor controller could be resumed, the control program had to be exited and restarted. The test was restarted as T114B at point H and the load of 500 N was regained and held before commencing the first VP test at point I. This sub-test was run from input file T114_A.INP and its data was stored on the ADU.

The ADU was run in an autonomous state during the fast sub-tests. Communication between the ADU and the host PC was restricted when the ADU was running in this mode. Because of the reduced communication between the ADU and the PC, the PC did not log some of the data of the fast sub-tests at real-time. Consequently, the background logging of the PC did not capture all of the data of the fast sub-tests. Thus the background logging data of file T114B.OUT shown in Figure 5.2, during the sub-test at point I, does not show the full response of the footing. Although the vertical load recorded by background logging does not change by much at point I in plot [a], the sub-test is clearly identifiable by the sudden changes in the vertical displacement and footing pore pressure (see point I in plots [d], [g], and [j]).

Immediately after the sub-test was finished, the test data that was stored on the ADU was automatically transferred to the host PC and stored in files T114B_1.RAW and T114B_1.DAT. Whilst the data from the sub-test was being transferred, background-logging could not be maintained. The data retrieval generally did not last for more than about one minute.

The vertical stepper motors were switched once again at point J after the VP test at 500 N. This was because the drained penetration rate could not be achieved with the large motor. The test was restarted as T114C at point L, and drained vertical penetration was resumed at point M. Once the footing load reached 1000 N at point N in Figure 5.2[a], the above procedure was repeated. That is, the load was held, the stepper motors were switched, the control program was restarted, input file T114_B.INP was run (point O in [a], [d], [g], and [j]), the sub-test was transferred to the host PC (files T114D_1.RAW and T114D_1.DAT), and the stepper motors were switched back. And finally, the control program was restarted as T114E at point P.

After the VP test at 1000 N, the footing was penetrated to 1500 N at point Q and held before

commencing the combined load partially-drained test at point R. In this moment sideswipe test (MSS), the footing was rotated at $\dot{\theta}$= 0.2 deg/s (d(2$R\theta$)/dt = 0.524 mm/s). This sub-test was characterised by a sudden reduction in the vertical load in [a], an increase in the moment load in [c], an increase in the rotation in [f] and [i], an increase in the vertical penetration in [g], and a reduction in the pore pressure in [j]. The sub-test was run from input file T114_C.INP and stored in files T114E_1.RAW and T114E_1.DAT. After the sideswipe, the footing was slowly retracted and the loads were reduced between points S and T. The footing was moved to its initialisation position at point T.

5.4 Partially-drained tests

The vertical load partially-drained tests (VP) were conducted at 500 N and 1000 N. The fastest of these tests (at $\dot{w}$= 5 mm/s) required the large vertical stepper motor. When the large motor was required, the motors were changed just before the VP tests. After the VP tests, the large motor was replaced by the small one.

Most of the combined load partially-drained tests were conducted from 1500 N. The combined load partially-drained tests are also referred to as horizontal or moment sideswipe tests (HSS or MSS tests). In some of the later main-tests, additional sideswipes tests were conducted at higher vertical loads than 1500 N.

The initial vertical load and the displacement rate of the partially-drained tests are listed in Table 5.1. Details of the VP, HSS, and MSS tests (including the multi-rate tests) are also listed in Table 6.6, 7.1, and 7.2 respectively. The procedures involved in the vertical and combined load partially-drained tests will be described in the following sections.

It should be noted that the footing displacements referred to were the displacements measured by the LVDT frame and not those measured by the long LVDTS.

5.4.1 Vertical load

The vertical load partially-drained tests (VP) were run from input files that were created before the main-tests were commenced. Each of these input files contained six commands, together with the parameters associated with these commands. The commands in the input file were read by the control program, which then performed the routines associated with the commands.

A typical input file is shown in Figure 5.3. This input file was used to control the VP test of T114 that was performed from 500 N (T114B_1, see Table 5.1). The first LIMITS command in Figure 5.3 was used to set the load soft limits that were active during the move event. Lower and upper limits were set. These were the loads at which the control program would automatically stop all the stepper motors. The vertical load soft limit was used to ensure that a VP test did not overshoot the vertical load from which the next sub-test was to be conducted. The effectiveness of this check was dependent on the speed of the load feedback mechanism in the control program and it was not reliable for fast tests.

The MTEST (move test) command in Figure 5.3 was used to allot and activate the test on the ADU, whilst simultaneously commanding the stepper motors to move the footing a finite distance at a specified velocity and acceleration. All three stepper motors could be moved at the same time with this command. For the VP tests, however, only parameters for the vertical stepper motor were included. The parameters in the first line of the MTEST command were used to set the test logging parameters required by the ADU. These were the test time in seconds and the number of scans per second. The time delay was used to set the delay between the start of ADU testing and the start of the footing displacements. The last three lines of the MTEST command contained the displacement parameters for the three axes of the stepper motor controller (w, u, and θ). The base speed was an extra parameter that was required by the vertical axis because two different stepper motors were sometimes used on this axis. A displacement of 1.5 mm was used in tests T101 to T107. This was reduced to 0.5 mm in the later tests because it was found that the relevant behaviour could be captured by smaller displacements. The displacement parameter in the MTEST command was also kept low so that a test would stop before reaching too high a vertical load.

A different set of soft limits was set immediately after the MTEST was complete in the input file in Figure 5.3. This was to accommodate any loads that overshot the initial limits. The ADUSTORE command was used to retrieve the test data from the ADU to the host PC. The MOVE command could be used to move the footing a finite distance. For example, back to its initial position before the VP test. But this command was only used to reset the base speed of the vertical stepper motor. At the END command, the input file was closed and the user regained access to the control program.

The scan rate chosen for each test was dependent on the displacement rate. Each test was comprised of three sections. An initial "delay" section before the move commenced (generally between $t = 0$ s and $t = 1$ s). A middle section during which the footing was displaced (the duration of this part of the test was dependent on the displacement rate). And a final part that captured the dissipation of pore pressures once the move had stopped.

The load, displacement, and pore pressure load time history of a slow VP test displaced at 0.01 mm/s is shown in Figure 5.4. The time history is that of test T317_1, which was controlled by input file T317_A (see Table 5.1). The logging and move parameters of test T317_1 are shown in Figure 5.4[b]. The ADU was set to log for 56 s and five scans were taken every second. The delay between the start of ADU logging and the start of stepper motor activity was set at one second. The three distinct sections of the VP test are indicated in plot [a].

The scan rate was adjusted to derive an adequate number of scans during the move section. In the slowest tests at $w = 0.01$ mm/s, the number of scans during the move section ($\cong 0.5$ mm) was limited to about 250. This limit was imposed to minimise the size of the data files. The total number of scans in a VP test was limited to about 500.

The move parameters sent to the stepper motor controller are listed in the second line below the MTEST command in Figure 5.4[b]. The first number was the magnitude of the move (MR), the second was the velocity (SV), and the third was the acceleration (SA). A base speed (SB) of 0.01 mm/s was also set. These move parameters are explained in Figure 3.6. The base speed was the velocity at which the footing started accelerating up to the required velocity. Since the base speed and the velocity were the same, the acceleration time was equal to zero.

The magnitude of the move in the MTEST command in Figure 5.4[b] was set at 0.5 mm but the measured displacement increment was less. It was equal to about 0.37 mm. The displacements implied by the stepper motors were not always equal to the displacements at the footing. This difference was due to the flexibility in the rig (the rig was not infinitely stiff). The ratios of the measured displacements to the intended displacements decreased as the stiffness of the sand samples increased. The rate of increase in the load and the pore pressure in Figure 5.4 was higher at the start of the move (between $t = 2$ s and $t = 6$ s). The rates then decreased to practically constant

values. This form of response was evident in most of the VP tests.

In the fastest tests at w = 5 mm/s, only 10 scans could be logged during the 0.5 mm move sections. The maximum scan rate of the ADU was 100 scans per second. The load, displacement, and pore pressure load time history of a fast VP test displaced at 5 mm/s is shown in Figure 5.5. The time history is that of test T114B_1, which was controlled by input file T114_A (see Table 5.1). The logging and move parameters of test T114B_1 are shown in Figure 5.5[b]. The relative size of the move section, and the quantity of data within, is small in relation to the rest of the test. Only about five percent of the data from the whole test is particularly useful. This data is shown in the inserts. Although the data from the very fast moves was limited, it was sufficient to define the load:deformation response. The rate of increase in the load, shown in the enlargement in Figure 5.4[a], was higher at the start of the move (between t = 1.18 s and t = 1.20 s). The rate then decreased to a constant value. As mentioned previously, this form of response was evident in most of the VP tests.

The number of scans in the first 0.05 mm of the move sections was important as it was noticed that the initial footing response was different from the subsequent response at larger displacements. In the fastest tests, only about two scans could be made during this initial part of the move sections. This is illustrated in Figure 5.5[a] by the data points in the enlargement of the move section. The ratio of acceleration to velocity was generally set at a value of 20 or more. In the fastest tests, where the duration of the move section was only about 0.1 s, a ratio of 50 was used to reduce the acceleration time. The base speed was also set at or close to the intended velocity.

Multi-rate tests

Vertical partially-drained tests with multiple displacement rates (VPM) were performed in main-test T120. These tests were conducted from 500 N and 1000 N and each was comprised of three sequences of events. Each sequence was comprised of two moves, a slow move and a fast move. In effect, six moves were run in immediate succession, a slow move at w = 0.01 mm/s alternating with a fast move at w = 1 mm/s. This form of displacement path was used to check the response of the footing to successive changes of displacement rate, and also to check if the response was similar to that in the normal vertical tests (VP tests).

The six daisy-chained moves of the VPM tests were run from a single input file. The input file was similar to that used in the VP tests (see Figure 5.3), but the MTEST command was replaced by three SEQTEST1 commands and the MOVE command was not included. The input file used to control the VPM tests is shown in Figure 5.6[a] (the same input file was used to control the VPM test from 500 N and the one from 1000 N). The SEQTEST1 command instructed the ADU to start logging and then ran subroutine SEQMOVE1 in the control program. The move parameters of the sequence event were not included in the SEQTEST1 command in the input file, these parameters were programmed directly into the subroutine SEQMOVE1 in the control program. This subroutine is listed in Figure 5.6[b]. Subroutine SEQMOVE1 sent a sequence, comprising two move events, to the stepper motor controller. The details of the moves are explained in Figure 5.6[b] (the move commands used to communicate with the stepper motor controller are illustrated in Figure 3.6).

Firstly, the details of the sequence are defined and sent to the stepper motor controller (lines one to eleven of the code in Figure 5.6[b]). The sequence is then executed at line twelve of the code. The total displacement of the three sequences was 0.48 mm and the total logging time was 19.3 s. Three output files were created of the events associated with input file T120_A.INP (one for each SEQTEST1 command). For the VPM test from 500 N, these are named T120A_1, T120A_2, and T120A_3. The test from 1000 N produced output files T120C_1, T120C_2, and T120C_3. A chronological list of the tests is given in Table 5.1.

The load, displacement, and pore pressure load time history of the test from 1000 N will be used to describe the typical characteristics of the VPM tests. The time history is shown in Figure 5.7. The VPM test is composed of three output files and these are plotted together in Figure 5.7. The time delay between the tests is estimated from the rate of pore pressure dissipation at the end of a test and the pore pressure at the start of a subsequent test (the pore pressure load U is shown in Figure 5.7[b]). There is a delay of about one second between the start of ADU logging and the start of the slow move in the first sequence (stored in T120C_1). The subsequent sequences do not include this time delay since ADU logging and the moves are started simultaneously. Although the displacement increment of the slow moves was set at 0.06 mm (see Figure 5.6[b]), the corresponding increment in the first sequence was only about 0.02 mm and in the last two

sequences they were about 0.05 mm. This was due to the flexibility of the rig. The displacement increments of the fast moves were about 0.06 mm. These were set at 0.1 mm.

5.4.2 Horizontal load

Most of the horizontal load partially-drained tests (HSS) were run from input files. The slowest tests at $\dot{u}$ = 0.001 mm/s, however, were logged directly onto the host PC as part of the background logging. The input files of the HSS tests were similar to those of the vertical load partially-drained tests (described in the previous section and shown in Figure 5.3). The only significant differences were in the LIMITS and MTEST commands. The MOVE command was also excluded from the input files of the HSS tests. In the LIMITS command, appropriate horizontal load soft limits were entered. These were generally H = -500 N to H = 500 N. The horizontal displacement parameters (u, $\dot{u}$ and $\ddot{u}$) were entered in the third line of the MTEST command.

The time history of a slow horizontal sideswipe test (HSS test T309_1) is shown Figure 5.8. The horizontal velocity in this test was 0.001 mm/s and the test lasted about 70 minutes. Test T309_1 was not run from an input file. It was manually controlled from the host PC. This was because the required logging rate was low. The PC was set to log at one scan every ten seconds during this test. The data file for this test (T309_1.DAT) was created from the background logging file (T309.OUT).

The start of the HSS is indicated by point A in Figure 5.8. The horizontal load and moment are not equal to zero at the start of the test. The initial horizontal load is about 20 N and the moment is about 40 N. These loads developed during the preceding vertical loading stage. The footing was loaded to V = 1500 N before the HSS test was started (as shown in plot [a]). At the start of horizontal displacement at point A, the horizontal load (in [b]) increases immediately even though the increase in the horizontal displacement (in [e]) is very small. The initial slope of the t:du curve in plot [e] is not linear because of the interaction between the horizontal flexibility of the rig and the changing stiffness of the footing response. After about 2000 seconds, the horizontal velocity is approximately constant. The vertical load shown in Figure 5.8[a] reduces throughout the test, but the change in the moment shown in plot [c] is small. The rotational displacement shown in

[f] increases slightly because of the increase in horizontal load. The penetration of the footing shown in [d] also changes. This was because of the vertical flexibility of the rig. The pore pressure load shown in [d] decreases at a constant rate throughout the test, but increases sharply at point B when the horizontal displacement is stopped.

The time history of a fast horizontal sideswipe test (HSS test T107A_3) is shown Figure 5.9. The horizontal velocity in this test was 0.4 mm/s and the test lasted for about eleven seconds. Test T107A_3 was run from input file T107_D.INP. The MTEST parameters of the input file are listed in Figure 5.9[a]. The ADU was set to log for 13 s and to take 40 scans every second. A delay of one second was also set. The move parameters that were sent to the horizontal axis of the stepper motor controller specified a move of three millimetres. The three sections of the HSS test are outlined in Figure 5.9[b]. These were similar to the sections of the vertical partially-drained tests.

The response of the footing in T107A_3 was broadly similar to that in the slow HSS test previously described (T309_1). The vertical load reduced, and the vertical and rotational displacements increased. A small negative moment shown in [c] was associated the HSS test. The total horizontal displacement was also less than the input value of 3 mm.

Multi-rate tests

Multi-rate horizontal partially-drained tests (HSSM) were performed in main-test T120. Two multi-rate sideswipes were performed, one from 1500 N and the other from 1700 N. The sideswipe from 1500 N was run from a single input file (T120_B.INP) and included five sequences. This input file was similar to that used for the multi-rate vertical tests. It included five SEQTEST2 commands. Each of these called a subroutine named SEQMOVE2 in the control program. This subroutine defined and executed a sequence that included two moves. There was a slow move at 0.001 mm/s and a fast move at 0.1 mm/s. Each sequence, or set of two moves, resulted in one output file. In effect, ten moves were made in immediate succession and generated files T120D_1.DAT to T120D_5.DAT.

Once the multi-rate moves had stopped and the input file had returned control to the interactive menu on the host PC, the footing was displaced horizontally at 0.001 mm/s under manual control. The data from this manually controlled section formed part of the HSSM test from 1500 N, and was extracted from the background logging file (T120D.OUT) and saved as

T120D_5A (see Table 5.1).

The sideswipe from 1700 N was run from input file T120_C.INP and was displaced in the negative horizontal direction (to the left). This file included six MTEST commands. Each MTEST command was used to perform a single move and generated a single output file. Slow and fast MTEST commands were alternated and these generated output files T120D_6.DAT to T120D_11.DAT. This form of testing was used to overcome a drawback of the sequence tests used in the sideswipe from 1500 N. In the sideswipe from 1500 N, the logging rate was fixed for the duration of each sequence. Thus there were only five scans during the fast moves. By running each move as a separate (MTEST) test, appropriate logging rates could be used. It was also possible to increase the magnitude of the move events. The only problem with the MTEST command was that there was a slight time delay between each of the MTESTs.

The sideswipe from 1700 N was continued after the events associated with input file T120_C.INP were complete. The sideswipe was continued (by manual control) at the drained displacement rate for about six minutes before input file T120_C.INP was once again run. The data of this drained section was extracted from the background logging file and stored as T120D_11A. The second execution of T120_C.INP generated output files T120D_12.DAT to T120D_17.DAT (see Table 5.1).

The time history of the HSSM sideswipe from 1700 N is shown in Figure 5.10. The filenames of the MTEST events are shown in Figure 5.10[b]. The first six files were created by the first execution of input file T120_C. The middle section between $t \cong 330$ s and $t \cong 730$ s (T120D_11A) is the manually controlled move at 0.001 mm./s. The last six filenames indicate the MTEST events associated with the second execution of the input file.

The fast events of the HSSM test resulted in a rapid decrease in the horizontal load and displacement (see Figure 5.10[b] and [e]). The changes in the horizontal load and displacement were negative because the footing was displaced in the negative horizontal direction. The pore pressure load increased during the fast events. This is evident from the spikes in the profile of U in plot [d]. The pore pressure was not equal to zero at the start of the test but the initial excess pressure was only 0.5 kPa. The response of the vertical load and displacement, shown in [a] and [d], is similar to that observed in the normal horizontal sideswipe tests (the HSS tests previously

discussed). Small changes in the moment and rotational displacement are also evident.

5.4.3 Moment load

The procedures for the moment load partially-drained tests (MSS) were the same as for the HSS tests (described in the previous section). The slowest tests at $\dot{\theta}$ = 0.001 deg/s ($2R\dot{\theta}$ = 0.0026 mm/s) were logged directly onto the host PC as part of the background logging. In the fast tests run from input files, appropriate moment load soft limits were entered in the LIMITS command. These were generally M = -30 Nm to M = 30 Nm (or $M/2R$ = ±200 N).

The time history of a slow moment sideswipe test (MSS test T311_3) is shown in Figure 5.11. The rotational velocity in this test was 0.0026 mm/s and the test lasted about 40 minutes. Test T311_3 was manually controlled from the host PC. The PC was set to log at one scan every five seconds. The data file for this test (T311_3.DAT) was created from the background logging file (T311.OUT).

The start of the MSS is indicated by point A in Figure 5.11. The footing was loaded to V = 1500 N before the MSS test was started (as shown in plot [a]). Displacement starts at point A in plot [c], and finishes at point B. The vertical load shown in Figure 5.11[a] reduces throughout the test. The change in the horizontal load shown in plot [b] is significant. In the sideswipe tests on the stiff samples, the passive component of the combined load also changed. The change in the horizontal displacement shown in [c] is negligible and the penetration of the footing shown in [d] increases by about 0.4 mm. This was because of the vertical flexibility of the rig. The pore pressure load shown in [d] decreases to a constant value, but increases at point B when the rotational displacement is stopped.

The time history of a fast moment sideswipe test (MSS test T114E_1) is shown Figure 5.12. The rotational velocity in this test was 0.524 mm/s (0.2 deg/s) and the test lasted for 26 s. Test T114E_1 was run from input file T114_C.INP. The MTEST parameters of the input file are listed in Figure 5.12[a]. The ADU was set to log for 26 s and to take 20 scans every second. A delay of one second was also set. The move parameters that were sent to the rotational axis of the stepper motor controller specified a move of three degrees. The three sections of the MSS test are outlined in Figure 5.12[c].

The response of the footing in T114E_1 was broadly similar to that in the slow MSS test previously described (T311_3). The vertical load reduced and the vertical displacement increased. There was a slight increase in the horizontal displacement as well. The horizontal load shown in [b] reduces by about 40 N. The total rotational displacement shown in [f] is also less than the input value of 7.9 mm (3 °). The pore pressure shown in [d] increases at the start of the move before reducing at an almost constant rate.

Multi-rate tests

Multi-rate moment partially-drained tests (MSSM) were performed in main-test T120. Two multi-rate sideswipes were performed, one from 1900 N and the other from 2100 N. The sideswipe from 1900 N was run from a single input file (T120_D.INP) and included five sequences. This input file was similar to that used for the multi-rate horizontal tests. It included five SEQTEST4 commands. Each of these called a subroutine named SEQMOVE4 in the control program. This subroutine defined and executed a sequence that included two moves. There was a slow move at 0.0026 mm/s and a fast move at 0.26 mm/s (0.001 deg/s and 0.1 deg/s). Each sequence, or set of two moves, resulted in one output file. In effect, ten moves were made in immediate succession and generated files T120D_18.DAT to T120D_22.DAT.

The sideswipe from 1900 N was continued after the events associated with input file T120_D.INP were complete. The sideswipe was continued (by manual control) at the drained displacement rate for about ten minutes before input file T120_D.INP was rerun. The data of this drained section was extracted from the background logging file and stored as T120D_22A. The second execution of T120_D.INP generated output files T120D_23.DAT to T120D_27.DAT (see Table 5.1).

The sideswipe from 2100 N was run from input file T120_E.INP and was displaced in the negative rotational direction (anti-clockwise). This file included eight MTEST commands. Each MTEST command was used to perform a single move and generated a single output file. Slow and fast MTEST commands were alternated and these generated output files T120E_1.DAT to T120E_8.DAT.

The time history of the MSSM sideswipe from 1900 N is shown in Figure 5.13. The filenames of the SEQTEST4 events are shown in Figure 5.13[e]. The first five files were created by

the first execution of input file T120_D. The middle section between $t \cong 200$ s and $t \cong 600$ s (T120D_22A) is the manually controlled move at 0.0026 mm./s. The last five filenames indicate the SEQTEST4 events associated with the second execution of the input file.

The fast events of the MSSM test resulted in a rapid increase in the moment load and displacement (see Figure 5.13[c] and [f]). The pore pressure load increased during the first two fast events but decreased during all the other fast events. This is evident from the spikes in the profile of U in plot [d]. The pore pressure was not equal to zero at the start of the test but the initial excess pressure was only 0.6 kPa. The response of the vertical load and displacement, shown in [a] and [d], is similar to that observed in the normal moment sideswipe tests (the MSS tests previously discussed). The horizontal load was not zeroed before the MSSM test. The initial horizontal shown in Figure 5.13[b] is equal to about -40 N and this load increased slightly during the test.

5.5 Unload-reload loops

The unload-reload loops were performed to investigate the elastic response of the footing. Five vertical unload-reload loops, and two load-unload-reload horizontal and moment loops, were performed.

5.5.1 Vertical loops

The first four ULRL tests were unloaded from 1000 N and the last was unloaded from 1900 N. The ULRL tests are listed in Table 5.1. The ULRL tests were controlled manually from the host PC and the test data was extracted from the relevant background logging files. The tests were initiated from the virgin-penetration curve and the footing was unloaded and reloaded at the drained displacement rate (0.001 mm/s). The VLUP command (VeLocity UP, retraction of the footing at a constant rate) was used to unload the footing and the VLDN command was used to reload the footing. A load of 200 N was set as the lower soft limit in all the tests except the last. In T118E_U, the footing was unloaded to 190 N. The unloading of the footing stopped automatically when the lower soft limit was reached. An upper soft limit was used to control the reloading phase. The minimum load was held for a few minutes before the footing was reloaded.

5.5.2 Horizontal and moment loops

The horizontal and moment cycles (HCYC and MCYC tests) were performed in main-test T120. These tests were controlled manually from the host PC and the test data was extracted from the relevant background logging files. The data files are listed in Table 5.1. The footing was unloaded vertically from 1000 N to 500 N before the first set of cycles. And before the second set of cycles, the footing was unloaded vertically from 1500 N to 1000 N, and also horizontally from about 250 N to 0 N. The cycles were performed at the drained displacement rates and the constant velocity commands, in combination with the soft load limits, were used to control the tests. The cycles were initiated from a horizontal and moment load of zero, and the maximum and minimum soft limits were set at about ±50 N (in both types of test).

5.6 Consolidation tests

Six consolidation tests (CONSL) were performed, three in main-test T118 and three in main-test T319. The CONSL tests were run from input files and were initiated at a vertical load of 700 N. Each set of three CONSL tests were run from a single input file. The input file contained an initial LIMITS command and three HTEST commands. An ADUSTORE and an END command were also included. The HTEST command set the logging parameters for the ADU (test length = 120 s, scans per second = 2, and delay = 1) and started ADU logging. It also set the parameters for the HOLD routine in the control program, as well as starting the routine. The HOLD routine was used to load (or unload) the footing, and to hold the target load by using a load feedback mechanism. The first and third HTEST commands loaded the footing from 700 N to 900 N, and the second unloaded the footing from 900 to 700 N. The target loads were held for 120 s and a tolerance of ±3 N was set. If the load moved out of the tolerance range, the footing was moved slightly to regain the target.

The consolidation tests performed in main-test T319 are shown in Figure 5.14. These three tests were run from input file T319_B and were stored as data files T319B_1 to T319B_3. In the first test shown in Figure 5.14[a], the footing is loaded from 700 N to 900 N and the target load is reached after about 20 s. It was hoped that the footing would reach the target load very quickly, as it does in the other two tests. The effectiveness of the HOLD routine was dependent on the stiffness

of the footing and the routine was programmed to work best at a particular stiffness. The routine was programmed to be effective at the elastic (or unload-reload) stiffness of the footing. Positive pore pressures are associated with the loading and reloading tests shown in Figure 5.14[b] and negative pressures with the unloading test. Most of the displacement shown in plot [c] occurs during the first test.

After the three HTEST events, the ADUSTORE command in the input file instructed the control program to download the test data from the ADU to the host PC. The END command returned the control program to manual operation.

5.7 Miniature cone penetrometer tests

The procedure for the cone tests was similar to that of the main-tests as the cone was attached to the rig. The footing was removed from the base plate and the bracket for the penetrometer was attached. The LVDT frame was not used in the cone tests. The long LVDT was used to measure the displacement of the cone. A QuickBASIC program similar to that used in the main-tests was used to control the cone tests. The cone tests were logged directly onto the host PC and one scan was usually taken every six seconds. The cone was penetrated between 100 mm and 170 mm into the sample. A penetration rate of 0.1 mm/s was used in most of the tests. This rate was calculated to ensure drained penetration, but the pore pressure was not measured so the drainage conditions could not be verified.

Cone tests were not performed on the first sample. On each of samples two to eleven, two tests were performed after the main-tests (footing tests). Between three and five cone tests were performed on each of samples 12 to 20, and some of these were before the main-tests. Tests were performed before the main-tests to check the progress of densification. The details of the cone tests are listed in Table 5.2. The different tests on a sample were performed in one of five locations. These were either at the centre or at the side of the sample. The tests at the side were either at the back, front, left, or right of the sample. The tests at the sides of the samples were located 75 mm from the tank wall, which was equivalent to 75 mm from the edge of the footing.

6 Results: Vertical Loading

6.1 Introduction

The drained load:deformation response, the consolidation behaviour, and the partially-drained behaviour of the footing is analysed. A partially-drained consolidation model is also developed.

The footing was not loaded to failure but bearing capacity estimates are compared with the drained load:deformation behaviour. The footing was subject to creep and this response is investigated. Elastic parameters are also derived from the unload-reload loops. The partially-drained consolidation model was used to deduce consolidation parameters from the consolidation tests. The consolidation tests were partially-drained. The model simulations were good when the response of the footing was mainly elastic. A framework for modelling the total stress response of the partially-drained tests is outlined.

6.2 Drained loading

The load:penetration behaviour of the footing was assumed to be fully drained at a vertical displacement rate of 0.001 mm/s. During virgin-penetration at this displacement rate, the pore pressure beneath the footing did not increase with increasing load. At very low loads, however, even small increases in the pore pressure did affect the load:deformation behaviour of the footing and this is discussed below. The tests only investigated behaviour at loads significantly below the bearing capacity, but estimates of the failure loads are discussed below. These estimates were based on the virgin-penetration stiffness measurements and the cone-penetrometer results. The creep response and the unload-reload behaviour of the footing are also investigated.

6.2.1 Bedding-in phase and associated pore pressure response

In some of the tests, the initial load:deformation behaviour of the footing, from $V = 0$ N to about $V = 100$ N, indicated that there was a thin layer of loose soil above the densified sample. The low virgin-penetration stiffness encountered at low loads could also have been caused by an uneven sample surface. A few virgin-penetration curves that illustrate the effect of a loose layer of soil on

the load:deformation behaviour are shown in Figure 6.1. The response in each test became consistent above a load of about V = 100 N. The footing stiffness measured between V = 400 N and V = 500 N was used to characterise the samples and was labelled the *characterisation stiffness* (as discussed in Section 4.6).

The displacement in T101 was greater than that in T108 even though the load:deformation behaviour at higher loads was similar, as shown in Figure 6.1. When considering the load:deformation curve at higher loads, as in Section 6.2.2 below, one should subtract the displacement associated with the anomalous initial response. One way of doing this is to assume that if a loose layer was not present the initial stiffness would have been similar to the stiffness at a higher load level. This procedure was followed in the comparison of virgin-penetration curves in Section 6.2.2. The stiffness from V = 200 N to V = 400 N was used and the procedure is illustrated in Figure 6.2. Tests T101, T204, T108 and T309, the tests used to describe virgin-penetration behaviour in the following section, are shown in Figure 6.2 with suggested virgin-penetration lines extrapolated down to the displacement axis.

The anomalous initial response could not be explained by the miniature cone penetration results. For example, consider the load:deformation curves of tests T103 and T108 shown in Figure 6.1. The characterisation stiffness of these two tests was roughly similar, 112 N/mm and 99 N/mm respectively, but the load:deformation curves were different. The response of T103 indicated the likelihood of a loose layer of soil. The cone penetration curves shown in Figure 6.3, however, did not suggest that the sample used in T108 was any stiffer than that used in T103. This may have been due to a lack of sensitivity in the cone-penetrometer measurements.

The pore pressure measurements at the centre of the footing supported the idea of a loose layer of soil as the cause of the anomalous initial footing response. The vertical load, pore pressure load, and effective load responses of the tests that are shown in Figure 6.1 are plotted in Figure 6.4. It is evident from Figure 6.4 that the effective loads in the tests with an anomalous initial response, particularly T102, T103 and T105, are almost equal to zero. Test T101 cannot be used in this comparison because the footing was initially penetrated at $\dot{w}$ = 0.005 mm/s before being slowed (at $w \cong 3$ mm) to a rate of $\dot{w}$ = 0.001 mm/s, the rate used in the other tests. The pore pressure loads

are calculated using Equation 2.30. A value of C_p = 0.5 was used to calculate the pore pressure loads in Figure 6.4. This value is representative of a parabolic pore pressure distribution, as discussed in Section 2.6. The initial response of tests T101, T102, T103 and T105, shown in Figure 6.4, was probably fully undrained, because of the loose layer of sand, and indicated that a value of C_p = 0.5 was appropriate. This value of C_p was deemed suitable because the effective load was greater than or equal to zero.

6.2.2 Virgin-penetration stiffness

The footing was subjected to a maximum vertical load of about V = 1500 N in most tests. Load:deformation curves of the main tests, those that did not include partially-drained sub-tests, are shown in Figure 6.5. Note that the unload-reload sub-tests, but not the sideswipe sub-tests, are shown in Figure 6.5. None of these tests except T108 exhibited softening behaviour. This indicated that the loads involved were probably well below the bearing capacity loads. In most of the tests, the virgin-penetration stiffness was still increasing at the maximum vertical load encountered. The virgin-penetration stiffness values are listed in Table 6.1. These values were measured over four load ranges in most of the tests, at 100-200 N, 400-500 N, 900-1000 N and 1400-1500 N. The values from Table 6.1 are shown in Figure 6.6. The stiffness measurements are plotted against the characterisation stiffness and best-fit lines (with zero intercepts) are included. The best-fit lines highlighted the general trend of increasing stiffness with rising load. This behaviour was not restricted to the tests on saturated samples because test T204 exhibited similar behaviour, only at loads higher than 500 N.

The characterisation stiffness values were compared to similar quantities from footing tests in the literature in Figure 6.7. The different tests should all follow a similar relationship since the initial stiffness is normalised by the radius. Some of the R_D:$(k_p/R^2\gamma')$ data could be approximated by an exponential relationship. The tests of Vesic (1975) and of Gottardi and Houlsby (1995) did not fit the trend. An exponential relationship between the initial stiffness and the relative density can be postulated from bearing capacity theory if it is assumed that the initial stiffness is proportional to the bearing capacity load, and hence to the bearing capacity factor.

6.2.3 Bearing capacity estimates

The discussion of load:deformation behaviour in Section 6.2.2 indicated that the maximum loads that the footing was subjected to were probably below the bearing capacity loads. The bearing capacity loads are estimated in this section. The characteristics of the estimation are as follows:

— The estimates of the relative density from the cone-penetrometer tests, as opposed to the bulk relative density measurements (Section 4.6.2), are used in the calculation of the peak friction angle.

— The R_D:p':ϕ'_{max} relationship outlined in Section 4.5.3 is used to calculate the peak friction angle. Note that the peak friction angle in the oil-saturated specimens was reduced by 1.5° and the effective mean stress along the failure surface is assumed equal to a tenth of the contact stress.

— The bearing capacity factors of Bolton and Lau (1993) for rough footings are used.

— Estimates of the bearing capacity load are incorporated into the Hardening Rule described by Equation 2.20.

The bearing capacity estimates are shown in Figure 6.8, and are also listed in Table 6.1. The bearing capacity of the specimen in test T204 (the dry specimen) was estimated at about 10 kN. The relative density in the top layer of this specimen was 79%. The bearing capacity estimates for the tests on the oil-saturated specimens varied from 2 kN to 8 kN (that is, test T108, and tests T309 and T313). The relative density values of the oil-saturated specimens varied from 54% to 91%. The variation of the bearing capacity caused by a ±1° variation of the peak friction angle is also indicated in Figure 6.8. For the dry specimen, a ±30% change of the bearing capacity was predicted for the aforementioned variation of the peak friction angle.

Byrne and Houlsby (1999) measured the bearing capacity of a 50 mm diameter footing on dry Baskarp Cyclone sand at approximately 900 N, at a relative density of 95%. Their bearing capacity factors were similar to the theoretical factors, if one calculated the peak friction angles using the low stress adjustment to Bolton's method that was outlined in Section 4.5.3. It is probable that the bearing capacity estimates shown in Figure 6.8 are representative, since the bearing

capacity factors of Byrne and Houlsby's tests are similar to those suggested by Bolton and Lau (1993).

The estimated values of the bearing capacity and the measured values of normalised initial stiffness are compared with some results from the literature in Figure 6.9[a]. The results from tests with the same size of footing (covering a range sand densities) should all follow a similar relationship since the initial stiffness is normalised by the radius. The results from tests with different sized footings should not all follow a similar relationship, however, because of the effect that scale has on the bearing capacity. The scale effect can explain the relatively larger N_γ values of the Byrne and Houlsby (1999) tests. The N_γ values of this investigation are unexpectedly larger than those from the other tests with a similar size of footing (for a constant normalised stiffness). The trend of each set of tests indicates that a linear relationship between the bearing capacity factor and the initial virgin-penetration stiffness is probable.

An indication of the displacement at bearing failure w_m for some of the footing tests was gained by considering the parameters used to fit the Hardening Law to the load:deformation curves in Figure 6.5. The estimated values of the bearing capacity factor and the displacement at bearing failure are compared with some values from the literature in Figure 6.9[b]. The lowest estimate of w_m is 10 mm and the highest is 40 mm, for tests T204 and T108. These values produced a similar trend to the results of de Beer (1970) and Vesic (1975) but the larger estimates of w_m were probably excessive.

The estimated values of V_m and the measured values of k_p were used to fit some of the virgin-penetration curves as shown in Figure 6.10. The theoretical curves were derived from Equation 2.20 and the fitting parameters are listed in Figure 6.10. These theoretical curves are used in the procedures in Chapter 7 to account for the vertical penetration that occurred during the sideswipe tests.

6.2.4 Constant-load time dependent behaviour

Creep behaviour of the footing was evident during the HOLD routines that were executed before each sub-test. For example, constant-load displacement of the footing occurred before each unload-reload sub-test as shown in Figure 6.11. Creep rates were measured at 500 N, 1000 N, and

1500 N and ranged between 0.2 mm/hr and 1.6 mm/hr as shown in Figure 6.12. The creep rate at similar loads was less in tests on stiffer soil. In each test, however, the rate increased with increasing penetration and load. This result was unexpected, as one would expect the rate to decrease with increasing stiffness. The creep values were usually measured over a period of five minutes and the creep rates should have decreased with time. If a creep rate of 1 mm/hr was assumed to be valid over a period of five hours, a typical test duration, a total creep displacement of 5 mm would have resulted. This was about half the typical total displacement during a test and was obviously not a realistic value.

Negative creep rates that resulted in heave of the footing were measured at the lowest loads during the HOLD routines in the unload-reload sub-tests, at V = 200 N in tests T101, T204, T108 and T309, as in Figure 6.11. A creep rate of approximately -0.07 mm/hr was measured in tests with saturated samples (tests T101, T108 and T309) and a rate of -0.16 mm/hr was measured in T204.

6.2.5 Unload-reload behaviour

Elastic parameters were deduced from the vertical unload-reload loops and the triaxial tests. These were compared with values in the literature.

Four vertical unload-reload (ULRL) sub-tests were performed from V_0 = 1000 N and one from V_0 = 1900 N. The symbol V_0 represented the maximum vertical load experienced by the footing. The ULRL loops are shown in Figure 6.11 and the associated parameters are listed in Table 6.2. The ULRL behaviour of the footing was non-linear, and in the sub-tests with a low characterisation stiffness, tests T101 and T108 in Figure 6.11[a] and [c], the footing penetrated significantly during the reloading phase. The effect of creep on ULRL behaviour was checked to verify if the large penetrations, sustained during reloading of the footing on samples of low characterisation stiffness, were due to creep. A relation between the rate of creep and load was assumed for test T101. The creep rate was measured during the HOLD routines: at V = 1000 N before unloading; at V = 200 N; and at V = 550 N during reloading. A power relationship that fit the three points was assumed valid for unloading and reloading. The ULRL curve of test T101 is compared with the creep-corrected curve in Figure 6.13. It is obvious from Figure 6.13[b] that the large penetrations during reloading could not be accounted for assuming the above creep

behaviour.

Two types of stiffness measurements were taken. The stiffness of the initial section of the unloading curve K'_{ul} was taken to represent small-strain stiffness at $\varepsilon_a = 0.05\%$. The gradient of a line drawn through the bottom and the top of the ULRL loop was taken to represent large-strain stiffness K'_{ulrl} at $\varepsilon_a \cong 0.2\%$. The axial strain was assumed equal to $w/2R$. The values of K'_{ul} and K'_{ulrl}, for the loops unloaded from 1000 N, are plotted against K'_{ch} in Figure 6.14. The data in Figure 6.14 indicates that K'_{ul} and K'_{ulrl} were proportional to the characterisation stiffness. The small-strain stiffness values were a factor of about two greater than the large-strain values. The ratio of K'_{ul} to K'_{eq} was also of interest as it indicated the ratio of elastic to plastic stiffness. K'_{eq} is used to represent the virgin-penetration stiffness before an event. In the case of the ULRL tests, K'_{eq} was the stiffness measured just before the footing was unloaded from 1000 N.

The stiffness values from the ULRL sub-test of T118 are not plotted in Figure 6.14 because the value of V_o and the relative size of the loop were different than in the other ULRL sub-tests. Plotting G against $V_o/V_{m\ dry}$ for a range of relative density values and for a constant value of strain resulted in a better comparison as shown Figure 6.15. This comparison included the effect of the relative density as well as the normalised stress level on the elastic shear modulus. Note that the drained bearing capacity was used, as the silicone oil does not seem to affect the elastic shear modulus. The elastic shear moduli that were derived from the unloading stiffness values are used, the values of G are listed in Table 6.2. Stiffness values derived from the relationship between G_o, p', and e that was suggested by Iwasaki *et al.* (1978), as given in Figure 2.2, are also plotted in Figure 6.15. The value of G_o was reduced by a factor of 0.2 so as to be representative of the strain level, and also to fit the ULRL test results. The match between the theoretical and experimental results was good. Lines representing constant values of V_o that were derived from the relationship of Iwasaki *et al.* are included in Figure 6.15.

The elastic shear moduli listed in Table 6.2 were calculated using the elastic solution of Poulos and Davis (1974) for the vertical displacement of a rigid disc on a finite layer,

$$G = \frac{K'_{ul}}{2\pi R(1+\nu)} I_\rho \qquad [6.1]$$

where I_ρ is an influence factor that is dependent on the Poisson's ratio and the ratio of the footing radius to layer depth. The value of h/R relevant to this enquiry is 3.3 and the drained Poisson's ratio is assumed to be 0.2. For these values the influence factor was found to be equal to 1.16. Rewriting Equation 6.1 with the values mentioned above gives,

$$G = 0.483\frac{K'_{ul}}{\pi R} \qquad [6.2]$$

The vertical stiffness of a footing on a finite layer, where h/R = 3.3, is approximately 20% greater than that of a similar footing on an infinite layer. The vertical stiffness on an infinite layer is given by Equation 2.5 and the K_1 coefficient, for a Poisson's ratio of 0.2, listed in Table 2.1.

The values of G deduced from the footing averaged 13 MPa at a relative density of 85%. This value of G is based on small-strain measurements at an effective mean stress of 30 kPa, that is for V = 1000 N and assuming σ'_h/σ'_v = 0.3. The estimates of G compare well with the theoretical values in Figure 2.2.

Elastic shear moduli for Baskarp Cyclone sand were also derived from triaxial and oedometer tests in Section 4.4. The triaxial values of G from tests BC10 to BC12, shown in Figure 4.3, are a factor of about six greater than the footing values. The mean effective stress in the triaxial tests was 87 kPa. This difference in stress level between the triaxial and footing tests cannot account for the difference in the value of elastic shear modulus. The elastic shear modulus can be assumed to be proportional to the square root of effective mean stress, as mentioned in Section 2.2.2. And an increase a factor of three in the effective mean stress should correspond with a 1.7 increase in G. The elastic shear moduli derived from the oedometer tests were a factor of about three greater than the values determined from the footing ULRL sub-tests.

The reloading sections of the ULRL loops were subject to varying degrees of plastic penetration as shown in Figure 6.11. The transition point from predominantly elastic reloading to that of predominantly plastic reloading seemed to be dependent on the ratio of V_o/V_m. This variation and the definition of the parameters involved are shown in Figure 6.16. The transition point from the reloading section of some of the sideswipe tests and from some of the combined load elastic loops are shown in Figure 6.16[a]. The penetration-corrected values of V_o are used for the sideswipe tests. The data indicated that the transition from predominantly elastic to plastic

reloading occurred at not less than 70% of the V_o load, when this load was less than 50% of the bearing capacity load.

6.3 Partially-drained consolidation model

Lambe and Whitman (1969) stated that the consolidation due to an increment of load proceeds independently of all preceding and succeeding increments of load. Although clearly only true for elastic soil, this suggested that some insight into the effects of partially-drained loading could be gained by dividing the applied load into increments and superimposing the solutions for each increment. A computer program was written in VisualBasic to investigate the problem of a time-varying load. The following values were used in the model in the subsequent sections if not otherwise stated: applied total load ΔV = 200 N (Δq = 5.66 kPa); coefficient of consolidation c_v = 1.2 x 10^{-3} m^2/s; height of sample h = 0.25 m; and radius of footing R = 0.075 m. A comparison of the model predictions and consolidation tests is performed in Section 6.4.5.

6.3.1 Description of model

The consolidation solution of Davis and Poulos (1972) that is outlined in Section 2.7.3 is used to describe the relationship between the degree of pore pressure dissipation and the dissipation time for each load increment. More precisely, the solution was for the average degree of pore pressure dissipation along the centre line of the footing. This was assumed to be representative of the degree of pore pressure dissipation at the pore pressure transducer in the footing, at the centre of the base of the footing.

The solution for a linearly increasing load with a rise time of 1.5 s is illustrated in Figure 6.17. The total pore pressure at any time was equal to the sum of the current values of all the previously occurring increments. In the model, the load increment was assumed to result in an elastic total stress distribution on the base of the footing, as defined in Figure 2.25. For an elastic total stress distribution, the total stress at the centre of the footing was half the value of the average total stress. Hence the C_q value of two in Figure 6.17.

Two types of ramped loading were incorporated into the model. A *linear load* of constant rate and a *non-linear load* of decreasing rate as shown in Figure 6.18. The non-linear load, resulting in a parabolic load curve, is defined as follows,

$$V = \Delta V \left[1 - \left(\frac{t_r - t}{t_r} \right)^2 \right] \qquad [6.3]$$

where ΔV is the total applied load, t_r is the rise time, and t is the time. This particular form of non-linear load was chosen for reasons of simplicity; not because it is similar to the actual form of ramped loading observed in the physical tests. A sinusoidal form of ramped loading would have been more realistic. It is evident from Figure 6.18 that the type of loading influenced the value of the peak pore pressure u_p as well as the time at which the peak occurred t_p. Under linear loading, t_p is always equal to t_r. But under non-linear loading, t_p is always less than t_r. It was also possible to investigate the effect of partially-drained loading on the peak pore pressure and the effect of partially-drained loading on the t_{50} time.

6.3.2 Sensitivity of model

The only known solution that the model could be compared with was that for an undrained increment of load. From Figure 6.19[a], it is evident that the predictions of the model tended to the undrained solution of Davis and Poulos (1972), as outlined in Section 2.7.3, as the rise time t_r approached zero. The trend is also obvious when the comparison is made in T_v:U_p space as shown in Figure 6.19[b].

The influence of the time increment on a linearly increasing load with a rise time of 5 s is shown in Figure 6.20[a]. The difference in the pore pressure predictions with t_{inc} = 0.05 s and t_{inc} = 0.01 s is negligible. Thus it would seem that a time increment of 0.05 s was acceptable. In Figure 6.20[b], the difference between a large and a small time increment for two rise times is compared. It is evident from the t_r = 5 s and t_r = 15 s predictions with the larger time increment (t_{inc} = 1.0 s), that the time increment alone should not be used as a parameter to indicate the accuracy of the prediction. Even though the two predictions had the same value of time increment, the value of the load increments of the t_r = 5 s prediction were greater because of the lower number of increments. Dividing the applied load into 100 increments resulted in satisfactory predictions.

6.3.3 Parametric analysis using model

The partially-drained consolidation model was used to investigate the effects of load rate on the peak pore pressure and the dissipation times.

The effect of load rate on the peak pore pressure u_p is illustrated by plotting u_p/u_m against t_p/t_{50m} as shown in Figure 6.21. Note that u_m is the maximum pore pressure under undrained conditions, t_p is the time to u_p, and t_{50m} is the t_{50} time under undrained conditions. The time to peak pore pressure t_p is equal to the rise time t_r when the ramped load is linear but it is less than t_r when the load is non-linear, as shown in Figure 6.18. The data in Figure 6.21 indicates that the peak pore pressure reduces with increasing time to peak, or rise time, as expected. When t_p is equal to the undrained t_{50}, the peak pore pressure is approximately 70% and 60% of the undrained peak pore pressure under linear and non-linear loading respectively. A few points with similar rise times are also compared in Figure 6.21. It is evident that at small rise times the peak pore pressure under linear loading was greater than that under non-linear loading. This trend is reversed at large rise times.

The effect of loading rate on the t_{50} time is illustrated in Figure 6.22. Note the definition of the t_{50} times and pore pressures shown in Figure 6.23. Under non-linear loading, dissipation is assumed to commence from the rise time and not the time to peak. From Figure 6.22 it is evident that when the rise time is equivalent to the undrained t_{50} time, when $t_r/t_{50m} \cong 1$, there is a 20% increase in the dissipation time under linear and non-linear loading. At large rise times the increase in the partially-drained dissipation time is approximately 70% and 150% under linear and non-linear loading respectively.

6.4 Consolidation behaviour

Six consolidation (CONSL) sub-tests were performed, three in T118 and three in T319. In the first sub-test the footing was loaded from 700 N to 900 N. In the second sub-test the footing was unloaded from 900 N back to 700 N. And in the third sub-test the footing was reloaded from 700 N to 900 N. The load increment was maintained for two minutes to allow dissipation of the pore pressures. The consolidation tests of T118 and T319 are shown in Figure 6.24 and Figure 6.25. In these figures, du is the change in pore pressure measured at the centre of the footing, dq is the change in the average applied total stress, and dw is the change in displacement. It should be noted that the pore pressure measured at the centre of the footing did not dissipate back to its initial value. The pore pressure measurements shown in Figures 6.24 and 6.25 were corrected, by

applying a weighting to ensure that the final excess pore pressure was zero (assuming full dissipation), as shown in Figure 6.26.

The consolidation tests were intended to be "true" consolidation tests; it was hoped that the load increment would be undrained. The first and second consolidation tests did not work properly because the efficiency of the HOLD routine with which the consolidation tests were performed was dependent on the stiffness of the footing (as discussed in Section 5.6). The stiffness factor programmed into the HOLD routine was applicable to the footing response in the final or reloading consolidation tests, that is in sub-tests T118B_3 and T319B_3. From the reloading consolidation tests shown in Figures 6.24 and 6.25, it is evident that the load increment of 200 N was achieved in approximately 1.5 s. Within this time one would expect approximately 30% pore pressure dissipation, assuming the T:U_p relationship outlined in Section 2.7.3 and a coefficient of consolidation of 0.8 x 10^{-3} m^2/s, as proposed in Section 4.3.3. Thus the load increment was partially-drained.

The pore pressure measurements in the tank from test T319B_3 are shown in Figure 6.27. The measurement in the footing is labelled pp_1 and those in the tank pp_2 and pp_3. One would expect the presence of the impermeable tank wall to reduce the rate of consolidation of the footing. It was not possible to clarify this but the fact that the measured coefficient of consolidation was of the same order of magnitude as that derived from the element tests indicated that the boundary effects might not have been significant.

The boundary effects could also be investigated by comparing the dissipation times of the transducers in the tank wall with the theoretical times for a semi-infinite layer. The t_{50} times of pp_2 and pp_3, from the third consolidation test shown in Figure 6.27 (test T319B_3), were 165 s and 240 s respectively. These values were compared with the solution for a triangular distribution in a half-closed layer (Craig, 1987) using the coefficient of consolidation from the element tests, c_v = 0.5 x 10^{-3} m^2/s. This solution resulted in a t_{50} of 24 s, indicating that the presence of the walls may have increased the dissipation times at the relevant points in the sand mass.

The consolidation settlements and the calculation of the coefficients of consolidation are discussed in Sections 6.4.1 and 6.4.3. The distribution of the total stress on the base of the footing is investigated in Section 6.4.2. This was necessary because the value of the total stress at the

centre of the footing was required. A brief insight into the effect of consolidation on the effective loads is given in Section 6.4.4. And finally, comparisons of some of the consolidation tests and predictions generated by the partially-drained consolidation model are made in Section 6.4.5.

6.4.1 Consolidation settlement

Three stages of settlement are evident in the consolidation tests, especially in T118B_3 and T319B_3, as shown in Figure 6.28. The results from the immediate and primary settlement stages from all of the consolidation tests are listed in Table 6.3. The drained or effective stiffness parameters were derived from the results at the end of primary consolidation, after full dissipation of the excess pore pressures.

In the initial consolidation tests, T118B_1 and T319B_1, one would expect the footing to consolidate back to the virgin-penetration line. In effect, the drained stiffness of the consolidation tests should be similar to the relevant virgin-penetration stiffness. This was indeed the case considering the virgin-penetration stiffness values listed in Table 6.1. The drained stiffness values of the unloading and reloading consolidation tests also compared well with the values derived from the ULRL tests, which are shown in Figure 6.14. The similarity between the load:deformation path of the three consolidation tests of T118 and the effective load:deformation path, determined from the virgin-penetration stiffness and the ULRL tests, is illustrated in Figure 6.29. The drained unload stiffness values of tests T118B_2 and T319B_2 are higher than those measured in the ULRL tests because of the smaller strain magnitude in the consolidation tests. The similarity mentioned above indicates that the drained stiffness values determined from the virgin-penetration curve and ULRL curve could be used to estimate the stiffness parameter in the calculation of the coefficient of consolidation. This also reinforces the applicability of the theory of effective stress and indicates the absence of degrading mechanisms induced by pore pressure change. The large variation in the effective stiffness values, which was dependent on the position in load:deformation space and the nature of loading, should be noted as it results in a similarly large variation in the coefficient of consolidation (assuming a constant coefficient of permeability).

The immediate settlement parameters listed in Table 6.3 were measured over the initial "immediate" stage of the consolidation tests, as illustrated in Figure 6.28. These immediate

settlements were not fully undrained as the rise time of the ramped load was about 1.5 s. The immediate stiffness values from the consolidation tests were plotted against the drained stiffness values in Figure 6.30. If the behaviour of a soil is assumed to be elastic, then the theoretical value of undrained stiffness can be used as the upper bound to the immediate stiffness, and the drained stiffness as the lower bound. The immediate stiffness under partially-drained loading should be a function of the rate of loading (or rate of displacement). The theoretical values of the undrained stiffness (1.8 times the drained stiffness) are also shown in Figure 6.30. The factor of 1.8 was derived from Equation 2.39 and the relevant values of ν and I_ρ given in Section 2.7.2. The partially-drained stiffness values from the consolidation tests were measured at an average displacement rate of 0.02 mm/s. This displacement rate was only a factor of ten greater than the average drained displacement rate (Table 6.3). For an undrained response, the rate of loading would have to be at least a factor of 100 greater than the drained rate of loading; this factor was estimated from the relation between the degree of consolidation and the dimensionless time factor in Figure 2.27. Thus the immediate stiffness values plotted in Figure 6.30 should be closer to the lower bound (drained values) than to the upper bound (undrained values). Considering the results in Figure 6.30, it would seem that the theoretical estimate of the undrained stiffness was only applicable to the unloading consolidation tests, tests T118B_2 and T319B_2, and was obviously not applicable in situations where there was significant plastic deformation.

If one assumes that the unloading tests represented elastic response and that the theoretical estimate of the undrained stiffness was applicable, then the question of what was the upper limit to the immediate stiffness values in the other tests arises. One possibility was that the undrained stiffness from the unloading tests, 18000 N/mm, was applicable to the loading and re-loading tests. This assumption was made in the calculation of the theoretical undrained settlements listed in Table 6.3; the theoretical undrained settlements were calculated in accordance with the methodology outlined in Section 2.7.2. The partially-drained stiffness data shown in Figure 6.30 do not provide adequate evidence for a relationship between the rate of loading, or rate of displacement, and the partially-drained stiffness to be postulated. If data was available for a range of loading rates, from loading, unloading, and reloading tests, then the influence of loading rate on the undrained stiffness could have been quantified. In addition, the effect of the degree of elasticity (the effect of the

drained stiffness) would also have become apparent.

There was considerable secondary settlement as shown in Figure 6.28. The rate of secondary settlement was highly non-linear but the average rate in tests T118B_3 and T319B_3 was about 0.8 mm/hr. This rate was about half the average rate of primary settlement (or consolidation settlement), measured over a similar time scale, and was similar to the creep rates shown in Figure 6.12 and discussed in Section 6.2.4. Davis and Poulos (1968) detected significant secondary settlements in their tests of model footings on clay. Significant secondary settlements were also evident in their three-dimensional element tests but not in their one-dimensional tests (triaxial and oedometer tests respectively). The secondary settlements observed in the consolidation tests of this investigation might have been caused by creep as well as consolidation of the sand mass in areas some distance from the footing.

6.4.2 Degree of elasticity during ramped load

It was postulated from the analysis of consolidation settlements and stiffness in Section 6.4.1, that the response in the loading tests was mainly plastic, and in the unloading tests it was mainly elastic. By comparing the applied stress at the centre of the footing and the measured pore pressure, it was possible to conclude that the response was not purely elastic in most of the tests. The pore pressure response and the implied total stress at the centre of the footing, for a range of possible stress distributions (as defined in Section 2.6), are compared in Figure 6.31. If the response was purely elastic, then the pore pressures could not be larger than the total stresses, calculated assuming an elastic distribution. In most of the tests, the peak pore pressures were greater than the elastic total stress, even in unloading test T319B_2. The fact that the pore pressure was not greater than the elastic total stress in test T118B_2 and T118B_3 did not necessarily mean that the response was purely elastic. One would also have to be sure that the degree of dissipation was very low ($u_p/u_m \cong 1$) before concluding that the response was purely elastic.

The degree of dissipation during the loading stage of consolidation test T118B_3 was estimated using the findings of the partially-drained consolidation model. The rise time in the consolidation test was approximately 2 s and t_{50m} was estimated at 1.92 s from Figure 6.22, which gave a t_p/t_{50m} ratio of 1.04. From Figure 6.21, it was estimated that the peak partially-drained pore

pressure u_p was about 60% of the maximum undrained pore pressure u_m. This suggested that the peak pore pressure in the consolidation test shown in Figure 6.31 was about 60% of the applied total stress.

It can be concluded that the response was mainly elastic during the ramped loading stage in T118B_3. This was based on the assumption that the applied total stress at the centre of the footing was about 67% greater than the measured peak pore pressure.

6.4.3 Estimation of undrained coefficient of consolidation

Preliminary estimates of the three-dimensional coefficient of consolidation c_3 were derived from the consolidation tests by assuming that the load increments were undrained. The consolidation tests were then compared with predictions from the partially-drained consolidation model.

From the discussion of the element tests in Section 4.3.3, it was postulated that c_1 = 0.8 x 10^{-3} m^2/s was representative of G = 13 MPa. The stiffness in the reloading footing tests, however, was approximately 8 MPa (Table 6.3). Thus the c_1 value for the footing tests was estimated at 0.5 x 10^{-3} m^2/s, assuming proportionality between c_1 and G. Converting the 1-D coefficient to the 3-D value resulted in c_3 = 0.25 x 10^{-3} m^2/s for a Poissons ratio of 0.2 (see Section 2.7.3).

Estimates of the partially-drained value of c_3 were also derived from the t_{80} times of the unloading and reloading consolidation tests. The t_{80} times were used instead of the t_{50} times because the applied loads overshot and cycled, before stabilising at the intended load increment of 200 N. The dissipation times and coefficients of consolidation are listed in Table 6.4. The average value of c_3 was 0.6 x 10^{-3} m^2/s for unloading and was 1.1 x 10^{-3} m^2/s for reloading. The effective stiffness in the unloading tests was a factor of about 2.6 greater than in the reloading tests (Table 6.3). It was expected that the values of c_3 would differ by a similar factor, assuming constant permeability. Considering the differences in the value of c_3 and the effective stiffness between the unloading and reloading tests suggests that either: the permeability in the reloading tests was about five times greater than in the unloading tests; or, the Poissons ratio in the reloading tests was about double that in the unloading tests(assuming ν = 0.2 in the unloading tests). The Poissons ratio should, if

anything, have been less in the reloading tests than in the unloading tests. Thus it was possible that the permeability was not constant, and that it differed by the factor mentioned above.

The partially-drained value of c_3 measured from the reloading consolidation tests was a factor of about four greater than the estimated undrained value of c_3 from the element tests. This contradicted the findings of the partially-drained consolidation model, which indicated that $t_{50}/t_{50m} \geq 1$, and hence that the partially-drained value of c_3 must be less than or equal to the undrained value of c_3. Thus the estimate of the undrained value of c_3 from the element tests was not applicable to the footing consolidation tests.

The undrained value of c_3 was estimated from the t_{50}/t_{50m}: t_r/t_{50m} relationship derived from the partially-drained consolidation model and shown in Figure 6.22. Values of t_r = 2 s and t_{50} = 2.4 s were deduced from consolidation test T118B_3 (the t_{50} value was calculated from the measured t_{80} value). The intersection of the curve for a non-linear load in Figure 6.22 and the curve created by plotting $2.4/t_{50m}$ against $2/t_{50m}$ indicated that t_{50m} = 1.92 s. This was equivalent to an undrained c_3 value of 1.6×10^{-3} m^2/s.

The rate of consolidation settlement, as opposed to the rate of pore pressure dissipation, was not investigated because the magnitude of the displacements was small compared to the noise level. The average rate of settlement, however, was compared with the average rate of drainage as follows.

The rate of volume change due to settlement was compared with an estimate of the rate of fluid flow out of a volume of sand beneath the footing. The shape of the volume of sand was taken to be a hemisphere for reasons of simplicity. Two forms of pore pressure distribution were assumed. An undrained distribution was taken to be applicable during the immediate stage of settlement, or during the period of ramped loading. And a partially-drained distribution was assumed during the primary stage of settlement (Figure 6.28). With the undrained distribution, the pore pressure at the edge of the footing was assumed to be twice the pore pressure at the centre and the volume of sand was divided into two sections, experiencing different hydraulic gradients. The pore pressure distributions and flow characteristics used in the calculation of the volumetric flow rate are shown in Figure 6.32, and the results are listed in Table 6.5. Only the unload and reload consolidation tests were analysed. The primary consolidation settlements were negligible in the

unload tests, thus only the immediate stage was considered in these tests. During the immediate stage of settlement, the rate of volume change derived from the settlement of the footing was, on average, a factor of two greater than that derived from the fluid flow. And during the primary stage, the values differed by a factor of about 0.35. These differences were not great considering the crudeness of the assumed flow characteristics and indicate a degree of coupling between volumetric change and flow.

6.4.4 Effective load during consolidation

The shape of the pore pressure distribution on the base of a footing founded on an elastic medium was discussed in Section 2.6. It was noted that the shape was a function of time. A parameter labelled C_p, from Equation 2.30, was introduced to account for the shape of the pore pressure distribution. Incorporating C_p into the calculation of the effective load on a footing, as opposed to assuming a uniform pore pressure distribution, results in a more rigorous calculation procedure.

The consolidation solutions of Davis and Poulos (1972) for a footing on a finite elastic medium can be used to estimate the dissipation of the average pore pressure below the centre of a footing. In practice, these solutions are used to model the dissipation of the average pore pressure assuming a uniform distribution over the whole of the base of a footing. The difference between the pore pressure at the centre of a footing and the average pore pressure is illustrated in Figure 6.33. The rate of dissipation of the average pore pressure over the whole base of the footing was significantly greater when C_p was taken to be a function of time, or when the pressure distribution was assumed to vary with time. This difference can be illustrated in terms of the effective foundation load as shown in Figure 6.34. The increase in effective load for a uniform pore pressure distribution, which is normally assumed in design, and a varying distribution is compared. It is evident that the more rigorous solution resulted in a greater rate of increase in effective load. Incorporating the effect of the change in shape of the pore pressure distribution may not be warranted considering that the common method of calculating the effective load is conservative. An implication of a greater rate of increase in effective load would be an increased rate of settlement. It should be remembered that the definition of the effect of dissipation on the pore

pressure distribution, that is the definition of C_p in Section 2.6, was only postulated by the author and was not based on experimental observation.

6.4.5 Comparison with model predictions

The undrained coefficient of consolidation derived above, and the relationship between u_m and u_p, were used to produce the simulation of test T118B_3 shown in Figure 6.35. Also shown is a simulation of test T319B_3. The model predictions and the experimental data compared well, considering that the response on the footing was most probably not fully elastic. The model could not be said to be accurate at this stage; it would have to be tested against a larger experimental database consisting of tests with a range of rise times. The simulation process is summarised as follows:

— Measure partially-drained t_{50} and t_r from consolidation tests.

— Derive t_{50m} from Figure 6.22 and calculate the undrained c_3.

— Derive the ratio u_p/u_m from Figure 6.21 and calculate u_m.

It should be noted that the degree of elasticity, or the shape of the total stress distribution on the footing, could not be predicted. Therefore u_m could not be predicted. It was derived from the experimental value of u_p and the model prediction of u_p/u_m.

The model performed well but a rigorous assessment of the model could not be undertaken. An important observation was the possible applicability of the model to, not only fully elastic behaviour, but also to elastic-plastic behaviour. The model also provided a framework for differentiating between the factors affecting the pore pressure. That is, the total stress distribution on the footing and the dissipation characteristics of the system.

6.5 Partially-drained tests

The partially-drained vertical displacement events (VP and VPM sub-tests) that were performed from V = 500 N and V = 1000 N are analysed in this section.

The vertical partially-drained tests were performed using a range of displacement rates: 0.01 m/s, 0.1 m/s, 1 m/s, and 5 m/s. The stiffness of the sand specimens was not constant and therefore the vertical stiffness of the footing was also a significant variable, in addition to the displacement rate. Constant sample stiffness was intended but this was difficult to achieve. The

distribution of the vertical partially-drained tests, in terms of displacement rate and characterisation stiffness, is shown in Figure 6.36. It should be noted that the displacement rates shown in Figure 6.36 are the intended rates, the actual or measured rates were slightly different because of the flexibility of the test rig. The interaction of the flexibility of the rig and the stiffness of the footing resulted in low displacement rate ratios in tests in which the stiffness of the footing response was high. The displacement rate ratio was defined as the actual rate divided by the intended rate. The effect of the footing stiffness on this ratio is shown in Figure 6.37. The measured displacement rate of each test is also listed in Table 6.6. A curve of the theoretical relationship between the displacement rate ratio and the footing stiffness is also shown in Figure 6.37[a] and [b]. This relationship was based on a system of two springs placed in series. The value of the vertical stiffness parameter K_{mf}, from Section 3.2.1, was estimated at 1944 N/mm. The stiffness parameter K_{vp-s} was the stiffness of the secondary section of the partially-drained tests, discussed in Section 6.5.2. The slower tests fit the theoretical curve well but the tests at 1 mm/s and at 5 mm/s exhibited greater displacement rates than expected.

Referring back to Figure 6.36, which shows the distribution of the intended displacement rates and the characterisation stiffness values, it can be seen that only certain tests could be compared when investigating the effect of either of these variables. Although the variation in characterisation stiffness was somewhat random, most of the tests fell into narrow stiffness bands. For example, the mean characterisation stiffness of tests 17, 15, 10 and 13 was 478.5 N/mm, with a range of 13 N/mm. Therefore, with this set of tests, the characterisation stiffness could be said to be constant, and these tests could be used to investigate the effect of displacement rate.

The load:deformation behaviour of the partially-drained tests was investigated. The control parameters were displacement rate and drained (or effective) vertical stiffness. The drained vertical stiffness of the footing was related to the sample stiffness and therefore to the relative density of the sample. Hence the control parameters were analogous to loading rate and sample density.

The stiffness of the load:deformation response in the partially-drained tests was proportional to the characterisation stiffness as expected. This trend is obvious from the tests shown in Figure 6.38, where different tests, with different K_{ch} values but having the same displacement rate, are plotted together. Note that the first column is of tests performed from 500 N and the second of tests

performed from 1000 N. Each row is of a set of tests at a particular displacement rate. The effect of the characterisation stiffness is observed over a range of displacement rates as shown in Figure 6.38.

The effect of displacement rate on the load:deformation response in the partially-drained tests is illustrated in Figure 6.39. Tests with similar values of characterisation stiffness are plotted together, the top row consists of tests with the lowest values of stiffness. The label in brackets adjacent to the test number indicate the displacement rate. Note that the partially-drained sub-tests in main test 20 were multi-rate tests, in which the footing was penetrated at alternating slow and fast rates. The general trend of increasing stiffness with rate is obvious from Figure 6.39, as the loads are higher in the faster tests. The multi-rate tests highlighted this trend well.

Analysis of the load:deformation behaviour of the VP tests indicated that three parameters could be used to define the observed response. An idealised shape of the partially-drained tests and the parameters involved are shown in Figure 6.40. The partially-drained load:deformation response could be separated into two distinct parts with differing stiffness values. The stiffness of the primary section is labelled $K_{vp\text{-}p}$ and that of the secondary section $K_{vp\text{-}s}$ (subscript "vp" signifies a vertical partially-drained test, and subscripts "p" and "s" signify the primary section and the secondary section respectively). The third parameter is $\Delta V_{vp\text{-}p}$, defined as the observed load increment of the primary section. Also shown is the equivalent drained stiffness K'_{eq}. This was the value of the virgin-penetration stiffness measured between 400 N and 500 N or between 900 N and 1000 N. That is, the value just before the partially-drained tests. Note that K'_{eq} is equivalent to K'_{ch} for the tests conducted from 500 N.

The shape of the idealised partially-drained load:deformation curve was similar to that observed in most of the partially-drained tests. The exceptions were the tests performed on the least stiff samples, which possessed low values of characterisation stiffness. All of the partially-drained tests on samples in which the characterisation stiffness was greater than 300 N/mm exhibited load:deformation curves similar to the idealised shape. The characterisation stiffness can be deduced from Figure 6.36. The tests in which the characterisation stiffness was less than 300 N/mm exhibited a reduction in load immediately after the primary section of the partially-drained move. After this reduction, the load:deformation curves tended to exhibit a constant stiffness. The footing

in tests T102_1, T103A_1, T103A_2, and T105_2 exhibited pronounced work softening type behaviour and the total load reduced below its initial value.

6.5.1 Primary section of partially-drained tests

A distinct initial section was observed in the load:deformation curves of the partially-drained tests, as discussed in the preceding paragraphs and illustrated in Figure 6.40. The measured values of the partially-drained primary stiffness $K_{vp\text{-}p}$ and load change $\Delta V_{vp\text{-}p}$ are listed in Table 6.7, and will be discussed in this section.

Primary Stiffness

The values of $K_{vp\text{-}p}$ from the partially-drained tests are shown in Figure 6.41. There is considerable scatter in the results shown in Figure 6.41 and the control parameters, K'_{eq} and w, do not seem to affect the partially-drained primary stiffness in any obvious manner. There is some evidence of proportionality in Figure 6.41[b] between the $K_{vp\text{-}p}$ and K'_{eq} in the partially-drained tests performed at V = 1000 N. Note that some of the K'_{eq} values measured between V = 900 N and V = 1000 N were not representative of the virgin-penetration stiffness, as outlined in Table 6.7. These included the two highest values of K'_{eq} in Figure 6.41[b]. The average value of $K_{vp\text{-}p}$ in the tests performed at V = 1000 N is slightly higher than that in the tests at V = 500 N.

The scatter in the values of $K_{vp\text{-}p}$ was due to a large extent on the lack of resolution in the displacement measurements used in the calculation of the stiffness values. The magnitude of the displacements over which the primary section occurred was sometimes only 0.02 mm. This resulted in a relative error of about ±40% in the values of $K_{vp\text{-}p}$, which translates to an absolute error of ±2000 N/mm for $K_{vp\text{-}p}$ = 5000 N/mm. It should also be noted that in the fastest moves, sometimes only two data points were recorded during the primary section of the moves.

It was probable that the creep that usually occurred during the holding of the vertical load had some influence on the primary stiffness (HOLD routines were performed before the partially-drained tests). Mitchell (1976) noted that creep loading usually increased the stiffness of subsequent virgin-penetration loading. The high initial values of stiffness were not due to the effects of over-consolidation. The partially-drained tests were performed from the virgin-penetration line in the majority of cases. It should be noted that a primary stiffness was evident in

the preliminary tests, which were performed to verify an applicable footing size and pore pressure measurement system. In some of the preliminary tests, an altogether different loading apparatus was used. This ruled out the possibility that the loading apparatus was the cause of the observed primary stiffness.

The primary stiffness was most probably a rate dependent phenomenon due to the permeability of the soil, as there was no evidence in the literature of such large initial stiffness values in the rapid loading of dry sand. In the consolidation tests, discussed in Section 6.4.1, similarly large initial (or immediate) values of stiffness were measured. The value of the initial stiffness was also found to be proportional to the equivalent drained stiffness. That is, it was higher in the unloading (elastic) consolidation tests than in the loading (plastic) consolidation tests. It was postulated in Section 6.4.1 that there was an upper limit to the partially-drained stiffness that was equivalent to the undrained stiffness (the undrained stiffness being calculated from the elastic drained stiffness measured in an unloading test). In Figure 6.42, the partially-drained primary stiffness values from the partially-drained tests are compared with the values from the consolidation tests (the partially-drained tests were added to Figure 6.30). The partially-drained stiffness measured in the partially-drained tests was consistent with the postulate on the undrained stiffness. It was possible, however, that the upper limit to the partially-drained stiffness of the loading tests (the tests on a predominantly plastically deforming base) was approximately half that of the possible undrained limit shown in Figure 6.42. The fastest of the partially-drained tests should have been almost undrained, considering the time scale and the probable coefficient of consolidation. That is, about 0.02 s and about 1.0×10^{-5} m^2/s respectively.

Load change

It was evident that the magnitude of the change in load during the primary section of the partially-drained tests, as defined in Figure 6.40, was a significant parameter. The measured values of $\Delta V_{vp\text{-}p}$ are shown in Figure 6.43. The $\Delta V_{vp\text{-}p}$ values were measured over a displacement of about 0.05 mm.

There was a definite trend of increase of $\Delta V_{vp\text{-}p}$ with the rate of displacement in the tests conducted both at V = 500 N and at V = 1000 N. This trend can be visualised by plotting the values

of $\Delta V_{vp\text{-}p}$ against each rate as shown in Figure 6.44 (plotted against the measured rate). From Figure 6.44[a], it is evident that at high values of displacement rate the sensitivity of $\Delta V_{vp\text{-}p}$ to changes in rate is reduced. Conversely, Figure 6.44[b] illustrates the behaviour at low values of displacement rate. The values of $\Delta V_{vp\text{-}p}$ tended toward constant values as the displacement rate reduced to zero. In both figures, inverse hyperbolic sine best-fit curves were included. The following expression is used to fit the data from V_o = 500 N,

$$\Delta V_{vp\text{-}p} = 23\sinh^{-1}(5\dot{w}) + 50 \qquad [6.4a]$$

and from V_o = 1000 N, the following expression is used,

$$\Delta V_{vp\text{-}p} = 46\sinh^{-1}(5\dot{w}) + 100 \qquad [6.4b]$$

Mitchell (1976) used this type of expression to model rate-dependent behaviour and it is the form of relationship expected if the rate-dependence could be modelled as a thermally activated process. The trend of the data at low displacement rates indicates the likelihood of an initial stiff response (like that of a primary stage in the partially-drained load:deformation curve) even at the drained rate of 0.001 mm/s. In the absence of stiffness enhancing rate effects, the value of $\Delta V_{vp\text{-}p}$ at the drained rate should have been approximately 10 N and 20 N for the tests conducted at V = 500 N and V = 1000 N respectively. These values were based on the average magnitude of displacement over which the values of $\Delta V_{vp\text{-}p}$ were measured, and the representative values of drained stiffness. The value of $\Delta V_{vp\text{-}p}$ at the creep rate should have been equal to zero. Taking 1 x 10^{-7} mm/s to be a representative creep rate, as determined in Section 6.2.4, suggests that the inverse hyperbolic sine functions cannot model the behaviour at very low rates of displacement.

The partially-drained tests performed at V = 1000 N also indicate a trend, although less definite, of an increase in $\Delta V_{vp\text{-}p}$ with the characterisation stiffness (Figure 6.43). This trend would have been reduced if the drained load increment were subtracted from the $\Delta V_{vp\text{-}p}$ values (the displacement increments of the primary sections were generally equal to 0.05 mm). Comparing the tests at V = 500 N and those at V = 1000 N, indicated that there was a significant increase in the values of $\Delta V_{vp\text{-}p}$ in the tests conducted at the higher load. That is, the $\Delta V_{vp\text{-}p}$ values in each test increased with penetration, or with an increase in the equivalent drained stiffness. The effect of the

characterisation stiffness on the value of $\Delta V_{vp\text{-}p}$ was, however, assumed to be negligible in light of the results of the preliminary tests. In the preliminary tests, $\Delta V_{vp\text{-}p}$ values of about 250 N were measured even though the characterisation stiffness was about 2000 N/mm. That is, similar $\Delta V_{vp\text{-}p}$ values even though the stiffness was a factor of four greater than in the partially-drained tests of the main-test series. The preliminary tests referred to were TP08_1 and TP09_1A. These consisted of the rapid penetration, $\dot{w} \cong 8$ mm/s from a vertical load of about 400 N, of a similar footing on the same oil-saturated sand base as in the main series of tests.

It should be noted that the discussions above related only to partially-drained loading from the virgin-penetration curve, not from over-consolidated states. Partially-drained loading from an unloaded state, in the elastic region, should result in an initial stiff response which then softened as the partially-drained load path traversed the virgin-penetration line.

6.5.2 Secondary section of partially-drained tests

A secondary section, as defined in Figure 6.40, was observed in all of the vertical partially-drained tests. In some of the tests on the looser samples with low values of characterisation stiffness, there was considerable reduction in the load immediately after the primary section. These tests are highlighted in Table 6.7. After the reduction in load, the load:deformation behaviour tended to a straight line indicating a constant stiffness. In such cases, the secondary stiffness was taken as the gradient of the latter, and constant, part of the load:deformation curves.

The secondary stiffness of the partially-drained tests conducted from V = 500 N and V = 1000 N are shown in Figure 6.45. Note that some of the values of K'_{eq} measured between V = 900 N and V = 1000 N were not representative of the virgin-penetration stiffness. Hence in Figure 6.45[b], the two rightmost points should be more to the left. The values of $K_{vp\text{-}s}$ were similar to the equivalent drained stiffness, even at the fastest displacement rates. This indicated that after the initial highly rate dependent section, the load:deformation behaviour of the partially-drained penetrating footing was rate insensitive. That is, after a strain of about 0.03%, in the tests in which work-softening was not evident, the load:deformation behaviour of the footing was not affected by the rate of displacement. Note that the above refers to the "total" load and not the "effective" load.

6.5.3 Pore pressure response in the partially-drained tests

In Sections 6.5.1 and 6.5.2 above, only the total loads were considered. The response of soil is dependent on effective stress. A methodology for estimating the effective load on a footing was outlined in Section 2.6. This required knowledge of the variation of the pore pressure distribution with time. Thereby allowing the pore pressure load and the effective load to be calculated. Realistically, only the pore pressure distribution in the latter stages of the partially-drained tests, after considerable pore pressure dissipation, could be assumed. This distribution should be parabolic in shape. Therefore the effective load could only be estimated in the latter stages of the tests. Note that the methodology outlined in Section 6.4.2 for estimating the total stress distribution, using the results of the partially-drained consolidation model, could not be used to deduce the effective stress at the centre of the footing in the partially-drained tests. This process was only applicable in cases where the total stress distribution was fairly constant over the period under consideration. That is, in cases where the response was predominantly elastic. The response in the partially-drained tests was not predominantly elastic as the moves were performed from the virgin-penetration line. In the following paragraphs, a qualitative analysis of the effects of the control parameters, the displacement rate and effective stiffness, on the pore pressure response will be undertaken. Note that the pore pressure response did not follow any clearly definable pattern.

A selection of tests with low and high drained stiffness, and at three rates of displacement (0.01 mm/s, 0.1 mm/s, and 1.0 mm/s), are shown in Figure 6.46. The first two columns include the low stiffness tests and the second two include the high stiffness tests. Tests from V = 500 N and from V = 1000 N are both included. The different rows of plots are of tests with different displacement rates. The partially-drained sub-tests from T105, T107, and T311 are taken to be representative of low stiffness samples, and T110, T315, and T317 of high stiffness samples. The characterisation stiffness of T311 is about 100 N/mm greater than the stiffness of tests T105 and T107 (Figure 6.36). The values of the characterisation stiffness of the chosen high stiffness samples are closer.

In Figure 6.46, the change in the pore pressure is compared with the change in the total stress for three possible total stress distributions. The pore pressure was measured at the centre of the

footing. The estimates of the total stress at the centre of the footing were derived from the measured total load and the possible distributions. Since the distribution of the total stress on the base of the footing could not be assumed, and was probably not constant, the total stress was calculated for a parabolic (or plastic; $C_q = 0.5$) distribution, a uniform distribution ($C_q = 1.0$), and a saddle shaped (or elastic; $C_q = 2.0$) distribution. The parameter C_q was defined in Section 2.6. Thus the top dq curves in Figure 6.46 represent plastic response and the bottom dq curves represent elastic response. The response in the high stiffness tests was likely to be more elastic than plastic, and vice versa in the low stiffness tests. The initial behaviour in the fastest tests was likely to be more elastic than plastic as well. Note that in test T105_2 the footing exhibited evidence of liquefaction.

First of all, the effect of rate in the low stiffness tests shown in Figure 6.46 is considered. These tests exhibited higher relative values of du, relative to the dq values, in the faster tests. In the slowest tests, tests T105_1 and T105_2, the pore pressures dissipated. In the intermediate rate tests, tests T311_1 and T311_2, the rate of fluid flow and the rate of loading were probably similar, and hence the relative values of du are higher. And in the sub-tests of T107, the relative values of du are higher still. Tests T107_1 and T107A_1 also showed evidence of a change from an initial semi-elastic response to a more plastic response.

The effect of rate in the high stiffness tests shown in Figure 6.46 is not similar to that in the low stiffness tests. The intermediate rate tests do exhibit slightly higher relative values of du than in the slowest tests. But in the fastest tests, tests T110_1 and T110_2, the relative values of du are lower than in the slower tests, contradicting the pattern observed in the low stiffness tests. This could be explained by considering the degree of elasticity of the response. The sub-tests of T110 may have resulted in predominantly elastic response, as the sample stiffness and the rate of loading were high. The total stress at the centre of the footing may have been similar to that predicted by an elastic distribution. That is, by the bottom dq curve with $C_q = 2.0$. If the footing was penetrated further in the sub-tests of T110, the total stress distribution may have become more plastic and the relative values of du could have increased.

In summary, there was a definite trend of increasing relative pore pressure with increasing rate of displacement. This could be best illustrated by comparing tests at the two extremes of rate,

at 0.01 mm/s and at 5.0 mm/s. The partially-drained sub-tests of T116 and T118, with similar values of characterisation stiffness, are shown in Figure 6.47. The displacement rates differ by a factor of 500 and relative pore pressures in T118 are significantly higher.

Comparing the low stiffness tests with the high stiffness tests in Figure 6.46, indicates a possible inverse relationship between the relative values of du and sample stiffness. This is particularly evident when comparing the fastest tests. That is, the sub-tests of T107 and T110. This was most probably due to the possible differences in the degree of elasticity of the responses.

From the above analyses of the tests shown in Figure 6.46, it is obvious that the pore pressure response at the centre of the footing could only be sensibly explained with reference to the total stress at that point. Averaging the pore pressure over the base of the footing, or assuming the vertical load resulted in a uniform total stress distribution, could not explain the observed behaviour.

6.5.4 Evidence of liquefaction

In the discussion of Figure 6.46 in Section 6.5.3 above, it is mentioned that test T105_2 exhibited a liquefaction type response. A number of the partially-drained tests on samples with low values of stiffness showed a similar response. All of these tests liquefied to some degree but none showed evidence of full liquefaction. That is, the estimated effective load did not reduce to zero. It should be noted that in estimating the effective load, a parabolic shaped pore pressure distribution was assumed. This assumption was particularly applicable to the latter stages of the tests.

All the tests that partially liquefied are shown in Figure 6.48. As mentioned above, the relevant tests were all on low stiffness samples. The average characterisation stiffness was 150 N/mm. Thus the displacement rate was the only control parameter of influence. In the slowest test, the test in the first row of plots, the partial liquefaction subsides and the effective load increases. The interaction between the rate of penetration and the rate of pore pressure dissipation in the fastest test leads to progressive liquefaction and a continual reduction in the effective load. It should be noted that all of these tests were performed under displacement control. Under load control, the observed liquefaction would have been much more pronounced.

The partial liquefaction most probably commenced in the very early stage of loading and at

the edge of the footing. At this stage, the pore pressure distribution could have been similar to the undrained shape, with high pressures at the edge of the footing. These high pore pressures would have resulted in substantial hydraulic gradients and the flow of pore fluid away from the edge. This flow could have caused local liquefaction.

There was a possible reason why the tests on the low stiffness samples liquefied and those on the high stiffness samples did not. Consider the definition of the effective stress at a depth δs below the edge of a footing with an upward hydraulic gradient of i,

$$\sigma'_v = \gamma_w \, \delta s \left[\left(\frac{\gamma}{\gamma_w} - 1 \right) - i \right] + q \qquad [6.5]$$

where q is the contact stress at the edge of the footing. If one assumes that the difference in the density of the samples was insignificant and that the hydraulic gradients were similar, then Equation 6.5 suggests that the contact total stress must have been greater in the tests that were not prone to liquefaction. That is, in the tests on the stiffer samples. It seemed more probable, however, that the density was the important parameter.

6.5.5 Effective load response in the partially-drained tests

Some general trends in the pore pressure behaviour are outlined in Section 6.5.3. The effective load response, deduced from estimated values of the pore pressure load and the measured total load, was also investigated. The change in the effective load dV', measured at $dw \cong 0.24$ mm, was calculated for a range of possible pore pressure distributions. The effective load was estimated at $dw \cong 0.24$ mm because the maximum penetration in some of the partially-drained tests was not much greater than $dw \cong 0.3$ mm. The drained stiffness of the partially-drained tests was also calculated. This was calculated from the point after a move at which the pore pressure returned to its ambient value.

The range of dV' in the partially-drained tests is shown in Figure 6.49. The first column is of tests performed from $V = 500$ N and the second column of tests from $V = 1000$ N. The different rows indicate different displacement rates, the slowest tests are in the first row of plots. The circular data points indicate the values of dV' calculated assuming a uniform pore pressure distribution. Error bars are used to indicate the possible range of dV'. As illustrated in Figure

6.49[a], the top bars represent the values of dV' calculated assuming a parabolic (partially-drained) pore pressure distribution and the bottom bars represent the values calculated assuming a saddle shaped (undrained) distribution. The dotted lines indicate the values of dV' that would be expected if the penetration over the displacement increment of 0.24 mm was at the equivalent effective stiffness. That is, at the probable drained penetration stiffness.

In the absence of degrading mechanisms, such as caused by liquefaction, one would expect the change in effective load to be similar to that predicted assuming drained penetration, indicated by the dotted line. This was indeed the case in the slowest tests in Figure 6.49[a] and [e]. In the slowest tests, the pore pressure distribution was most probably parabolic in shape and the top bars should be indicative of the values of dV'. Note that the second partially-drained sub-test of T105, shown in Figure 6.49[e], shows evidence of substantial liquefaction as there is a definite reduction in the effective load in this test.

The tests at $\dot{w}$ = 0.1 mm/s, in Figure 6.49[b] and [f], also show evidence of an effective load response similar to that predicted by the drained stiffness. That is, the partially-drained sub-tests of T311 and T315. Both the partially-drained sub-tests of T103 liquefied to some extent. The pore pressure distribution was most probably parabolic in shape, as the time increment was of a similar order of magnitude to the t_{50} time. Hence the top bars should be indicative of the values of dV'.

In the fast tests at $\dot{w}$ = 1 mm/s and $\dot{w}$ = 5 mm/s, it could not be assumed that the pore pressure distributions were parabolic in shape and that the top bars were indicative of the values of dV'. Therefore it was possible that the effective load response in the fast tests was less than the expected drained response. This seemed to be the case in the tests at $\dot{w}$ = 1 mm/s. Some of the fastest tests from V = 1000 N, however, produced larger values of dV' than predicted by the expected drained stiffness, see tests 14 and 13 in Figure 6.49[h].

The discussions above indicate that the effective load response, at a specific point during the slower partially-drained tests, was similar to the expected drained response. In the faster tests, the evidence was inconclusive.

Analysis of the response at the end of the partially-drained tests indicated lower values of effective stiffness at higher rates of penetration. The overall drained stiffness of the partially-

drained tests was measured between the start of the moves, and the point after the moves at which the excess pore pressures were zero. The values of the overall drained stiffness are shown in Figure 6.50. The overall drained stiffnesses at the slower rates of $\dot{w}$ = 0.01 mm/s and $\dot{w}$ = 0.1 mm/s are similar to the values of drained stiffness measured just before the partially-drained tests, indicated by the dotted lines. The faster tests produce significantly less stiff responses. This reduction in stiffness was not due to increased creep in the faster tests, as the time scales over which the measurements were taken were similar.

6.5.6 Multi-rate tests

Two multi-rate vertical partially-drained tests (VPM) were performed in main-test T120. The displacement rate was alternated between 0.01 mm/s and 1 mm/s. The details of these tests are listed in Table 6.6 and Table 5.1. The results from the constant-rate partially-drained tests that are shown in Figure 6.44, and expressed by Equation 6.4a, indicate that the load changes (or $\Delta V_{vp\text{-}p}$ values) associated with rates of 0.01 mm/s and 1 mm/s are 50 N and 100 N. That is, when the initial vertical load is 500 N. The load changes are 100 N and 200 N when the initial load is 1000N, as deduced from Equation 6.4b. One would expect similar load changes in the multi-rate tests.

The multi-rate tests are shown in Figure 6.51. The test from an initial vertical load of 500 N is shown in the plot on the left and the test from 1000 N is shown on the right. The pore pressure load U, calculated for a parabolic distribution, is also included. The extrapolated drained penetration line (or virgin-penetration line), and the partially-drained penetration lines along which the slow and fast moves tended, are shown. The symbols represent the data points along the loading sections of the fast moves. The motor stalled during the second fast move of the test from 500 N. Lines indicating the initial stiff response of the partially-drained moves are shown. The primary stiffness $K_{vp\text{-}p}$ varied between 2kN/mm and 10 kN/mm in all of the moves, but lines with a gradient of 10 kN/mm are shown in Figure 6.51. These values are similar to the values measured in the normal partially-drained tests, which are shown in Figure 6.41.

The $\Delta V_{vp\text{-}p}$ values in the test from 500 N shown in Figure 6.51[a] are 60 N and 125 N. These values are very similar to those predicted by Equation 6.4a. The values during the second and third slow moves were slightly less, but the values during both of the fast moves are consistent. The

$\Delta V_{vp\text{-}p}$ values in the test from 1000 N shown in Figure 6.51[b] are 90 N and 210 N. Again these values are very similar to those predicted, in this case by Equation 6.4b.

The findings of the multi-rate tests substantiate and extend the results of the constant-rate partially-drained tests. The multi-rate tests indicate that the rate dependent penetration lines deduced from the constant-rate tests might be unique, in so much as they are not affected by the prior w:V state. That is, the $\Delta V_{vp\text{-}p}$ values might not influenced by prior moves at different rates.

The pore pressure at the end of each slow move increased as the tests progressed. This indicates that there might have been some degradation in the effective load since the total load at the end of each test increased in parallel with the drained penetration line.

7 Results: Combined Loading

7.1 Introduction

Sideswipes tests were performed at different rates to investigate the effect of partially-drained loading on the yield surface. The results of the drained horizontal and moment sideswipe tests are compared with tests in the literature. The drained load:deformation behaviour within the yield surface is investigated and elastic parameters are derived. The drained load:deformation behaviour of the footing during yield is also investigated, in the context of a flow rule. The effects of partially-drained behaviour, or the rate of loading, on the yield surfaces tracked by sideswipes is analysed.

7.2 Drained *V*:*H* sideswipe tests

Five drained horizontal sideswipes (HSS) were performed. The sideswipe of test T204 was performed on dry sand. In addition to these, two multi-rate sideswipe tests (HSSM) with drained components were performed in test T120. A comprehensive set of plots of the drained horizontal sideswipe tests (in the three axes of load and displacement) is shown in Figure 7.1. From these plots it can be seen that tests T118D_2 and T120D_H2 were displaced in the negative horizontal direction, or to the left. The majority of tests were commenced from V_{0i} = 1500 N, but tests T101_1, T120D_H2 and T118D_2 were commenced from V_{0i} values between 1600 N and 1700 N (see Figure 7.1[a]). Although the tests performed at a horizontal displacement rate of 0.001 mm/s were assumed to be drained, low values of pore pressure were measured at the centre of the footing. The pore pressure load shown in Figure 7.1[f], calculated assuming a parabolic pore pressure distribution on the base of the footing, varied between -5 N and -20 N. A pore pressure load of -20 N is equivalent to a pore pressure of only -2.3 kPa.

The values of V_{0i} and the intended and measured displacement rates of the horizontal sideswipe tests are listed in Table 7.1. The measured displacement rates were generally less than the intended rates because of the flexibility in the rig. This is illustrated Figure 7.2. The displacement rate ratio is plotted against the characterisation stiffness in Figure 7.2. In Section 4.6

it was suggested that the characterisation stiffness was indicative of the density of the samples. The distribution of the displacement rates and the characterisation stiffness values of the horizontal sideswipe tests is shown in Figure 7.3. From Figure 7.2 it would seem that the displacement rate ratio of the drained sideswipe tests was not influenced by the characterisation stiffness. It should be noted that the measured rates were averaged over the whole duration of each sideswipe and that some of the variations of displacement with time were not linear.

7.2.1 Shape of the yield surfaces

The sideswipes are shown in V:H space and in V_0-normalised space in Figure 7.4. The sideswipe of T101 was started from an overconsolidated state. The footing was unloaded from V = 1700 N before the sideswipe was commenced. Tests T120D_H1 and T120D_H2 were multi-rate tests in which the horizontal displacement rate was alternated between 0.001 mm/s and 0.1 mm/s. The flatter sections of the multi-rate tests represent the slower displacement rate.

The effect of the characterisation stiffness on the shape of the sideswipe curves is evident in Figure 7.4[a]. The peak values of the horizontal load are larger in the tests with the larger values of characterisation stiffness. This effect is better illustrated by plotting the tests in V_0-normalised space as shown in Figure 7.4[b]. Note that V_0 was the equivalent vertical load along the extrapolated virgin penetration curve. Thus the tests shown in Figure 7.4[b] are corrected for the vertical penetration that occurred during the tests. This correction procedure is discussed in Section 2.3.3 and illustrated in Figure 2.8.

The difference between V_{0i} and V_0 normalisation is shown in Figure 7.5. The magnitude of the correction is greatest in the stiffest samples, as small penetrations during the sideswipe tests resulted in relatively large increases in the value of V_0. The sideswipe of T101 was also corrected for the initial overconsolidated state. The probable degrading effect of the excess pore pressures in the multi-rate tests was not accounted for. The effect of excess pore pressures on the vertical load:deformation behaviour was discussed in Section 6.5.5.

The shapes of the sideswipe tests in Figure 7.4[b] are generally parabolic, except that of test T204_1 that was on the stiffest sample. The peak V_0-normalised horizontal load (or h_0 value as referred to in Section 2.3.3) increased with increasing characterisation stiffness. A parabola defined

by Equation 2.9 with $h_0 = 0.12$ is also shown in Figure 7.4[b]. This parabola was representative of the V_m-normalised yield surface of the horizontal sideswipe tests of Gottardi and Houlsby (1995) (see Section 2.3.3 and Figure 2.9). But in accordance with the tests of Gottardi and Houlsby, the sideswipes do not converge to this probable yield surface when plotted in V_0-normalised space.

The shape of the sideswipe of test T101 shown in Figure 7.4 is peculiar. Cyclic shearing of the soil or slippage of the drive system may have caused the saw-tooth shaped load path (as discussed in Section 5.3.1). If this phenomenon was due to the response of the soil, then localised partially-drained shearing had probably developed. The unstable nature of the shearing might also have been influenced by the flexibility in the displacement-controlled loading rig (there was a load-controlled component in the application of the loads). A section of the saw-tooth shaped sideswipe is shown in Figure 7.6. From Figure 7.6[a] it can be seen that the unloading sections are characterised by rapid shearing and penetration, whilst the loading sections are characterised by slow shearing and penetration, which is followed by heave in some cycles. From the plot of the vertical load and pore pressure load in Figure 7.6[b], it is evident that the rapid shearing and penetration (and hence contraction) were associated with negative pore pressures. One would expect the contraction of a sand mass to be associated with positive pore pressures. Although the mass as a whole was contracting, the layer of sand immediately beneath the footing might have been dilating. Low negative pore pressures were associated with all of the sideswipe tests even though the footing was penetrating in each test (see Figure 7.1[f]). This illustrates the complex localised nature of the mechanism beneath the footing.

The analysis of the combined load tests of Gottardi and Houlsby (1995) in Section 2.3.3 indicated that the shape of the surfaces tracked by sideswipe tests was influenced by the ratio of V_{0i} to V_m. That is, the shape was influenced by the ratio of the initial vertical load to the bearing capacity load. Normalisation by V_m, as opposed to V_0, resulted in a more sensible framework for analysing the sideswipe tests.

The evidence that h_0 was dependent on the value of V_{0i}/V_m was reinforced by sideswipe tests conducted by Byrne and Houlsby (1999) on dense Baskarp Cyclone sand (the same sand as used in this project). The value of h_0 decreased as V_{0i}/V_m increased, or as the initial vertical load approached the bearing capacity load. The relationship between V_{0i}/V_m and h_0 shown in Figure

2.10, and expressed by Equation 2.11, is assumed to be applicable to the tests in this project. This assumption could not be verified, as the bearing capacity loads of the tests in this project were not measured, they were estimated. The above postulate inferred that the aforementioned relationship was valid for a larger footing than that from which the relationship was derived. The relationship should be sufficiently generic considering that data from tests on two very different sands (in terms of grain size and shape, and also with relative densities that differed by 20%) were used to derive the relationship.

The results of this investigation indicate a similar trend to that inferred by Equation 2.11, as the values of h_o shown in Figure 7.4[b] were larger in the tests on the stiffer samples. Note that in Section 6.2.3 it was suggested that the characterisation stiffness was proportional to the bearing capacity. Therefore the value of V_{oi}/V_m for test T204_1 should be substantially less than that for test T101_1. The two tests of T118 did not fit the general trend between h_o and V_{oi}/V_m. One would expect the value of h_o in test T118D_2 to be less than the value in test T118D_1, as the value of V_{oi} was greater in test T118D_2. The value of V_m in the two tests was constant as they were performed on the same sample.

Equation 2.9 was used to fit parabolas to the drained sideswipe tests shown in Figure 7.7, so as to derive values of h_o. The measured load paths in Figure 7.7 do not represent points along a single yield surface because of the vertical penetration that occurs during the sideswipe tests. In cases where the value of V_o/V_m changed considerably during the sideswipe, where the vertical penetration was significant, the value of h_o would change accordingly.

The data in Figure 2.10 indicates that the value of h_o, and hence the shape of the V:H yield surface, is particularly sensitive at low values of V_{oi}/V_m. The values of V_o/V_m at the start and at the end of the sideswipe tests are listed in the table included in Figure 7.7. Two yield surfaces, representative of the start and the end of the sideswipes, are also shown in some of the plots where the value of h_o is expected to change significantly. By fitting parabolas to different sections of the load paths shown in Figure 7.7, it is implied that if constant vertical displacement sideswipes were conducted at the different sections they would produce parabolic shaped surfaces. The evidence from the tests of Gottardi and Houlsby (1995), of Byrne and Houlsby (1999), and from test T204_1 indicated that V:H yield surfaces at low values of V_o/V_m could not be modelled by a parabolic

curve. Extrapolating a parabolic curve from the start of a sideswipe could also lead to an overestimate of the value of h_0, as the presence of an overconsolidated state would affect the initial section of a sideswipe. The values of h_0 deduced from the parabolic curves, which are fitted to the start and end of the sideswipes in Figure 7.7, should be viewed as extreme values.

The values of V_0/V_m at the start and at the end of tests T204_1, T309_1, T118D_1 and T118D_2 indicated that the shape of the yield surface probably changed during these tests. The values of h_0 at the end of all of the aforementioned tests, except test T204_1, are lower than at the start. This is in agreement with the expected trend between h_0 and V_{0i}/V_m. The load path of test T204_1 indicates that a parabolic shape cannot be used to model the surface at very low values of V_0/V_m. The complex response observed in test T204_1 was due to strong dilatant shearing of the foundation sand. The dilatant shearing resulted in heave of the footing and a consequent increase in the vertical load. This is illustrated in Figure 7.1[g] and Figure 7.1[d] respectively. On exhaustion of the dilatant behaviour at the peak horizontal load, the vertical and horizontal load reduced. Both of these loads would probably have reduced to zero, or to a critical state, if the sideswipe were continued.

The values of h_0 deduced from Figure 7.7 are compared to the results of Gottardi and Houlsby (1995) and of Byrne and Houlsby (1999) in Figure 7.8. The values of h_0 for the surfaces fitted to the start of the sideswipes are generally higher than those that were indicated by Equation 2.11. This is expected since the aforementioned values of h_0 are probably not representative. It should be noted that in the derivation of Equation 2.11, values of V_0/V_m at the start of sideswipes were correlated with peak values of h_0. This methodology is acceptable when the shape of the surfaces traversed by a sideswipe do not change considerably. In modelling the effect of footing penetration on the shape of the yield surface, it may be better to correlate peak values of h_0 with the corresponding values of V_0/V_m. It should be remembered that the values of V_m are estimated from the cone penetrometer tests. The variability in the value of V_0/V_m of test T204_1, caused by a $\pm 1°$ variation in the estimate of the peak friction angle, is shown in Figure 7.8.

The V_m-normalised sideswipes are shown in Figure 7.9. One would expect the load paths to follow a similar trend to the sideswipes of Gottardi and Houlsby (1995) (shown in Figure 2.9[b]) where the peak values of H/V_m were proportional to the corresponding values of V/V_m. It is evident

from Figure 7.9, however, that the paths of test T204_1 and T309_1 cross those of the other tests. This is probably due to unrepresentative bearing capacity estimates. The bearing capacity values of tests T204 and T309 are either underestimated or those of the other tests are overestimated, or a combination of both. The range due to a ±1° variation in the estimate of the peak friction angle for tests T204 and T118 is shown in Figure 7.9. The parabola that fit the V_m-normalised results of Gottardi and Houlsby (Equation 2.9 with $h_0 = 0.12$) is also shown in Figure 7.9. The end points of T204_1 and T309_1 are a substantial way outside of this parabola. This reinforces the idea that the bearing capacity values of these two tests are underestimated.

7.2.2 Shape of the yield surfaces on reversal of horizontal displacement

Reverse displacement sideswipes were performed at the end of some of the drained sideswipes and these are shown in Figure 7.10. These sideswipes were performed to investigate the shape of the yield surfaces after load reversal. Most of the reverse displacement sideswipes were displaced at rates greater than 0.001 mm/s, but the rates on the saturated samples were not more than a factor of ten greater than the drained rate. The pore pressure loads calculated assuming a parabolic distribution are shown in Figure 7.10[d]. The maximum pore pressures measured during the reverse-displacement sideswipes were about twice those measured during the initial drained sideswipes, and were of an opposite sign as well. The change from negative to positive pore pressure was due to the increased rate of contraction (or penetration as shown in Figure 7.10[c]) associated with the particle rearrangement. After the reversal, the pore pressures decreased and probably would have tended to steady negative values once again.

The initial and reverse-displacement yield surfaces are shown in Figure 7.10[e] and the attached enlarged view. The fitted yield surfaces in the *V*:*H* plane are representative of the end points of the initial sideswipes and those in the *V*:(-*H*) plane are representative of the end points of the reverse displacement sideswipes. The fitted surfaces were corrected for the associated vertical penetration, as well as the probable change in the shape of the surfaces. The reverse-displacement sideswipes of tests T101_1, T309_1, and T118D_2 approached the probable yield surfaces. This indicates that the findings relating to the shape of the yield surfaces are applicable even after load reversal. Yield surfaces are not fitted to the sideswipes of tests T204_1 and T118D_1. This is

because parabolic yield surfaces cannot model the path tracked by a sideswipe test performed at very low values of V_o/V_m, and because the reverse-displacement sideswipe of T118D_1 was not displaced sufficiently.

The shape of the loading and reverse loading sideswipes in Figure 7.10[e] is very similar to the drained constant volume load paths investigated by Luong (1980). The p':q triaxial load paths tracked by Luong were initially parabolic, but then moved upwards along a "characteristic state line" once they approached the failure surface. Tests T204_1 and T118D_2 behaved in a similar fashion. Thus the sliding line evident in footing tests may be analogous to the characteristic state line. The load paths in the undrained triaxial tests performed by Luong were also very similar to the drained constant volume paths.

7.2.3 Location of the critical state point

The point at which a footing could be displaced *continuously* at constant load and vertical displacement was labelled the critical state point. Tan (1990) referred to this point as the "line of parallel points". If a critical state point exists in V:H space, one would expect load paths from high values of V/V_m to move down towards this point and for load paths from low values of V/V_m to move up towards this point. The model footing tests of Gottardi and Houlsby (1995) indicated that a critical state point did not exist in V:H space at values of V/V_m greater than 0.05 (as discussed at the end of Section 2.4.2).

Consideration of the vertical load, horizontal load, and vertical displacement of the sideswipe tests (shown in Figure 7.1[d], [e] and [g]) indicates that none of the tests reached a critical state point. Consequently, from the V_m-normalised sideswipe tests shown in Figure 7.9, it can be seen that a critical state point did not exist at values of V/V_m greater than about 0.05 (assuming that the estimated bearing capacity value for test T118 was representative). Test T204_1 did achieve a temporary state of constant load and penetration after the footing heaved, but the load path reversed after reaching this state at peak horizontal load. This is clear from Figure 7.4[b]. If a critical state point does not exist in V:H space, then the load path of test T204_1 shown in Figure 7.4[b] and Figure 7.9 would approach the origin after backtracking on itself. For this to happen, the shearing of the foundation soil would have to result in volumetric contraction (the dilatant shearing

would have to be unsustainable). There is evidence in the literature of unstable dilatant shearing of sand at large strains. Han and Vardoulakis (1991) measured post failure volumetric contraction in the shear bands that developed in biaxial element tests.

The sideswipes that were tracked on the reversal of the horizontal displacement did not reach critical state points (the footing was displaced in the opposite horizontal direction after some of the sideswipe tests, see Section 7.2.2). At least one component of the two loads and displacements shown in Figure 7.10 is changing at the end of the reverse displacement sideswipes. Although the load paths of the reverse displacement sideswipes of T204_1 and T118D_2 shown in Figure 7.10[e] are tracking up probable yield surfaces, these paths would probably backtrack on themselves and approach the origin. That is, if they behave in a similar fashion to that observed in the positive sideswipe of T204_1.

7.3 Drained *V*:*M* sideswipe tests

Five drained moment sideswipes (MSS) were performed. In addition to these, two multi-rate sideswipe tests (MSSM) with drained components were performed in test T120. A comprehensive set of plots of the drained moment sideswipes is shown in Figure 7.11. It can be seen from these plots that tests T319D_2 and T120E_M2 were displaced in the negative rotational direction (or anti-clockwise). The tests were commenced from V_{oi} values between 1500 N and 2100 N (see Figure 7.11[a]). The V_{oi} values of each test are listed in Table 7.2.

Low values of pore pressure were measured at the centre of the footing, even though the tests performed at a rotational displacement rate of 0.0026 mm/s are assumed to be drained. The rotational displacement was defined as $2R\theta$. The pore pressure load shown in Figure 7.11[f] is calculated assuming a parabolic pore pressure distribution on the base of the footing. This load varies between zero and -20 N.

The values of V_{oi} and the intended and measured displacement rates of the moment sideswipe tests are listed in Table 7.2. Note that a rotational displacement rate of 1 mm/s is equivalent to an angular rate of 0.38 deg/s. The measured displacement rates shown in Figure 7.12 are not less than 80% of the intended rates. The variation of the displacement rates with the characterisation stiffness values of the moment sideswipe tests is shown in Figure 7.13.

7.3.1 Shape of the yield surfaces

The sideswipes are shown in V:$M/2R$ space and in V_0-normalised space in Figure 7.14. Tests T120D_M1 and T120E_M2 were multi-rate tests in which the rotational displacement rate was alternated between 0.0026 mm/s and 0.262 mm/s. The flatter sections of the multi-rate tests represented the slower displacement rate.

There is a trend between the values of the characterisation stiffness and the shape of the sideswipes of tests T102, T311 and T319 shown in Figure 7.14[a]. The results from the multi-rate sideswipes of T120 do not fit this trend. Although the characterisation stiffness and the estimated bearing capacity values of tests T319 and T120 are similar, the surfaces tracked in T120 are smaller than those in T319 are. This difference is better illustrated in Figure 7.14[b] where the loads are normalised by V_0. It was possible that the response in the slow (and drained) sections of the multi-rate sideswipes was affected by the fast moves. The sideswipes of T319D_1 and T319D_2 were commenced from slightly overconsolidated states. The initial vertical loads were about 5% overconsolidated. Consequently, the sideswipes started from V/V_0 values of about 0.95 (as shown in Figure 7.14[b]).

The tests shown in Figure 7.14[b] are corrected for the vertical penetration that occurred during the tests. The difference between V_{0i} and V_0 normalisation is shown in Figure 7.15. The magnitude of the correction is greatest in the stiffest samples. The probable degrading effect of the excess pore pressures in the multi-rate tests is not accounted for.

The shapes of the sideswipe tests in Figure 7.14[b] are generally parabolic. The sideswipes of test T319 were stopped at the upper soft limits that were set on the moment load. These limits were set to protect the load cell. A parabola defined by Equation 2.14 with $m_0 = 0.09$ is also shown in Figure 7.14[b]. This parabola was representative of the V_m-normalised yield surface of the moment sideswipe tests of Gottardi and Houlsby (1995) shown in Figure 2.12. But in accordance with the tests of Gottardi and Houlsby, the sideswipes do not converge to this probable yield surface when plotted in V_0-normalised space.

The analysis of the combined load tests of Gottardi and Houlsby (1995) and of Byrne and Houlsby (1999) in Section 2.3.4 indicates that the shape of the moment yield surfaces is influenced

by the ratio of V_{oi} to V_m. Their results relating to V:H response indicate a similar dependency. The relationship between V_{oi}/V_m and m_o shown in Figure 2.10, and expressed by Equation 2.15, should be applicable to the tests in this project (for reasons outlined in Section 7.2.1).

Equation 2.14 is used to fit parabolas to the drained sideswipe tests shown Figure 7.16, so as to derive values of m_o. The measured load paths in Figure 7.16 do not represent points along a single yield surface because of the vertical penetration that occurred during the sideswipe tests. In cases where the value of V_o/V_m changed considerably during the sideswipe, the value of m_o would change accordingly. The similar feature relating to the horizontal sideswipes was discussed in detail in Section 7.2.1. This discussion should be applicable to the moment sideswipe results as well.

The values of V_o/V_m at the start and at the end of the sideswipe tests are listed in the table included in Figure 7.16. Two yield surfaces (representative of the start and the end of the sideswipes) are also shown in some of the plots where the sideswipes tracked into the post-peak region. That is, in the plots of tests T102A_2 and T311_3. The initial shape of the sideswipes of test T319 in Figure 7.16 is affected by the overconsolidation that was present. The load path of these tests is parabolic once the value of V_o increases beyond the overconsolidation load.

The values of m_o deduced from Figure 7.16 were compared with the results of Gottardi and Houlsby (1995) and of Byrne and Houlsby (1999), in the form of Equation 2.15, in Figure 7.17. The values of m_o deduced from the end points of the sideswipes of test T319 are similar to the values of Equation 2.15. The values of m_o of the other sideswipes are all substantially less than the values implied by Equation 2.15. Even the values of m_o that are deduced from the start of the sideswipes of T102A_2 and T311_3 are less. It is possible that the estimate of the bearing capacity of T102 is too high. The estimated value of V_m of T102 is about 50% larger than the value of T311, although the characterisation stiffness is less. The difference between the m_o values of the sideswipes of test T120 and T319 could not be explained. The measured values of characterisation stiffness and the estimated values of bearing capacity of the two different samples are both similar. It is possible that the partially-drained components of the multi-rate sideswipes of T120 had a degrading effect.

The V_m-normalised sideswipes are shown in Figure 7.18. The load paths do not follow a

similar trend to the sideswipes of Gottardi and Houlsby (1995), shown in Figure 2.12[b], where the peak values of $M/2RV_m$ were proportional to the corresponding values of V/V_m. The path of the sideswipes of test T319 shown in Figure 7.18 cross those of the other tests. This was probably due to unrepresentative bearing capacity estimates. The sideswipes were all within the parabola that fit the V_m-normalised results of Gottardi and Houlsby (Equation 2.14 with $m_o = 0.09$). This indicates that the V_m yield surface under moment loading in this project is probably smaller than that implied by the tests of Gottardi and Houlsby.

7.3.2 Shape of the yield surfaces on reversal of rotation

A reverse rotation sideswipe was only performed at the end of test T102A_2, and not at the end of the other moment sideswipe tests. The pattern of behaviour on reversal of rotation at the end of test T102A_2 was very similar to that observed in the horizontal sideswipes. The load path approached the probable yield surface in V:($-M/2R$) space.

7.3.3 Location of the critical state point

The definition of the critical state point relevant to the footing problem was outlined in Section 7.2.3. The moment sideswipe tests of Gottardi and Houlsby (1995) indicated that a critical state point was probable at $V/V_m \cong 0.25$ (this is discussed at the end of Section 2.4.2).

Tests T102A_2 and T311_3 were approaching a critical state at the end of the tests. The vertical and moment loads shown in Figure 7.11[d] and [e] are stabilising, and the rates of penetration shown in Figure 7.11[g] are reducing. If the estimated values of V_m for tests T102 and T311 are accurate, then the V_m-normalised data in Figure 7.18 implies that the critical state point is located at $V/V_m \cong 0.1$. It is probable, however, that the estimated values of V_m are unrepresentative. If the V_m values of tests T102 and T311 are reduced so as to locate the end points of these tests at $V/V_m \cong 0.25$, the required values of V_m would be unrealistically low (equal to about 2000 N). This indicates that the critical state point suggested by the moment sideswipe tests in this project is probably located at a V/V_m ratio less than 0.25.

7.4 Drained load:deformation behaviour

7.4.1 Load:deformation behaviour within the yield surface

Two sets of horizontal and moment load-unload loops were performed in test T120. The loops were performed at load states within the *V*:*H*:*M* yield surface. The load-unload loops, and the load and vertical displacement time histories, are shown in Figure 7.19. The first set of loops shown in Figure 7.19[a] to [d] indicates that the vertical load and displacement are constant, implying that the loops are mainly elastic and that the load-unload stiffness values are representative. The vertical load reduces substantially during the second set of loops shown in Figure 7.19[e] to [h]. This indicates that the sand base was subjected to significant plastic deformation. The plastic deformation is pronounced during the negative loading section of the horizontal loop (see Figure 7.19[g] and [h]). This results in the open loop shown in Figure 7.19[e].

The vertical unload-reload stiffness associated with the first set of combined load loops was 5560 N/mm. This value is similar to the small strain stiffness values listed in Table 6.2. Thus the ratios of the combined load stiffness values to the vertical stiffness are $H/u = 0.5V/w$ and $M/(R^2\theta) = 0.3V/w$. These ratios are about half the value of those derived from elastic theory and about twice the value of those measured in the footing tests of Gottardi and Houlsby (1995). Ratios are not calculated for the second set of loops because of the plastic deformation that occurred.

The load paths preceding the loop events, the proximity of the probable yield surfaces in *V*:*H* space, and the proximity of the elastic-to-plastic transition surfaces in *V*:*H* space are investigated with the aim of explaining the difference between the two sets of events shown in Figure 7.19. The transition surfaces are deduced from the vertical reloading response that is analysed in Section 6.2.5 and illustrated in Figure 6.16. The load paths preceding the first set of loop events are shown Figure 7.20[a] to [f], and those preceding the second set are shown in Figure 7.20[g] to [l]. Although both sets of events were performed at states within the *V*:*H*:*M* yield surface, the first set of events were performed after unloading, whilst the second set were performed after unloading and some reloading. Both of the loop events are also within the *V*:*H* elastic-to-plastic transition surfaces shown in Figure 7.20[f] and [l]. These surfaces are representative of the start position of the loop events.

The yielding observed in the horizontal loading part of the second set of loop events cannot be explained by the proximity of the transition surface. This response indicates that the combined loading behaviour within the yield surface cannot be assumed to be predominantly elastic. The response of the footing during the reverse displacement moves, which were performed after some of the horizontal sideswipes, was also highly plastic, even though the load paths were within the yield surfaces. The reverse displacement moves are discussed in 7.2.2 and shown in Figure 7.10.

7.4.2 Load:deformation behaviour on the yield surface

A feature of plasticity theory is that the plastic strain increment vectors are only governed by the ratio of stresses at the relevant point, and not by the stress path. The relationship between the stress ratio and the plastic strain increment vectors is called a flow rule. The variation between the load ratio and the plastic displacement increment vectors, derived from some of the drained horizontal sideswipe tests, is investigated. It is possible to deduce plastic displacement increment vectors because there was significant vertical penetration during the sideswipe tests. The plastic load:deformation behaviour of the tests is compared with the results of footing tests in the literature.

The load ratio is defined as H/V and is presented as the angle $\tan^{-1}(H/V)$. The plastic displacements (and hence the plastic displacement increments) are calculated by subtracting the estimated elastic component from the measured displacements. A vertical elastic stiffness of 3 kN/mm and a horizontal elastic stiffness of 2.5 kN/mm were assumed (see Section 6.2.5 and 7.4.1). An illustration of the elastic and plastic displacements in w:V space is given in Figure 2.8[b]. The plastic displacement increment vector is presented as the angle $\tan^{-1}(du_p/dw_p)$.

The $\tan^{-1}(du_p/dw_p)$:$\tan^{-1}(H/V)$ results from some of the drained sideswipe tests of this investigation are compared to the results from the model footing tests of Gottardi and Houlsby (1995) in Figure 7.21. The results from a constant V test and from an overconsolidated sideswipe test are included in the data from Gottardi and Houlsby in Figure 7.21[a]. The variation between the load and displacement ratios shown in Figure 7.21[b], of the sideswipe tests of this investigation, are similar to those of Gottardi and Houlsby. The load and displacement ratios increase as the sideswipes progressed.

The load ratios shown in Figure 7.21[b] are still increasing at the end of the tests, except the ratio in test T204_1 that reduces slightly after reaching a peak value. This is consistent with the shape of the load paths shown in Figure 7.4. The load ratios would have tended to constant values at low values of V/V_m if the paths were to follow sliding lines. The displacement ratios indicate that the vertical component of the vectors tend to zero as the sideswipes progressed. The footing heaves in the sideswipe initiated from the lowest value of V/V_m (in test T204_1).

The displacement vectors shown in Figure 7.21[b] are angled between 60° and 90° to the horizontal over most of the length of the sideswipes. These angles are larger than those indicated by the plastic potentials suggested by Tan (1990) and Cassidy (1996), and shown in Figure 2.18. That is, the vertical component of the vectors measured in this research is significantly less than that suggested by the aforementioned authors. This difference is probably due to the variation in the direction of the load paths used to expand the yield surface. Tan used constant V probes and Cassidy used the constant V tests and constant load-ratio tests performed by Gottardi and Houlsby (1995). Cassidy (1999) also noted a difference in the flow rules suggested by the constant V probes and constant load-ratio tests of Gottardi and Houlsby.

The flow response of the sideswipe tests shown in Figure 7.21[b] is not appreciably affected by the wide range of the V_o/V_m values between the tests. The relationship between the load ratio and plastic displacement increment vectors of the moment sideswipes were also investigated. The ratios of the displacements at the start of the moment sideswipes were equal to approximately 70°. At the end of the moment sideswipes, the load ratios were about 12° and the displacement ratios were about 85°.

The horizontal stiffness over the initial section of the horizontal sideswipes range between 2 kN/mm and 3 kN/mm (measured to 25% of the peak horizontal load). Thus the load:deformation response of the initial sections of the sideswipes is similar to the elastic response. The comparable moment stiffness was about 500 N/mm, which is a factor of about three less than the relevant elastic stiffness.

7.5 Partially-drained *V*:*H* sideswipe tests

Six partially-drained horizontal sideswipes (HSS) were performed. In addition to these, two

multi-rate sideswipes (HSSM) with partially-drained components were performed in test T120. The footing was displaced horizontally at rates of 0.1 mm/s and 0.4 mm/s in the partially-drained sideswipe tests (the rate in the drained tests was 0.001 mm/s). The distribution of the displacement rates with the characterisation stiffness of the samples is shown in Figure 7.3. The values of V_{oi} and the intended and measured displacement rates of the tests are listed in Table 7.1. The ratio of the measured rates to the intended rates is plotted against the characterisation stiffness in Figure 7.2. This ratio decreased with increasing characterisation stiffness because of the flexibility in the rig.

A comprehensive set of plots of the partially-drained tests at $\dot{u}$ = 0.1 mm/s and $\dot{u}$ = 0.4 mm/s are shown in Figure 7.22 and Figure 7.23 respectively. All of the tests shown in Figure 7.22[a] and Figure 7.23[a], except T103A_3, were commenced from V_{oi} values of about 1500 N. Test T103A_3 was commenced from V_{oi} = 1340 N. Tests T103A_3 and T315C_1 were conducted from overconsolidated states. The footing was unloaded from V = 1600 N before test T103A_3. A sideswipe was attempted from V = 1500 N before T315C_1 was performed. There was an error in the input file of this initial sideswipe, which was recorded as test T315_3. The failed sideswipe resulted in expansion of the yield surface to an extrapolated virgin-penetration load of V = 1650 N.

7.5.1 Displacements and associated pore pressures

The pore pressure response of sand undergoing shear loading in element tests is dependent on the potential for volumetric strains associated with the shear strains. Sand that dilates when sheared under drained conditions results in negative pore pressures when sheared under undrained conditions. And sand that contracts when sheared under drained conditions results in positive pore pressures when sheared under undrained conditions. If the vertical and the horizontal displacements of a footing are representative of the volumetric and the shear strains respectively, one would expect the pore pressure response under partially-drained loading to be dependent on the potential for vertical penetration or heave. The pore pressure responses in the partially-drained sideswipe tests are compared with the vertical displacements in the drained sideswipe tests (tests with similar values of characterisation stiffness being comparable).

The ratio of plastic displacements from the drained sideswipe tests shown Figure 7.21[b] indicates that the rate of vertical displacement decreased as the sideswipes progressed. In the latter

stages of the test on the stiffest sample (T204_1), the footing heaved. The effect of the characterisation stiffness on the vertical displacement is evident from Figure 7.1[g]. If the low pore pressures measured in the drained sideswipe tests did not affect the displacements, then under partially-drained loading one would expect an initial positive pore pressure, which should reduce as the horizontal displacement increased. The pore pressure should not decrease continuously, however, as the footings penetrate after heaving.

The pore pressure response of the partially-drained tests shown in Figure 7.22[g] and Figure 7.23[g] followed the expected trend, except the tests initiated from overconsolidated states. Tests T103A_3 and T315C_1, which were performed from overconsolidated states, did not develop initial positive pore pressures. This is understandable since overconsolidation results in increased dilatancy. This is also evident when comparing the ratio of the plastic displacements of the overconsolidated sideswipe with the normal sideswipes in Figure 7.21[a].

The coupling between the pore pressure response and the vertical displacement is evident from the effect that the horizontal displacement rate has on the slope of the u:w curves shown in Figure 7.1[g], Figure 7.22[h] and Figure 7.23[h]. The vertical penetration (comparing tests on samples with similar values of characterisation stiffness) reduced with increasing horizontal displacement rate. At very fast horizontal displacement rates, as the drainage reduces to zero, one would expect the vertical penetration to tend to a minimum.

7.5.2 Shape of the yield surfaces

The probable drained yield surfaces of each of the partially-drained sideswipe tests were deduced from the relationship between the shape of the surfaces in the drained sideswipe tests and the characterisation stiffness values. The sideswipe test results of Gottardi and Houlsby (1995) and of Byrne and Houlsby (1999) indicated that the shape of a sideswipe was dependent on the ratio of V_{oi}/V_m. This relationship was not used to deduce the probable drained yield surfaces because the V_m estimates in this investigation were unrepresentative. The normalised peak horizontal loads of the drained tests are plotted against the characterisation stiffness in Figure 7.24. The peak values in Figure 7.24[a] are not corrected for the vertical penetration, as they are normalised by the initial vertical load. The values in Figure 7.24[b] are normalised by V_0 and are therefore corrected for the

vertical penetration. The effect of the correction on the normalised peak horizontal load is negligible at low values of K_{ch}, and reduces the load by about 0.03 at high values of K_{ch}.

The effect of the horizontal displacement rate on the uncorrected (for vertical penetration) sideswipes was deduced by comparing probable drained and partially-drained V_{oi}-normalised sideswipes. The procedure for correcting the partially-drained sideswipes (or for choosing an appropriate value of V_o with which to normalise the loads) was not straightforward. Some possible methods for choosing the penetration corrected normalising load V_o are illustrated in Figure 7.25.

The vertical load:deformation behaviour is shown in Figure 7.25[a] and interaction of the loads is shown in Figure 7.25[b]. The sideswipe is commenced from the initial virgin-penetration load V_{oi}. The effective load V' at a point in the sideswipe is less than the total load V since a positive pore pressure load is assumed. The analysis of the vertical partially-drained tests in Section 6.5 indicates that there are unique partially-drained penetration curves. These are above the virgin-penetration curve and their heights are dependent on the rate of penetration. The stiffness $K_{vp\text{-}p}$ of the w:V path from the drained virgin-penetration curve up to the partially-drained penetration curves is higher than the drained unload-reload stiffness K'_{ulrl} (and is probably rate dependent as well). The analysis of the consolidation tests in Section 6.4 also indicates that the unload-reload stiffness is rate dependent.

Therefore it is possible that the total load V in Figure 7.25[a] should be normalised by the loads at either points $V_{o\text{-}pd2}$ or $V_{o\text{-}pd3}$, as opposed to the load at point $V_{o\text{-}pd1}$. The normalising load $V_{o\text{-}pd2}$ was extrapolated up to the partially-drained penetration curve at some drained elastic stiffness K_d and the normalising load $V_{o\text{-}pd3}$ was extrapolated up at some partially-drained (and vertical rate dependent) stiffness K_{pd}. Although the vertical penetration associated with the sideswipe shown in Figure 7.25 is zero, the plastic vertical penetration is greater than zero. Hence a plastic vertical penetration rate can be deduced.

The partially-drained sideswipes were not corrected for the vertical penetration because of the ambiguity concerning the choice of an appropriate normalising load. Although the procedure for correcting the effective load V' is straightforward (as shown in Figure 7.25[a]), this was not undertaken because the single pore pressure measurement at the centre of the footing was most

probably not representative of the pore pressures on the whole of the footing. This was due to the unsymmetrical *V:H* loading. The total load and effective load sideswipes are compared with probable drained parabolas in the following paragraphs.

The V_{oi}-normalised partially-drained sideswipes are shown in Figure 7.26. The tests in the left column were displaced at 0.1 mm/s and those in the right column were displaced at 0.4 mm/s. The rows represent three ranges of characterisation stiffness. The values of the characterisation stiffness are listed in the individual plots. The total load and the probable drained parabola are shown as thick lines. The thin dotted lines represent the parabolas that were fitted to the total load sideswipes. The effective load sideswipes are also shown.

The total load sideswipes shown in Figure 7.26 track surfaces that are larger than the drained parabola, except the sideswipe of T103A_3. This suggests that the size of yield surfaces tracked by horizontal sideswipe tests is rate dependent. Although two of the slower sideswipes were overconsolidated, there is a noticeable increase in the size of the surfaces tracked at the faster displacement rate as well. The parabolas fitted to the total load sideswipes indicate that the intermediate section of the partially-drained surfaces can be modelled by an increased partially-drained V_{oi} value. This is in accord with the findings of the vertical partially-drained tests.

The following two parameters were adjusted to fit the parabolas to the total load sideswipes in Figure 7.26: the intercept with the horizontal axis (or V_{oi} value); and the normalised peak horizontal load (or h_o value). The intercept value affected the size and the peak value affected the shape. The magnitudes of these values, relative to the drained parabolas, are shown in Figure 7.27. The percentage change in size and peak are plotted against the measured horizontal displacement rates. The values from the overconsolidated tests are not shown. The change in the peak value is erratic but a trend of increasing size with rate is evident in Figure 7.27. The increase in the value of V_{oi} in the fastest tests was about 12%.

The effective load sideswipes (calculated assuming a parabolic pore pressure distribution on the base of the footing) shown in Figure 7.26 do not match the drained parabolas. This suggests that the estimates of the pore pressure loads were unrepresentative or that there was effective stress hardening in the foundation sand, or both. The assumption that the effective load path under partially-drained conditions is similar to the drained load path may not be valid.

Drained load paths were followed after some of the horizontal partially-drained tests. This was done to check the position of the *V*:*H* load point after pore pressure dissipation and to check the yield surface at low values of vertical load. The loads paths followed after three of the partially-drained tests are shown in Figure 7.28. The data was taken from the background logging files. After pore pressure dissipation, the *V*:*H* load point approached the drained parabola in all of the tests. This indicates that there was not much hardening during these partially-drained sideswipes (if the effects of creep are ignored).

7.5.3 Multi-rate sideswipe tests

Two multi-rate horizontal sideswipes tests (HSSM) were performed in which the horizontal displacement rate was alternated between 0.001 mm/s and 0.1 mm/s. The details of these tests are listed in Table 7.1. The measured displacement rates varied between about one tenth and one half of the intended rates. The average measured value of the fast rates was 0.01 mm/s in the first test and 0.025 mm/s in the second test. The results from the partially-drained tests that are shown in Figure 7.27 indicate that the yield surface should expand by about three to five percent during the fast moves of the multi-rate tests. The expanded yield surface is compared with the multi-rate sideswipes in Figure 7.29. A parabola that is five percent larger than the drained sideswipes fit the peaks of the fast moves. The fast moves were not displaced for a sufficient distance to verify if the fast (partially-drained) sections would have tracked along the expanded surface. If the expanded surfaces shown in Figure 7.29 are representative, then the results indicate that the partially-drained surfaces may be unique. That is, the positions of the rate dependent partially-drained surfaces may not affected by the initial load state in *V*:*H* space.

7.6 Partially-Drained *V*:*M* sideswipe Tests

Six partially-drained moment sideswipes (MSS) were performed. In addition to these, two multi-rate sideswipes (MSSM) with partially-drained components were performed in test T120. The footing was rotated at rates of 0.026 mm/s, 0.26 mm/s, and 0.524 mm/s in the partially-drained sideswipe tests (or 0.01 deg/s, 0.1 deg/s, and 0.2 deg/s respectively). The rate in the drained tests was 0.0026 mm/s. The distribution of the displacement rates with the characterisation stiffness of the samples is shown in Figure 7.13. The values of V_{oi} and the intended and measured displacement

rates of the tests are listed in Table 7.2. The ratio of the measured rates to the intended rates is plotted against the characterisation stiffness in Figure 7.12. This ratio decreased with increasing characterisation stiffness because of the flexibility in the rig.

A comprehensive set of plots of the partially-drained tests at $2R\dot{\theta} = 0.026$ mm/s and $2R\dot{\theta} = 0.26$ mm/s, and at $2R\dot{\theta} = 0.524$ mm/s are shown in Figure 7.30 and Figure 7.31 respectively. All of the tests shown in Figure 7.30[a] and Figure 7.31[a], except T317A_1, were commenced from V_{oi} values of about 1500 N. Test T317A_1 was commenced from V_{oi} = 1700 N and from an overconsolidated state. The footing was unloaded from V = 1830 N before test T317A_1. The soft load limit on the moment load was set too low in test T317_3. This test was repeated from a higher vertical load as T317A_1.

7.6.1 Displacements and associated pore pressures

The ratio of plastic displacements of the drained moment sideswipes was similar to that of the horizontal sideswipes. Thus a similar pattern of pore pressure measurements was expected. That is, an initial increase in the pore pressure followed by a reduction. The pore pressure response of the partially-drained moment sideswipes shown in Figure 7.30[g] and Figure 7.31[g] followed the expected trend. The rate of decrease of the pore pressures also reduced at large rotations. In the sideswipe on the least stiff sample (test T105_3 in Figure 7.30[g]), the pore pressure was increasing at the end of the test.

The coupling between the pore pressure response and the vertical displacement is evident from the effect that the rotational displacement rate has on the slope of the $2R\theta$:w curves shown in Figure 7.11[g], Figure 7.30[h] and Figure 7.31[h]. The vertical penetration (comparing tests on samples with similar values of characterisation stiffness) reduced with increasing rotational displacement rate. A similar pattern was observed in the horizontal sideswipe tests.

7.6.2 Shape of the yield surfaces

The probable drained yield surfaces of the partially-drained moment sideswipe tests were estimated from the characterisation stiffness. The relationship between the V_{oi}-normalised peak moments from the drained sideswipes and the characterisation stiffness values was deduced. The procedure was the same as employed with the horizontal tests. The effect of the rotational

displacement rate on the uncorrected (for vertical penetration) sideswipes was deduced by comparing probable drained and partially-drained V_{oi}-normalised sideswipes. The partially-drained moment sideswipes were not corrected for the vertical penetration for the same reasons as outlined in Section 7.5.2.

The V_{oi}-normalised partially-drained sideswipes are shown in Figure 7.32. The tests in the left column were displaced at rates of 0.026 and 0.26 mm/s. The first test in the left column was displaced at 0.26 mm/s. The tests in the right column were displaced at 0.524 mm/s. The rows represent three ranges of characterisation stiffness. The values of the characterisation stiffness are listed in the individual plots. The total load and the probable drained parabola are shown as thick lines. The thin dotted lines represent the parabolas that were fitted to the total load sideswipes. The effective load sideswipes are also shown.

The total load sideswipes shown in Figure 7.32 track surfaces that are larger than the drained parabolas, except the sideswipe of T317A_1 that was overconsolidated. This suggests that the size of yield surfaces tracked by moment sideswipe tests is rate dependent, which is in accord with the results of the horizontal tests. The increase in the size of the partially-drained surfaces is more consistent in the faster tests. The parabolas fitted to the total load sideswipes indicate that the intermediate section of the partially-drained surfaces can be modelled by an increased partially-drained V_{oi} value. This is in accord with the findings of the vertical partially-drained tests.

The following two parameters were adjusted to fit the parabolas to the total load sideswipes in Figure 7.32: the intercept with the x-axis (or V_{oi} value); and the normalised peak moment load (or m_o value). The intercept value affected the size and the peak value affected the shape. The magnitudes of these values, relative to the drained parabolas, are shown in Figure 7.33. The percentage change in size and peak are plotted against the measured horizontal displacement rates. The values from the overconsolidated test is not shown. The change in the peak value is erratic but the trend of increasing size with rate is evident in Figure 7.33. The increase in the value of V_{oi} in fastest tests was about 12%. These results are very similar to those observed in the partially-drained horizontal tests.

The effective loads in the moment sideswipes shown in Figure 7.32 do not differ by much from the total loads. This is not surprising since the positive pressures on the downward half of the

footing and the negative pressures on the upward half of the footing should cancel each other out. This statement is based on the assumption that there is symmetry between loading and unloading, which is not strictly true. The response of the sand subjected to unloading will be predominantly elastic and the response of the sand subjected to loading will be plastic.

The position of the *V:M* load point after pore pressure dissipation was checked for a few of the tests. The load paths followed after three of the partially-drained tests are shown in Figure 7.34. The data was taken from the background logging files. After pore pressure dissipation, the *V:M* load point approaches the drained parabola in test T114E_1 but traverses the drained parabola in the other two tests. This indicates that there was probably some degradation in tests T112E_1 and T313D_1. One would expect, however, a greater degree of degradation in the test on the less stiff sample.

7.6.3 Multi-rate sideswipe tests

Two multi-rate moment sideswipes tests (MSSM) were performed in which the rotational displacement rate was alternated between 0.0026 mm/s and 0.26 mm/s. The details of these tests are listed in Table 7.2. The measured displacement rates were approximately equal to the intended rates. The average measured value of the fast rates was 0.2 mm/s in the first test and 0.28 mm/s in the second test. The results from the partially-drained tests that are shown in Figure 7.33 indicate that the yield surface should expand by about five percent during the fast moves of the multi-rate tests. The expanded yield surface is compared with the multi-rate sideswipes in Figure 7.35. Parabolas that are eight percent and six percent larger than the drained sideswipes fit the peaks of the fast moves of the two tests (T120D_M1 and T120E_M2 respectively). These results are in accord with the results from the horizontal multi-rate tests, and reinforce the postulate that there may be unique partially-drained surfaces.

8 Conclusions

This thesis is concerned with the partially-drained load:deformation behaviour of shallow footings. A flat circular model footing was tested on a sand base under 1-g conditions. The sand was saturated with oil to reduce its permeability. The effects of partial drainage were investigated by varying the displacement rate of the footing. The effect of displacement rate on the vertical and combined load response has been analysed. The vertical virgin-penetration and unload-reload behaviour, and the combined load yield surfaces (V:H and V:M) were investigated.

8.1 Main findings

1 Rig for model testing

The displacement-controlled rig was capable of investigating the partially-drained behaviour of the model footing. For example, vertical displacement rates that differed by a factor of 5000 were investigated. Fully undrained behaviour was probably not attained, however, because of the velocity limits of the drive system. The logging speed of the data acquisition system was also not sufficient for logging the velocities required for fully undrained behaviour.

A displacement measuring system that was capable of measuring the three components of displacement to an accuracy of about ten microns was developed.

2 Sample preparation

Apparatus and procedures were developed for preparing oil-saturated (low-permeability) sand samples. An automated densification process that involved alternate application of downward hydraulic gradient and vibration was successful at preparing dense samples. It was possible to liquefy the samples by applying an upward hydraulic gradient but an automated stirring device was developed to ensured that the samples were fully fluidised.

3 Characterisation of oil-saturated sand samples

The bulk relative density measurements did not correlate well with the response of the footing. The density of the top layer of the samples was gauged from miniature cone penetrometer tests.

4 Initial virgin-penetration stiffness as a characterising parameter

The correlation between the vertical and combined load (drained and partially-drained) behaviour and the drained virgin-penetration stiffness was good.

5 R_D:p':ϕ'_{max} relationship for very low stress levels

A low stress adjustment to Bolton's (1986) method was developed. This was required because the stresses associated with the 1-g miniature cone penetrometer tests were very low.

6 Vertical load: Initial loading and risk of liquefaction

The initial loading of the footing (immediately after touchdown) on the loose samples was prone to liquefaction. This indicates that full drainage should be provided on the underside of foundations during touchdown and the initial stages of loading.

7 Vertical load: Partially-drained consolidation model

An incremental partially-drained consolidation was developed. This model was capable of simulating the partially-drained behaviour of the footing when the response was predominantly elastic.

8 Vertical load: Partially-drained unload-reload behaviour

The partially-drained unloading and reloading of the footing during the consolidation tests indicated that the unload and reload stiffness were rate dependent. The stiffness increased with displacement rate.

9 Vertical load: Partially-drained virgin-penetration behaviour

The virgin-penetration response was dependent on the rate of penetration. This investigation suggests that there are indeed unique penetration curves, which are mainly dependent on the rate of penetration and the drained penetration stiffness (or density of the sand). Two distinct load:deformation sections were evident in the partially-drained penetration curves. The primary section was highly rate dependent and the load change associated with this section could be modelled using an expression derived from rate process theory. The stiffness of the secondary section was similar to the drained virgin-penetration stiffness.

10 Vertical load: Partially-drained virgin-penetration behaviour and risk of liquefaction

Partially-drained loading from the drained virgin-penetration curve resulted in localised liquefaction in some of the loose samples. This highlights the coupling between the density and the

rate on the risk of liquefaction.

11 Vertical load: Partially-drained virgin-penetration behaviour and effective stress

The overall change in the effective load between the start and the end of the partially-drained moves was checked. This indicated that the partially-drained moves resulted in degradation of the effective stiffness, as compared to the drained virgin-penetration stiffness.

12 Combined load: Drained yield surfaces and dependency of shape on V_0/V_m

Analysis of test data in the literature indicated that the shape of combined load yield surfaces tracked by sideswipe tests (horizontal or rotational displacement at constant vertical displacement) is dependent on the ratio of the current vertical load to the vertical bearing capacity load. The results of this investigation showed a similar trend. It is believed that this dependency will only be evident in cases where the foundation sand is prone to dilation. That is, when a general or local shear failure mechanism is probable.

13 Combined load: Drained yield surfaces and critical state points

Investigators have suggested that there are points on the combined load yield surfaces at which constant load and constant vertical displacement shearing occur. The analysis of the results of this investigation, and the analysis of test data in the literature, suggests that there is a critical state point along the *V*:*M* failure surface. With regard to the *V*:*H* failure surface, if a critical state point does exist, its position would be very close to the origin.

14 Combined load: Pore pressures associated with partially-drained moves

The general nature of the pore pressure response during the partially-drained combined load moves could be predicted from the flow rule deduced from similar drained moves. This highlights the coupling between the pore pressure and volumetric strain (vertical displacement).

15 Combined load: Partially-drained yield surfaces

The *V*:*H* and *V*:*M* yield surfaces expanded as the horizontal and rotational rate increased. That is, the partially-drained yield surfaces were larger than the comparable drained surfaces. This investigation suggests that there are unique partially-drained yield surfaces, which are mainly dependent on the rate and the drained response (or density of the sand). Partially-drained loading also resulted in a change in the shape of the surfaces. The effect of increasing rate in the partially-drained tests was similar to the effect of lower values of V_0/V_m in the drained tests. The effective

load yield surfaces (V':H and V':M) might also have expanded.

8.2 Concluding remarks

Aspects of the (total stress) vertical and combined load behaviour of a footing on sand were shown to be rate dependent. The vertical response was stiffer, and the combined load yield surfaces expanded, as the displacement rate increased (or as the degree of drainage decreased). The rate dependent expansion of the virgin-penetration curve was modelled using an expression deduced from rate process theory. Sufficient data were not available to quantify the expansion of the combined load yield surface. But the trend of the results indicated that the initial expansion of the yield surfaces could be modelled using a similar expression to that used to model the vertical load.

The typical dimensions of shallow offshore foundations are such that, when loaded by environmental forces, the loading will be partially-drained. Current design procedures do not account for partial drainage. If the results of this investigation are representative of the prototype situation, then a design based on drained behaviour might be conservative since the partially-drained total stress behaviour is stiffer.

Good analytical models for the drained and undrained monotonic behaviour of footings exist. These models were developed from the results of experiments on model footings. The objective of this investigation was to provide experimental evidence that could be used in the development of an analytical partially-drained footing model. The ultimate objective of further research should be the development of such a model. This, however, is still not possible with the current experimental database. Much more data on partially-drained behaviour is required. Some aspects that need exploring are listed below:

— The effective stress response has to be investigated. The pore pressure distribution on the base of the footing will be required.

— The effects of sustained partially-drained loading, up to failure, on the vertical response have to be studied.

— Monotonic partially-drained loading can trigger liquefaction (or partial liquefaction) in loose samples. Pore pressure measurements across the whole area of a footing, and especially at the edge, would be required to investigate this problem.

— It is important that the fully undrained response be investigated as this, along with the drained response, help define the limits of the problem.

— More data on the effect of rate on the combined load yield surface is needed. The effect on other combined load paths and on the work-softening region has to be investigated as well. The combined load:deformation behaviour, on and within the yield surface, will also be affected by the degree of drainage.

Offshore loading is cyclic, and load reversals can have dramatic effects on the response of sand. Cyclic behaviour is highly complex and difficult to model, but the next step after the development of a monotonic partially-drained model would be the development of a cyclic partially-drained model.

Appendix A

Bearing capacity formulae

The drained bearing capacity formula is as follows,

$$V_{max} = A'\left(\tfrac{1}{2}\gamma B' N_\gamma s_\gamma d_\gamma i_\gamma + q N_q s_q d_q i_q \right) \qquad [A.1]$$

where

V_{max}	vertical failure load
γ'	effective unit weight
q	overburden pressure, $q = z\gamma'$ where z is foundation embedment
A'	effective foundation area
B'	minimum effective foundation dimension
N_γ, N_q	bearing capacity factors
s_γ, s_q	shape factors
d_γ, d_q	depth factors
i_γ, i_q	load inclination factors

The definitions of the factors in Equation A.1 - suggested by Brinch Hansen (1970), Meyerhof (1963) and Vesic (1975) - are listed in Table A.1. The API (1993) procedure for determining the effective foundation dimensions (see Figure 2.6) gives

$$A' = B'L' = \pi R^2 - 2e\sqrt{R^2 - e^2} - 2R^2 \sin^{-1}_{\text{radians}}\left(\frac{e}{R}\right) \qquad [A.2a]$$

$$\frac{L'}{B'} = \sqrt{\frac{R+e}{R-e}} \qquad [A.2b]$$

In the case of a central load (*i.e.* when $e = 0$), using B' derived from Equations A.2a and A.2b instead of $2R$ results in a reduction of 13% in the ultimate load. De Beer (1970) used $B' = 2R$ when developing the shape factors.

Appendix B

Footing displacements from small LVDTs

An arrangement of three small LVDTs was used to measure the displacement of the footing relative to the specimen container. This is discussed in Section 3.3.3 and the LVDT frame is shown in Figure 3.11. A calculation procedure for deriving the displacements of the footing from the measurements of the three small LVDTs is given below.

The parameters used in the calculation are shown in Figure B.1. Points *A*, *B*, and *C* represent the ends of the LVDTs that were fixed to the LVDT frame, which was fixed to the specimen container. Points *D* and *E* represent the ends of the LVDTs that were fixed to the footing. The thick dotted lines in Figure B.1 represent the three LVDTs. These lengths change as the footing displaces. Point *G* represents the load and displacement reference point at the centre of the bottom of the footing. Point *A* is set as the origin and the downward (y) and rightward (x) directions are taken as positive. The position of point *E* is determined from transducers DSV2 and DSH. Points *D* and *G* are then determined by considering DSV1. The length of *DE* and *GH* are fixed, and point *H* is located midway along *DE*.

Point *E*

Consider the triangle *BCE* in Figure B.1. By the cosine rule,

$$\angle BCE = \cos^{-1}\left(\frac{BC^2 + CE^2 - BE^2}{2(BC)(CE)}\right) \qquad [B.1]$$

where *BE* and *CE* are given by DSV2 and DSH respectively, and *BC* is fixed and known from the geometry of the frame. Angle *BCE* is used to deduce the co-ordinates of *E*,

$$x_E = x_C - (CE)\sin(\pi - \angle BCE - \angle BCF)$$
$$y_E = y_C + (CE)\cos(\pi - \angle BCE - \angle BCF) \qquad [B.2a;B.2b]$$

where the co-ordinates of *C* and the angle *BCF* are known.

Point *D*

The length *AE* and angle *DAB* are needed to find the co-ordinates of *D*. From the co-ordinates of *A* and *E*,

$$AE = \sqrt{x_E^2 + y_E^2} \qquad [B.3]$$

since A is taken as the origin. The angle DAB is equal to the sum of angles BAE and DAE, and is given by,

$$\angle DAB = \cos^{-1}\left(\frac{AB^2 + AE^2 - BE^2}{2(AB)(BE)}\right) + \cos^{-1}\left(\frac{AD^2 + AE^2 - DE^2}{2(AD)(AE)}\right) \qquad [B.4]$$

Angle DAB is used to deduce the co-ordinates of D,

$$\begin{aligned} x_D &= (AD)\cos\angle DAB \\ y_D &= (AD)\sin\angle DAB \end{aligned} \qquad [B.5a;B.5b]$$

Point G

The rotation of the G about the vertical is equivalent to the rotation of the footing (θ) and is given by,

$$\theta = \tan^{-1}\left(\frac{y_E - y_D}{x_E - x_D}\right) \qquad [B.6]$$

The co-ordinates of G are,

$$\begin{aligned} x_G &= x_D + (DG)\sin\left(\frac{\pi}{2} - \angle GDH - \theta\right) \\ y_G &= y_D + (DG)\cos\left(\frac{\pi}{2} - \angle GDH - \theta\right) \end{aligned} \qquad [B.7]$$

where length DG and angle GDH are known from the geometry of the footing and the footing/LVDT connecting beam shown in Figure 3.11.

The co-ordinates of G (x_G, y_G) represent the linear displacements of the footing (w, u) and the angle θ represents the rotation. The footing tests were initialised with the LVDT frame and the footing level ($y_A = y_B = 0$ and $y_D = y_E$ respectively), and with DSV1 and DSV2 vertical.

References

Aas, P. M. & Andersen, K. H. (1992). Skirted foundations for offshore structures. *Proc. 9th Offshore South East Asia Conf., Singapore*, 1-8.

Allard, M. A., Andersen, K. H. and Hermstad, J. (1994). Centrifuge model tests of a gravity platform on very dense sand. I: Testing technique and results. *Proc. 7th Conf. on Behaviour of Offshore Structures, Boston*, **1**, pp. 231-254.

Altaee, A. & Fellenius, B. H. (1994). Physical modeling in sand. *Canadian Geotechnical Journal* **31**(3), 420-431.

Americam Petroleum Institute (1993). *Recommended practice for planning, designing and constructing fixed offshore platforms - load and resistance factor design*. RP 2A-LRFD, 1st ed. Washington DC: American Petroleum Institute.

Andersen, K. H. (1972). Bearing capacity of shallow foundations on cohesionless soils. *Internal report 51404-1*.Oslo: Norwegian Geotechnical Institute.

API (1993). *See* American Petroleum Institute (1993).

Atkinson, J. H. (1992). A note on modelling small strain stiffness in Cam-Clay. *Predictive Soil Mechanics (Proc. Wroth Memorial Sym., Oxford)*, 34-39. London: Thomas Telford.

Barltrop, N. D. P. & Adams, A. J. (1991). *Dynamics of fixed marine structures*. 3rd ed. UK: Butterworth-Heinemann Ltd.

Basma, A. A. (1994). Risk-reduction factor for bearing capacity of shallow foundations. *Canadian Geotechnical Journal* **31**(1), 12-16.

Been, K., and Jefferies, M. G. (1985). A state parameter for sands. *Géotechnique* **35**(2), 99-112.

Been, K., Jefferies, M. G. and Hachey, J. (1991). The critical state of sands. *Géotechnique* **41**(3), 365-381.

Bell, R. W. (1991). *The analysis of offshore foundations subjected to combined loading*. M.Sc. thesis, University of Oxford.

Bielby, F. (1989). *Triaxial tests on oil saturated sand*. Part II project report, Cambridge University Engineering Department.

Biot, M. A. (1941). General theory of three-dimensional consolidation. *J. Applied Physics* **12**, 155.

Bolton, M. D. (1986). The strength and dilatancy of sands. *Géotechnique* **36**(1), 65-78.

Bolton, M. D. (1987). The strength and dilatancy of sands (discussion). *Géotechnique* **37**(2), 219-226.

Bolton, M. D. and Lau, C. K. (1993). Vertical bearing capacity factors for circular and strip footings on Mohr-Coulomb soil. *Canadian Geotechnical Journal* **30**(6), 1024-1033.

Bossinesq, J (1885). Application des potentiels à l' équilibre et du mouvements des solides élastiques. Paris: Gauthier-Villars.

Bransby, P. L. (1973). Cambridge contact stress transducers. *Report no. CUED/C-SOILS/LN2*, Cambridge University Engineering Deparment.

Brinch Hansen, J. (1970). A revised and extended formula for bearing capacity. *Bulletin no. 28*, 5-11. Copenhagen: Danish Geotechnical Institute.

Butterfield, R. (1981). Another look at gravity platform foundations. Presented at CISM course *Soil Mech. and Foundation Eng. in Offshore Technology, Udine.*

Butterfield, R. & Gottardi, G. (1994). A complete three-dimensional failure envelope for shallow footings on sand (technical note). *Géotechnique* **44**(1), 181-184.

Butterfield, R., Houlsby, G. T. & Gottardi, G. (1997). Standardised sign conventions and notation for generally loaded foundations. *Géotechnique* **47**(5), 1051-1054.

Butterfield, R. & Ticof, J. (1979). Design parameters for granular soils (discussion contribution). *Proc. 7th European Conf. on Soil Mech. and Foundation Eng., Brighton*, **4**, 259-261.

Bye, A., Erbrich, C., Rognlien, B. & Tjelta, T. (1995). Geotechnical design of bucket foundations. *Proc. 27th Offshore Technology Conf., Houston*, OTC 7793.

Byrne, P. M. & Finn, W. D. L. (1978). Breakout of submerged structures buried to a shallow depth. *Canadian Geotechnical Journal* **15**(2), 146-154.

Byrne, B. W. & Houlsby, G. T. (1999). Drained behaviour of suction caisson foundations on very dense sand. *Proc. 31st Offshore Technology Conf., Houston*, OTC 10994.

Cassidy, M. J. (1996). *The behaviour of jack-up platforms*. First year report, University of Oxford.

Cassidy, M. J. (1999). *The non-linear dynamic response of jack-up units subjected to random wave loading*. D.Phil. thesis (to be published), University of Oxford.

Chiarella, C. & Booker, J. R. (1975). The time-settlement behaviour of a rigid elastic die resting on a deep clay layer. *Q. J. Mech. Appl. Math.* **28**(3), 317-328.

Chu, J. (1995). An Experimental examination of the critical state and other similar concepts for granular soils. *Canadian Geotechnical Journal* **32**(6), 1065-1075.

Corté, J. F. (1989). Model testing - geotechnical model tests (general report, discussion session 11). *Proc. 12th Int. Conf. on Soil Mech. and Foundation Eng., Rio de Janeiro*, **3**, 2553-2571.

Cox, A. D. (1962). Axially symmetric plastic deformations in soils - II. Indentation of ponderable soils. *Int. J. Mech. Sciences* **4**, 371-380.

Cox, A. D., Eason, G. & Hopkins, H. G. (1961). Axially symmetric plastic deformations in soils. *Phil. Trans. Royal Soc. London*, Series A, **25**, 1-45.

Craig, R. F. (1987). *Soil mechanics*. 4th ed. London: Van Nostrand Reinhold.

Davis, E. H. & Poulos, H. G. (1963). Triaxial testing and three-dimensional settlement analysis. *Proc. 4th Aust.-N.Z. Conf. on Soil Mech.* 233.

Davis, E. H. & Poulos, H. G. (1968). The use of elastic theory for settlement prediction under three-dimensional conditions. *Géotechnique* **18**(1), 67-91.

Davis, E. H. & Poulos, H.G. (1972). Rate of settlement under two- and three-dimensional conditions. *Géotechnique* **22**(1), 95-114.

de Beer, E. E. (1965a). Influence of the mean normal stress on the shear strength of sand. *Proc. 6th Int. Conf. on Soil Mech. and Foundation Eng., Montreal*, **1**, 165-169.

de Beer, E. E. (1965b). The scale effect on the phenomenon of progressive rupture in cohesionless soils. *Proc. 6th Int. Conf. on Soil Mech. and Foundation Eng., Montreal*, **2**, 13-17.

de Beer, E. E. (1970). Experimental determination of the shape factors and the bearing capacity factors of sand. *Géotechnique* **20**(4), 387-411.

Dean, E. T. R. (1991). Some potential approximate methods for the preliminary estimation of excess pore pressures and settlement-time curves for submerged circular spud foundations subjected to time-dependent loading. *Report no. CUED/D-Soils/TR240*, Cambridge University Engineering Department.

Dean *et al.* (1992a). *See* Dean, E. T. R., James, R. G., Schofield, A. S., Tan, F. S. C. & Tsukamoto, Y. (1992).

Dean *et al.* (1992b). *See* Dean, E. T. R., James, R. G., Schofield, A. S. & Tsukamoto, Y. (1992).

Dean, E. T. R., James, R. G., Schofield, A. S., Tan, F. S. C. & Tsukamoto, Y. (1992). The bearing capacity of conical footings on sand in relation to the behaviour of spudcan footings of jack-ups. *Predictive Soil Mechanics (Proc. Wroth Memorial Sym., Oxford)*, 230-253. London: Thomas Telford.

Dean, E. T. R., James, R. G., Schofield, A. S. & Tsukamoto, Y. (1992). Combined vertical, horizontal, and moment loading of circular spuds on dense sand foundations. *Report no. CUED/D-Soils/TR244*, Cambridge University Engineering Department.

Douglas, J. F., Gasiorek, J. M. & Swaffield, J. A. (1985). *Fluid mechanics*. 2nd ed. New York: John Wiley and Sons.

Erbrich, C. (1996). Bucket Foundations. *Aust. Centre for Geomech. News Letter* **5**, 1-2.

Eyton, D. G. P. (1982). *Triaxial tests on sands with viscous pore fluid*. Project report, Cambridge University Engineering Department.

Faber, O. (1933). Pressure distribution under bases and the stability of foundations. *Struct. Eng.* **11**(3), 116-125.

Finnie, I. M. S. (1993). *Performance of shallow foundations in calcareous soil*. Ph.D. thesis, University of Western Australia.

Gazetas, G., Dobry, R. & Tassoulas, J. L. (1985). Vertical response of arbitrarily shaped embedded foundations. *Proc. ASCE, J. of the Geotechnical Eng. Div.* **111**(6), 750-771.

Gazetas, G. & Tassoulas, J. L. (1987). Horizontal stiffness of arbitrarily shaped embedded foundations. *Proc. ASCE, J. of the Geotechnical Eng. Div.* **113**(5), 440-457.

Georgiadis, M. & Butterfield, R. (1988). Displacements of footings on sand under eccentric and inclined loads. *Canadian Geotechnical Journal*. **25**(2), 199-212.

Goodman, L. J., Lee, C. N. & Walker, F. J. (1961). The feasibility of vacuum anchorage in soil (correspondence). *Géotechnique* **11**(3), 356-359.

Gottardi, G. & Butterfield, R. (1993). On the bearing capacity of surface footings on sand under general planar loads. *Soils and Foundations* **33**(3), 68-79.

Gottardi, G. & Butterfield, R. (1995). The displacement of a model rigid surface footing on dense sand under general planar loading. *Soils and Foundations* **35**(3), 71-82.

Gottardi, G. & Houlsby, G. T. (1995). Model Tests of Circular Footings on Sand Subjected to Combined Loading. *Report no. OUEL 2071/95*, Oxford University Engineering Laboratory.

Gottardi, G., Houlsby, G. T. & Butterfield, R. (1997). The plastic response of circular footings on sand under general planar loading. *Report no. OUEL 2143/97*, Oxford University Engineering Laboratory.

Griffiths, D. V. (1982). Computation of bearing capacity factors using finite elements. *Géotechnique* **32**(3), 195-202.

Gue, S. S. (1984). *Ground heave around driven piles in clay*. D.Phil. thesis, University of Oxford.

Han, C. & Vardoulakis, I. G. (1991). Plane-strain compression experiments on water-saturated fine-grained sand. *Géotechnique* **41**(1), 49-78.

Hettler, A. & Gudehus, G. (1985). A pressure-dependent correction for displacement results from 1-g model tests with sand. *Géotechnique* **35**(4), 497-510.

Hettler, A. & Gudehus, G. (1988). Influence of the foundation width on the bearing capacity factor. *Soils and Foundations* **28**(4), 81-92.

Hicher, P. Y. (1996). Elastic properties of soils. *Proc. ASCE, J. of the Geotechnical Eng. Div.* **122**(8), 641-648.

Hicks, M. A. & Smith, I. M. (1988). Class A prediction of arctic caisson performance. *Géotechnique* **38**(4), 589-612.

Holubec, I. & D'Appolonia, E. (1973). Effect of particle shape on the engineering properties of granular soils. In *Evaluation of relative density and its role in geotechnical projects involving cohesionless soils*, ASTM STP 523, American Society for Testing and Materials, 304-318.

Houlsby, G. T. (1995). *Geotechnical model testing - Sleipner Vest project*. Main report 1-3 (draft), Civil Engineering Group, University of Oxford.

Houlsby, G. T. & Hitchman, R. (1988). Calibration chamber tests of a cone penetrometer in sand. *Géotechnique* **38**(1), 39-44.

Isaacson, E. de St. Q. & Isaacson, M. de St. Q. (1975). *Dimensional analysis*. London: Edward Arnold.

Ingra, T. S. & Baecher, G. B. (1983). Uncertainty in bearing capacity of sands. *Proc. ASCE, J. of the Geotechnical Eng. Div.* **109**(7), 899-914.

Iwasaki, T., Tatsuoka, F. & Takagi, Y. (1978). Shear moduli of sands under cyclic torsional shear loading. *Soils and Foundations* **18**(1), 39-56.

Jackson, N. & Dhir, R. K. (1988). *Civil engineering materials*. 4th ed. London: MacMillan Education.

Janbu, N. (1985). Soil models in offshore engineering. *Géotechnique* **35**(3), 239-281.

Kerr, A. D. (1989). Tests and analyses of footings on a sand base. *Soil and Foundations* **29**(3), 83-94.

Kolbuszewski, J. (1948). An experimental study of the maximum and minimum porosities of sand. *Proc. 2nd Int. Conf. on Soil Mech. and Foundation Eng., Rotterdam*, **1**, 158-165.

Kolk, H. J. & Campbell, K. J. (1997). Significant developments in offshore geosciences. *Proc. 8th Int. Conf. on Behaviour of Offshore Structures, Delft*, **1**, 3-40.

Lambe, T. W. & Whitman, R. V. (1969). *Soil mechanics - SI version*. New York: John Wiley and Sons.

Lau, C. K. (1988). *Scale effects in tests on footings*. Ph.D. thesis, University of Cambridge.

Lo Presti, D. (1987). *Mechanical behaviour of Ticino sand from resonant column tests*. Ph.D. thesis, Politecnico di Torino.

Luong, M. P. (1980). Stress-strain aspects of cohesionless soils under cyclic and transient loadings. *Proc. Int. Sym. on Soils under Cyclic and Transient Loading, Swansea*, 315-324.

McBean, H. F. & West, C. G. (1987). *The miniature cone penetrometer*. Third year project report, Department of Engineering Science, University of Oxford.

McManus, K. J. & Davis, R. O. (1997). Dilation-induced pore fluid cavitation in sands. *Géotechnique* **47**(1), 173-177.

McNeilan, T. W. (1985). Jack-up rig performance in predominantly silty soils, offshore california. *Proc. 17th Offshore Technology Conf., Houston*, OTC 5082.

Mangal, J. (1994). *Transient loading of offshore foundations*. First year report, Department of Engineering Science, University of Oxford.

Martin, C. M. (1994). *Physical and numerical modelling of offshore foundations under combined loads*. D.Phil. thesis, University of Oxford.

Meyerhof, G. G. (1953). The bearing capacity of foundations under eccentric and inclined loads. *Proc. 3rd Int. Conf. on Soil Mech. and Foundation Eng., Zurich*, **1**, 440-445.

Meyerhof, G. G. (1961). The ultimate bearing capacity of wedge shaped foundations. *Proc. 5th Int. Conf. on Soil Mech. and Foundation Eng., Paris*, **2**, 105-109.

Meyerhof, G. G. (1963). Some recent research on the bearing capacity of foundations. *Canadian Geotechnical Journal* **1**(1), 16-26.

Mitchell, J. K. (1976). *Fundamentals of soil behaviour*. New York: John Wiley and Sons.

Montrasio, L. & Nova, R. (1997). Settlements of shallow foundations on sand: geometrical effects. *Géotechnique* **47**(1), 49-60.

NGI (1993). *see* Norwegian Geotechnical Institute (1993).

NGI (1994a). *see* Norwegian Geotechnical Institute (1994a).

NGI (1994b). *see* Norwegian Geotechnical Institute (1994b).

Ngo-Tran, C. L. (1996). *The analysis of offshore foundations subjected to combined loading*. D.Phil. thesis, University of Oxford.

Noble Denton & Associates (1987). *Foundation fixity of jack-up units: a joint industry study*. London: Noble Denton & Associates.

Norwegian Geotechnical Institute (1993). Model testing of plated skirt foundation in sand - pilot study. *Report no. 933006-1*, 4th August. Oslo: Norwegian Geotechnical Institute.

Norwegian Geotechnical Institute (1994a). Statoil model tests - preliminary results. *Report no. 933013*. Oslo: Norwegian Geotechnical Institute.

Norwegian Geotechnical Institute (1994b). Sleipner T - special laboratory testing. *Report no. 932514-1*, 5th April. Oslo: Norwegian Geotechnical Institute.

Nova, R. & Montrasio, L. (1991). Settlements of shallow foundations on sand. *Géotechnique* **41**(2), 243-256.

Os, A. G. van & Van Leussen, W. (1987). Basic research on cutting forces in saturated sand. *Proc. ASCE, J. of the Geotechnical Eng. Div.* **113**(12), 1501-1516.

Ovesen, N. K. (1979). The use of physical models in design (discussion contribution). *Proc. 7th European Conf. on Soil Mech. and Foundation Eng., Brighton*, **4**, 319-323.

Poorooshasb, H. B. (1995). One gravity model testing. *Soils and Foundations* **35**(3), 55-59.

Poulos, H. G. (1988). *Marine geotechnics*. London: Unwin Hyman.

Poulos, H. G. & Davis, E. H. (1974). *Elastic solutions for soil and rock mechanics*. New York: John Wiley and Sons.

Prandtl, L. (1921). Uber die eindringungfestigkeit plastisher baustoffe und die festigkeit von schneiden. *Zeitschrift fur Angewandte Mathematik und Mechanik*, **1**(1). Basel, Switzerland.

Ricceri, G. & Simonini, P. (1989). Interaction diagrams for shallow footings on sand. *Proc. 12th Int. Conf. on Soil Mech. and Foundation Eng., Rio de Janeiro*, **2**, 967-972.

Roscoe, K. H. & Poorooshasb, H. (1963). A fundamental principle of similarity in model tests for earth pressure problems. In *Proc. 2nd Asian Regional Conf. on Soil Mech., Bangkok*, **1**, 134-140.

Roscoe, K. H. & Schofield, A. N. (1956). The stability of short pier foundations on sand. *British Welding Journal*, January, 12-18.

Scott, C. R. (1980). *An introduction to soil mechanics and foundations*. 3rd ed. London: Applied Science Publishers.

Selvadurai, A. P. S. (1979). Elastic analysis of soil-foundation interaction. Asterdam: Elsevier.

Shi, Q. (1988). *Centrifugal modelling of surface footings subjected to combined loading*. Ph.D. thesis, University of Cambridge.

Shield, R. T. (1955). On the plastic flow of metals under conditions of axial symmetry. *Proc. Royal Soc. London*, Series A, **233**, 267-287.

Simonini, P. (1993). Influence of relative density and stress level on the bearing capacity of sands. *Int. J. Numerical and Analytical Methods in Geomechanics* **17**, 871-890.

SINTEF (1992). Model development for light skirt foundations. *Report no. STF69 F92031*. Norway: SINTEF.

Small, J. C., Booker, J. R. & Davies, E. H. (1976). Elasto-plastic consolidation of soil. *Int. J. Solids and Structures* **12**, 431-448.

Spence, D. A. (1968). Self similar solutions to adhesive contact problems with incremental loading. *Proc. Royal Soc. London*, Series A, **305**, 55-80.

Stephens, R. C. (1970). *Strength of Materials*. London: Edward Arnold.

Tan, F. S. C. (1990). *Centrifuge and theoretical modelling of conical footings on sand*. Ph.D thesis, University of Cambridge.

Taylor, D. W. (1948). *Fundamentals of soil mechanics*. New York: John Wiley and Sons.

Terzaghi, K. (1943). *Theoretical soil mechanics*. New York: John Wiley and Sons.

Vesic, A. S. (1975). Bearing capacity of shallow foundations. In *Foundation Engineering Handbook* (ed. H. F. Winterkorn & H. Y. Fang), 121-147. New York: Van Nostrand

Vesic, A. S., Banks, D. C. & Woodard, J. M. (1965). An experimental study of dynamic bearing capacity of footings on sand. *Proc. 6th Int Conf. on Soil Mech. and Foundation Eng., Montreal*, **2**, 209-213.

Wang, M. C., Demars, K. R. & Nacci, V. A. (1977). Breakout capacity of model suction anchors in soil. *Canadian Geotechnical Journal*. **14**(2), 246-257.

Watson, P. G. & Randolph, M. F. (1997). A yield envelope design approach for caisson foundations in calcarreous sediments. *Proc. 8th Int. Conf. on Behaviour of Offshore Structures, Delft*, **1**, 259- 689.

Wood, D. M. (1990). *Soil behaviour and critical state soil mechanics*. Cambridge: Cambridge University Press.

Wroth, C. P. & Houlsby, G. T. (1985). Soil mechanics - property characterization and analysis procedures. *Proc. 11th Int. Conf. on Soil Mech. and Foundation Eng., San Francisco*, **1**, 1-50.

Yamaguchi, H., Kimura, T. & Fujii, N. (1977). On the scale effect of footings in dense sand. *Proc. 9th Int. Conf. on Soil Mech. and Foundation Eng., Tokyo*, **1**, 795-798.

Yamamuro, J. A. & Lade, P. V. (1998). Steady-state concepts and static liquefaction of silty sands. *Proc. ASCE, J. Geotechnical and Geoenvironmental Eng.* **122**(8), 641-648.

Youd, T. L. (1972). Compaction of sand by repeated shear straining. *Proc. ASCE, J. Soil Mech. and Foundations Div.* **98**(7), 709-725.

Yue, Z. Q., Selvadurai, A. P. S. & Law, K. T. (1994). Excess pore pressure in a poroelastic seabed saturated with a compressible fluid. *Canadian Geotechnical Journal* **31**(6), 898-1003.

Table 1.1 Failure mechanisms of shallow footings

	Sand		Clay	
	Drained	Undrained	Drained	Undrained
Dense sand or Stiff clay	general shear	punching shear	general shear	punching shear
Loose sand or Soft clay	punching shear	*general shear*	punching shear	general shear

Note:
Normal letters — Based on experimental evidence
Italic letters — Postulated

Table 2.1 Elastic stiffness factors of Ngo-Tran (1996) for a rough flat circular footing embedded in an isotropic homogeneous elastic material

w/R	$\nu = 0.2$				$\nu = 0.49$			
	K_1	K_2	K_3	K_4	K_1	K_2	K_3	K_4
0.0	5.406	4.652	3.816	-0.573	8.197	5.554	5.563	-0.015
0.5	5.951	6.117	4.586	-0.843	8.810	7.226	6.583	-0.402

Table 2.2 Scaling factors for different modelling scenarios

Quantity	Prototype P	Equivalent Void Ratio Model M2	Centrifuge Model M3	Equivalent State Parameter Model M1
Length	1	$1/n$	$1/n$	$1/n$
Area	1	$1/n^2$	$1/n^2$	$1/n^2$
Volume	1	$1/n^3$	$1/n^3$	$1/n^3$
Acceleration	1	1	n	1
Stress	1	~ $1/n$	1	$1/n$
Strain	1	?	1	1
Displacement	1	?	$1/n$	$1/n$
Force	1	~ $1/n^3$	$1/n^2$	$1/n^3$
Moment		~ $1/n^4$	$1/n^3$	$1/n^4$
Void Ratio	e_P	$e_M = e_P$	$e_M = e_P$	$e_M > e_P$
State Parameter	ψ_P	$\psi_M > \psi_P$	$\psi_M = \psi_P$	$\psi_M = \psi_P$
Undrained strength	1	$1/n$ to 1	1	$1/n$
Soil stiffness	1	~ $1/n^{1/2}$	1	~ $1/n^{1/2}$
Vertical and horizontal footing stiffness	1	~ $1/n^{3/2}$	$1/n$	~ $1/n^{3/2}$
Moment footing stiffness	1	~ $1/n^{7/2}$	$1/n^3$	~ $1/n^{7/2}$
Scaling factors below include an additional viscosity scaling factor of n				
Permeability	1	$1/n$	$1/n$	$1/n$
M' (elastic)	1	~ $1/n^{1/2}$	1	~ $1/n^{1/2}$
M' (plastic)	1	~ $1/n$	1	$1/n$
c_v (elastic)	1	~ $1/n^{3/2}$	$1/n$	~ $1/n^{3/2}$
c_v (plastic)	1	~ $1/n^2$	$1/n$	~ $1/n^2$
t (elastic)	1	~ $1/n^{1/2}$	$1/n$	~ $1/n^{1/2}$
t (plastic)	1	~ 1	$1/n$	~ 1

Table 3.1 Stepper motor specifications

Control axis	Type of displacement	Step count conversion	Velocity range
1	rotational	1 deg = 47,240 steps	0.001 - 0.2 deg/s
2	horizontal	1 mm = 50,340 steps	0.001 - 0.4 mm/s
3	vertical	1 mm = 10,000 steps	0.001 - 1 mm/s
3	vertical (fast)	1 mm = 200 steps	1 - 5 mm/s

Table 3.2 Details of preliminary tests

Test	Diameter of footing (mm)	Loading apparatus	Position and type of pore pressure transducer [a]	Hydraulic surcharge	Rate of penetration (mm/s)	$\frac{\Delta U}{\Delta V}$ [b] (%)
TP01	100	rig	external, Druck	—	0.3	10
TP02	100	rig	external, Druck	—	0.8	4
TP03	100	rig	external, Druck	-3.8	1.4	2
TP04	100	hanger & weights	external, Druck	—	9.3	2
TP05	100	hanger & weights	internal, Druck	—	7.9	3
TP06	100	hanger & weights	internal, Gaeltec	—	3	27
TP07	100	hanger & weights	internal, Gaeltec	—	7	22
TP08	150	hanger & weights	internal, Gaeltec	—	10.0	64
TP09	150	hanger & weights	internal, Gaeltec	-4.0	6.8	62

Note:

a *External* indicates that the transducer was connected to the centre of the footing via tubing and *internal* indicates that the transducer was connected directly to the centre of the footing.

b A uniform pore pressure distribution assumed.

Table 3.3 Verification of the load cell calibration and errors involved

Applied loads			Measured loads			Absolute errors			Relative errors (%)		
V (N)	H (N)	M (Nm)	V (N)	H (N)	M (Nm)	V (N)	H (N)	M (Nm)	V	H	M
656.1	0	0	657.1	-0.9	-0.06	1.0	-0.9	-0.06	0.15	-	-
656.1	457.9	0	657.4	461.2	0.18	1.3	3.3	0.18	0.20	0.72	-
656.1	0	26.24	655.3	-0.13	26.42	-0.8	-0.13	0.18	0.12	-	0.69
656.1	287.75	26.24	652.5	287.7	26.41	-3.6	-0.1	0.17	0.55	0.04	0.65
656.1	287.75	-26.24	660.3	289.9	-26.35	4.2	2.2	0.11	0.64	0.76	0.42
656.1	0	-26.24	661.2	0.32	-26.50	5.1	0.32	-0.26	0.78	-	0.99

Table 3.4 LVDT specifications

LVDT	Displacement		Type	Range (mm)	Standard error in calibration coefficient (%)
DLV	vertical (w)	coarse measurements	ACT600C	±150	0.08
DLH	horizontal (u)		D5/1000A	±25	0.05
DLM	rotational (θ)		ACT2000C	±50	0.04
DSV1	transformed to w, u, and θ	fine measurements	D5/200AG	±5	0.04
DSV2			D5/200AG	±5	0.12
DSH			D5/200AG	±5	0.03

Note: All LVDTs supplied by RDP Electronics.

Table 3.5 Pore pressure transducer specifications

Pore pressure transducer	Location	Type	Range (kPa)	Standard error in calibration coefficient (%)
pp_1	centre of footing	custom built (Gaeltec Ltd.)	±100	0.10
pp_2	wall of specimen container (upper)	PDCR910 (Druck Ltd.)	±70	0.06
pp_3	wall of specimen container (lower)	PDCR910 (Druck Ltd.)	±70	0.04

Note: Pressures were referenced to atmospheric pressure.

Table 3.6 Methods used in the preparation of the sand specimens

Test	Specimen	Method of densification	Fully fluidised before densification ?
T101	1	dhg/vibration, manual	yes
T102	1	dhg/vibration, manual	no
T103	1	dhg/vibration, manual	no
T204	2	poured and vibrated	no
T105	1	dhg/vibration, manual	no
T106	1	dhg/vibration, automatic	no
T107	1	dhg/vibration, automatic, surcharge	no
T108	1	dhg/vibration, automatic	no
T309	3	dhg/vibration, automatic, surcharge	yes
T110	1	dhg/vibration, automatic	yes
T311	3	dhg/vibration, automatic	yes
T112	1	dhg/vibration, automatic	yes
T313	3	dhg/vibration, automatic	yes
T114	1	dhg/vibration, automatic	yes
T315	3	dhg/vibration, automatic	yes
T116	1	dhg/vibration, automatic	yes
T317	3	dhg/vibration, automatic	yes
T118	1	dhg/vibration, automatic	yes
T319	3	dhg/vibration, automatic	yes
T120	1	dhg/vibration, automatic	yes

Note:
- *dhg* abbreviates downward hydraulic gradient.
- *manual* indicates that the switching between the densification components was done manually, and *automatic* indicates that the asynchronous switch and solenoid valve apparatus was used.
- *surcharge* indicates a weight was applied to the surface of the sand during the densification process.

Table 4.1 Permeability tests on oil-saturated Baskarp Cyclone sand

Test	Time (min)	Head difference in manometer tubes (m)	Flow (ml)	Flow rate (m^3/s)	Permeability k (m/s)
1	123	0.855 ± 0.005	51.0	6.91×10^{-9}	1.77×10^{-7}
2	85	0.863 ± 0.003	35.5	6.96×10^{-9}	1.77×10^{-7}
3	214	0.865	93.0	7.24×10^{-9}	1.83×10^{-7}

Table 4.2 Elastic and consolidation parameters derived from NGI (1994b) element tests

Test Number	Type of test	R_D (%)	p' (kPa)	k $\times 10^{-5}$ (m/s)	Loading			Unloading		
					ε_q (%)	G (MPa)	c_v (m^2/s)	ε_q (%)	G (MPa)	c_v (m^2/s)
BC10	CIU_{Oedo}	60	87	2.0	0.53	5	0.04	-0.04	57	0.54
BC11	CIU_{Oedo}	70	87	1.6	0.33	7	0.05	-0.04	64	0.42
BC12	CIU_{Oedo}	90	87	0.8	0.15	17	0.04	-0.04	101	0.23
BC13	Oedo	60	30	2.0	0.23	4	0.02	-0.04	22	0.12
BC14	Oedo	90	30	0.8	0.03	27	0.06	-0.02	45	0.09
NTH93-1	CAD_{Oedo}	60	136	1.8	1.08	3	0.02	-0.06	57	0.35
NTH93-2	CAD_{Oedo}	85	98	0.9	0.70	8	0.02	-0.02	66	0.16

Note:

σ'_{consol} = 10 kPa and $\Delta\varepsilon_r \neq 0$ in tests BC10 to BC12.

σ'_{consol} = 0 kPa and $\Delta\varepsilon_r = 0$ in tests NTH93-1 and NTH93-2.

Table 4.3 Drained triaxial test parameters of Baskarp Cyclone sand (NGI, 1994b)

Test	Type of Test	Pore Fluid	R_D (%)	Consol. p' (kPa)	Peak State		Critical State	
					ϕ'_{max} (deg)	p' (kPa)	ϕ'_{crit} (deg)	p' (kPa)
BC15	CID_c	water	79	10	44.0	27.1	33.4	21.8
BC16	CID_c	water	81	50	42.5	124.0	34.9	98.4
BC17	CID_c	water	80	200	36.4	400.7	31.1	348.3
BC23	CID_c	oil	81	10	41.9	26.2	33.1	21.7
BC18 [a]	CID_{cy}	water	79	10	44.2	28.3	34.5	24.7
BC20 [a]	CID_{cy}	water	80	8 [b]	43.1	26.8	31.8	23.5

Note:

a Undrained cyclic test performed before drained static test.

b Anisotropic consolidation, σ'_{ac} = 4.6 kPa and σ'_{rc} = 9.7 kPa

Table 4.4 Undrained triaxial test parameters of Baskarp Cyclone sand (NGI, 1994b)

Test	Type of Test	Pore Fluid	R_D (%)	p'_{con} (kPa)	Back Pressure (kPa)	Critical State	
						ϕ'_{crit} (deg)	p' (kPa)
BC1	CIU_c	water	50	10	1471	35.0	185
BC2	CIU_c	water	79	20	1471	35.3	1913
BC24	CIU_c	oil	82	20	1569	32.6	1778
BC3 [a]	CIU_{cy}	water	90	20	1471	31.6	2258
BC6 [a]	CIU_{cy}	water	70	20	1569	33.6	840
BC8 [a]	CIU_{cy}	water	80	20	1471	32.9	1824
BC9 [a]	CIU_{cy}	water	90	18 [b]	1765	34.2	3120

Note:

a Undrained cyclic test performed before drained static test.

b Anisotropic consolidation, σ'_{ac} = 13.5 kPa and σ'_{rc} = 20.0 kPa

Table 4.5 Properties of Baskarp Cyclone sand specimens

Specimen	Type	Mass of sand (kg)
1	oil-saturated	67.052
2	dry	65.069
3	oil-saturated	66.997

Table 4.6 Cone penetrometer test results

Test	Bulk R_D (%)	K_{ch} (N/mm)	q_c [a] (kPa)				Local ϕ'_{max} [d] (deg)	Local R_D [e] (%)
			Before footing test		After footing test			
			Centre	Side	Centre	Side		
T101	87	144						
T102	86	180	332 [b]		**200**	**230**	43.9	81
T103	81	112	66 [b]		**40**	**130**	41.3	67
T204	84	628	1162 [b]		**700**	**1000**	45.3	80
T105	89	156	199 [b]		**120**	**200**	43.1	77
T106	91	337	664 [b]		**400**	**400**	45.1	88
T107	84	173	166 [b]		**100**	**140**	42.8	75
T108	82	99	17 [b]		**10**	**50**	39.0	54
T309	90	476	996 [b]		**600**	**950**	45.7	91
T110	94	483	747 [b]		**450**	**550**	45.2	89
T311	73	259	116 [b]		**70**	**100**	42.3	72
T112	88	350	315 [c]	**450**	**180**	**300**	43.8	81
T313	91	480	996 [b]	**600**	**600**	**500**	45.7	91
T114	91	234	399 [c]	**570**	**100**		44.2	83
T315	92	470	840 [c]	**1200**	**250**		45.5	90
T116	96	385	634 [c]	**905**	**200**		45.0	87
T317	88	481	770 [c]	**1100**	**450**		45.3	89
T118	100	409	823 [c]	**1175**			45.4	89
T319	102	342	665 [c]	**950**			45.0	88
T120	98	345	543 [c]	**775**			44.7	86

Note:
q_c values in bold font refer to measured values.
q_c values in normal font refer to estimated values.
a q_c measured between 50 mm and 100 mm of penetration.
b Estimated from after-centre measured values, *i.e.* equal to measured value multiplied by 1.66.
c Estimated from before-side measured values, *i.e.* equal to measured value multiplied by 0.70
d Estimated from before-centre cone penetrometer results using Equation 4.11.
e Estimated from before-centre cone penetrometer results using Equation 4.12 for the dry specimens and Equation 4.13 for the oil-saturated specimens.

Table 5.1 Chronological list of tests (page 1 of 4)

Test name	Main-test files [a]	Sub-Tests					Notes
		Input files [b]	Output files [c]	Type of test	Intended displace-ment rate (mm/s)	Initial vertical load (N)	
T101	T101		*T101_U*	ULRL	±0.001	1000	
			T101_1	HSS	0.001	1630	
T102	T102	T102_A	T102_1	VP	1	500	
	T102A	T102_B	T102A_1	VP	1	1000	
			T102A_2	MSS	0.0026	1500	
T103	T103						
	T103A	T103_A	T103A_1	VP	0.1	500	
		T103_B	T103A_2	VP	0.1	1000	
		T103_C	T103A_3	HSS	0.1	1340	
T204	T204		*T204_U*	ULRL	±0.001	1000	
			T204_1	HSS	0.001	1500	
T105	T105	T105_A	T105_1	VP	0.01	500	
		T105_B	T105_2	VP	0.01	1000	
		T105_C	T105_3	MSS	0.26	1500	
T106	T106	T106_A	T106_1	VP	2	500	motor stalled
		T106_A	T106_2	VP	2	500	reduced acceleration in input file but motor still stalled
		T106_A	T106_3	VP	1	500	reduced velocity in input file
		T106_B	T106_4	VP	1	1000	
		T106_C	T106_5	HSS	0.4	1500	
T107	T107	T107_A	T107_1	VP	1	500	
		T107_B		VP	1	1000	no activity
		T107_B		VP	1	1000	no activity, error in control program, program stopped
	T107A	T107_B	T107A_1	VP	1	1000	
		T107_C	T107A_2	HSS	0.4	1500	motor stalled, error in input file
		T107_D	T107A_3	HSS	0.4	1500	
T108	T108						
	T108A						
	T108B						
	T108C						
	T108D						
	T108E		*T108E_U*	ULRL	±0.001	1000	
T309	T309		*T309_U*	ULRL	±0.001	1000	
			T309_1	HSS	0.001	1500	
T110	T110	T110_A	T110_1	VP	1	500	
		T110_B	T110_2	VP	1	1000	
		T110_C	T110_3	HSS	0.4	1500	

Table continued on next page.
See notes on page three.

Table 5.1 (cont.) Chronological list of tests (page 2 of 4)

Test name	Main-test files [a]	Sub-Tests					Notes
		Input files [b]	Output files [c]	Type of test	Intended displace-ment rate (mm/s)	Initial vertical load (N)	
T311	T311	T311_A	T311_1	VP	0.1	500	
		T311_B	T311_2	VP	0.1	1000	
			T311_3	MSS	0.0026	1500	
T112	T112						
	T112A						
	T112B	T112_A	T112B_1	VP	1	500	
	T112C						
	T112D	T112_B	T112D_1	VP	1	1000	
	T112E	T112_C	T112E_1	MSS	0.524	1500	
T313	T313						
	T313A	T313_A	T313A_1	VP	5	500	
	T313B						
	T313C	T313_B	T313C_1	VP	5	1000	
	T313D	T313_C	T313D_1	MSS	0.524	1500	
T114	T114						
	T114A						
	T114B	T114_A	T114B_1	VP	5	500	
	T114C						
	T114D	T114_B	T114D_1	VP	5	1000	
	T114E	T114_C	T114E_1	MSS	0.524	1500	
T315	T315	T315_A	T315_1	VP	0.1	500	
		T315_B	T315_2	VP	0.1	1000	
		T315_C	T315_3	HSS	0.4	1500	error in input file
	T315A						
	T315B	T315_D	T315B_1	HSS	0.4	1500	new input file, motor stalled
		T315_D	T315B_2	HSS	0.4	1500	motor stalled
	T315C	T315_E	T315C_1	HSS	0.1	1500	new input file with reduced velocity
	T315D						
	T315E						
T116	T116	T116_A	T116_1	VP	0.01	500	
		T116_B		VP	0.01	1000	error in control program, file not retrieved
	T116A	T116_B	T116A_1	VP	0.01	1000	
		T116_C	*T116A_2*	HSS	0.1	1500	test not logged on ADU, file T116A_2 created from background data
	T116B						
	T116C						
	T116D						
	T116E						
	T116F						

Table continued on next page.
See notes on page three.

Table 5.1 (cont.) Chronological list of tests (page 3 of 4)

Test name	Main-test files [a]	Sub-Tests					Notes
		Input files [b]	Output files [c]	Type of test	Intended displace-ment rate (mm/s)	Initial vertical load (N)	
T317	T317	T317_A	T317_1	VP	0.01	500	
		T317_B	T317_2	VP	0.01	500	
		T317_C	T317_3	MSS	0.026	1500	the limit on the moment load in the input file was set too low
	T317A	T317_D	T317A_1	MSS	0.026	1800	new input file
T118	T118						
	T118A	T118_A	T118A_1	VP	5	500	
	T118B	T118_B	T118B_1	CONSL		700	
			T118B_2	CONSL		900	
			T118B_3	CONSL		700	
	T118C	T118_C	T118C_1	VP	5	1000	
	T118D		*T118D_1*	HSS	0.001	1500	
			T118D_2	HSS	-0.001	1700	
	T118E		*T118E_U*	ULRL	±0.001	1900	
	T118F						
	T118G						
T319	T319						
	T319A	T319_A	T319A_1	VP	5	500	
	T319B	T319_B	T319B_1	CONSL		700	
			T319B_2	CONSL		900	
			T319B_3	CONSL		700	
	T319C	T319_C	T319C_1	VP	5	1000	
	T319D		*T319D_1*	MSS	0.0026	1500	
			T319D_2	MSS	-0.0026	1700	
			T319D_3	MSS	0.0026	2000	

Table continued on next page.

Note:

a The main-test files are the background logging files that were logged directly onto the host PC. The filename extension of these files is .OUT.

b The filename extension of the input files is .INP.

c The filename extension of the output files is .DAT. Output files shown in italic were created from the background logging data.

ULRL Vertical unload-reload test.
HCYC Horizontal load-unload-reload test.
MCYC Moment load-unload-reload.
VP Vertical partially-drained test.
HSS Horizontal sideswipe test.
MSS Moment sideswipe test.
CONSL Vertical consolidation test.
VPM Vertical partially-drained test with alternating slow and fast rates.
HSSM Horizontal sideswipe test with alternating slow and fast rates.
MSSM Moment sideswipe test with alternating slow and fast rates.

Table 5.1 (cont.) Chronological list of tests (page 4 of 4)

Test name	Main-test files [a]	Sub-Tests					Notes
		Input files [b]	Output files [c]	Type of test	Intended displace-ment rate (mm/s)	Initial vertical load (N)	
T120	T120						
	T120A	T120_A	T120A_1 T102A_2 T120A_3	VPM	0.01 1	500	
	T120B		*T120B_HC*	HCYC	0.001	1000	
			T120B_MC	MCYC	0.0026	1000	
	T120C	T120_A	T120C_1 T120C_2 T120C_3	VPM	0.01 1	1000	
	T120D	T120_B	T120D_1 to T120D_5	HSSM	0.001 0.1	1500	the data files of this sideswipe were merged into a single file labelled T120D_H1
			T120D_5A				
			T120D_HC	HCYC	0.001	1500	
			T120D_MC	MCYC	0.0026	1500	
		T120_C	T120D_6 to T120D_11	HSSM	-0.001 -0.1	1700	the data files of this sideswipe were merged into a single file labelled T120D_H2
			T120D_11A				
		T120_C	T120D_12 to T120D_17				
		T120_D	T120D_18 to T120D_22	MSSM	0.0026 0.26	1900	the data files of this sideswipe were merged into a single file labelled T120D_M1
			T120D_22A				
		T120_D	T120D_23 to T120D_27				
	T120E	T120_E	T120E_1 to T120E_8	MSSM	-0.0026 -0.26	2100	the data files of this sideswipe were merged into a single file labelled T120E_M2
	T120F						
	T120G						

See notes on page three.

Table 5.2 Details of the miniature cone penetration tests

Sample	Specimen	Cone test [a]	Timing [b]	Rate (mm/s)
2	1	CP02C	after	0.3
		CP02L	after	0.3
3	1	CP03C	after	0.3
		CP03L	after	0.3
4	2	CP04C	after	0.3
		CP04L	after	0.3
5	1	CP05C	after	0.3
		CP05L	after	0.3
6	1	CP06C	after	0.3
		CP06L	after	0.1
7	1	CP07C	after	0.1
		CP07L	after	0.1
8	1	CP08C	after	0.1
		CP08L	after	0.1
9	3	CP09C	after	0.1
		CP09L	after	0.1
10	1	CP10C	after	0.1
		CP10L	after	0.1
11	3	CP10C	after	0.1
		CP10L	after	0.1
12	1	CP12C	after	0.1
		CP12F	before	0.1
		CP12L	after	0.1
13	3	CP13B	before	0.1
		CP13C	after	0.1
		CP13F	before	0.1
		CP13L	after	0.1
		CP13R	before	0.1
14	1	CP14B	before	0.1
		CP14C	after	0.1
		CP14F	before	0.1
		CP14L	before	0.1
		CP14R	before	0.1
15	3	CP15B	before	0.1
		CP15C	after	0.1
		CP15F	before	0.1
		CP15L	before	0.1
		CP15R	before	0.1
16	1	CP16B	before	0.1
		CP16C	after	0.1
		CP16F	before	0.1
		CP16L	before	0.1
		CP16R	before	0.1
17	3	CP17B	before	0.1
		CP17C	after	0.1
		CP17F	before	0.1
		CP17L	before	0.1
		CP17R	before	0.1
18	1	CP18B	before	0.1
		CP18F	before	0.1
		CP18L	before	0.1
		CP18R	before	0.1
19	3	CP19B	before	0.1
		CP19F	before	0.1
		CP19L	before	0.1
		CP19R	before	0.1
20	1	CP20B	before	0.1
		CP20F	before	0.1
		CP20L	before	0.1
		CP20R	before	0.1

Note:

a The last character of the test name indicates the position of the test in the tank:
- B back
- C centre
- F front
- L left
- R right

b Indicates whether the cone tests were performed *before* or *after* the main-test.

Table 6.1 Virgin-penetration stiffness and estimated bearing capacity values

Test	Virgin-penetration stiffness (N/mm)				Local [c] R_D (%)	V_m [f] (kN)
	100 - 200 N	400 - 500 N [a]	900 - 1000 N	1400 - 1500 N		
T101	111	144	160	166		
T102	116	180	255	408	81	5.5
T103	90	112	136	136	67	3.2
T204	670	628	766	890	80	9.8
T105	87	156	223	233	77	4.6
T106	267	337	514 [b]	600 [b]	88	6.9
T107	133	173	220 [c]	248	75	4.3
T108	108	99	110	[d]	54	2.0
T309	328	476	603	702	91	7.9
T110	313	483	925 [b]	946 [b]	89	7.2
T311	189	259	264	250	72	3.8
T112	294	350	412	459	81	5.4
T313	333	480	657	803	91	7.9
T114	135	234	354	445	83	5.8
T315	322	470	593	682	90	7.5
T116	263	385	517	599	87	6.8
T317	313	481	659	731	89	7.3
T118	322	409	910 [b]	673	89	7.4
T319	167	342	661 [b]	536	88	6.9
T120	225	345	638 [b]	582	86	6.4

Note:

a The 400-500 N stiffness was equivalent to the characterisation stiffness, K'_{ch}.

b The sample was most probably overconsolidated at this stage.

c The value was estimated from Figure 6.6.

d The maximum vertical load of the test was less than 1400 N.

e The relative density of the top layer of the specimens was estimated from the cone penetrometer tests, see Table 4.6.

f The bearing capacity was estimated from the local R_D values, see Section 6.2.3.

Table 6.2 Vertical stiffness parameters derived from unload-reload footing tests

				Type of stiffness measurement			
				Initial section of unloading curve, ε_a = 0.05 %			Whole ULRL loop
Test number	K'_{ch} (N/mm)	K'_{eq} [a] (N/mm)	V (N)	K'_{ul} (N/mm)	K'_{ul}/K'_{eq}	G (MPa)	K'_{ulrl} (N/mm)
T101	144	160	1000-200	6000	37.5	12.3	2500
T204	628	766	1000-200	6667	8.6	13.7	4000
T108	99	110	1000-200	5417	49.2	11.1	2597
T309	476	603	1000-200	6750	11.2	13.8	3496
T118	409	520	1900-190	11000	21.2	22.6	3448

Note: a K'_{eq} measured over the 100 N of virgin-penetration preceding the loops.

Table 6.3 Consolidation settlements

Test	Type of loading	Load range (N)	Immediate (partially-drained)				Primary (drained)					Theoretical undrained settlement [a]
			dV (N)	dw (mm)	K (N/mm)	dw/dt (mm/s)	dV (N)	dw (mm)	K (N/mm)	G (MPa)	dw/dt (mm/s)	(mm)
T118b_1	loading	700 - 900	131	0.047	2787	0.0313	200	0.315	635	1.3	0.0035	0.007
T118b_2	unloading	900 - 700	-272	-0.025	10880	-0.0167	-200	-0.020	10000	20.5	-0.0002	-0.015
T118b_3	reloading	700 - 900	218	0.035	6229	0.0233	200	0.050	4000	8.2	0.0017	0.012
T319b_1	loading	700 - 900	123	0.036	3417	0.0240	200	0.345	580	1.2	0.0035	0.007
T319b_2	unloading	900 - 700	-230	-0.017	13529	-0.0113	-200	-0.020	10000	20.5	-0.0002	-0.013
T319b_3	reloading	700 - 900	210	0.035	6000	0.0233	200	0.055	3636	7.5	0.0014	0.012

Note:

a Calculated using Equation 2.39 and elastic shear modulus from unloading tests, *i.e.* 20.5 MPa.

Table 6.4 Dissipation times and coefficients of consolidation (unloading and reloading tests)

Test	t_{50} (s)	c_3 (m^2/s)
T118B_2	11.7	0.7×10^{-3}
T118B_3	6.3	1.3×10^{-3}
T319B_2	15.5	0.5×10^{-3}
T319B_3	9.5	0.9×10^{-3}

Note:
A time factor T_v of 0.135 was taken to be representative of t_{50}, see Figure 2.27.

Table 6.5 Settlement and fluid flow data from unloading and reloading consolidation tests

Test	dt (s)	Settlement		Flow			
		dw (mm)	A dw/dt (mm^3/s)	d$u_{average}$ (kPa)	i		Aki (mm^3/s)
T118B_2	1.5	-0.02	-236	-3.5	Section 1	-38.1	-136
					Section 2	-4.8	
T118B_3	2	0.04	353	3	Section 1	32.6	117
					Section 2	4.1	
	26	0.016	11	3		4.1	26
T319B_2	1.5	-0.017	-200	-4.25	Section 1	-46.2	-165
					Section 2	-5.8	
T319B_3	1.5	0.033	389	4.25	Section 1	46.2	165
					Section 2	5.8	
	40	0.022	10	4.25		5.8	37

Note:
Refer to Figure 6.32.

Table 6.6 Displacement rates of vertical partially-drained tests

Test	K'_{ch} (N/mm)	V_o (N)	dw/dt (mm/s)		Displacement rate ratio
			Intended	Measured	
T102_1	180	500	1	1.014	1.01
T102A_1		1000		0.952	0.95
T103A_1	112	500	0.1	0.101	1.01
T103A_2		1000		0.102	1.02
T105_1	156	500	0.01	0.009	0.91
T105_2		1000		0.009	0.90
T106_3	337	500	1	0.853	0.85
T106_4		1000		0.808	0.81
T107_1	173	500	1	0.920	0.92
T107A_1		1000		0.918	0.92
T110_1	483	500	1	0.963	0.96
T110_2		1000		0.902	0.90
T311_1	259	500	0.1	0.088	0.88
T311_2		1000		0.088	0.88
T112B_1	350	500	1	1.052	1.05
T112D_1		1000		0.978	0.98
T313A_1	480	500	5	4.611	0.92
T313C_1		1000		3.800	0.76
T114B_1	234	500	5	4.773	0.95
T114D_1		1000		4.582	0.92
T315_1	470	500	0.1	0.081	0.81
T315_2		1000		0.075	0.75
T116_1	385	500	0.01	0.009	0.85
T116A_1		1000		0.008	0.82
T317_1	481	500	0.01	0.008	0.77
T317_2		1000		0.007	0.74
T118A_1	409	500	5	4.479	0.90
T118C_1		1000		4.028	0.81
T319A_1	342	500	5	4.543	0.91
T319C_1		1000		[a]	[a]
T120A_1	345	500	0.01	0.006	0.55
			1	0.857	0.86
T120A_2			0.01	0.009	0.93
			1	[a]	[a]
T120A_3			0.01	0.009	0.93
			1	0.759	0.76
T120C_1			0.01	0.006	0.61
			1	0.559	0.56
T120C_2		1000	0.01	0.009	0.86
			1	0.410	0.41
T120C_3			0.01	0.009	0.88
			1	0.455	0.46

Note:

a Stepper motor stalled.

Table 6.7 Measured parameters from the vertical partially-drained tests

Test	K'_{eq} (N/mm)	V_o (N)	Primary Section		Secondary Section
			$K_{vp\text{-}p}$ (N/mm)	$\Delta V_{vp\text{-}p}$ (N)	$K_{vp\text{-}s}$ (N)
T102_1	180	500	3690	80	148 [c]
T102a_1	255	1000	3930	160	160 [c]
T103a_1	112	500	3260	65	82 [c]
T103a_2	136	1000	3770	100	70 [c]
T105_1	156	500	1700	50	171
T105_2	223	1000	4290	60	230 [c]
T106_3	337	500	6290	75	357
T106_4	514 [a]	1000	8170	200	488
T107_1	173	500	2450	100	132
T107a_1	220 [b]	1000	4680	175	159
T110_1	483	500	2500	125	624
T110_2	925 [a]	1000	4820	250	832
T311_1	259	500	3350	60	261
T311_2	264	1000	3820	100	274
T112b_1	350	500	2520	125	250
T112d_1	412	1000	4980	210	291
T313a_1	480	500	9140	150	469
T313c_1	657	1000	23900	240	930
T114b_1	234	500	7390	150	191
T114d_1	354	1000	5420	250	248
T315_1	470	500	4400	75	524
T315_2	593	1000	5690	150	652
T116_1	385	500	3000	60	410
T116a_1	517	1000	6580	150	537
T317_1	481	500	4000	50	582
T317_2	659	1000	7000	100	715
T118a_1	409	500	4590	125	414
T118c_1	910 [a]	1000	10290	300	397
T319a_1	342	500	3000	150	310
T319c_1	661 [a]	1000	6970	300	[d]

Note:

a These values of K'_{eq} that were measured between 900 N and 1000 N may not have been representative of the virgin-penetration stiffness because of over-consolidation.

b Estimated value, see Table 6.1.

c Significant work softening was evident before the secondary section.

d Motor stalled.

Table 7.1 Displacement rates of horizontal sideswipe tests

Name	K_{ch} (N/mm)	V_{oi} (N)	du/dt (mm/s)	
			Intended	Measured
T101_1	144	1630	0.001	0.0008
T103A_3	112	1340	0.1	0.0969
T204_1	628	1500	0.001	0.0008
T106_5	337	1500	0.4	0.3167
T107A_3	173	1500	0.4	0.3464
T309_1	476	1500	0.001	0.0008
T110_3	483	1500	0.4	0.2128
T315_3	470	1500	0.04	0.009
T315C_1		1500	0.1	0.0617
T116A_2	385	1500	0.1	0.0688
T118D_1	409	1500	0.001	0.0009
T118D_2		1700	-0.001	-0.001
T120D_1	345	1500	0.001	0.0001
			0.1	0.0165
T120D_2			0.001	0.0003
			0.1	0.0029
T120D_3			0.001	0.0005
T120D_H1			0.1	0.0115
T120D_4			0.001	0.0006
			0.1	0.0186
T120D_5			0.001	0.0007
			0.1	0.0044
T120D_5A			0.001	0.0001
T120D_6		1700	-0.001	-0.0002
T120D_7			-0.1	-0.0167
T120D_8			-0.001	-0.0004
T120D_9			-0.1	-0.0291
T120D_10			-0.001	-0.0005
T120D_11			-0.1	-0.0219
T120D_11A T120D_H2			-0.001	-0.0006
T120D_12			-0.001	-0.0006
T120D_13			-0.1	-0.0297
T120D_14			-0.001	-0.0007
T120D_15			-0.1	-0.0195
T120D_16			-0.001	-0.0008
T120D_17			-0.1	-0.0359

Note:
Tests T120D_1 to T120D_5A composed a single sideswipe that was labelled T120D_H1.
Tests T120D_6 to T120D_17 composed a single sideswipe that was labelled T120D_H2.

Table 7.2 Displacement rates of moment sideswipe tests

Name	K'_{ch} (N/mm)	V_{oi} (N)	d(2Rθ)/dt (mm/s)	
			Intended	Measured
T102A_2	180	1500	0.0026	0.0026
T105_3	156	1500	0.26	0.2616
T311_3	259	1500	0.0026	0.0026
T112E_1	350	1500	0.524	0.4926
T313D_1	480	1500	0.524	0.4639
T114E_1	234	1500	0.524	0.5036
T317_3	481	1500	0.026	0.0213
T317A_1		1800	0.026	0.0216
T319D_1	342	1500	0.0026	0.0023
T319D_2		1700	-0.0026	-0.0022
T319D_3		2000	0.0026	0.0023
T120D_18	345	1900	0.0026	0.0017
			0.26	0.1465
T120D_19			0.0026	0.0019
			0.26	0.1833
T120D_20			0.0026	0.0021
			0.26	0.2182
T120D_21			0.0026	0.0022
			0.26	0.2121
T120D_22			0.0026	0.0023
			0.26	0.2286
T120D_22A T120D_M1			0.0026	0.0023
T120D_23			0.0026	0.0026
			0.26	0.2339
T120D_24			0.0026	0.0023
			0.26	0.1833
T120D_25			0.0026	0.0022
			0.26	0.1676
T120D_26			0.0026	0.0021
			0.26	0.1833
T120D_27			0.0026	0.0026
			0.26	0.2294
T120E_1		2100	-0.0026	-0.002
T120E_2			-0.26	-0.2755
T120E_3			-0.0026	-0.0019
T120E_4			-0.26	-0.2686
T120E_5 T120E_M2			-0.0026	-0.002
T120E_6			-0.26	-0.313
T120E_7			-0.0026	-0.0023
T120E_8			-0.26	-0.2696

Note:
Tests T120D_18 to T120D_27 composed a single sideswipe that was labelled T120D_M1.
Tests T120E_1 to T120D_8 composed a single sideswipe that was labelled T120E_M2.

Table A.1 Factors for bearing capacity formulae

Factor	Brinch Hansen (1970)	Meyerhof (1963)	Vesic (1975)
N_γ	$1.5(N_q - 1)\tan\phi$	$(N_q - 1)\tan(1.4\phi)$	$2(N_q + 1)\tan\phi$
N_q	$e^{\pi\tan\phi}\tan^2\left(45° + \frac{\phi}{2}\right)$	$e^{\pi\tan\phi}\tan^2\left(45° + \frac{\phi}{2}\right)$	$e^{\pi\tan\phi}\tan^2\left(45° + \frac{\phi}{2}\right)$
s_γ	$1 - 0.4 i_\gamma \frac{B'}{L'}$	$1 + 0.1\tan^2\left(45° + \frac{\phi}{2}\right)\frac{B'}{L'}$	$1 - 0.4\frac{B'}{L'}$
s_q	$1 + i_q \sin\phi \frac{B'}{L'}$	$1 + 0.1\tan^2\left(45° + \frac{\phi}{2}\right)\frac{B'}{L'}$	$1 + \tan\phi\frac{B'}{L'}$
d_γ	1	$1 + 0.1\tan\left(45° + \frac{\phi}{2}\right)\frac{z}{B'}$	1
d_q	$1 + 2\tan\phi(1 - \sin\phi)^2\frac{z}{B'}$	$1 + 0.1\tan\left(45° + \frac{\phi}{2}\right)\frac{z}{B'}$	$1 + 2\tan\phi(1 - \sin\phi)^2\frac{z}{B'}$
i_γ	$\left(1 - 0.7\frac{H}{V}\right)^5$	$\left(1 - \frac{\alpha}{\phi}\right)^2$	$\left(1 - \frac{H}{V}\right)^{m+1}$
i_q	$\left(1 - 0.5\frac{H}{V}\right)^5$	$\left(1 - \frac{\alpha}{90}\right)^2$	$\left(1 - \frac{H}{V}\right)^m$

Note:

See Appendix A for definitions not mentioned below.

ϕ in degrees.

For circular footings use the triaxial friction angle in Meyerhof's and Vesic's formulae but use the plane-strain friction angle in Brinch Hansen's formulae.

L' is the maximum effective foundation dimension.

$\alpha = \tan^{-1}(H/V)$ where H/V is the ratio of horizontal to vertical load and $\alpha < \phi$.

$$m = \frac{2 + B'/L'}{1 + B'/L'}$$

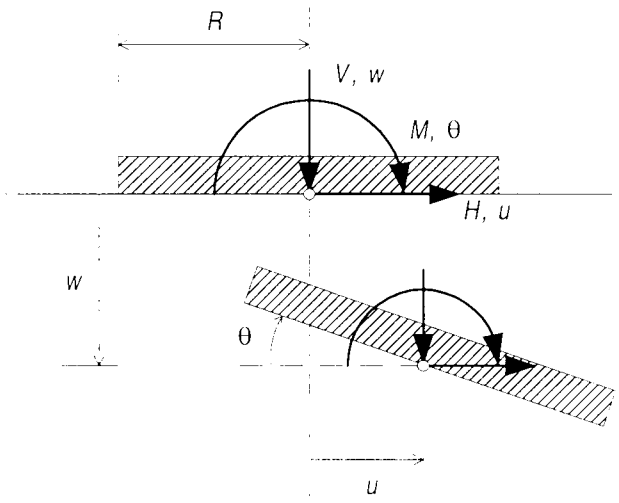

Figure 2.1
Sign convention for combined loads and displacements

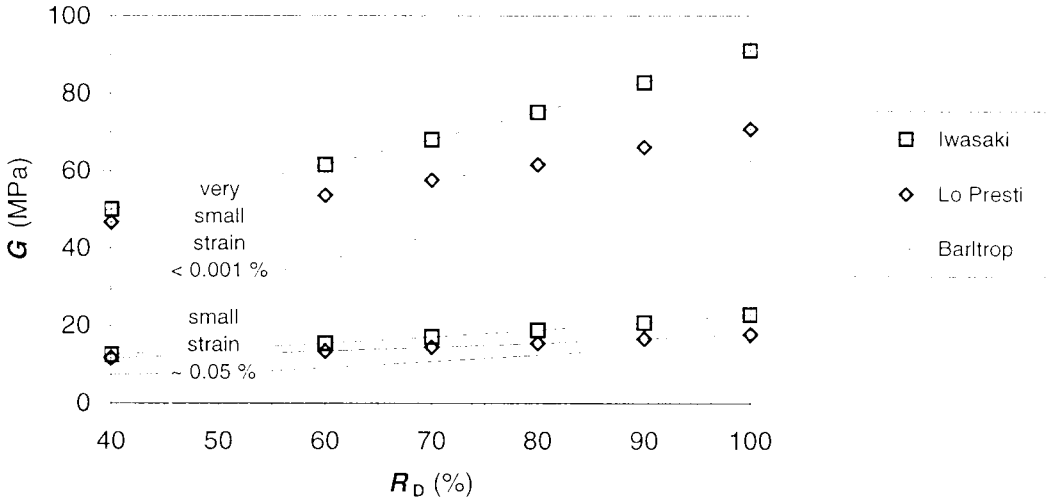

Notes:

Iwasaki et.al.(1978) :

$$\frac{G_o}{p_a} = 900 \left(\frac{p'}{p_a}\right)^{0.4} \frac{(2.17 - e)^2}{(1 + e)}$$

Lo Presti (1987) :

$$\frac{G_o}{p_a} = 591 \left(\frac{p'}{p_a}\right)^{0.34} e^{-2.093\,R_D}$$

Barltrop & Adams (1991) :

$G_o = 600\sqrt{p_a p'}$ for $e = 0.8$

$G_o = 1300\sqrt{p_a p'}$ for $e = 0.5$

$p' = 30$ kPa; $p_a = 100$ kPa; $G_{small\ strain} = 0.25 G_o$

Figure 2.2 Elastic shear moduli from the literature

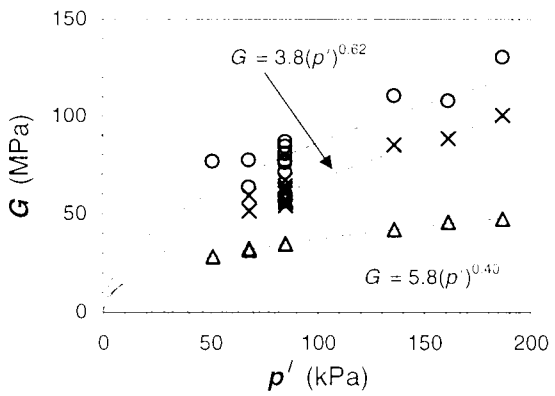

Gottardi & Houlsby (1995); Ea =0.025%
Gottardi & Houlsby (1995); Ea = 0.05%
Iwasaki, et. al. (1978)
power best-fit lines

Note:
- Relative density ranged from 74% to 79%.
- Radius equal to 50 mm.
- $p' = 0.67q$ for $K_o = 0.5$.
- $G = (d[V/w])/5R$ for a Poisson's ratio of 0.2.
- See Figure 2.2 for Iwasaki, *et. al.* (1978). Small strain values plotted.

Figure 2.3 Elastic shear moduli from the footing tests of Gottardi and Houlsby (1995)

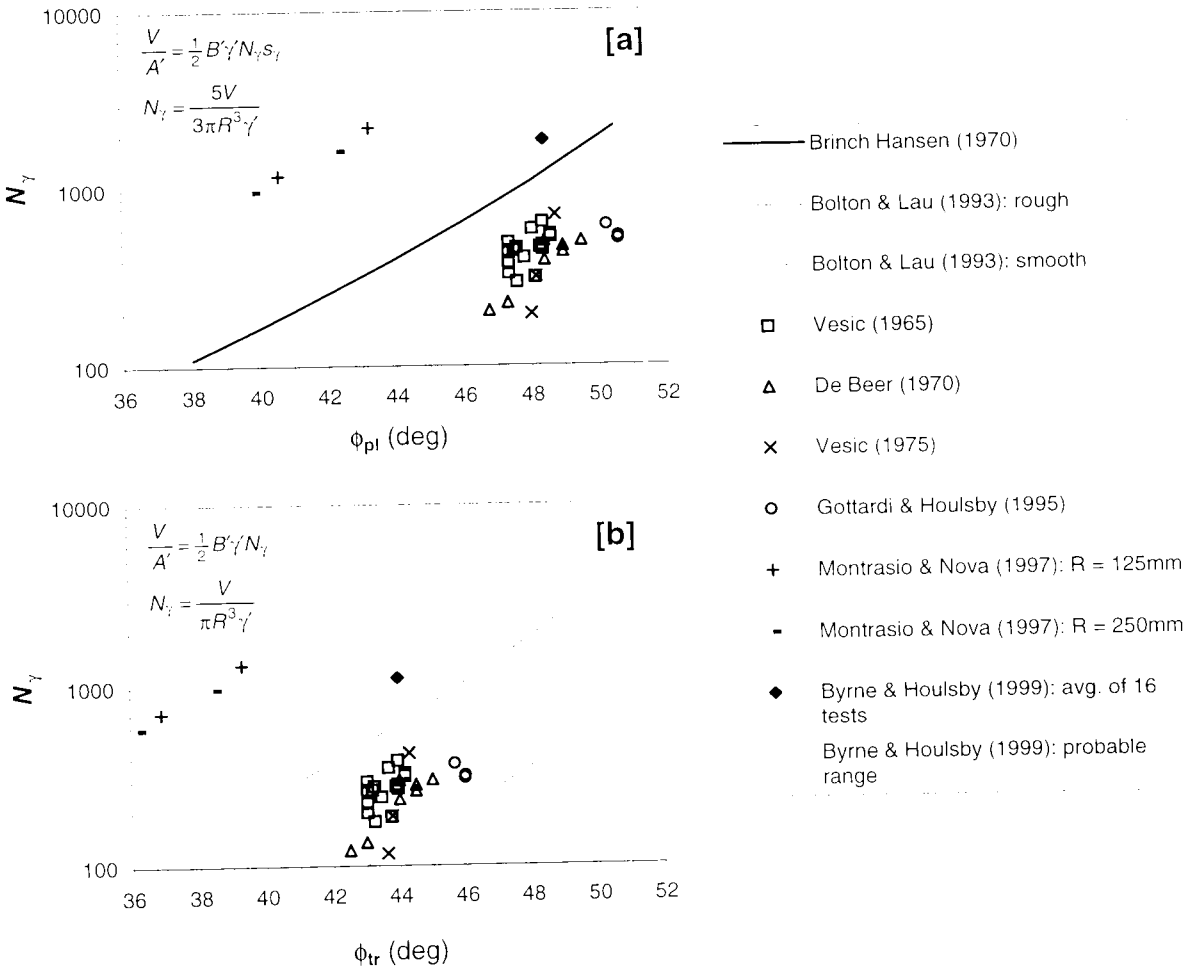

Source	R (mm)	R_D (%)	p' [a] (kPa)	Derivation of ϕ_{max}	ϕ_{crit} (deg)
Vesic (1965)	50	76 - 82	14 - 30	$\phi = \tan^{-1}(0.68/e)$ [b]	n/a
De Beer (1970)	75	65 - 89	14 - 37	$\phi = f(R_D, p')$ [c]	n/a
Vesic (1975)	76	61 - 78	13 - 49	Bolton (1986)	33 [d]
Gottardi & Houlsby (1995)	50	75	28	Bolton (1986)	34
Montrasio & Nova (1997)	125 & 500	45 & 70	132 - 382	Bolton (1986)	33 [d]
Byrne & Houlsby (1999)	25	97	47	Bolton (1986)	32 [e]

Note:
a Effective mean stress along shear plane at failure taken as one tenth of contact stress, see de Beer (1970).
b Relationship stated to be relevant for p' < 70 kPa.
c See Figure 10 in de Beer (1970).
d Value of ϕ_{crit} assumed.
e Byrne's tests were on Baskarp Cyclone sand, see Section 4.5 for relevant data.
All footings were classified as "rough".
Plane strain friction angles used in Brinch Hansen's method, $\phi_{tr} = 1.1\phi_{tr}$.

Figure 2.4 A comparison of theoretical and experimental bearing capacity factors: **[a]** Brinch Hansen (1970); and **[b]** Bolton and Lau (1993)

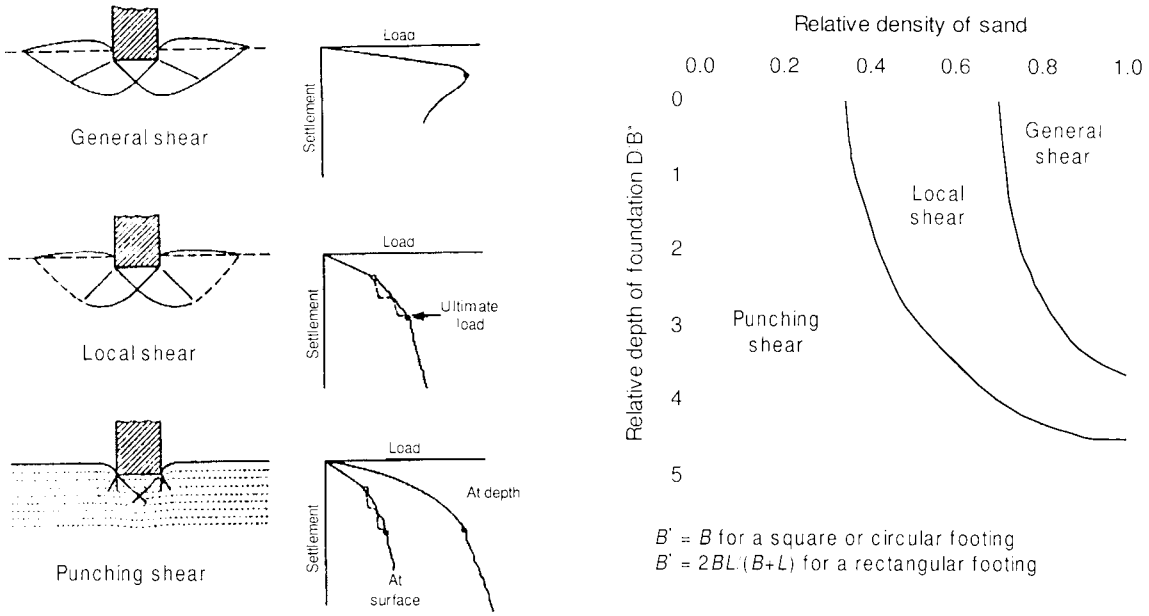

Figure 2.5 Bearing capacity failure mechanisms (after Vesic, 1975)

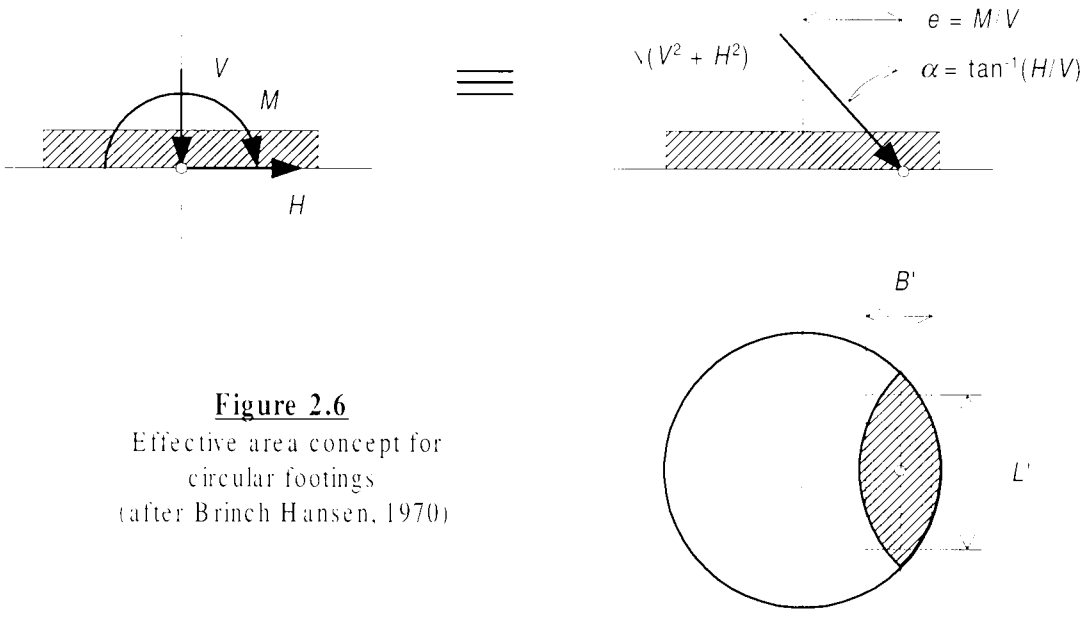

Figure 2.6
Effective area concept for circular footings (after Brinch Hansen, 1970)

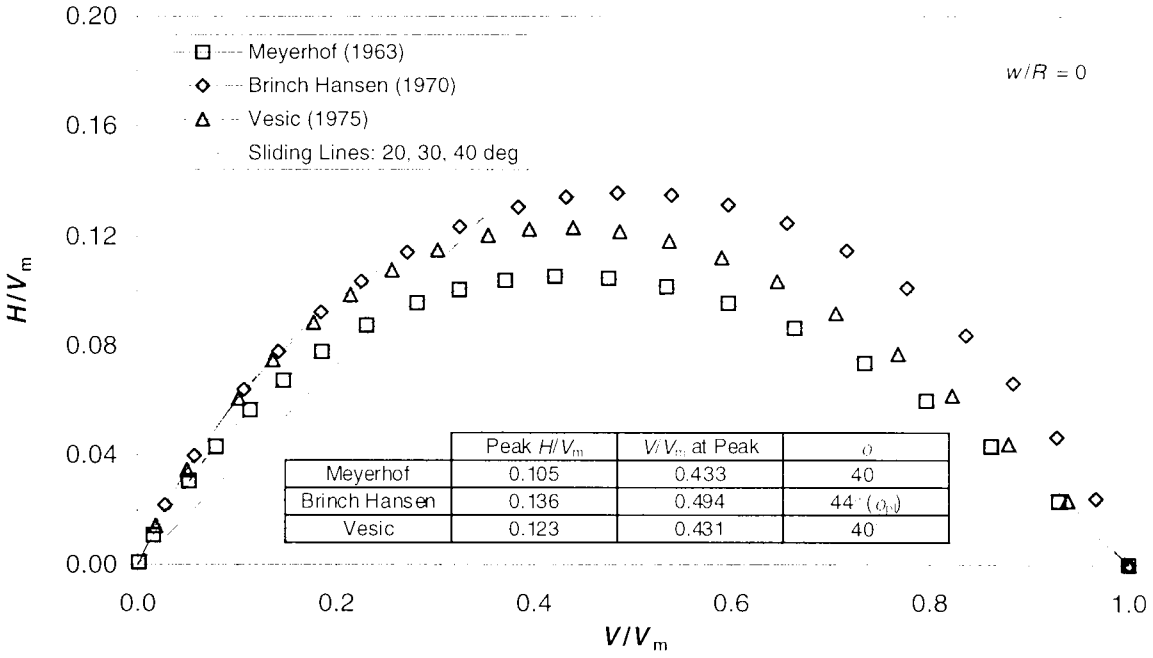

	Peak H/V_m	V/V_m at Peak	ϕ
Meyerhof	0.105	0.433	40
Brinch Hansen	0.136	0.494	44 (ϕ_{cv})
Vesic	0.123	0.431	40

Figure 2.7 V:H yield surfaces deduced from the traditional bearing capacity methods

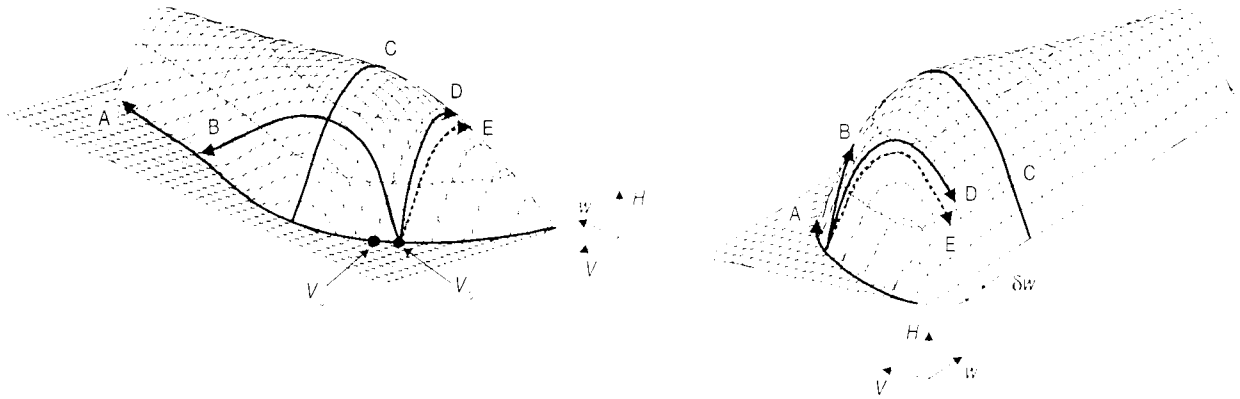

[a]

V_o is the initial virgin-penetration load
V_i is the extrapolated virgin-penetration load
w_e is the elastic vertical displacement
w_p is the plastic vertical displacement

A Virgin-penetration curve
B Constant-V test
C V_o:H failure envelope
D Sideswipe with $\delta w > 0$
E Sideswipe with $\delta w = 0$

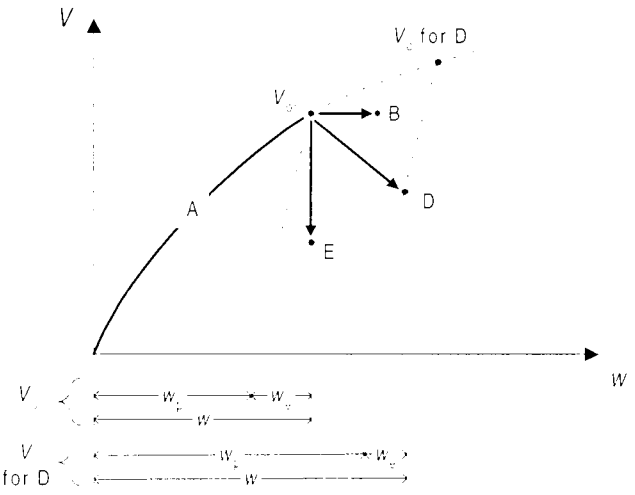

[b]

Figure 2.8
Illustration of sideswipe and constant-V tests:
[a] in w:V:H space; and
[b] in w:V space

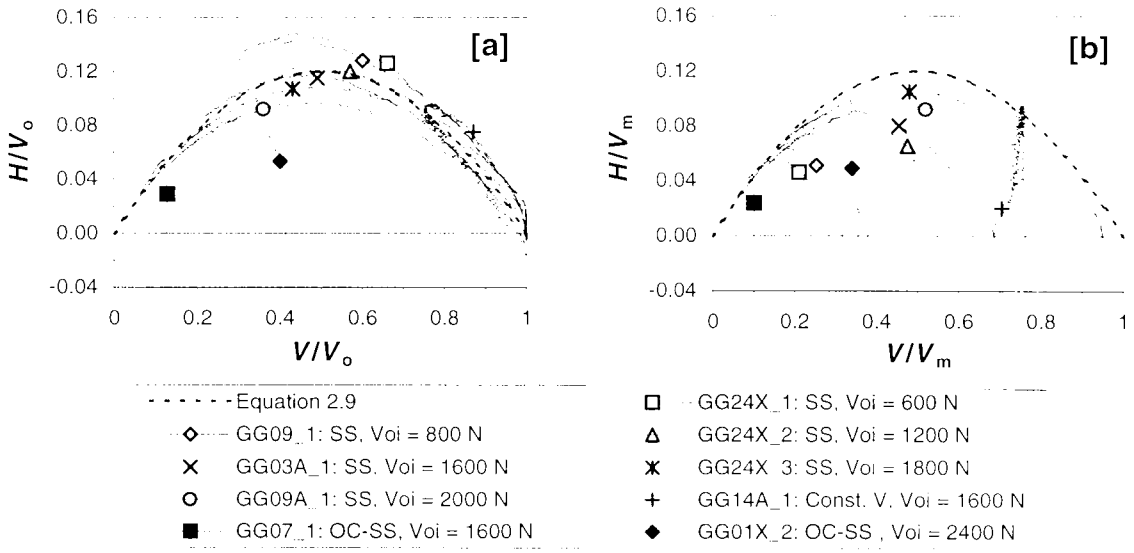

Note.
- SS = sideswipe test, Const. V = constant V test, and OC-SS = overconsolidated sideswipe test.
- In the OC-SS tests, the footing was loaded up to the indicated V_{oi} values before unloading and performance of the sideswipes.

Figure 2.9 Effect of normalisation on V:H yield surfaces: **[a]** V_o-normalised; and **[b]** V_m-normalised (data from Gottardi and Houlsby, 1995)

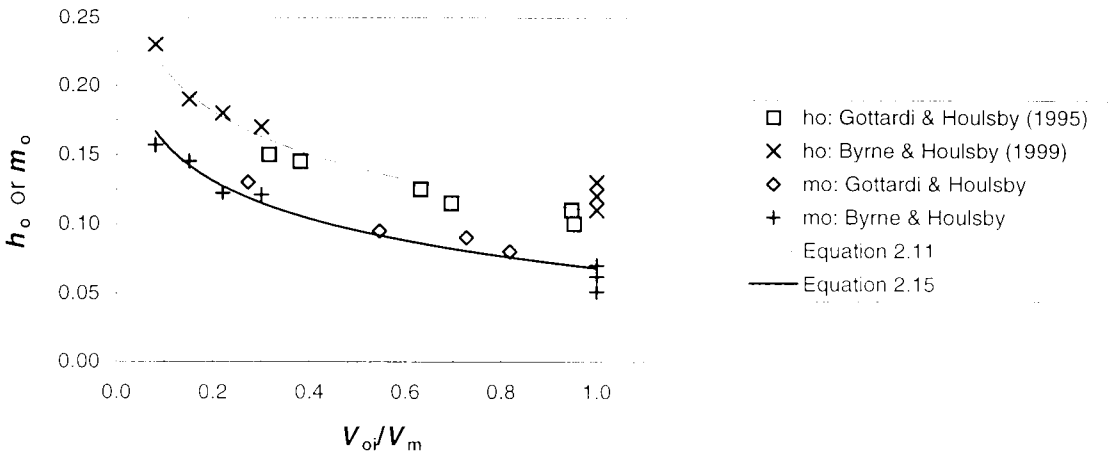

Figure 2.10 Relationship between normalised peak loads and V_{oi}/V_m ratio from sideswipe tests in the literature

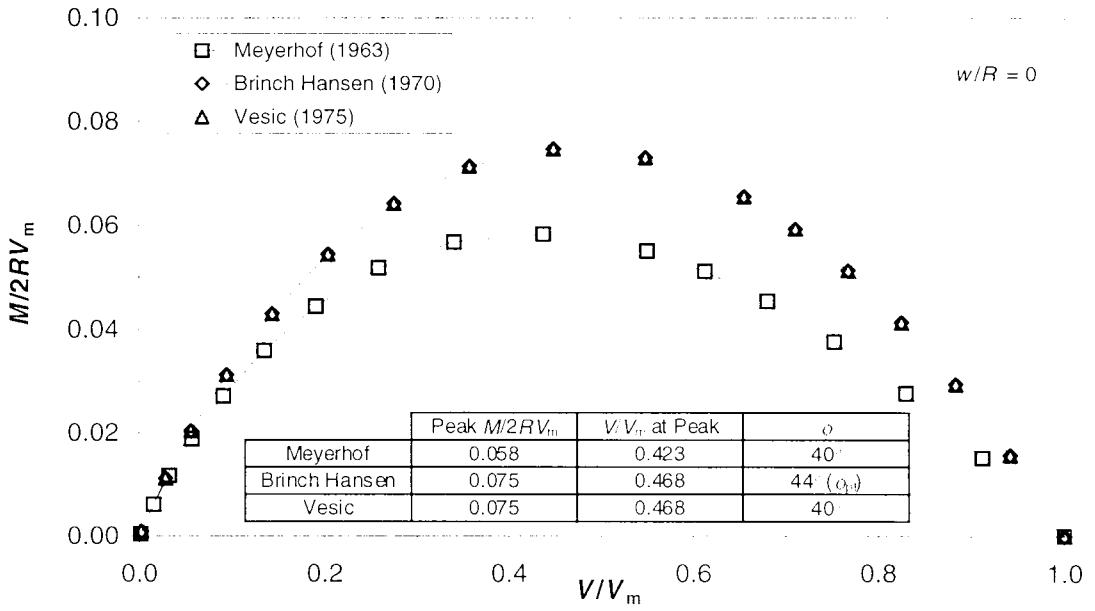

	Peak $M/2RV_m$	V/V_m at Peak	ϕ
Meyerhof	0.058	0.423	40°
Brinch Hansen	0.075	0.468	44° (ϕ_{cv})
Vesic	0.075	0.468	40°

Figure 2.11 V:M interaction loci deduced from traditional bearing capacity methods

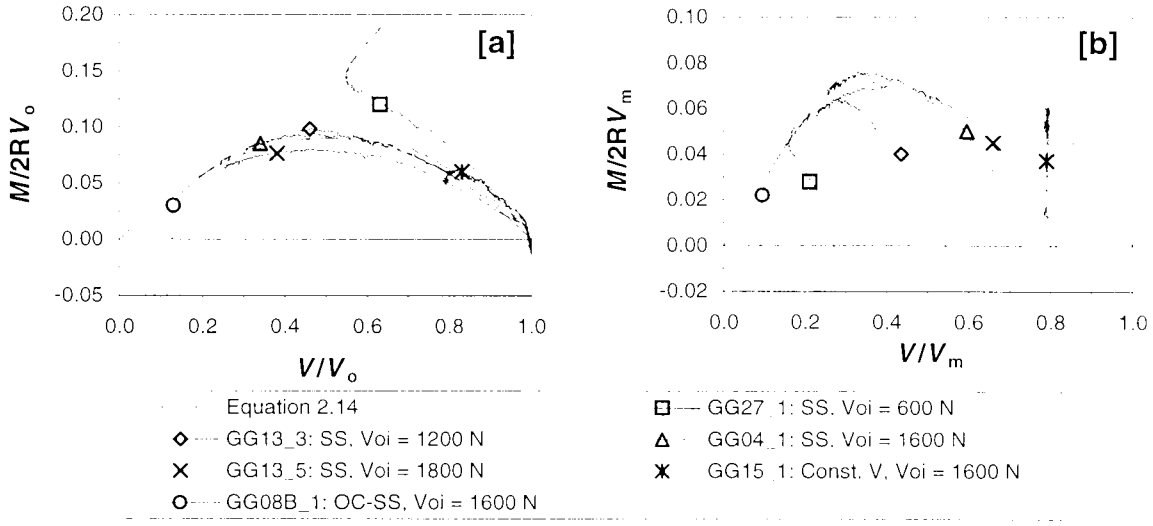

Note:
- SS = sideswipe test, Const. V = constant V test, and OC-SS = overconsolidated sideswipe test.
- In the OC-SS tests, the footing was loaded up to the indicated V_{oi} values before unloading and performance of the

Figure 2.12 Effect of normalisation on V:M yield surfaces:
[a] V_o-normalised; and **[b]** V_m-normalised (data from Gottardi and Houlsby, 1995)

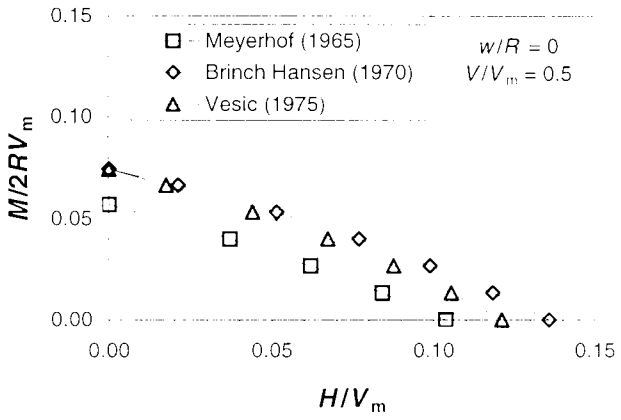

Figure 2.13
H:M failure surfaces derived using the traditional bearing capacity methods (plotted in the $(+H)$:$(+M)$ quadrant only)

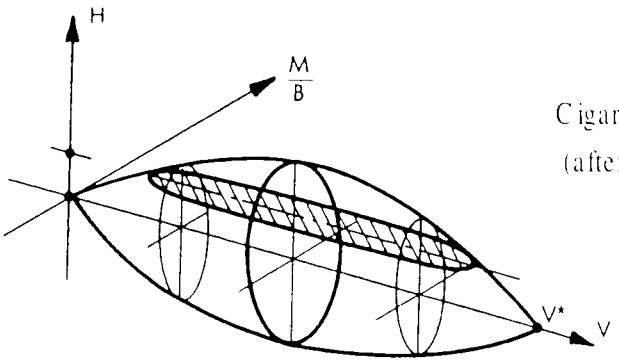

Figure 2.14
Cigar shaped V:H:M failure surface
(after Butterfield and Ticof, 1979)

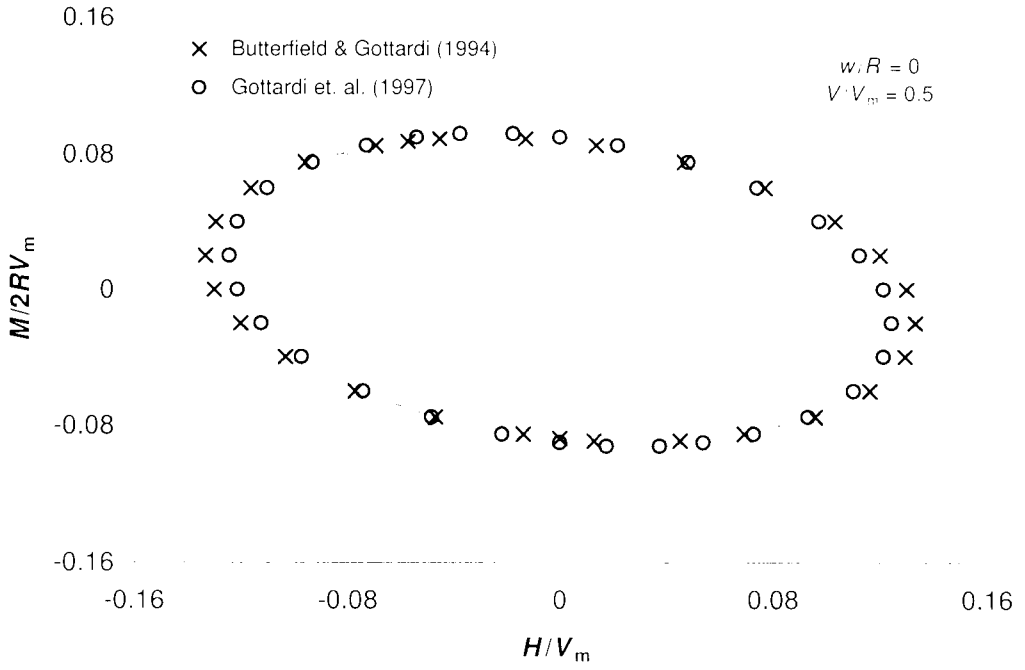

Figure 2.15 H:M failure surfaces derived from combined load tests

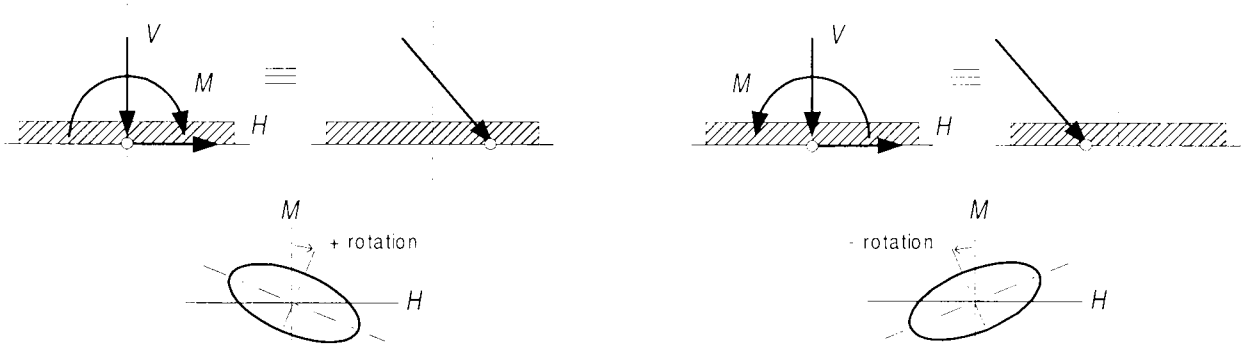

clockwise moment positive

anti-clockwise moment positive

Figure 2.16 Effect of sign convention on eccentricity of H:M ellipse

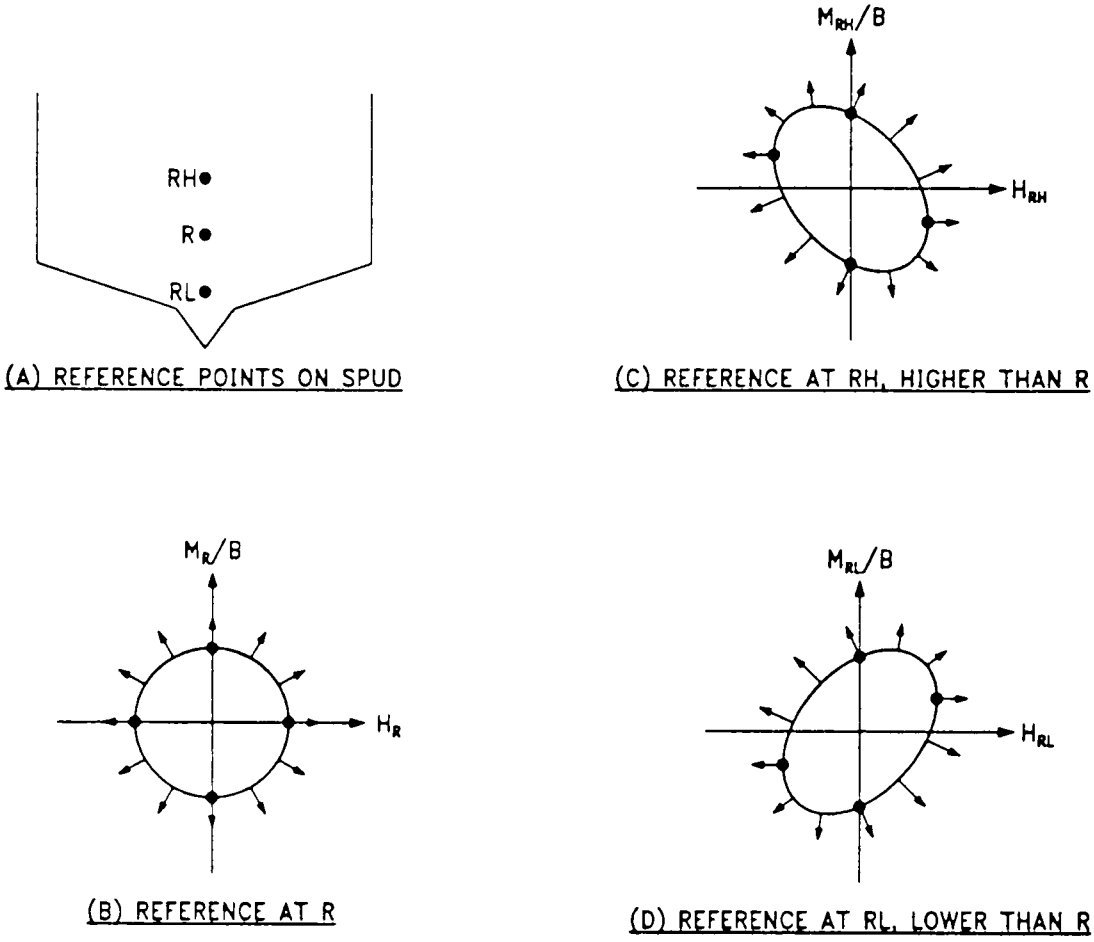

Figure 2.17 Effect of the position of the load/displacement reference point (after Dean *et al.*, 1992b)

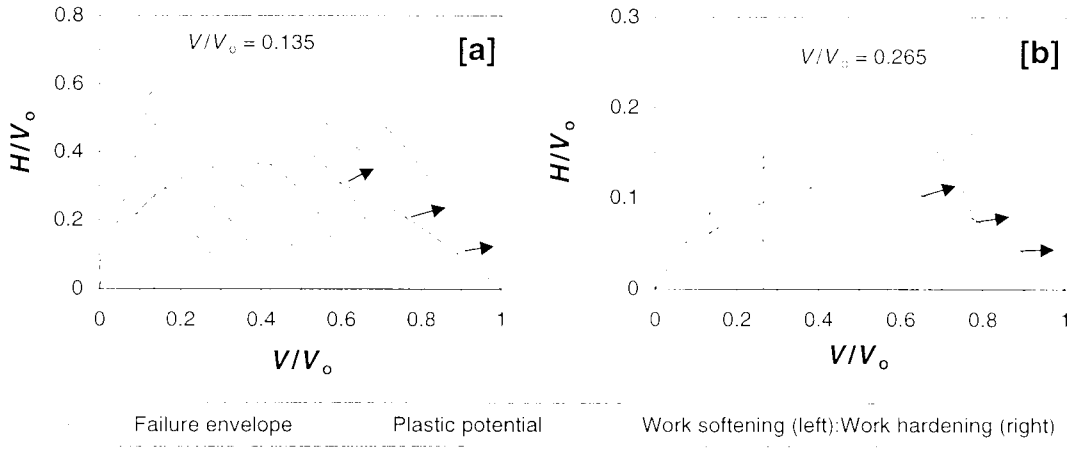

Note: Arrows indicate direction of plastic displacement increment vectors, *i.e.* perendiculuar to plastic potential

Figure 2.18 Failure envelope, plastic potentials and work softening/work hardening regions: **[a]** Tan (1990); and **[b]** Cassidy (1996)

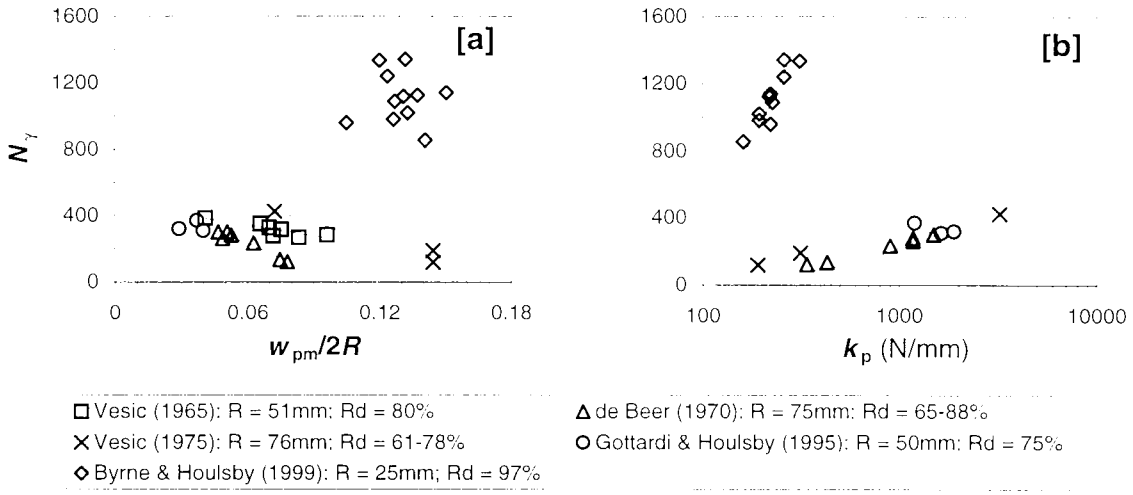

Note: Some linear trendlines shown. Intercepts set to zero in [b].

Figure 2.19 Relationship between load:deformation parameters of experimental data in the literature: **[a]** bearing capacity factor against normalised displacement at failure; and **[b]** bearing capacity factor against initial virgin-penetration stiffness

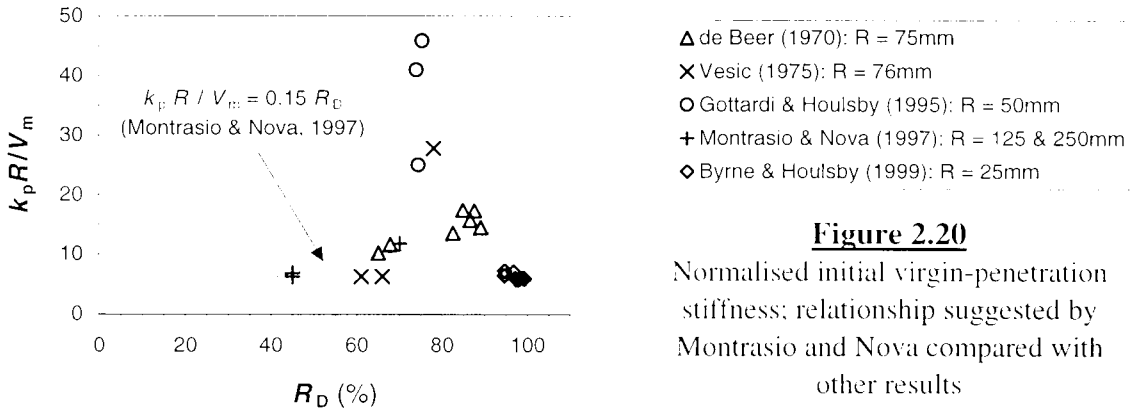

Figure 2.20
Normalised initial virgin-penetration stiffness; relationship suggested by Montrasio and Nova compared with other results

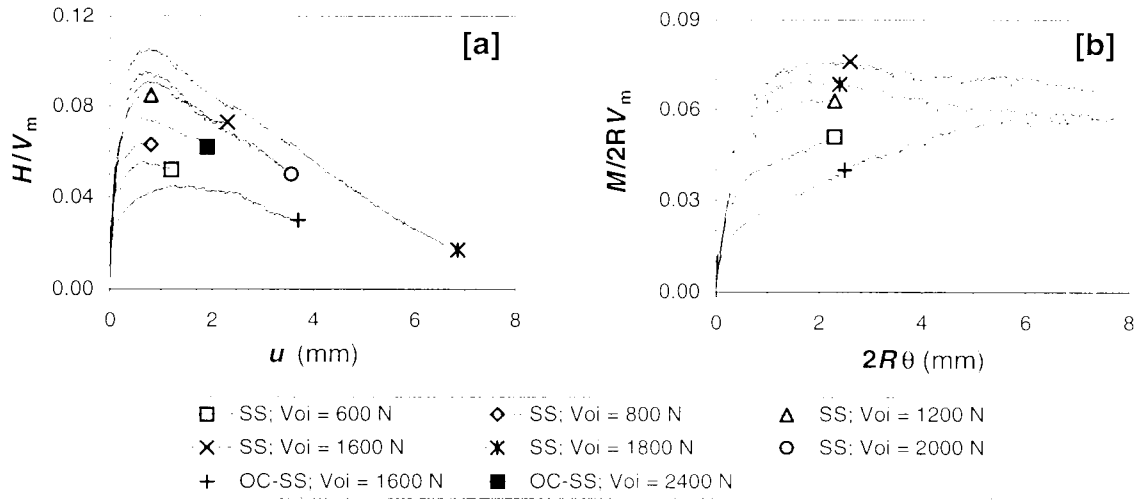

Note:
- SS = sideswipe test and OC-SS = overconsolidated sideswipe test.
- In the OC-SS tests, the footing was loaded up to the indicated V_{oi} values before unloading and performance of the sideswipes.

Figure 2.21 Normalised load:deformation response of sideswipe tests: **[a]** horizontal sideswipes; and **[b]** moment sideswipes (data from of Gottardi & Houlsby, 1995)

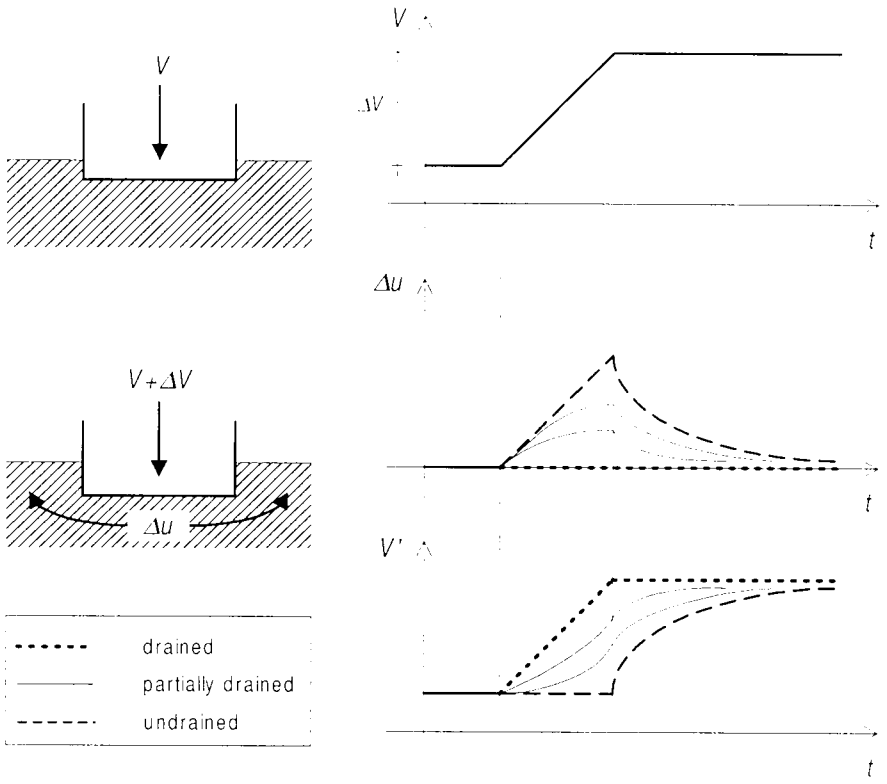

Figure 2.22
Effect of drainage conditions on a transient load increment

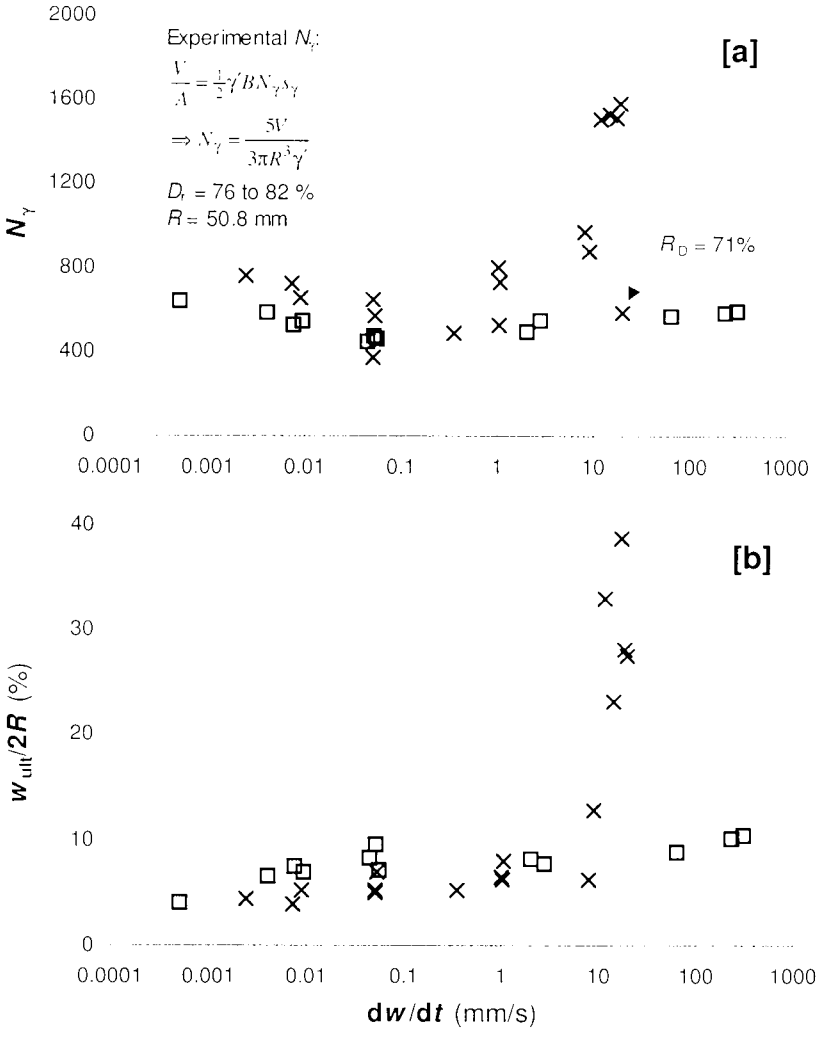

Figure 2.23
Dynamic model footing tests:
[a] effect of penetration rate on bearing capacity; and
[b] effect of penetration rate on ultimate settlement
(after Vesic *et al*., 1965)

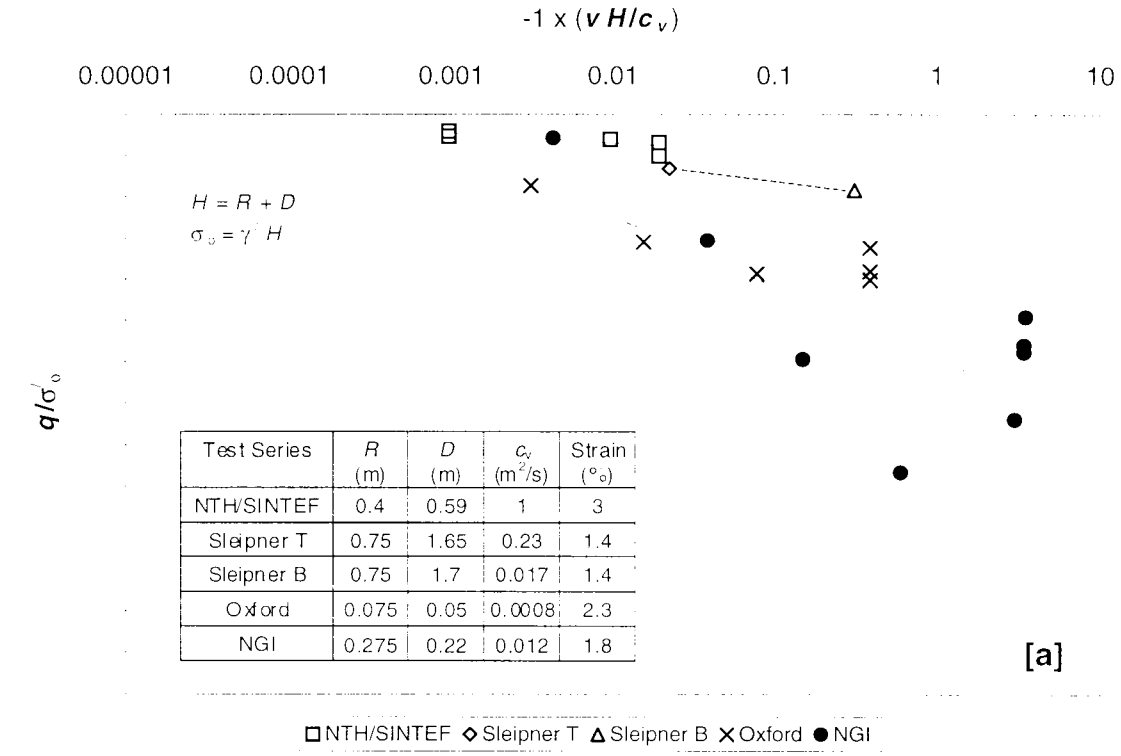

Test Series	R (m)	D (m)	c_v (m^2/s)	Strain (%)
NTH/SINTEF	0.4	0.59	1	3
Sleipner T	0.75	1.65	0.23	1.4
Sleipner B	0.75	1.7	0.017	1.4
Oxford	0.075	0.05	0.0008	2.3
NGI	0.275	0.22	0.012	1.8

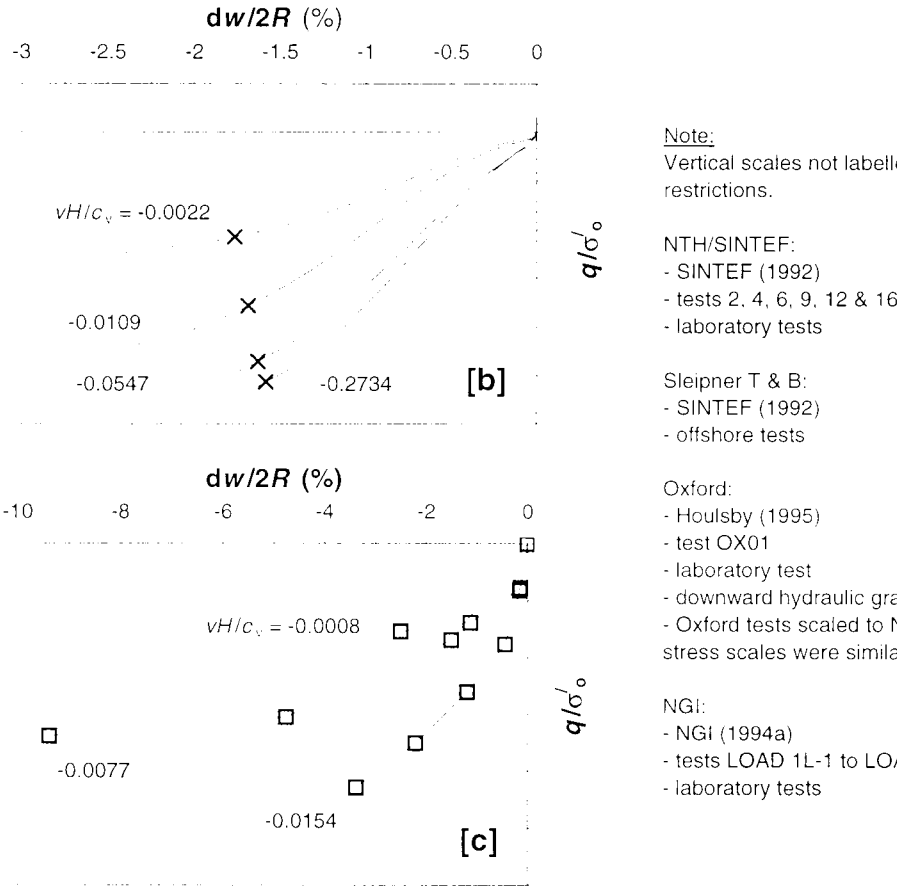

Note:
Vertical scales not labelled because of confidentiality restrictions.

NTH/SINTEF:
- SINTEF (1992)
- tests 2, 4, 6, 9, 12 & 16
- laboratory tests

Sleipner T & B:
- SINTEF (1992)
- offshore tests

Oxford:
- Houlsby (1995)
- test OX01
- laboratory test
- downward hydraulic gradient of 3.6
- Oxford tests scaled to NGI as geometric and effective stress scales were similar

NGI:
- NGI (1994a)
- tests LOAD 1L-1 to LOAD 1L-9
- laboratory tests

Figure 2.24 Effect of pull-out rate on load:deformation behaviour of suction caisson foundations: **[a]** trend of increasing load with increasing pull-out velocity; **[b]** Oxford tests; and **[c]** NTH/SINTEF tests

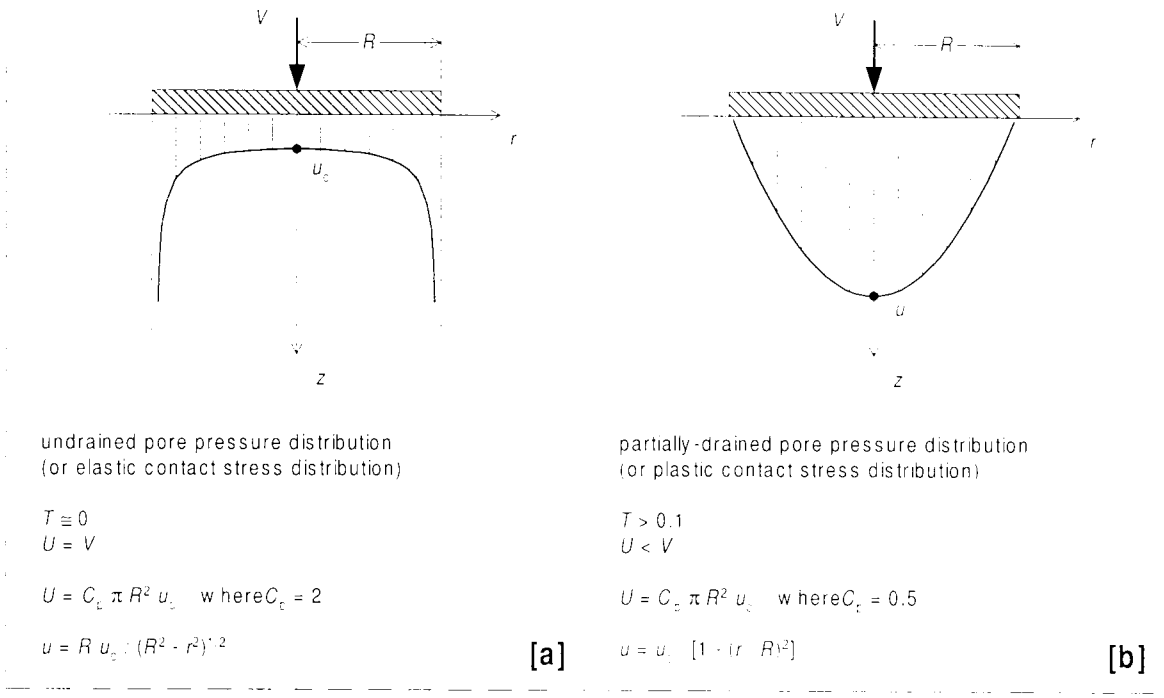

Figure 2.25 Pore pressure distributions beneath a rigid circular footing: [a] undrained distribution; and [b] partially-drained distribution

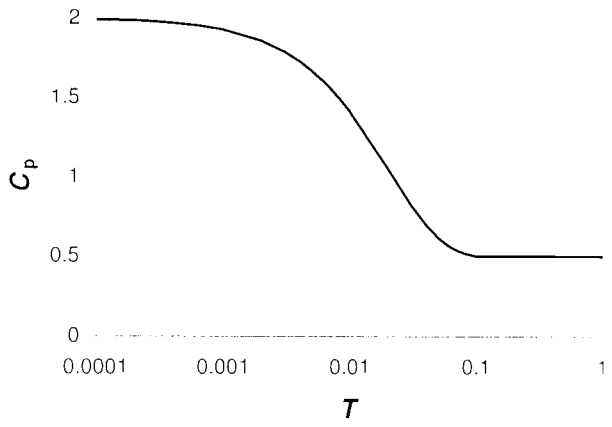

Figure 2.26
Variation of the coefficient of pore pressure distribution with the non-dimensional time factor

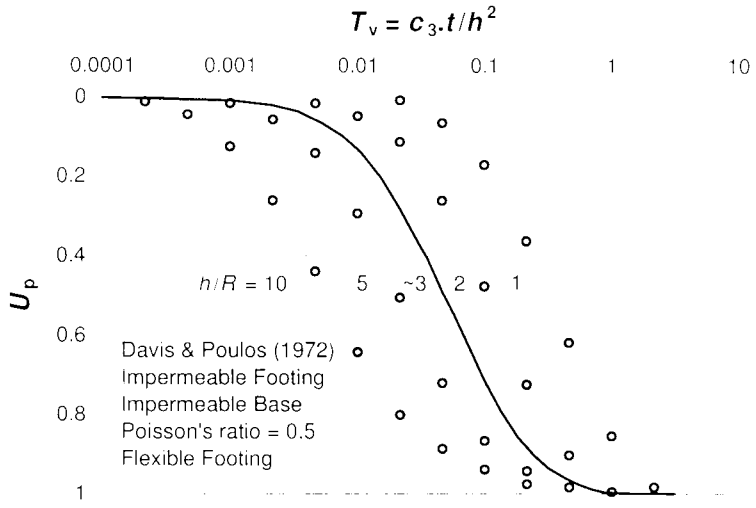

Figure 2.27
Rate of pore pressure dissipation

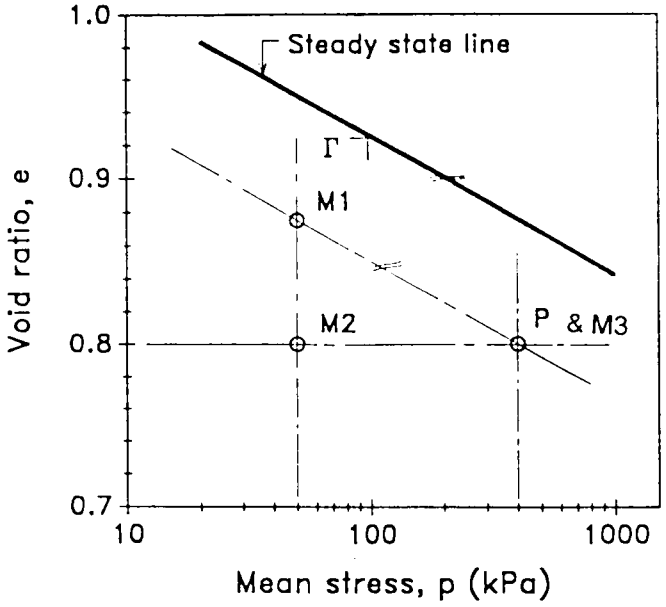

P - prototype

M1 - equivalent state parameter 1-g model

M2 - equivalent void ratio 1-g model

M3 - centrifuge model

Figure 2.28 Reference states of models and prototype
(after Altaee and Fellenius, 1994)

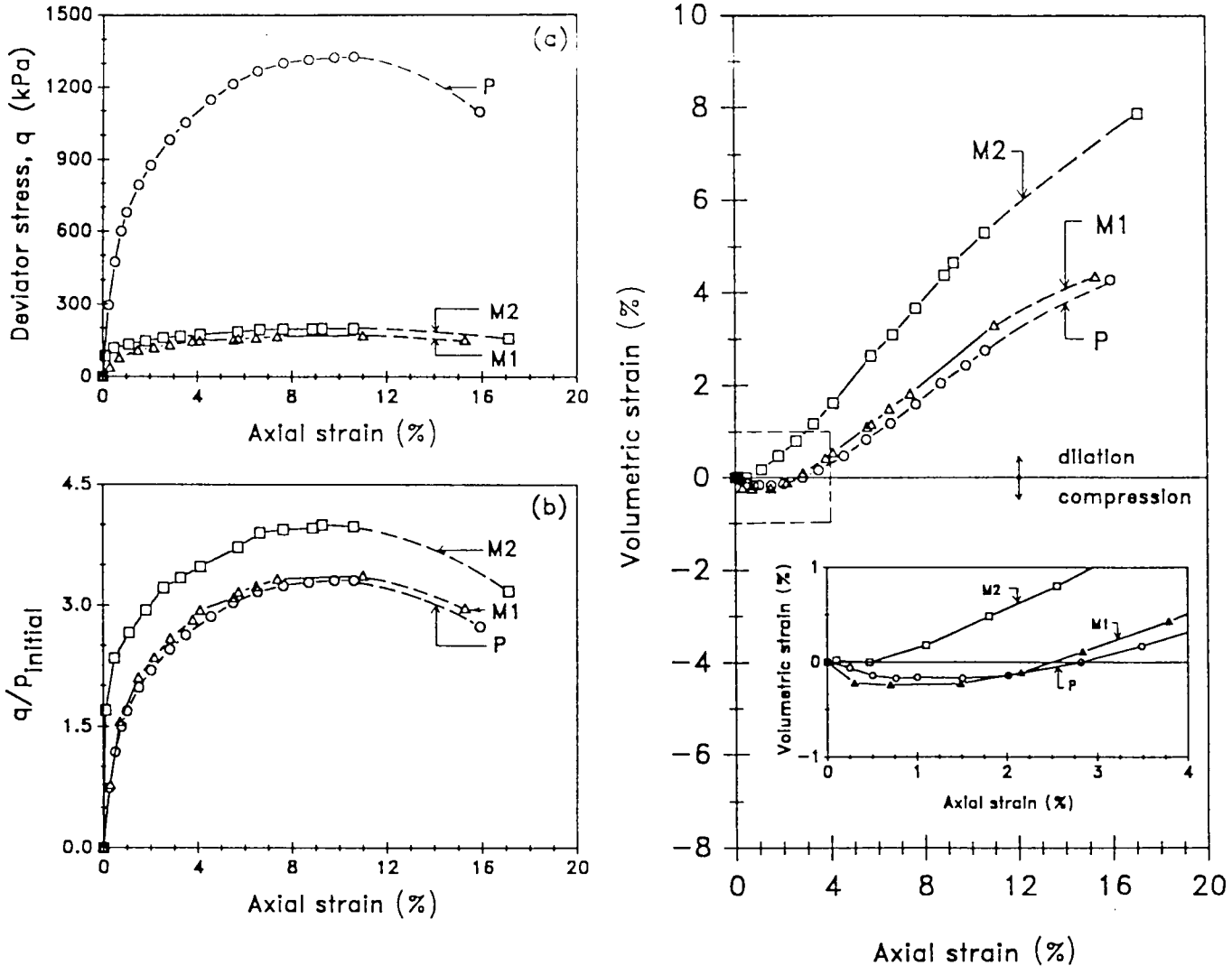

P - prototype; M1 - equivalent state parameter 1-g model; M2 - equivalent void ratio 1-g model

Figure 2.29 Triaxial drained response of reference states P, M1, and M2
(after Altaee and Fellenius, 1994)

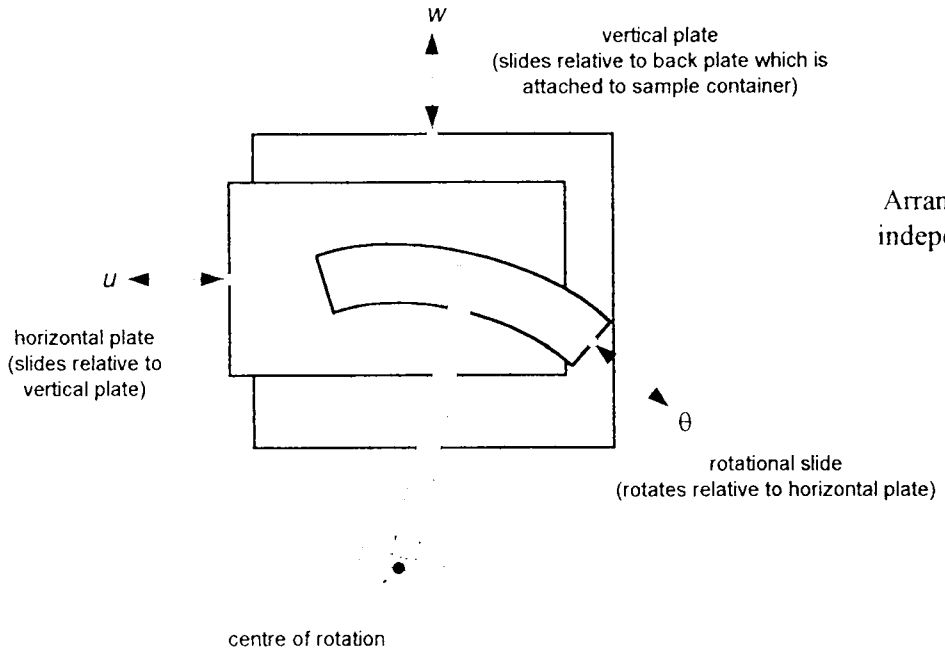

Figure 3.1
Arrangement of the three independent displacement systems

Figure 3.2 Shaft connecting footing to rotational slide

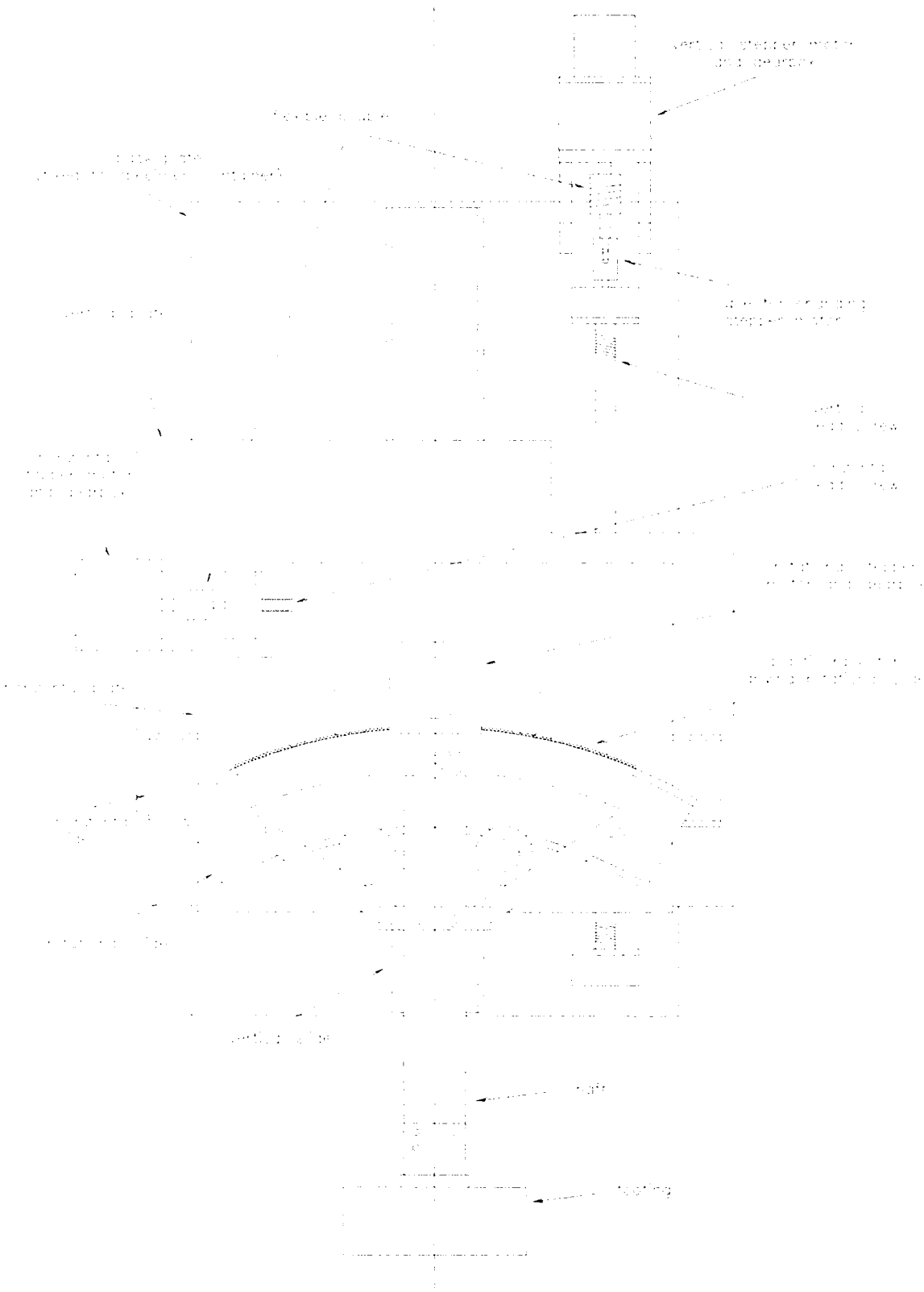

Figure 3.3 Stepper motor arrangement and drive system

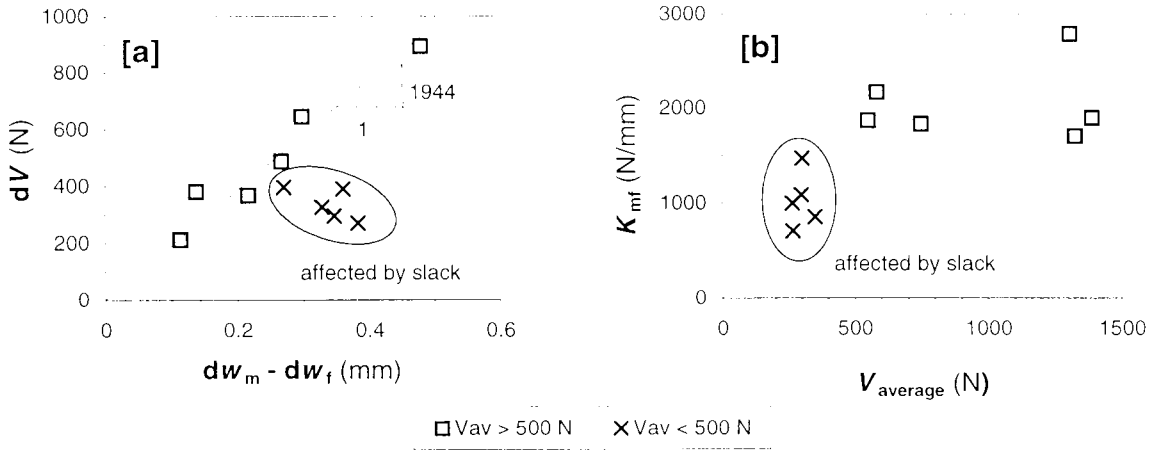

Note:
- dw_m was the vertical displacement at the stepper motor.
- dw_f was the vertical displacement at the footing.
- K_{mf} was the vertical stiffness of the rig measured between the stepper motor and the footing.

Figure 3.4 The vertical stiffness of the rig and slack in the vertical displacement system: **[a]** average vertical stiffness of rig; and **[b]** effect of slack on vertical rig stiffness

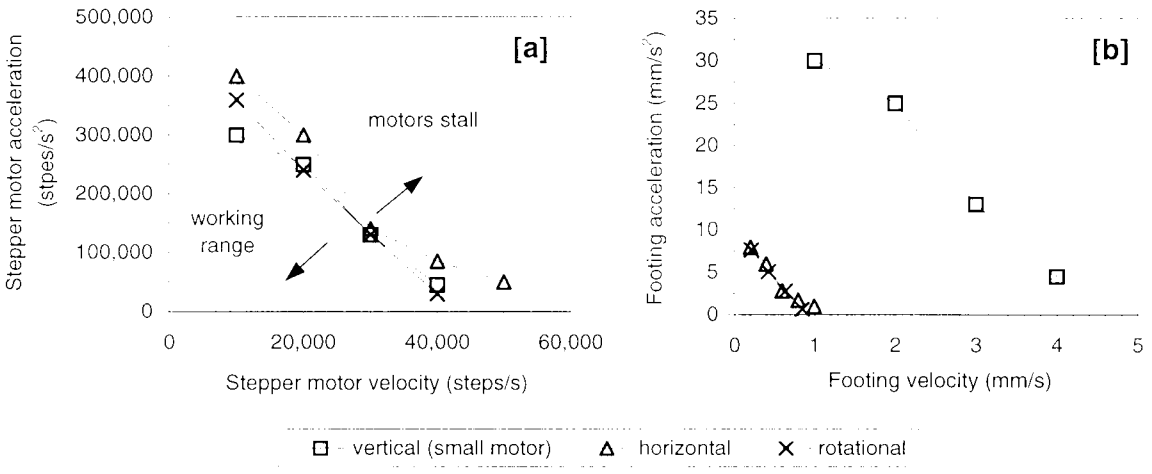

Figure 3.5 Working range of the stepper motors under minimal load: **[a]** in steps; and **[b]** in millimeters

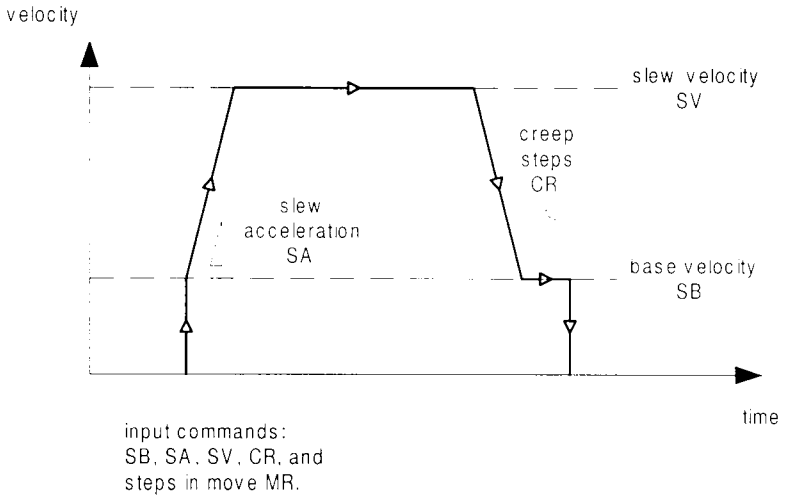

Figure 3.6 Velocity path and stepper motor commands for a Move Relative (MR) event

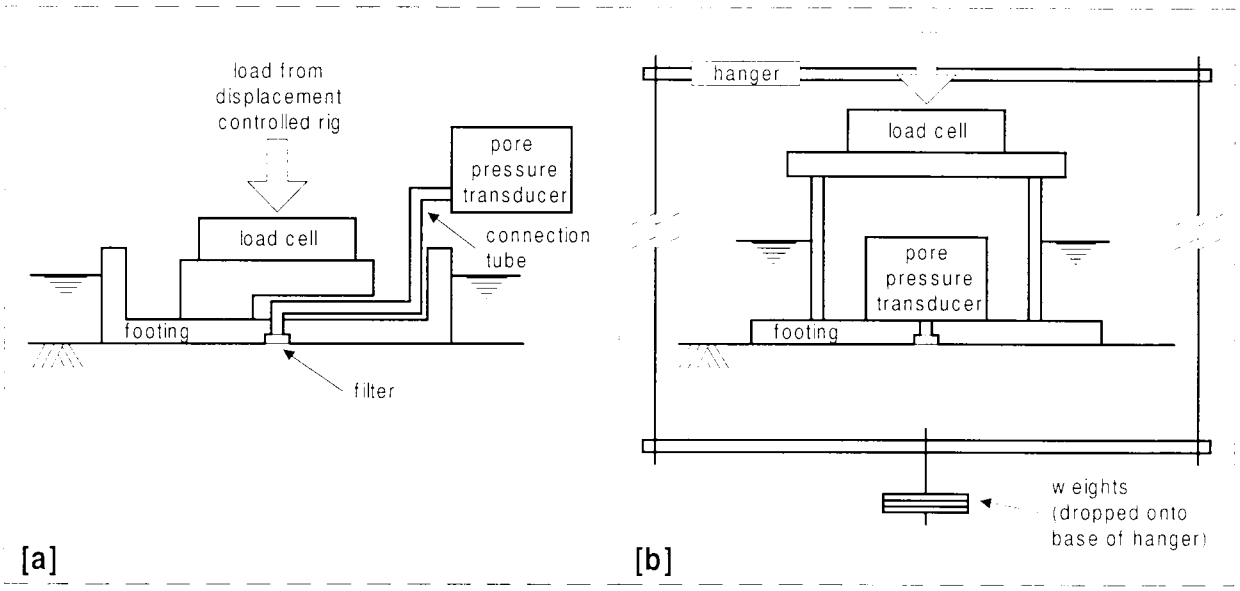

Figure 3.7 Apparatus of preliminary tests:
[a] 100 mm diameter footing with external pore pressure transducer; and
[b] 150 mm diameter footing with internal pore pressure transducer

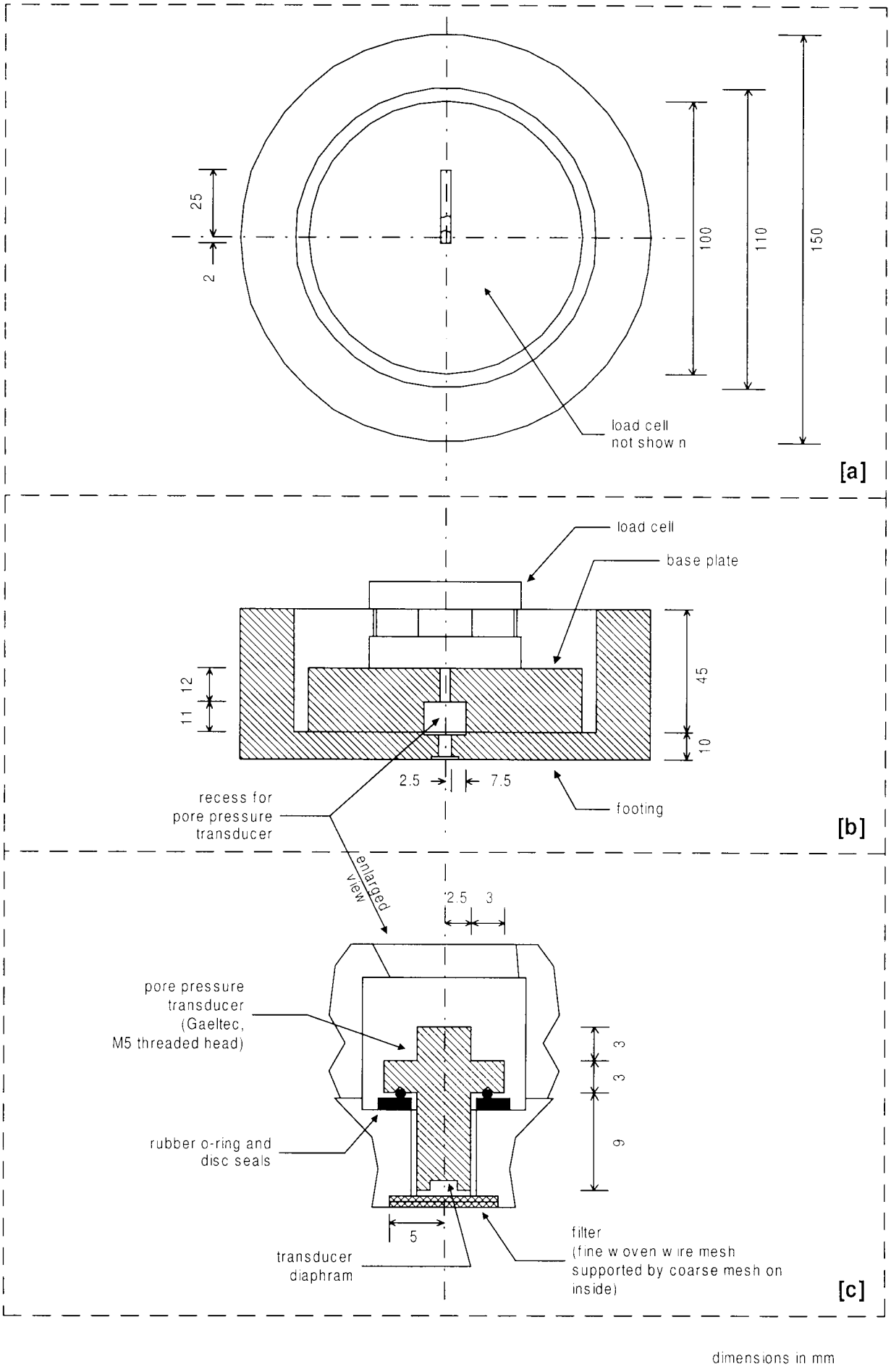

Figure 3.8 The footing and base plate, and pore pressure transducer: [a] plan view of footing and base plate; [b] section through footing and base plate; and [c] detail of pore pressure transducer

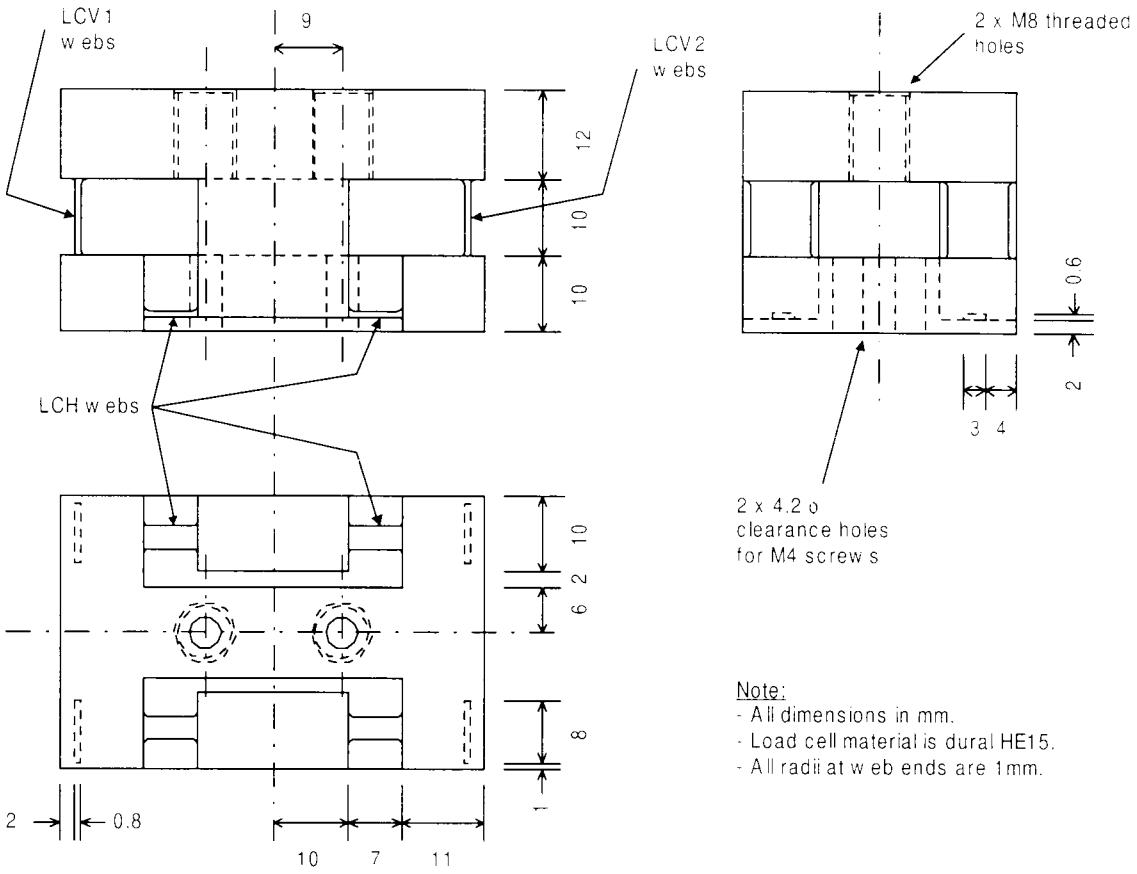

Figure 3.9 Load cell for measuring V, H, and M loads on footing

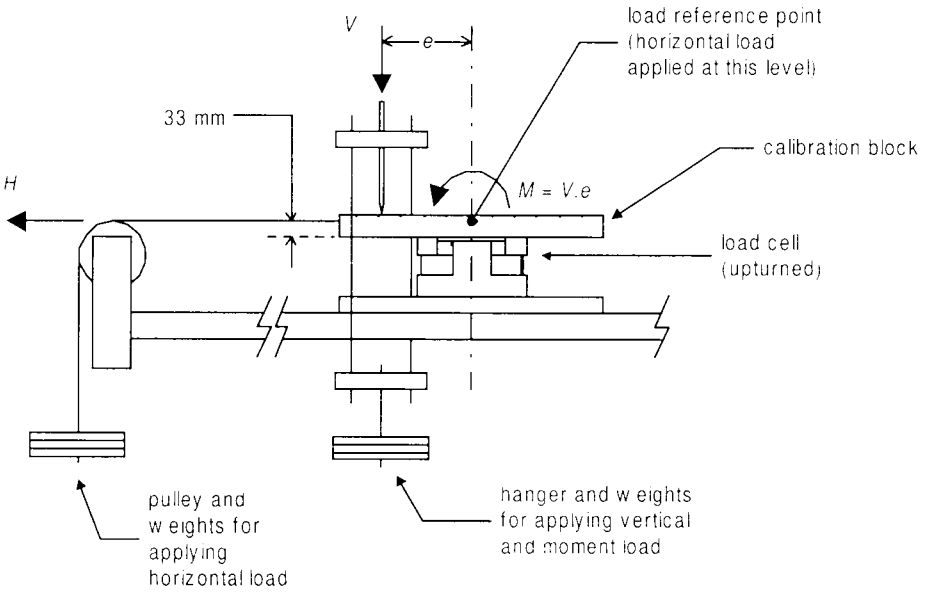

Figure 3.10 Load cell calibration apparatus

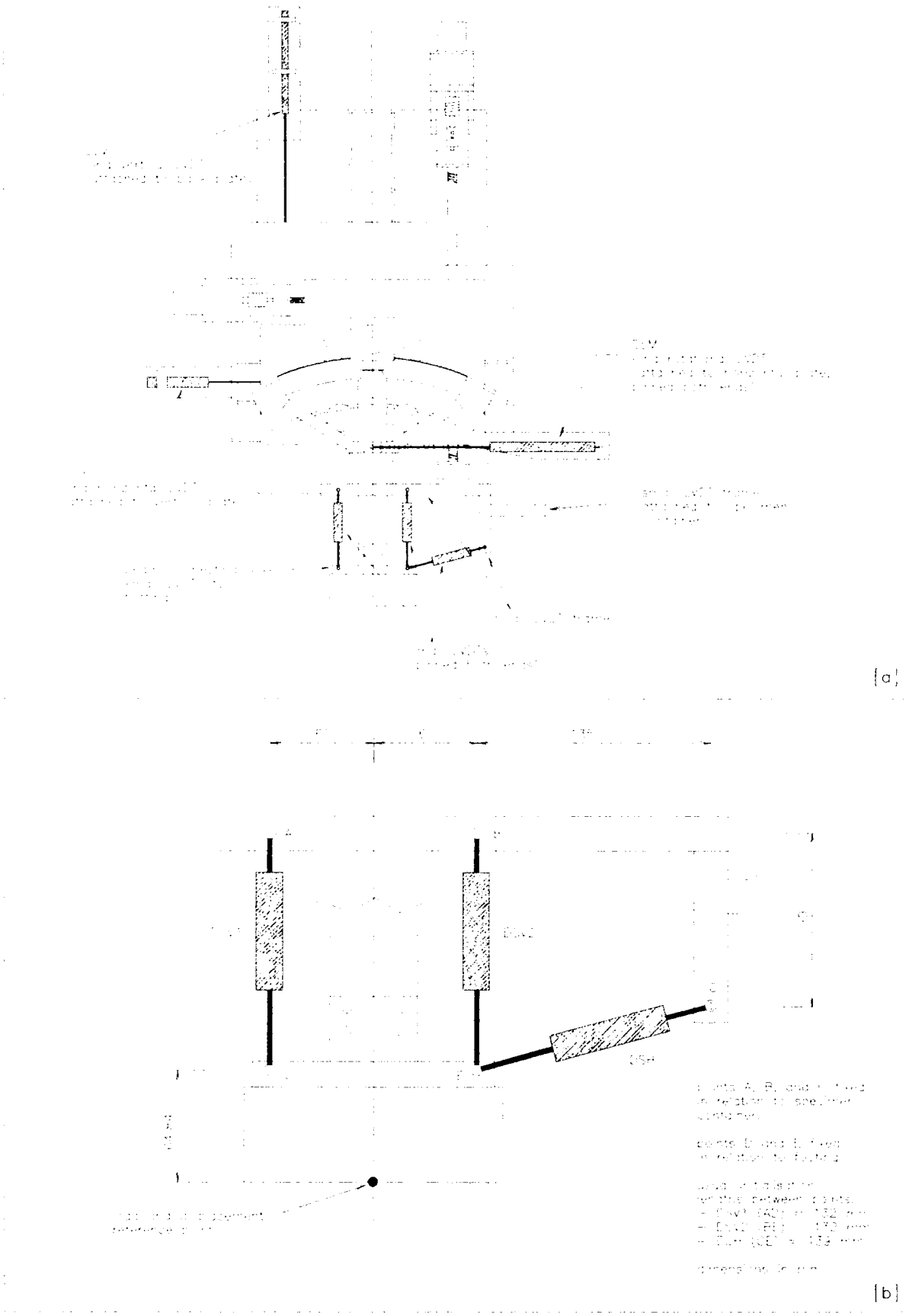

Figure 3.11 Arrangement of long and small LVDTs:

[a] position of all LVDTs on rig; and **[b]** detail of LVDT frame

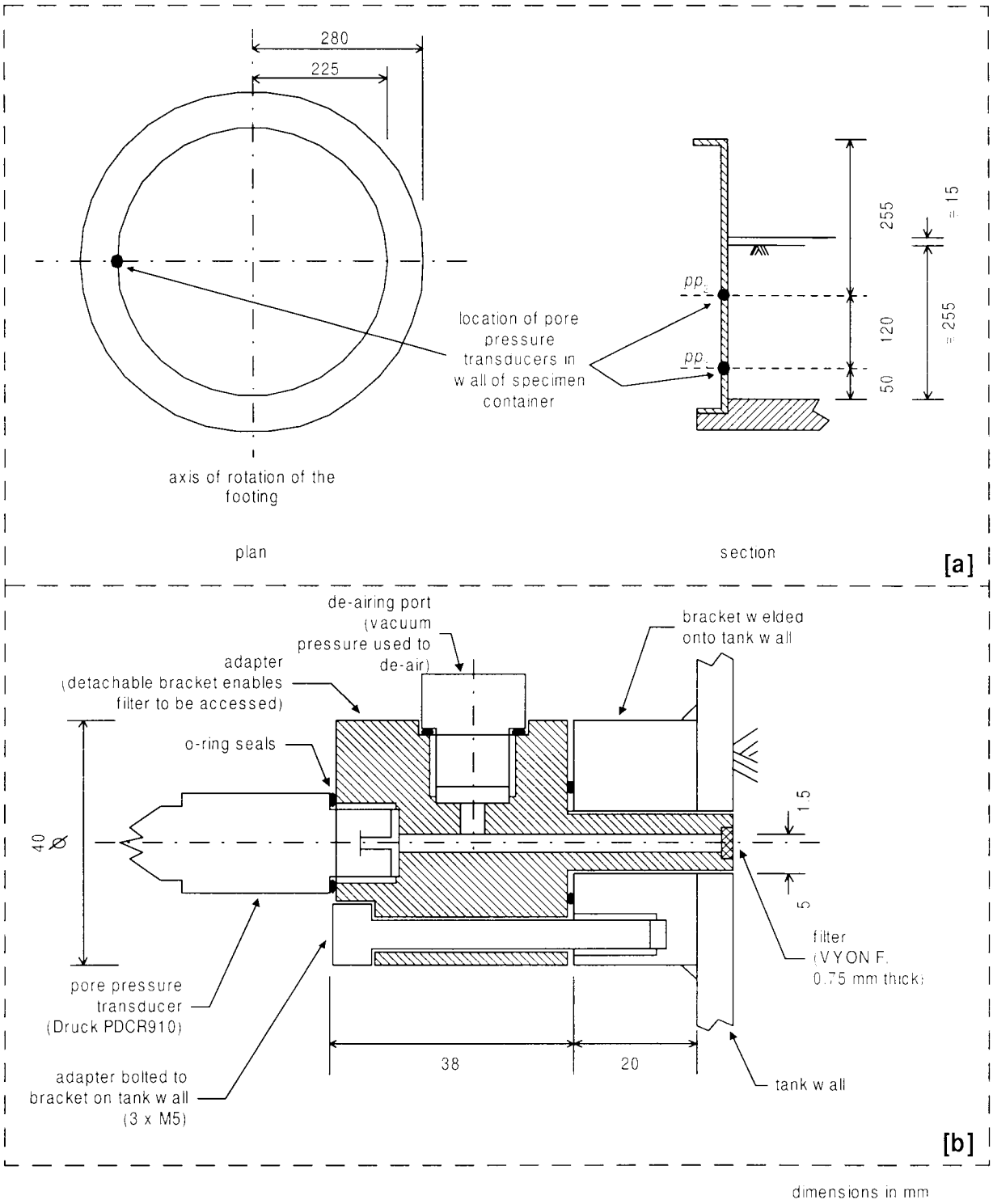

Figure 3.12 Pore pressure transducers in the wall of the specimen container: [a] location of transducers; and [b] detail of connection

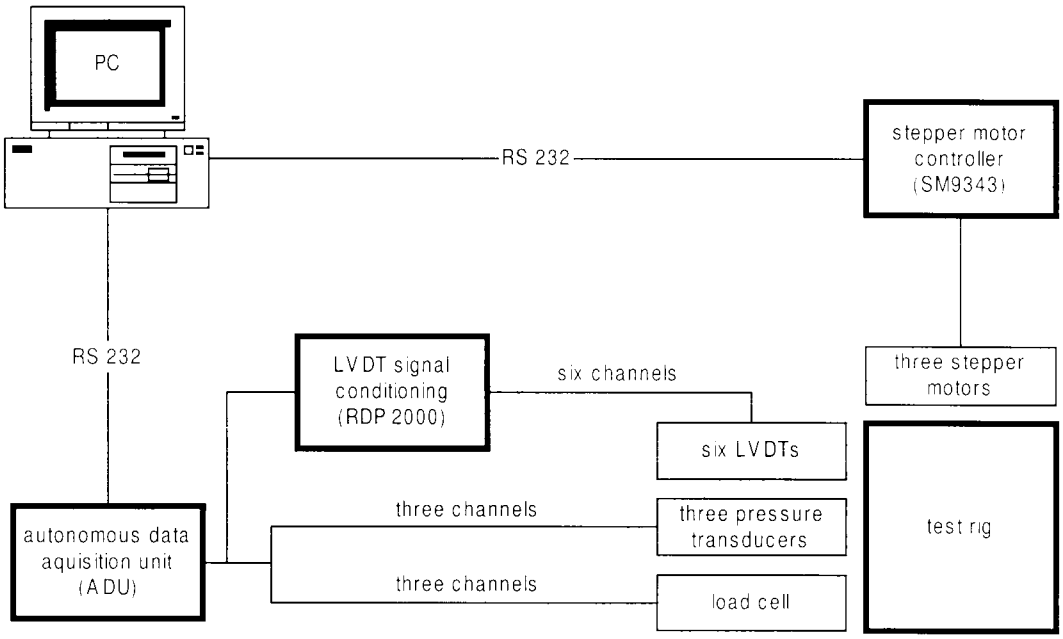

Figure 3.13 Control and monitoring layout

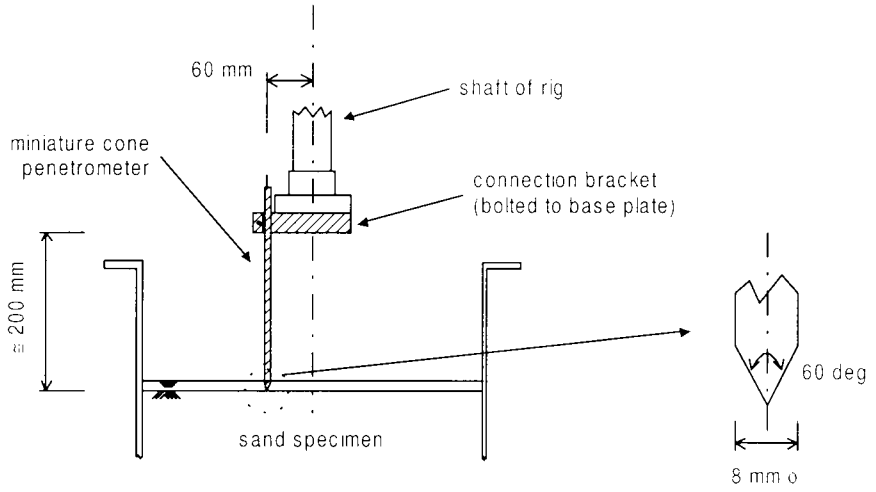

Figure 3.14 Miniature cone penetrometer

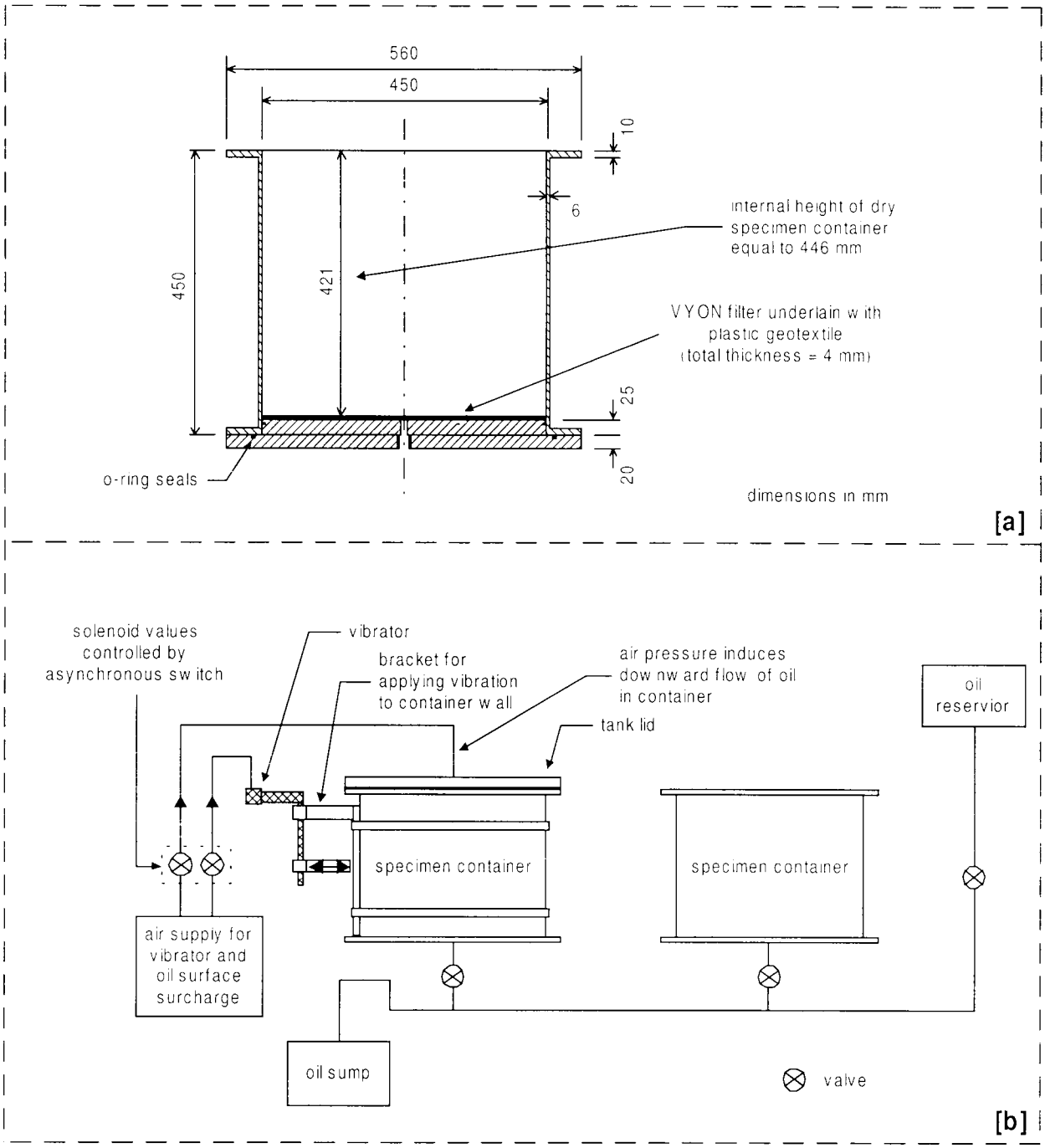

Figure 3.15 Containers for saturated specimens: [a] dimensions of containers; and [b] hydraulics and densification apparatus

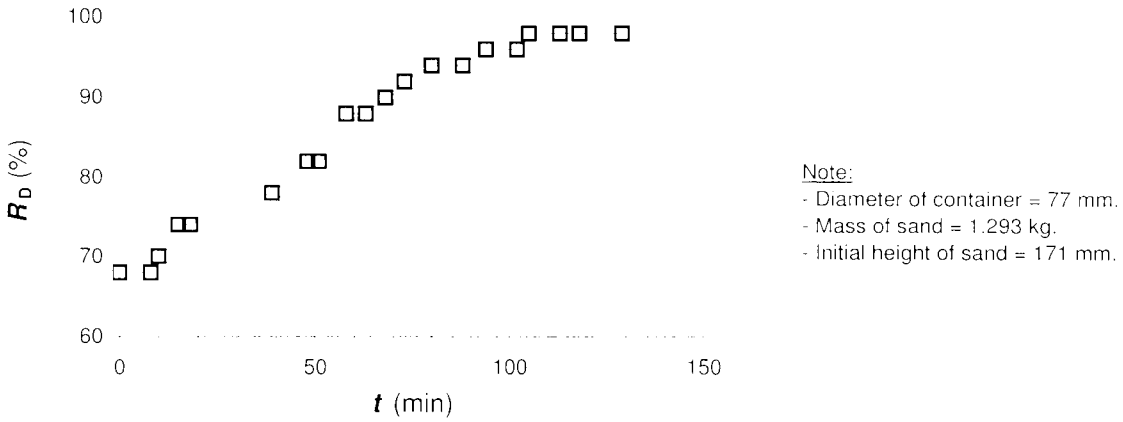

Figure 3.16 Densification of sand using vibration and downward hydraulic gradient

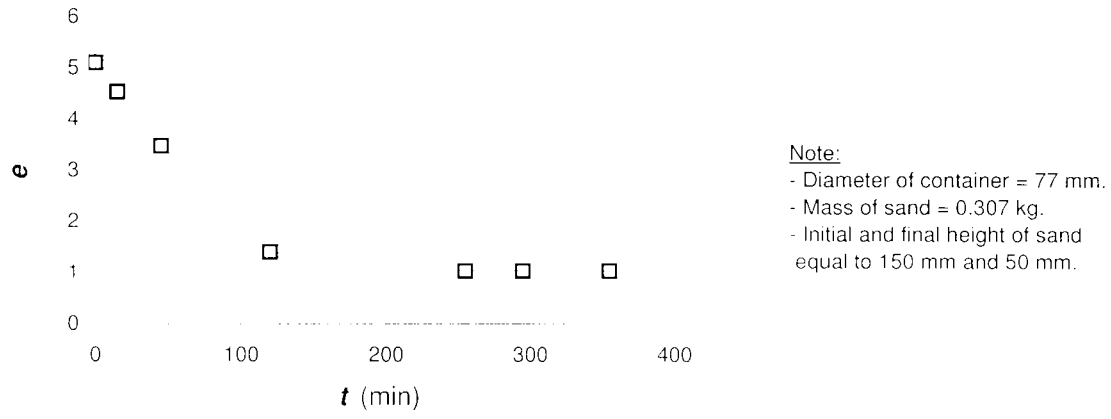

Figure 3.17 Sedimentation of sand

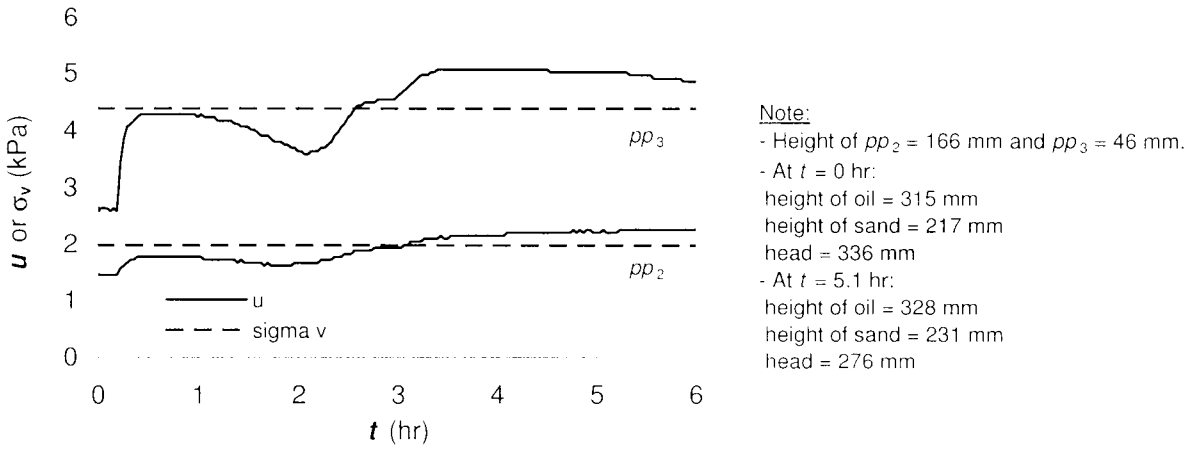

Figure 3.18 Pore pressure and total stress during liquefaction of sand specimen

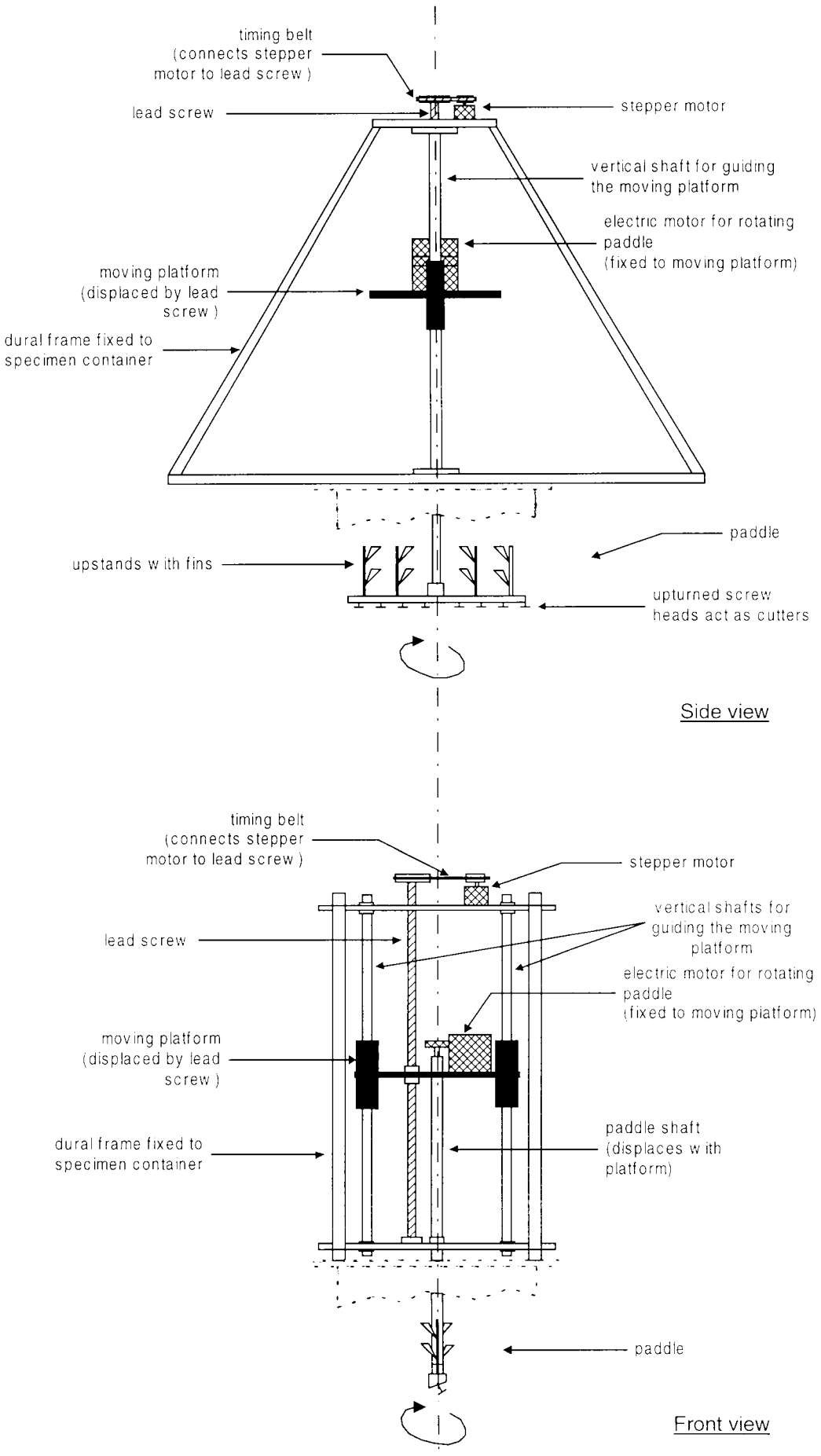

Figure 3.19 Stirrer used to fluidise sand specimens

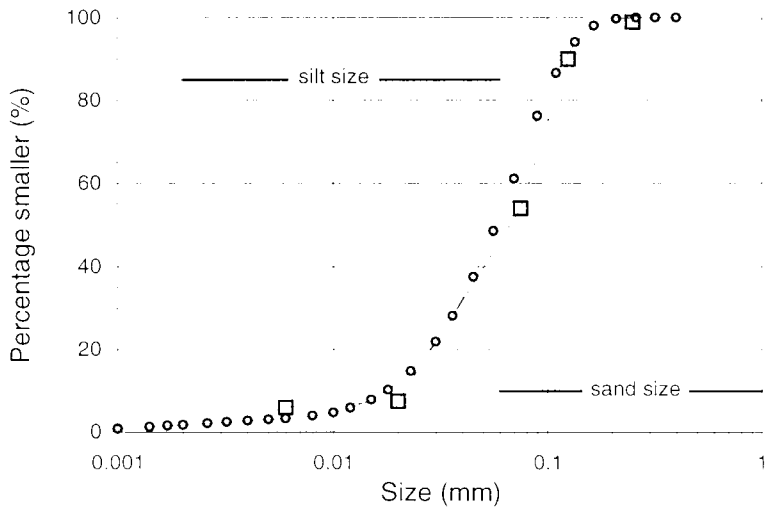

Figure 4.1
Particle size distribution of Baskarp Cyclone sand

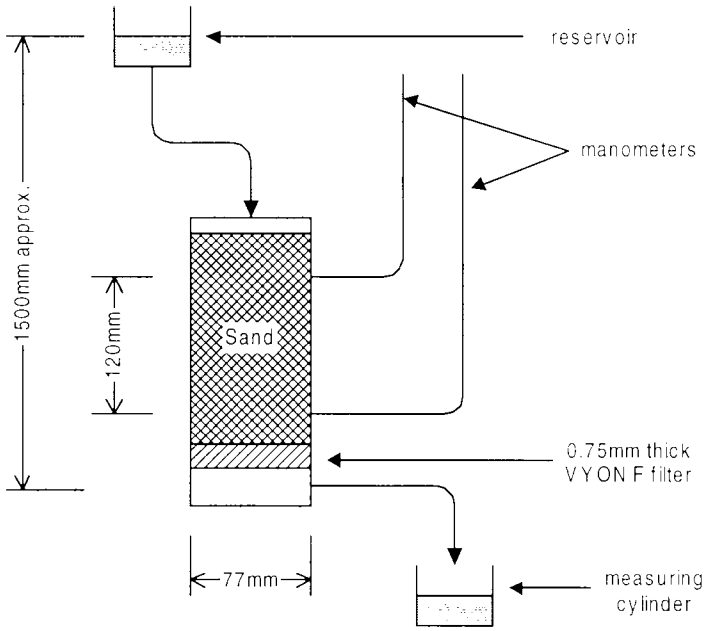

Figure 4.2
Apparatus for permeability tests

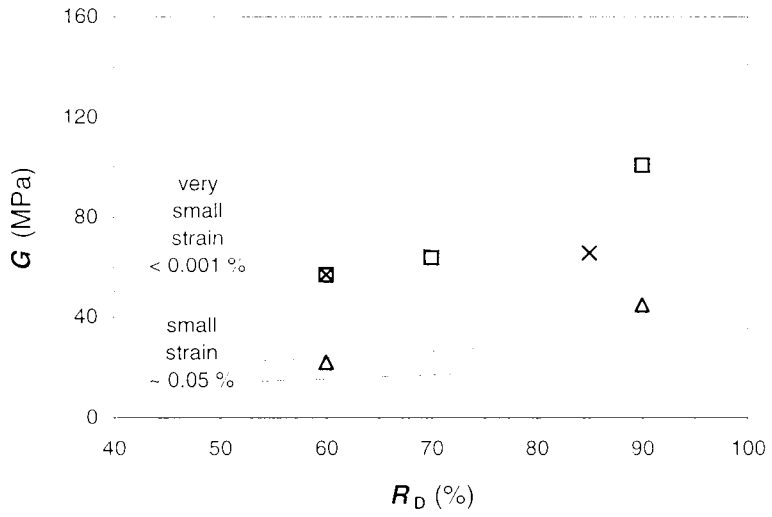

Notes:
- The theoretical values were derived from Iwasaki *et. al.* (1978), see Figure 2.2.
- Refer to Table 4.2 for details of NGI and NTH tests.

Figure 4.3 Comparison of small-strain elastic shear moduli of Baskarp Cyclone sand, derived from NGI (1994b) element tests, with values from the literature

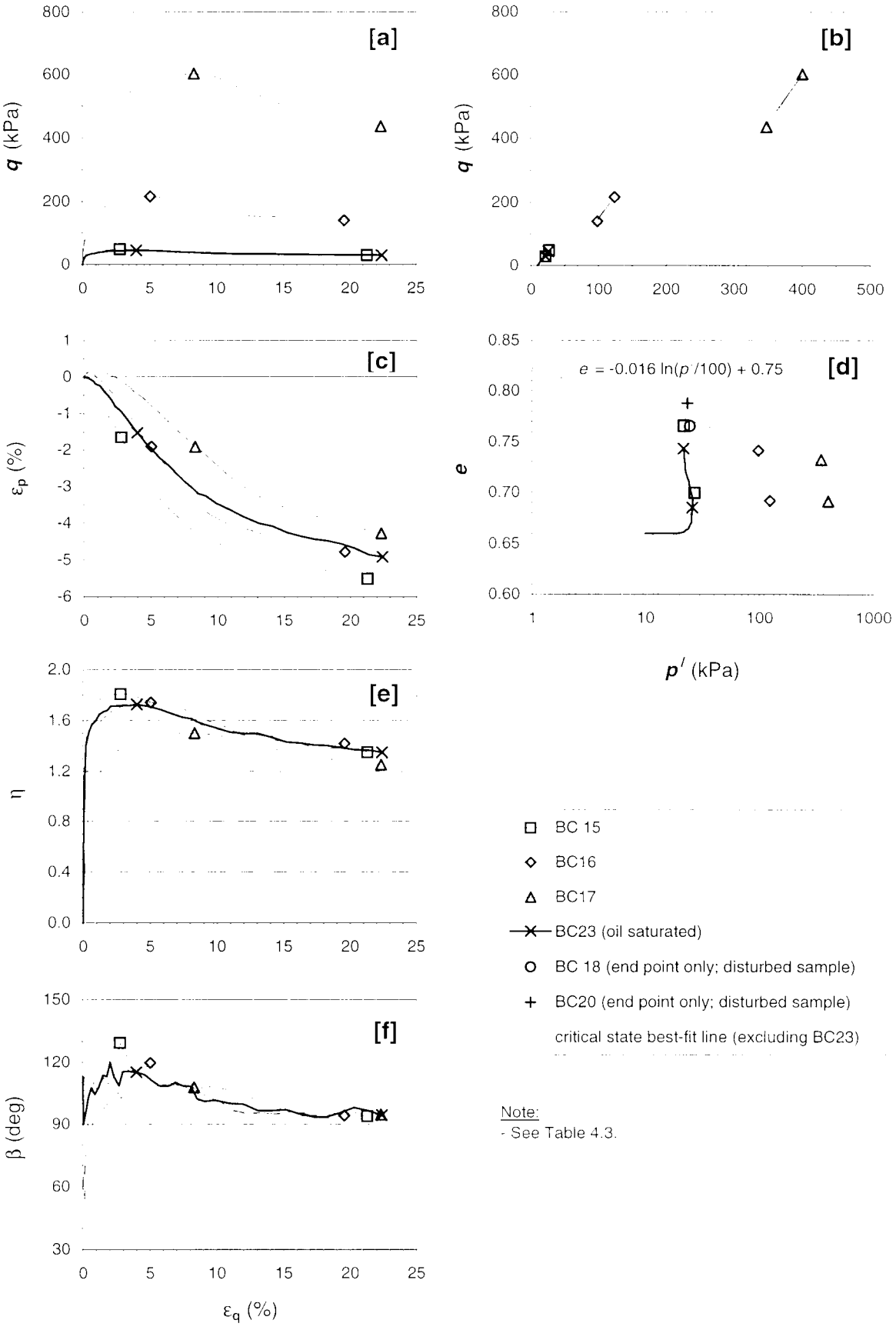

Figure 4.4 Drained triaxial tests on Baskarp Cyclone sand

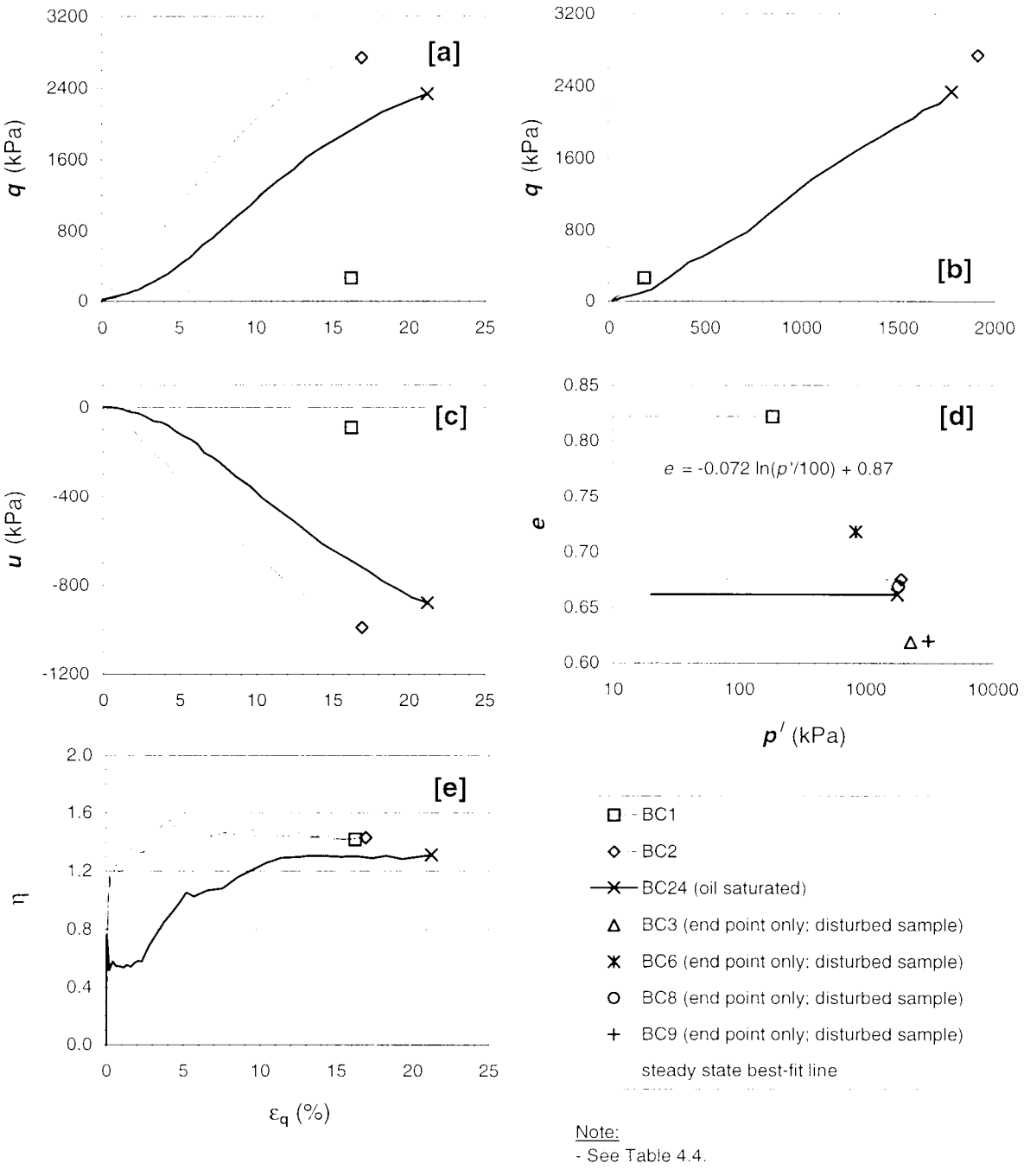

Figure 4.5 Undrained triaxial tests on Baskarp Cyclone sand

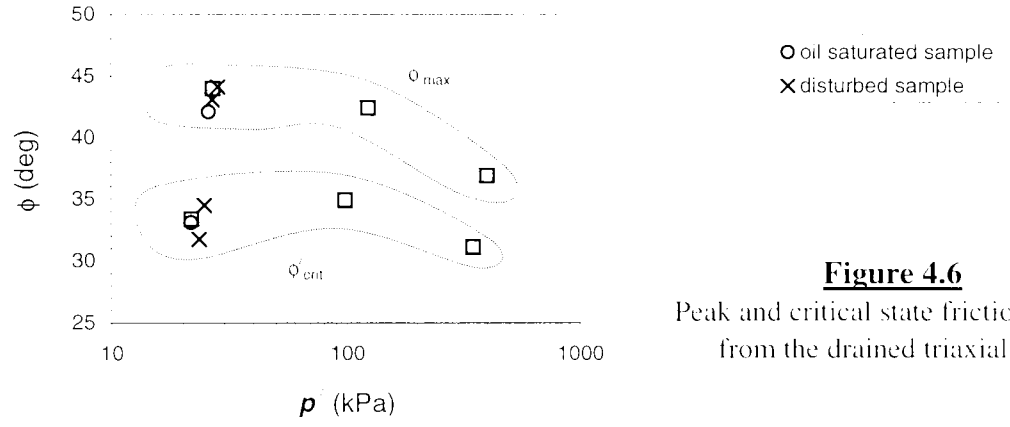

Figure 4.6
Peak and critical state friction angles from the drained triaxial tests

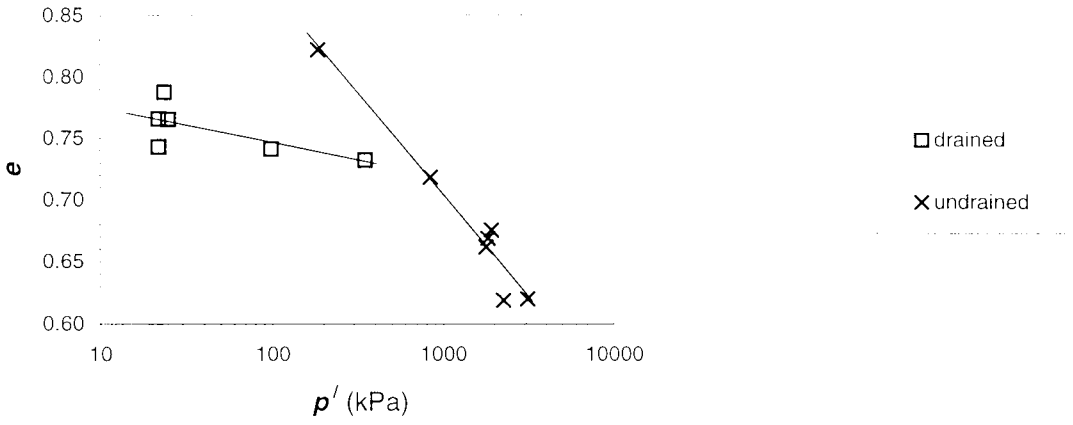

Figure 4.7 Probable drained critical state and undrained steady state lines of Baskarp Cyclone sand

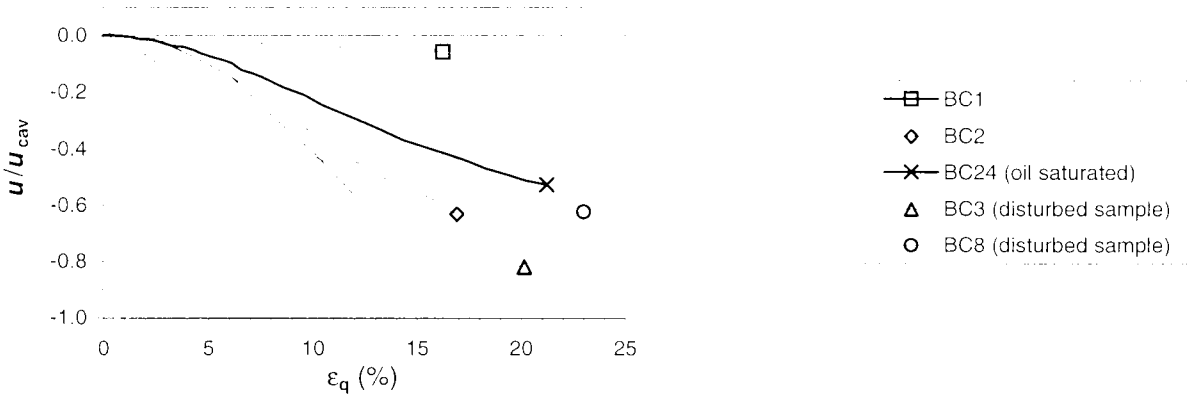

Figure 4.8 Pore pressure normalised by cavitation increment

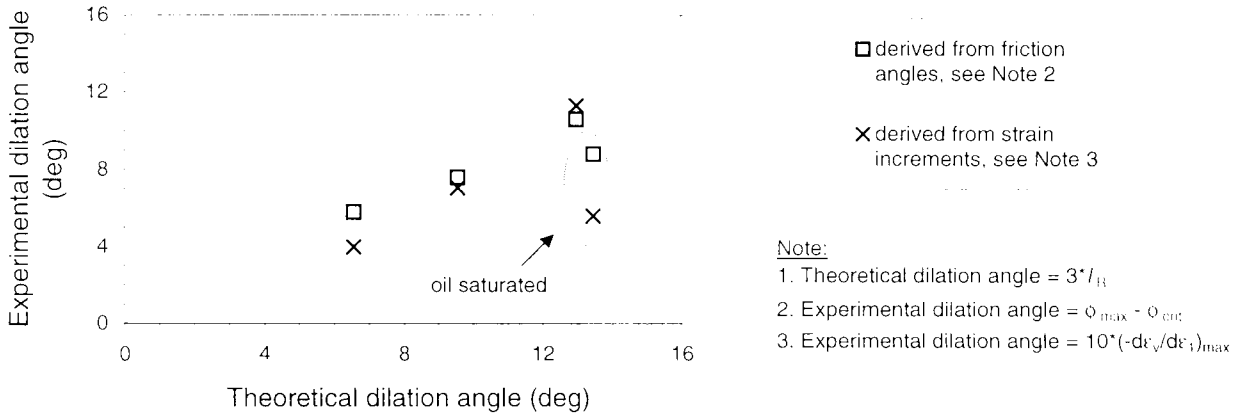

Figure 4.9 Comparison of maximum theoretical and experimental dilation angles of Baskarp Cyclone sand

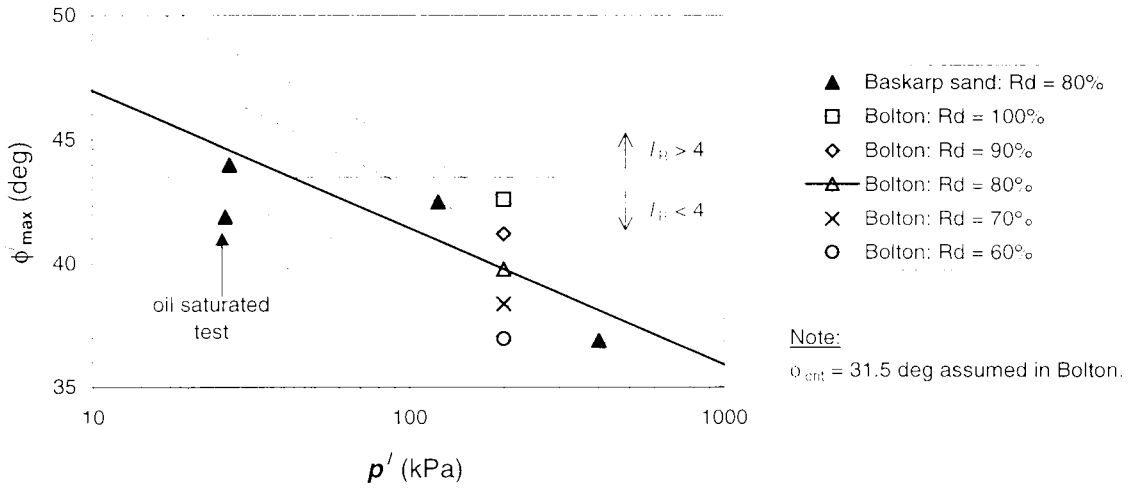

Figure 4.10 Comparison of triaxial test results of Baskarp Cyclone sand with predictions using Bolton's method

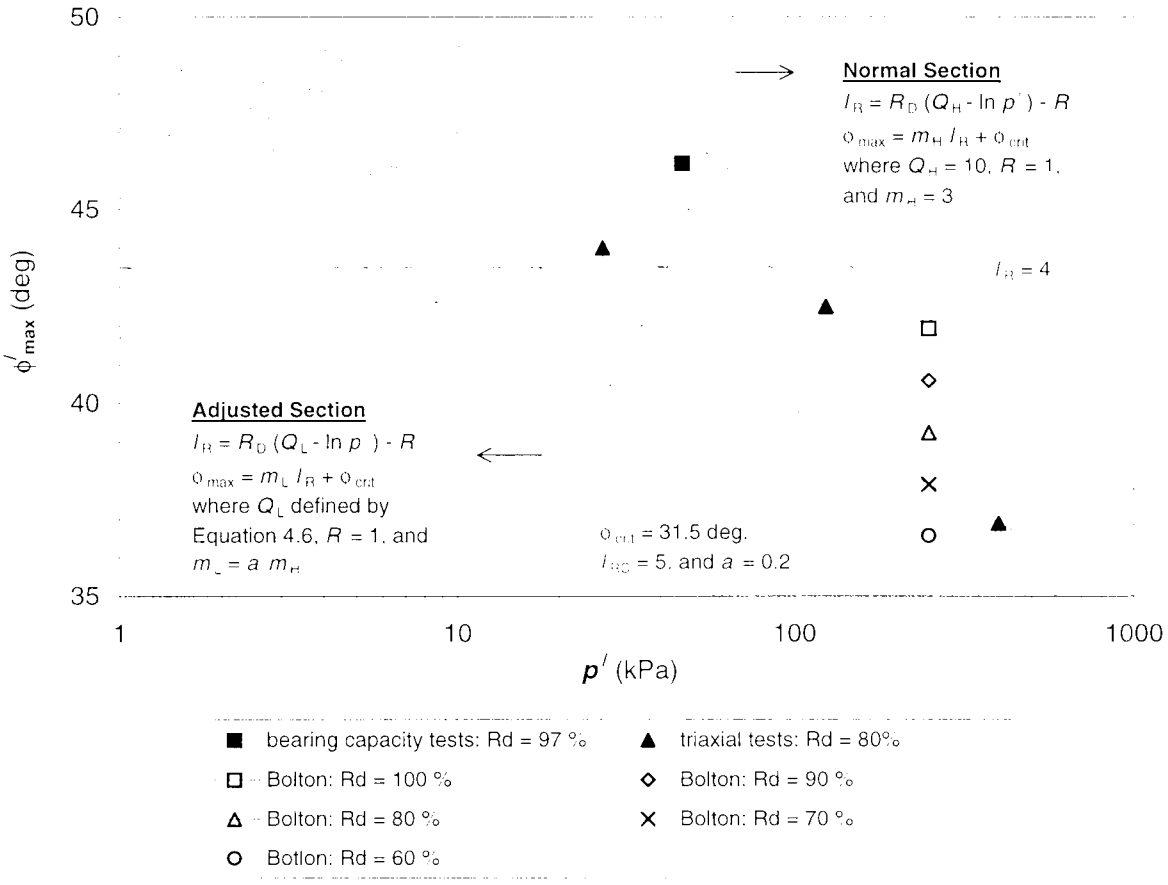

Note:
- The bearing capacity tests were performed by Byrne and Houlsby (1999), see Section 2.3.1 and Figure 2.4. The friction angle of the tests was derived from the ϕ:N_q relationship of Bolton and Lau (1993).

Figure 4.11 Bolton's (1986) R_D:p':ϕ'_{max} relationship with low stress adjustment

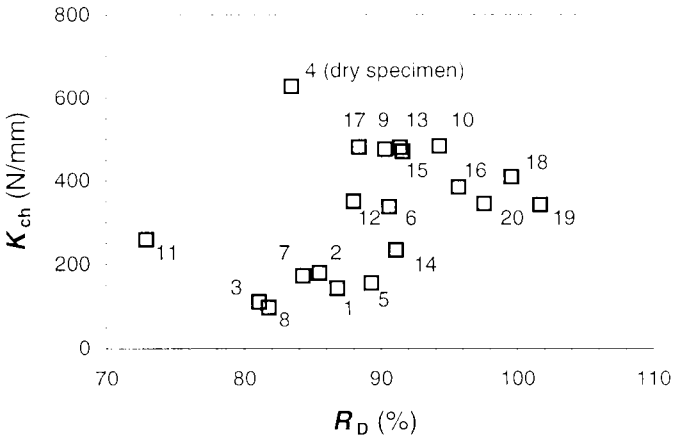

Figure 4.12
Distribution of the footing tests in terms of the characterisation stiffness and the bulk relative density of the samples

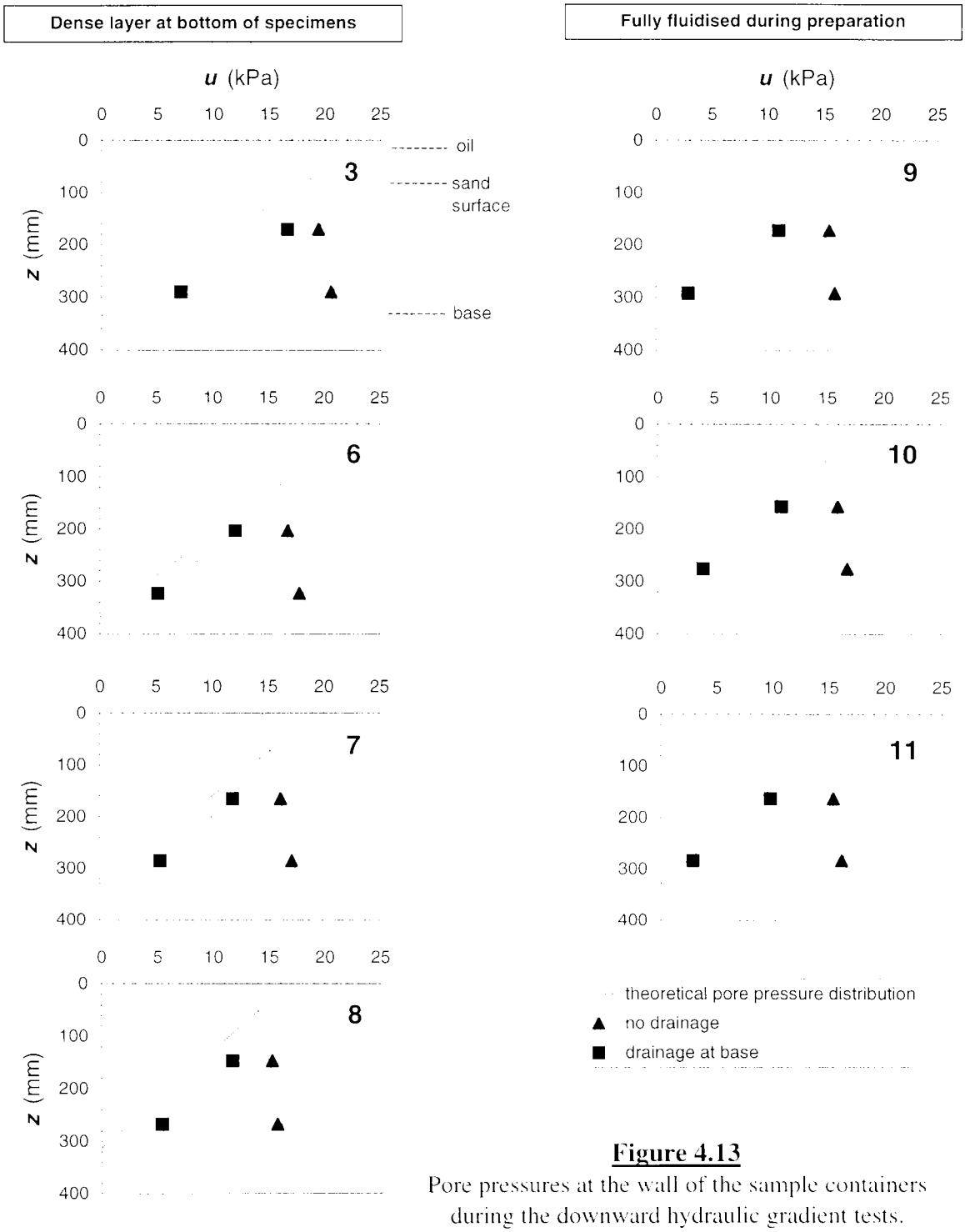

Figure 4.13
Pore pressures at the wall of the sample containers during the downward hydraulic gradient tests.

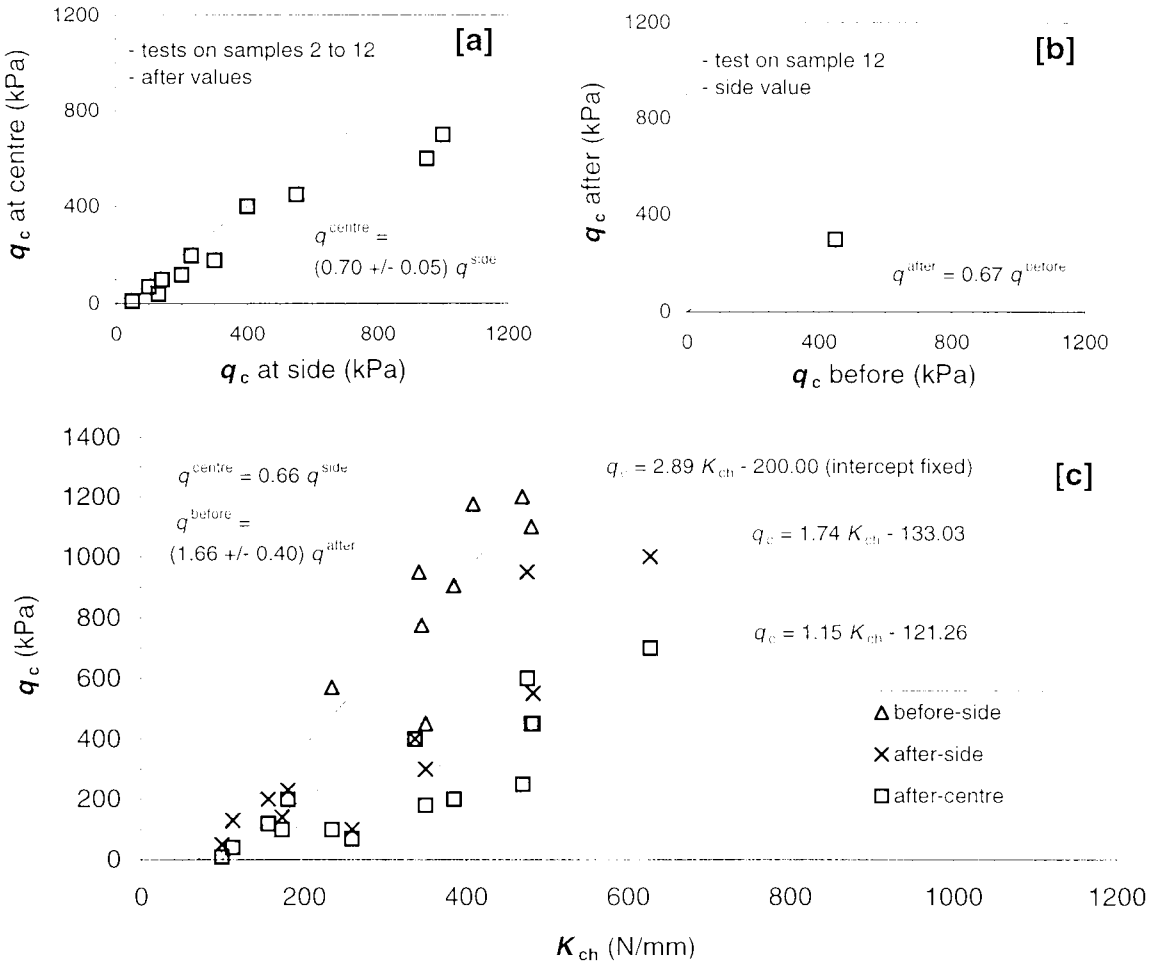

Note:
- Results from tests performed on sample 13 excluded.
- See Table 4.6.

Figure 4.14 Correlation between the different types of cone penetrometer test: **[a]** tests performed at the centre of the samples versus those at the side; **[b]** tests performed after the footing tests versus those before; and **[c]** the three different types of q_c result plotted against the characterisation stiffness

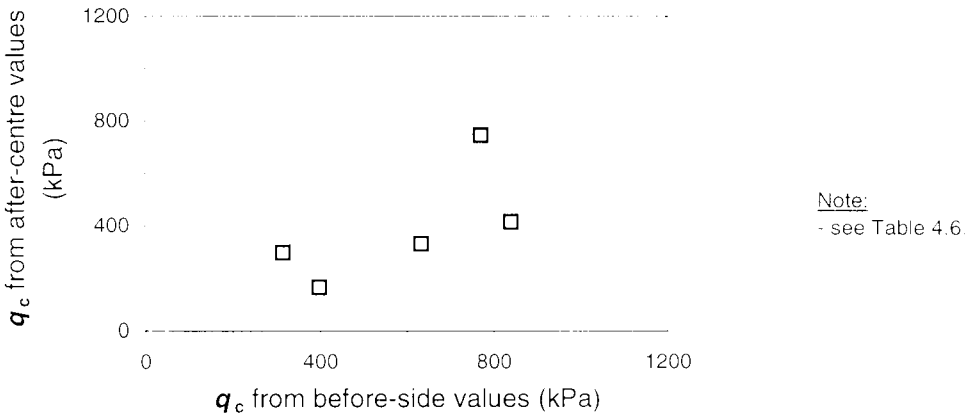

Figure 4.15 Comparison of before-centre q_c values calculated from two different sets of measured values, from tests on samples 12 and 14 to 17

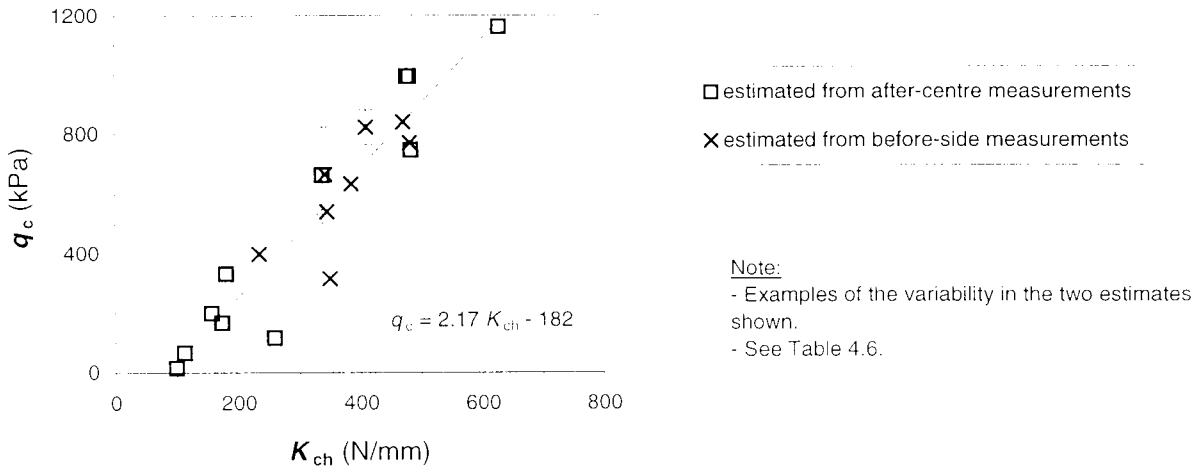

Figure 4.16 Estimated before-centre q_c values

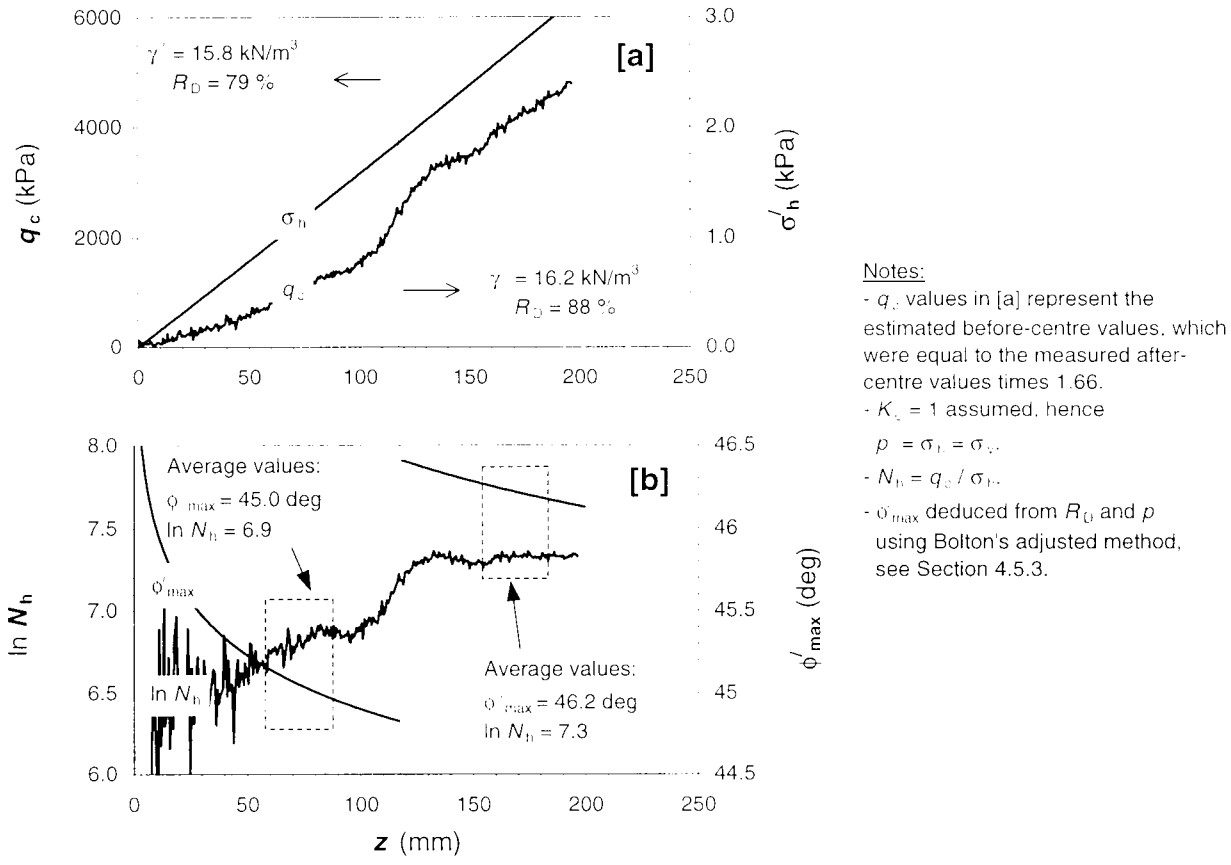

Figure 4.17 Cone penetrometer results from CP04C, *i.e.* test at centre of sample T204:
[a] cone tip resistance and effective horizontal stress; and
[b] tip resistance factor and peak friction angle

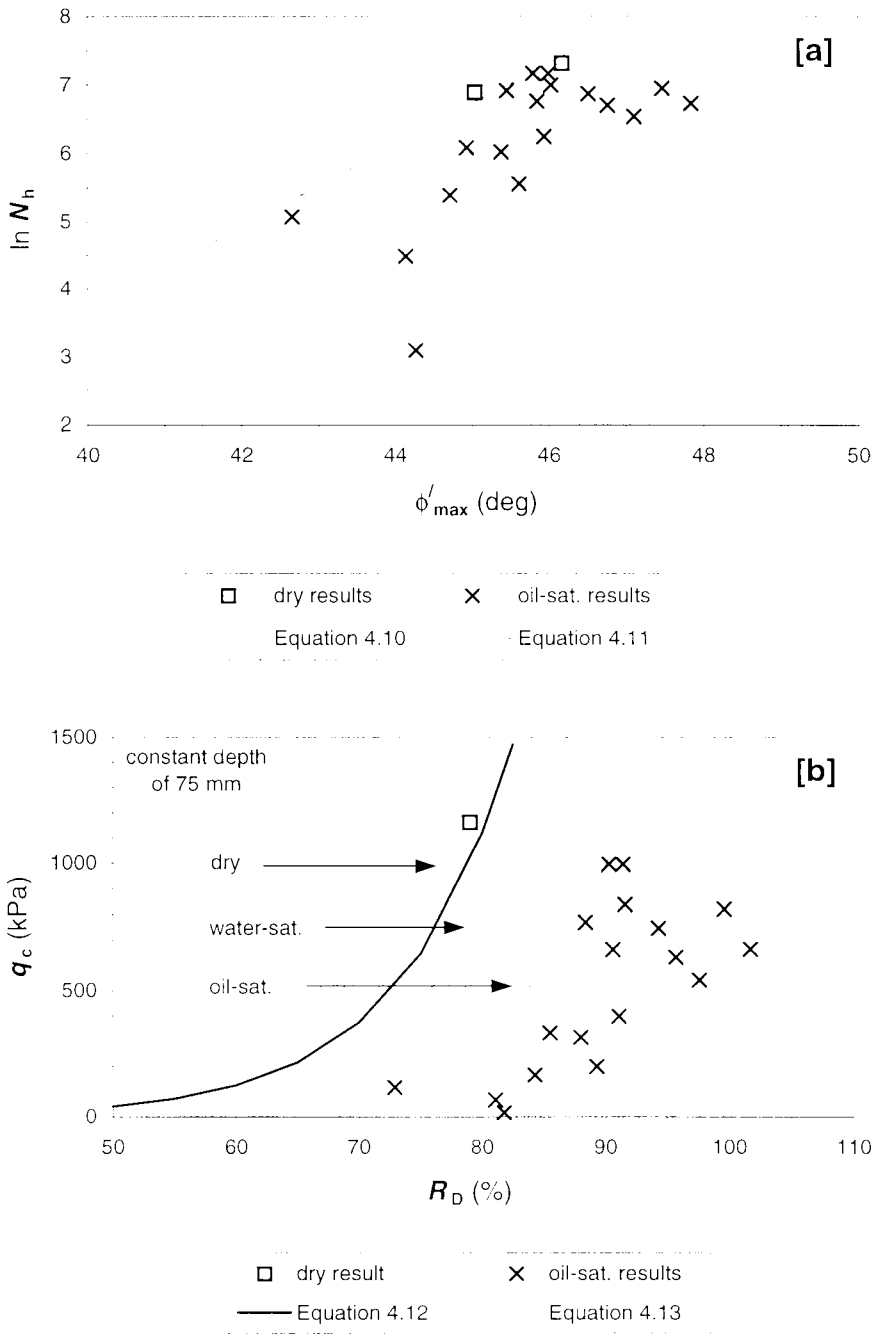

Figure 4.18 Correlation between cone penetrometer results and sand properties:
[a] cone tip resistance factor versus peak friction angle; and
[b] cone tip resistance versus relative density

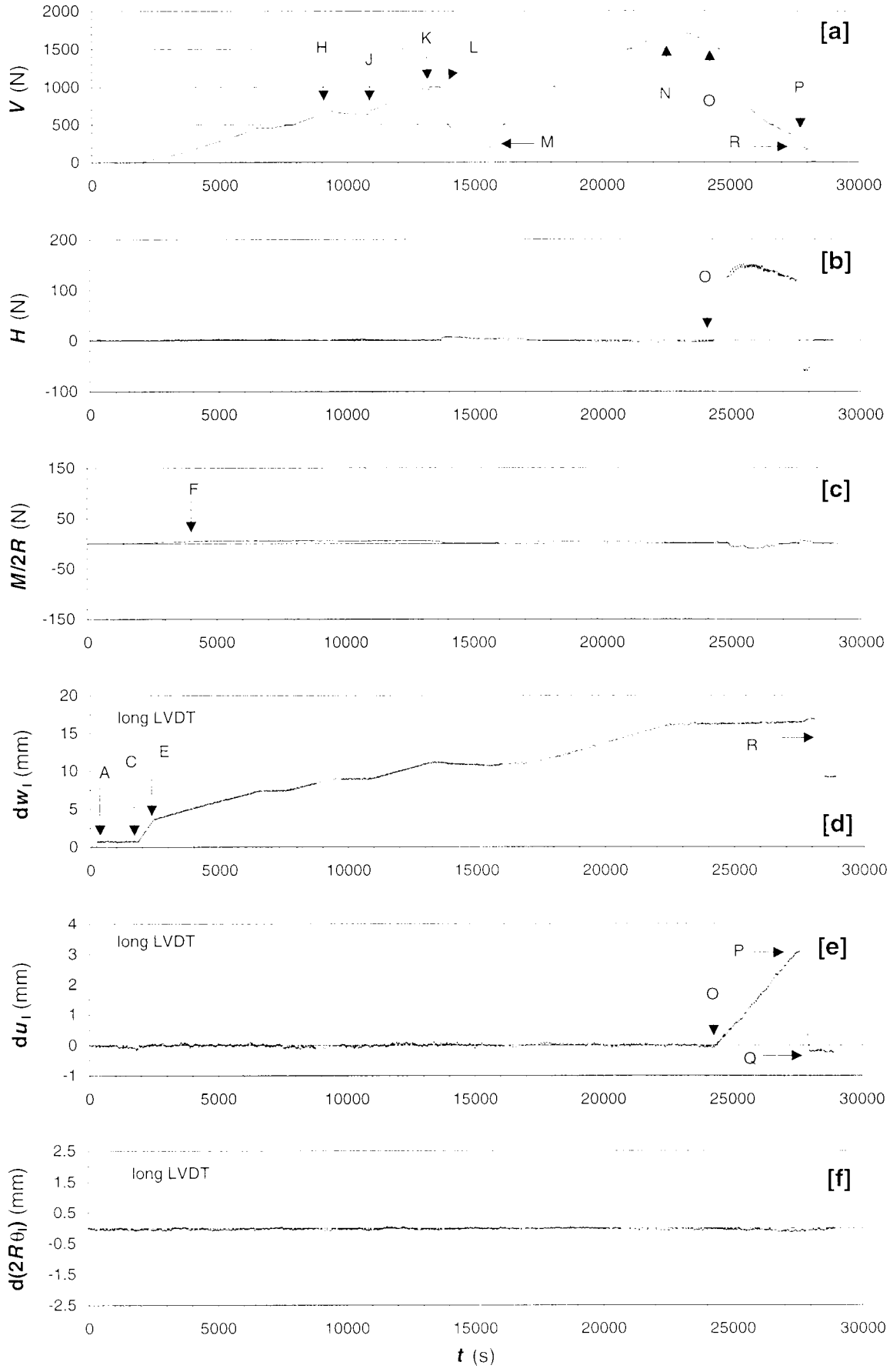

Figure 5.1 Time history of test T101

(continued on next page)

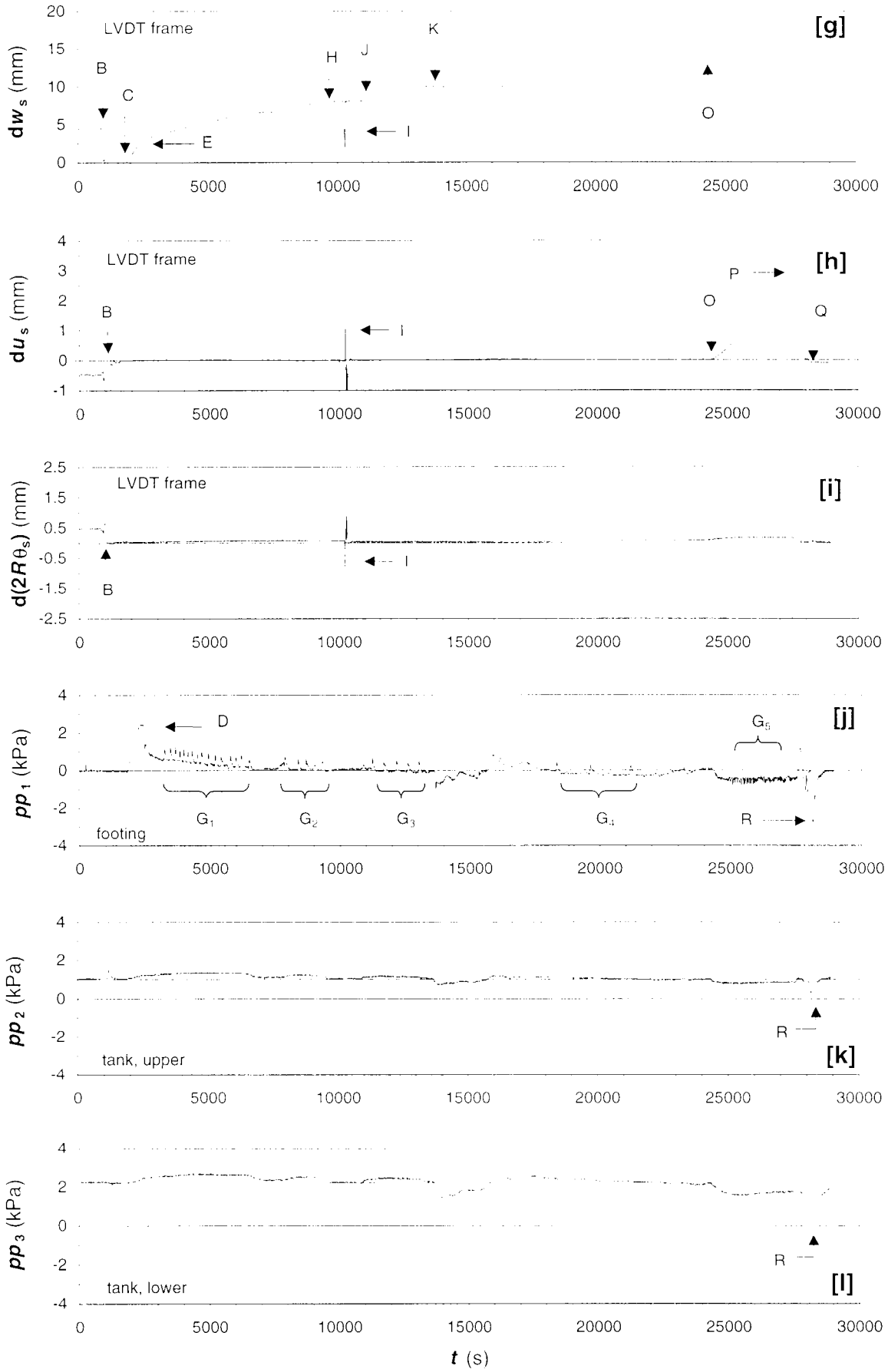

Figure 5.1 (cont.) Time history of test T101

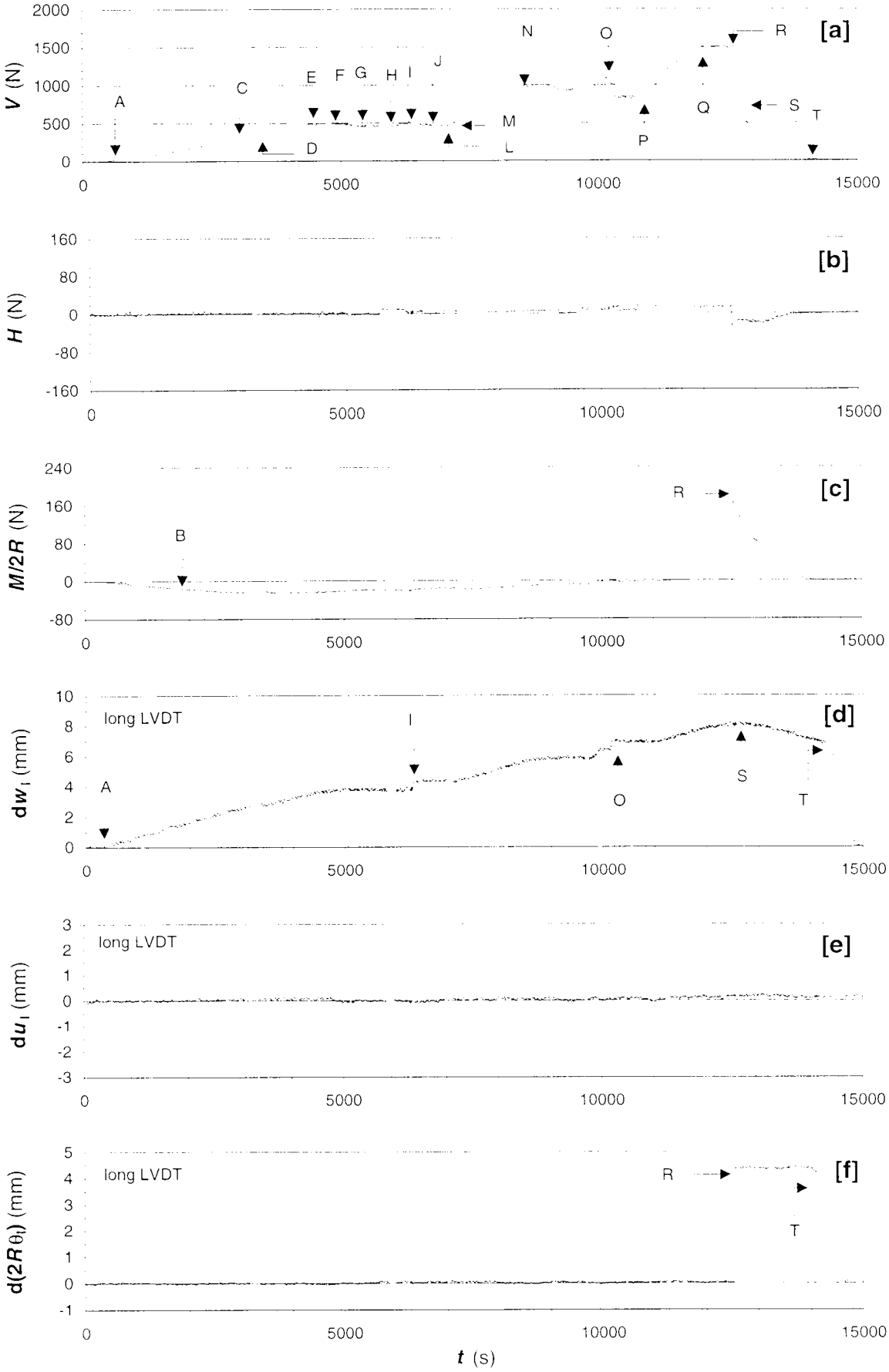

Figure 5.2 Time history of test T114

(continued on next page)

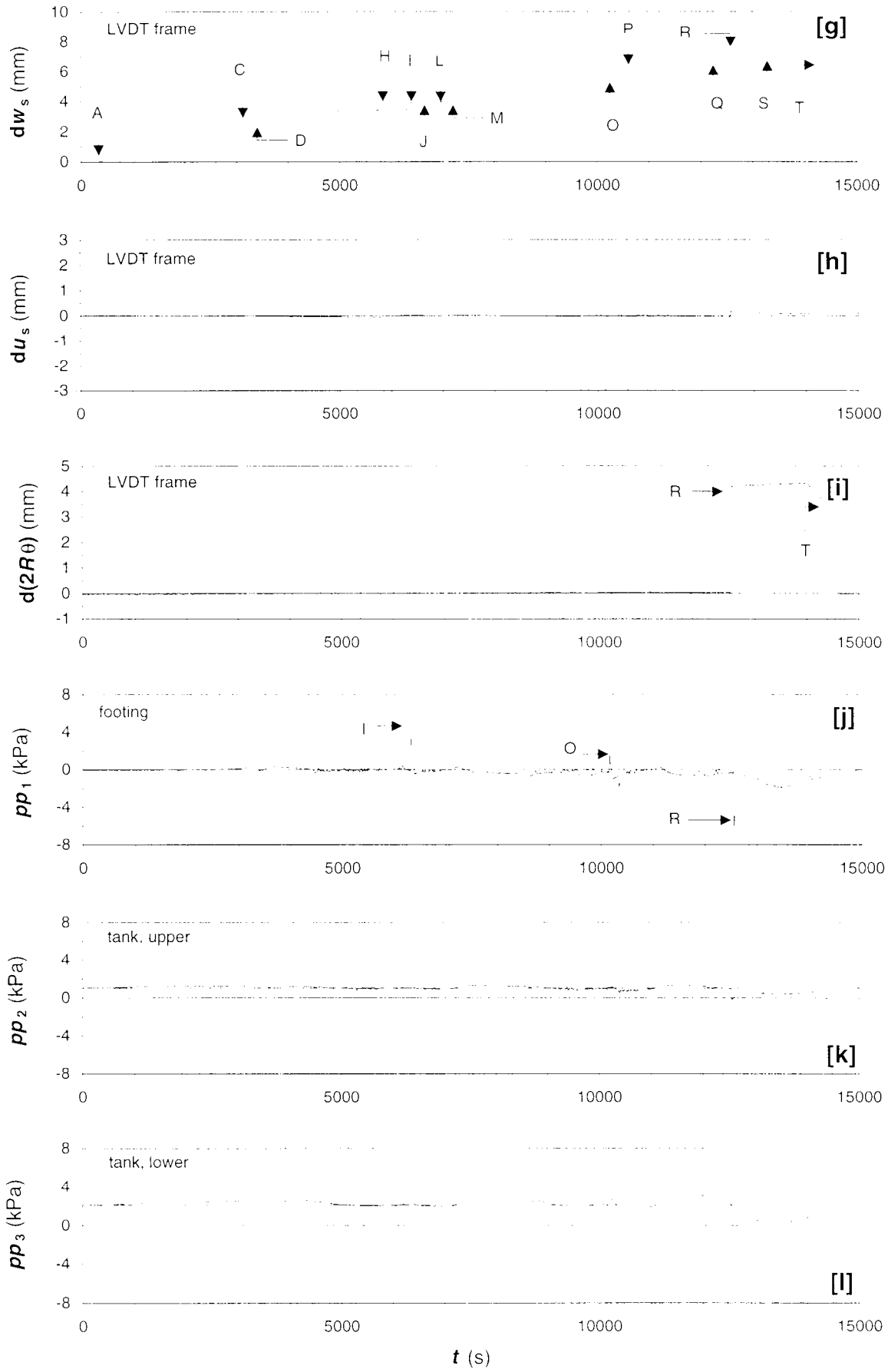

Figure 5.2 (cont.) Time history of test T114

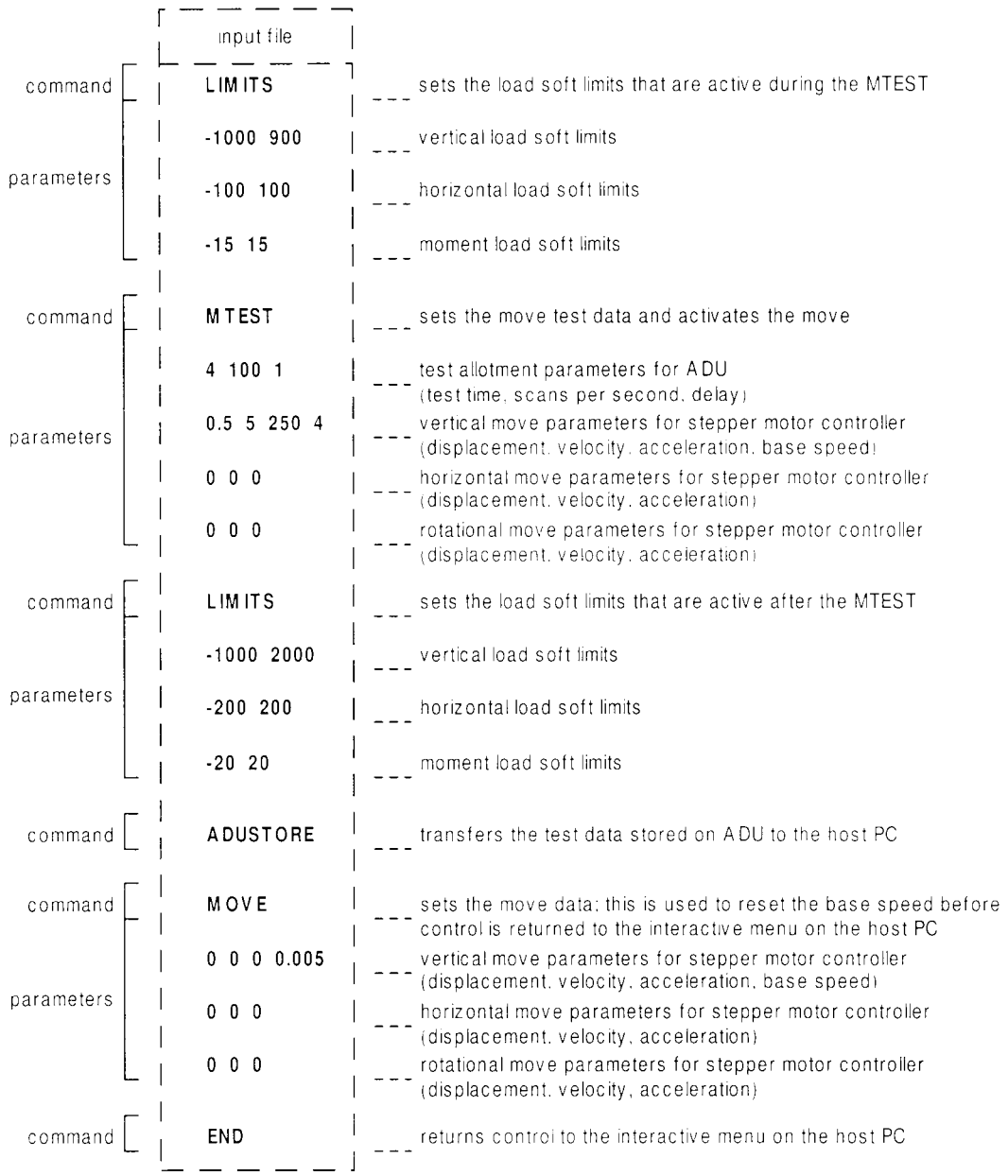

Figure 5.3 Input file T114_A.INP

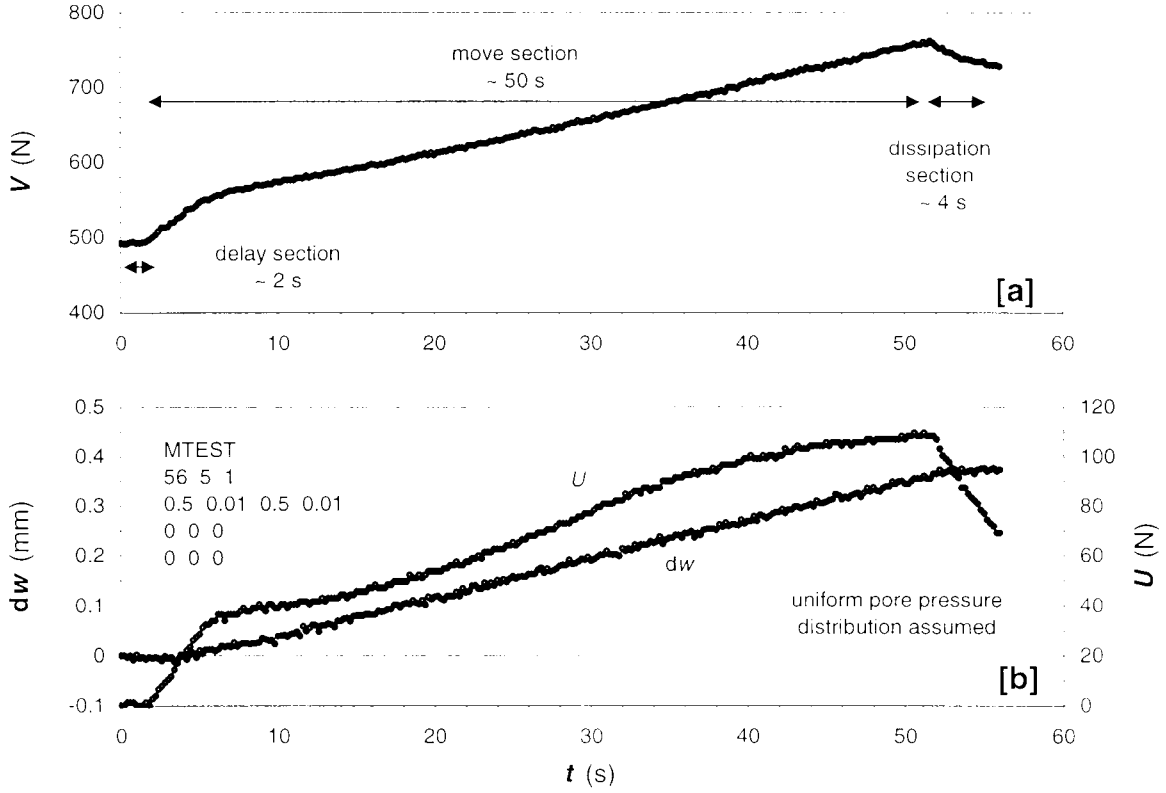

Figure 5.4 Time history of a slow vertical partially-drained test (T317_1, dw/dt = 0.01 mm/s)

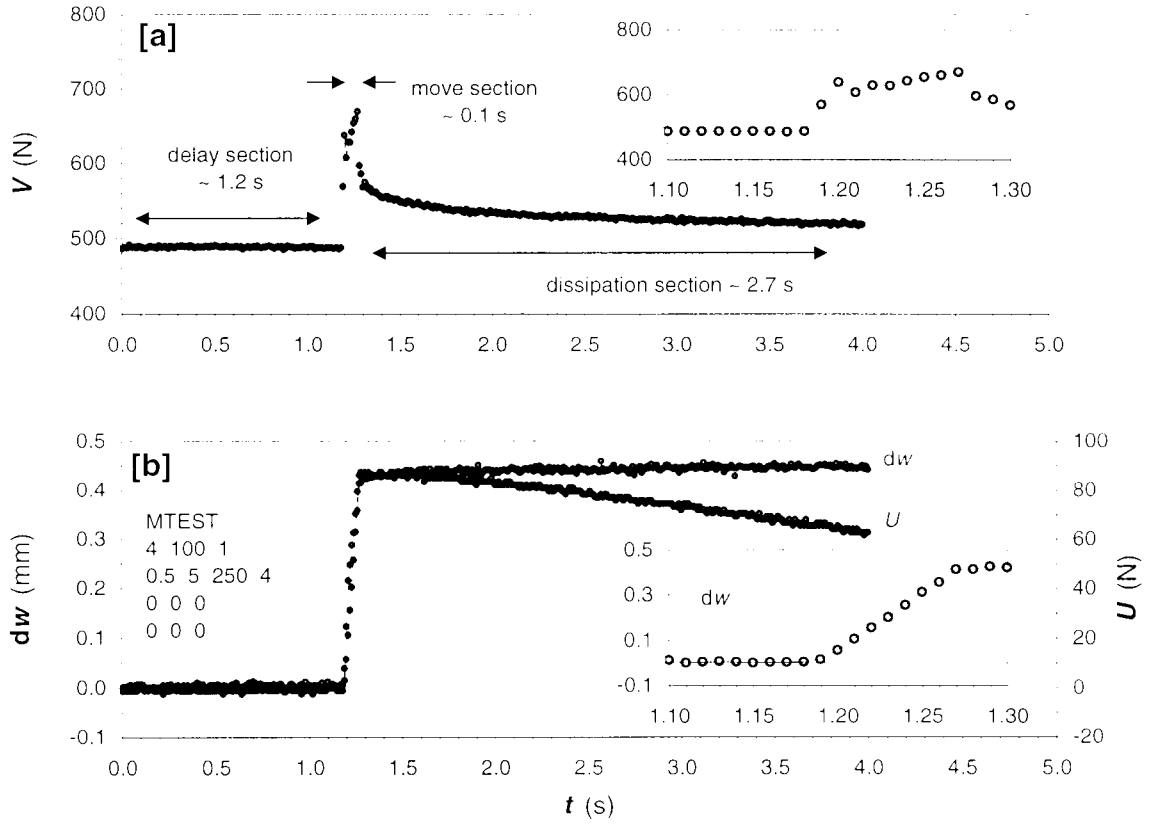

Figure 5.5 Time history of a fast vertical partially-drained test (T114B_1, dw/dt = 5 mm/s)

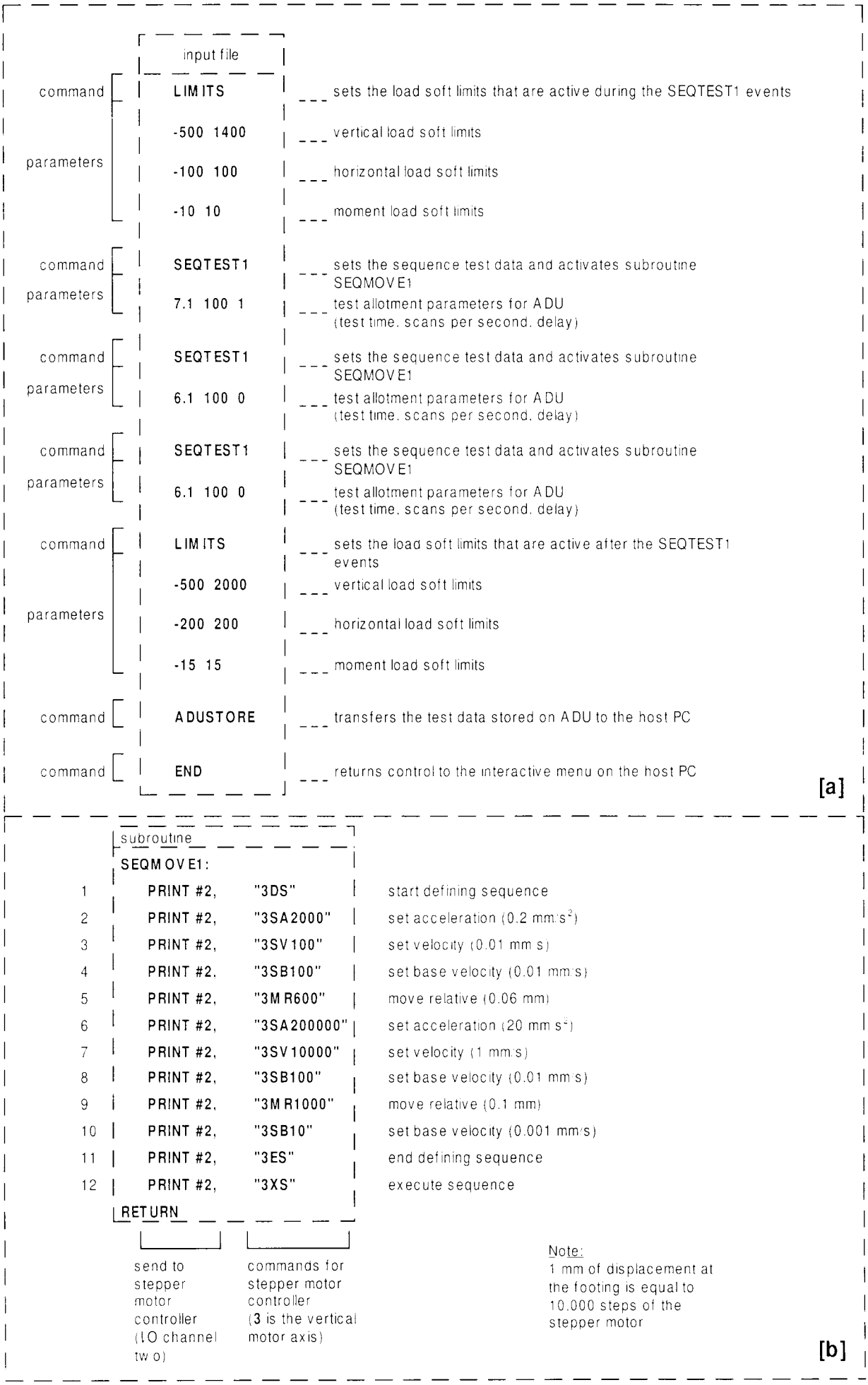

Figure 5.6 Control of multi-rate vertical partially-drained tests: [a] input file T120_A.INP; and [b] subroutine SEQMOVE1 in control program

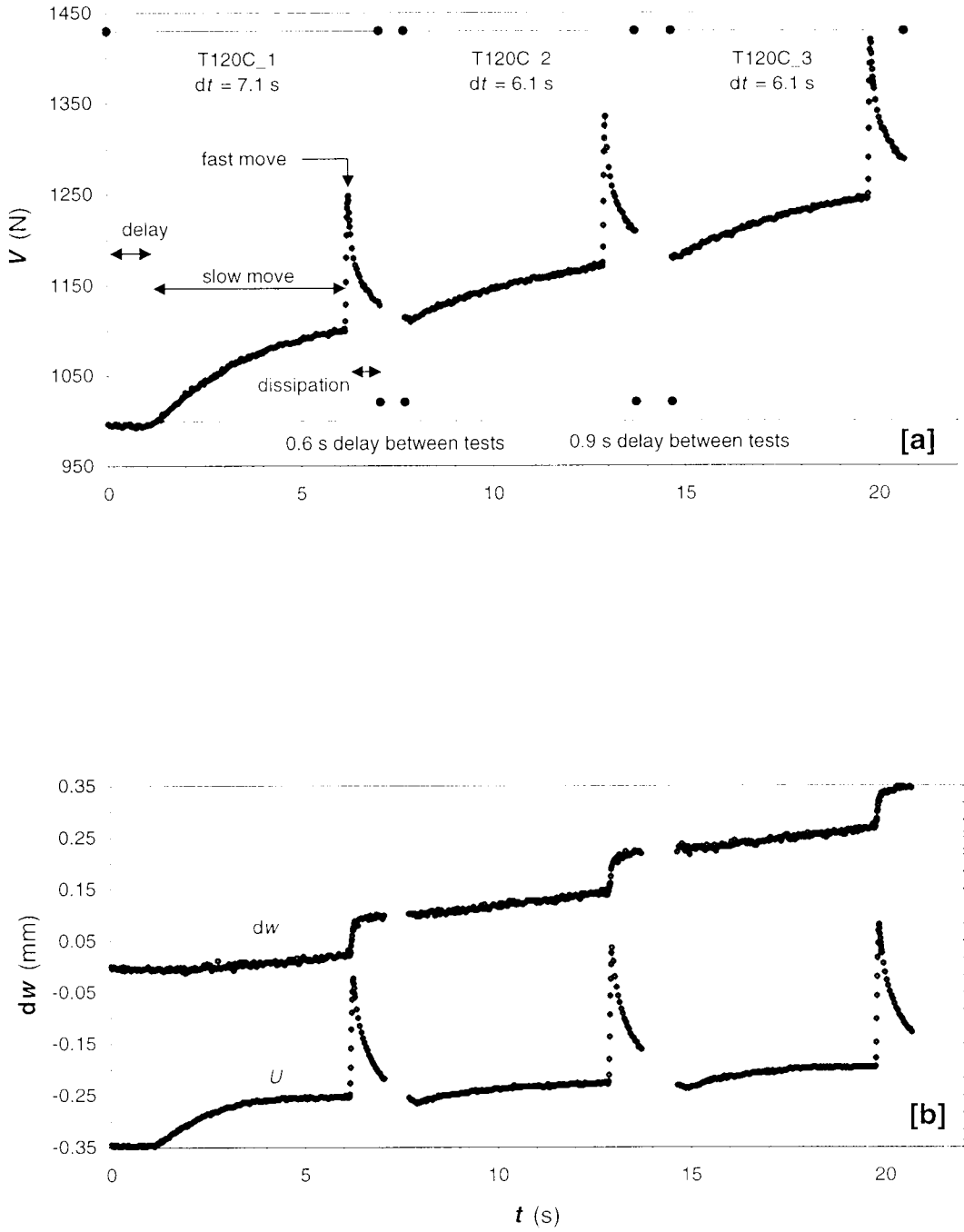

Figure 5.7 Time history of the multi-rate vertical partially-drained test from 1000 N

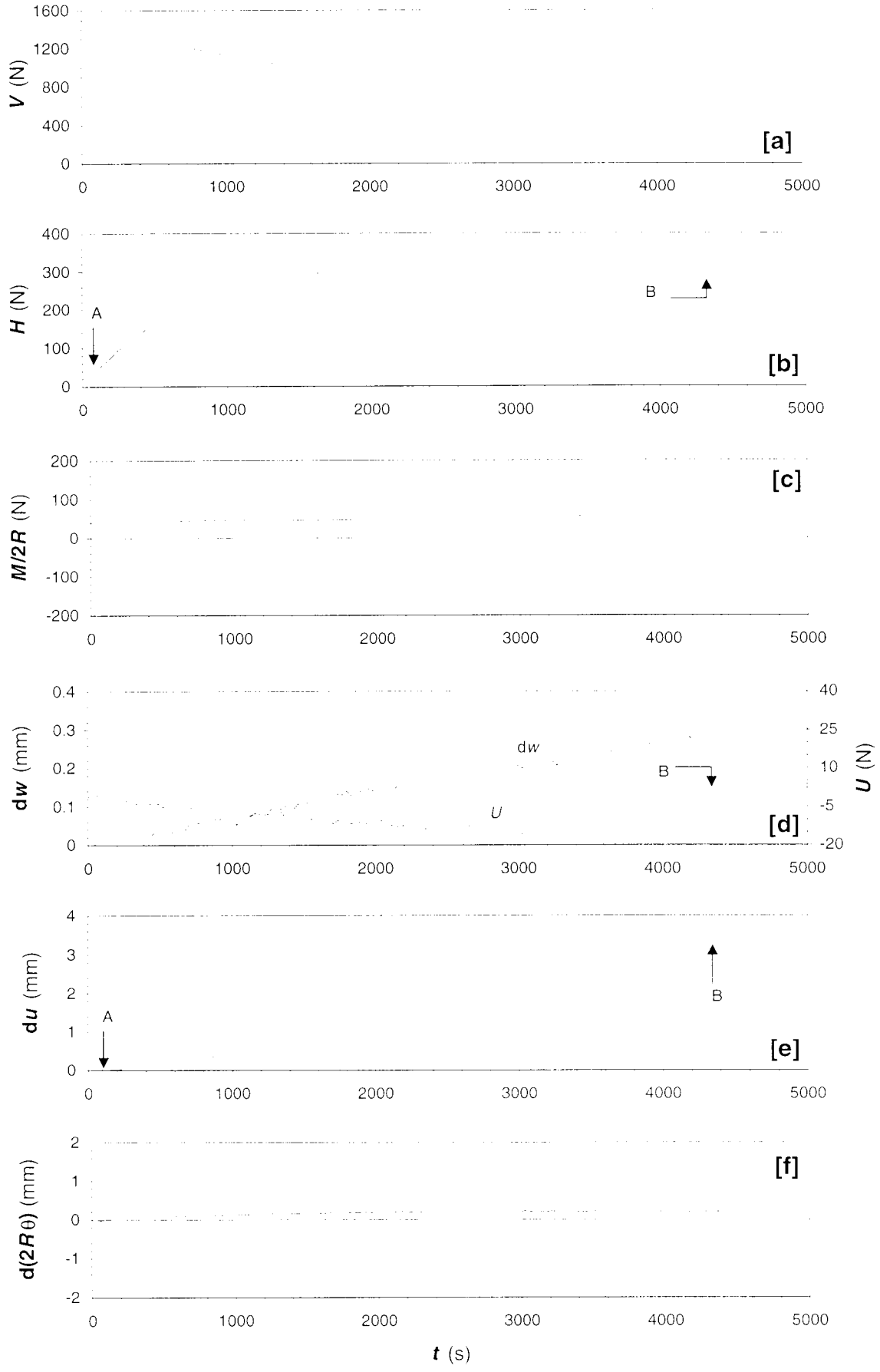

Figure 5.8 Time history of a slow horizontal sideswipe test (T309_1, $du/dt = 0.001$ mm/s)

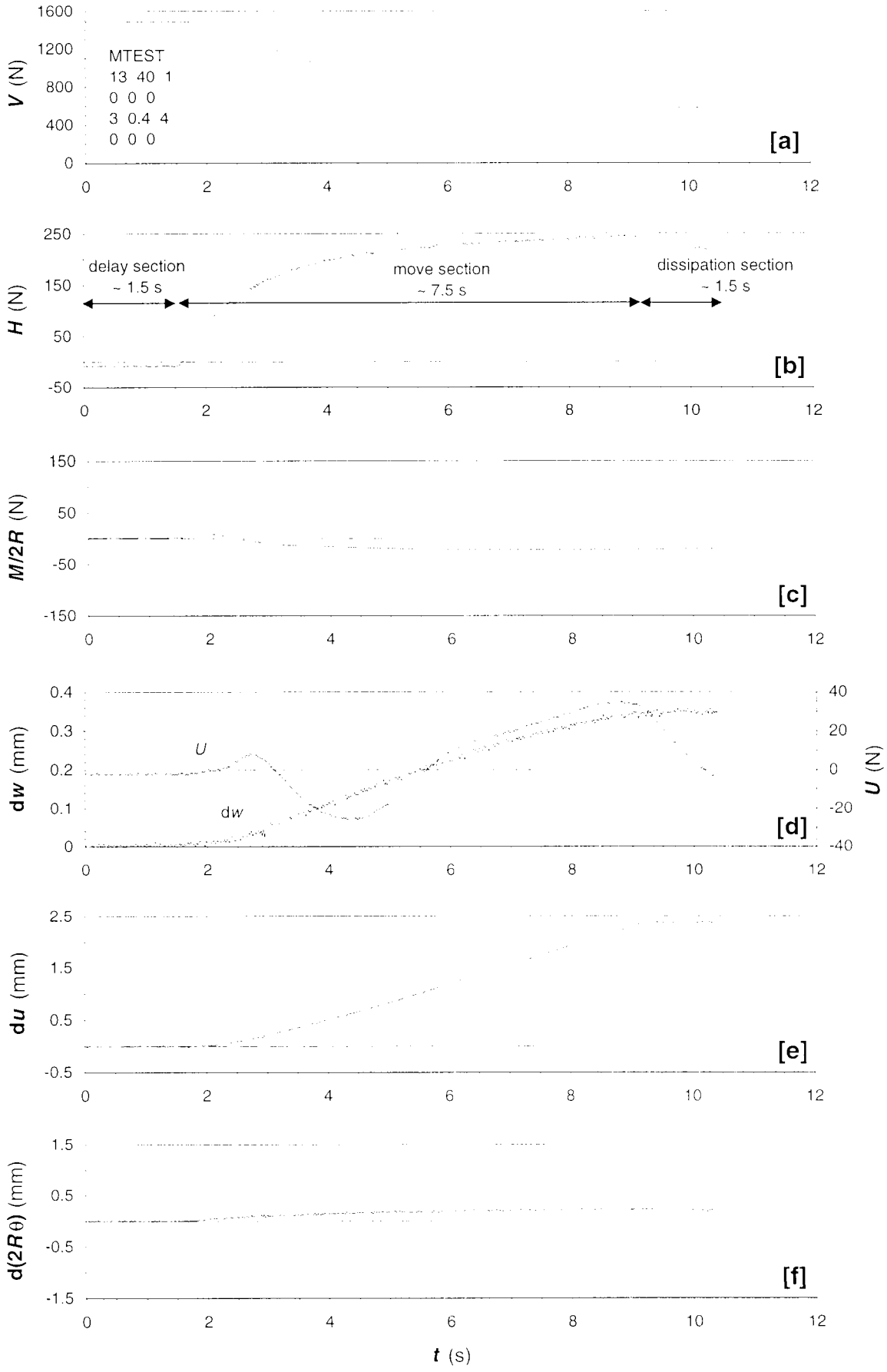

Figure 5.9 Time history of a fast horizontal sideswipe test (T107A_3, du/dt = 0.4 mm/s)

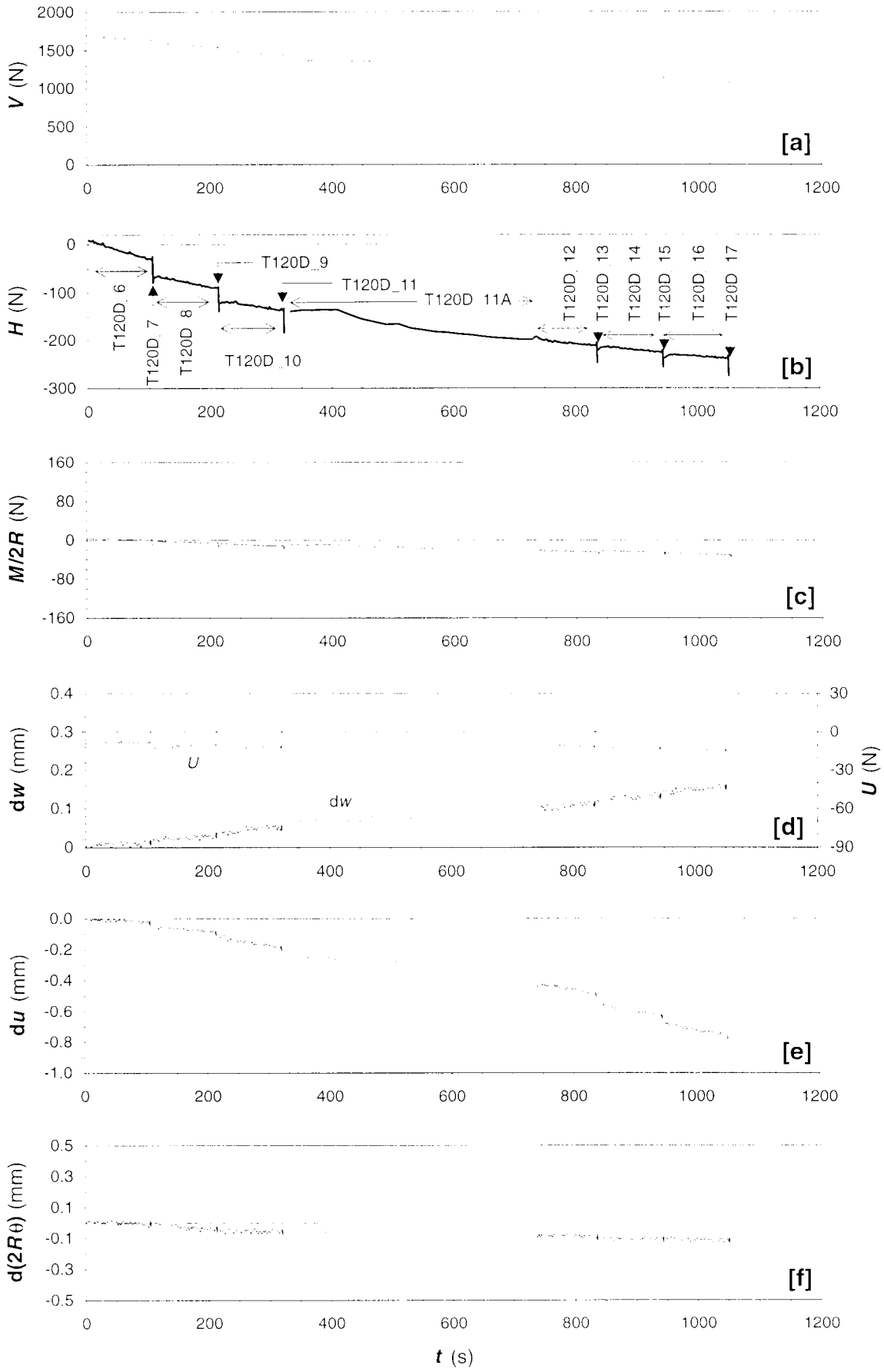

Figure 5.10 Time history of the multi-rate horizontal sideswipe test from 1700 N

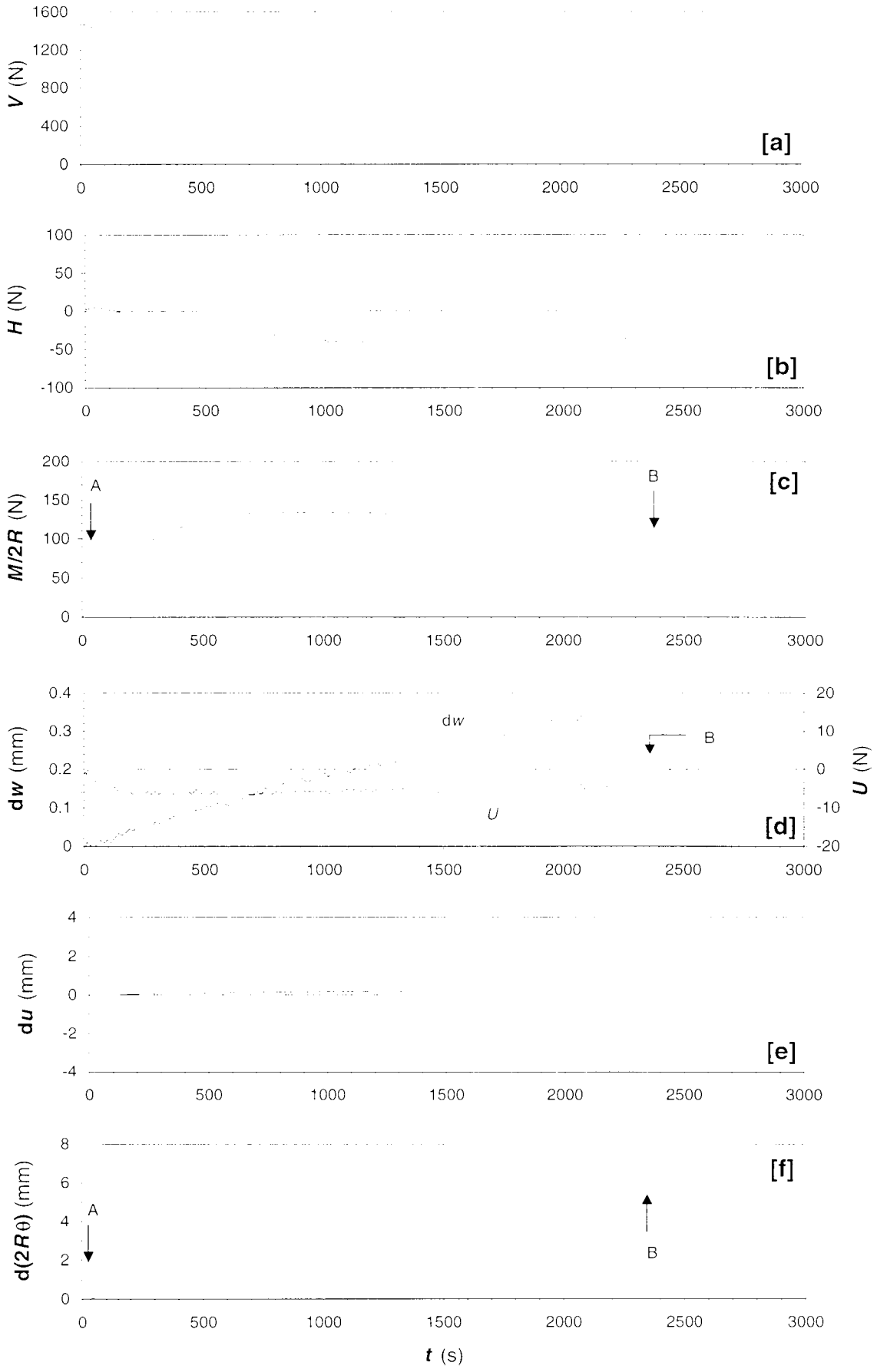

Figure 5.11 Time history of a slow moment sideswipe test
(T311_3, $d(2R\theta)/dt = 0.0026$ mm/s)

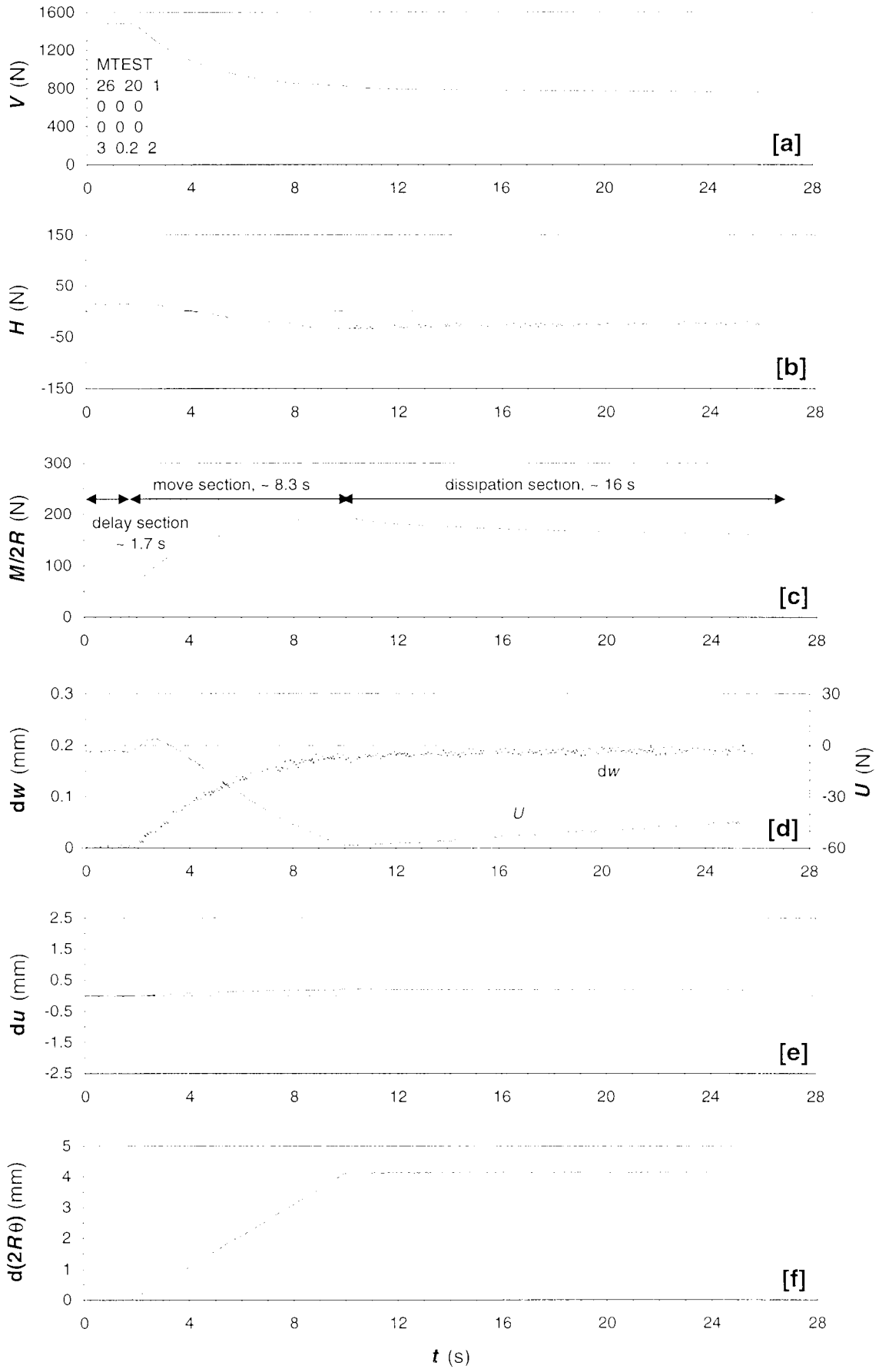

Figure 5.12 Time history of a fast moment sideswipe test (T114E_1, $d(2R\theta)/dt = 0.524$ mm/s)

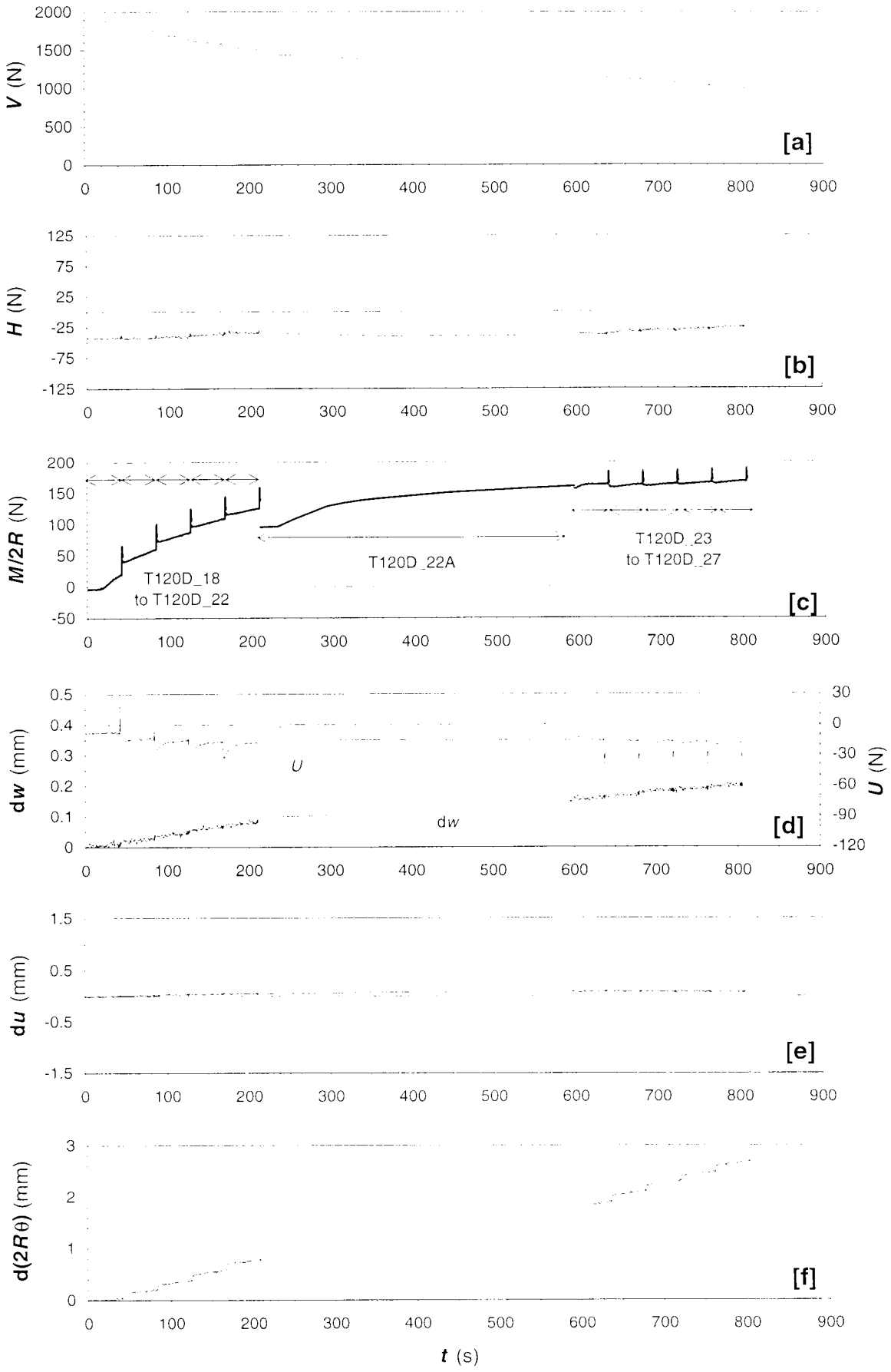

Figure 5.13 Time history of the multi-rate moment sideswipe test from 1900 N

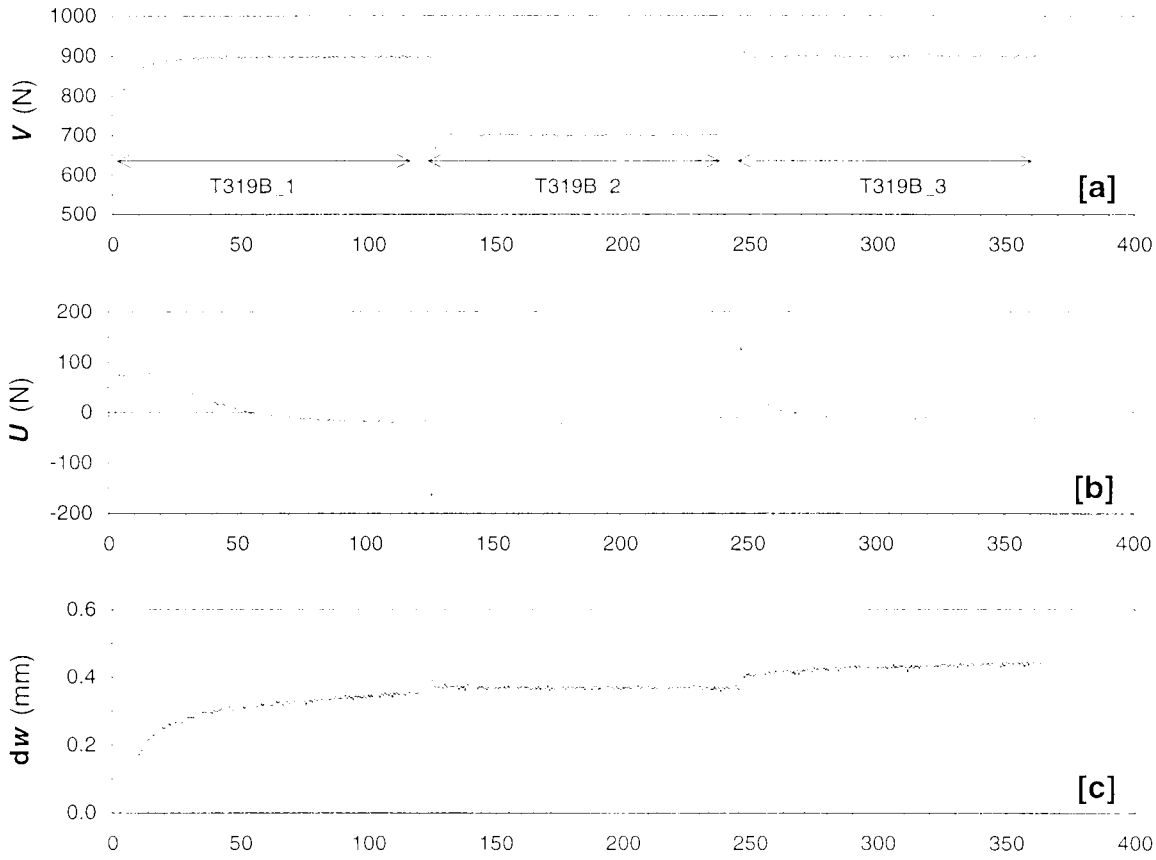

Figure 5.14 Time history of the consolidation tests in T319

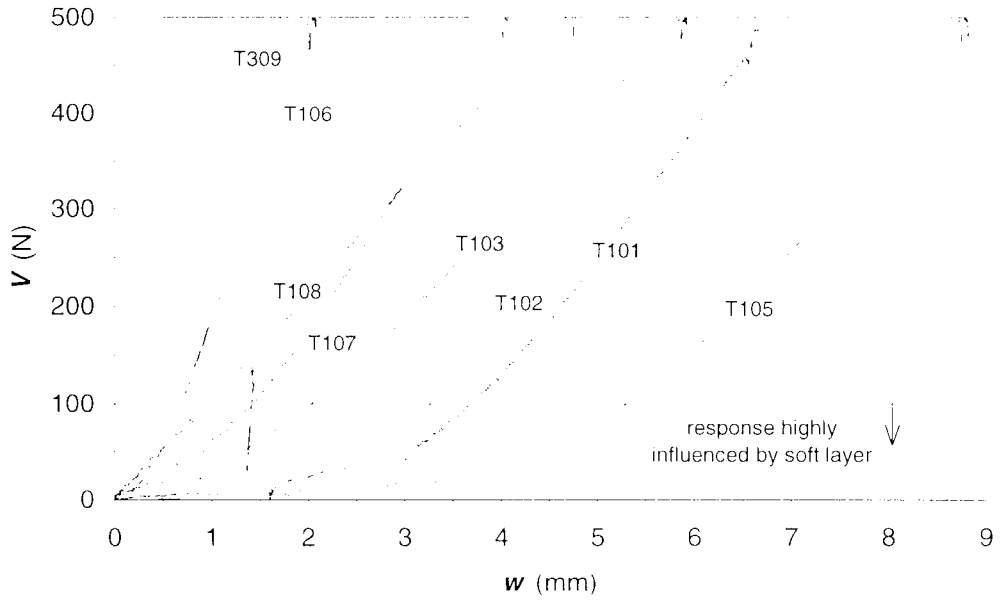

Figure 6.1 Differences in the initial load:deformation response of the footing

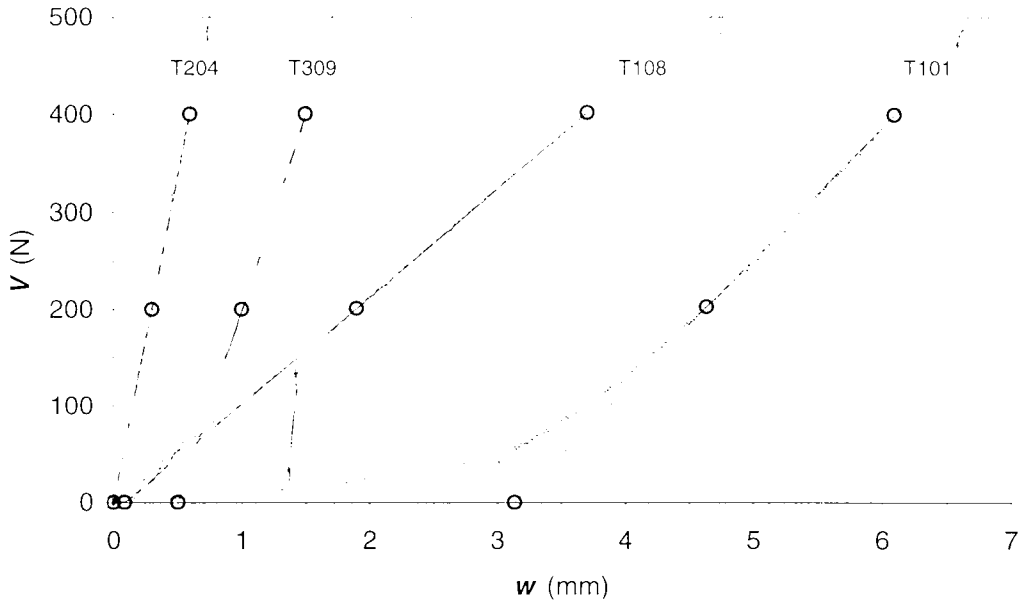

Figure 6.2 Extrapolated origin of load:deformation curves

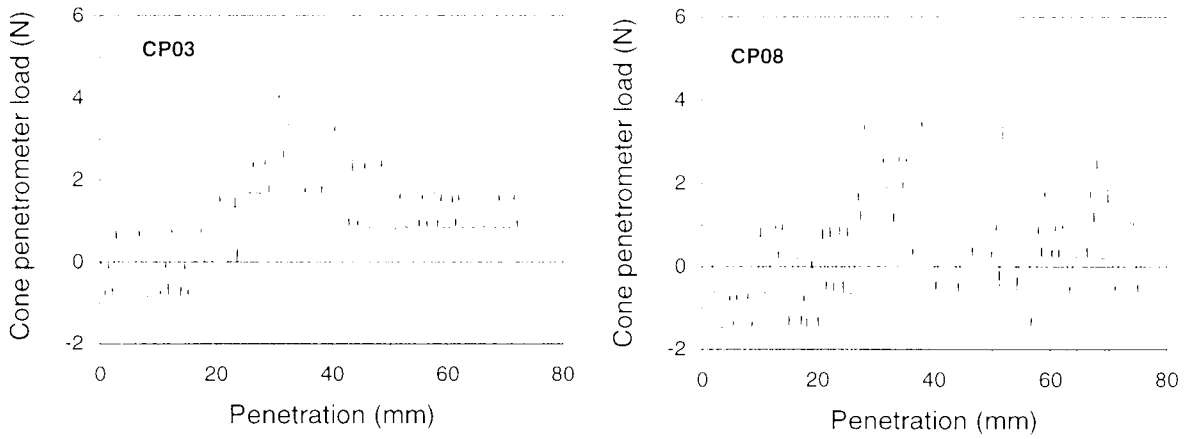

Figure 6.3 Cone penetration tests at the centre of samples T103 and T108

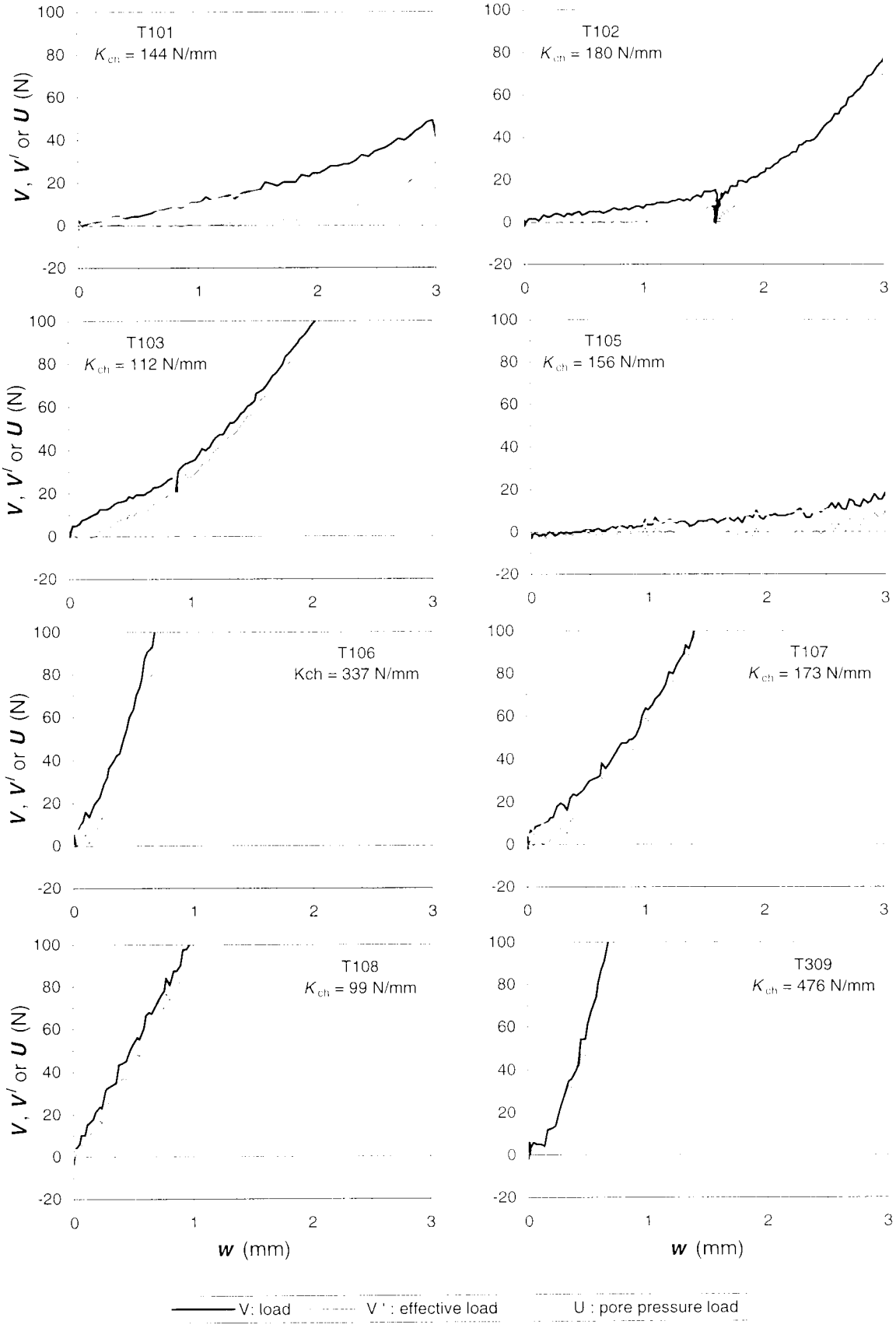

Figure 6.4 Effect of loose layer of soil and pore pressures on initial load:deformation response

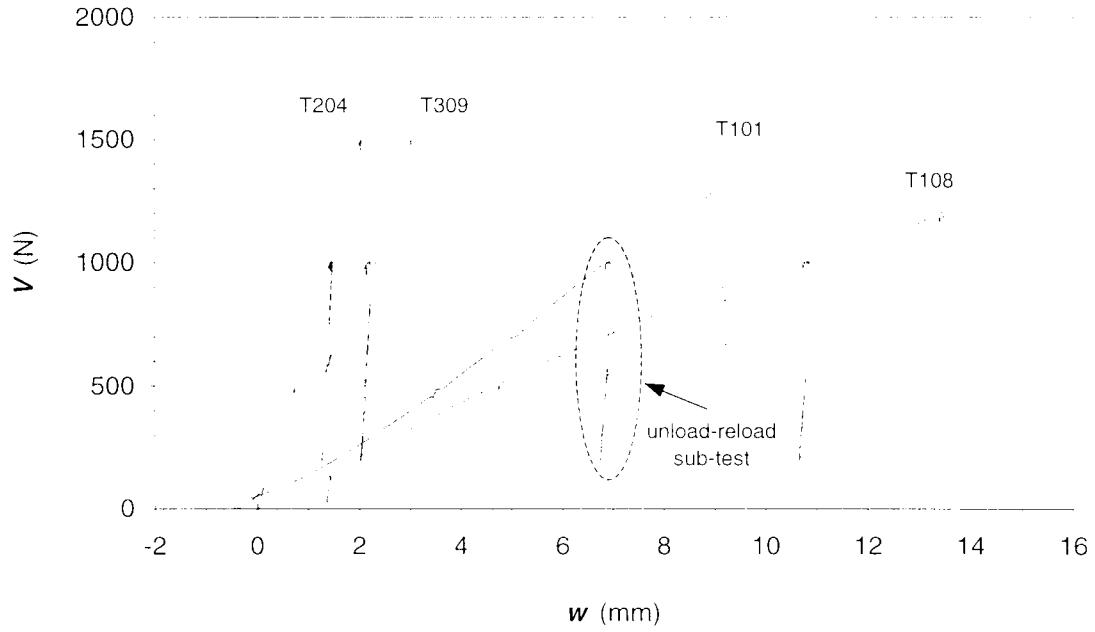

Note:
- The sideswipe sub-tests at end of virgin-penetration curves are not shown.

Figure 6.5 Load:deformation curves of the tests that did not include partially-drained sub-tests

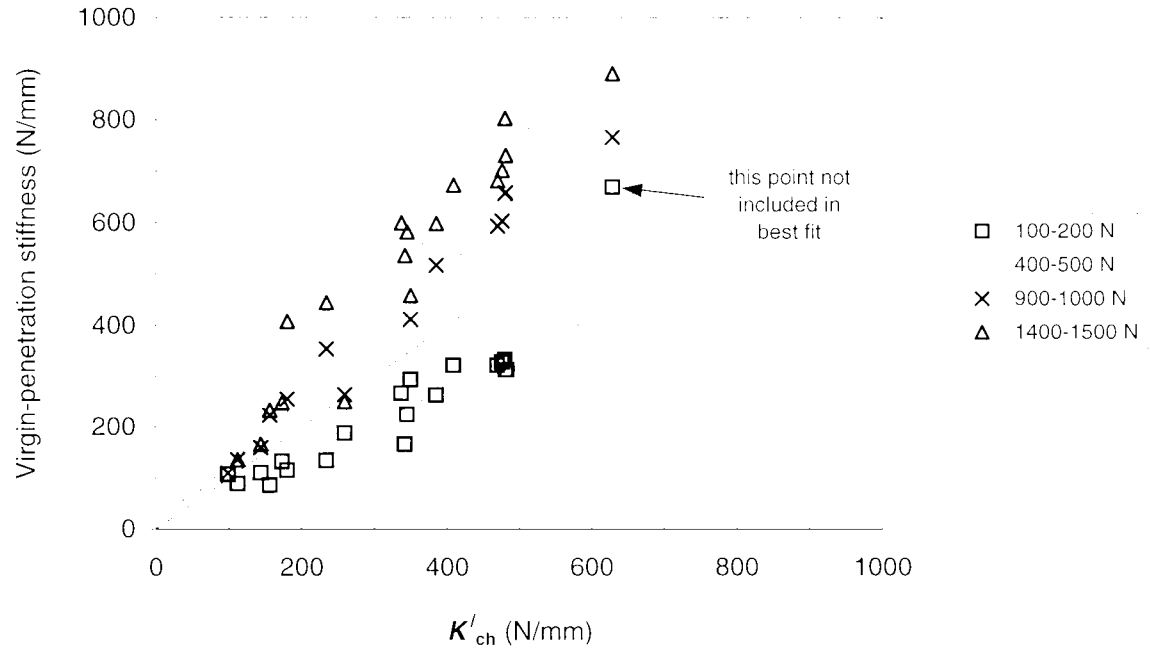

Figure 6.6 The virgin-penetration stiffness values plotted against the characterisation stiffness

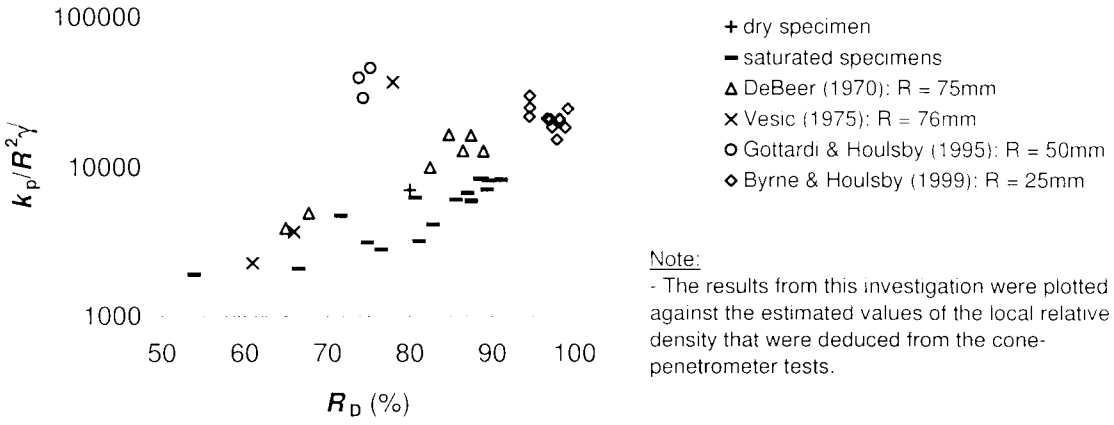

Figure 6.7 The initial virgin-penetration stiffness versus the relative density; results from this investigation compared with some of those in the literature

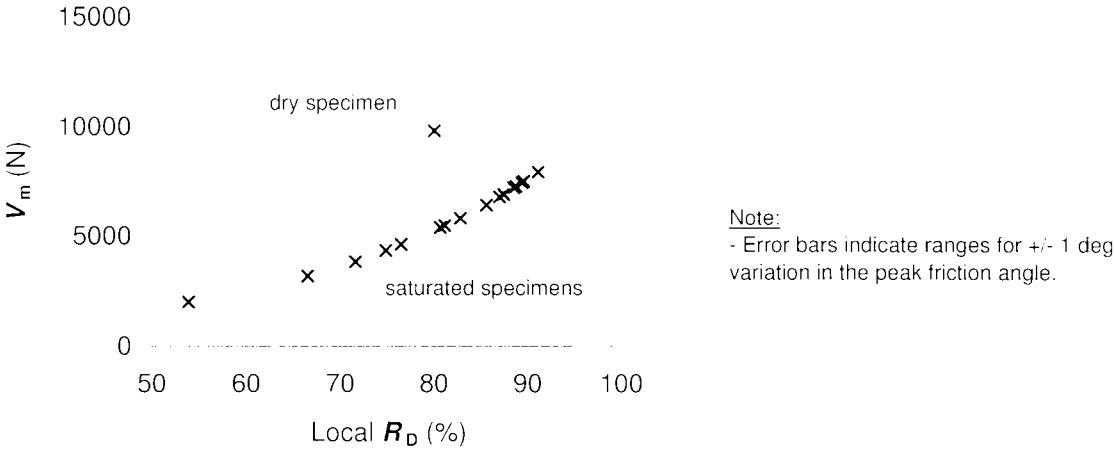

Figure 6.8 Predictions of the bearing capacity plotted against the estimated values of the relative density in the top layer of the specimens

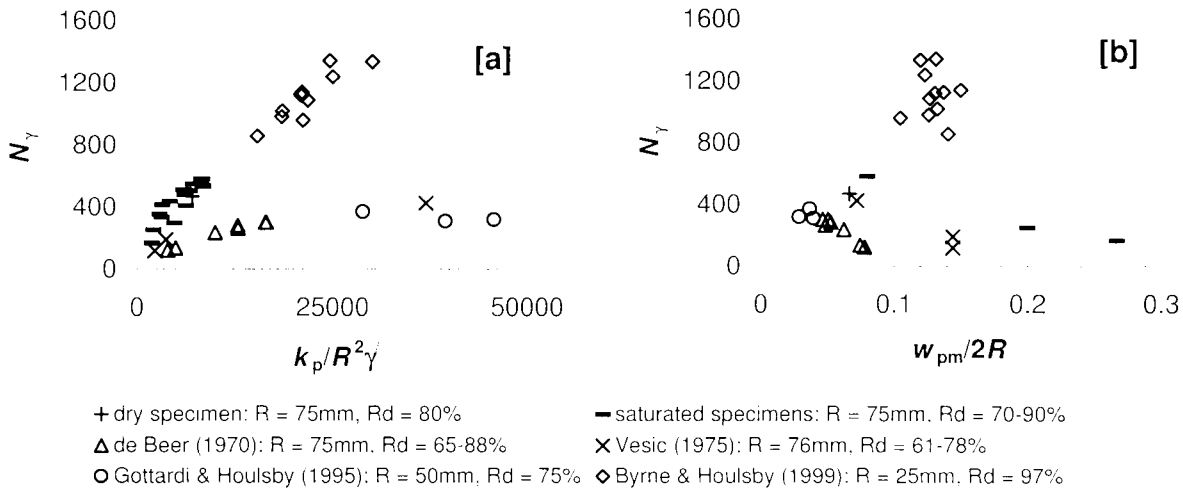

Figure 6.9 Relationships between bearing capacity and initial stiffness parameters (estimated values from this investigation compared with some measured values from the literature):
[a] bearing capacity factor against initial stiffness; and
[b] bearing capacity factor against normalised displacement at failure

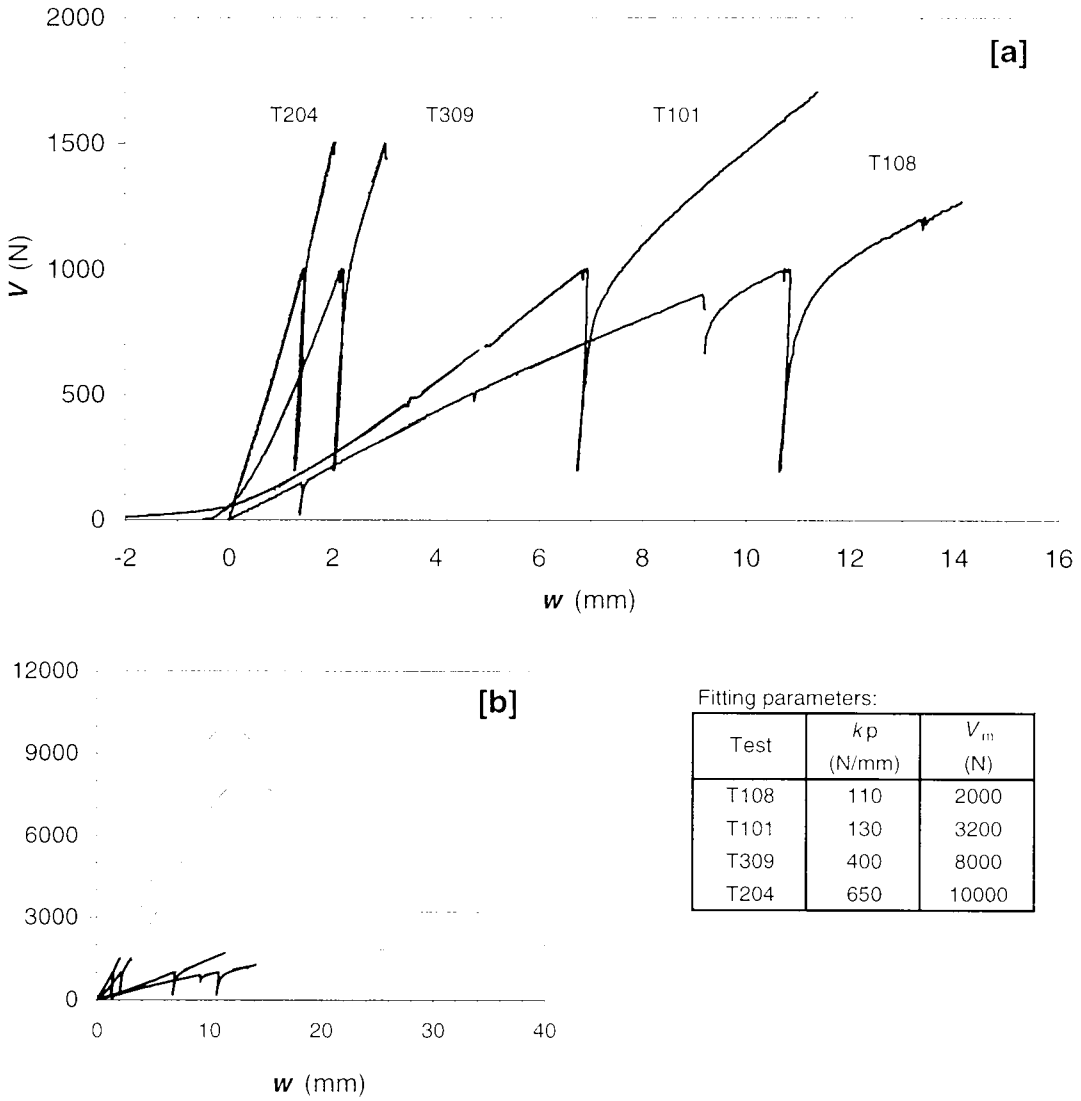

Fitting parameters:

Test	kp (N/mm)	V_m (N)
T108	110	2000
T101	130	3200
T309	400	8000
T204	650	10000

Figure 6.10 Comparison of virgin-penetration curves and fitted curves: **[a]** at small displacement; and **[b]** large displacement

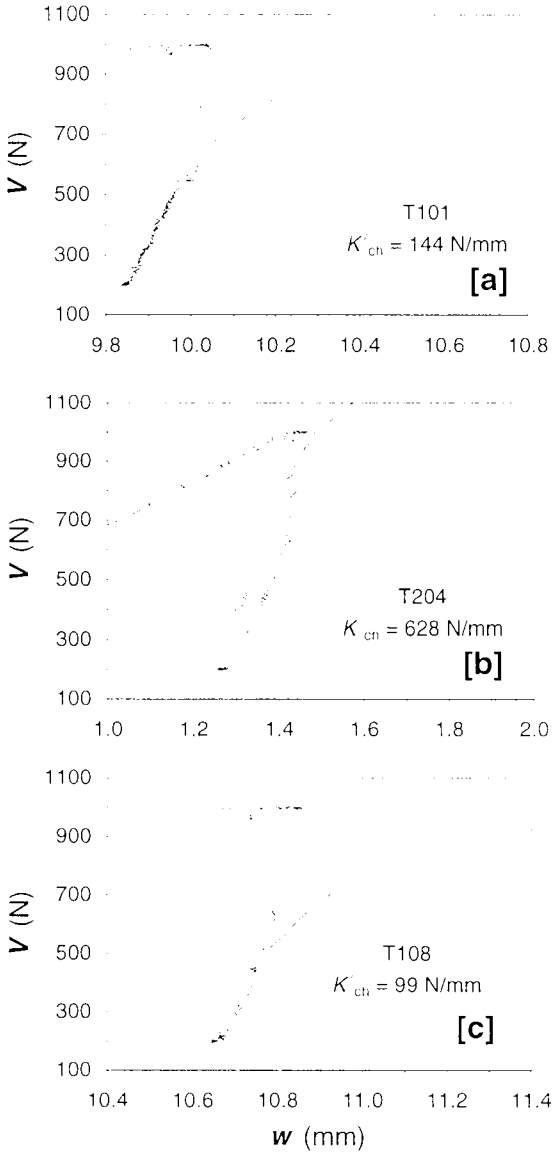

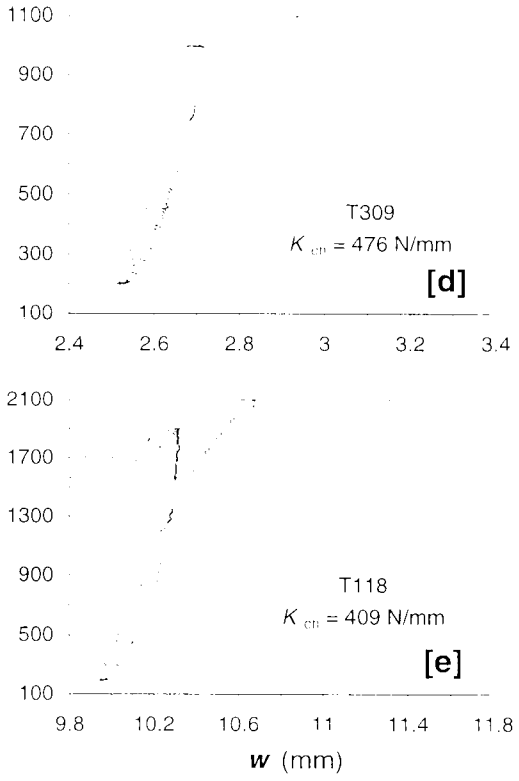

Note:
- The scale of plot [e] differs from the rest.

Figure 6.11 Load:deformation plots of unload-reload sub-tests

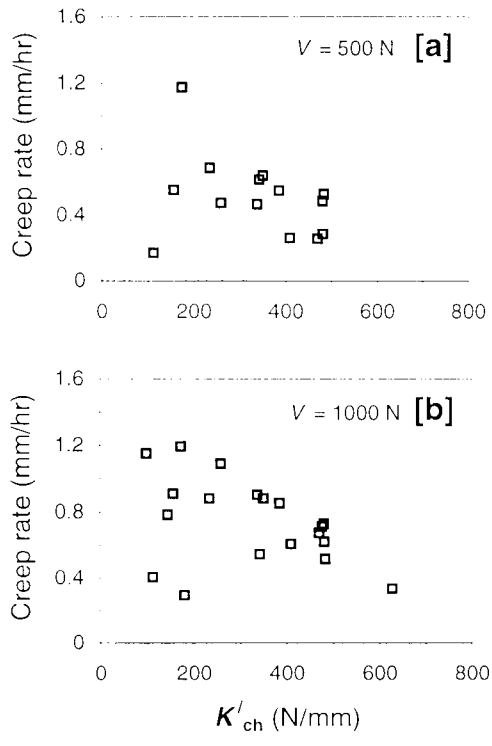

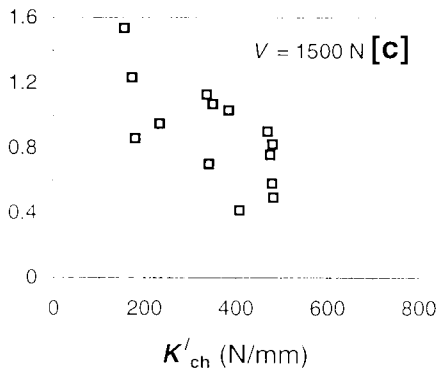

Figure 6.12 Creep rates measured during the HOLD routines:
[**a**] at V = 500 N;
[**b**] at V = 1000 N; and
[**c**] at V = 1500 N

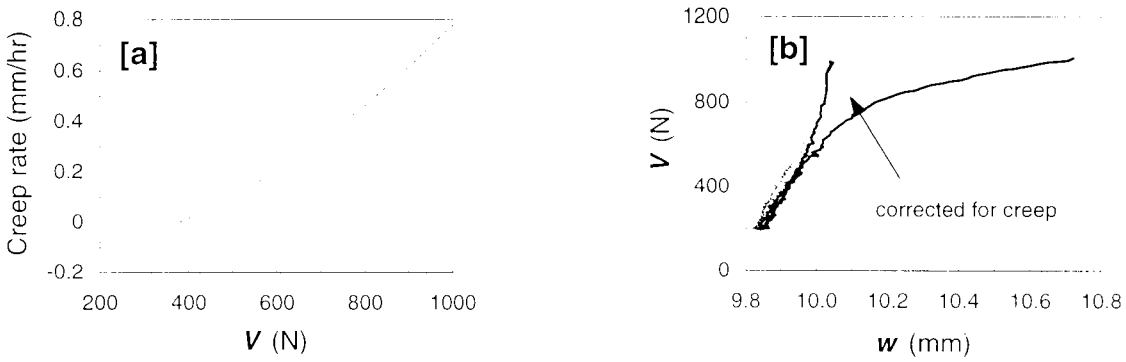

Figure 6.13 The effect of creep on the unload-reload sub-test of T101: **[a]** assumed creep relationship; and **[b]** actual response compared with corrected response

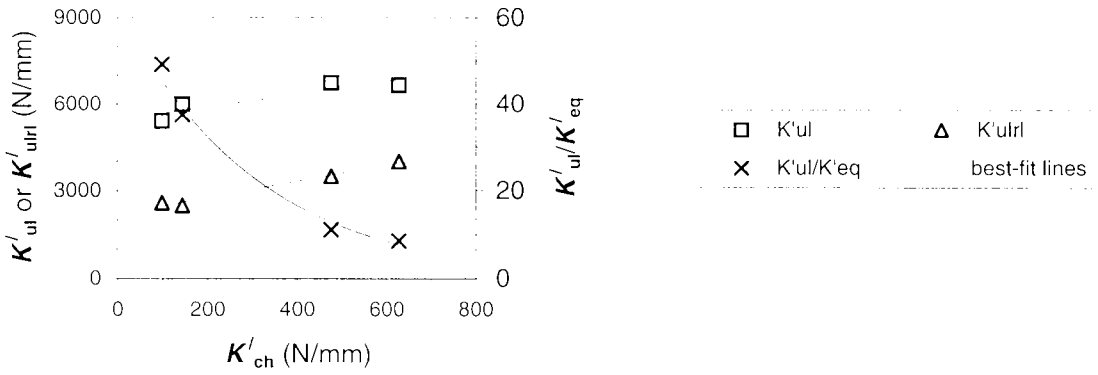

Figure 6.14 Vertical stiffness parameters derived from the unload-reload footing tests

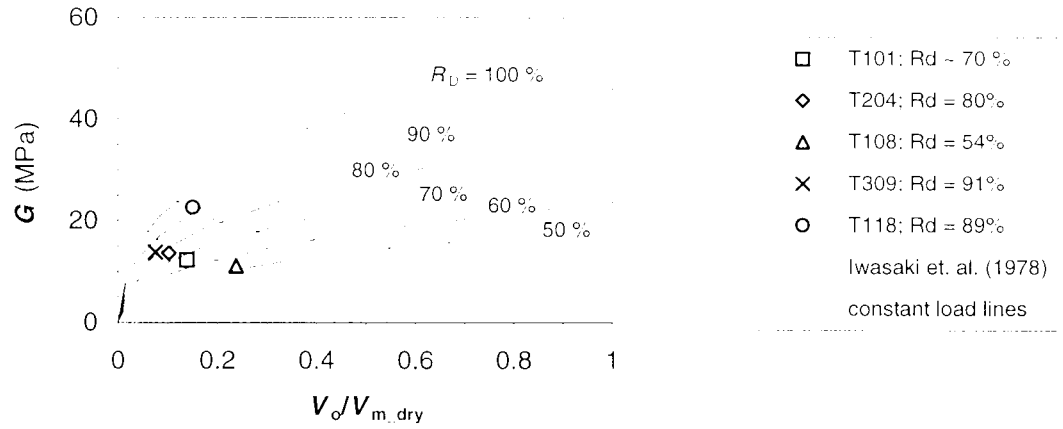

Note:
- See Figure 2.2 for Iwasaki *et. al.* relationship.
- In Iwasaki *et. al.*, the effective mean stress was assumed equal to 0.53 times the contact stress on the footing ($K_o = 0.3$) and the elastic shear modulus was taken as $0.2G_o$.
- The constant load lines represented V_o = 1000 N and V_o = 2000 N.
- The relative density measurements from the cone penetrometer tests were used, see Table 4.6.

Figure 6.15 Elastic shear moduli from vertical unload-reload tests.

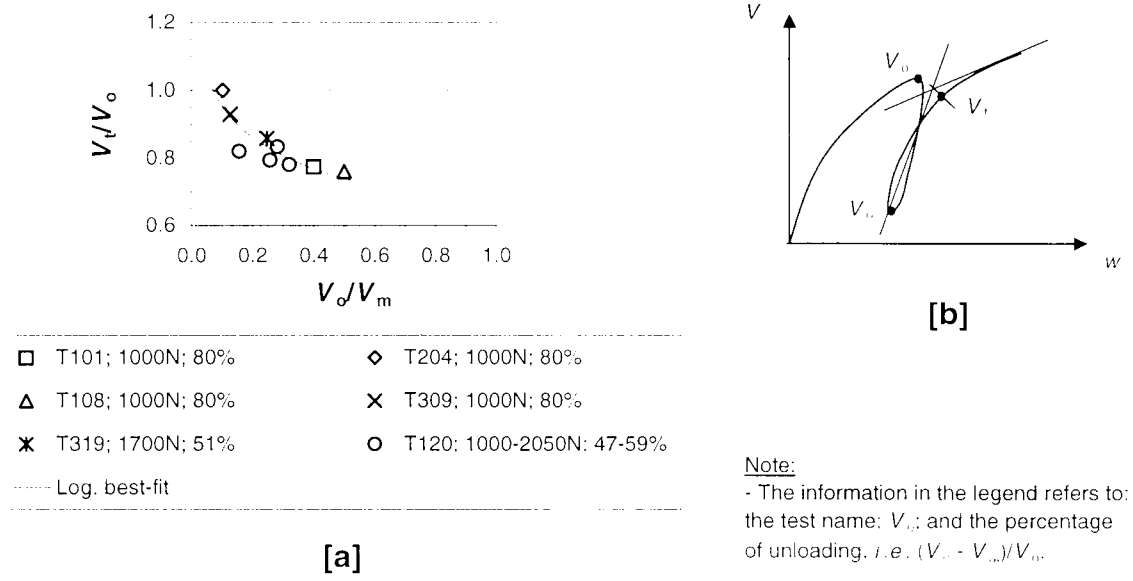

Figure 6.16 Transition point of the reloading section of the vertical ULRL tests and after some of the sideswipe tests: **[a]** measured points; **[b]** diagram showning parameters involved

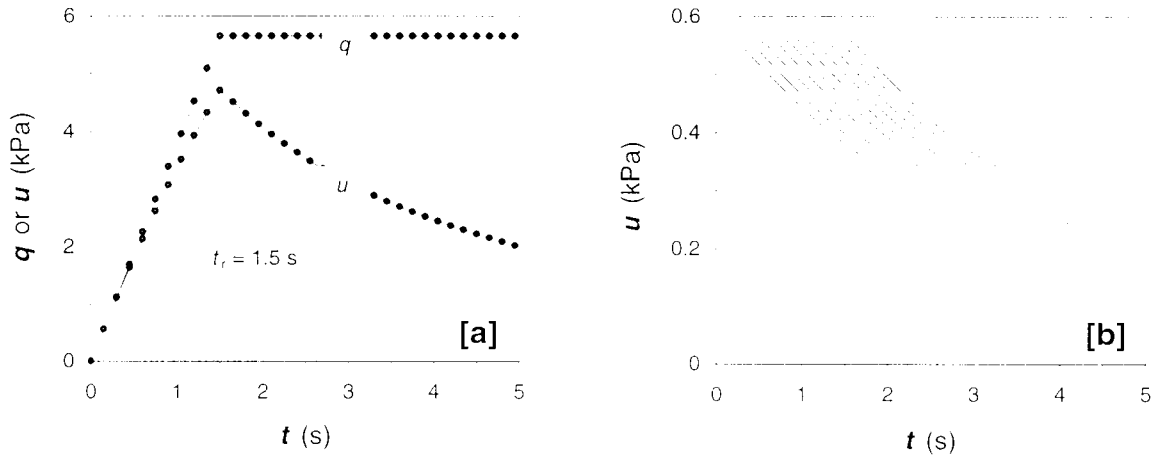

Note:
- $(du)_{t=0} = (dq)_{t=0}$
- Ten load increments.
- Dissipation of each increment given by relation in Figure 2.27.
- $dq = dV/(C_q \pi R^2)$ where $C_q = 2$.

Figure 6.17 Illustration of partially-drained consolidation model: **[a]** total stress and sum of pore pressure increments at centre of footing; and **[b]** pore pressure increments

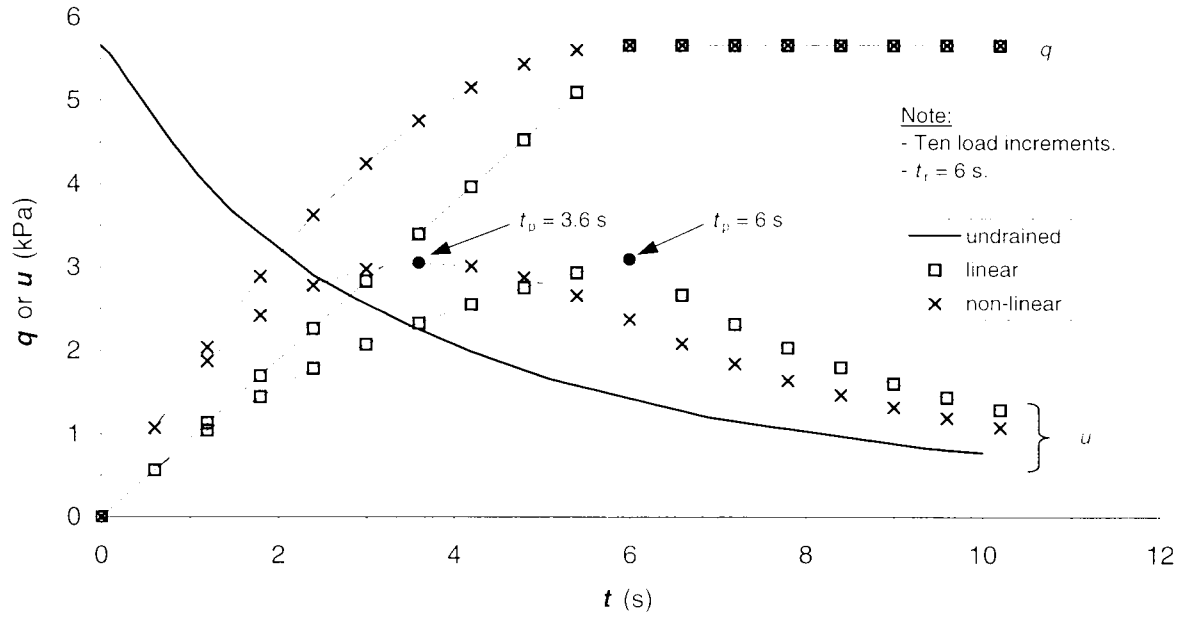

Figure 6.18 Types of ramped loading and resulting pore pressures of partially-drained consolidation model

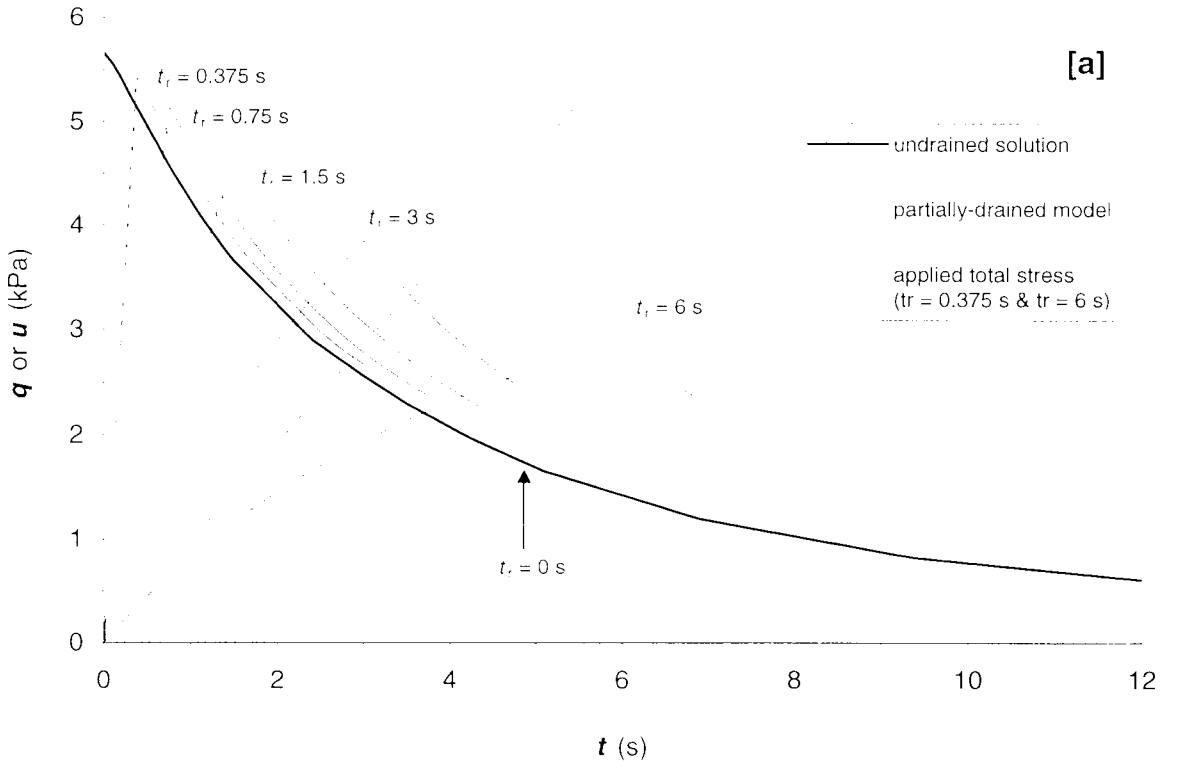

Figure 6.19 Comparison of the Davis and Poulos (1972) undrained solution and partially-drained consolidation model: **[a]** $t:u$ space; and **[b]** $T_v:U_p$ space

(continued on next page)

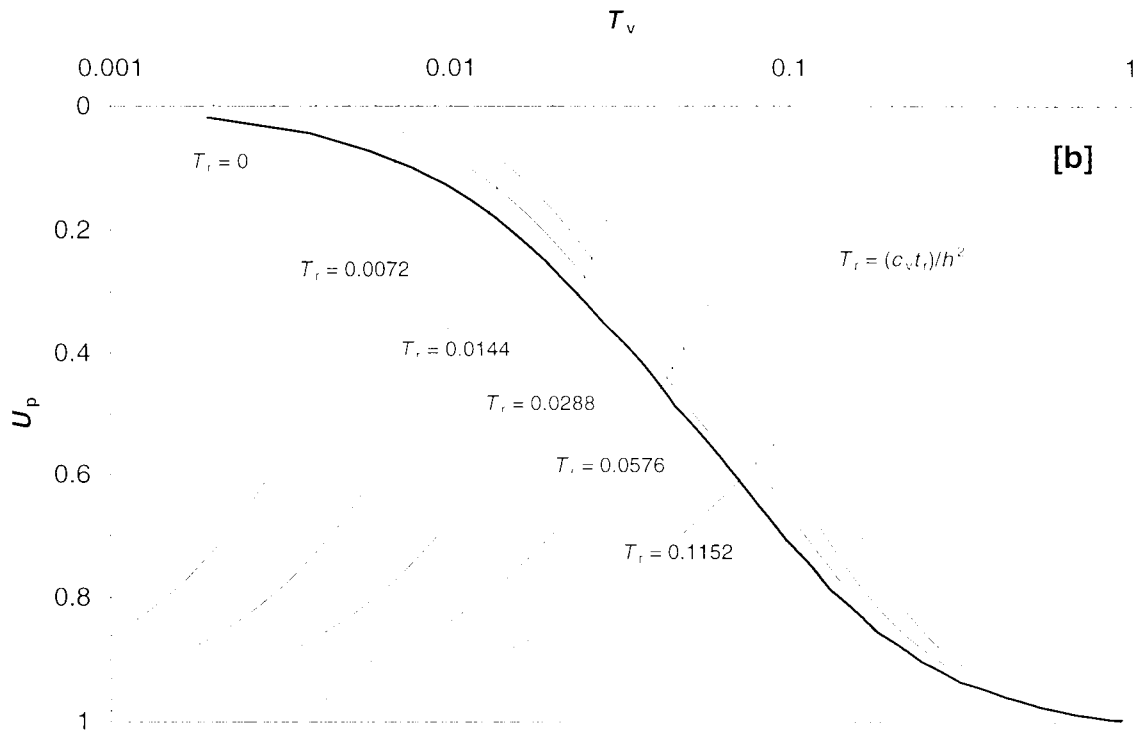

Figure 6.19 (cont.) Comparison of the Davis and Poulos (1972) undrained solution and partially-drained consolidation model: **[a]** t:u space; and **[b]** T_v:U_p space

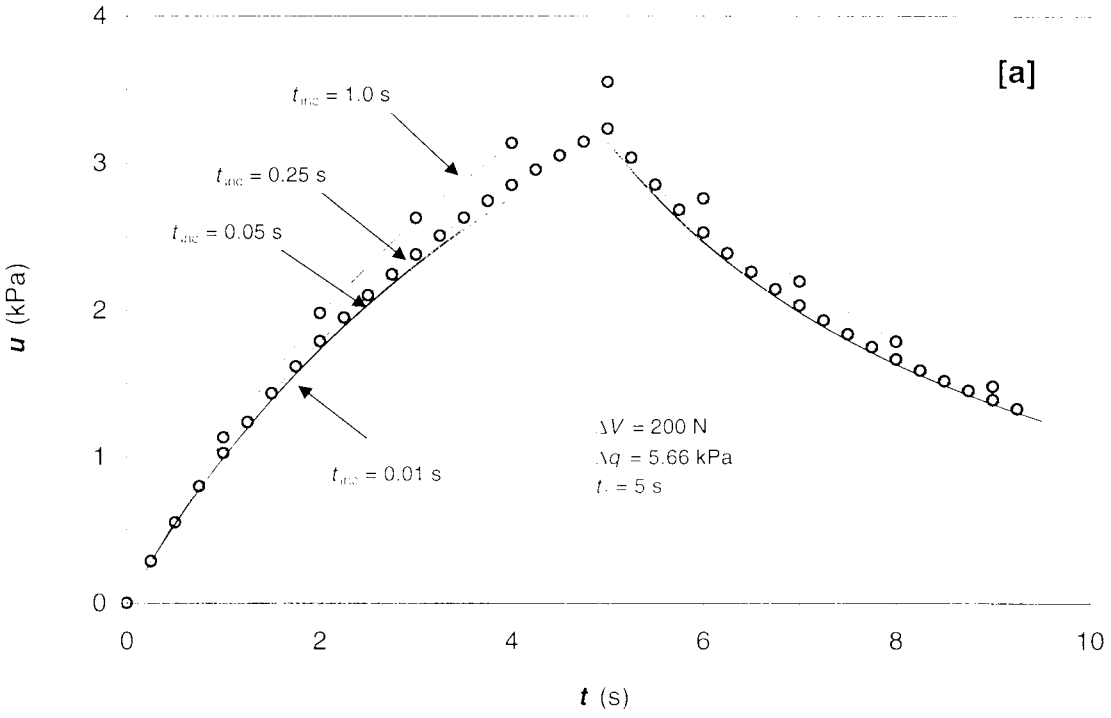

Figure 6.20 Effect of the time increment on predictions of the partially-drained consolidation model: **[a]** trend of decreasing time increment; and **[b]** effect of time increment on different rise times

(continued on next page)

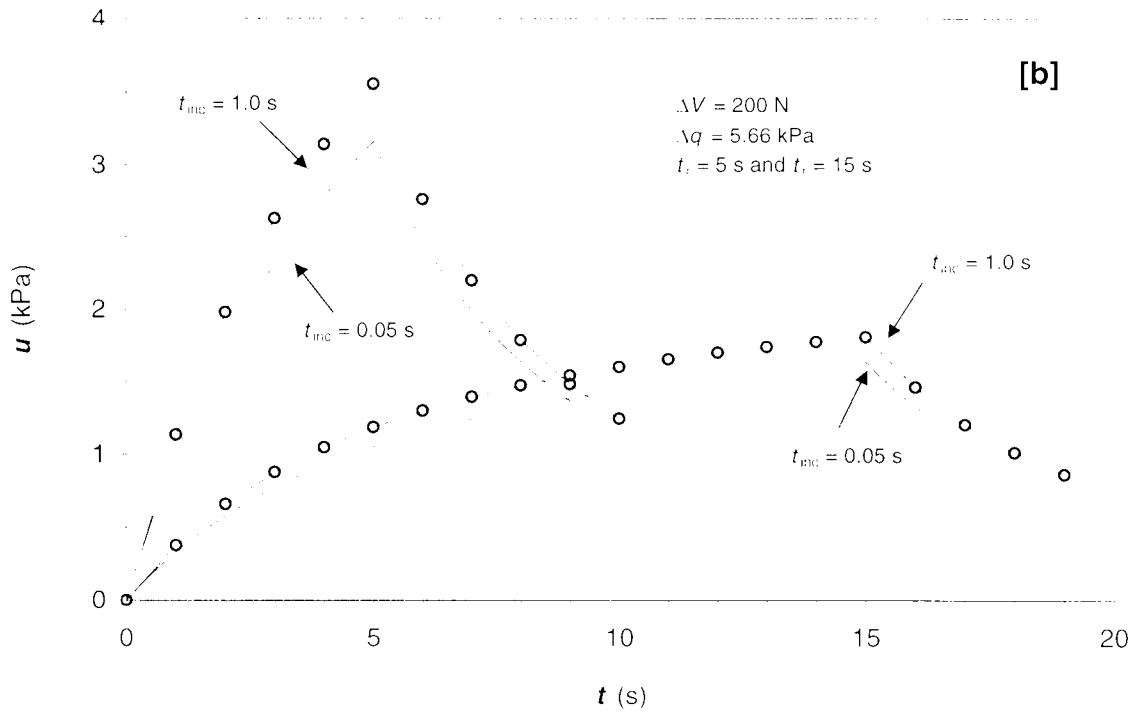

Figure 6.20 (cont.) Effect of the time increment on predictions of the partially-drained consolidation model: **[a]** trend of decreasing time increment; and **[b]** effect of time increment on different rise times

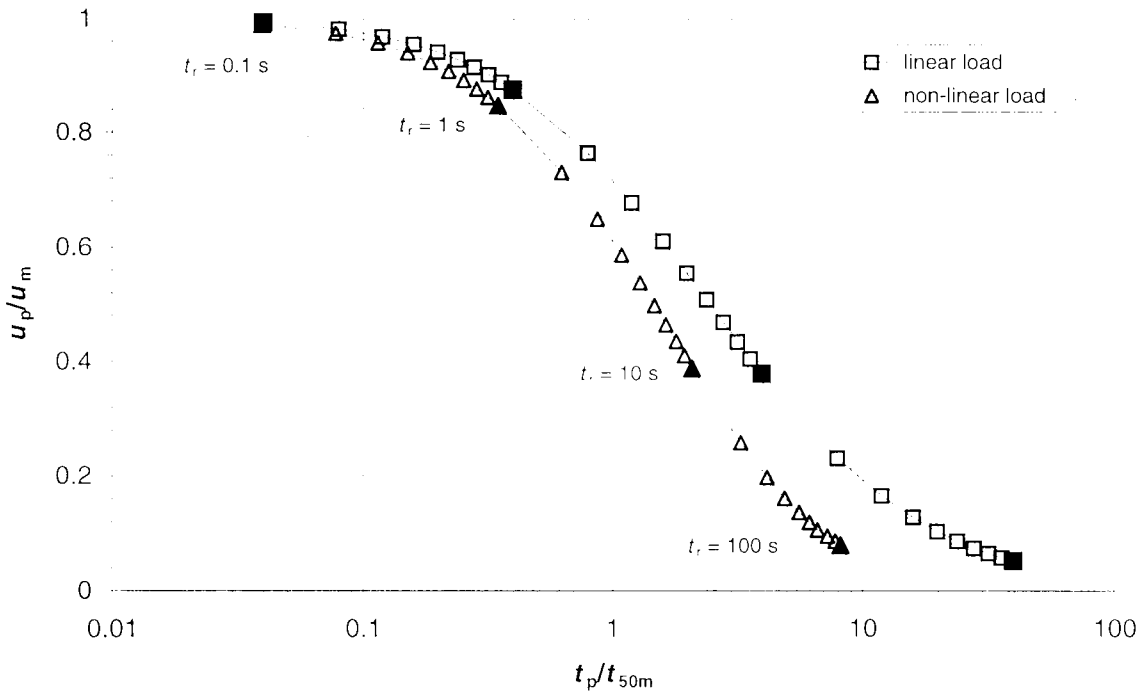

Figure 6.21 Peak pore pressure as a function of time to peak, from partially-drained consolidation model

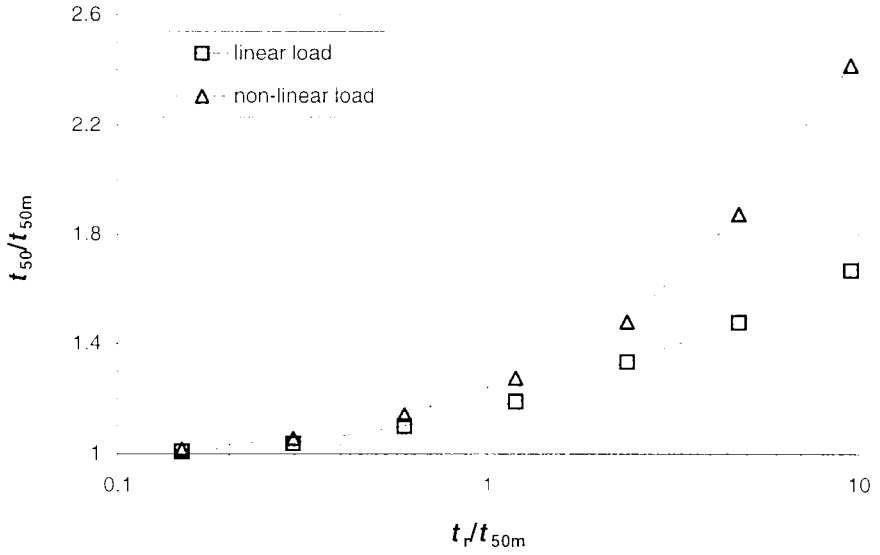

Figure 6.22 Effect of rise time on t_{50} time, from partially-drained consolidation model

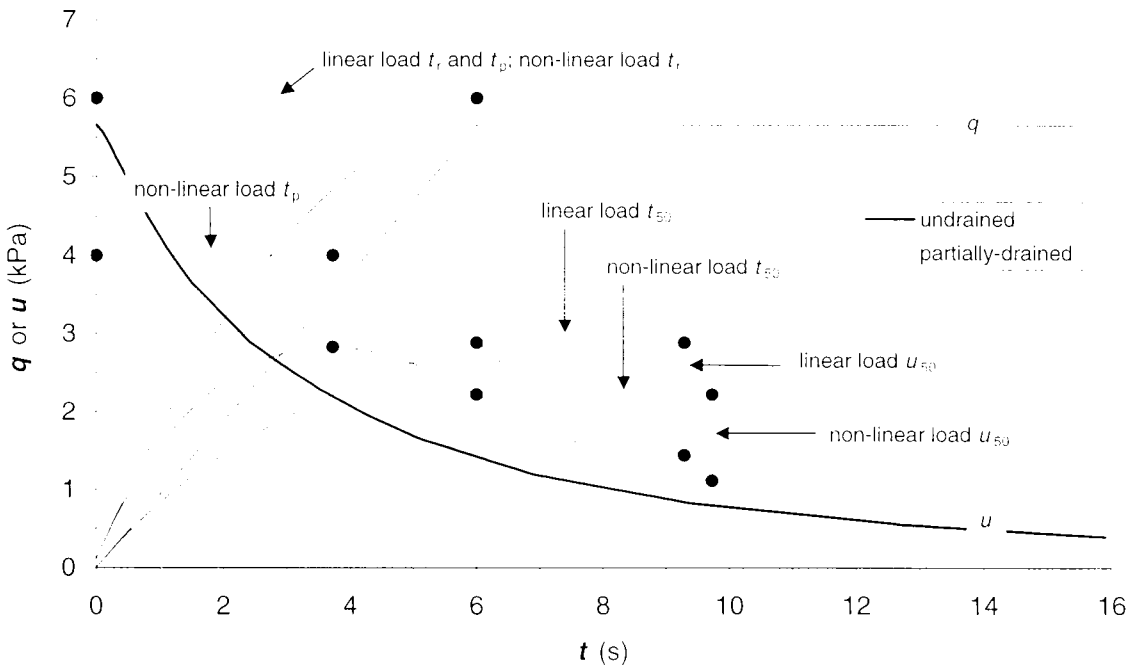

Figure 6.23 Definition of t_{50} time and u_{50} pore pressure

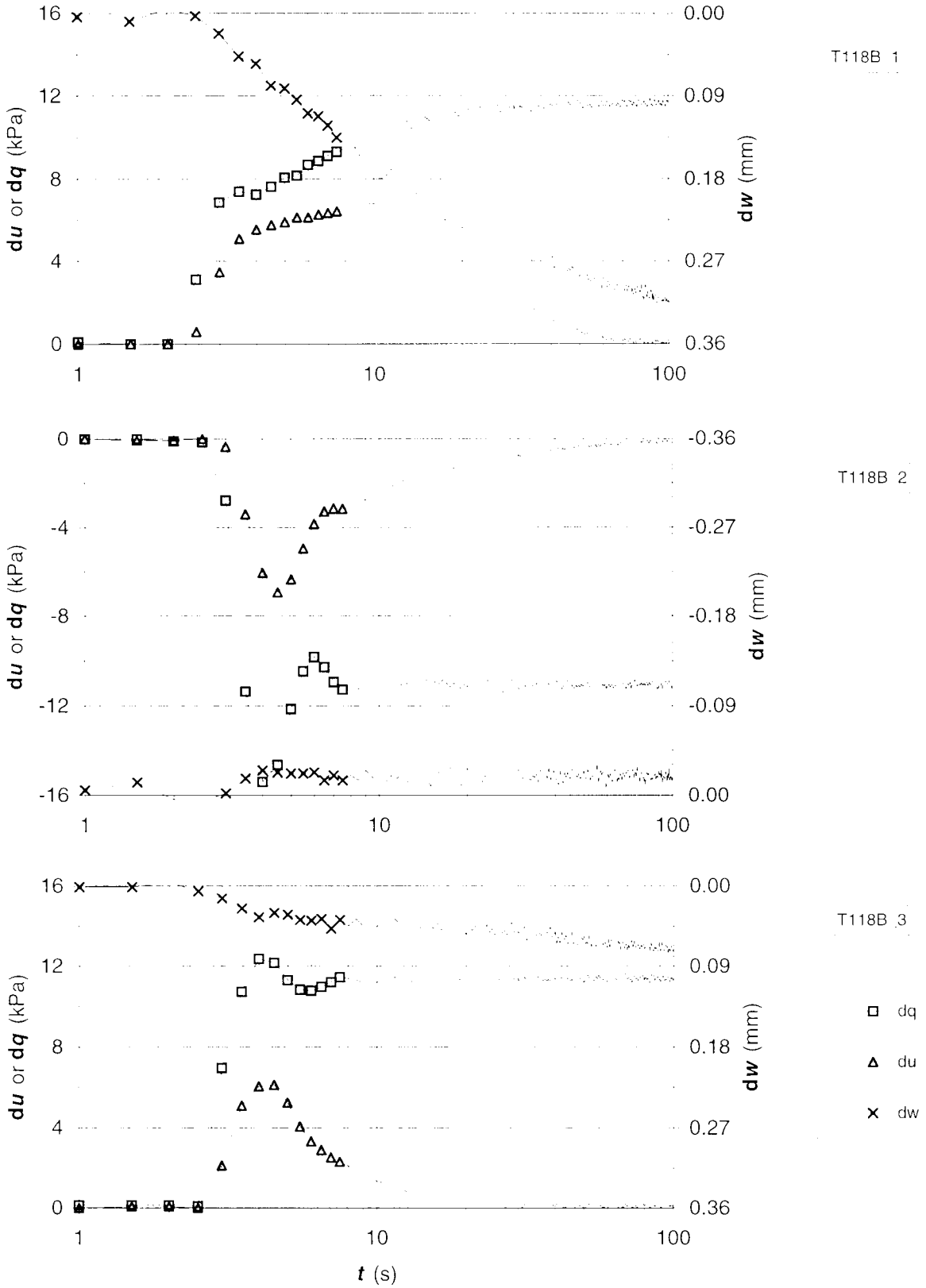

Figure 6.24 Consolidation sub-tests of T118

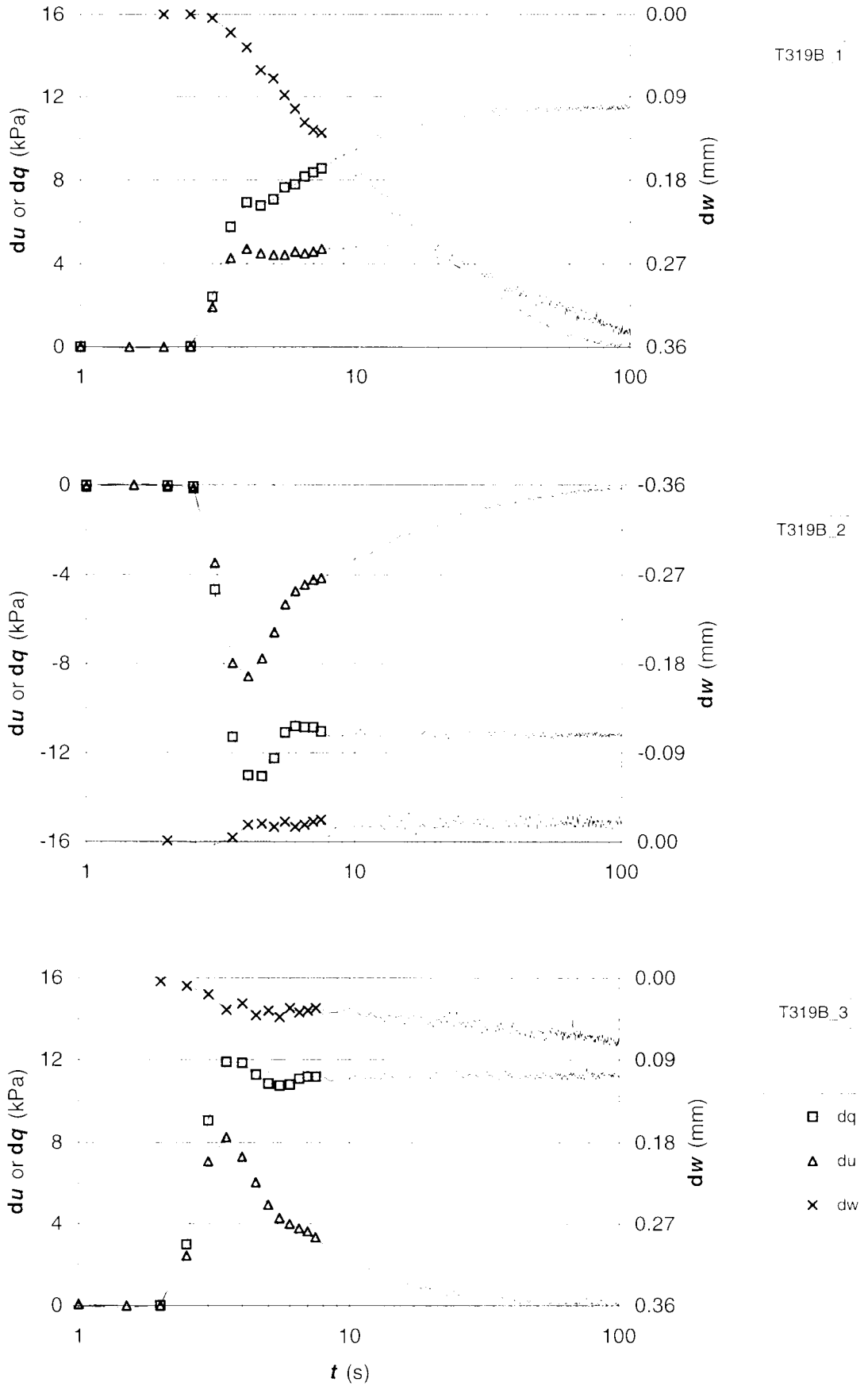

Figure 6.25 Consolidation sub-tests of T319

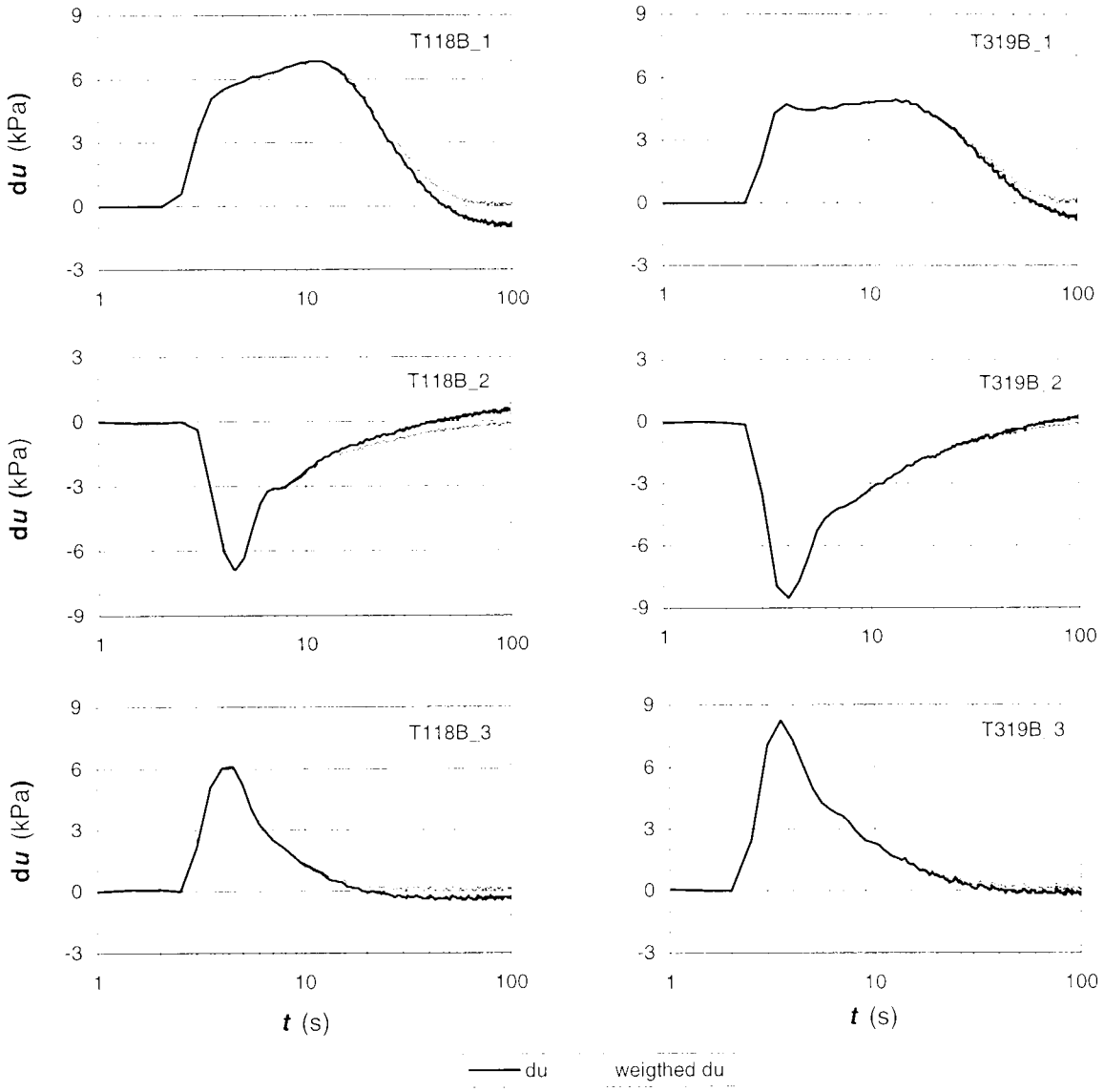

Figure 6.26 Alteration of pore pressure measurements in consolidation tests

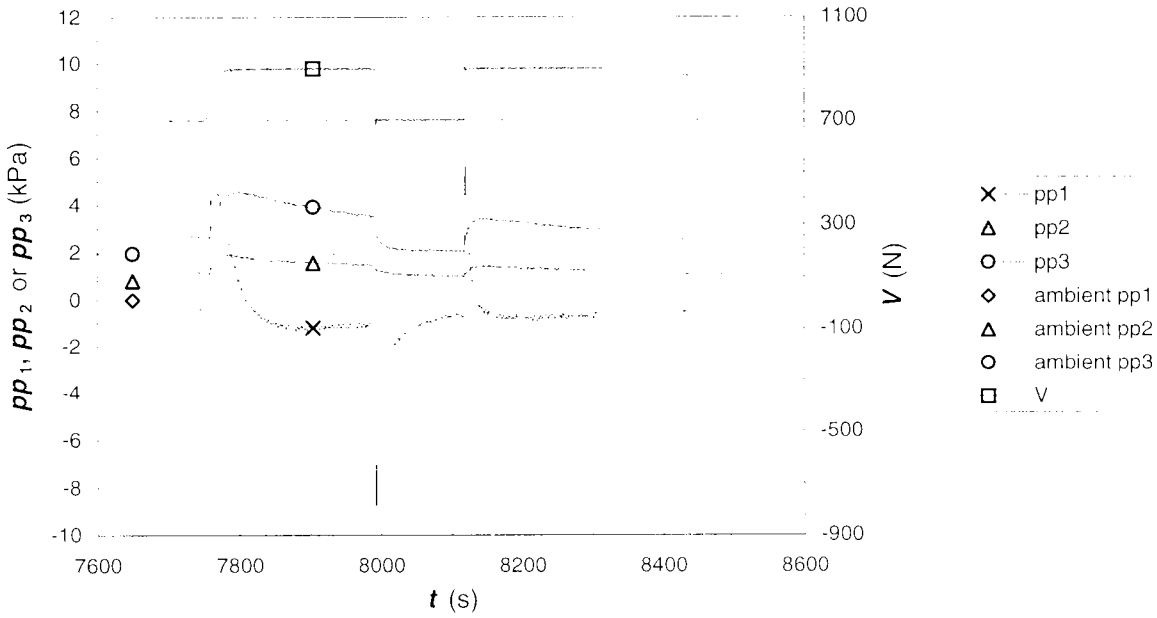

Figure 6.27 Pore pressure measurements in footing and tank wall during consolidation tests of T319 (background logging only)

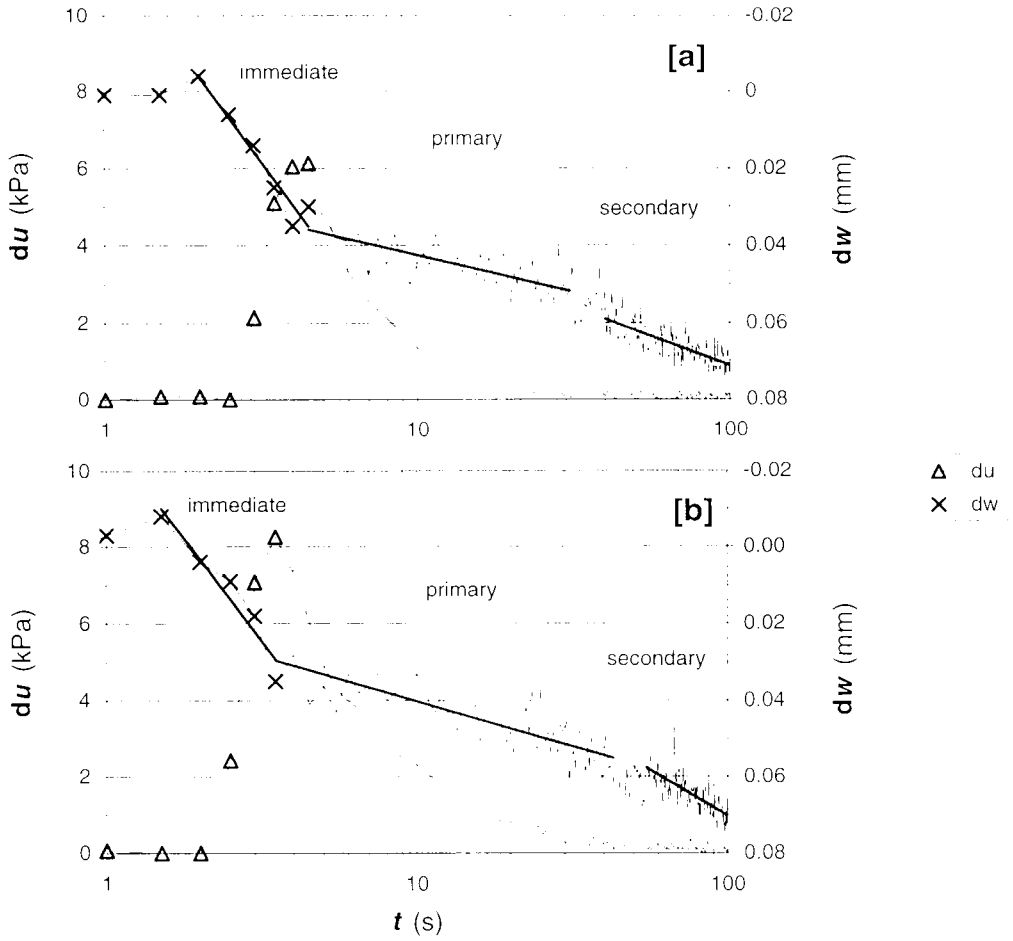

Figure 6.28 The three stages of settlement in reloading consolidation tests: **[a]** test T118B_3; and **[b]** test T319B_3

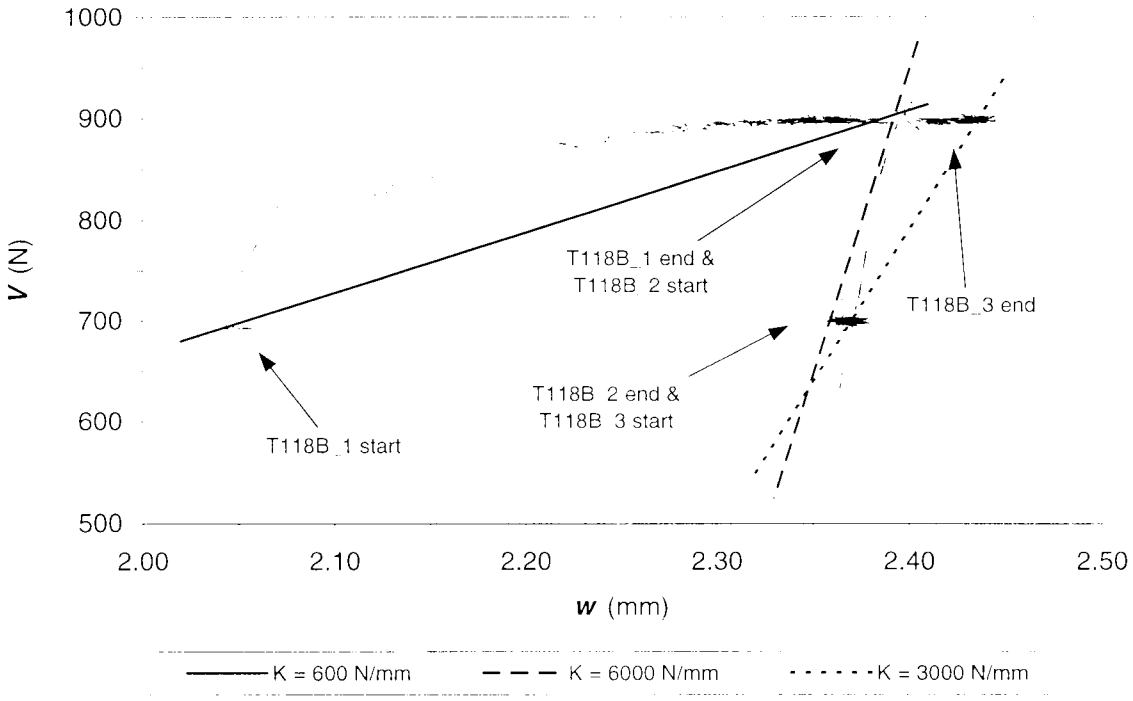

Figure 6.29 Comparison of consolidation and drained load paths of test T118

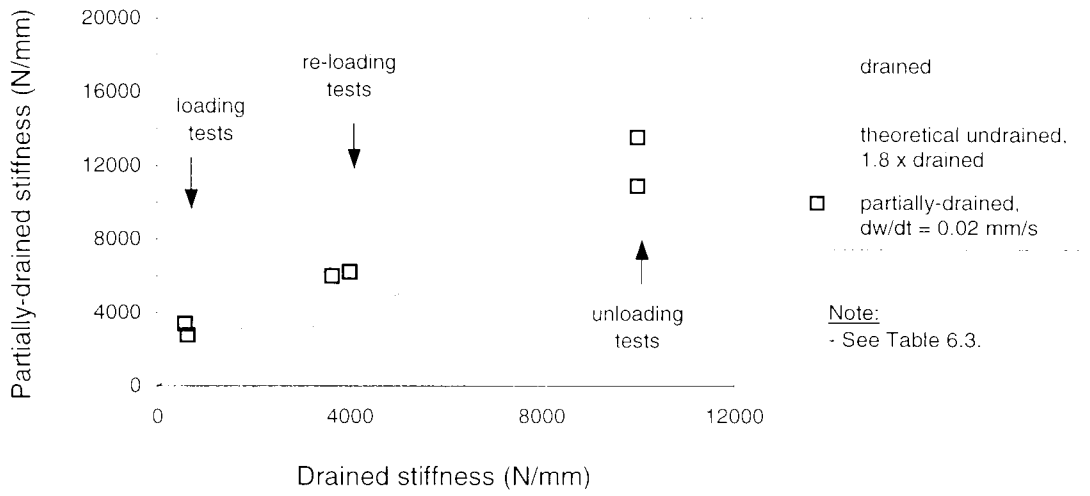

Figure 6.30 Partially-drained (or immediate) vertical stiffness from the consolidation tests

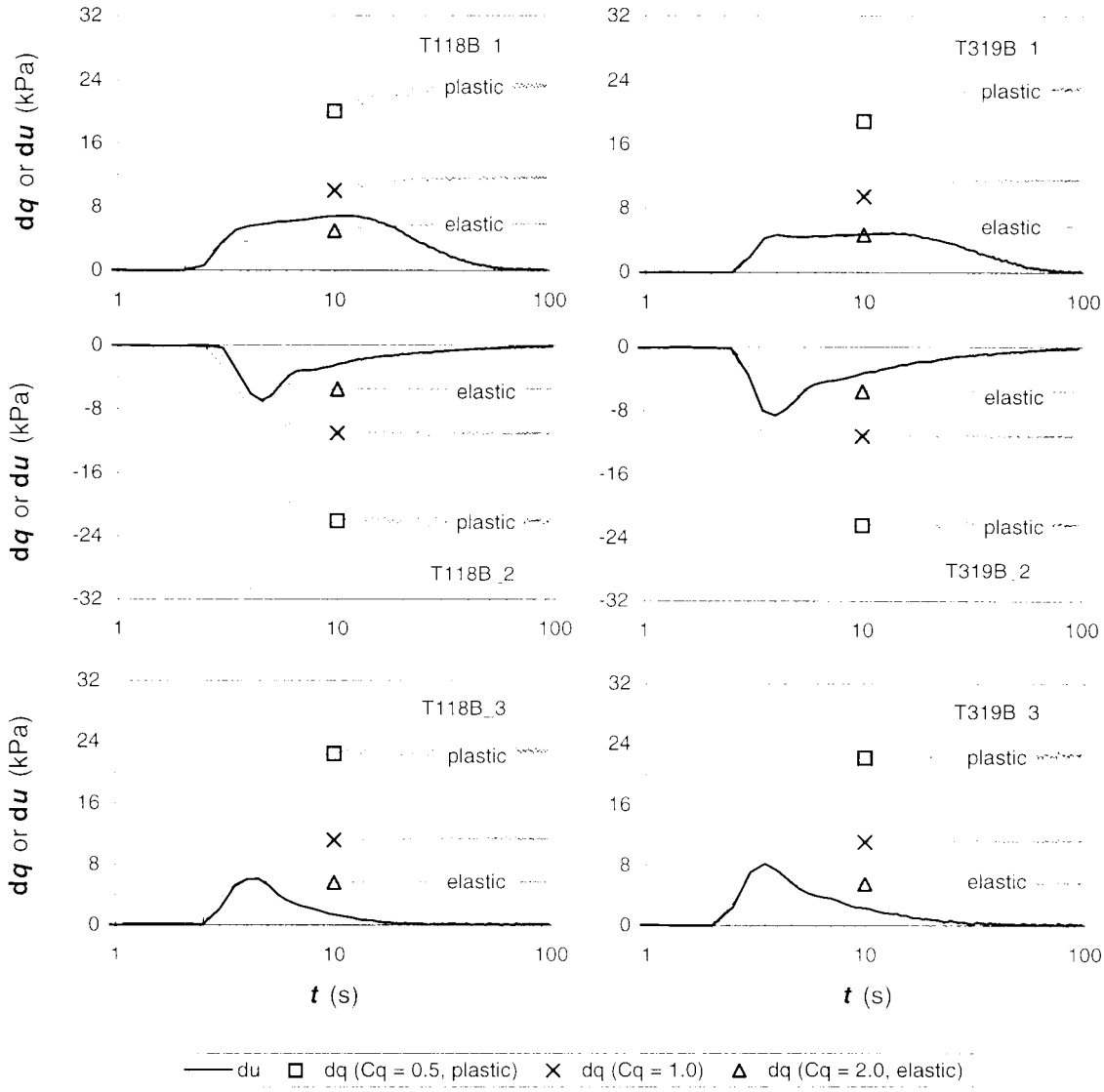

Figure 6.31 Comparison of the measured pore pressure and the estimated total stress during the consolidation tests of T118 and T319
(at the centre of the footing for a range of total stress distributions)

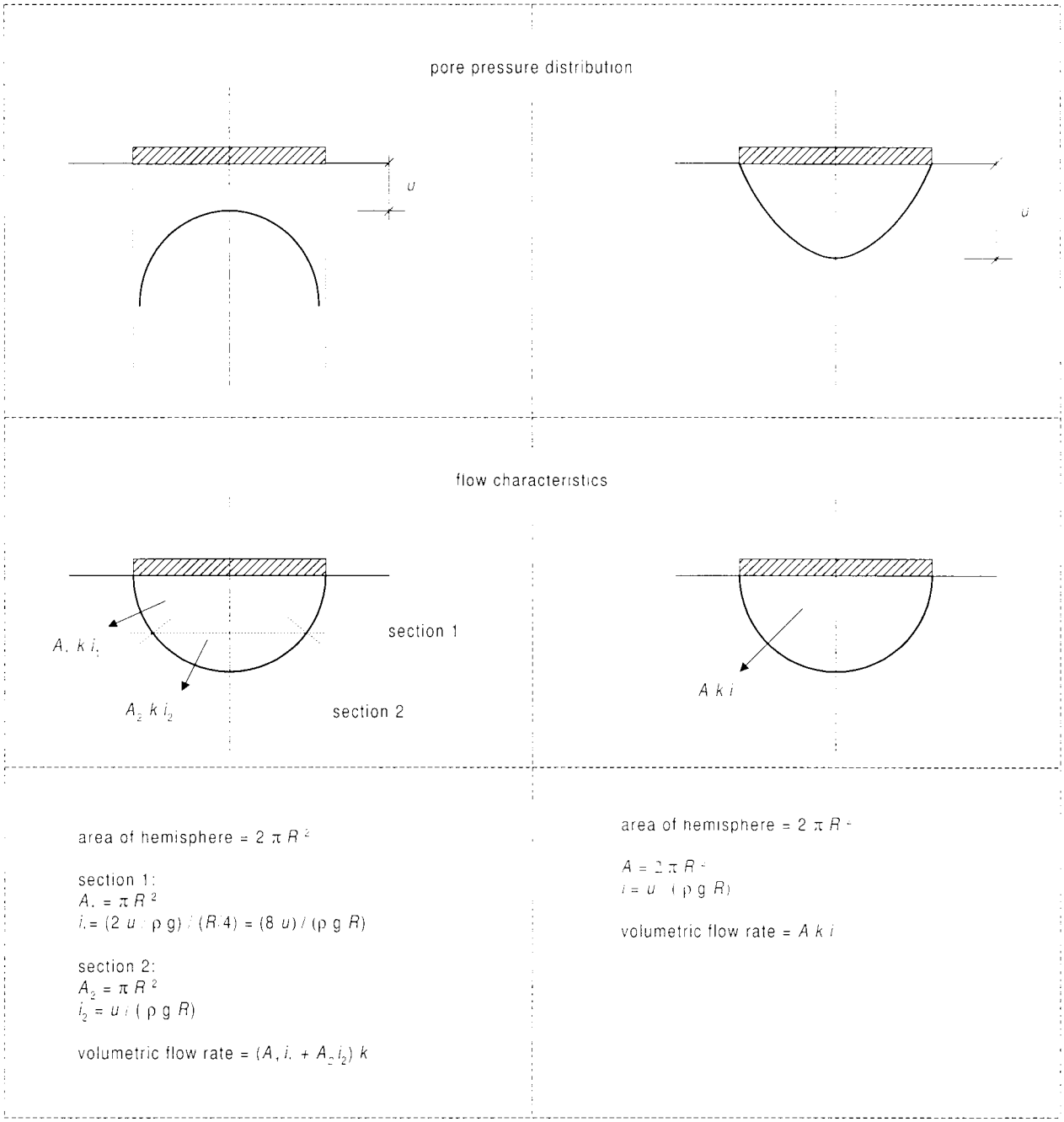

Figure 6.32 Definitions used in calculation of volumetric flow rate during consolidation: [a] immediate stage; and [b] primary stage

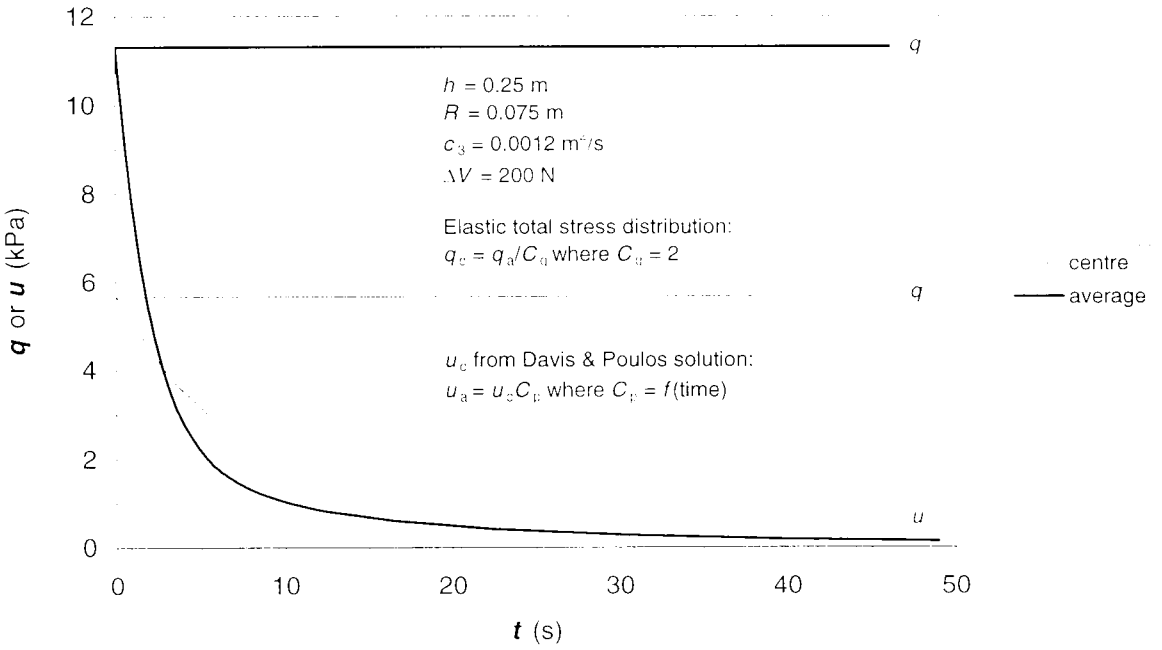

Figure 6.33 Comparison of the pore pressure at the centre of a footing and the average pore pressure during consolidation

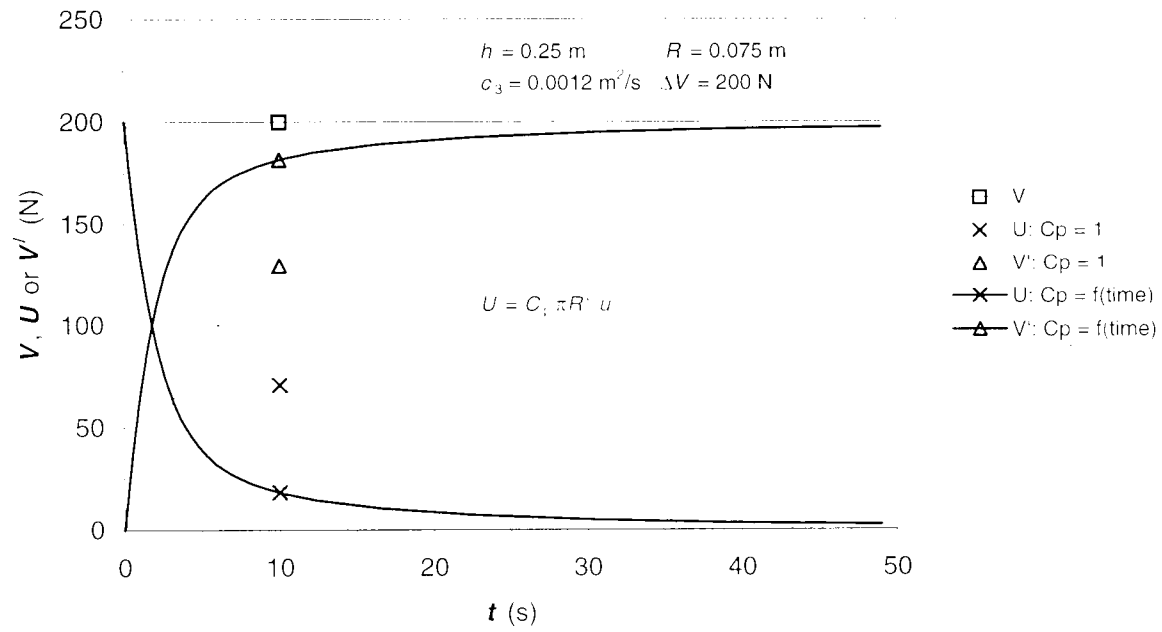

Figure 6.34 Comparison of the effective load calculated assuming a uniform pore pressure distribution and a distribution that varies with dissipation

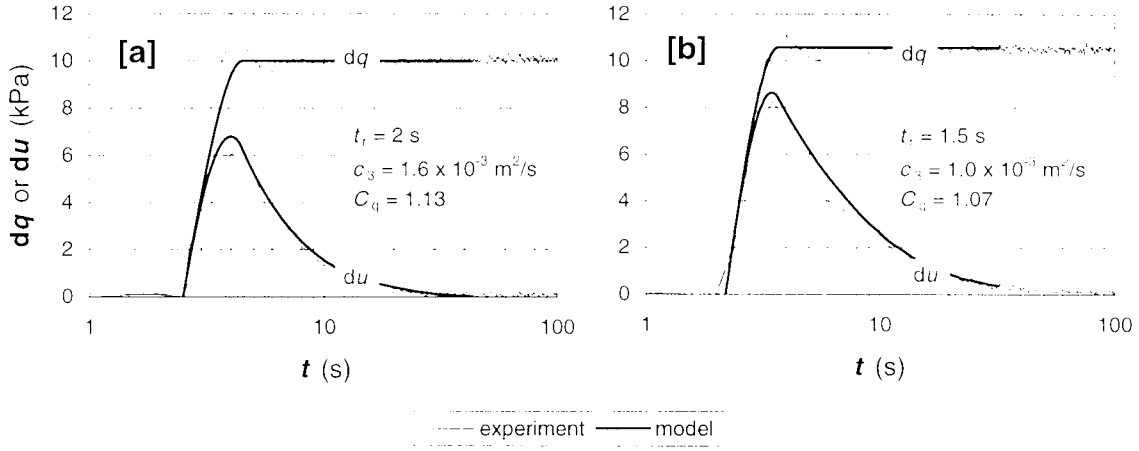

Figure 6.35 Comparison of partially-drained consolidation model with tests: **[a]** with T118B_3; and **[b]** with T319B_3

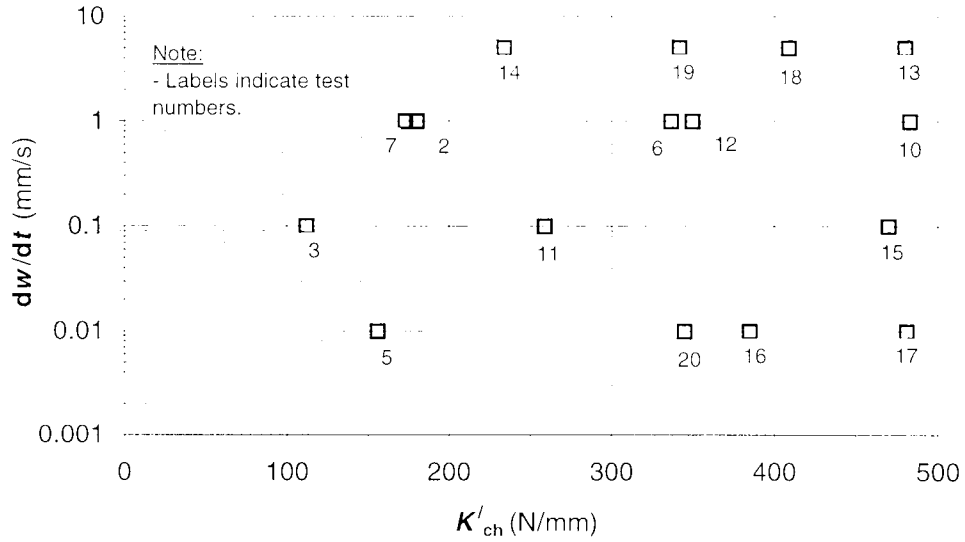

Figure 6.36 Distribution of the displacement rate of the vertical partially-drained tests with the characterisation stiffness

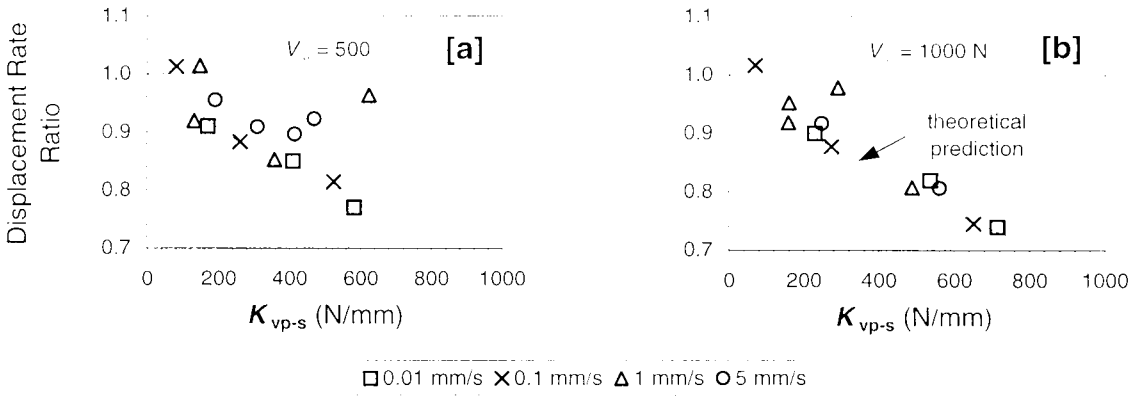

Note:
- Displacement ratio defined as measured displacement rate divided by intended displacement rate
- $K_{vp\text{-}s}$ was the stiffness of the secondary section of the partially-drained tests
- Theoretical prediction defined as $K_{rig} / (K_{vp\text{-}s} + K_{rig})$ where K_{rig} was the rig stiffness measured between the stepper motor and the footing

Figure 6.37 The variation of displacement rate ratio with stiffness from the vertical partially-drained tests: **[a]** tests from 500 N; and **[b]** tests from 1000 N

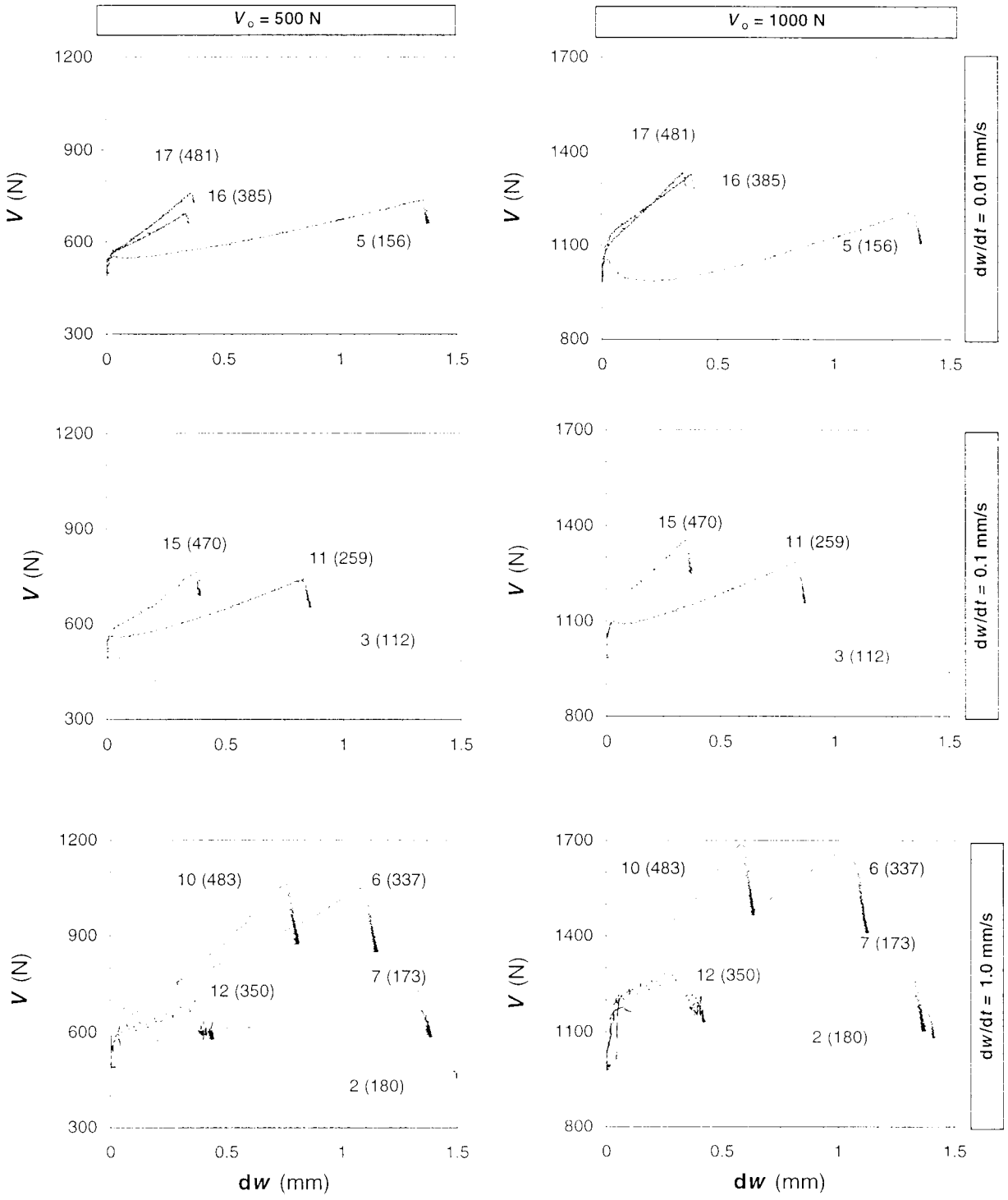

Note:
- Labels refer to the test number and the characterisation stiffness.

Figure 6.38 Effect of characterisation stiffness on load:deformation response of the vertical partially-drained tests, at three different displacement rates

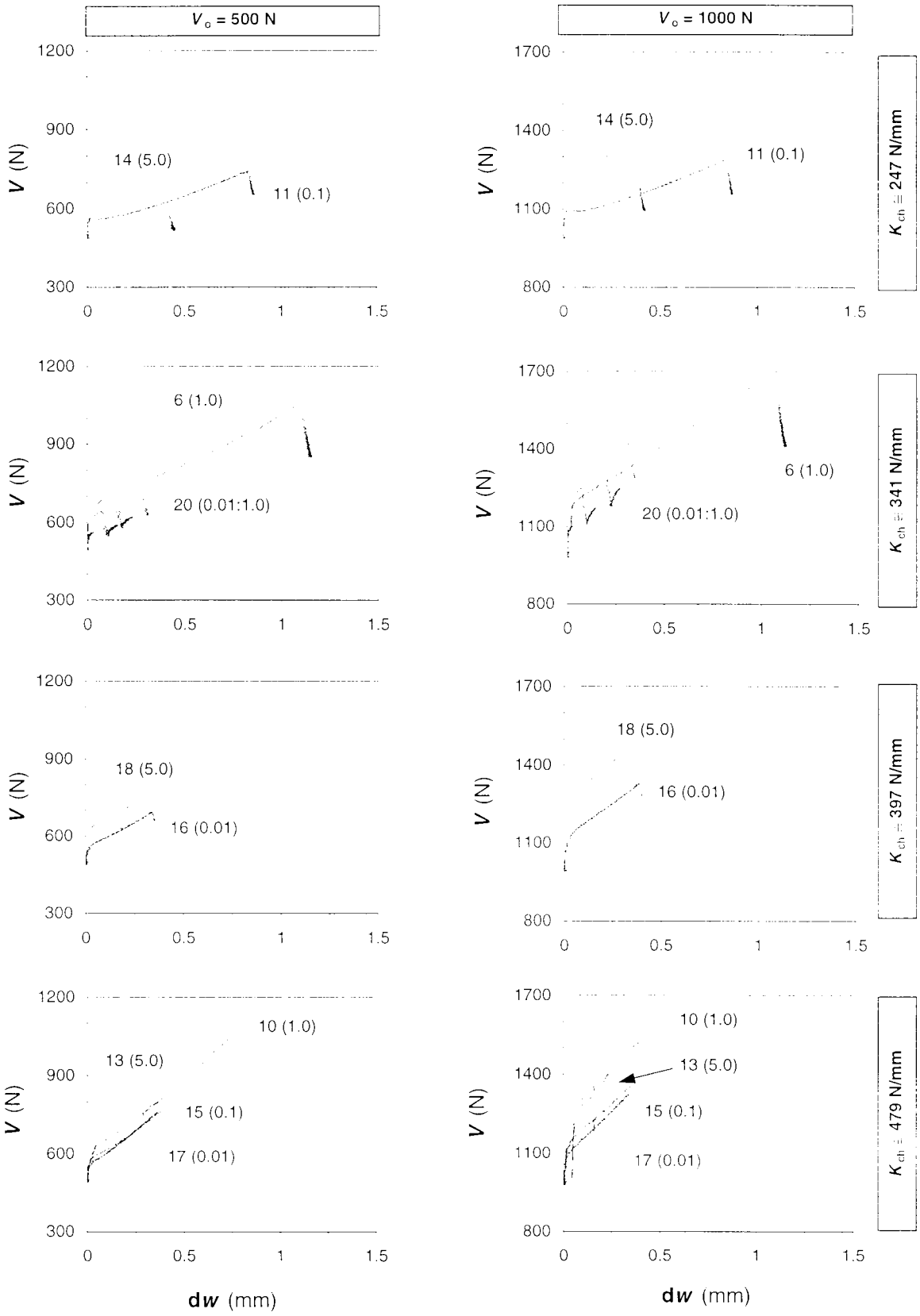

Note:
- Labels refer to the test number and vertical displacement rate.

Figure 6.39 Effect of displacement rate on load:deformation response of vertical partially-drained tests, at four different values of characteristic stiffness

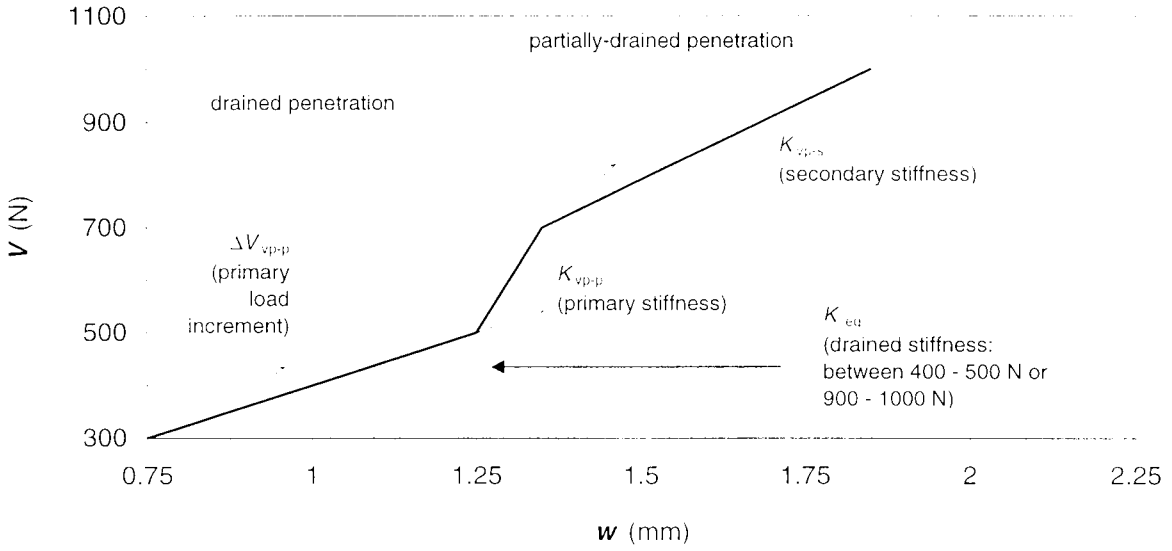

Figure 6.40 Idealised load:deformation behaviour of vertical partially-drained tests

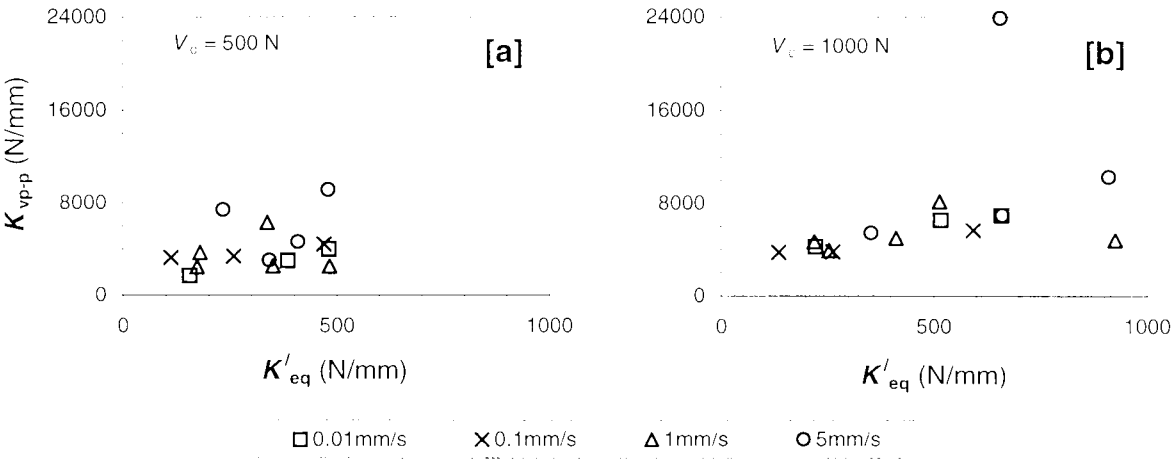

Figure 6.41 The primary stiffness of the vertical partially-drained tests: **[a]** from 500 N; and **[b]** from 1000 N

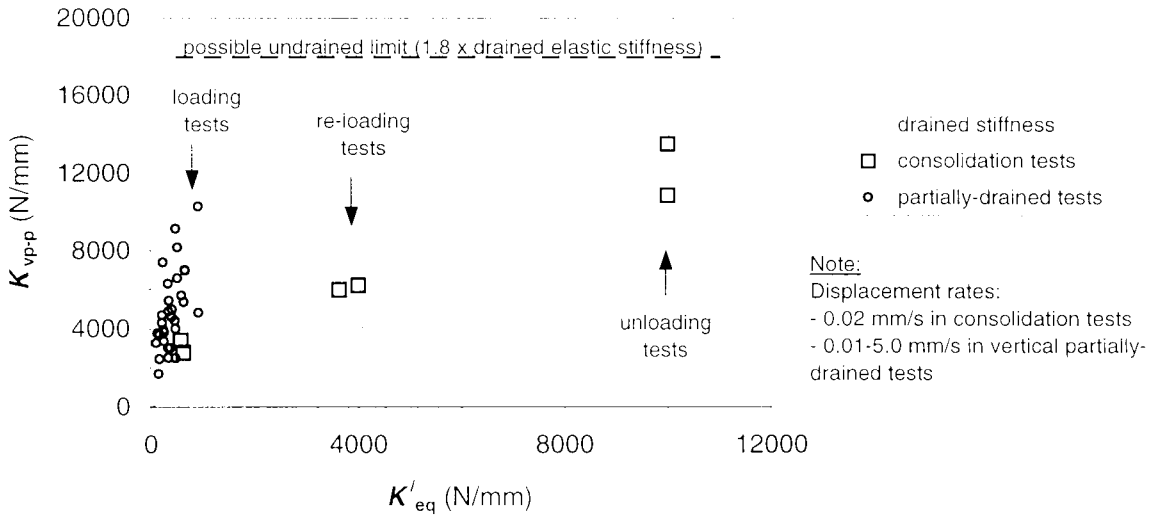

Figure 6.42 Comparison of the partially-drained vertical stiffness from the consolidation tests and the vertical partially-drained tests

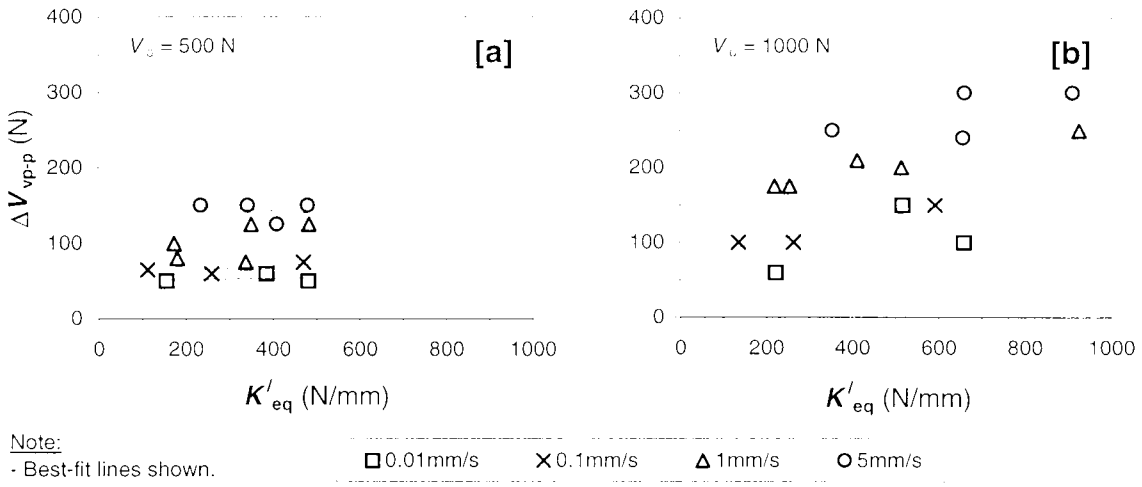

Figure 6.43 The magnitude of the change in load over the primary section of the vertical partially-drained tests: **[a]** from 500 N; and **[b]** from 1000 N

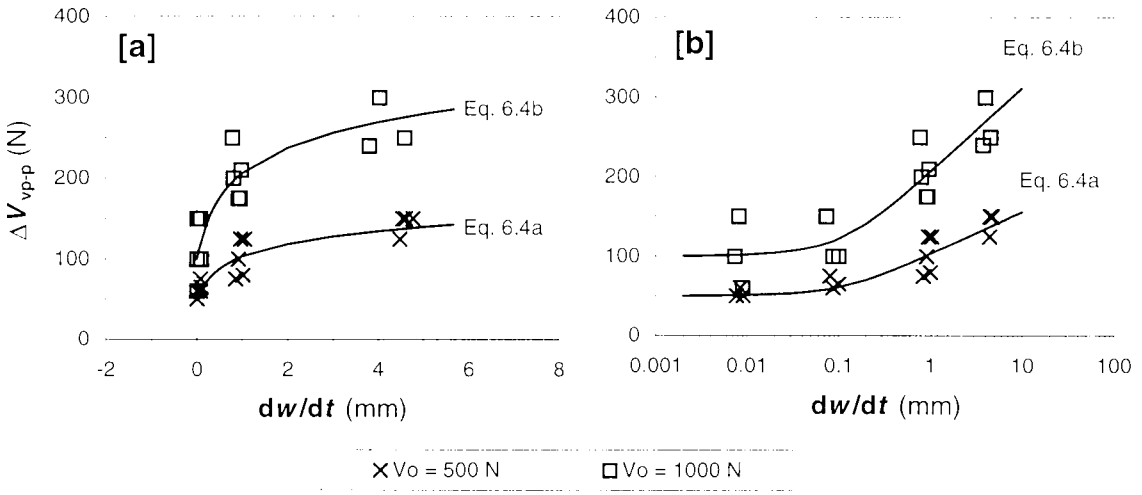

Figure 6.44 The measured load increment during the primary stage of the vertical partially-drained tests versus the measured displacement rate: **[a]** normal x-axis; and **[b]** logarithmic x-axis

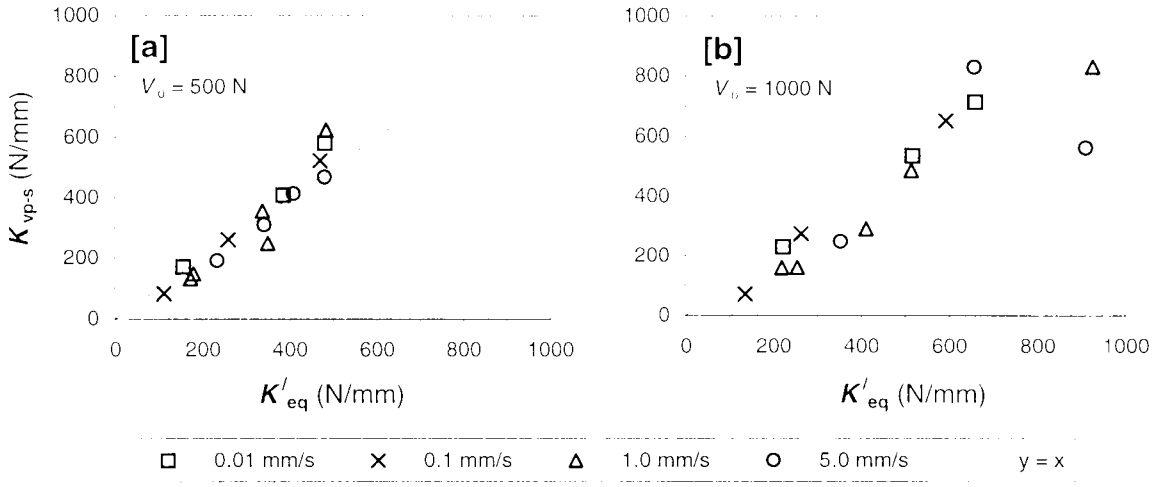

Figure 6.45 The secondary stiffness of the vertical partially-drained tests: **[a]** from 500 N; and **[b]** from 1000 N

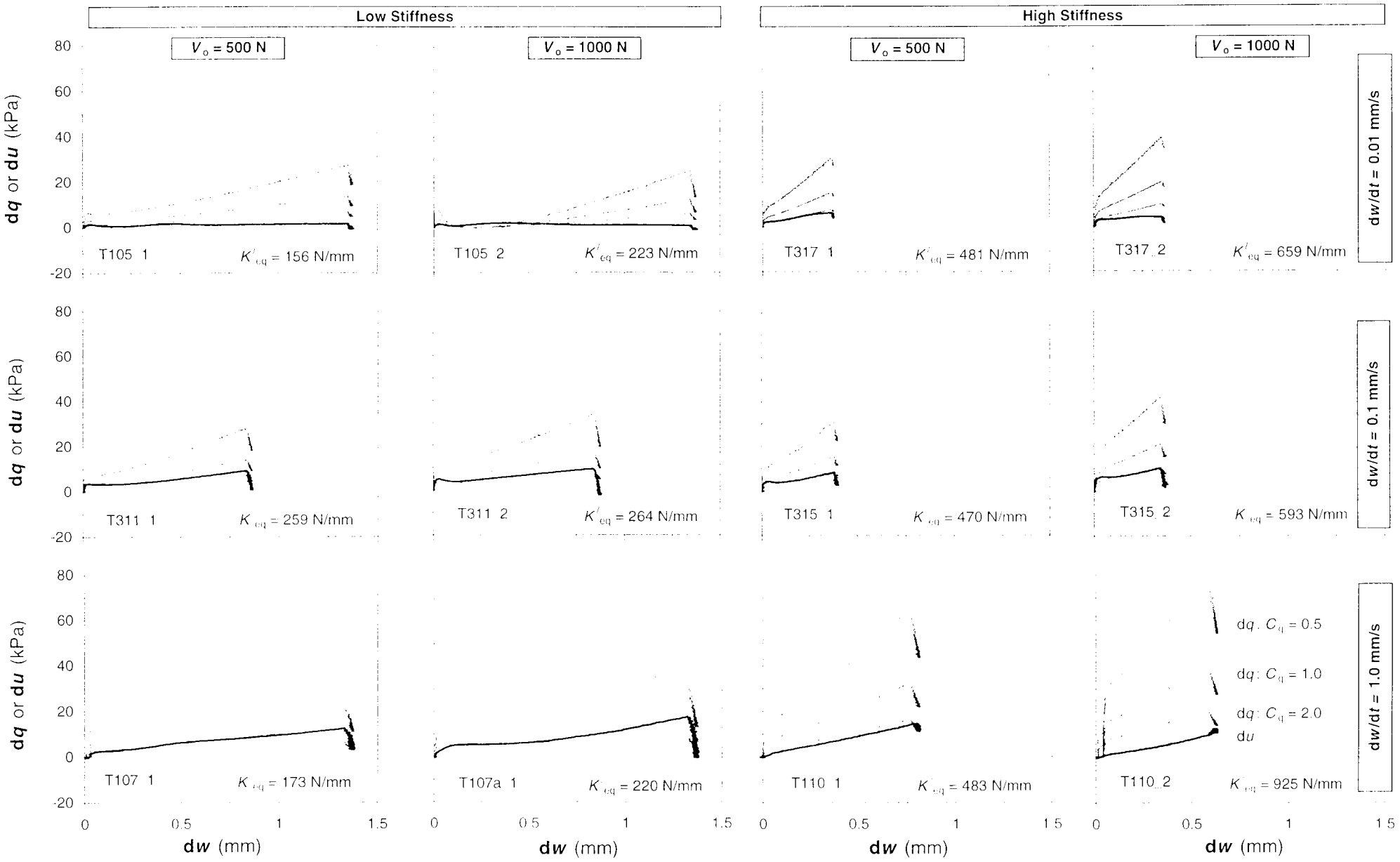

Figure 6.46 Pore pressure response compared with total stress response at centre of footing (total stress for C_q values of 2.0, 1.0 and 0.5)

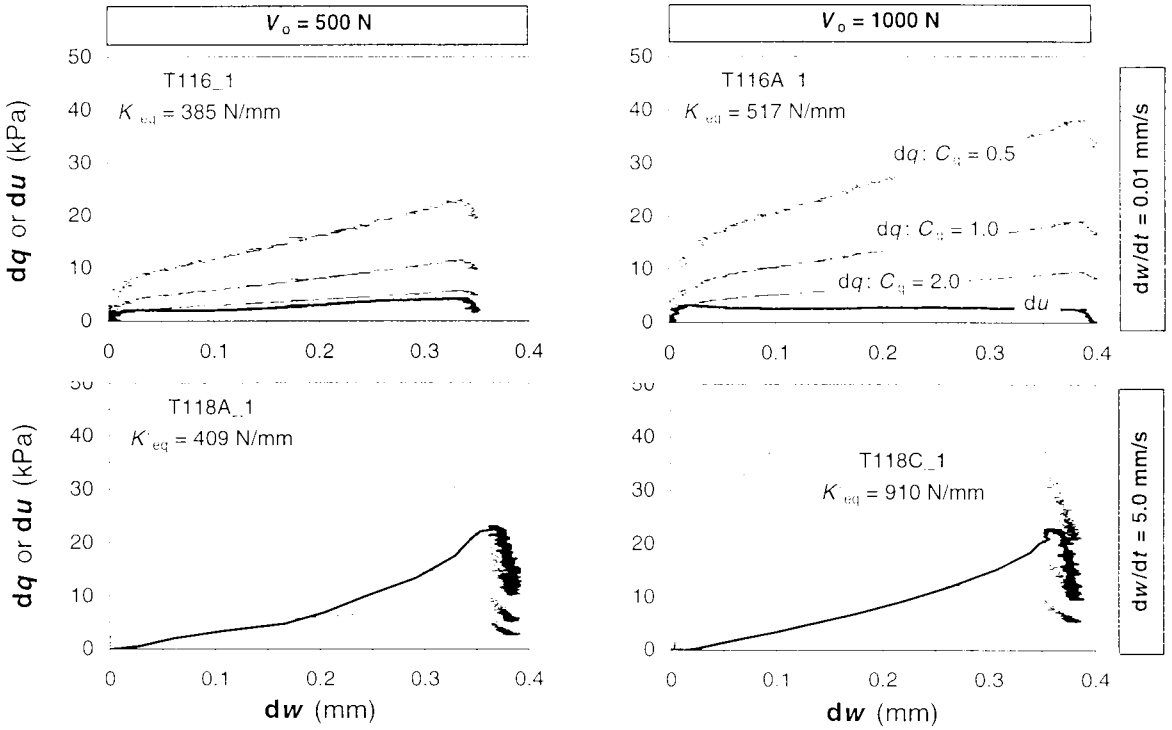

Figure 6.47 Effect of a change in the displacement rate on the pore pressure response, in vertical partially-drained tests with similar sample stiffnesses
(estimated total stress at the centre of the footing for C_q values of 2.0, 1.0 and 0.5)

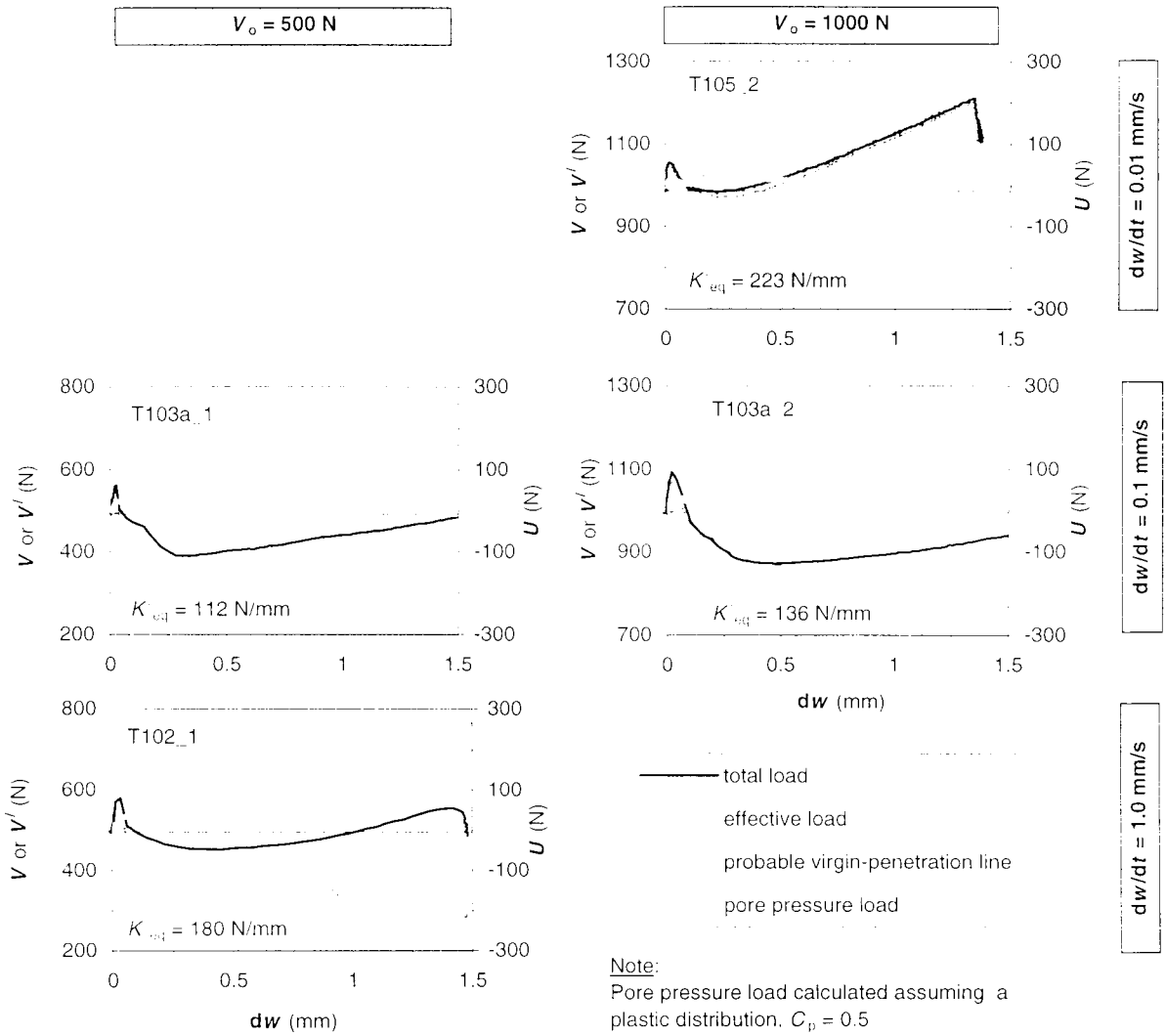

Figure 6.48 Load:deformation behaviour of vertical partially-drained tests that exhibited evidence of liquefaction

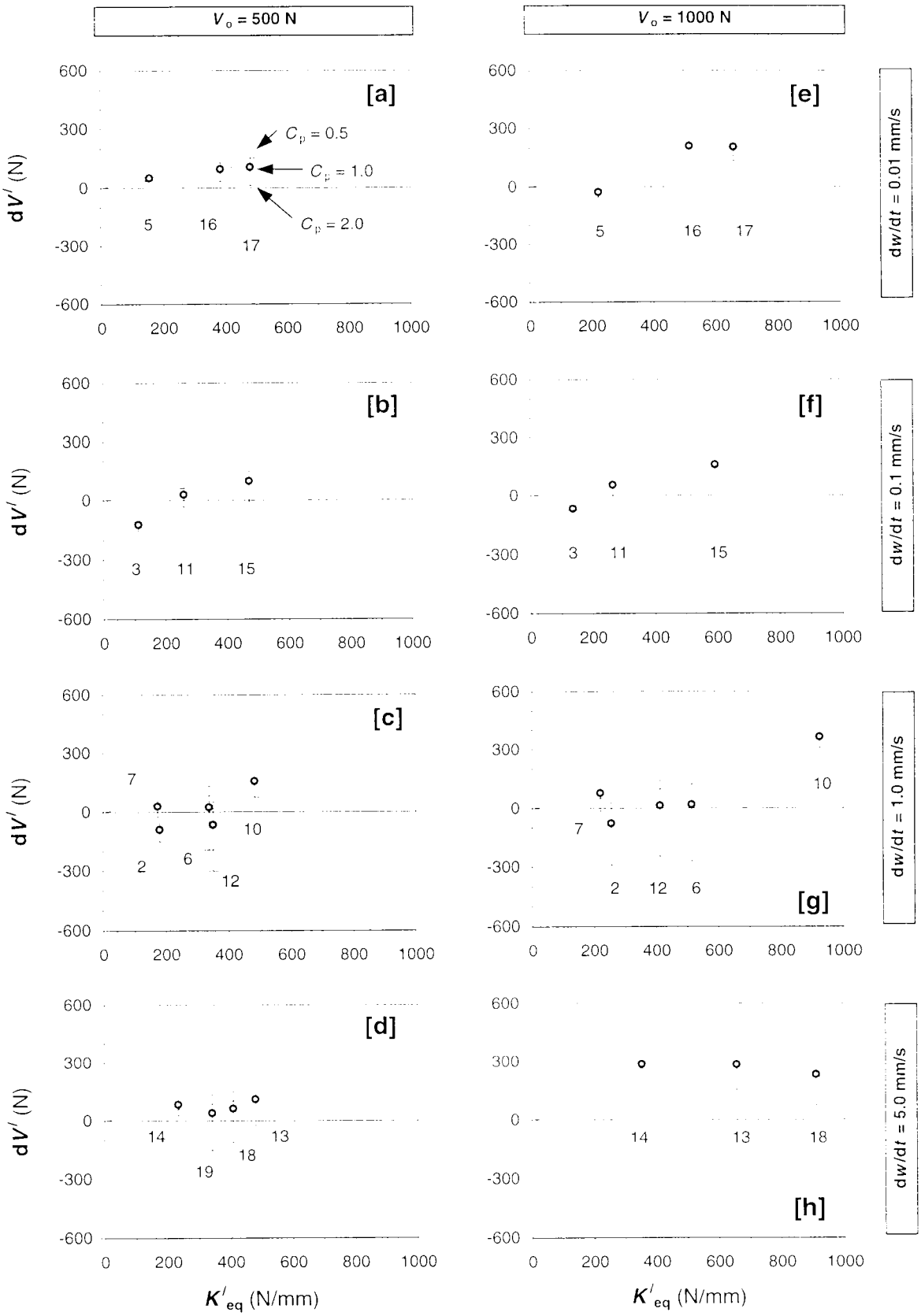

Note:

- The values of dV were calculated for dw approximately equal to 0.24 mm. The maximum and minimum values of dw were 0.194 mm and 0.252 mm, and the standard deviation was 0.0147 mm.
- The dotted lines indicate the value of dV for 0.24 mm of penetration at the equivalent effective stiffness.

Figure 6.49 The range of possible values of the change in effective load in the vertical partially drained tests

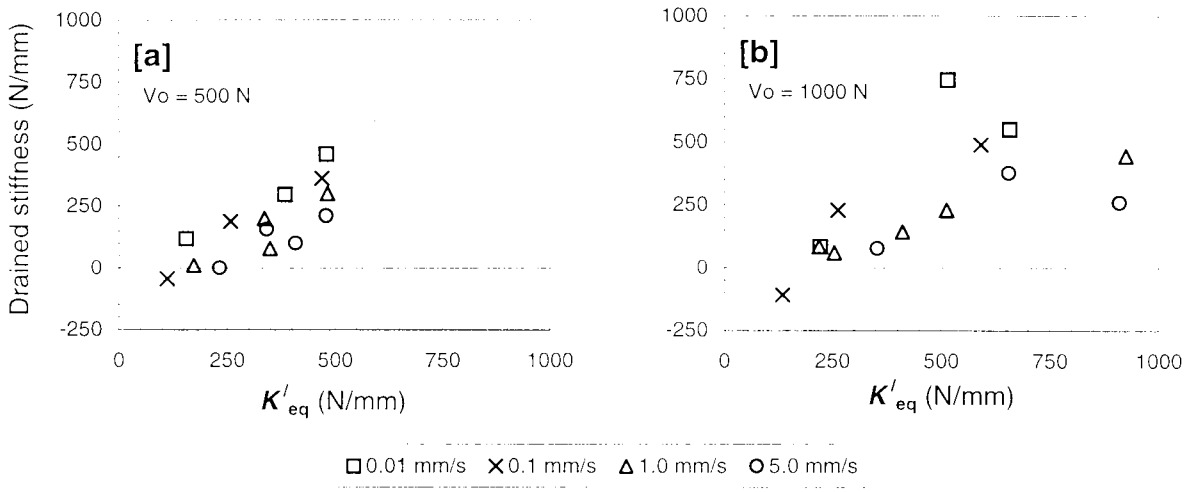

Notes:
- Drained stiffness measured from start of move to point after end of move at which the excess pore pressures were zero

Figure 6.50 The overall drained stiffness of the vertical partially-drained tests: **[a]** from V = 500 N; and **[b]** from V = 1000 N

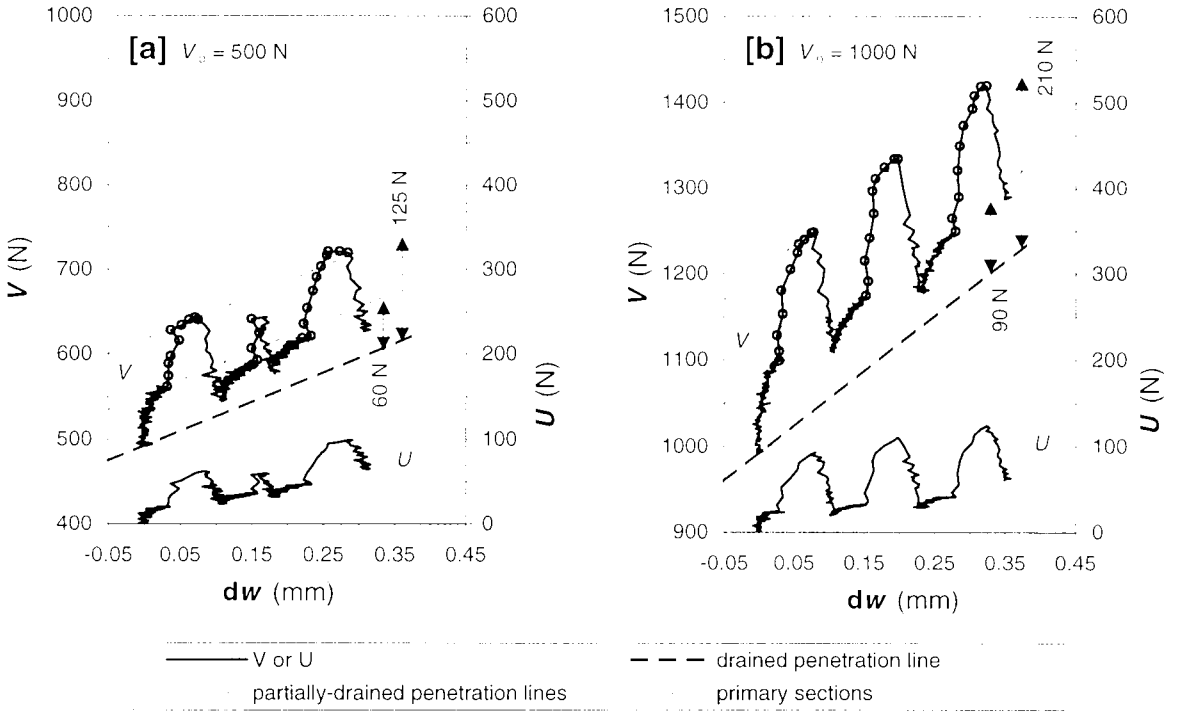

Note:
- Drained rate = 0.001 mm/s.
- Partially-drained rates = 0.01/1.00 mm/s.
- Drained stiffness equal to 350 N/mm at 500N and equal to 640 N/mm at 1000 N.

Figure 6.51 The multi-rate vertical tests in T120: **[a]** from 500 N; and **[b]** from 1000 N

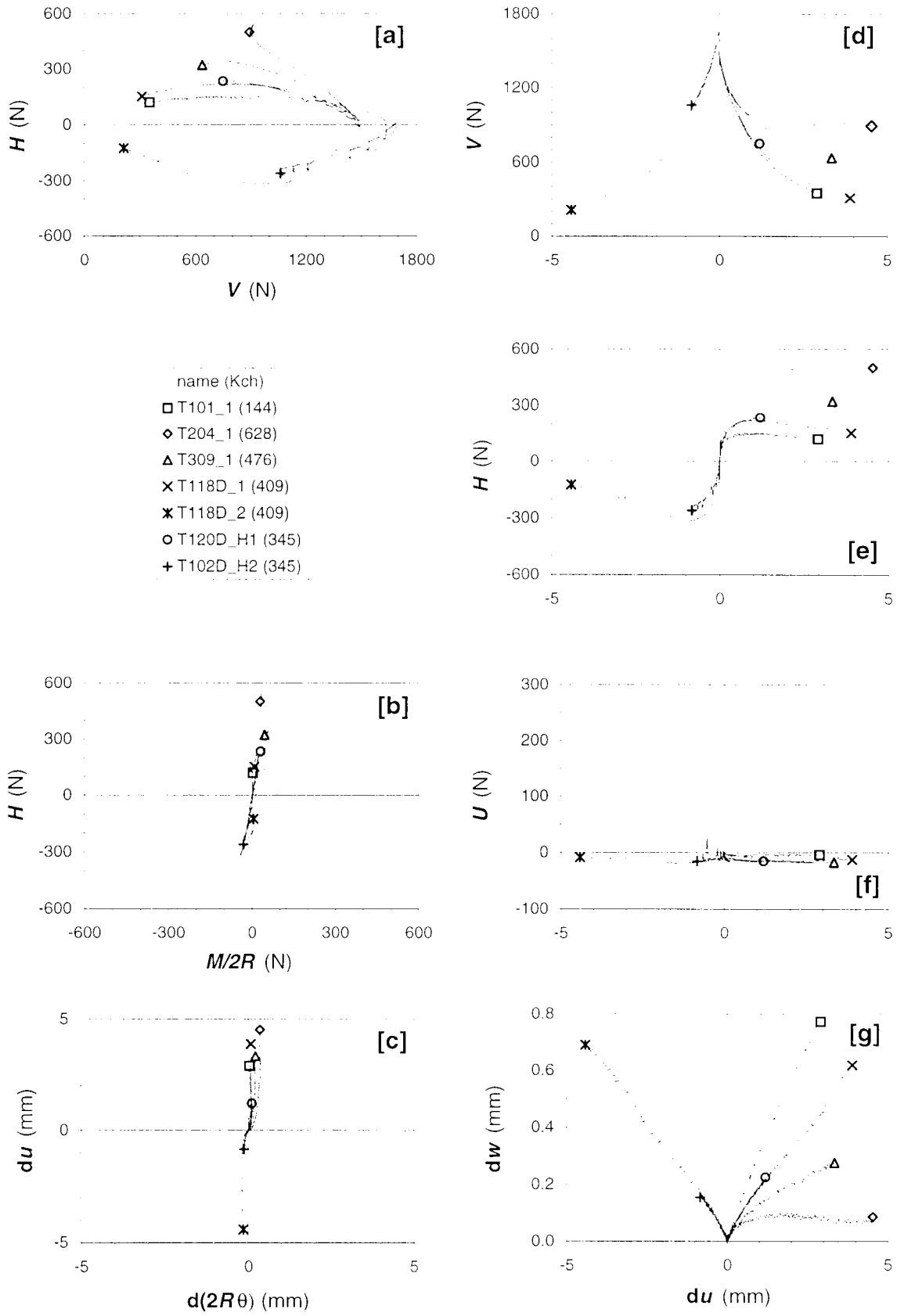

Figure 7.1 Load and displacement interaction diagrams of the drained horizontal sideswipe tests (intended $du/dt = 0.001$ mm/s)

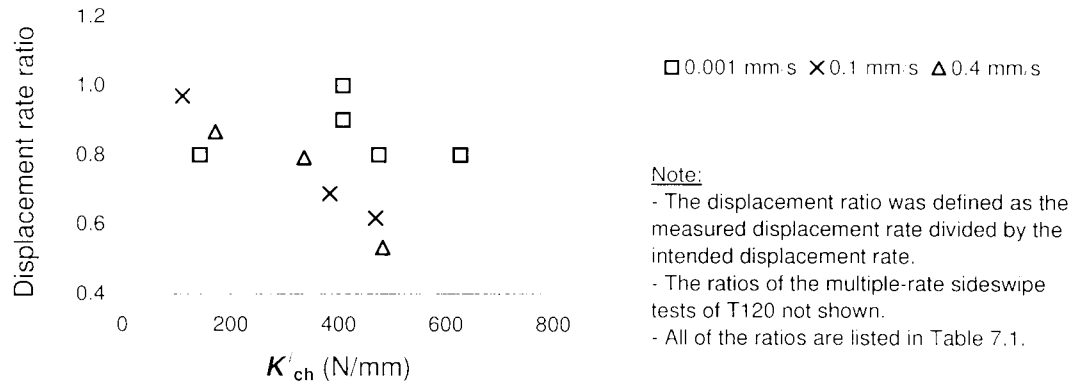

Figure 7.2 The variation of the displacement rate ratio of the horizontal sideswipe tests with the characterisation stiffness

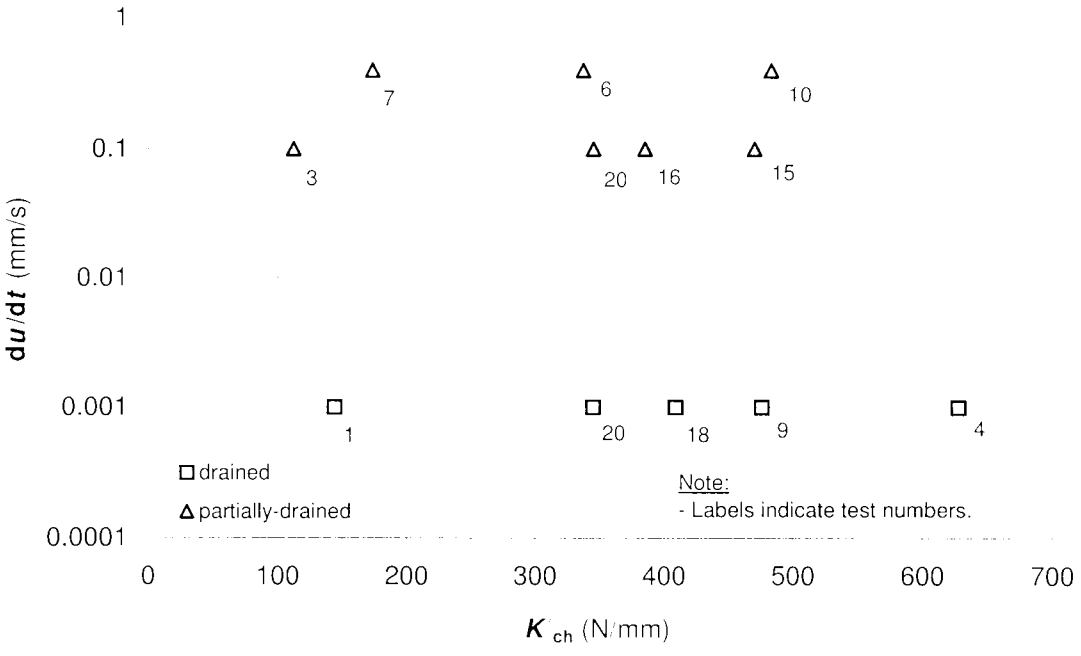

Figure 7.3 Distribution of the displacement rate of the horizontal sideswipe tests with the characterisation stiffness

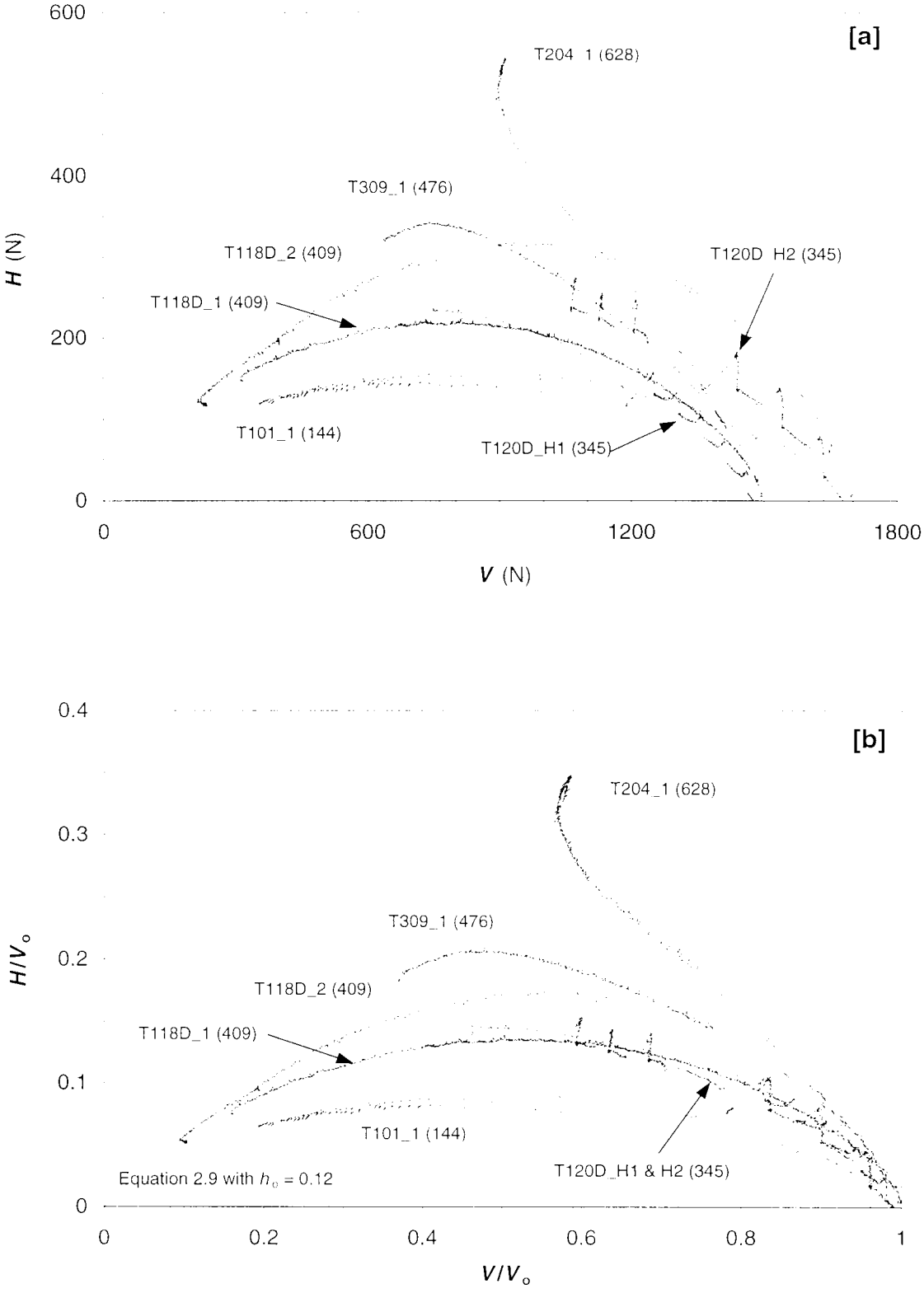

Note:
- Labels give test number and characterisation stiffness (in brackets).
- Tests T118D_2 and T120D_H2 were displaced in the negative horizontal direction.

Figure 7.4 Drained horizontal sideswipe tests: **[a]** in V:H space; and **[b]** normalised by V_o

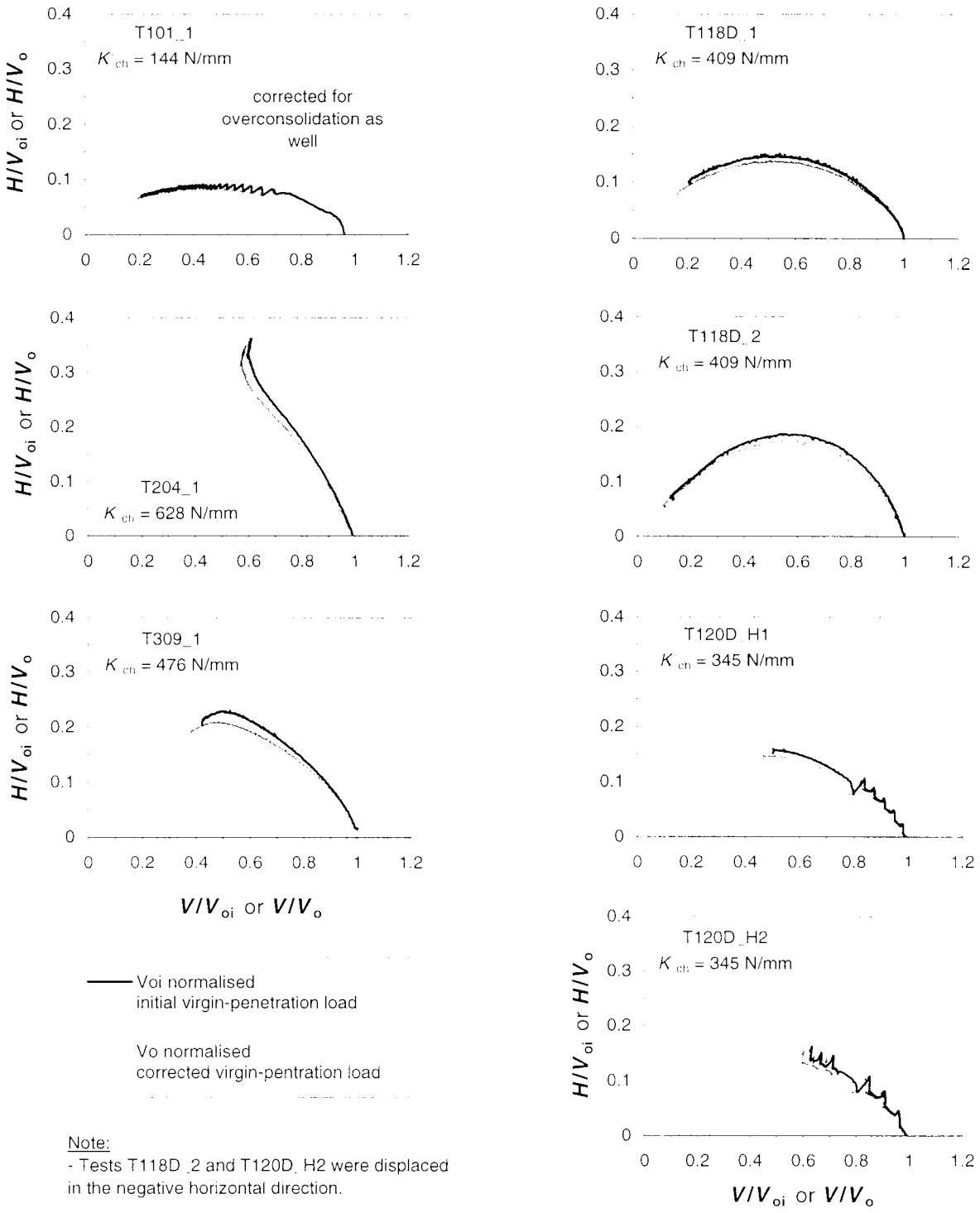

Note:
- Tests T118D_2 and T120D_H2 were displaced in the negative horizontal direction.

Figure 7.5 Correction for vertical penetration of the drained horizontal sideswipe tests

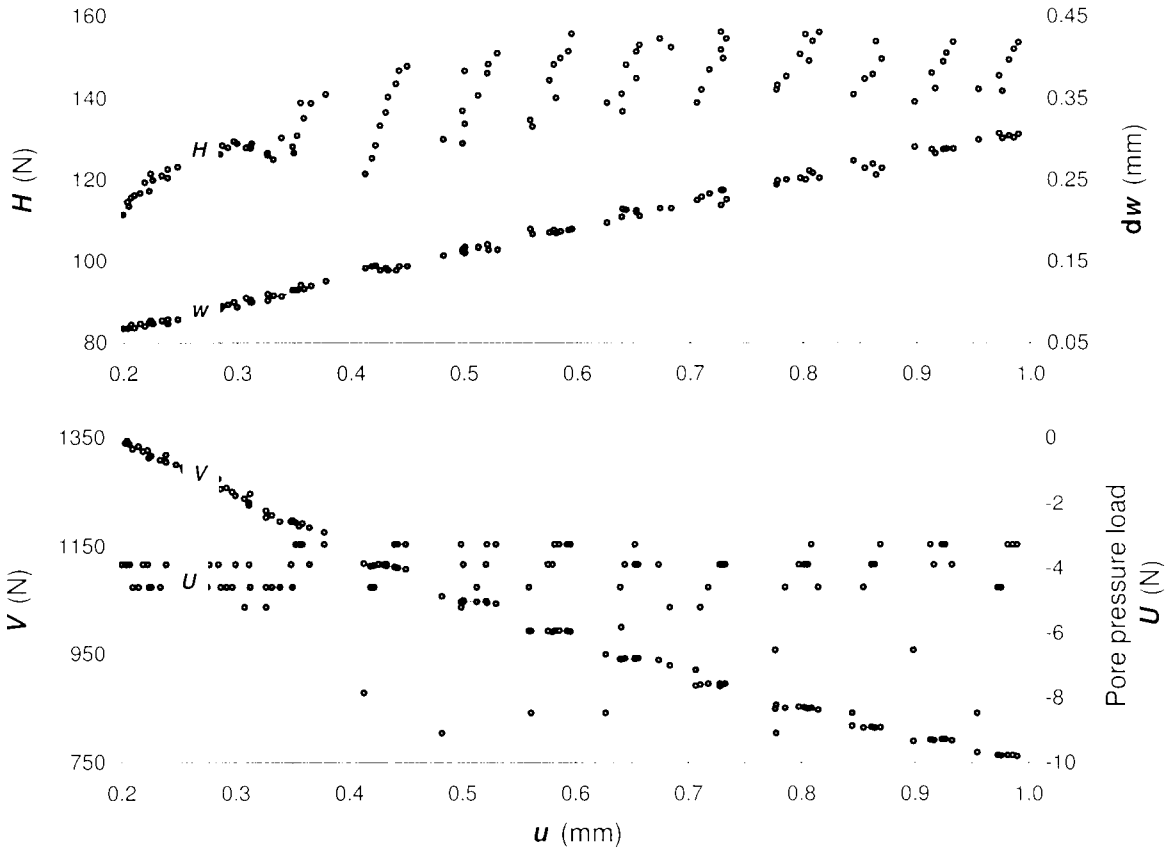

Figure 7.6 Detail of the saw-tooth shaped sideswipe of test T101

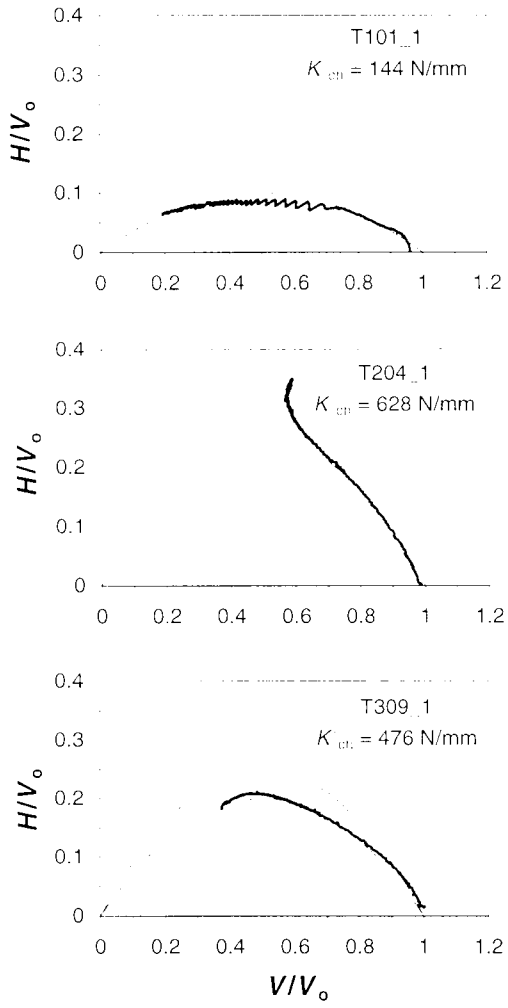

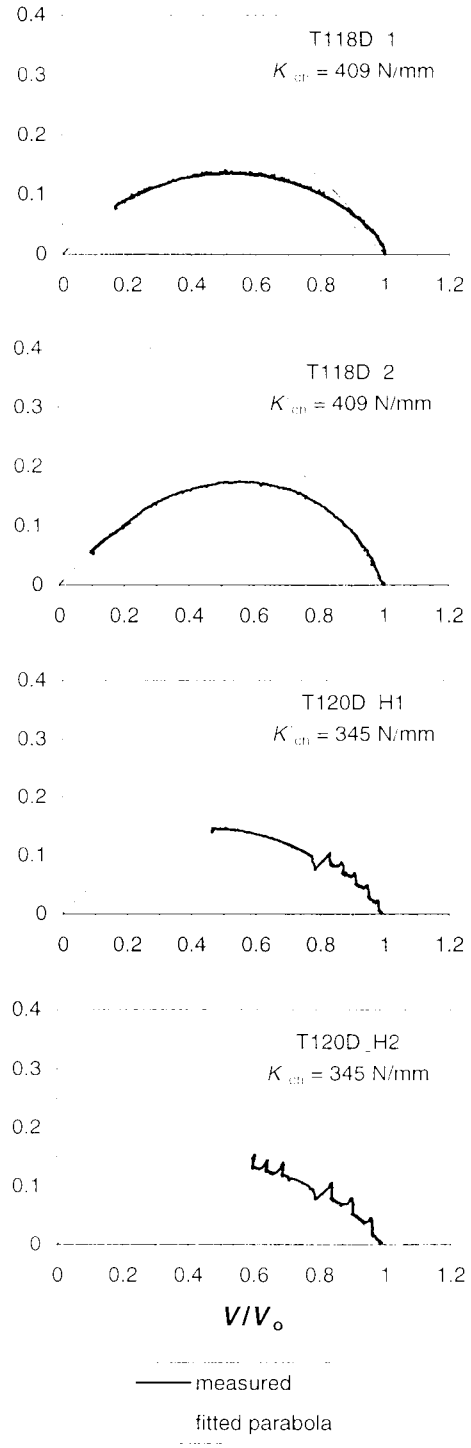

Test	Position	V_o	V_c/V_{cn}	h_c
T101_1	start	1700	0.68	0.100
	end	1827	0.73	
T204_1	start	1500	0.15	0.250
	end	1580	0.16	
T309_1	start	1495	0.19	0.250
	end	1707	0.22	0.200
T118D_1	start	1495	0.20	0.200
	end	1955	0.26	0.135
T118D_2	start	1700	0.23	0.250
	end	2250	0.30	0.150
T120D_H1	start	1489	0.23	0.145
	end	1623	0.25	
T120D_H2	start	1693	0.26	0.140
	end	1790	0.28	

Note:
- Tests T118D_2 and T120D_H2 were displaced in the negative horizontal direction.

Figure 7.7 Drained horizontal sideswipe tests and fitted parabolas

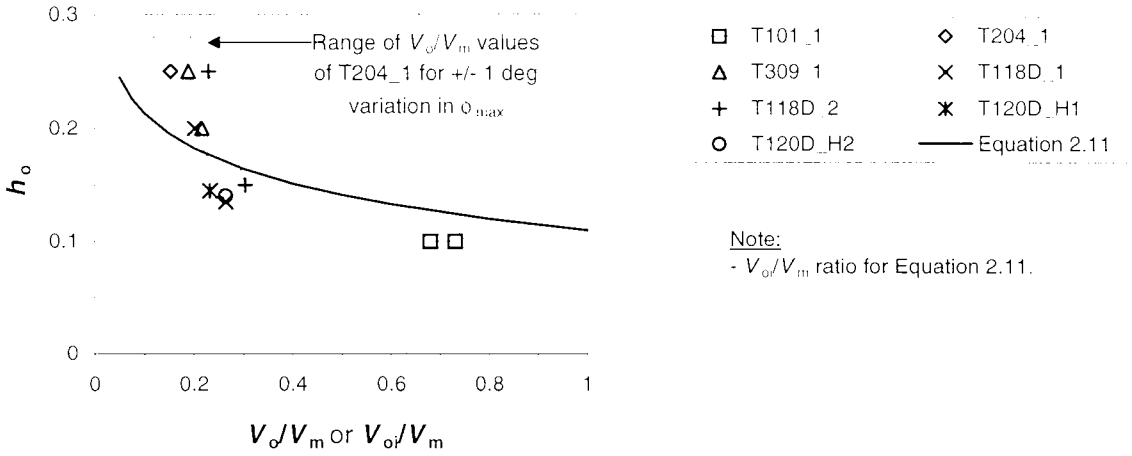

Figure 7.8 Relationship between normalised peak horizontal load and V_o/V_m ratio

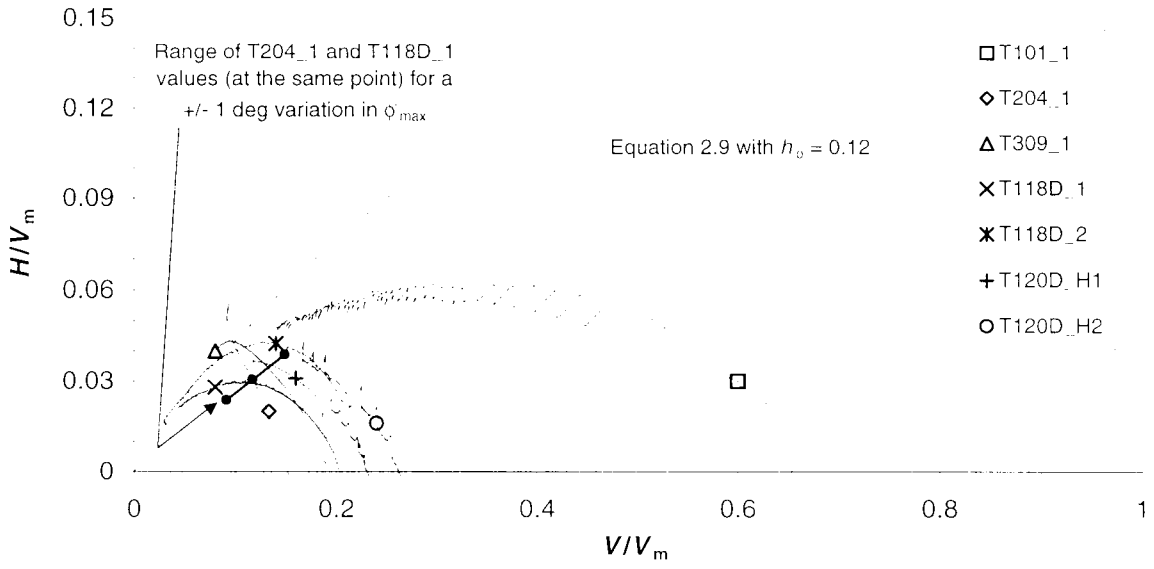

Figure 7.9 Drained horizontal sideswipe tests normalised by estimated values of V_m

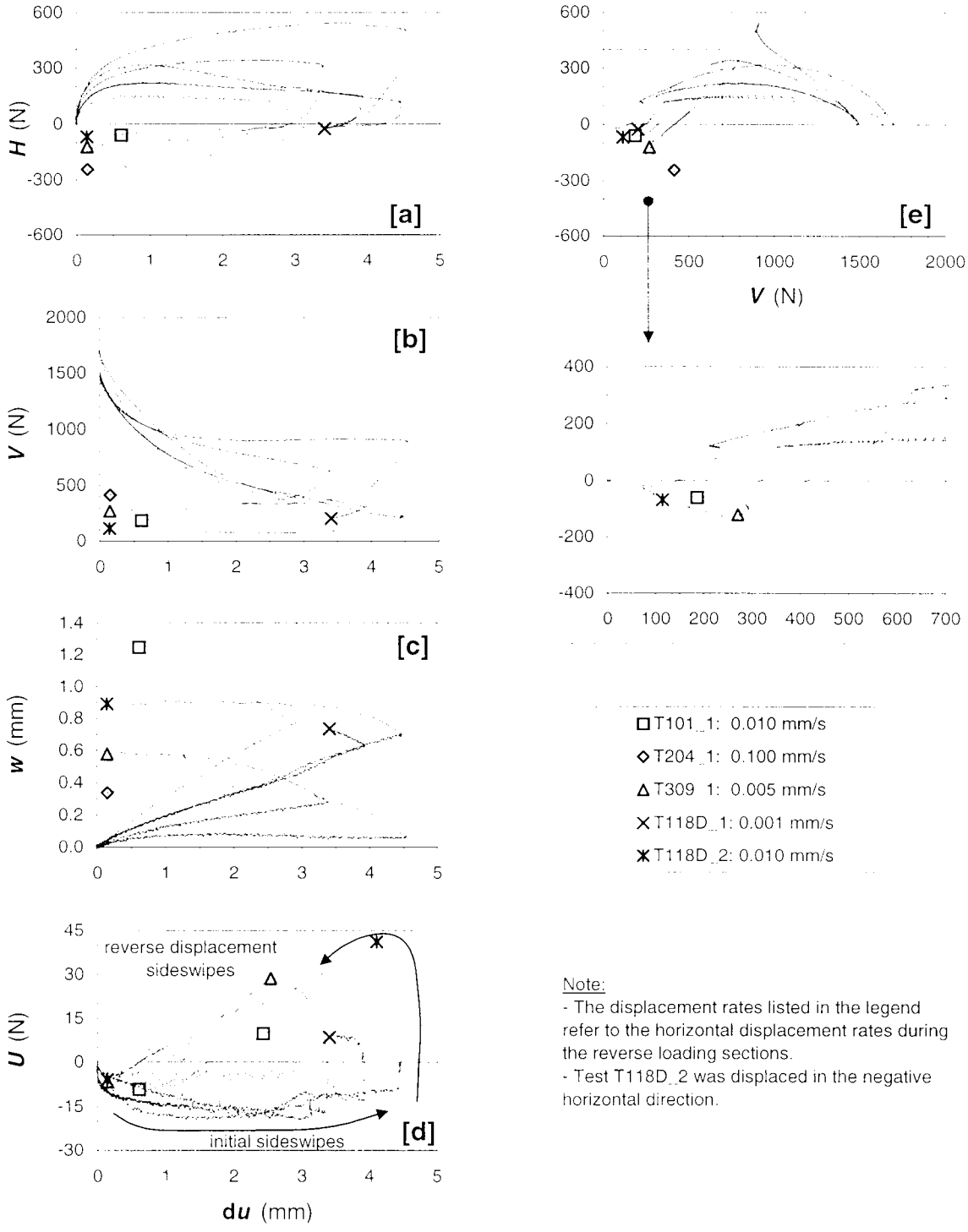

Figure 7.10 The reverse displacement sections associated with the drained horizontal sideswipe tests

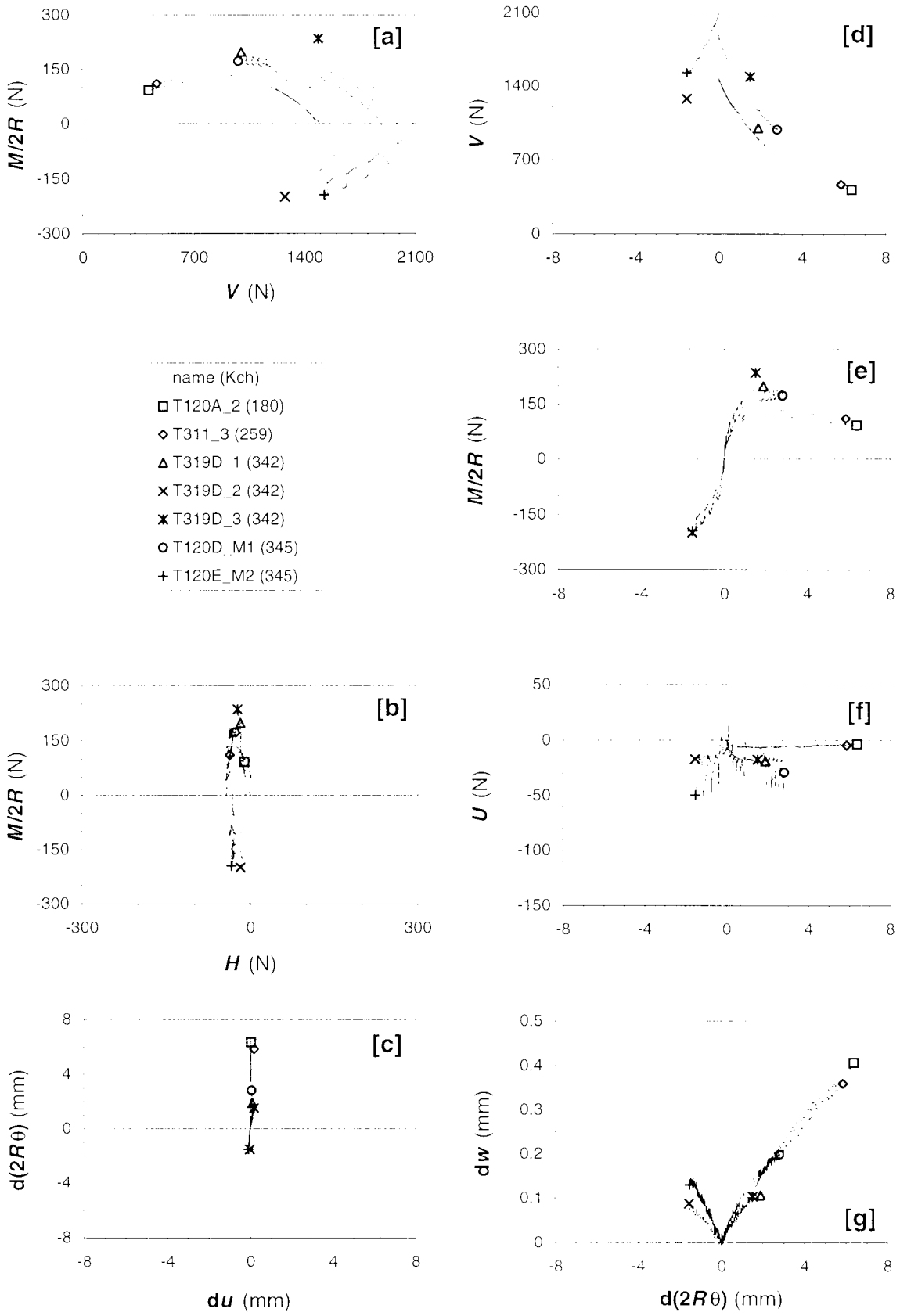

Figure 7.11 Load and displacement interaction diagrams of the drained moment sideswipe tests (intended $d(2R\theta)/dt = 0.0026$ mm/s)

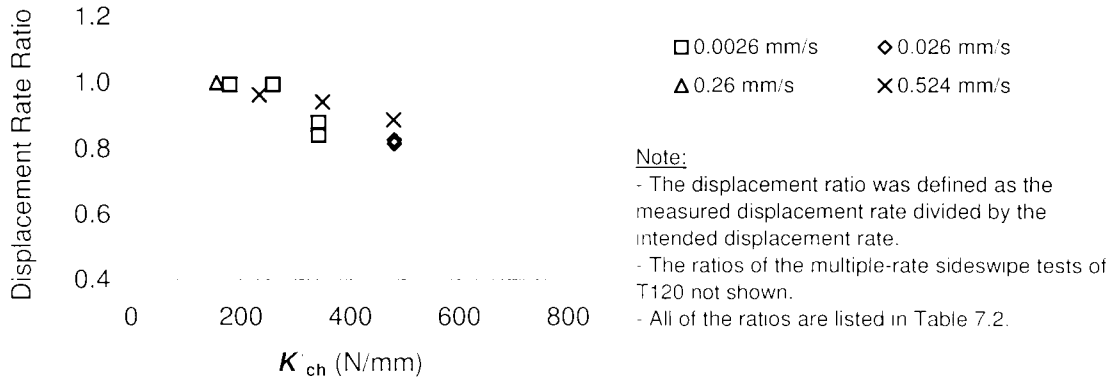

Figure 7.12 The variation of the displacement rate ratio of the moment sideswipe tests with the characterisation stiffness

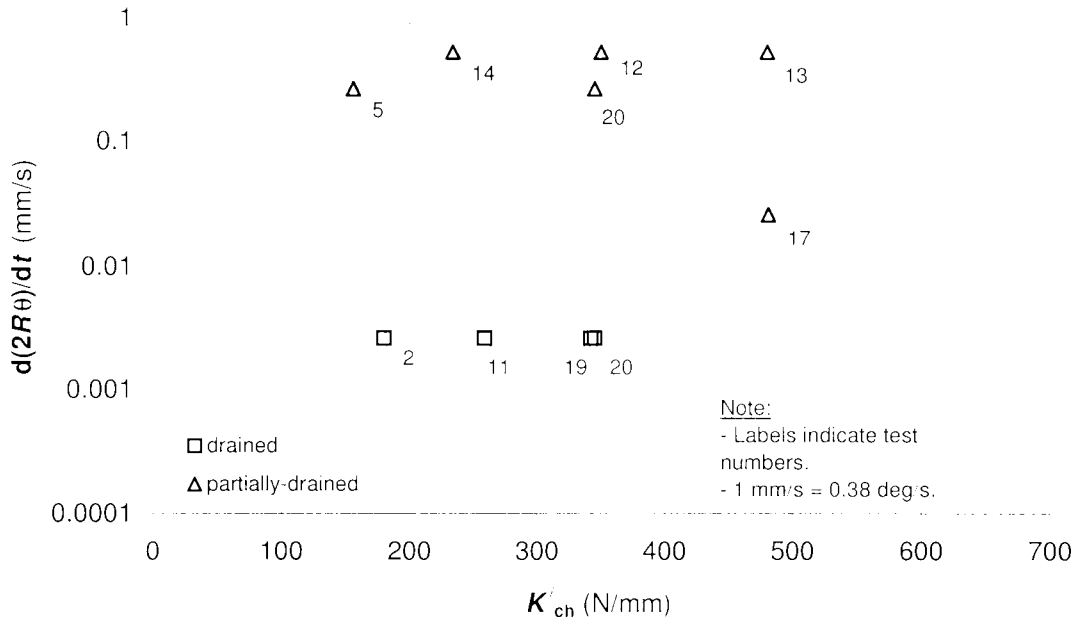

Figure 7.13 Distribution of the displacement rate of the moment sideswipe tests with the characterisation stiffness

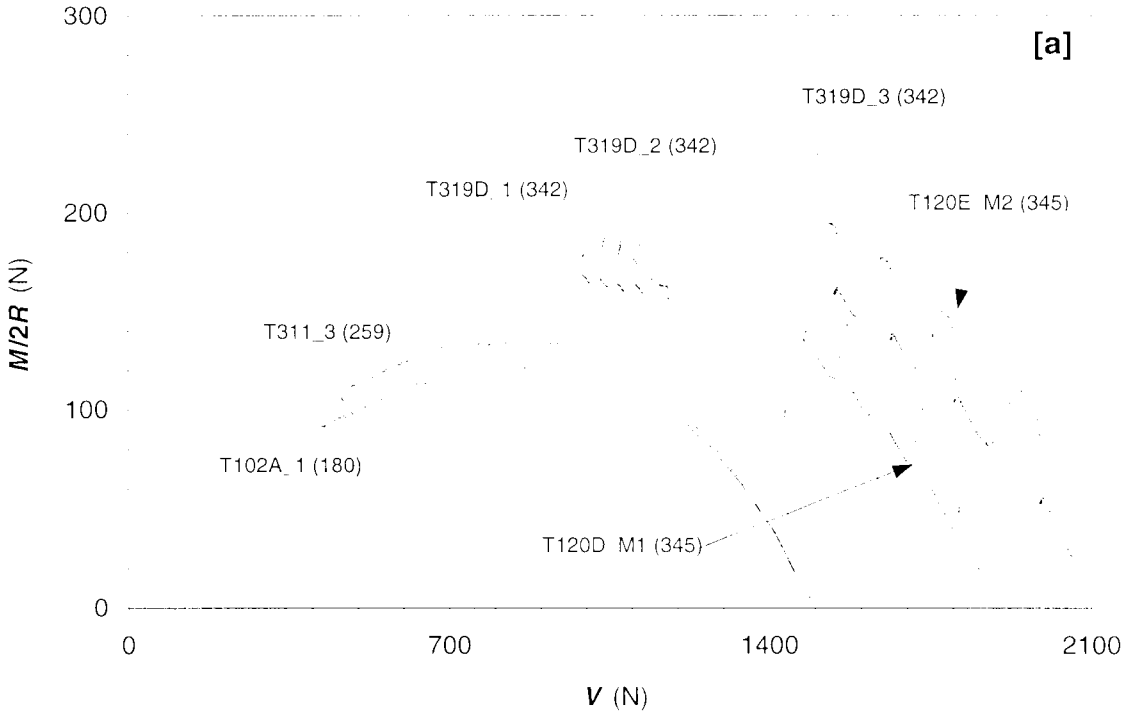

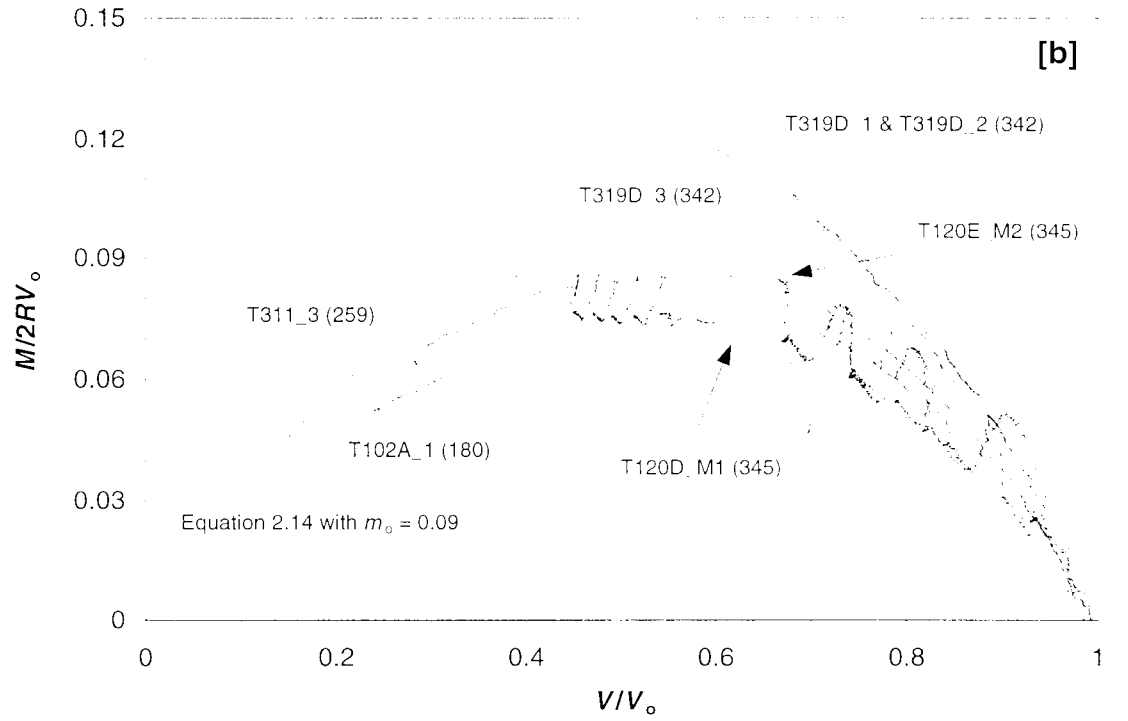

Note:
- Labels give test number and characterisation stiffness (in brackets).
- Tests T319D_2 and T120E_M2 were displaced in the negative horizontal direction.

Figure 7.14 Drained moment sideswipe tests: **[a]** in $V:M/2R$ space; and **[b]** normalised by V_o

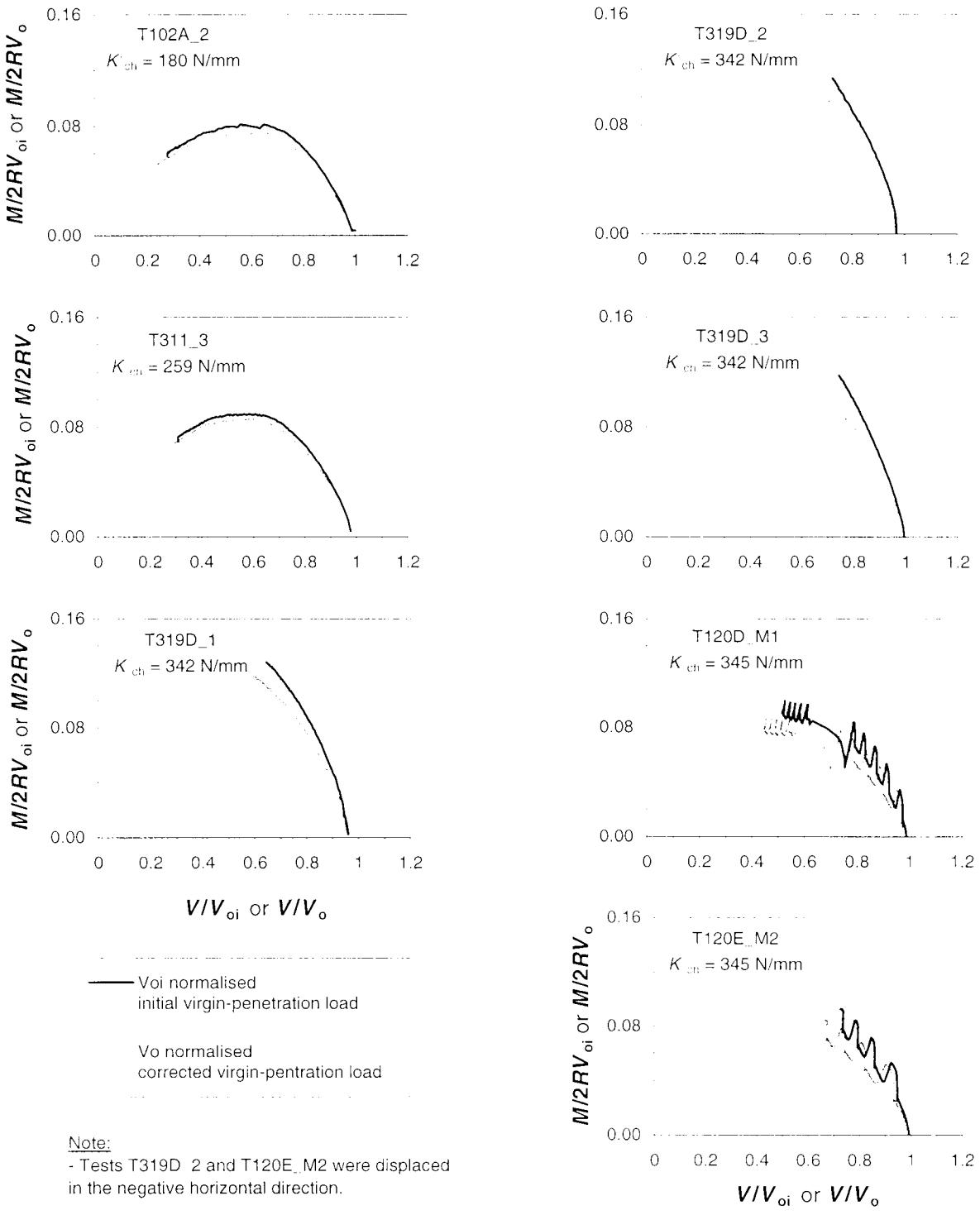

Figure 7.15 Correction of the drained moment sideswipe tests for vertical penetration

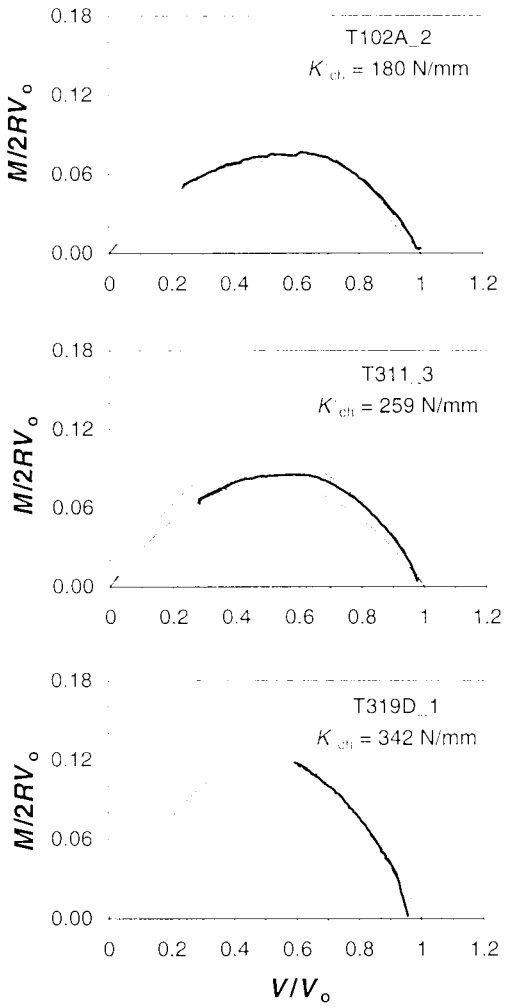

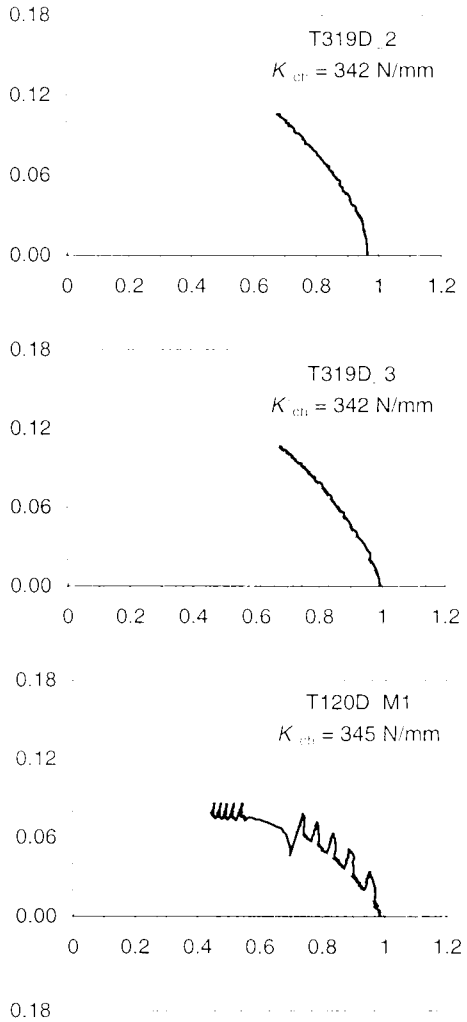

Test	Position	V_o	V_o/V_m	m_o
T102A_2	start	1500	0.27	0.09
	end	1752	0.32	0.07
T311_3	start	1500	0.39	0.10
	end	1640	0.43	0.08
T319D_1	start	1500	0.22	
	end	1627	0.24	0.12
T319D_2	start	1700	0.25	
	end	1825	0.26	0.12
T319D_3	start	2000	0.29	
	end	2200	0.32	0.12
T120D_M1	start	1900	0.30	0.08
	end	2200	0.34	
T120E_M2	start	2100	0.33	0.08
	end	2293	0.36	

measured

fitted parabola

Note:
- Tests T319D_2 and T120_M2 were displaced in the negative horizontal direction.

Figure 7.16 Drained moment sideswipe tests and fitted parabolas

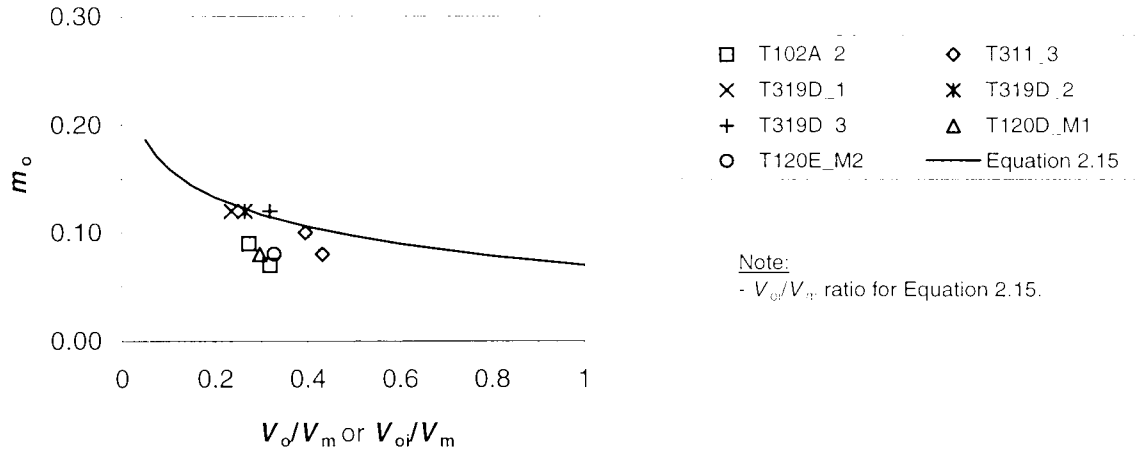

Figure 7.17 Relationship between normalised peak moment load and V_o/V_m ratio

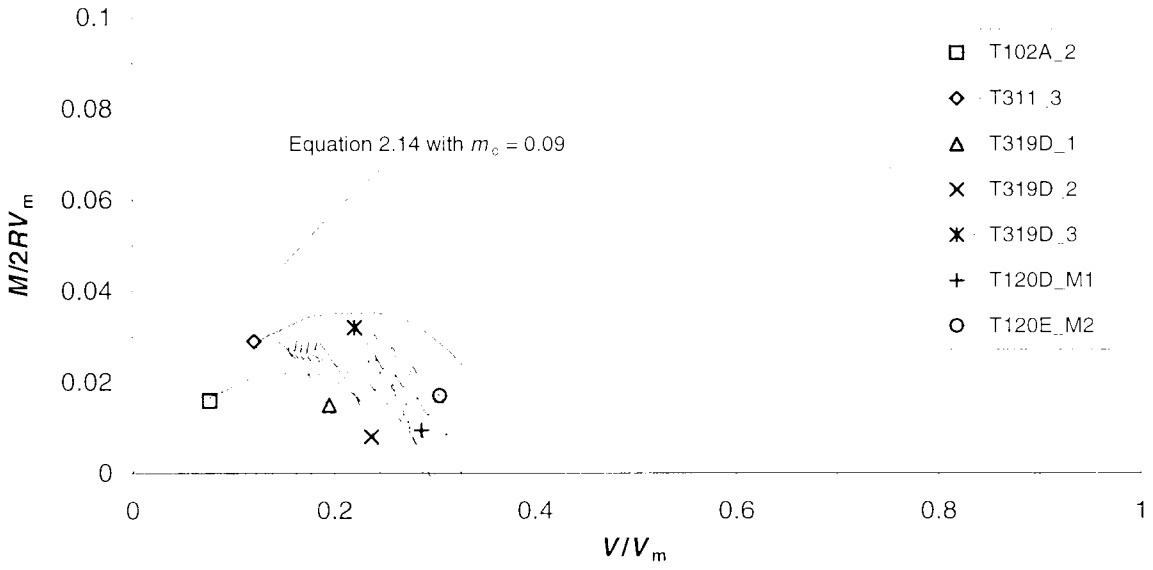

Figure 7.18 Drained moment sideswipe tests normalised by estimated values of V_m

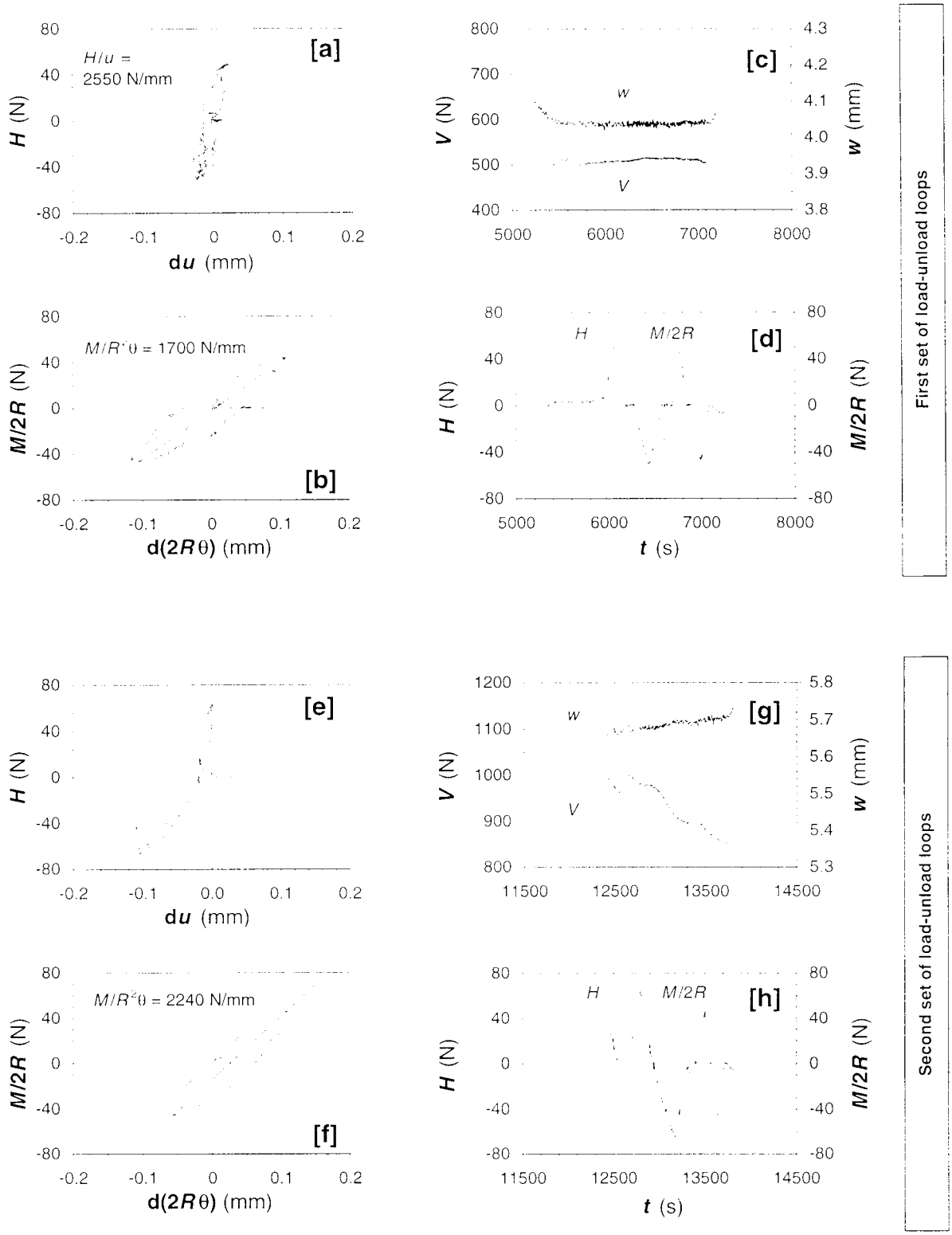

Figure 7.19 Horizontal and moment load-unload loops and associated time histories

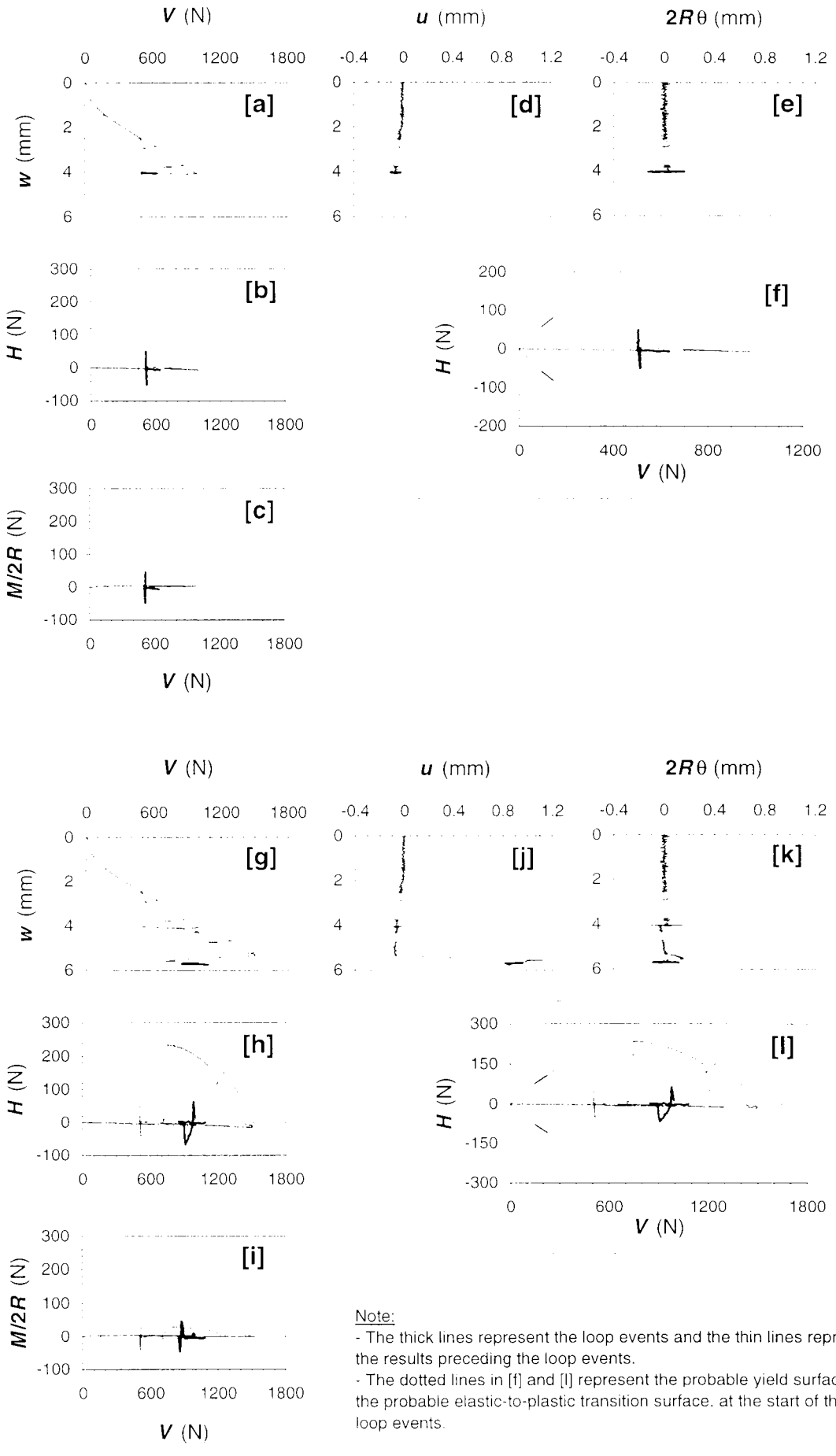

Note:
- The thick lines represent the loop events and the thin lines represent the results preceding the loop events.
- The dotted lines in [f] and [l] represent the probable yield surface and the probable elastic-to-plastic transition surface, at the start of the loop events.

Figure 7.20 Load and deformation history of horizontal and moment load-unload loops

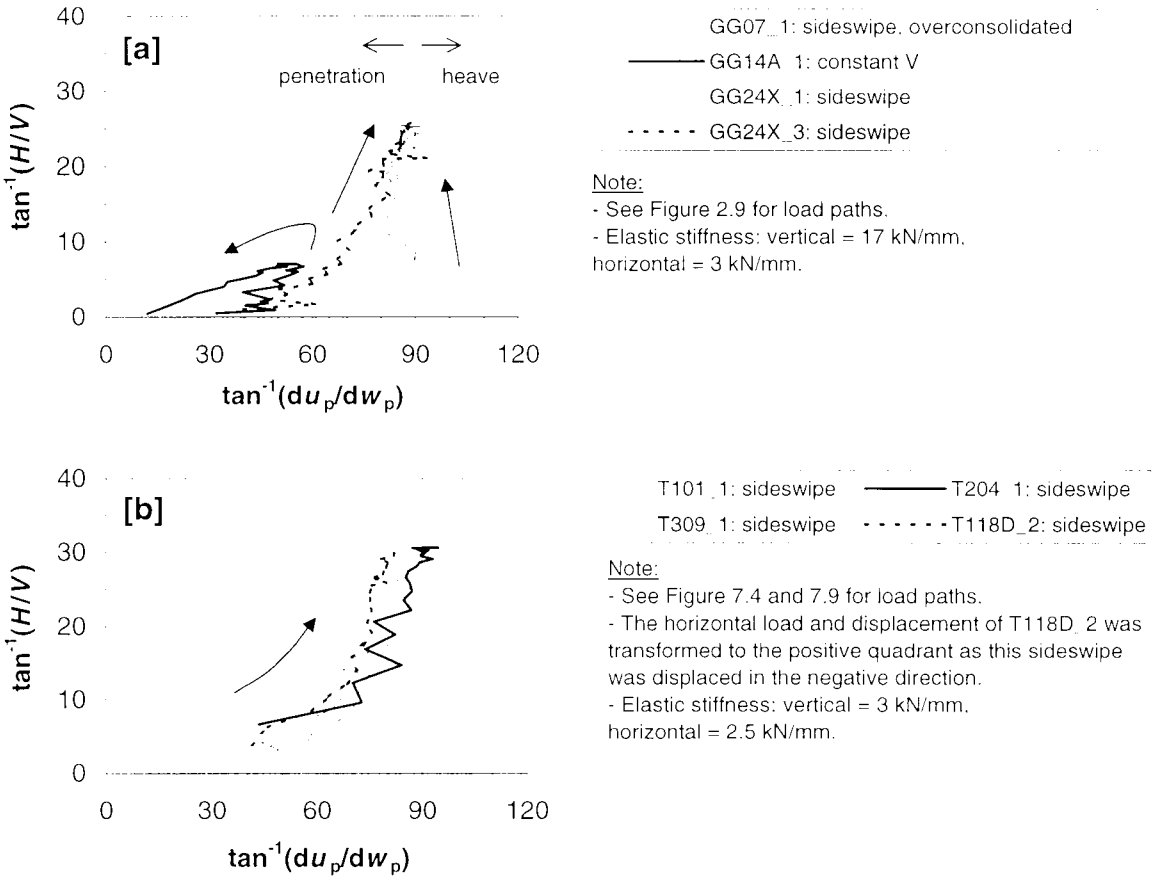

Figure 7.21 The load and plastic displacement ratios from the horizontal sideswipe tests of this project compared with data from other tests in the literature:
[a] data from Gottardi and Houlsby (1995); and **[b]** data from this investigation

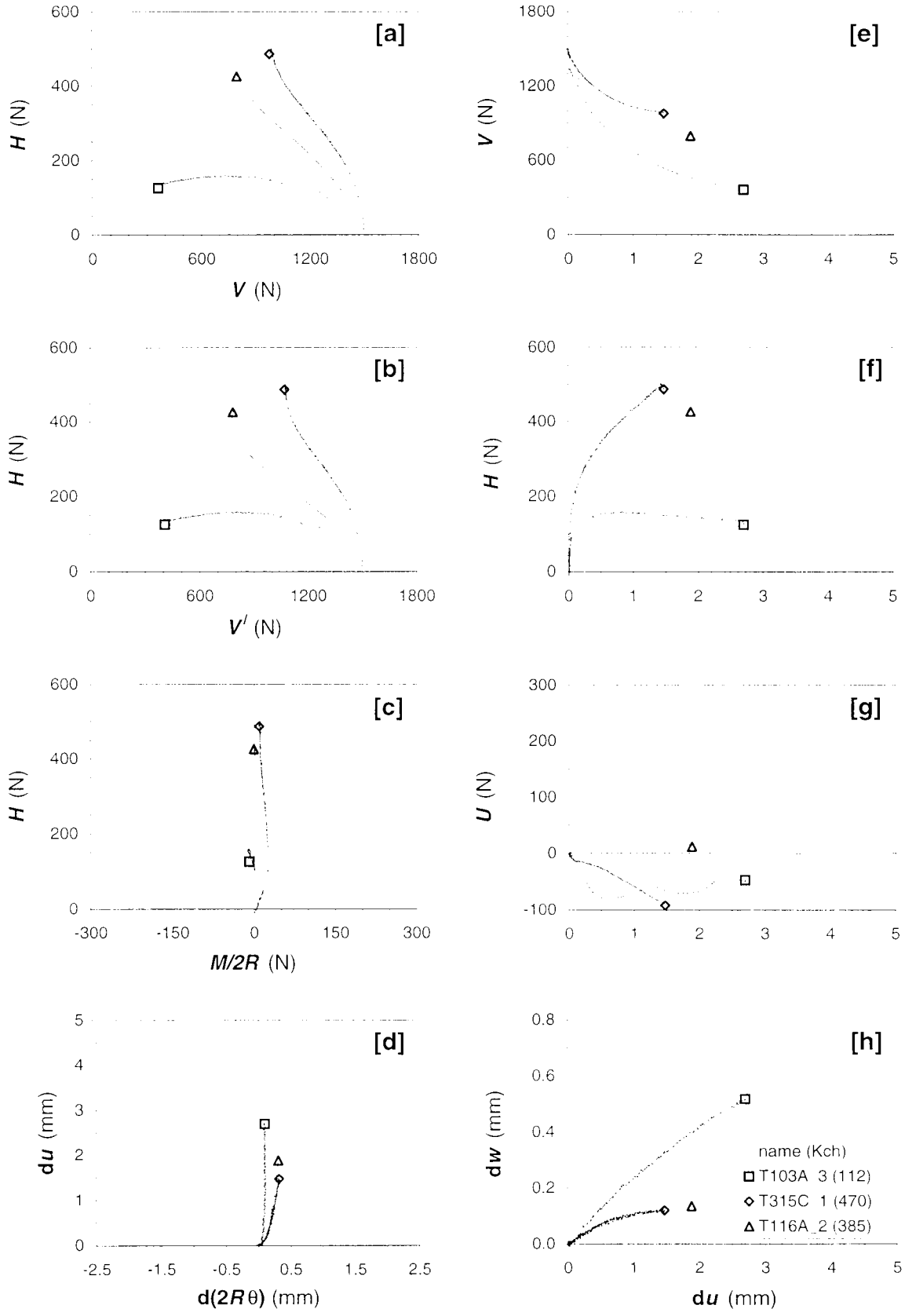

Figure 7.22 Load and displacement interaction diagrams of the partially-drained horizontal sideswipe tests (intended $du/dt = 0.1$ mm/s)

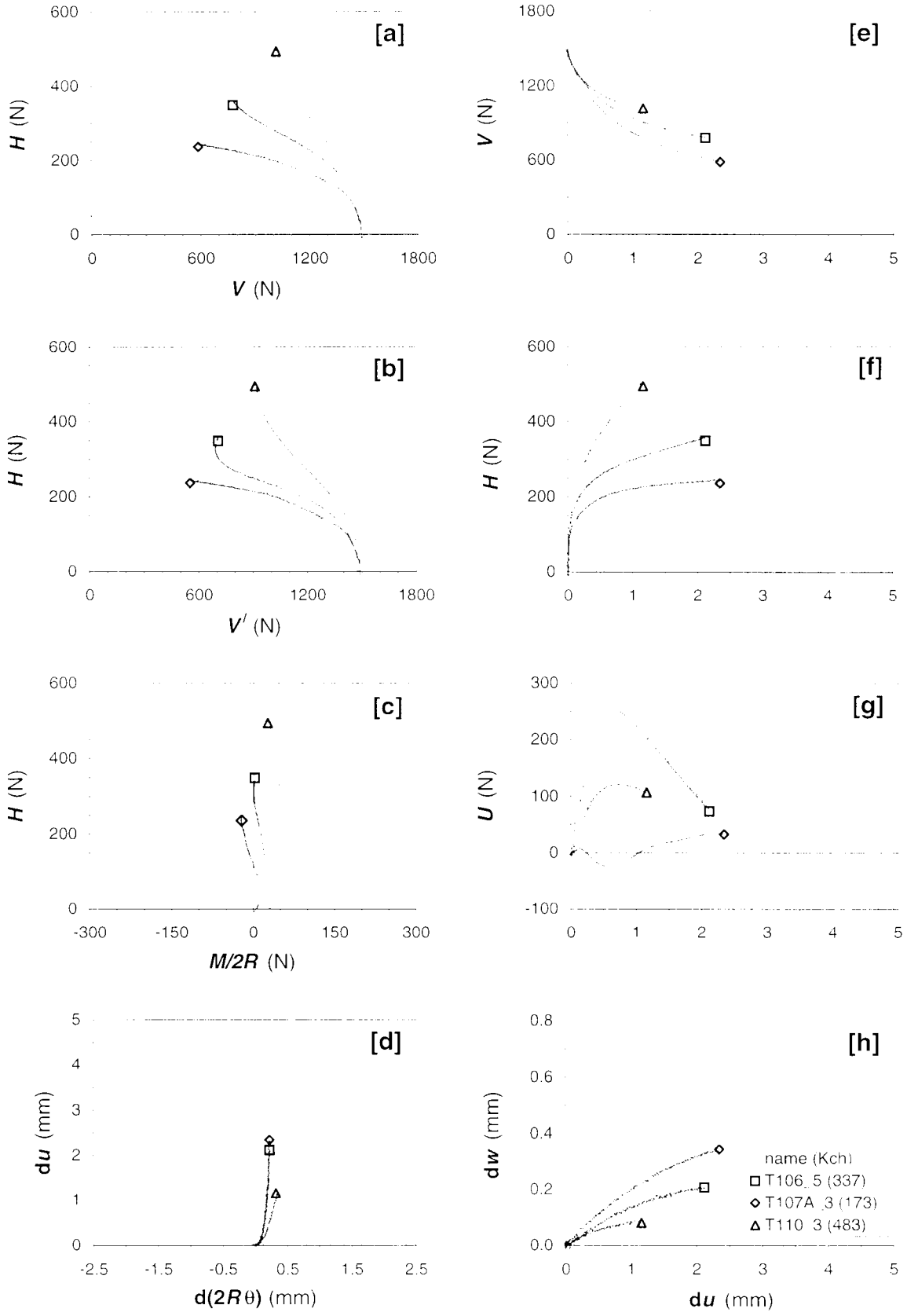

Figure 7.23 Load and displacement interaction diagrams of the partially-drained horizontal sideswipe tests (intended $du/dt = 0.4$ mm/s)

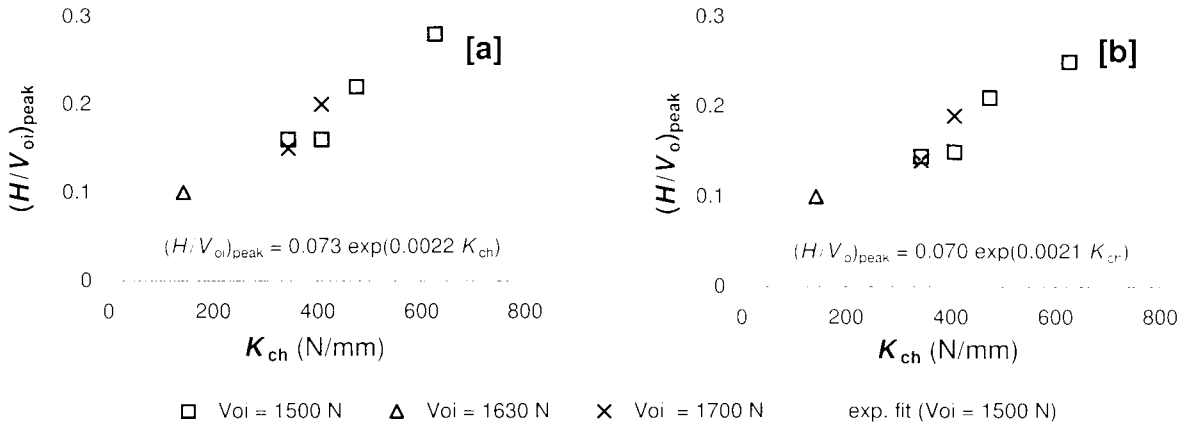

Figure 7.24 Relationship between the normalised peak horizontal load and the characteriastion stiffness from the drained sideswipe tests:
[a] not corrected for vertical penetration; and **[b]** corrected for vertical penetration

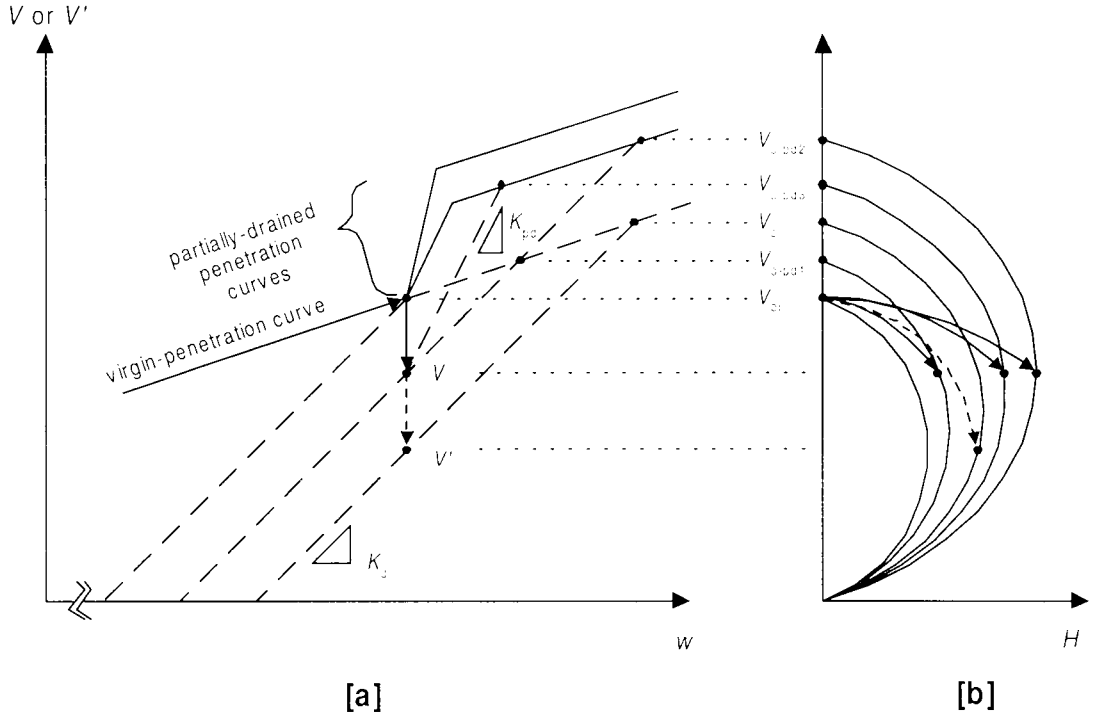

Figure 7.25 Correction for the vertical penetration in a partially-drained sideswipe test:
[a] vertical load versus penetation; and **[b]** vertical load versus horizontal load

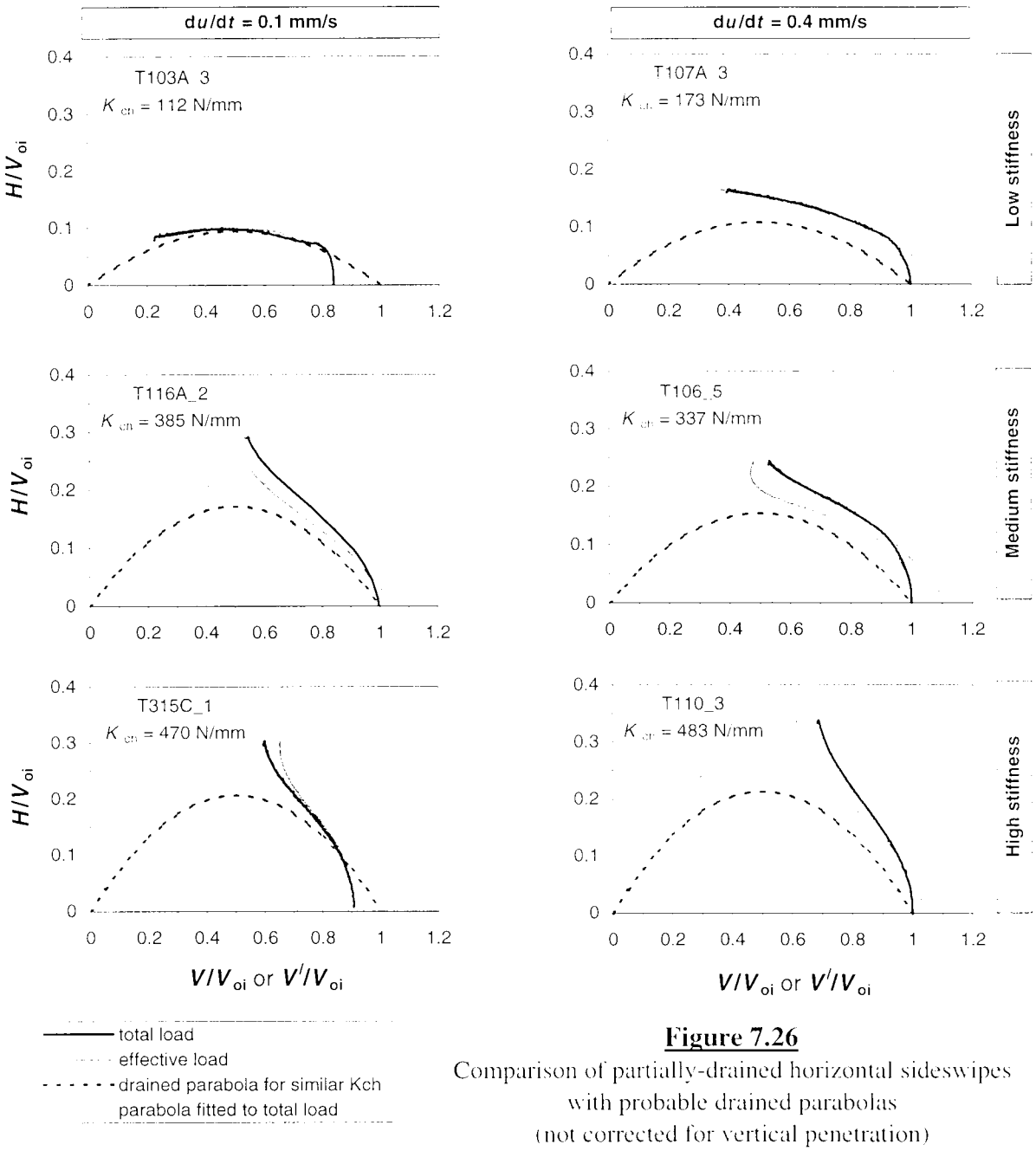

Figure 7.26
Comparison of partially-drained horizontal sideswipes with probable drained parabolas (not corrected for vertical penetration)

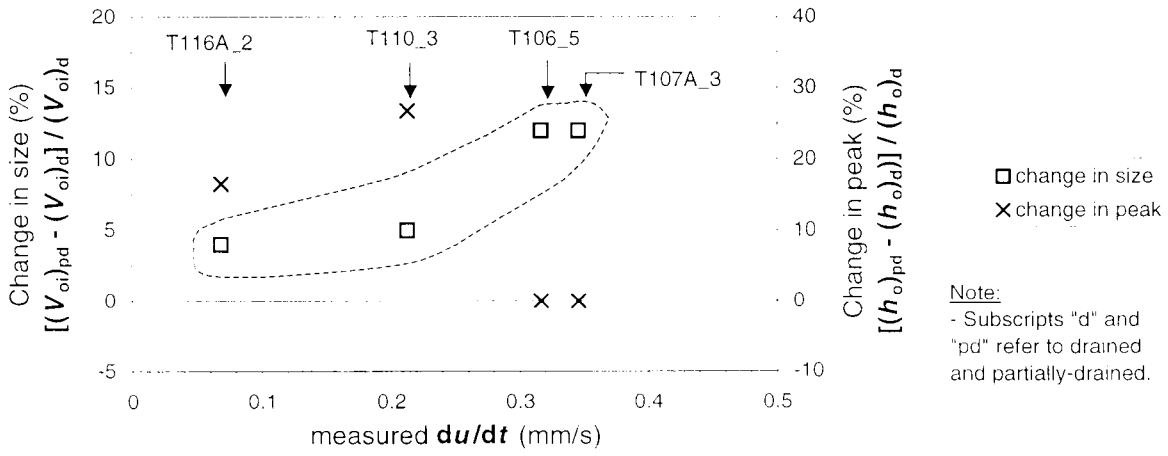

Figure 7.27 The difference between the drained horizontal sideswipes and the parabolas fitted to the partially-drained sideswipes

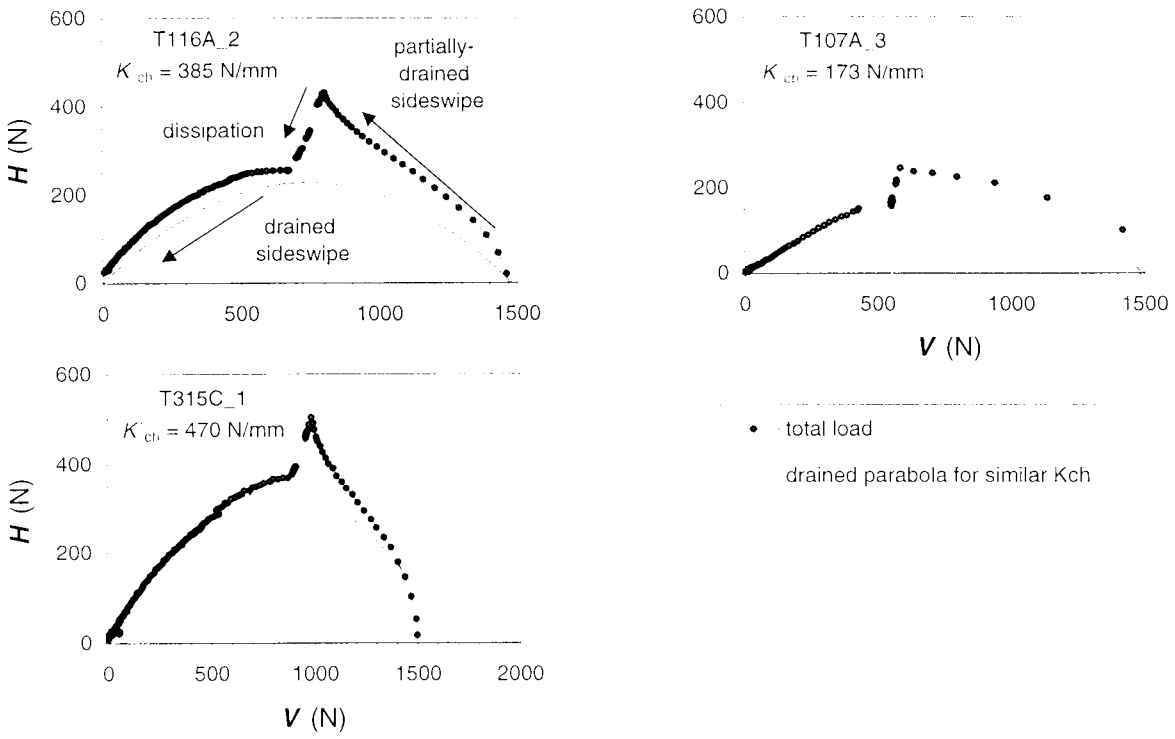

Figure 7.28 Load paths after some of the partially-drained horizontal sideswipe tests

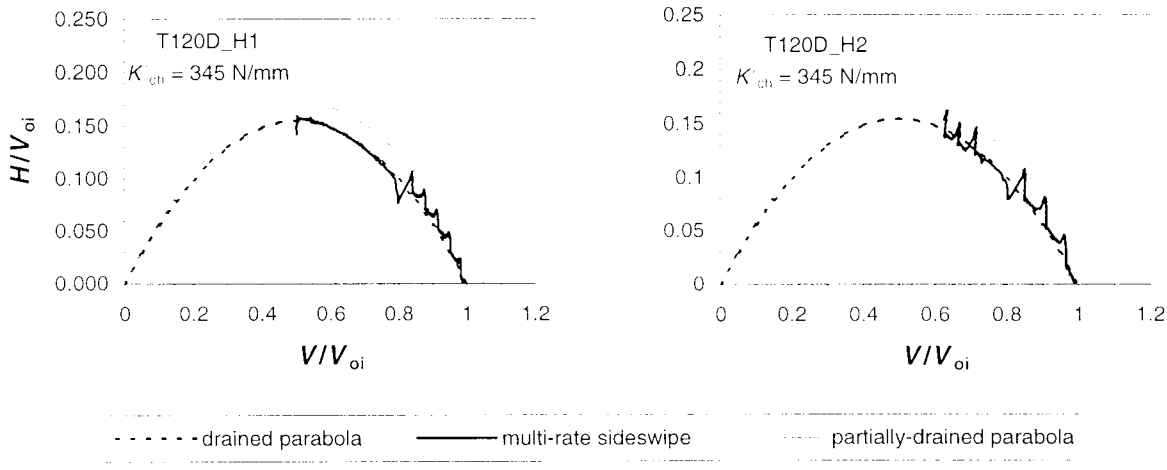

Figure 7.29 The multi-rate horizontal sideswipe tests

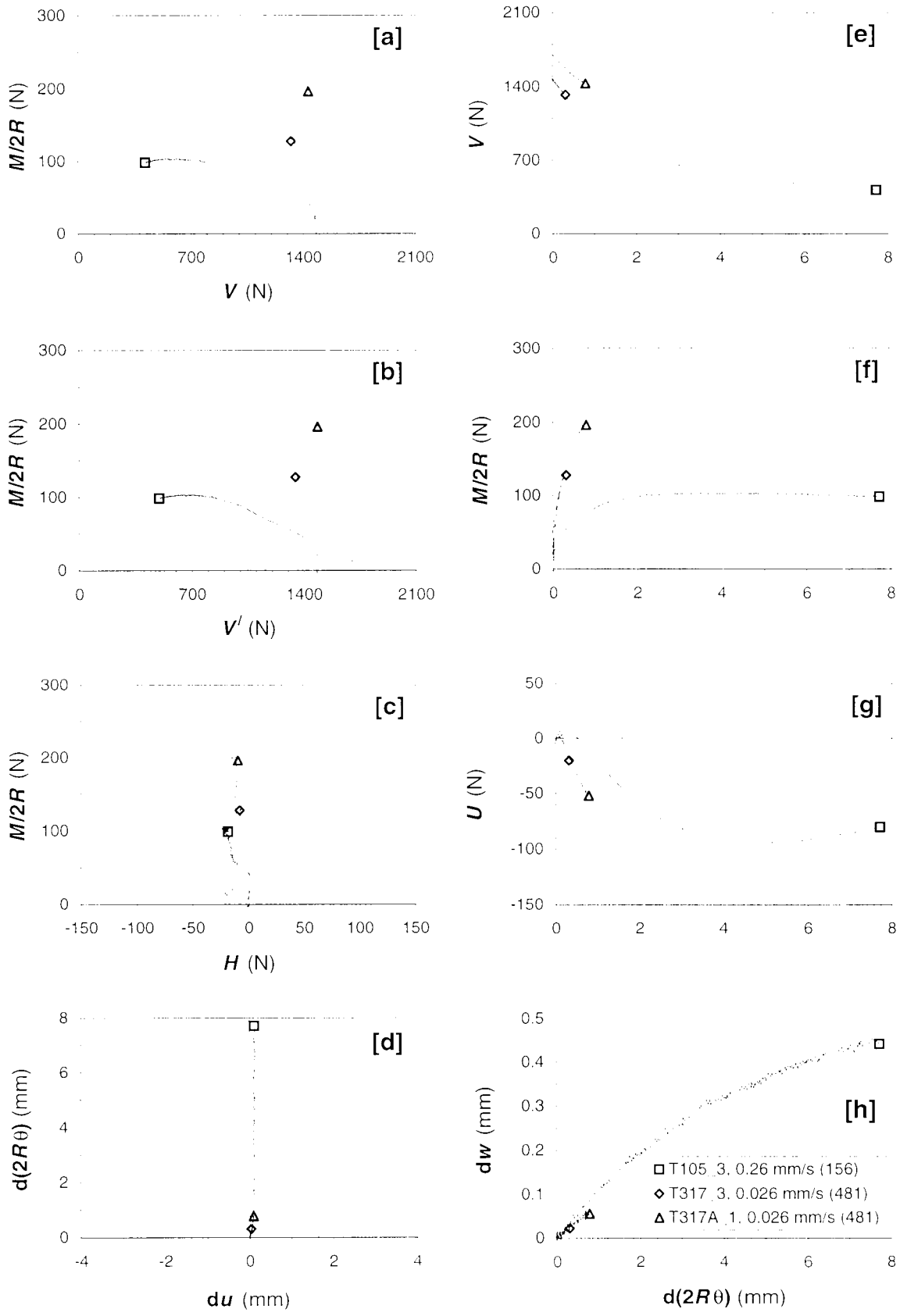

Figure 7.30 Load and displacement interaction diagrams of the partially-drained moment sideswipe tests (intended $d(2R\theta)/dt = 0.26$ mm/s and 0.026 mm/s)

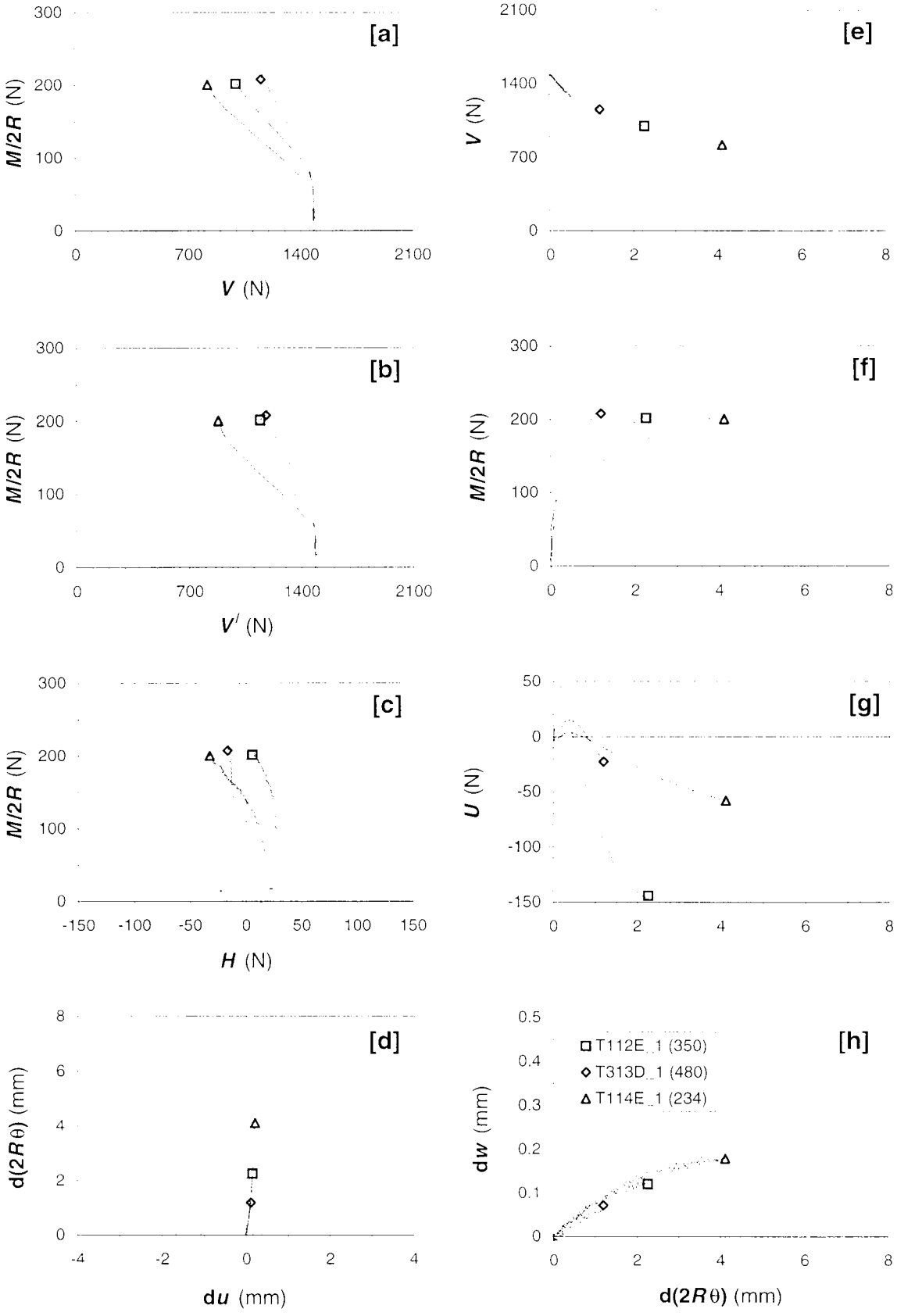

Figure 7.31 Load and displacement interaction diagrams of the partially-drained moment sideswipe tests (intended $d(2R\theta)/dt = 0.524$ mm/s)

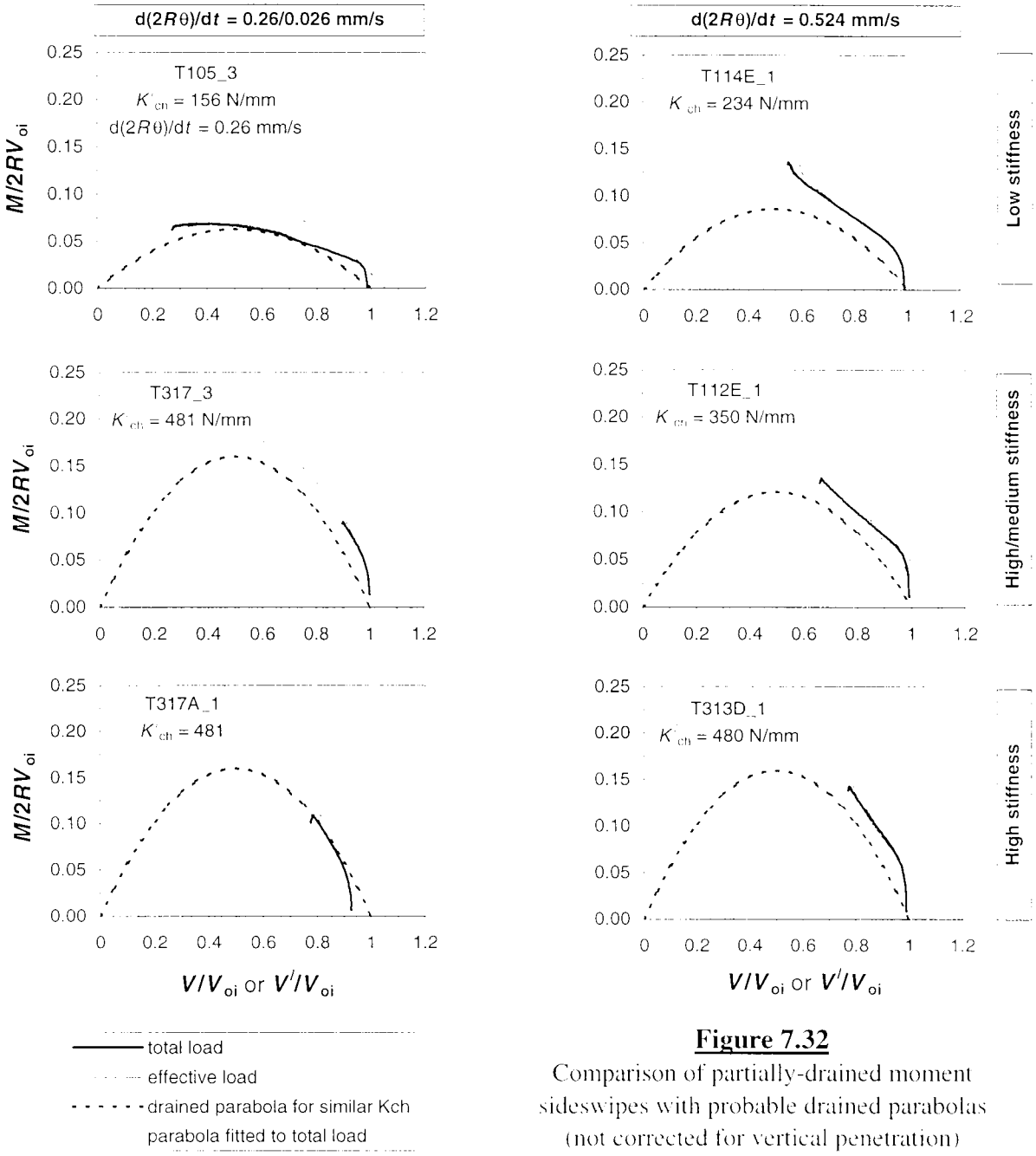

Figure 7.32
Comparison of partially-drained moment sideswipes with probable drained parabolas (not corrected for vertical penetration)

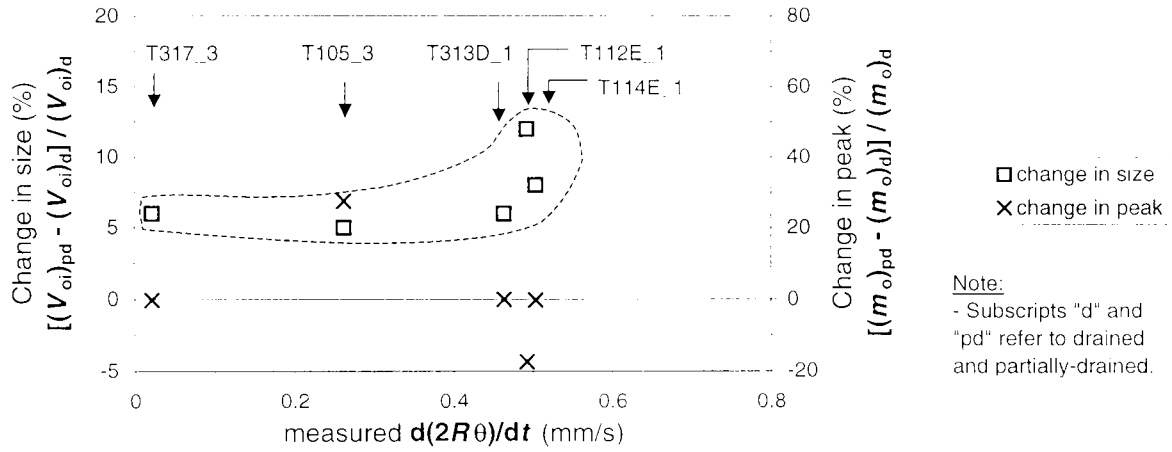

Figure 7.33 The difference between the drained moment sideswipes and the parabolas fitted to the partially-drained sideswipes

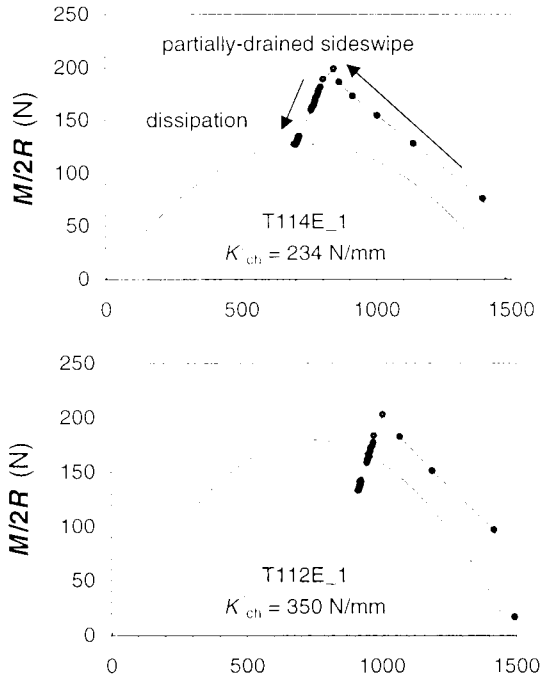

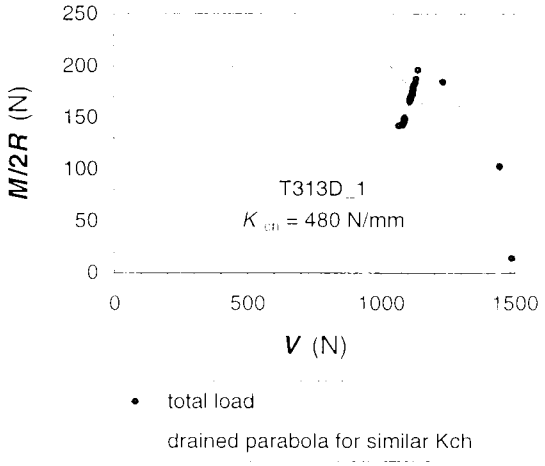

Figure 7.34
Load paths after some of the partially-drained moment sideswipe tests

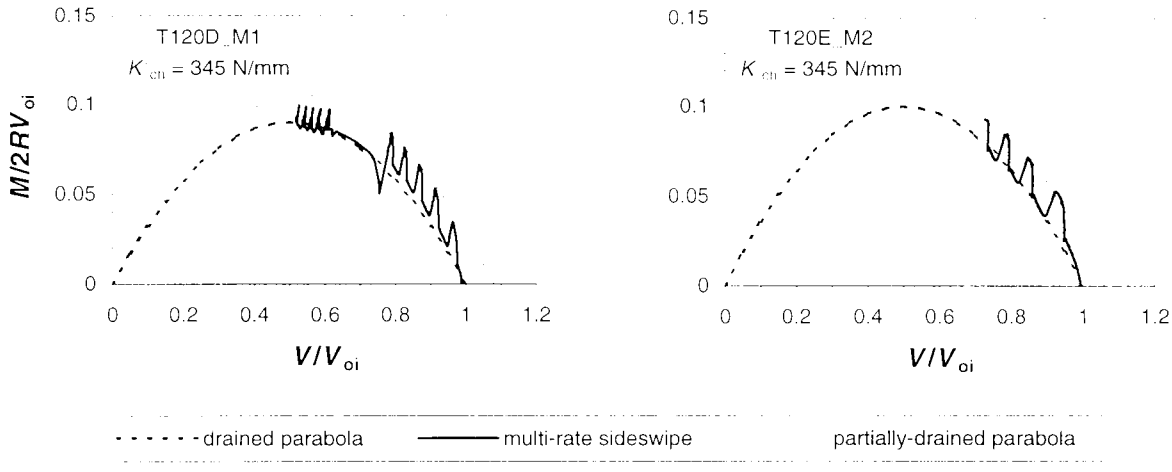

Figure 7.35 The multi-rate moment sideswipe tests

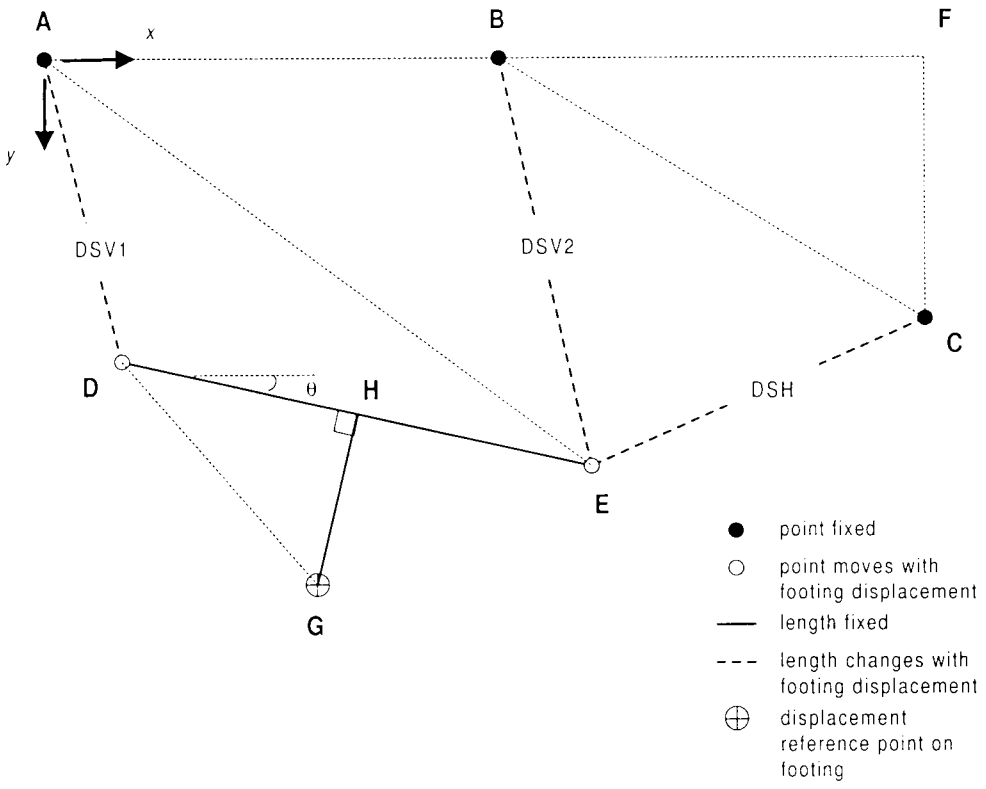

Figure B.1 Parameters used in the derivation of the footing displacements from the small LVDTs